



HAL
open science

Structure and dynamics of aluminosilicate glasses and melts

Alexey Novikov

► **To cite this version:**

Alexey Novikov. Structure and dynamics of aluminosilicate glasses and melts. Other. Université d'Orléans, 2017. English. NNT: 2017ORLE2041 . tel-01951698

HAL Id: tel-01951698

<https://theses.hal.science/tel-01951698>

Submitted on 11 Dec 2018

HAL is a multi-disciplinary open access archive for the deposit and dissemination of scientific research documents, whether they are published or not. The documents may come from teaching and research institutions in France or abroad, or from public or private research centers.

L'archive ouverte pluridisciplinaire **HAL**, est destinée au dépôt et à la diffusion de documents scientifiques de niveau recherche, publiés ou non, émanant des établissements d'enseignement et de recherche français ou étrangers, des laboratoires publics ou privés.

ÉCOLE DOCTORALE
ENERGIE, MATERIAUX, SCIENCES DE LA TERRE ET DE L'UNIVERS

Laboratoire CEMHTI

THÈSE présentée par :
Alexey NOVIKOV

soutenue le : **11 octobre 2017**

pour obtenir le grade de : **Docteur de l'université d'Orléans**

Discipline/ Spécialité : Science des matériaux

**Structure and dynamics of aluminosilicate
glasses and melts**

THÈSE dirigée par :

Pierre FLORIAN
Daniel NEUVILLE

Ingénieur de Recherche, CNRS-CEMHTI, France
Directeur de Recherche, CNRS-IPGP, France

RAPPORTEURS :

Christiane ALBA-SIMIONESCO
Bernard HEHLEN

Directrice de Recherche, LLB CEA-CNRS, France
Professeur, LCC Université Montpellier II, France

JURY :

Christiane ALBA-SIMIONESCO
Pierre FLORIAN
Bernard HEHLEN
Florian KARGL

Directrice de Recherche, LLB CEA-CNRS, France
Ingénieur de Recherche, CNRS-CEMHTI, France
Professeur, LCC Université Montpellier II, France
Professeur, Deutsches Zentrum für Luft- und
Raumfahrt, Allemagne

Dominique MASSIOT

Directeur de Recherche, CNRS-CEMHTI, France
Président du jury

Daniel NEUVILLE
Anita ZEIDLER

Directeur de Recherche, CNRS-IPGP, France
Chercheur, University of Bath, Royaume-Uni

“The deepest and most interesting unsolved problem in solid state theory is probably the theory of the nature of glass and the glass transition.”

Philip W. Anderson, 1995

(Nobel Prize in Physics in 1977)

Acknowledgements

These three years of the PhD have gone so fast, filled with both good and bad moments. But these are not the moments (especially the bad ones) that I am going to carry through my life but rather memories of the people that were around all this time, helping in word and deed, supporting during difficult moments and sharing good ones.

First of all, I would like to thank the CEMHTI's direction for welcoming me at the laboratory. Catherine Bessada, Patrick Echegut and Ludovic Brutinot, I am very grateful for your pieces of advice, encouragements and interest you showed in CEMHTI students' life.

Many thanks are to both of my thesis directors, Pierre Florian and Daniel Neuville, for inviting me to France to work on a very interesting and challenging subject. Your trust in me, your support at every step of my PhD work and discussions with you are highly appreciated. Special acknowledgement is due to Louis Hennet, my unofficial supervisor and the kindest person I have ever met, who was (and is!) always ready to help.

I would also like to thank all the jury members Anita Zeidler, Florian Kargl, Dominique Massiot and, especially two reviewers, Christiane Alba-Simionesco and Bernard Hehlen, for carefully studying my manuscript and giving thoughtful feedbacks. Thank you all for the evaluation of my PhD thesis (a quintessence of the three-year study), for interesting and stimulating questions, for the discussion that we had during the defence.

All the staff and students of both CEMHTI (Orléans) and Géomatériaux (Paris) labs are gratefully acknowledged. I would like to express my particular gratitude to the NMR team, especially to Franck Fayon, Vincent Sarou-Kanian and Aydar Rakhmatullin.

Thanks to all the PhD students and postdocs from Orléans: Babacar Diallo, , Pierre-Alexandre Martin, Charlotte Monteiro, Ghenima Oukali, Mouna Sassi, William Asplet, Alberto José Fernández Carrión, Charles-Emmanuel Dutoit and Roman Shakhovoy, but especially to those, who started their PhD at the same time with me (Assia Mabrouk, Kelly Machado, Eric-Stephane Fotso-Gueutue and Maxime Yon). I am really glad that I have met you! You made my stay at CEMHTI very comfortable and cheerful, thank you!

My “comrades in arms” from Paris: Lucie Grousset, Ilyes Ben Kacem, Rawan El Hayek, Mariona Tarragó Aymerich. Thank you so much for such a great environment and all the fun we had together! I wish we had seen each other more often.

My final but the most important acknowledgement goes to my beloved wife Anastasia, without her support I would probably not be able to finish the PhD and to write anything of this. Thank you for your constant moral support and the positive mood you shared with me! I love you, darling! Je t’aime ma chérie! Я люблю тебя, моя милая Настёна!!!

Table of Contents

Introduction	3
Chapter I. Glass. General representation	11
From liquids to crystalline and amorphous solids	13
Theories of glass structure	14
Glass building blocks: case of aluminosilicates	21
Literature overview.....	25
Silicate glasses	25
Aluminate glasses.....	35
Aluminosilicate glasses.....	38
Conclusion	43
Chapter II. Methods and experimental techniques	55
Synthesis of glasses and ceramics	57
Classic melting-quenching procedure	57
Glass synthesis from ceramic	58
Direct synthesis on the levitator	59
Chemical composition analysis	59
Density measurements	60
Differential scanning calorimetry	61
Viscosity measurements	62
Raman spectroscopy.....	66
Nuclear magnetic resonance spectroscopy	69
Neutron diffraction	75
Chapter III. Strontium aluminosilicates	83
Tectosilicate join ($R = 1$).....	86
Silicates domain ($R = \infty$)	97
Peralkaline domain ($R = 3$)	108
Peraluminous domain ($R < 1$).....	121
High-temperature melts	129
Conclusion.....	139

Chapter IV. Barium aluminosilicates	149
Tectosilicate join ($R = 1$).....	152
Silicates domain ($R = \infty$)	158
Peralkaline domain ($R = 3$).....	168
Peraluminous domain ($R < 1$).....	179
High-temperature melts	185
Conclusion.....	189
Chapter V. Zinc aluminosilicates	197
Tectosilicate join ($R = 1$).....	203
Peralkaline domain ($R = 3$)	219
Conclusion.....	231
General conclusion and perspectives	239
Annex I. Sr tectosilicate glasses (Chemical Geology)	245
Annex II. Ba tectosilicate glasses (Journal of Non-Crystalline Solids)	261
Annex III. Supplementary information	283

Introduction

French version

Le verre est l'un des plus anciens et plus polyvalents matériaux créés par l'Homme. L'histoire du verre élaboré par l'Homme peut être retracée jusqu'à 3000 av. J.-C. en Mésopotamie et en Égypte ([Rasmussen, 2012](#)). Mais les premiers verres utilisés par l'Homme ont été trouvés dans la nature, résultant du refroidissement du magma éjecté lors des éruptions volcaniques. La facilité d'obtention d'arêtes tranchantes à partir d'obsidiennes a permis, entre autres, la production de couteaux, de pointes de flèches et d'autres outils de coupe. De nos jours, le verre est utilisé dans de nombreux domaines de la vie quotidienne comme par exemple pour des objets d'art ou des fibres de verre. Mais à quoi fait référence habituellement le terme « verre » ? Les verres naturels ont une composition complexe, mais la plupart d'entre eux sont à base de silice, ce qui signifie que l'oxyde de silicium (SiO_2) en est le composant principal. Le reste est généralement composé d'oxydes d'alcalins et/ou d'alcalino-terreux, d'alumine et d'autres. Un bon exemple d'une composition industrielle typique est celle du verre à vitre constitué de SiO_2 (63-81 mol%), Na_2O (9-15 mol%), CaO (7-14 mol%), MgO (0-6 mol%), Al_2O_3 (0-2 mol%), K_2O (0-1,5 mol%) et d'autres composants mineurs.

Le but de cette thèse était d'explorer des systèmes ternaires d'aluminosilicates de Sr, Ba et Zn globalement peu étudiés (SAS, BAS et ZAS, respectivement). Les compositions obtenues dans ces systèmes présentent une stabilité chimique et une résistance mécanique élevées et sont très intéressantes pour la conception de produits d'étanchéité à haute température ([Arora et al., 2011](#); [Da Silva et al., 2016](#)), de céramiques transparentes ([Boyer et al., 2016](#); [Duan et al., 2003](#)), de verres bioactifs ([Goel et al., 2013](#); [Kaur et al., 2012](#)), de vitrocéramiques diélectriques et réfractaires ([Beall, 2009](#)), de verres et vitrocéramiques photoactifs ([Ehrt, 2011](#)), de céramiques radio-transparentes ([Lisachuk et al., 2015](#)) ainsi que de nombreuses autres applications. Néanmoins, presque aucune étude systématique de la structure et des propriétés macroscopiques des systèmes SAS, BAS et ZAS n'a été réalisée auparavant. Par conséquent, plusieurs objectifs ont été fixés au début de la thèse. Premièrement, l'accroissement de nos connaissances sur les domaines de vitrification de ces systèmes. En effet, les compositions élaborées au cours de la thèse varient du silicate au peralumineux couvrant ainsi une partie significative des diagrammes ternaires. Le deuxième objectif était l'étude systématique des propriétés macroscopiques et de la structure des

verres élaborés. Les propriétés macroscopiques mesurées ont été la densité, la viscosité et la température de transition vitreuse ; pour les études structurales, la spectroscopie RMN ^{27}Al et ^{29}Si , la diffraction des neutrons et la spectroscopie Raman ont été utilisées. Une telle approche multi-échelle a permis d'établir des liens entre les propriétés et la structure des verres dans les systèmes SAS, BAS et ZAS. Enfin, la caractérisation de la structure et de la dynamique des aluminosilicates fondus à haute température a été réalisée. Pour cette partie de la thèse, la diffraction neutronique à haute température et la RMN ^{27}Al ont été employées.

Ce manuscrit est divisé en cinq chapitres. Dans le premier chapitre, nous discuterons de quelques théories de la structure du verre ainsi que des éléments structuraux typiques trouvés dans les verres aluminosilicatés. Un aperçu de la littérature sera donné à la fin du chapitre afin de fournir au lecteur les informations sur les études qui ont déjà été réalisées à propos des trois systèmes ternaires. Le deuxième chapitre présentera toutes les techniques et les méthodes utilisées pour étudier la structure et les propriétés macroscopiques des aluminosilicates vitreux et fondus. Les détails concernant l'élaboration du verre seront également donnés. Le troisième chapitre sera consacré au système SAS. Quatre domaines vitreux différents avec un rapport $\text{SrO}/\text{Al}_2\text{O}_3$ variable seront décrits en termes de structures et de propriétés macroscopiques. Les résultats obtenus sur des verres de différents domaines seront comparés et discutés. En fin de chapitre, quelques résultats d'études à hautes températures seront présentés. Le quatrième chapitre présentera les résultats des expériences réalisées sur des verres d'aluminosilicate de Ba. Quatre domaines vitreux seront également considérés. Dans le dernier chapitre, nous présenterons les données les plus récentes obtenues sur le système ZAS. Nous verrons la complexité de ce système pour lequel le domaine de vitrification est fortement réduit en raison de problèmes de cristallisation et de séparation de phase. Une comparaison des verres dans les systèmes ternaires d'aluminosilicates des alcalino-terreux (Mg, Ca, Sr et Ba) et de Zn sera faite afin de montrer l'influence de la nature du cation sur les propriétés macroscopiques et les caractéristiques structurelles.

English version

The glass is one of the world's oldest and most versatile human-created materials. The history of the man-made glass can be tracked back to 3000 BCE in Mesopotamia and Egypt (Rasmussen, 2012). But the earliest glasses used by man were found in nature, resulting from the cooling of the magma ejected during volcanic eruptions. The ease of formation of sharp edges on obsidians, for example, allowed the production of knives, arrow heads, and other cutting tools. Nowadays, glass is used in many domains of human life: from objects of art to glass fibers. But what do people usually imply using the word “glass”? Natural glasses have complex composition but most of them are silica-based meaning that silicon oxide (SiO_2) is the major component. The rest is typically composed of alkali and/or alkaline earth oxides, alumina and some others. A good example of a typical industrial composition is window glass consisting of SiO_2 (63-81 mol%), Na_2O (9-15 mol%), CaO (7-14 mol%), MgO (0-6 mol%), Al_2O_3 (0-2 mol%), K_2O (0-1.5 mol%) and some other minor components.

The goal of this PhD thesis was to investigate poorly studied and hence challenging Sr, Ba and Zn aluminosilicate ternary systems (SAS, BAS and ZAS, respectively). Compositions obtained in these systems demonstrate high chemical stability and mechanical resistance, and are very attractive for the design of high-temperature sealants (Arora et al., 2011; Da Silva et al., 2016), transparent ceramics (Boyer et al., 2016; Duan et al., 2003), bioactive glasses (Goel et al., 2013; Kaur et al., 2012), dielectric and refractory glass-ceramics (Beall, 2009), photoactive glasses and glass-ceramics (Ehrt, 2011), radio-transparent ceramics (Lisachuk et al., 2015) and many other applications. Nevertheless, almost none systematic studies of structure and macroscopic properties of the SAS, BAS and ZAS systems has been carried out. Therefore, several goals were set at the beginning of the thesis. First of all, the extension of our knowledge on the vitrification domains in these systems. The compositions elaborated during the thesis vary from silicate to peraluminous ones covering a significant part of the ternary diagrams. Secondly, systematic study of macroscopic properties and the structure of elaborated glasses. Among the macroscopic properties measured were density, viscosity and glass transition temperature; for structural studies ^{27}Al and ^{29}Si NMR spectroscopy, neutron diffraction and Raman spectroscopy were used. Such multi-scale multi-technique approach allowed consequently establishing links between the properties

and the structure of glasses in the SAS, BAS and ZAS systems. Thirdly, the characterization of high-temperature melts' structure and dynamics. For this part of the thesis, high-temperature neutron diffraction and ^{27}Al NMR were used.

This manuscript is divided into five chapters. In the first chapter, we will discuss some theories of glass structure as well as typical structural elements found in aluminosilicate glasses. A literature overview will be given at the end of the chapter in order to provide the readers with the information on studies that have already been carried out in the three ternary systems. The second chapter will present all the techniques and methods used for studying the structure and macroscopic properties of aluminosilicate glasses and melts. The details of glass synthesis will also be given. The third chapter will be devoted to the SAS system. Four different glass domains with varying $\text{SrO}/\text{Al}_2\text{O}_3$ ratio will be described in terms of the structure and macroscopic properties. The results obtained on glasses from different domains will be compared and discussed. In the end of the chapter, some results of high-temperature studies will be presented. The fourth chapter will present results of the experiments carried out on Ba aluminosilicate glasses. Four glass domains will be considered as well. In the last fifth chapter, we will present the most recent data obtained on the ZAS system. We will see the complexity of the system for which the vitrification domain is greatly reduced due to crystallization and phase separation issues. A comparison of glasses in alkaline earth (Mg, Ca, Sr and Ba) and Zn aluminosilicate ternary systems will be made in order to show the influence of the cation's nature on macroscopic properties and structural features.

Bibliography

- Arora, A., Singh, K., Pandey, O.P., 2011. Thermal, structural and crystallization kinetics of SiO₂–BaO–ZnO–B₂O₃–Al₂O₃ glass samples as a sealant for SOFC. *Int. J. Hydrogen Energy* 36, 14948–14955. doi:10.1016/j.ijhydene.2011.03.036
- Beall, G.H., 2009. Refractory glass–ceramics based on alkaline earth aluminosilicates. *J. Eur. Ceram. Soc.* 29, 1211–1219. doi:10.1016/j.jeurceramsoc.2008.08.010
- Boyer, M., Alahraché, S., Genevois, C., Licheron, M., Lefevre, F.-X., Castro, C., Bonnefont, G., Patton, G., Moretti, F., Dujardin, C., Matzen, G., Allix, M., 2016. Enhanced Transparency through Second Phase Crystallization in BaAl₄O₇ Scintillating Ceramics. *Cryst. Growth Des.* 16, 386–395. doi:10.1021/acs.cgd.5b01374
- Da Silva, M.J., Bartolomé, J.F., De Aza, A.H., Mello-Castanho, S., 2016. Glass ceramic sealants belonging to BAS (BaO–Al₂O₃–SiO₂) ternary system modified with B₂O₃ addition: A different approach to access the SOFC seal issue. *J. Eur. Ceram. Soc.* 36, 631–644. doi:10.1016/j.jeurceramsoc.2015.10.005
- Duan, X.L., Yuan, D.R., Xu, D., Lu, M.K., Wang, X.Q., Sun, Z.H., Wang, Z.M., Sun, H.Q., Lu, Y.Q., 2003. Preparation and characterization of Co²⁺-doped ZnO–Al₂O₃–SiO₂ glass-ceramics by the sol–gel method. *Mater. Res. Bull.* 38, 705–711. doi:10.1016/S0025-5408(03)00009-6
- Ehrt, D., 2011. Photoactive glasses and glass ceramics. *IOP Conf. Ser. Mater. Sci. Eng.* 21, 12001. doi:10.1088/1757-899X/21/1/012001
- Goel, A., Kapoor, S., Tilocca, A., Rajagopal, R.R., Ferreira, J.M.F., 2013. Structural role of zinc in biodegradation of alkali-free bioactive glasses. *J. Mater. Chem. B* 1, 3073. doi:10.1039/c3tb20163e
- Kaur, G., Sharma, P., Kumar, V., Singh, K., 2012. Assessment of in vitro bioactivity of SiO₂–BaO–ZnO–B₂O₃–Al₂O₃ glasses: An optico-analytical approach. *Mater. Sci. Eng. C* 32, 1941–1947. doi:10.1016/j.msec.2012.05.034
- Lisachuk, G. V., Kryvobok, R. V., Fedorenko, E.Y., Zakharov, A. V, 2015. Ceramic

radiotransparent materials on the basis of BaO-Al₂O₃-SiO₂ and SrO-Al₂O₃-SiO₂ systems. Epa. - J. Silic. Based Compos. Mater. 67, 20–23. doi:10.14382/epitoanyag-jsbcm.2015.4

Rasmussen, S.C., 2012. Origins of Glass: Myth and Known History, in: SpringBriefs in History of Chemistry. pp. 11–19. doi:10.1007/978-3-642-28183-9_2

Chapter I

Glass:

General representation

From liquids to crystalline and amorphous solids

Let's consider an aluminosilicate melt at high temperature. It can flow with the rate depending on its viscosity and can take any shape depending on the container where it is poured. When cooled down, at some point the melt becomes solid and loses the ability to flow under normal conditions and, as a consequence, to change its shape. If the melt is cooling down slow enough it can crystallize to produce a crystalline solid. During the crystallization, some properties (such as volume, for instance) change abruptly (Figure I.1) due to the transformation of disordered liquid to ordered crystals. The atoms composing the aluminosilicate become well-ordered forming a periodic crystal lattice extending in all directions. Under further cooling the volume of the crystalline solid changes continuously with temperature.

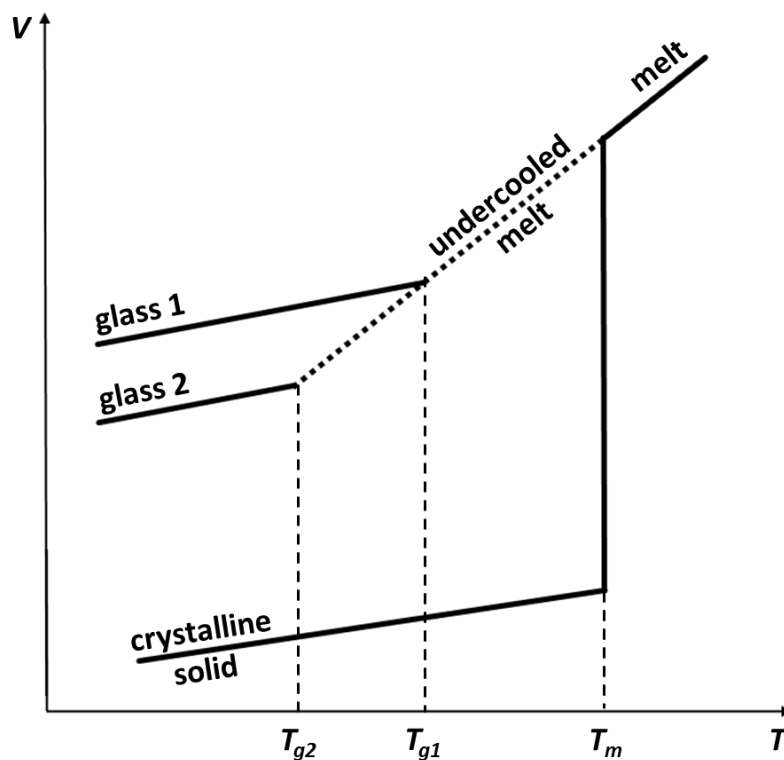


Figure I.1. The volume-temperature (V-T) diagram for a glass-forming liquid (modified from [Vogel, 1971](#)).

Another scenario can take place while cooling the melt. If the cooling is fast enough the melt, being undercooled (i.e. being at a temperature below its melting point), freezes into an amorphous solid, namely glass. In this case, no discontinuities in the V-T diagram are observed (Figure I.1). What happens is a rapid increase of the melt's viscosity that prevents

structural motifs to rearrange themselves. The motifs become less and less mobile and, finally, the undercooled melt starts to behave as a solid (i.e. the glass is obtained). A temperature at which the structure of the undercooled melt is frozen to produce the glass is called the glass transition temperature (T_g) and determined as the intersection of volume curves for the glass and the undercooled liquid. One should notice that different cooling rates provide a different degree of undercooling and, therefore, T_g in these cases will differ as well. For example, slower cooling allows the liquid to rearrange itself more, hence, its volume and T_g will be lower than at fast cooling (see, for example, [\(Moynihan et al., 1974\)](#)).

Now, when it is clear how to produce the glass (rapid cooling to avoid crystallization), let's focus on the theories of glass structure given in the following subsection.

Theories of glass structure

Several structural theories of glass formation were developed over the last century. Some of them were found inconsistent with experimental results and were discarded, the other proved their worth. Further in this subsection we will discuss the most valuable theories contributing in our comprehension of the glass formation. For a complete review of other structural theories, the reader is invited to check out books of W. Vogel ([\(Vogel, 1971\)](#)) and J. E. Shelby ([\(Shelby, 2005\)](#)).

Lebedev's crystallite theory ([Lebedev, 1921](#))

In 1921 Lebedev proposed that the structure of silica glass can be regarded as an accumulation of microcrystalline clusters composed of one of the crystalline modifications of SiO_2 . In compound glasses, the microcrystals may either be definite chemical compounds or solid solutions of these modifications with other components. Therefore, glasses according to this theory are to be considered as multi-phase and micro-heterogeneous in their structure (Figure 1.2). The microcrystals, optically undetectable should be imagined as greatly deformed structural units which possess a higher or lower degree the structure of a normal lattice. For example, it was thought that vitreous silica consists of cristobalite crystallites with the average linear dimension of around 15 Å. Such representation of the glass structure led, however, to discrepancy between observed and calculated glass

properties such as density, for instance. This theory was refuted by further diffraction and small-angle scattering experiments.

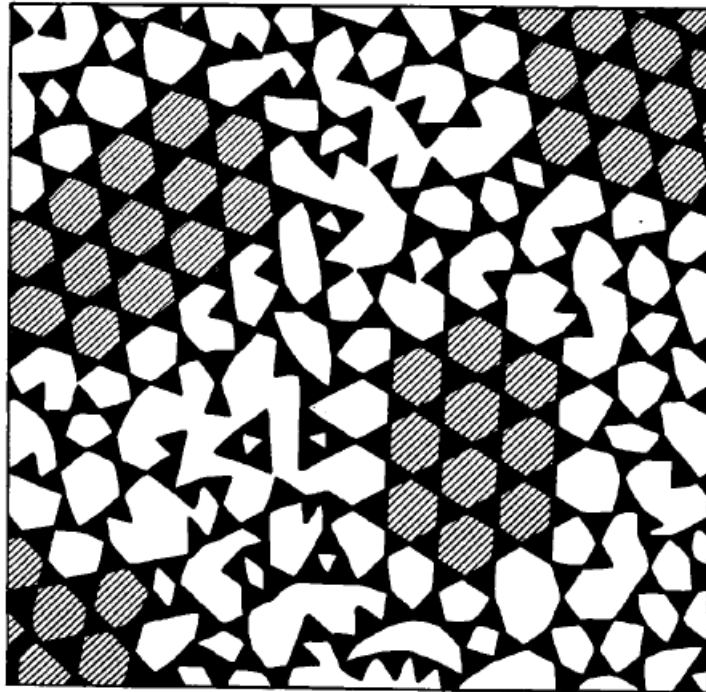


Figure I.2. Schematic representation of crystallite structures in vitreous silica (from [\(Vogel, 1971\)](#)).

Goldschmidt's radius ratio criterion ([Goldschmidt, 1926](#))

Based on his crystallochemical studies, Goldschmidt concluded that the ratio of cation's radius (r_c) to anion's radius (r_a) should lie in a range of 0.2-0.4 for a simple oxide to easily vitrify. This criterion worked for the principal glass formers (e.g., SiO_2 and P_2O_5) but could not explain why, for example, BeO does not form a glass ($r_c/r_a \sim 0.22$).

Zachariasen's random network theory ([Zachariasen, 1932](#))

Before Zachariasen most of the efforts had been made to interpret and order available data on glass properties. Zachariasen, trying to describe the atomic arrangement in simple oxide glasses, have put forward a model with following postulates:

- the atomic forces in both glass and the corresponding crystal must be similar;
- glass consists of a three-dimensional random network;
- glass has a slightly higher internal energy than the crystal but the energy difference is not sufficient to induce crystallization;

- structural units are similar in glass and the crystal.

He proposed four rules for glass formation for an oxide of A_mO_n formula:

- an oxygen atom is linked to not more than two atoms A;
- the number of oxygen atoms surrounding atoms A must be small;
- the oxygen polyhedra share corners with each other, not edges or faces;
- at least three corners in each oxygen polyhedron must be shared.

According to Zachariasen, oxides A_2O and AO do not satisfy these requirements and cannot be vitrified. For other oxides he has concluded that only those composed of oxygen triangles and/or tetrahedra will give glass. Therefore, only oxides A_2O_3 , AO_2 and A_2O_5 are considered as glass-forming ones (Figure I.3). The Zachariasen's model of an AO_2 glass' structure was confirmed by (Huang et al., 2012) who studied a two-dimensional (only 2 layers) silica glass grown on graphene.

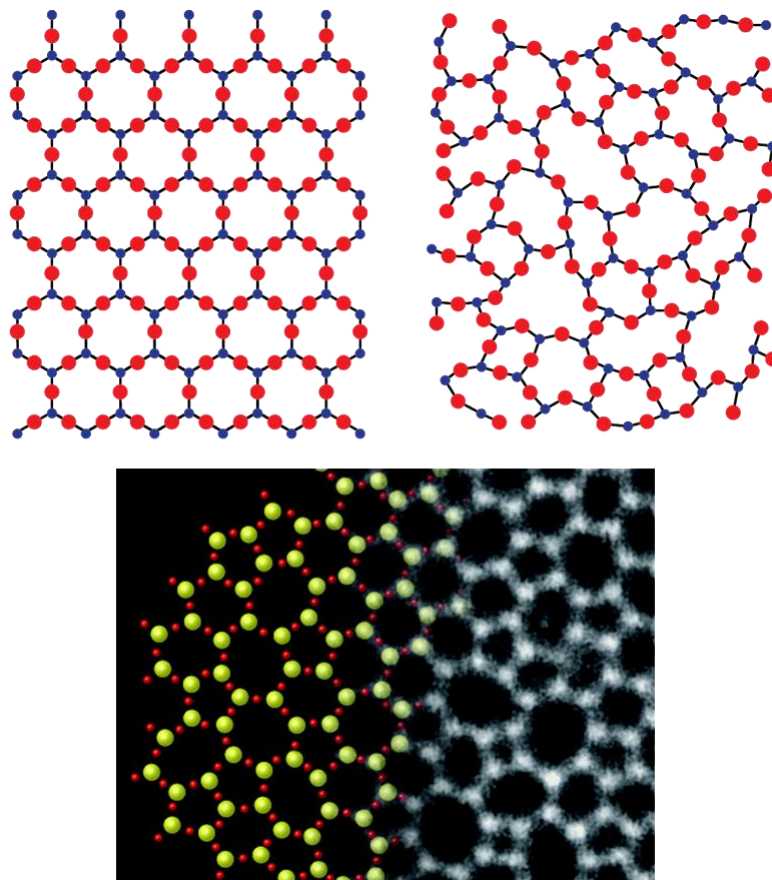


Figure I.3. Two-dimensional representation of 3D network of A_2O_3 crystal (*top left*) and glass (*top right*) (modified from (Zachariasen, 1932)). Experimental ADF-STEM image (*bottom*) of 2D amorphous silica (from (Huang et al., 2012)).

3D Continuous Random Network theory (Warren and Bischoe, 1938)

Original Zachariasen's theory did not consider multi-component oxide glasses. It was extended by Warren and Bischoe to systems containing non-network forming cations and in this form is known as the 3D Continuous Random Network (3D CRN or just CRN) model. With the introduction into vitreous silica of an alkali metal oxide, the glass network is disrupted with some Si-O bonds being broken. The alkali cations are held in the various voids of the network being connected to an oxygen atom produced from the broken Si-O bond (Figure I.4).

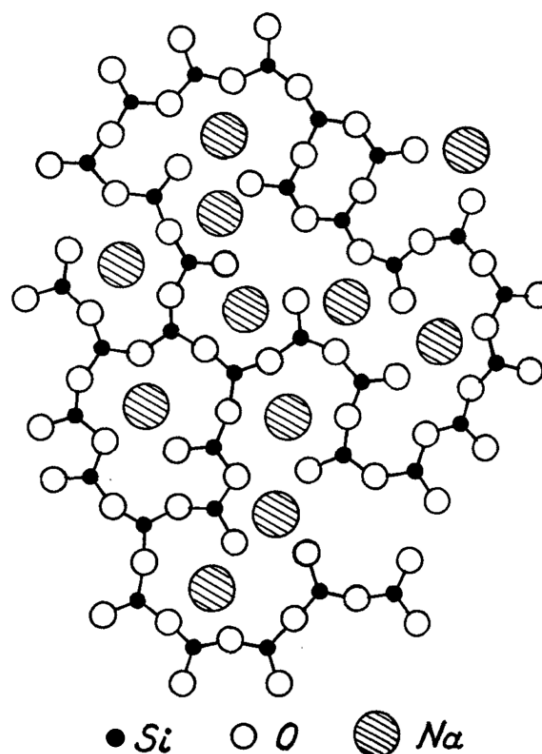


Figure I.4. Schematic representation in two dimensions of the structure of a Na silicate glass (from (Warren and Bischoe, 1938)).

Dietzel's field strength theory (Dietzel, 1942)

In 1942 Dietzel proposed that it is not only an ion's size that rules the glass formation but also its electronic properties (e.g., charge, polarizability etc.). In fact, it was an extension of the Goldschmidt's radius ratio criterion. He introduced a factor called "cation field strength" (CFS), Z/a^2 (where Z is the cation's charge and a is the distance between cation and oxygen) and divided cations according to it into network formers, network modifiers and intermediates (Figure I.5). In this classification network formers are cations with

$Z/a^2 = 1.4-2.0$, network modifiers – with $Z/a^2 = 0.1-0.4$ and intermediates – with $Z/a^2 = 0.5-1.0$.

Element	Valency	Ionic radius (for coord. no. 6)	The most common coordination no.	Interval between the oxide ions	Field strength of the O ²⁻ -ions across the interval	
	Z	r(Å)	Z = 6	a(Å)	Z/a ²	
K	1	1.33	8	2.77	0.13	} Network modifier Z/a ² ≈ 0.1-0.4
Na	1	0.98	6	2.30	0.19	
Li	1	0.78	6	2.10	0.23	
Ba	2	1.43	8	2.86	0.24	
Pb	2	1.32	8	2.74	0.27	
Sr	2	1.27	8	2.69	0.28	
Ca	2	1.06	8	2.48	0.33	
Fe	2	0.91	6	2.23	0.40	
Fe	2	0.83	6	2.15	0.43	
Mn	2	0.83	4	2.03	0.49	} Intermediate oxides Z/a ² ≈ 0.5-1.0
Mg	2	0.78	6	2.10	0.45	
			4	1.96	0.53	
Zr	4	0.87	8	2.28	0.77	
Be	2	0.34	4	1.53	0.86	
Fe	3	0.67	6	1.99	0.76	
			4	1.88	0.85	
Al	3	0.57	6	1.89	0.84	
Ti	4	0.64	6	1.77	0.96	
			4	1.96	1.04	
B	3	0.20	4	1.50	1.34	} Network formers Z/a ² ≈ 1.4-2.0
			3	1.36	1.63	
Si	4	0.39	4	1.60	1.57	
P	5	0.34	4	1.55	2.1	

Figure I.5. Classification of the cations according to their field strength Z/a^2 (after (Dietzel, 1942)).

Thus, he demonstrated that small and highly charged cations act as network formers while huge and/or possessing low charge cations act as network modifiers.

Sun's single bond strength criterion (Sun, 1947)

Sun suggested a link between the strength of cation-oxygen bonds and the glass formation ability. The stronger the bonds, the harder it is to be rearranged in the melt for crystallization and, hence, the easier the glass formation. Calculating the single bond strength (SBS) of the cation-oxygen bond he divided cations (Figure I.6) into glass formers (SBS > 80 kcal/mol), modifiers (SBS < 60 kcal/mol) and intermediates (60 kcal/mol ≤ SBS ≤ 80 kcal/mol). The main limitation of the Sun's theory is the exclusion of the whole class of chalcogenide glasses for which the SBS is about 40 kcal/mol for covalent bonds and less for Van der Waals bonds.

	M in MO _x	Valence	Dissociation energy E _r per MO _x (kcal)	Coordination number ^b	Single-bond strength (kcal)
Glass formers	B	3	356	3	119
	Si	4	424	4	106
	Ge	4	431	4	108
	Al	3	402-317	4	101-79
	B	3	356	4	89
	P	5	442	4	111-88
	V	5	449	4	112-90
	As	5	349	4	87-70
	Sb	5	339	4	85-68
	Zr	4	485	6	81
Intermediates	Ti	4	435	6	73
	Zn	2	144	2	72
	Pb	2	145	2	73
	Al	3	317-402	6	53-67
	Th	4	516	8	64
	Be	2	250	4	63
	Zr	4	485	8	61
	Cd	2	119	2	60
Modifiers	Sc	3	362	6	60
	La	3	406	7	58
	Y	3	399	8	50
	Sn	4	278	6	46
	Ga	3	267	6	45
	In	3	259	6	43
	Th	4	516	12	43
	Pb	4	232	6	39
	Mg	2	222	6	37
	Li	1	144	4	36
	Pb	2	145	4	36
	Zn	2	144	4	36
	Ba	2	260	8	33
	Ca	2	257	8	32
	Sr	2	256	8	32
	Cd	2	119	4	30
	Na	1	120	6	20
	Cd	2	119	6	20
	K	1	115	9	13
	Rb	1	115	10	12
Hg	2	68	6	11	
Cs	1	114	12	10	

Figure I.6. Single bond strengths for different cations (after (Sun, 1947)).

Smekal's mixed bonding rule (Smekal, 1951)

Pure covalent bonds incompatible with the random arrangement (sharply defined bond-lengths and bond-angles). Purely ionic or metallic bonds lack any directional characteristics. Therefore, Smekal suggested that the presence of mixed chemical bonds is necessary. According to him, the mixed bond is the characteristic feature determining the linkage relationships of glasses. Materials with pure ionic or homopolar linkage fuse at relatively low temperatures, have a low hardness and crystallize easily, but materials with mixed linkages, such as for example quartz, have a high hardness, a high fusion temperature, a high viscosity in the fused state and the property of vitrifying readily after fusion.

Modified Random Network theory (Greaves, 1985)

In 1985 Greaves introduced the Modified Random Network (MRN) theory. In this theory the glass network is divided into zones rich in network formers and those rich in network modifiers (Figure I.7). The latter ones connecting with NBOs form percolation channels, while the former ones are organised into the CRN. The principles of the MRN theory were later extended to aluminosilicate glasses to become the so-called Compensated Continuous Random Network (CCRN) theory (Greaves and Ngai, 1995). In the CCRN aluminium tetrahedra are fully charge-compensated by modifying cations. The clustering of the cations is accompanied by the grouping of aluminium atoms as well. In 2004, by means of inelastic neutron scattering and molecular dynamics simulation, it was demonstrated the existence of cations rich channels in a sodium silicate (Meyer et al., 2004).

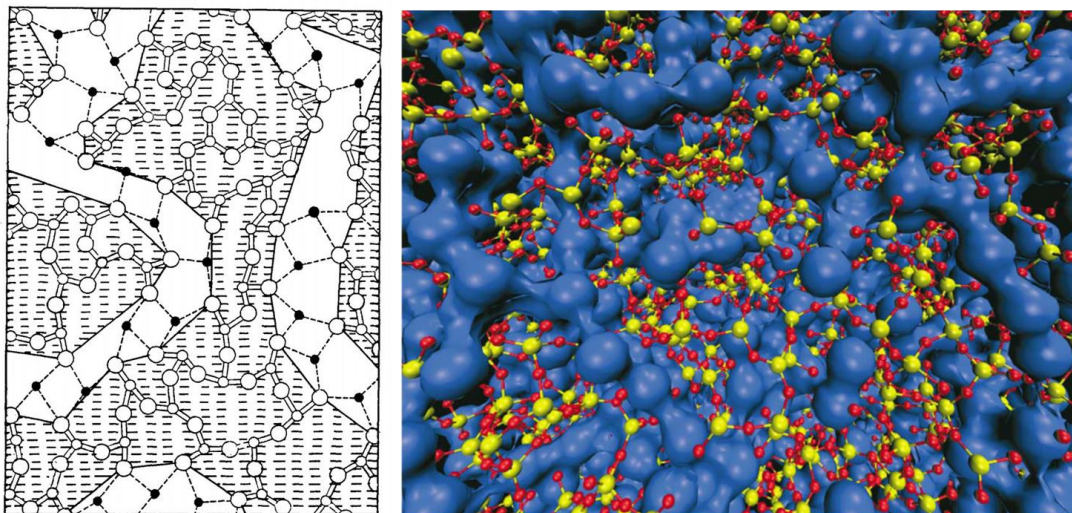


Figure I.7. *Left*: illustration of the MRN concept with the channels of modifying cations percolating through the network (from (Greaves, 1985)). *Right*: MD simulation of the melt's structure of $\text{Na}_2\text{O}-3\text{SiO}_2$ with emphasis on the sodium channel-like clusters (from (Meyer et al., 2004)).

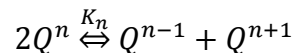
To summarize this subsection:

- Network formers – can form glass on their own, have strong directional bonds, CN is 3 or 4 (Si^{4+} , B^{3+} , P^{5+} etc.).
- Network modifiers – break the bonds between network formers and oxygens, have undirectional bonds, CN is greater than or equal to 6 (Na^+ , K^+ , Mg^{2+} , Ca^{2+} etc.).

- Intermediates (conditional network formers) – cannot form glass on their own but are able to do so in the presence of modifying oxides, may reinforce (CN = 4) or break the network further (CN ≥ 6). A good example of such conditional network former is Al³⁺.

Glass building blocks: case of aluminosilicates

As it has been shown above, vitreous silica is composed of interconnected corner-sharing silicon tetrahedra. The network is fully polymerized and only bridging oxygens are present. In this case, one says that all the tetrahedra are in Q⁴ species (Figure 1.8), meaning that all four oxygens are BOs. When a modifier oxide is introduced into the silica glass network, the connections between the tetrahedra break and a certain fraction of non-bridging oxygens is created. Following the depolymerisation of the network, tetrahedra with one, two, three or four NBOs appear (Q³, Q², Q¹ and Q⁰ species, respectively). These Qⁿ species are created in the melt by a disproportionation reaction:



The corresponding equilibrium constant, K_n , can be calculated as

$$K_n = \frac{x(Q^{n-1}) \cdot x(Q^{n+1})}{x(Q^n)^2}$$

where $x(Q^n)$ is the mole fraction of the Qⁿ species. If K_n is zero the Qⁿ distribution is binary, i.e. only two Qⁿ species can coexist in the glass network at once at given content of a network-modifier. Otherwise, a set of Qⁿ species will be present in the network according to the values of the equilibrium constants. The constants K_n depend on cation's nature and temperature. It has been shown that the equilibrium of the disproportionation reaction shifts to the right both with increasing temperature ([Brandriss and Stebbins, 1988](#)) and the CFS of the network-modifier ([Maekawa et al., 1991](#)).

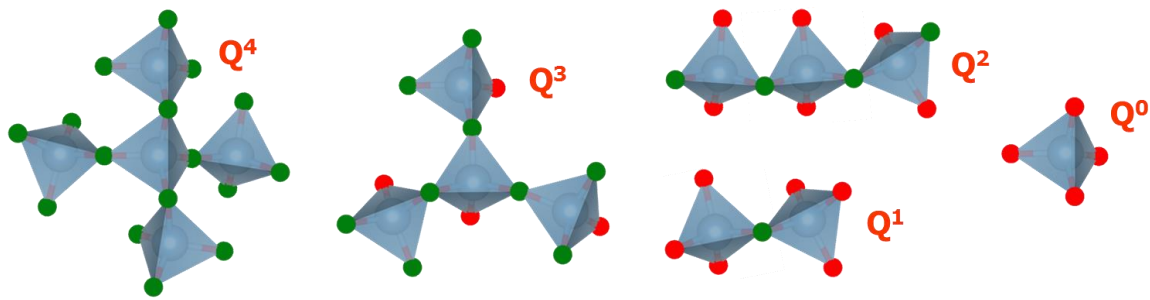


Figure I.8. Schematic representation of Q^n species (n is the number of BOs). The green spheres are BOs and the red ones are NBOs. The notation of Q^n species has been introduced by (Engelhardt et al., 1975).

In an aluminosilicate, a silicon tetrahedron can be surrounded by other silicon tetrahedra as well as by aluminium tetrahedra, or a mixture of both (the same applies to an aluminium tetrahedron). To distinguish between different surroundings, the notation of Q_m^n species is introduced (Figure I.9), where $m \leq n$.

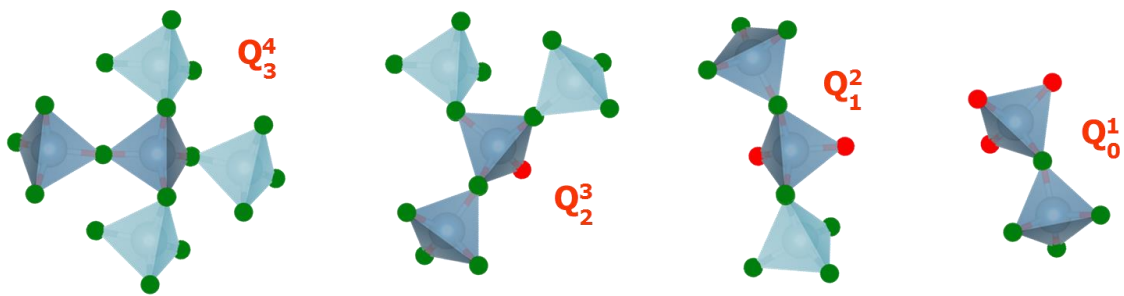


Figure I.9. Schematic representation of Q_m^n species (n is the number of BOs and m is the number of aluminium tetrahedra connected to the central silicon one). Silicon tetrahedra are dark blue and aluminium ones are light blue.

It was the description of the short-range scale in aluminosilicate glasses that is also applicable for crystals. On the medium-range silicon and aluminium tetrahedra form rings of different sizes (Figure I.10). Non-network forming cations are close to non-bridging oxygens and/or to negatively charged aluminium tetrahedra. According to this, they are defined to act either as network modifiers (creation of NBOs provoking the depolymerisation of the network) or charge compensators (charge balancing of AlO_4^-).

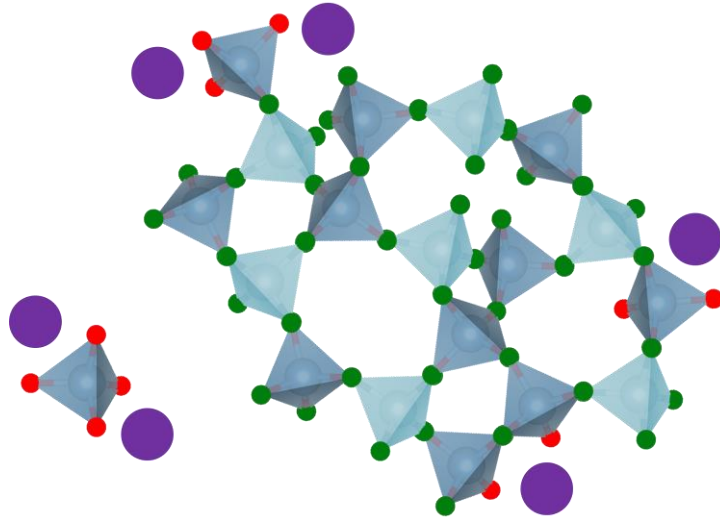


Figure I.10. Two-dimensional representation of 3D network of an aluminosilicate glass with three-, four- and higher-membered rings. The dark and light blue tetrahedra represent silicon and aluminium tetrahedra, green and red spheres – BOs and NBOs, respectively. Violet spheres are metal cations.

Before we discussed only silicon and aluminium tetrahedra, bridging and non-bridging oxygens, network modifiers and charge compensators. Yet there are few structural units that could exist in the network and that are left unmentioned. In particular, high-coordinate aluminium AlO_5 and AlO_6 (Figure I.11) were detected in alkali and alkaline earth aluminosilicate glasses (Neuville et al., 2008, 2004; Stebbins et al., 2000; Toplis et al., 2000). Other entities that were proposed to exist in aluminosilicate glasses and melts are oxygen triclusters (Lacy, 1963; Toplis et al., 1997; Toplis and Dingwell, 2004). These are oxygens which are shared by three tetrahedra at the same time (Figure I.11).

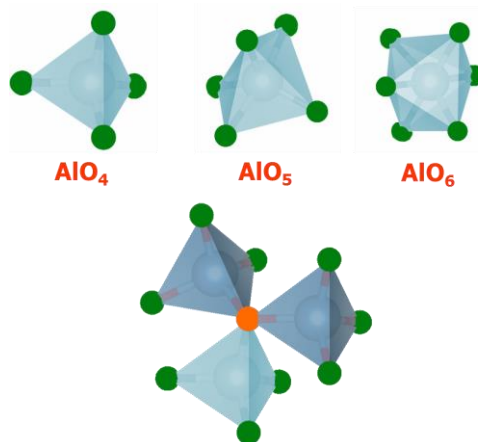


Figure I.11. *Top*: AlO_x speciation in glass. *Bottom*: an oxygen tricluster (an orange sphere) formed by the fusion of two silicon and one aluminium tetrahedra.

A good summary of reactions involving above-described species is given by (Stebbins et al., 2013) and visualized in Figure I.12.

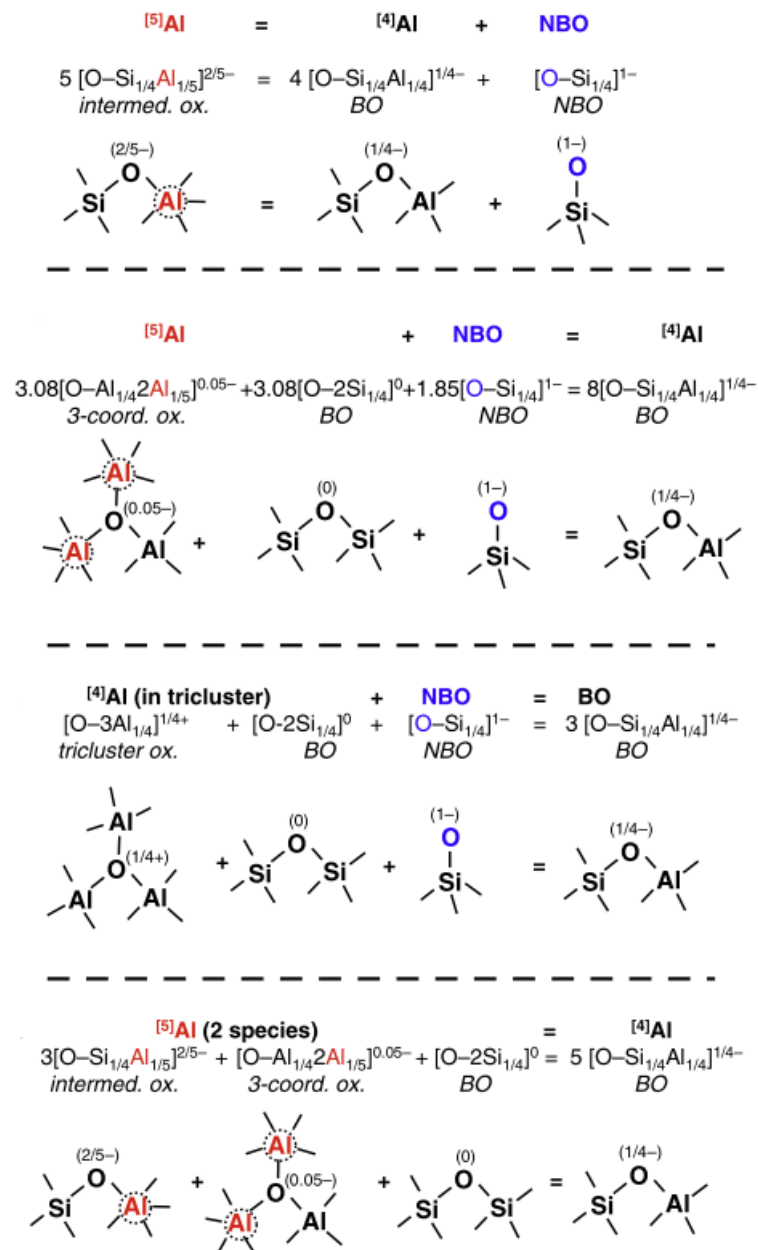


Figure I.12. Equilibria involving high-coordinate aluminium species as well as BOs, NBOs and three-coordinate oxygens (from (Stebbins et al., 2013)).

Literature overview

In this section, we present a review of studies carried out on SAS, BAS and ZAS ternary systems. The main goal of this review is to show how poorly the three systems are studied in comparison with Ca and Mg aluminosilicates, for instance. Here we include neither publications on mixed systems (e.g., BaO-ZnO-Al₂O₃) nor on the systems with additional components (e.g., SrO-B₂O₃-Al₂O₃-SiO₂).

This section is divided into three subsections (silicate glasses, aluminate glasses and aluminosilicate glasses), consisting of two major parts each: Vitrification domains and Structure and properties. The latter part is logically split into two parts: Glasses and Melts.

1. Silicate glasses

The investigation of SAS, BAS and ZAS ternary systems began from corresponding silicates. The interest was due to the abundance of silicate compounds in nature and their relatively low melting points allowing obtaining glass by traditional quenching procedures.

1.1. Vitrification domains

SrO-SiO₂. Strontium silicate glasses were reported by several authors (Cormier et al., 1999a, 1999b; Creux et al., 1995; Doweidar, 1999; Eskola, 1922; Frantz and Mysen, 1995; Murdoch et al., 1985; Neuville, 2005; Richet et al., 2009; Shelby, 1979). According to compositions reported, Sr silicates can be vitrified in a 46-80 mol% range of SiO₂.

BaO-SiO₂. According to the literature data (Cormier et al., 1999b; Doweidar, 1999; Eskola, 1922; Frantz and Mysen, 1995; Hasegawa and Yasui, 1987; Lenoir et al., 2008; Mysen et al., 1982; Mysen and Frantz, 1993; Schlenz et al., 2002; Schneider et al., 2003; Shelby, 1979; Stebbins et al., 1997; Thomas, 1950; Thompson et al., 2012) the vitrification domain of Ba silicates is in a 38-90 mol% range of SiO₂.

ZnO-SiO₂. Only two glasses are known for Zn silicates. Ehrt and Flugel (Ehrt and Flügel, 2011) reported a Zn metasilicate glass (ZnSiO₃) and Van Tran et al. reported a Zn silicate glass with 85 mol% of SiO₂ obtained by the sol-gel process (Van Tran et al., 2017).

1.2. Structure and properties

Glasses. A ^{29}Si MAS NMR study on a Sr silicate glass with 66.7 mol% of silica has been performed by Murdoch et al. (Murdoch et al., 1985). From the NMR linewidth analysis they found the effect of the CFS on the NMR linewidth reflecting the distribution of silicate environments. Namely, the NMR linewidth increases with increasing the CFS, meaning a greater variety in the distribution of silicon tetrahedra for smaller highly charged cations (Figure I.13). The NMR peak position and its deconvolution suggested the presence of Q^2 , Q^3 and Q^4 units with Q^3 being dominating species.

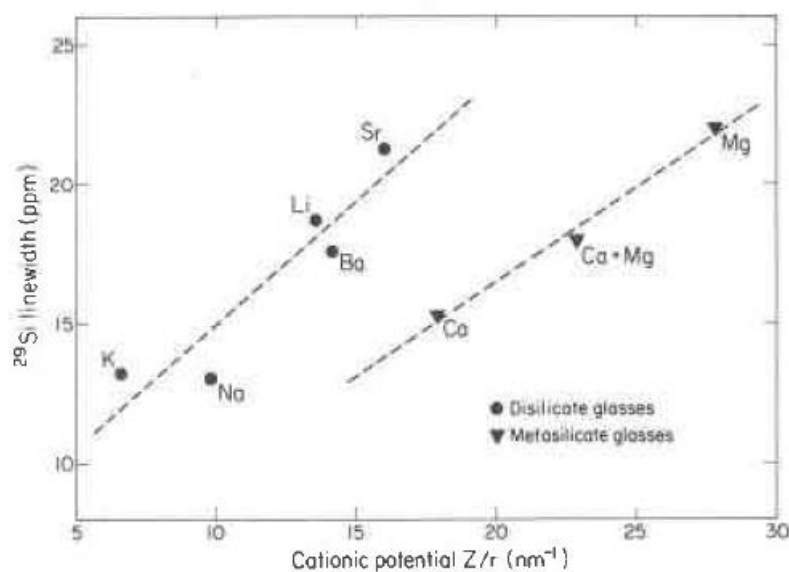


Figure I.13. Integrated linewidth of disilicate and metasilicate glasses as a function of the ionic potential of the network-modifying cation (from (Murdoch et al., 1985)).

Neuville (Neuville, 2005) also found these Q^n species in the silicate network of a glass with 60 mol% of silica by deconvoluting the high-frequency region of a Raman spectrum. He also reported density and viscosity measurements with estimated values of glass transition temperature (T_g), heat capacities of glass and liquid at T_g , configurational heat capacity and entropy at T_g .

Richet et al. (Richet et al., 2009) measured heat capacities and other thermodynamic properties at low temperatures (2-300 K) of Sr and Ba metasilicate glasses (50 mol% SiO_2). They found that heat capacity and vibrational entropy vary as a function of cation's nature, namely, it increases in alkaline earth group from Mg to Ba (Figure I.14).

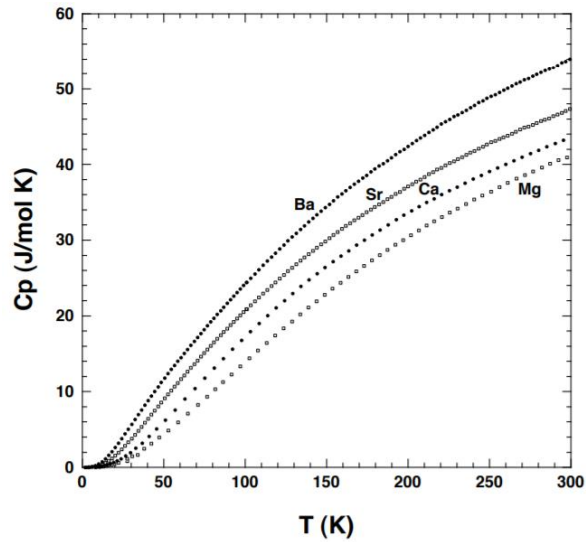


Figure I.14. Heat capacity of alkaline earth metasilicate glasses (from (Richet et al., 2009)).

Densities and molar volumes of Sr and Ba silicate glasses were reported by (Doweidar, 1999). It has been pointed out that at high concentrations of network-modifying cations the molar volume curves change the slope and seem to reach a plateau (Figure I.15). The author suggested that some changes in the glass structure should take place at the concentrations where the inflection points occur. Worth noticing, that the inflection point for Ba silicates is observed at a lower concentration of the network-modifying cation than in the case of Sr silicates.

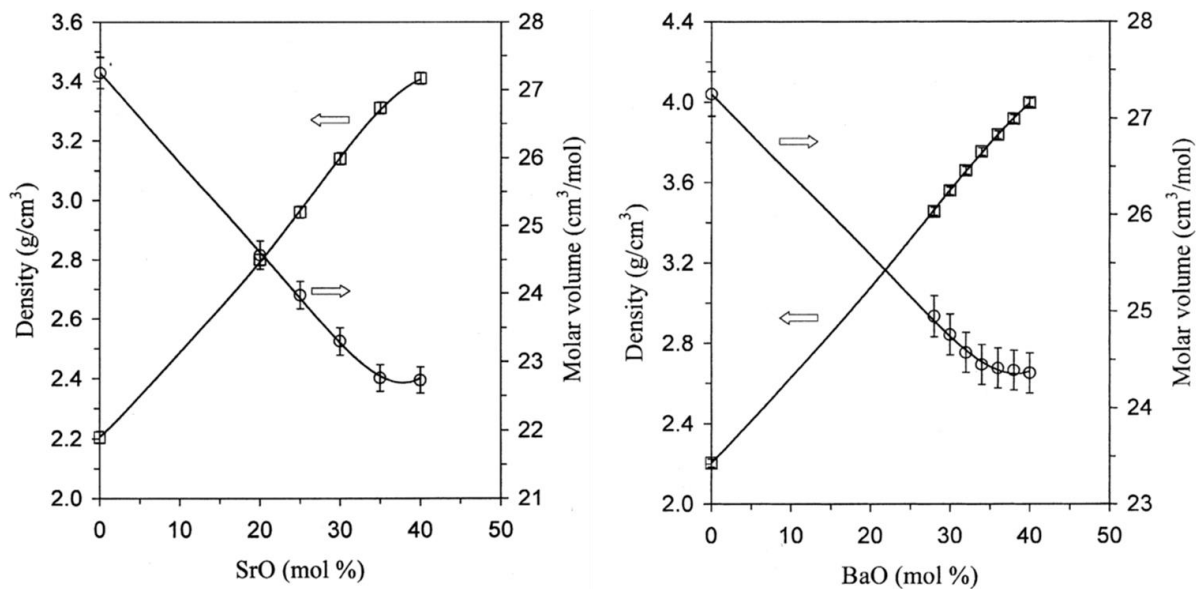


Figure I.15. Evolution of density and molar volume of Sr (left) and Ba (right) silicate glasses (from (Doweidar, 1999)).

Rabukhin demonstrated a complex dependence of the molar volume (V_m) of alkali and alkaline earth silicate glasses on the nature and concentration of the cation (Rabukhin, 1999). He showed (Figure I.16) that in each group the V_m increases with decreasing the CFS and that the curves are not monotonous but, in some cases, have inflection points implying structural changes involved.

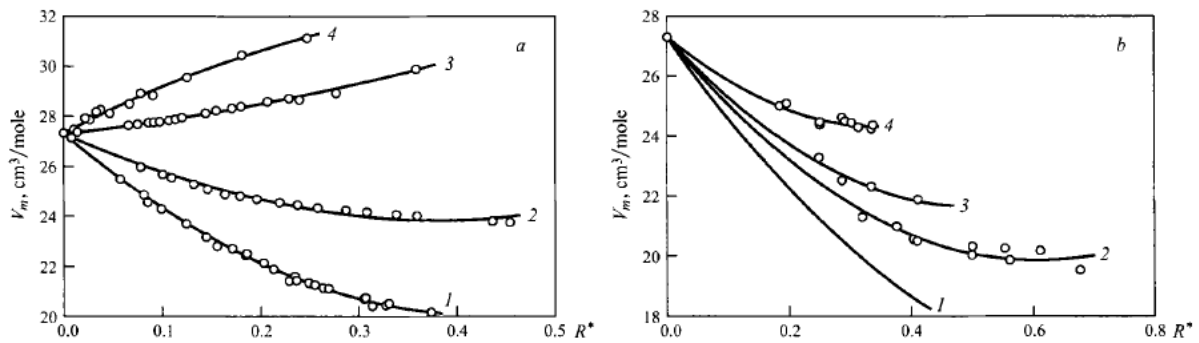


Figure I.16. *Left*: molar volume of glasses in the $R_2\text{O-SiO}_2$ system (1 - Li, 2 - Na, 3 - K, 4 - Rb). *Right*: molar volume of glasses in the RO-SiO_2 system (1 - Mg, 2 - Ca, 3 - Sr, 4 - Ba) (from (Rabukhin, 1999)).

(Shelby, 1979) reported results of measurements of various macroscopic properties (density, T_g etc.) for Sr and Ba silicate glasses. He found that in the case of Sr silicates, glass transition temperature does not evolve much at low SrO content and starts increasing with increasing SrO content above 40 mol% (Figure I.17). An identical trend was observed for Ca silicates as well. At the same time, no such tendency was observed for Ba silicates, although no compositions with more than 40 mol% of BaO were studied. Interestingly, reported T_g of Ca, Sr and Ba silicate glasses increases in the row $\text{Ba} < \text{Sr} < \text{Ca}$.

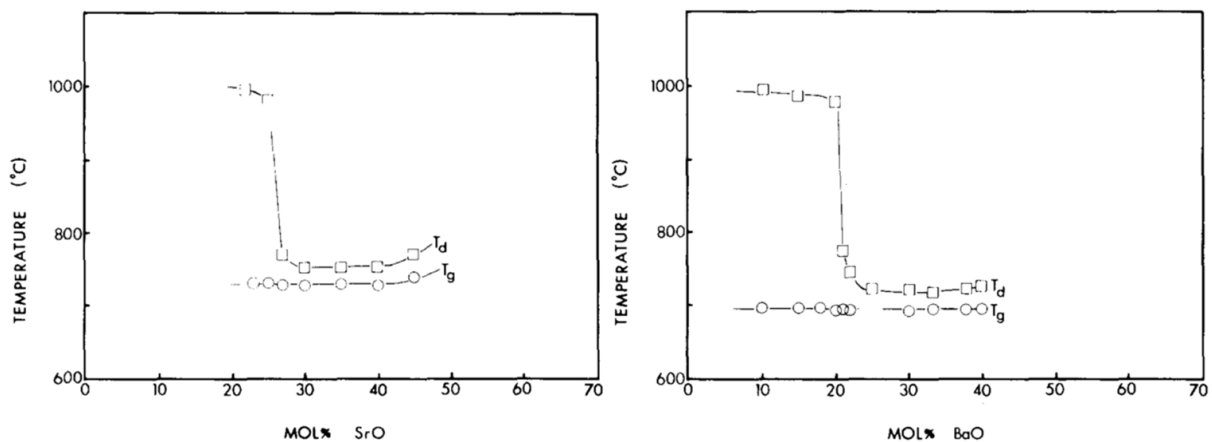


Figure I.17. Evolution of glass transition temperature of Sr (*left*) and Ba (*right*) silicates (from (Shelby, 1979)).

Among Ba silicate glasses, one with 66.7 mol% of SiO₂ (Ba disilicate) received much attention and has been studied by various methods. The first group of researches concentrated on the determination of the Qⁿ speciation by means of Raman and ²⁹Si NMR spectroscopy. Mysen et al. and Murdoch et al. (Murdoch et al., 1985; Mysen et al., 1982) demonstrated the presence of Q², Q³ and Q⁴ species with the overwhelming majority of silicon tetrahedra existing as Q³ species. Quantitative Raman and NMR studies on Qⁿ speciation in the glass were carried out by several authors. Schneider et al. (Schneider et al., 2003) found 24±7 % of Q², 62±5 % of Q³ and 14±5 % of Q⁴ species. They also calculated Qⁿ species distribution on the basis of a thermodynamic model – 17.9, 64.0 and 17.9 % for Q², Q³ and Q⁴ species, respectively – and found a satisfactory agreement between the two. Schlenz et al. (Schlenz et al., 2002) showed the existence of Q² and Q³ species as the major components (20.0±1.7 % and 77.7±5.3 %, respectively) with a negligible amount of Q¹ (0.6±0.7 %) and Q⁴ (1.6±0.8 %) species, while Lenoir et al. (Lenoir et al., 2008) reported Q² (11.89 %), Q³ (48.88 %) and Q⁴ (16.48 %) species.

The second group of researches based on diffraction and modelling methods focused mainly on interatomic distances and coordination of the elements. Hasegawa and Yasui (Hasegawa and Yasui, 1987) studied the structure of the disilicate glass by means of X-ray and neutron diffraction. They found mean interatomic distances to be 1.60 Å for Si-O pair, 2.60 Å for O-O pair and 2.75 Å for Ba-O pair. By comparison with structural data on crystalline BaSi₂O₅, they proposed a model in which the glass network consists of a folded layer structure differing from that of the crystal. Schlenz et al. applied a multi-technique approach to study the disilicate and a compositionally close silicate glass with 63 mol% of silica (Schlenz et al., 2002). Among the techniques the authors used were X-ray diffraction (XRD), anomalous wide angle X-ray scattering (AWAXS), electron diffraction (ED), atomic force microscopy (AFM), ²⁹Si MAS NMR, Raman spectroscopy, Si K-edge X-ray absorption spectroscopy (XAS), X-ray photoelectron spectroscopy (XPS), X-ray excited Auger electron spectroscopy (XAES), molecular dynamics (MD) simulation and Reverse Monte Carlo (RMC) modelling. The interatomic distances determined in their study are summarized in (Figure I.18). Raman and ²⁹Si MAS NMR results are discussed above. The authors compared the observed mean distances of Si-O, O-O and Ba-O bonds with those of crystalline analogue, BaSi₂O₅, and found that they are comparable. The model proposed by (Hasegawa

and Yasui, 1987) implied the existence of the glass network consisting of six-membered rings of SiO₄ tetrahedra arranged in folded layers with Ba ions located in voids and CN(Ba-O) = 9-10. However, Schlenz et al. found CN(Ba-O) = 6.76±0.12 with CN(Si-O) = 4.06±0.01 and CN(Ba-Ba) = 6.41±1.60. This led them to conclusion that smaller tetrahedral rings should exist in the glass network as well. They assumed that the glass structure should be made of folded layers of tetrahedral rings (from smaller ones to six-membered) altered with layers and/or chains of Ba ions with possible occurrence of additional tetrahedral chains, isolated rings and of silica-like regions. The last assumption brings to mind the Greaves' Modified Random Network model (Greaves, 1985).

BS333							BS370		Correlation
HXD	(DAS(2))	DAS(3)	ED	Neutron [9]	MD	RMC	HXD	ED	
1.62			1.61	1.60	1.62	1.62	1.62	1.62	Si-O (C-?)
2.66			2.72	2.63	2.60	2.69	2.68	2.72	O-O, Ba-O, (Si-Si)
2.96	2.94				3.10		3.02	2.93	Ba-O, (Si-Si)
	3.51								Ba-Si
4.15	3.91	3.93	4.15	4.15	4.0	4.12	4.09	4.16	Ba-Ba, (O-O), (Si-O)
	4.28								Ba-X
	4.73	4.63			4.70			4.80	Ba-Ba
5.17	5.15		4.95	4.94			5.07	5.14	Ba-X
				5.30					
	5.84								Ba-X
	6.58	6.45							Ba-Ba
6.86	6.96					6.87	6.95		Ba-X
7.09									Ba-X
	7.39		7.29	7.30	7.40		7.20	7.33	Ba-X
		7.61							Ba-Ba
8.31	8.37	8.38							Ba-Ba
11.24		11.28					11.20		Ba-Ba

For sample BS333 comparable literature data are included. Assumed correlations are in brackets. X = Ba, O, Si.

Figure I.18. Interatomic distances in Ba silicates (in Å) determined by different methods (modified from (Schlenz et al., 2002)).

Other authors reported values for the glass transition temperature for the Ba disilicate (Frantz and Mysen, 1995; Lenoir et al., 2008). However, the reported values of 835 °C (Frantz and Mysen, 1995) and 657 °C (Lenoir et al., 2008) differ very much. The reason for such enormous discrepancy is difficult to trace since the method used for T_g determination is not reported in the first work. In the second work, T_g was determined from viscosity data and it is consistent with other T_g values for the series of Ba borosilicate glasses reported therein. Lenoir et al. also reported density of the glass together with calculated thermodynamic parameters such as heat capacities and configurational entropy.

Mysen et al. studied the structure of Ba silicate glasses 54-75 mol% of silica by means of Raman spectroscopy (Mysen et al., 1982). They described the structure of the glasses in

terms of coexisting anionic species (SiO_2 , $\text{Si}_2\text{O}_5^{2-}$, $\text{Si}_2\text{O}_6^{4-}$, $\text{Si}_2\text{O}_7^{6-}$ and $\text{SiO}_4^{4-} - \text{Q}^4$ to Q^0 species, respectively). By deconvoluting the high-frequency region of the Raman spectra, they established compositional ranges in which the anionic species exist. It has been mentioned by the authors that the cations with high CFS prefer the most depolymerized structural units. They summarized available data on the activation energies of viscous flow (E_η) for alkali and alkaline earth silicate melts and found that in each group the E_η drops with increasing CFS (Figure I.19).

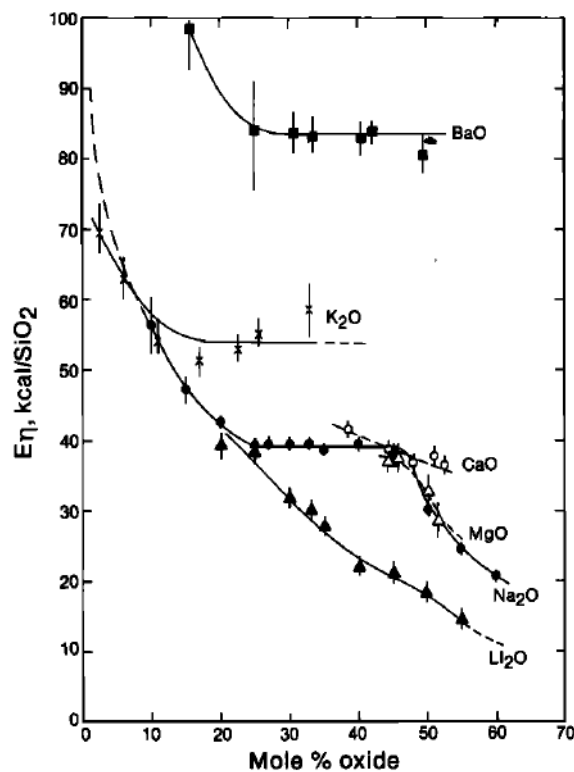


Figure I.19. Activation energies of viscous flow of melts on binary metal oxide-silica joins (from [Mysen et al., 1982](#)).

Stebbins et al. ([Stebbins et al., 1997](#)) and Thompson et al. ([Thompson et al., 2012](#)) probed an oxygen environment in a Ba silicate glass with 55 mol% of silica by ^{17}O NMR. They showed that the fraction of non-bridging oxygens (NBOs) is $58.8 \pm 0.8\%$ (Figure I.20) and is close to that expected from stoichiometry. Based on their and previously published data they concluded that modifier cations do not interact solely with NBOs but an extensive interaction with BOs exists as well.

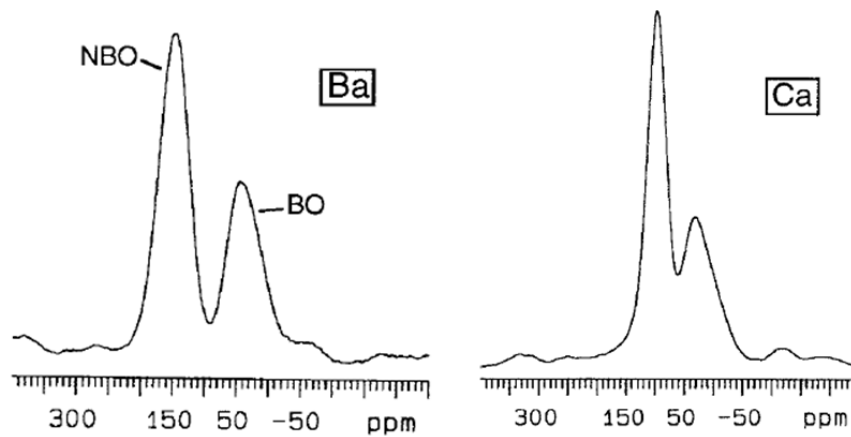


Figure I.20. ^{17}O MAS NMR spectra for Ba and Ca silicates with 55 mol% of silica (reproduced from [Stebbins et al., 1997](#)).

Rosenthal and Garofalini studied series of silica-rich Zn silicates (60-95 mol% of SiO_2) by MD simulation ([Rosenthal and Garofalini, 1987, 1986](#)). They found that at low ZnO concentrations most of Zn is four-coordinate. The concentration of ZnO_4 decreases with increasing ZnO content, giving an increase in six-coordinate Zn with a certain small amount of five-coordinate Zn (Figure I.21). The authors estimated the average $\text{CN}(\text{Zn-O})$ to range from 4.15 to 4.41 and $\text{CN}(\text{Si-O}) = 4.15-4.4$. A Huge fraction of oxygen triclusters was also found in the glasses together with some edge-sharing polyhedra. The authors concluded that even though a tetrahedral coordination implies a network-former role of a cation, zinc, nevertheless, disrupts the silica network by introducing edge-sharing polyhedra, oxygen triclusters and high-coordinate silicon species.

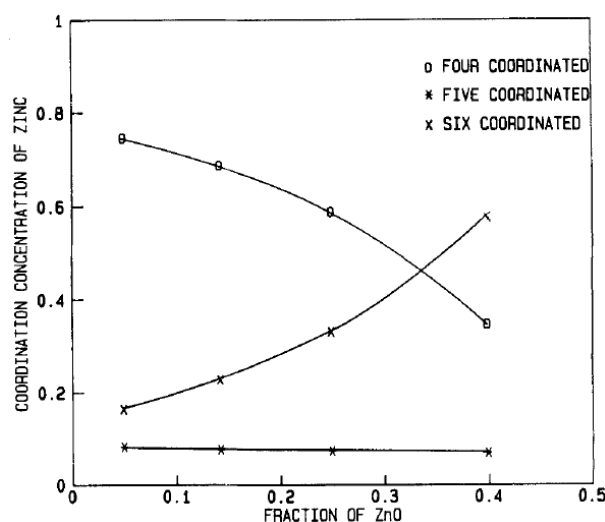


Figure I.21. Concentration of four-, five- and six-coordinate Zn as a function of ZnO content in Zn silicate glasses (from [Rosenthal and Garofalini, 1987](#)).

Ehrt and Flugel (Ehrt and Flügel, 2011) reported density and T_g of a Zn metasilicate glass (ZnSiO_3 , ZnO-SiO_2). Van Tran et al. reported results of Raman, FT-IR, XRD and TEM made on a Zn silicate glass with 85 mol% of silica obtained by the sol-gel process (Van Tran et al., 2017). The Raman spectrum of the silicate glass resembles that of pure silica glass. They also showed that the glass was phase separated into regions of amorphous ZnO and amorphous SiO_2 .

Melts. Viscosities of Sr, Ba and Zn silicate melts with 50-80, 50-96.3 and 45-50 mol% of SiO_2 , respectively, were reported in (Bockris et al., 1955; Mizoguchi et al., 1982; Urbain et al., 1982). Bockris et al. determined activation energies for viscous flow and suggested presence in the melts of discrete units of a general formula $(\text{Si}_n\text{O}_{2n+3})^{6-}$ with $n \geq 3$. It has been proposed that at low silica content such species have mostly chain structure while with increasing silica content the chains are converted to planar rings. They also demonstrated that silicate melts with cation possessing high CFS are less viscous (Figure I.22). At the same time, alkaline earth silicate melts are more viscous than alkali ones. They proposed that Ba^{2+} ions participate in the linking of the network by connecting with two NBOs, while K^+ is attached to only one NBO.

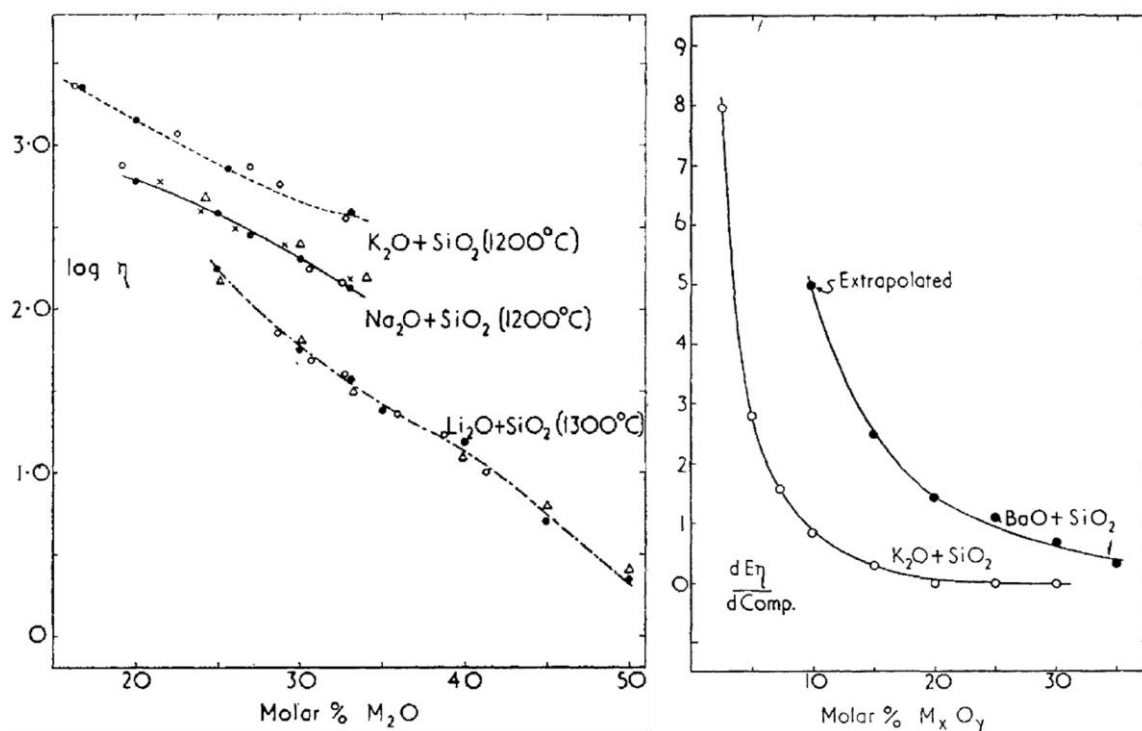


Figure I.22. Left: $\log(\eta)$ as a function of composition for alkali silicate melts. Right: $dE_\eta/d\%M_xO_y$ as a function of composition (reproduced from (Bockris et al., 1955)).

Tomlinson et al. (Tomlinson et al., 1958) carried out measurements of densities for Sr and Ba silicate melts with 45-65 and 45-95 mol% of SiO_2 , respectively. They showed that molar volume of silicate melts depends on the nature of the cation: the higher the CFS, the lower the molar volume (Figure I.23). Their observation is in agreement with that made on the alkali and alkaline earth glasses by (Rabukhin, 1999). They also noticed that the molar volume of Ba silicates deviates from a simple additivity curve (as it also does for potassium). They suggested that incorporation of huge cations into the network is accompanied by a structural rearrangement involving an increase in volume. Their calculations of the molar volume for the SrO-SiO_2 and BaO-SiO_2 systems indicate the presence of three-membered planar rings at low SiO_2 content and of four- and five-membered rings at high silica content.

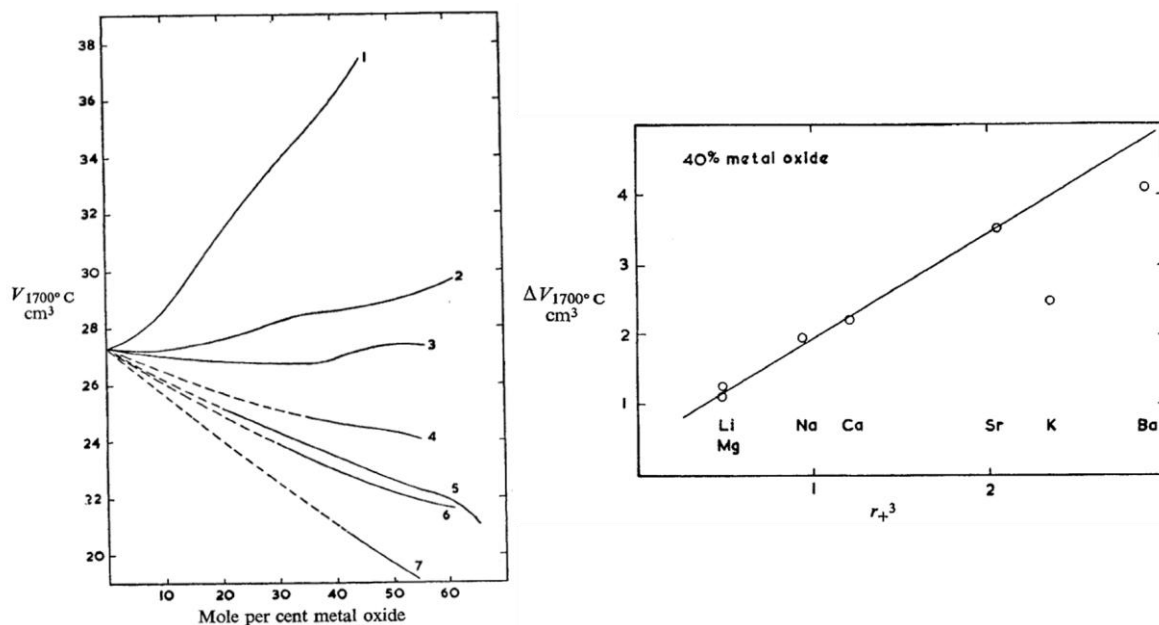


Figure I.23. *Left*: Molar volumes at 1700 °C for M_2O and MO silicate systems as a function of composition (1 - K, 2 - Na, 3 - Ba, 4 - Sr, 5 - Li, 6 - Ca, 7 - Mg). *Right*: Deviation from additivity of molar volume at 40 mol% of metal oxide as a function of the cube of the radius of the metal cation (reproduced from (Tomlinson et al., 1958)).

Richet and Bottinga (Richet and Bottinga, 1985) measured heat capacities of Sr disilicate (66.7 mol% of SiO_2) and barium trisilicate (75 mol% of SiO_2) melts by means of drop calorimetry. They calculated partial molar heat capacities of silica, SrO and BaO, combination of which can be used for estimation of thermodynamic parameters for other silicate compositions.

Mysen and Frantz ([Frantz and Mysen, 1995](#); [Mysen and Frantz, 1993](#)) carried out high-temperature Raman measurements on Sr and Ba silicate melts with 55.6-66.7 and 55.6-80 mol% of silica, respectively. They found that at all temperatures studied silica-rich melts consist only of three structural units: Q^2 , Q^3 and Q^4 species. However, the proportion of Q^3 species decreases with increasing temperature. The number of Q^4 species decreases while the quantity of Q^1 species increases for more depolymerized melts. The authors calculated the equilibrium constant for the reaction of Q^n species exchange at different temperatures and estimated the enthalpy of the reaction $2Q^n \leftrightarrow Q^{n+1} + Q^{n-1}$ to be 34 ± 4 kJ/mol. They also mentioned that the relative abundance of Q^3 species is higher in alkali silicates than in ones containing alkaline earth cations.

2. Aluminate glasses

Aluminate glasses are generally difficult to obtain due to elevated melting points and the high tendency of corresponding melts to crystallize under cooling. These glasses are interesting by the fact that they are not composed of classic network formers. Instead, their network formed by intermediates and network modifiers. It is only recently that Sr and Ba aluminate glasses could be obtained by fast aerodynamic levitation quench.

2.1. Vitrification domains

SrO-Al₂O₃. The vitrification domain for Sr aluminates was investigated by ([Kato et al., 2015](#); [Licheron et al., 2011](#)). They reported two domains of vitrification in a 25-45 and 55-75 mol% range of Al₂O₃. Shinozaki et al. claimed to obtain a glass of 50 SrO-50 Al₂O₃ (SrAl₂O₄) composition ([Shinozaki et al., 2016](#)). However, there are some doubts about the glass composition that are needed to be explained here. First, the reported melting point (1790 °C) is almost 200 °C lower than the one (2015 °C) reported by other authors ([Capron et al., 2001](#)). Second, density and the glass transition temperature values do not fit well the reported in this thesis density and T_g values for the series of compositions with the same SrO/Al₂O₃ ratio (see Chapter III). The last argument is that at least three different researchers from our lab have tried to obtain the aluminate glass under the same conditions on two slightly different levitation setups but have never succeeded to do so. This leads to a thought that the glass obtained by Shinozaki et al. might be not of the stated stoichiometry since no elemental analysis is reported.

BaO-Al₂O₃. Several authors determined the vitrification domain for the BaO-Al₂O₃ system (Allix et al., 2012; Boyer et al., 2016; Licheron et al., 2011; Skinner et al., 2012). It was found that two vitrification domains exist. The first one in a 25-38 and the second one in a 52-66.7 mol% range of Al₂O₃. Skinner et al. reported for the first time glass obtained by levitation quench for BaAl₂O₄ (50 BaO-50 Al₂O₃) composition (Skinner et al., 2006). Here again, some comments should be inserted. First, some authors do not report this glass composition in their subsequent paper (Skinner et al., 2012) where they investigated glass-forming regions of the BaO-Al₂O₃ system. Second, no elemental analysis was carried out and, therefore, the claimed glass might be of different composition. It should be noted that a small variation in stoichiometry may lead to a composition with 52 mol% of alumina for which glass exists. Finally, in our laboratory, the reported glass could not be obtained under variable conditions (different researchers, experimental setups and conditions).

ZnO-Al₂O₃. To our knowledge, no Zn aluminate glasses have been reported in the literature so far.

2.2. Structure and properties

Glasses. Glass transition temperatures of Ba aluminate glasses were reported in two papers (Allix et al., 2012; Boyer et al., 2016). Skinner et al. (Skinner et al., 2012, 2006) studied two Ba aluminate glasses with 50 (see discussion above) and 60 mol% of Al₂O₃ with X-ray and neutron diffraction, combined with MD and RMC methods. For the former glass the authors found that the glass structure resembles that of the crystalline BaAl₂O₄ with interconnected aluminium tetrahedra and Ba cations surrounded by nine oxygens (Huang et al., 1994). For the glass with 60 mol% alumina they showed that the network of the studied glass consists mainly of corner-sharing AlO₄⁻ tetrahedra where Ba²⁺ cations are surrounded by an average of 7.4 oxygens. They also found a huge amount of oxygen triclusters (21 %) connecting three aluminium tetrahedra (Figure I.24).

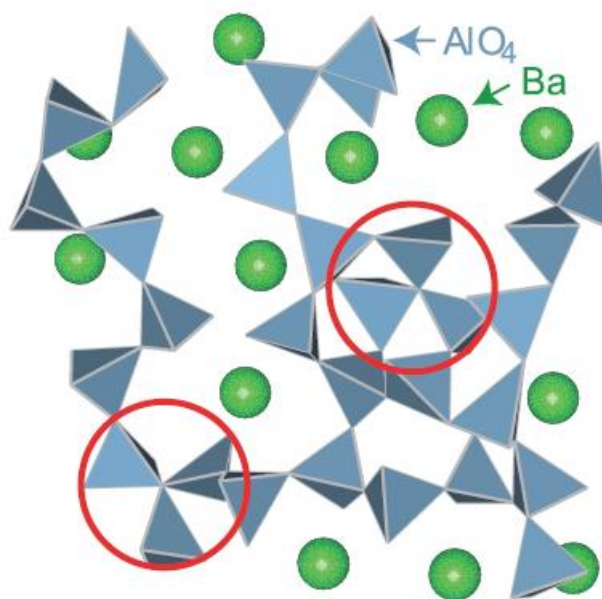


Figure I.24. Model of 40 BaO-60 Al₂O₃ glass with oxygen triclusters in red circles (from (Skinner et al., 2012)).

Licheron et al. (Licheron et al., 2011) performed ²⁷Al NMR and Raman measurements on series of Sr and Ba aluminate glasses with 25-45 and 25-38 mol% of alumina, respectively. They showed that aluminium sites are all four-coordinate (no high-coordinate sites) and its speciation in Qⁿ species changes from Q⁴ to Q³ and then to Q² under decrease in alumina content. Thus, the structure becomes more depolymerized with the substitution of alumina by SrO or BaO.

Melts. Capron et al. (Capron et al., 2001) studied Sr aluminate melts with 20-85.7 mol% of Al₂O₃ by means of ²⁷Al NMR and Sr K-edge XAS. They found that the CN(Al-O) is changing with increasing SrO content from 4.7±0.3 Å in liquid Al₂O₃ to about 4.0 Å for the melt with 80 mol% of Sr oxide. From the NMR linewidth analysis they showed that compositions with 40-50 mol% of SrO possess the maximum viscosity and, as the consequence, maximum in the melt's polymerization. XAS performed on SrAl₂O₄ sample indicated a change in Sr-O distance and coordination number from 2.81 Å and CN = 9 in the crystal at room temperature to 2.75-2.78 Å and CN = 7.2-7.7 in liquid aluminate. The latter values of Sr-O distance and coordination number are very close to ones for high-temperature hexagonal SrAl₂O₄ phase. This similarity suggests that the CN(Al-O) is about 4 in the liquid Sr aluminate.

3. Aluminosilicate glasses

Aluminosilicates, being a “mixture” of silicates and aluminates are expected to possess a mixed structure composed of interconnected silicon and aluminium tetrahedra. Their properties should depend on the degree of randomness of this mixing as well as on the $\text{SiO}_2/\text{Al}_2\text{O}_3$ and $\text{MO}/\text{Al}_2\text{O}_3$ ratios (where MO is an alkaline earth oxide). However, this picture is too simplified and, as it has been previously mentioned, other than tetrahedral units can exist in the glass network.

3.1. Vitrification domains

$\text{SrO}-\text{Al}_2\text{O}_3-\text{SiO}_2$. In the SAS system all reported aluminosilicate glasses have the ratio $\text{SrO}/\text{Al}_2\text{O}_3 = 1$. It has been shown that it is possible to obtain glasses with 10 to 66.7 mol% of SiO_2 on this join (Al Saghir, 2014; Al Saghir et al., 2015; Creux et al., 1995; Weigel et al., 2016).

$\text{BaO}-\text{Al}_2\text{O}_3-\text{SiO}_2$. Aluminosilicate glasses reported in the BAS system are generally alumina-poor with < 15 mol% of Al_2O_3 and 34.6-80.6 mol% of silica (Borhan et al., 2016; Thomas, 1950; Tredway and Risbud, 1988). However, several glasses with $\text{BaO}/\text{Al}_2\text{O}_3 \approx 1$ and SiO_2 content about 30 and 50 mol% are reported as well (Thompson and Stebbins, 2012; Weigel et al., 2016).

$\text{ZnO}-\text{Al}_2\text{O}_3-\text{SiO}_2$. As in case of BAS system, reported Zn aluminosilicate glasses are alumina-poor with < 15 mol% of Al_2O_3 and with 40-55 mol% of SiO_2 (Ehrt et al., 2008; Shimbo, 1987). Only two glasses are reported on the join with $\text{ZnO}/\text{Al}_2\text{O}_3 = 1$, namely with 50 and 75 mol% of silica (Varshal, 1990; Weigel et al., 2016) and one glass in a slightly peraluminous domain with 75.5 mol% of SiO_2 (Cormier et al., 2015).

3.2. Structure and properties

Glasses. Short and medium range order of a Sr aluminosilicate glass with 66.7 mol% of SiO_2 and $\text{SrO}/\text{Al}_2\text{O}_3 = 1$ were studied by Creux et al. (Creux et al., 1995) and by Cormier et al. (Cormier et al., 1999a, 1999b) by means of neutron diffraction (ND), AWAXS and Reverse Monte Carlo (RMC) modelling. From the AWAXS data they found the $\text{CN}(\text{Sr}-\text{O}) = 6$ with the mean Sr-O distance 2.685 Å. From ND the authors found the Sr-O distance to be 2.63 Å and

CN = 7.0 (2.7 Å and CN = 5.9 from RMC). The reported CN(Sr-O) is lower than in SrAl₂O₄ (SrO/Al₂O₃ = 1), both crystalline (CN = 9) and liquid (CN = 7.2-7.7) (Capron et al., 2001). Sr-Sr distances in the aluminosilicate glass were found to be at about 4 and 7 Å, which led the authors to a conclusion about the inhomogeneous distribution of Sr cations in the glass network. They proposed that Sr polyhedra are attached to the tetrahedral units (more likely to Al tetrahedra).

Glass transition temperatures of some Sr aluminosilicate glasses were reported in (Al Saghir, 2014; Al Saghir et al., 2015; Weigel et al., 2016). Weigel et al. found that T_g and molar volume of aluminosilicate glasses of a tectosilicate composition (namely with 50 mol% of SiO₂) decrease with increasing the cation field strength of the modified cation, both in alkali and alkaline earth series (Figure I.25).

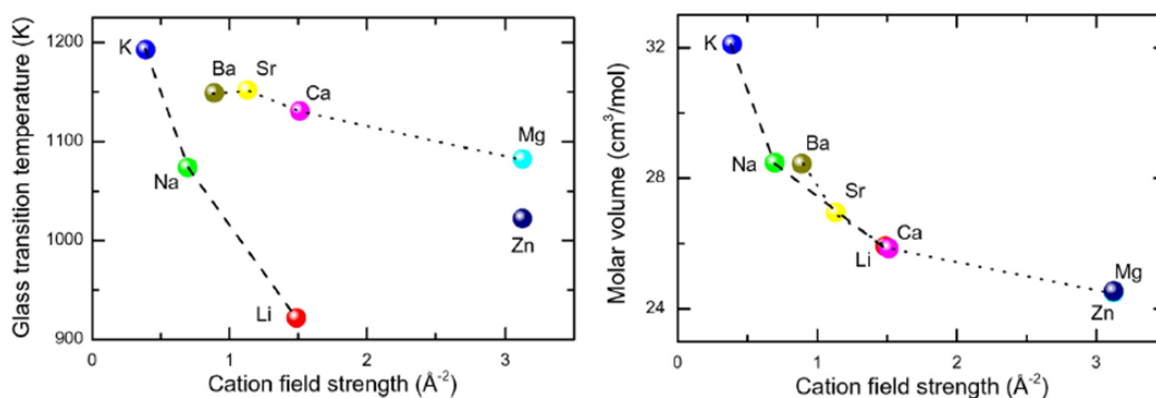


Figure I.25. Glass transition temperature T_g (left) and molar volume V_m (right) as a function of the CFS for aluminosilicate glasses of identical composition with 50 mol% of SiO₂ and 25 mol% of Al₂O₃ (from (Weigel et al., 2016)).

Thompson and Stebbins studied series of Ba aluminosilicates with BaO/Al₂O₃ ≈ 1 using ²⁷Al and ¹⁷O NMR (Thompson and Stebbins, 2012). They found that the number of NBOs increases from 1.9 % in the peraluminous field to 6.9 % in the peralkaline field, while at the same time proportion of five-coordinate Al drops down from 3.5 % to 1.5 %, respectively. They demonstrated that even for theoretically fully polymerized glasses a small fraction of NBOs is to expect and that there is no correlation between the formation of NBOs and five-coordinate Al. They also suggested that it is cation's charge and not its size that influences NBOs stabilization (more NBOs in alkaline earth aluminosilicates than in alkali ones). Nevertheless, they mentioned that AlO₅ content clearly correlates with CFS being higher for cations with higher field strength (Figure I.26).

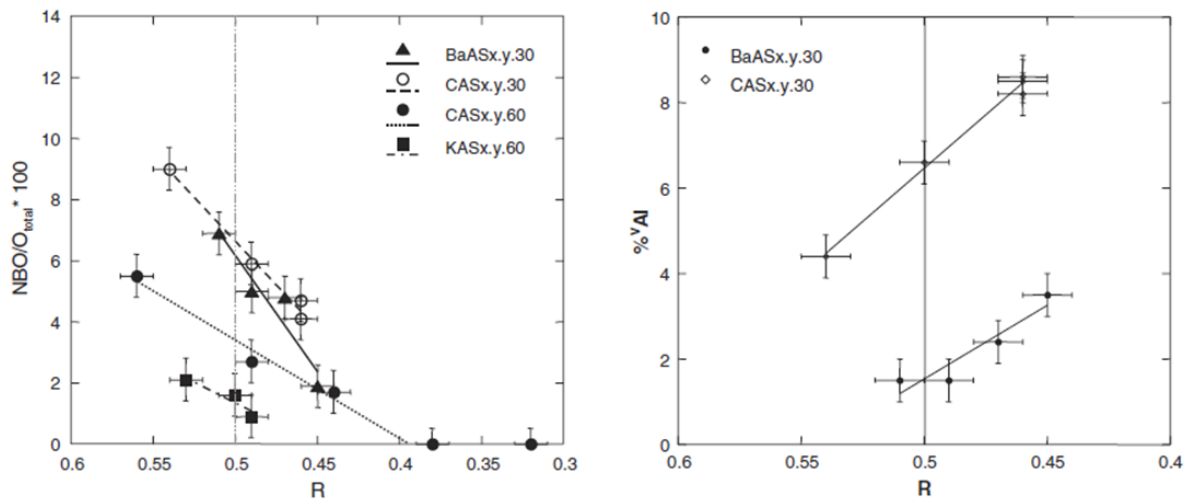


Figure I.26. *Left*: NBO content for K, Ca and Ba aluminosilicate glasses. *Right*: Al^V content for Ca and Ba aluminosilicates (from (Thompson and Stebbins, 2012)).

Ehrt et al. (Ehrt et al., 2011, 2008) reported densities and T_g for series of Zn aluminosilicate glasses with low alumina content. The authors assumed that Zn is four- and six-coordinate in the studied compositions.

As in the case of alkali and alkaline earth silicate glasses, Rabukhin (Rabukhin, 2000) demonstrated that the molar volume of alkali and alkaline earth aluminosilicate glasses increases with decreasing the CFS (Figure I.27).

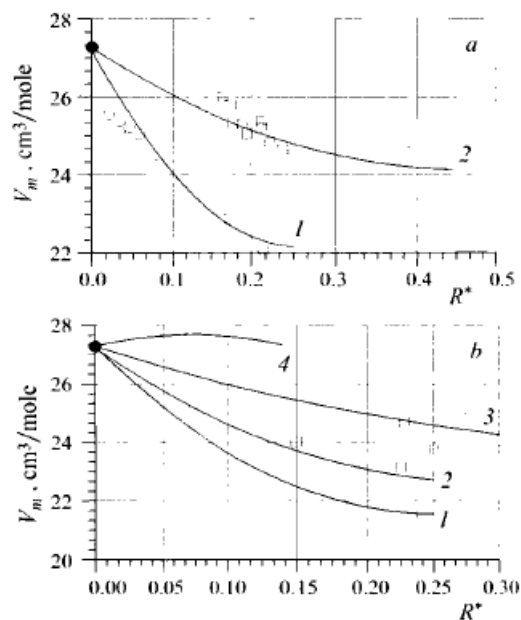


Figure I.27. *Top*: molar volume of glasses in the $R_2O-Al_2O_3-SiO_2$ system (1 - Li, 2 - Na). *Bottom*: molar volume of glasses in the $RO-Al_2O_3-SiO_2$ system (1 - Mg, 2 - Ca, 3 - Sr, 4 - Ba) at constant alumina content (from (Rabukhin, 2000)).

Melts. Viscosities of Sr, Ba and Zn aluminosilicate melts were reported in (Mizoguchi et al., 1982; Urbain et al., 1982). From the experimental data Mizoguchi et al. calculated the fraction X of Al^{3+} incorporated into tetrahedral units: $X(\text{Ba}) = 0.90$, $X(\text{Sr}) = 0.78$ and $X(\text{Zn}) = 0.50$. Therefore, they demonstrated a correlation between the fraction of high coordinate aluminium species and the cation field strength (CFS) in melts (Figure I.28). They also demonstrated that even for compositions with an excess of modifier oxides (for which one would expect all Al^{3+} to be charge compensated) Al incorporated not solely into tetrahedral units.

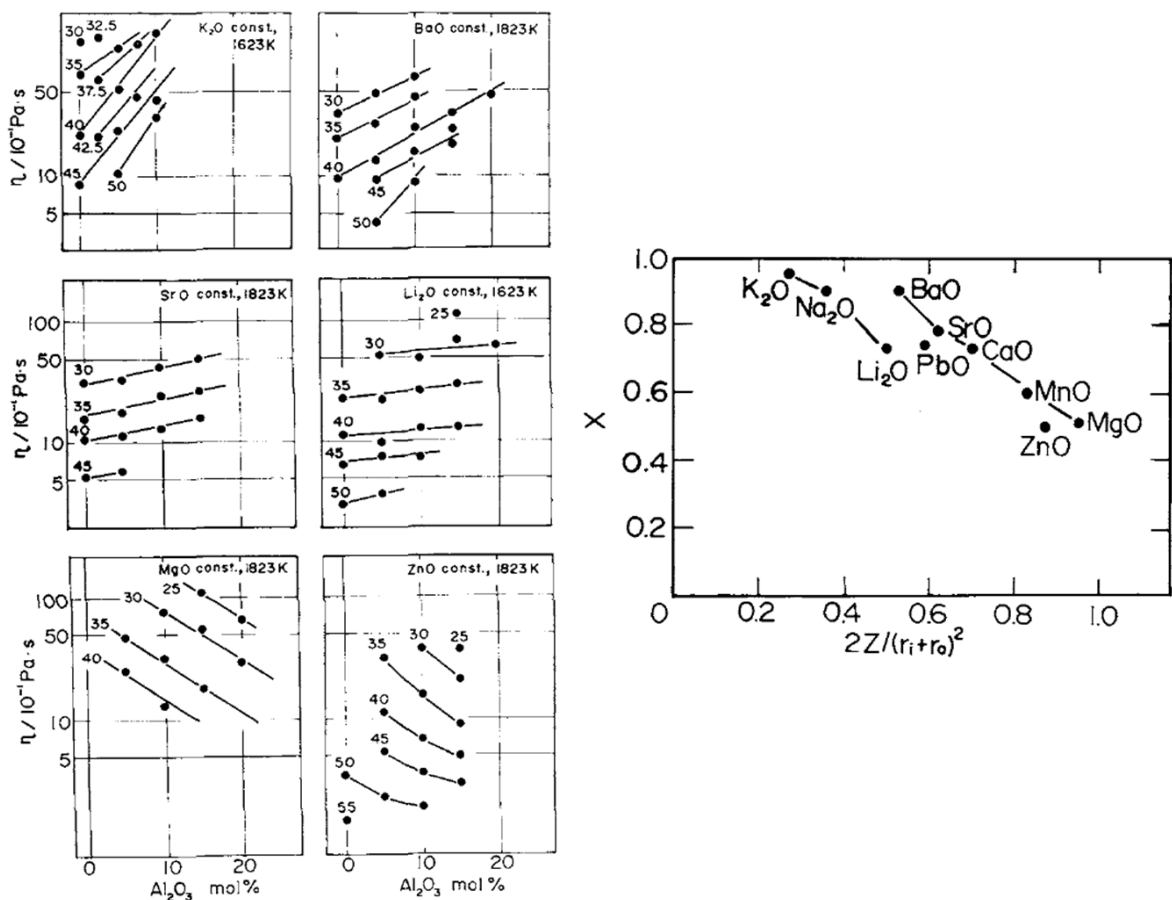


Figure I.28. Left: viscosity as a function of alumina content. Right: fraction of four-coordinate Al as a function of ion oxygen attraction (from (Mizoguchi et al., 1982)).

Urbain et al. noticed that, unlike for liquid silicates, viscosities of liquid aluminosilicates deviate from Arrhenian behaviour. Moreover, they showed that viscosities of liquid aluminosilicates of the similar composition depend on the CFS: viscosities of Ba aluminosilicate melts being higher than those containing Sr, Ca or Mg (Figure I.29).

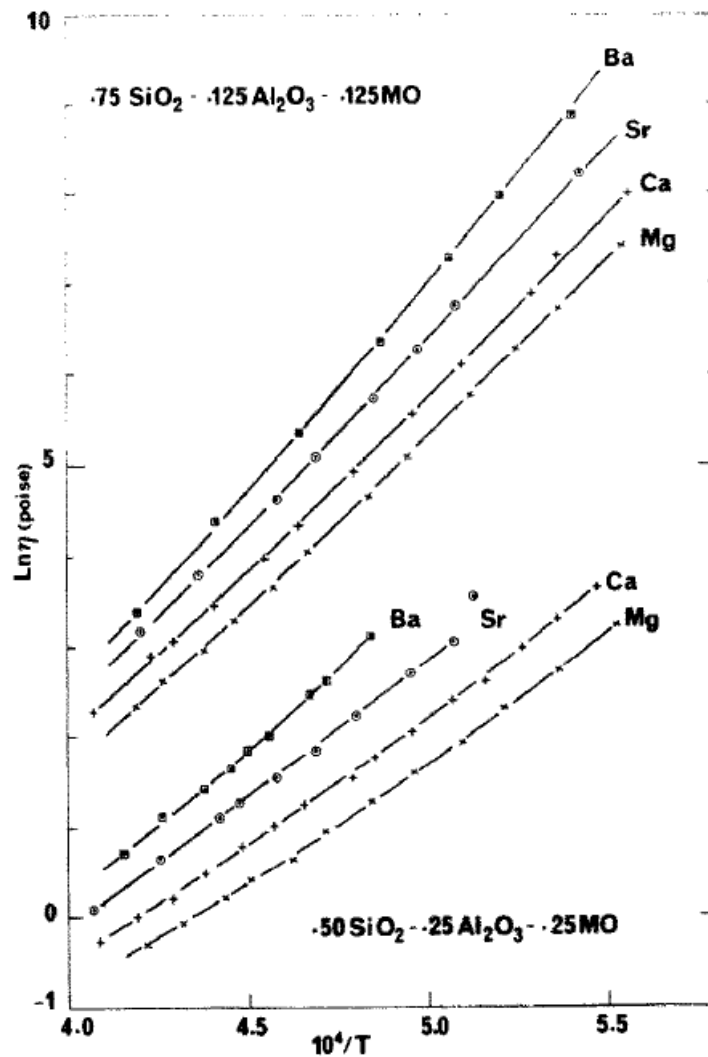


Figure I.29. $\text{Log}(\eta)$ versus reciprocal temperature for liquids of $\text{MO-Al}_2\text{O}_3\text{-SiO}_2$, where $\text{M} = \text{Mg/Ca/Sr/Ba}$ (from (Urbain et al., 1982)).

Varshal (Varshal, 1990) determined the Arrhenius activation energy for viscous flow from viscosity measurements for one Zn aluminosilicate ($12.5 \text{ ZnO}-12.5 \text{ Al}_2\text{O}_3-75 \text{ SiO}_2$). Unfortunately, he did not provide any experimental details and viscosity data itself. Nevertheless, using literature data he calculated activation energies for analogous alkali and alkaline aluminosilicates and compared them on the basis of cation electronegativity (Figure I.30). It appeared that aluminosilicates containing less electronegative cations possess higher activation energy. The author associated this trend with the stability of the aluminium tetrahedron: the higher the ionicity of cation-oxygen bond the stronger Al-O bonds in tetrahedra.

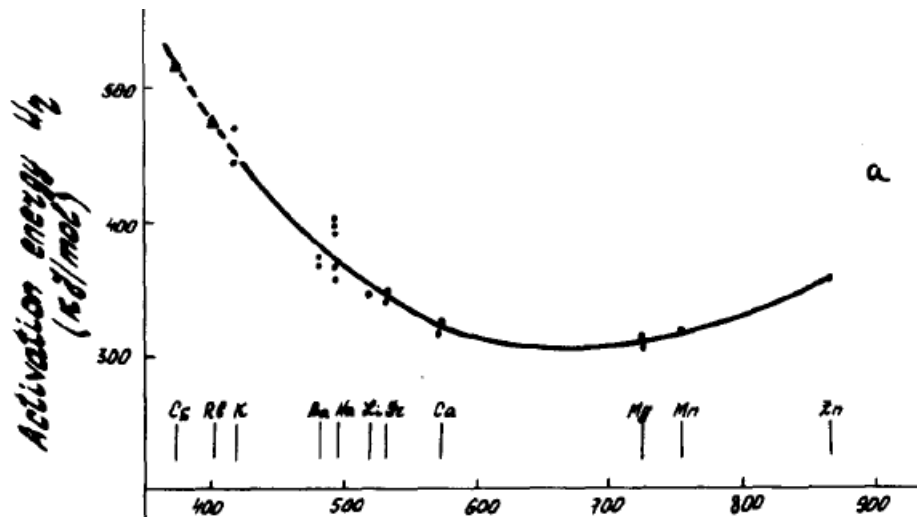


Figure I.30. The activation energy of viscous flow as a function of the cation electronegativity (from (Varshal, 1990)).

Abel et al. (Abel et al., 2013) noticed that for alkaline earth aluminosilicates with $MO/Al_2O_3 = 1$ ($M = Mg/Ca/Sr$) decrease in the CFS leads to decrease in the liquidus temperature. However, for $MO/Al_2O_3 > 1$ (peralkaline field) a minimum in liquidus for Ca aluminosilicate compositions is observed (Figure I.31).

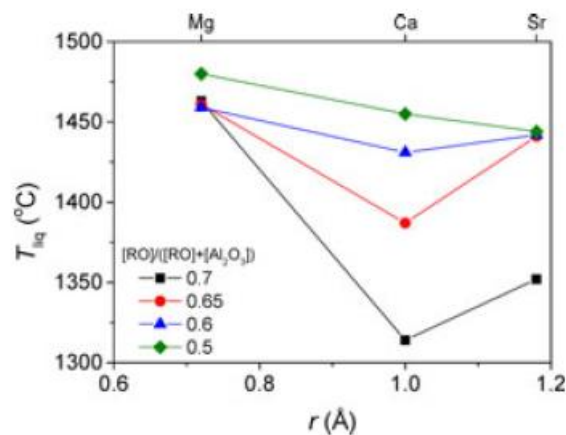


Figure I.31. Dependence of liquidus temperature on the ionic radius of the alkaline earth cation in $RO-Al_2O_3-SiO_2$ systems with different RO/Al_2O_3 ratios (from (Abel et al., 2013)).

Conclusion

The review has revealed several points that should be stated here:

- There is a strong dependence of glass and melt's properties on the cation's nature (size, CFS etc.).

- High-coordinate aluminium species are to be expected even in the peralkaline ($\text{MO}/\text{Al}_2\text{O}_3 > 1$) domain of the ternary diagram.
- Non-bridging oxygens exist for the compositions on the charge compensation line ($\text{MO}/\text{Al}_2\text{O}_3 = 1$) and in the peraluminous domain ($\text{MO}/\text{Al}_2\text{O}_3 < 1$).
- It has been demonstrated the presence of oxygen triclusters for aluminate glasses, so they might exist in aluminosilicate glasses as well.

In Figure I.32 we summarize all reported in the literature glass compositions in SAS, BAS and ZAS systems. As one can see, among the three systems the BAS one has been studied the most. Nevertheless, there are still huge gaps in all the ternary systems, especially in the peraluminous field. Moreover, the reported glasses were studied in most cases by one or two methods, which definitely didn't allow authors to make solid conclusions on the structure-properties relation in the systems. To our knowledge, no systematic studies were carried out in neither of the ternary systems.

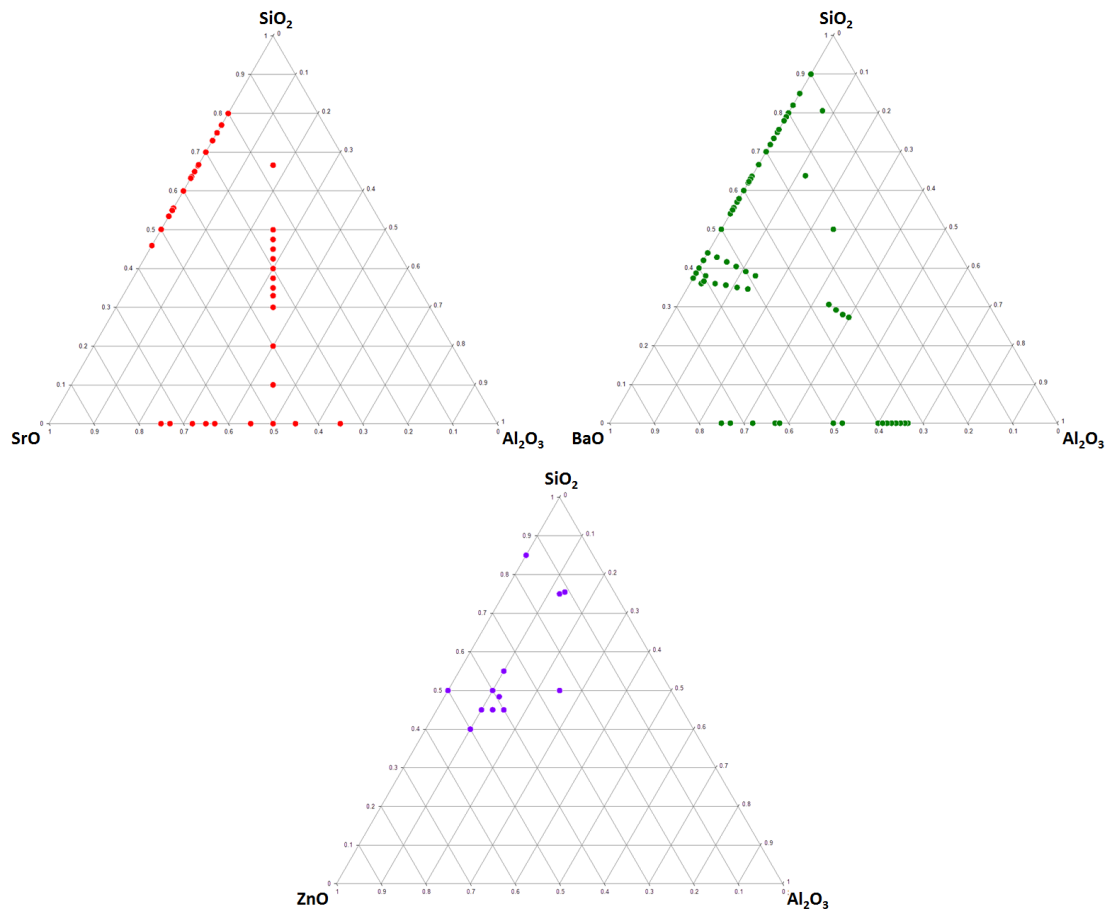


Figure I.32. Ternary diagrams for SAS (*top left*), BAS (*top right*) and ZAS (*bottom*) systems summarizing glass compositions reported in the literature.

In the following chapters we will discuss results obtained for the glasses and melts in the three systems. The techniques and methods used in the experiments are described in Chapter II.

Bibliography

- Abel, B.M., Morgan, J.M., Mauro, J.C., Smedskjaer, M.M., 2013. Liquidus Temperature of SrO-Al₂O₃-SiO₂ Glass-Forming Compositions. *Int. J. Appl. Glas. Sci.* 4, 225–230. doi:10.1111/ijag.12017
- Al Saghir, K., 2014. Céramiques transparentes par cristallisation complète du verre: application aux aluminosilicates de strontium.
- Al Saghir, K., Chenu, S., Veron, E., Fayon, F., Suchomel, M., Genevois, C., Porcher, F., Matzen, G., Massiot, D., Allix, M., 2015. Transparency through Structural Disorder: A New Concept for Innovative Transparent Ceramics. *Chem. Mater.* 27, 508–514. doi:10.1021/cm5037106
- Allix, M., Alahrache, S., Fayon, F., Suchomel, M., Porcher, F., Cardinal, T., Matzen, G., 2012. Highly Transparent BaAl₄O₇ Polycrystalline Ceramic Obtained by Full Crystallization from Glass. *Adv. Mater.* 24, 5570–5575. doi:10.1002/adma.201202282
- Bockris, J.O., Mackenzie, J.D., Kitchener, J.A., 1955. Viscous flow in silica and binary liquid silicates. *Trans. Faraday Soc.* 51, 1734–1748. doi:10.1039/TF9555101734
- Borhan, A.I., Gromada, M., Nedelcu, G.G., Leontie, L., 2016. Influence of (CoO, CaO, B₂O₃) additives on thermal and dielectric properties of BaO–Al₂O₃–SiO₂ glass–ceramic sealant for OTM applications. *Ceram. Int.* 42, 10459–10468. doi:10.1016/j.ceramint.2016.03.199
- Boyer, M., Alahraché, S., Genevois, C., Licheron, M., Lefevre, F.-X., Castro, C., Bonnefont, G., Patton, G., Moretti, F., Dujardin, C., Matzen, G., Allix, M., 2016. Enhanced Transparency through Second Phase Crystallization in BaAl₄O₇ Scintillating Ceramics. *Cryst. Growth Des.* 16, 386–395. doi:10.1021/acs.cgd.5b01374
- Brandriss, M.E., Stebbins, J.F., 1988. Effects of temperature on the structures of silicate liquids: ²⁹Si NMR results. *Geochim. Cosmochim. Acta* 52, 2659–2669. doi:10.1016/0016-7037(88)90034-8
- Capron, M., Florian, P., Fayon, F., Trumeau, D., Hennet, L., Gaihlhanou, M., Thiaudière, D.,

- Landron, C., Douy, A., Massiot, D., 2001. Local structure and dynamics of high temperature SrO–Al₂O₃ liquids studied by ²⁷Al NMR and Sr K-edge XAS spectroscopy. *J. Non. Cryst. Solids* 293–295, 496–501. doi:10.1016/S0022-3093(01)00762-1
- Cormier, L., Calas, G., Creux, S., Gaskell, P., Bouchet-Fabre, B., Hannon, A., 1999a. Environment around strontium in silicate and aluminosilicate glasses. *Phys. Rev. B* 59, 13517–13520. doi:10.1103/PhysRevB.59.13517
- Cormier, L., Dargaud, O., Calas, G., Jousseau, C., Papin, S., Trcera, N., Cognigni, A., 2015. Zr environment and nucleation role in aluminosilicate glasses. *Mater. Chem. Phys.* 152, 41–47. doi:10.1016/j.matchemphys.2014.12.008
- Cormier, L., Gaskell, P.H., Creux, S., 1999b. Comparison of the low-Q features in diffraction data for silicate glasses and crystals containing Sr or Ba. *J. Non. Cryst. Solids* 248, 84–91. doi:10.1016/S0022-3093(99)00102-7
- Creux, S., Bouchet-Fabre, B., Gaskell, P.H., 1995. Anomalous wide angle X-ray scattering study of strontium silicate and aluminosilicate glasses. *J. Non. Cryst. Solids* 192 & 193, 360–363.
- Dietzel, A., 1942. Die Kationenfeldstärken und ihre Beziehungen zu Entglasungsvorgängen, zur Verbindungsbildung und Schmelzpunkten von Silikaten. *Zeitschrift für Elektrochemie und Angew. Phys. Chemie* 48, 9–23. doi:10.1002/bbpc.19420480104
- Doweidar, H., 1999. Density-structure correlations in silicate glasses. *J. Non. Cryst. Solids* 249, 194–200. doi:10.1016/S0022-3093(99)00310-5
- Ehrt, D., Flügel, S., 2011. Properties of Zinc Silicate Glasses and Melts. *Mater. Sci. Eng.* 1, 312–320.
- Ehrt, D., Herrmann, A., Tiegel, M., 2011. Glasses and glass ceramics with blue, green and red photoluminescence. *Eur. J. Glas. Sci. Technol. Part B Phys. Chem. Glas.* 52, 68–76.
- Ehrt, D., Vu, H.T., Herrmann, A., Volksch, G., 2008. Luminescent ZnO–Al₂O₃–SiO₂ Glasses and Glass Ceramics. *Adv. Mater. Res.* 39–40, 231–236. doi:10.4028/www.scientific.net/AMR.39-40.231

- Engelhardt, L.G., Zeigan, D., Jancke, H., Wieker, W., Hoebbel, D., 1975. ^{29}Si -NMR spectroscopy of silicate solutions. 2. On the dependence of the structure of silicate anions in water solutions from the Na:Si ratio. *Zeitschrift für Anorg. und Allg. Chemie* 418, 17–28. doi:10.1002/zaac.19754180103
- Eskola, P., 1922. The silicates of strontium and barium. *Am. J. Sci.* s5-4, 331–375. doi:10.2475/ajs.s5-4.23.331
- Frantz, J.D., Mysen, B.O., 1995. Raman spectra and structure of BaO-SiO₂, SrO-SiO₂ and CaO-SiO₂ melts to 1600C. *Chem. Geol.* 121, 155–176.
- Goldschmidt, V., 1926. *Geochemische Verteilungsgesetze der Elemente.* 6. Über die Kristallstrukturen vom Rutiltypus, mit Bemerkungen zur Geochemie zweiwertiger und vierwertiger Elemente. *Skr. utg. av det Nor. Videnskaps-akademi i Oslo* 1.
- Greaves, G.N., 1985. EXAFS and the structure of glass. *J. Non. Cryst. Solids* 71, 203–217. doi:10.1016/0022-3093(85)90289-3
- Greaves, G.N., Ngai, K.L., 1995. Reconciling ionic-transport properties with atomic structure in oxide glasses. *Phys. Rev. B* 52, 6358–6380. doi:10.1103/PhysRevB.52.6358
- Hasegawa, H., Yasui, I., 1987. X-ray and neutron diffraction analyses of barium silicate glass. *J. Non. Cryst. Solids* 95–96, 201–208. doi:10.1016/S0022-3093(87)80111-4
- Huang, P.Y., Kurasch, S., Srivastava, A., Skakalova, V., Kotakoski, J., Krashennnikov, A. V., Hovden, R., Mao, Q., Meyer, J.C., Smet, J., Muller, D.A., Kaiser, U., 2012. Direct Imaging of a Two-Dimensional Silica Glass on Graphene. *Nano Lett.* 12, 1081–1086. doi:10.1021/nl204423x
- Huang, S.-Y., Von Der Mühl, R., Ravez, J., Chaminade, J.P., Hagenmuller, P., Couzi, M., 1994. A propos de la ferroélectricité dans BaAl₂O₄. *J. Solid State Chem.* 109, 97–105. doi:10.1006/jssc.1994.1077
- Kato, K., Masuno, A., Inoue, H., 2015. Containerless solidification of undercooled SrO–Al₂O₃ binary melts. *Phys. Chem. Chem. Phys.* 17, 6495–6500. doi:10.1039/C4CP05861E
- Lacy, E.D., 1963. Aluminium in glasses and in melts. *Phys. Chem. Glas.* 4, 234–238.

- Lebedev, A.A., 1921. Polymorphism and annealing of glass. *Trans. Opt. Inst.* 2, 1–20.
- Lenoir, M., Grandjean, A., Linard, Y., Cochain, B., Neuville, D.R., 2008. The influence of Si,B substitution and of the nature of network-modifying cations on the properties and structure of borosilicate glasses and melts. *Chem. Geol.* 256, 316–325.
doi:10.1016/j.chemgeo.2008.07.002
- Licheron, M., Montouillout, V., Millot, F., Neuville, D.R., 2011. Raman and ^{27}Al NMR structure investigations of aluminate glasses: $(1-x)\text{Al}_2\text{O}_3-x\text{MO}$, with $\text{M}=\text{Ca}, \text{Sr}, \text{Ba}$ and $0.5 < x < 0.75$. *J. Non. Cryst. Solids* 357, 2796–2801.
doi:10.1016/j.jnoncrysol.2011.03.001
- Maekawa, H., Maekawa, T., Kawamura, K., Yokokawa, T., 1991. The structural groups of alkali silicate glasses determined from ^{29}Si MAS-NMR. *J. Non. Cryst. Solids* 127, 53–64.
doi:10.1016/0022-3093(91)90400-Z
- Meyer, A., Horbach, J., Kob, W., Kargl, F., Schober, H., 2004. Channel Formation and Intermediate Range Order in Sodium Silicate Melts and Glasses. *Phys. Rev. Lett.* 93, 27801. doi:10.1103/PhysRevLett.93.027801
- Mizoguchi, K., Okamoto, K., Suginoara, Y., 1982. Oxygen Coordination of Al^{3+} Ion in Several Silicate Melts Studied by Viscosity Measurements. *J. Japan Inst. Met.* 46, 1055–1060.
- Moynihan, C.T., Easteal, A.J., Wilder, J., Tucker, J., 1974. Dependence of the glass transition temperature on heating and cooling rate. *J. Phys. Chem.* 78, 2673–2677.
doi:10.1021/j100619a008
- Murdoch, J.B., Stebbins, J.F., Carmichael, I.S.E., 1985. High-resolution ^{29}Si NMR study of silicate and aluminosilicate glasses: the effect of network-modifying cations. *Am. Mineral.* 70, 332–343.
- Mysen, B.O., Frantz, J.D., 1993. Structure of silicate melts at high temperature: In-situ measurements in the system BaO-SiO_2 to 1669 C. *Am. Mineral.* 78, 699–709.
- Mysen, B.O., Virgo, D., Seifert, F.A., 1982. The structure of silicate melts: Implications for chemical and physical properties of natural magma. *Rev. Geophys. Sp. Phys.* 20, 353.

doi:10.1029/RG020i003p00353

- Neuvill, D.R., 2005. Structure and properties in (Sr, Na) silicate glasses and melts. *Phys. Chem. Glas.* 46, 112–118.
- Neuvill, D.R., Cormier, L., Flank, A.-M., Briois, V., Massiot, D., 2004. Al speciation and Ca environment in calcium aluminosilicate glasses and crystals by Al and Ca K-edge X-ray absorption spectroscopy. *Chem. Geol.* 213, 153–163.
doi:10.1016/j.chemgeo.2004.08.039
- Neuvill, D.R., Cormier, L., Montouillout, V., Florian, P., Millot, F., Rifflet, J.-C., Massiot, D., 2008. Structure of Mg- and Mg/Ca aluminosilicate glasses: ²⁷Al NMR and Raman spectroscopy investigations. *Am. Mineral.* 93, 1721–1731. doi:10.2138/am.2008.2867
- Rabukhin, A.I., 2000. Structural interpretation of the concentration dependence of molar volume in ternary aluminosilicate glasses containing oxides of the first and second groups of the periodic system. *Glas. Ceram.* 57, 154–157. doi:10.1007/BF02681263
- Rabukhin, A.I., 1999. Structural interpretation of concentration dependences of molar volume of glasses in R₂O-SiO₂ and RO-SiO₂ systems. *Glas. Ceram.* 56, 339–342.
doi:10.1007/BF02681337
- Richet, P., Bottinga, Y., 1985. Heat capacity of aluminum-free liquid silicates. *Geochim. Cosmochim. Acta* 49, 471–486.
- Richet, P., Nidaira, A., Neuvill, D.R., Atake, T., 2009. Influence of cation size on the low-temperature heat capacity of alkaline earth metasilicate glasses. *Am. Mineral.* 94, 1591–1595. doi:10.2138/am.2009.3240
- Rosenthal, A.B., Garofalini, S.H., 1987. Structural Role of Zinc Oxide in Silica and Soda-Silica Glasses. *J. Am. Ceram. Soc.* 70, 821–826. doi:10.1111/j.1151-2916.1987.tb05634.x
- Rosenthal, A.B., Garofalini, S.H., 1986. Molecular dynamics simulation of amorphous zinc silicate. *J. Non. Cryst. Solids* 87, 254–262. doi:10.1016/S0022-3093(86)80081-3
- Schlenz, H., Kirfel, A., Schulmeister, K., Wartner, N., Mader, W., Raberg, W., Wandelt, K., Oligschleger, C., Bender, S., Franke, R., Hormes, J., Hoffbauer, W., Lansmann, V.,

- Jansen, M., Zotov, N., Marian, C., Putz, H., Neuefeind, J., 2002. Structure analyses of Ba-silicate glasses. *J. Non. Cryst. Solids* 297, 37–54. doi:10.1016/S0022-3093(01)00922-X
- Schneider, J., Mastelaro, V.R., Zanotto, E.D., Shakhmatkin, B.A., Vedishcheva, N.M., Wright, A.C., Panepucci, H., 2003. Qn distribution in stoichiometric silicate glasses: thermodynamic calculations and ²⁹Si high resolution NMR measurements. *J. Non. Cryst. Solids* 325, 164–178. doi:10.1016/S0022-3093(03)00332-6
- Shelby, J.E., 2005. Principles of glass formation, in: Shelby, J.E. (Ed.), *Introduction to Glass Science and Technology*. Royal Society of Chemistry, Cambridge, pp. 7–25. doi:10.1039/9781847551160-00007
- Shelby, J.E., 1979. Effect of morphology on the properties of alkaline earth silicate glasses. *J. Appl. Phys.* 50, 8010–8015. doi:10.1063/1.325986
- Shimbo, M., 1987. Thermal Stability and Acid Resistivity of Glasses Based on ZnO-Al₂O₃-SiO₂. *J. Am. Ceram. Soc.* 70, C-101-C-102. doi:10.1111/j.1151-2916.1987.tb05013.x
- Shinozaki, K., Honma, T., Affatigato, M., Komatsu, T., 2016. Long afterglow in hexagonal SrAl₂O₄:Eu²⁺, Dy³⁺ synthesized by crystallization of glass and solidification of supercooled melts. *J. Lumin.* 177, 286–289. doi:10.1016/j.jlumin.2016.05.013
- Skinner, L.B., Barnes, A.C., Crichton, W., 2006. Novel behaviour and structure of new glasses of the type Ba–Al–O and Ba–Al–Ti–O produced by aerodynamic levitation and laser heating. *J. Phys. Condens. Matter* 18, L407–L414. doi:10.1088/0953-8984/18/32/L01
- Skinner, L.B., Barnes, A.C., Salmon, P.S., Fischer, H.E., Drewitt, J.W.E., Honkimäki, V., 2012. Structure and triclustering in Ba-Al-O glass. *Phys. Rev. B* 85, 64201. doi:10.1103/PhysRevB.85.064201
- Smekal, A.G., 1951. On the Structure of Glass. *J. Soc. Glas. Technol.* 32, 392–395.
- Stebbins, J.F., Kroeker, S., Lee, S.K., Kiczenski, T.J., 2000. Quantification of five- and six-coordinated aluminum ions in aluminosilicate and fluoride-containing glasses by high-field, high-resolution ²⁷Al NMR. *J. Non. Cryst. Solids* 275, 1–6. doi:10.1016/S0022-3093(00)00270-2

- Stebbins, J.F., Oglesby, J. V., Xu, Z., 1997. Disorder among network-modifier in silicate glasses : cations New constraints from triple-quantum ^{17}O NMR. *Am. Mineral.* 82, 1116–1124.
- Stebbins, J.F., Wu, J., Thompson, L.M., 2013. Interactions between network cation coordination and non-bridging oxygen abundance in oxide glasses and melts: Insights from NMR spectroscopy. *Chem. Geol.* 346, 34–46. doi:10.1016/j.chemgeo.2012.09.021
- Sun, K.-H., 1947. FUNDAMENTAL CONDITION OF GLASS FORMATION. *J. Am. Ceram. Soc.* 30, 277–281. doi:10.1111/j.1151-2916.1947.tb19654.x
- Thomas, R.H., 1950. Phase Equilibrium in a Portion of the Ternary System $\text{BaO-Al}_2\text{O}_3\text{-SiO}_2$. *J. Am. Ceram. Soc.* 33, 35–44.
- Thompson, L.M., McCarty, R.J., Stebbins, J.F., 2012. Estimating accuracy of ^{17}O NMR measurements in oxide glasses: Constraints and evidence from crystalline and glassy calcium and barium silicates. *J. Non. Cryst. Solids* 358, 2999–3006. doi:10.1016/j.jnoncrysol.2012.07.032
- Thompson, L.M., Stebbins, J.F., 2012. Non-stoichiometric non-bridging oxygens and five-coordinated aluminum in alkaline earth aluminosilicate glasses: Effect of modifier cation size. *J. Non. Cryst. Solids* 358, 1783–1789. doi:10.1016/j.jnoncrysol.2012.05.022
- Tomlinson, J.W., Heynes, M.S.R., Bockris, J.O., 1958. The structure of liquid silicates. Part 2.—Molar volumes and expansivities. *Trans. Faraday Soc.* 54, 1822–1833. doi:10.1039/TF9585401822
- Toplis, M.J., Dingwell, D.B., 2004. Shear viscosities of $\text{CaO-Al}_2\text{O}_3\text{-SiO}_2$ and $\text{MgO-Al}_2\text{O}_3\text{-SiO}_2$ liquids: Implications for the structural role of aluminium and the degree of polymerisation of synthetic and natural aluminosilicate melts. *Geochim. Cosmochim. Acta* 68, 5169–5188. doi:10.1016/j.gca.2004.05.041
- Toplis, M.J., Dingwell, D.B., Lenci, T., 1997. Peraluminous viscosity maxima in $\text{Na}_2\text{O-Al}_2\text{O}_3\text{-SiO}_2$ liquids: The role of triclusters in tectosilicate melts. *Geochim. Cosmochim. Acta* 61, 2605–2612. doi:10.1016/S0016-7037(97)00126-9

- Toplis, M.J., Kohn, S.C., Smith, M.E., Poplett, I.J.F., 2000. Fivefold-coordinated aluminum in tectosilicate glasses observed by triple quantum MAS NMR. *Am. Mineral.* 85, 1556–1560. doi:10.2138/am-2000-1031
- Tredway, W.K., Risbud, S.H., 1988. Gel synthesis of glass powders in the BaO-Al₂O₃-SiO₂ system. *J. Non. Cryst. Solids* 100, 278–283. doi:10.1016/0022-3093(88)90032-4
- Urbain, G., Bottinga, Y., Richet, P., 1982. Viscosity of liquid silica, silicates and aluminosilicates. *Geochim. Cosmochim. Acta* 46, 1061–1072. doi:10.1016/0016-7037(82)90059-X
- Van Tran, T.T., Dung Cao, T.M., Lam, Q.V., Le, V.H., 2017. Emission of Eu³⁺ in SiO₂-ZnO glass and SiO₂-SnO₂ glass-ceramic: Correlation between structure and optical properties of Eu³⁺ ions. *J. Non. Cryst. Solids* 459, 57–62. doi:10.1016/j.jnoncrysol.2016.12.040
- Varshal, B.G., 1990. Viscosity of aluminosilicate glasses of R₂O(RO) · Al₂O₃ · 6SiO₂ composition. *J. Non. Cryst. Solids* 123, 344–348. doi:10.1016/0022-3093(90)90806-W
- Vogel, W., 1971. THE DEVELOPMENT OF THE CLASSICAL STRUCTURE THEORIES, in: *Structure and Crystallization of Glasses*. Elsevier, pp. 14–20. doi:10.1016/B978-0-08-006998-2.50005-0
- Warren, B.E., Bischof, J., 1938. FOURIER ANALYSIS OF X-RAY PATTERNS OF SODA-SILICA GLASS. *J. Am. Ceram. Soc.* 21, 259–265. doi:10.1111/j.1151-2916.1938.tb15774.x
- Weigel, C., Le Losq, C., Vialla, R., Dupas, C., Clément, S., Neuville, D.R., Rufflé, B., 2016. Elastic moduli of XAlSiO₄ aluminosilicate glasses: effects of charge-balancing cations. *J. Non. Cryst. Solids* 447, 267–272. doi:10.1016/j.jnoncrysol.2016.06.023
- Zachariasen, W.H., 1932. THE ATOMIC ARRANGEMENT IN GLASS. *J. Am. Chem. Soc.* 54, 3841–3851. doi:10.1021/ja01349a006

Chapter II

Methods and experimental techniques

1. Synthesis of glasses and ceramics

Glass/ceramic samples of the studied aluminosilicates were prepared by three methods described in details below. Following chemicals were used for the syntheses: SiO₂ (pure silica from Saint-Gobain Quartz & Silice), Al₂O₃ (Merck 1.01095, ≥ 99.5 %), SrCO₃ (Merck 1.07861, ≥ 99.0 %), BaCO₃ (Merck 1.01714, ≥ 99.0 %) and ZnO (Merck 1.08846, ≥ 99.0 %). The names of the glasses are given as SA_{xx.yy}, BA_{xx.yy} or ZA_{xx.yy}, where *xx* is the SiO₂ content in mol%, *yy* is the Al₂O₃ content in mol%, the remaining being the content of SrO, BaO or ZnO, respectively.

1.1. Classic melting-quenching procedure

Powders of SiO₂, Al₂O₃ and SrCO₃/BaCO₃/ZnO were pre-dried at 1000 °C (silica, alumina), 550 °C (carbonates) and 400 °C (zinc oxide) before being mixed in a stoichiometric amount to make ~100 g batches. The powders were crushed together in an agate mortar under ethanol for 1 h and then decarbonated in a platinum or platinum-iridium (Pt-Ir10%) crucible at temperatures up to 1200 °C in an electric muffle furnace for at least two hours. After this, the mixture was melted at the temperature up to 1750 °C and quenched either by dipping the bottom of the crucible in water or by pouring the melt on a large copper plate. Quenching method depended on the viscosity of each particular melt. The grinding, melting, quenching procedures were repeated three more times to ensure the homogeneity of the final product.

The advantage of the procedure is the possibility to obtain a great quantity of a sample (~100 g in our case). In fact, it is limited only by the volume of the crucible. On the other hand, the procedure has certain disadvantages. For example, it is only applicable for compositions with $T_m \leq 1750$ °C (the limiting factors are the maximum temperature that can be achieved by the laboratory furnaces and the melting point of the crucible's material). Another negative point is a relatively low cooling rate of the melt during the quench. It has been evaluated to be something around 15 °C/s (Neuville et al., 2008) and sometimes it is not fast enough for the vitrification of the compositions tending to crystallize readily. The last thing to keep in mind is the contamination of samples with a tiny amount (tens to hundreds of ppm) of Pt. It has been previously shown by different authors (Amosse et al., 1990; Farges et al., 1999; Ginther, 1971) that platinum can enter silicate and aluminosilicate

melts from a crucible. Even though such amounts of Pt should not affect noticeably the structure and macroscopic properties of the studied glasses and melts it is worth remarking that it does change the colour of the glasses from colourless to dark yellow (Figure II.1).



Figure II.1. Samples of BA60.10 (*left*) BA50.12 (*centre*) and BA42.14 (*right*) glasses illustrating increasing capacity of melts to incorporate Pt from the crucible.

1.2. Glass synthesis from ceramic

If glass samples could not be obtained directly by traditional quenching, ceramic samples were prepared following the above-described procedure and an aerodynamic levitation device coupled with two CO₂ lasers (Coté et al., 1992; Hennet et al., 2006) was used to prepare small glass spheres. For this, a small piece of ceramic was placed into the levitator's nozzle, heated up to the temperature just above the liquidus (typically determined visually) by means of the lasers. Each sample was held at a high temperature in order to obtain bubble-free glass and quenched by turning the power of the lasers off (Figure II.2).

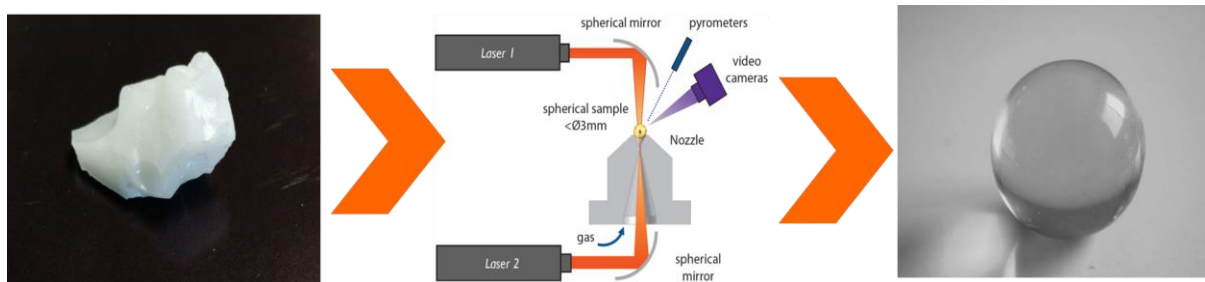


Figure II.2. Schematic representation of glass syntheses from ceramic samples using the levitation device.

With this procedure, a very high temperature ($> 2500\text{ }^{\circ}\text{C}$) can be reached and therefore refractory compositions for which $T_m > 1750\text{ }^{\circ}\text{C}$ can be melted. The cooling rate of the melt during the quench with this technique is around $300\text{ }^{\circ}\text{C/s}$ (Neuville et al., 2008) and this allows vitrifying the compositions readily crystallized using a traditional quench procedure described above. However, one should pay attention not to increase the temperature too

much since some components of melt could easily volatilize and, as a consequence, the composition of the melt will not be the same afterwards. Another limitation of the technique is a glass sample's size. Depending on the vitrification ability of a particular system it can vary between 1 and 3 mm but generally, it never exceeds 4 mm in diameter (due to difficulties in levitating massive samples), keeping in mind that the smaller the droplet size the higher the quench rate.

1.3. Direct synthesis on the levitator

Two samples (BA33.43 and BA50.40) were synthesised in a different manner. Dry powders of SiO_2 , Al_2O_3 and BaCO_3 were mixed in a stoichiometric amount to make 5 g batches. The powders were ground together in an agate mortar under ethanol for 30 minutes and compressed into several pellets each. Then the pellets were broken into small pieces and those pieces were used to make glass spheres by means of the levitation device (as it is described before).

2. Chemical composition analysis

Chemical compositions of glasses/ceramics were verified by means of electron micro probe analysers (EMPA) at CAMPARIS (Paris, France).

2.1. Method's description

Under the exposure of a sample to a beam of electrons, the atoms composing the sample are ionized. Filling in the vacancy with another atom's electron produces X-rays. The energy of the X-rays is element-dependent and their intensity depends on the element's concentration. Detection of the X-rays produced by the ionization of the atoms allows determining the chemical composition of the material. However, before any measurements, an EMPA needs to be calibrated with standard materials with known composition and the concentration of the elements.

2.2. Limitations

- Samples should not be exposed to the beam of electrons of high intensity. Long exposures to the beam should be avoided as well. Otherwise, some elements may volatilize under the exposure.

- Ideally, standards used for the calibration should be compositionally close to analysed samples and be in the same state (i.e., glass standards for analysis of glasses etc.). Nevertheless, this condition is rarely satisfied which produce an absolute error of 1 % order.
- The elements lighter than boron cannot be measured directly, so their content is typically estimated as the difference.

2.3. Experimental details

In order to carry out the analysis, small pieces of glasses/ceramics were incorporated into silicone resin. Then the pieces were polished with SiC abrasive papers of different grain size and diamond polishing paste in order to produce optical quality surfaces. Afterwards, the surface was metallized by depositing some graphite on it. It was made for improving the electrical conductivity of the exposed surface in order to avoid accumulation of charges under the action of the beam of electrons. Two instruments were used to carry out the analysis: a Cameca SX100 EMPA and a Cameca SXFive EMPA. The accelerating voltage of 15 kV and the counting time of 90 s were used, with a current of 10 and 40 nA, respectively. Each composition is an average of at least 10 measurements. The results of the analyses are given in Annex III.

3. Density measurements

The densities of the glasses were measured using the Archimedean method.

3.1. Method's description

The principle of the method is that a sample is weighed in air and then in an immersed liquid. Then its density can be calculated using these two values and the density of the immersed liquid.

3.2. Limitations

The method gives erroneous density values for glasses if the sample is partially crystalline, has bubbles captured by melt during the quench or has pores that cannot be filled with the liquid (due to poor wetting etc.).

3.3. Experimental details

Bubble-free pieces of glass were weighed in air and in toluene at a given temperature, and density, d (in g/cm^3), was calculated as

$$d = \frac{m_{air} \cdot d_{tol}(t)}{m_{air} - m_{tol}}$$

where m_{air} is a mass of an object in the air (in g), m_{tol} is a mass of an object immersed into toluene (in g), $d_{tol}(t)$ is temperature dependent density of toluene that can be calculated as

$$d_{tol}(t) = 0.8845 - 0.9159 \cdot 10^{-3} \cdot t + 0.368 \cdot 10^{-6} \cdot t^2$$

where t is an ambient temperature (in °C).

Before each run of measurements, a standard sample of sapphire was taken through the procedure. The run was started only if three consecutive measurements of the sapphire's density gave $3.987 \pm 0.001 \text{ g}/\text{cm}^3$ value. All the densities are listed in Annex III and are an average of at least 3 measurements performed on different pieces of the same glass.

4. Differential scanning calorimetry

4.1. Method's description

Differential Scanning Calorimetry (DSC) is an analytical technique allowing detection of exothermic or endothermic events (e.g., glass transition, crystallization, melting) in a sample under temperature change. For this, a studied sample and a reference sample are placed into a DSC apparatus and subjected to a concurrent temperature change. In this condition, the difference in the amount of heat required to change the temperature of both samples is measured as a function of time. Further data treatment allows extracting values of glass transition temperatures, melting points etc.

4.2. Limitations

The values obtained from DSC measurements depend strongly on the heating/cooling rate (rate of the temperature change). Usually, at higher heating rate the crystallization peak shifts to higher temperatures. It is also important in which form the sample is studied. A bulk sample and powder of the same composition give different values of the melting point, for example. The grain size also affects DSC measurements.

4.3. Experimental details

Glass transition temperatures (T_g) of some SAS glasses and tectosilicate and silicate glasses in the BAS system were measured using a Setaram® L96 Evo TGA-DTA/DSC apparatus at the IPGP (Paris, France). A glass sphere of the studied glasses was put in a platinum crucible and placed into the apparatus together with an empty platinum crucible used as a reference. The experimental chamber was evacuated first and then filled with Ar. Further heating was conducted with a rate of 5 °C/min up to 1500 °C. T_g were determined from the curves of heat flow versus temperature as an inflection point. Glass transition temperatures of ZAS glasses and peralkaline glasses in the BAS system were measured with Setaram® MHTC 96 apparatus at the CEMHTI (Orléans, France). For these measurements, glass powders instead of glass spheres were used. The heating rate was 10 °C/min and before the measurements, each sample was thermostated at 150 °C for 30 minutes. Glass transition temperatures were determined as inflection points of the heat flow curves.

To have T_g values comparable to those obtained from viscosity measurements, a correction of - 22 K was applied to all T_g obtained from DSC following the idea of (Neuville et al., 2010) and as implemented in (Le Losq, 2012; Novikov et al., 2017).

5. Viscosity measurements

The high-viscosity measurements on glasses at temperatures below 1000 °C were carried out using a creep apparatus (Figure II.3) described in more details elsewhere (Neuville, 2006, 1992; Neuville and Richet, 1991).

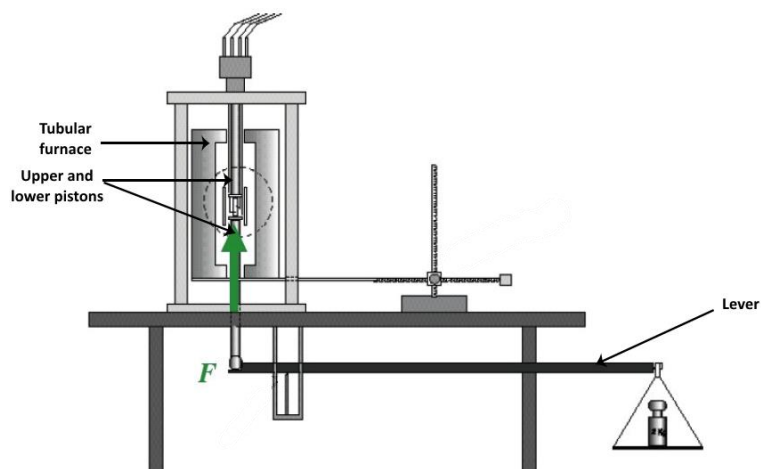


Figure II.3. Schematic representation of the creep apparatus used for viscosity measurements (reproduced after (Le Losq, 2012)).

5.1. Method's description

The principle of operation of the apparatus is following. A glass sample is exposed to a constant uniaxial compressive stress at a given temperature. Thus, the sample's deformation rate is measured and the viscosity at a given temperature can be calculated further. The dynamic (shear) viscosities, η (in Pa·s), are calculated from the experimental measurements by the following equation:

$$\eta = \frac{\sigma}{3\left(\frac{d \ln l}{dt}\right)}$$

where σ is the applied constant stress (in N/m²), l is the length of the sample (in m), and t is the deformation time (in s). The applied constant stress, σ , can be determined from the relation

$$\sigma = \frac{M \cdot g}{S(\tau)}$$

where M is the load applied to the sample on a shorter lever's arm (in kg), g is the gravitational acceleration (taken as 9.81 m/s²), and $S(\tau)$ is the cylinder's surface area at given time τ . $S(\tau)$ depends on the initial surface area $S(0)$ (an uncompressed sample), the height of the sample $L(\tau)$ at the time τ , and the deformation dL occurring during the time τ , and is given by

$$S(\tau) = S(0) \cdot \frac{L(\tau)}{L(\tau) - dL}$$

The load M applied to the sample is defined as

$$M = -263.94 + 4.0695m - m_x$$

where m is the load applied on a longer lever's arm (in kg), m_x is the sum of masses of alumina plates, platinum foils and of a sample. The part of the previous equation (namely, $-263.94+4.0695m$) was determined experimentally through the lever's calibration. Details of such a calibration are given elsewhere ([Neuville, 1992](#)) and the calibration curve is presented in Figure II.4.

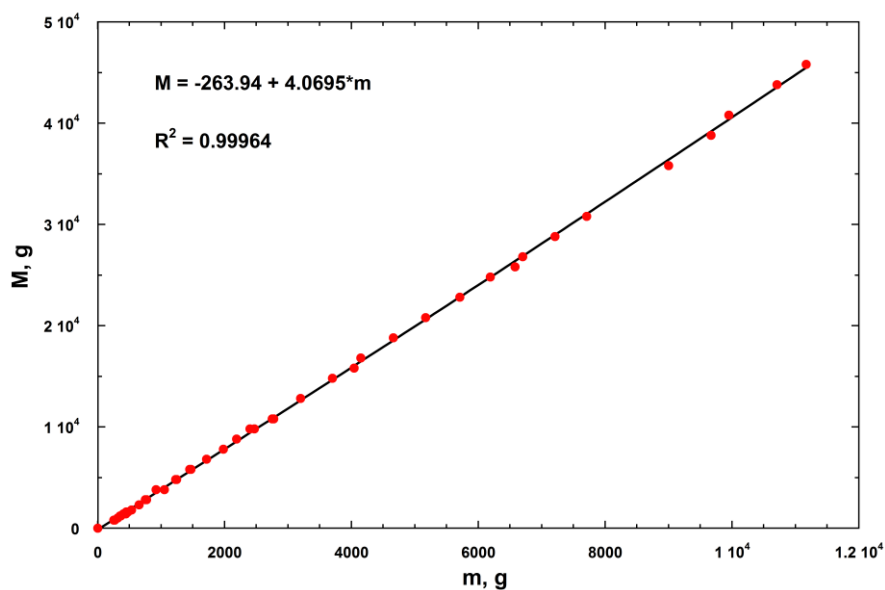


Figure II.4. The load calibration curve used for viscosity calculations.

5.2. Limitations

The apparatus allows measuring viscosities in the range of $10^8 - 10^{13}$ Pa·s at temperatures up to 1000 °C. A few things to pay attention to are crystallization and deformation of a sample. The first thing can happen in the case when the sample spends too much time under the pressure at an elevated temperature. The presence of crystals will increase the viscosity of the sample producing erroneous results. The second one concerns the loss by the sample of its cylindrical shape with time under applying stress. In this case, the above-described formulae cannot be used anymore. Therefore, the samples with deformation exceeding 50 % were not used.

5.3. Experimental details

Samples used for the measurements were glass cylinders with height to diameter ratio $H/D \approx 2$ ($H = 10-15$ mm, $D = 5-7$ mm). To produce bubble-free samples for the high-viscosity measurements, at the final stage of syntheses the products were maintained at the temperatures above their melting points for several hours. Next, the melt was poured into holes of different diameters drilled in a graphite bar (Figure II.5). Still hot glass was then placed together with the bar into a furnace preheated to a temperature below the estimated T_g values (typically, in the range of 600-800 °C). It was left there overnight to remove internal stress and, thus, to avoid its breaking under further sawing and polishing. Then glass cylinders were cut off from the rest of the glass mass and polished from the two

sides in order to have parallel faces. If the viscosity of the bubble-free melt was too high to pour it out of the crucible, another strategy was employed. The crucible was cooled down by putting its bottom into cold water and placed into a furnace preheated to a temperature below T_g . It was left there overnight to remove internal stress. Then glass cylinders were directly drilled out from the glass and polished from the two sides in order to have parallel faces.



Figure II.5. An example of glass produced by pouring melt into a graphite mould.

For viscosity measurements, a cylindrical sample was put between two pistons – a fixed upper one and a mobile lower one – separated from them by thin platinum foils and thick alumina plates. Temperature measurements were made with two thermocouples (90%Pt/10%Rh-Pt alloy) placed at the top and bottom positions and on the opposite sides of the cylinder (Figure II.6).

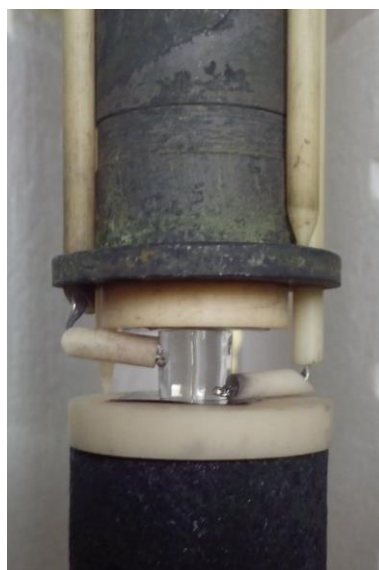


Figure II.6. A cylindrical glass sample put between the pistons. The thermocouples and the thick alumina plates are also visible.

To reduce temperature gradient along the sample a silver cylinder was placed around the sample and fixed on the upper piston. This measure allowed reducing the temperature difference between the top and the bottom of the sample down to 0.2-0.3 °C. For the measurements of viscosity in the temperature range from 950 to 1000 °C the silver cylinder was taken out. In this case, the gradient was more important but still less than 1 °C. Constant stress to the sample was applied through the lower mobile piston connected with a lever's shorter arm. Putting loads of different masses on the longer arm of the lever allowed applying different stresses at a given temperature. The changes in samples height were registered by means of two linear variable differential transformers kept in touch with two alumina rods resting on the pistons. The reported viscosity values at one temperature are the result of an average of 20-40 measurements at different applied stresses. The difference in viscosity measurements was not greater than 0.03 log₁₀(Pa·s). The reported temperatures are an average of measurements of the two thermocouples (taking into account cold-junction corrections).

6. Raman spectroscopy

The organization of the studied glasses at the medium range scale was investigated by means of Raman spectroscopy. Raman spectroscopy is a spectroscopic technique allowing observation of vibrational modes in a system. This technique relies on inelastic scattering of excitation light, also known as Raman scattering ([Landsberg and Mandelstam, 1928](#); [Raman, 1928](#)).

6.1. Method's description

Light can interact with matter in different ways. For example, it can be transmitted, absorbed or reflected. A certain fraction of transmitted and/or reflected light can be, in its turn, scattered due to irregularities in the propagation medium (such as fluctuations in density and/or composition). In a scattering event, light interacts with the atoms' electron clouds causing them to distort. This polarization creates an induced dipole which vibration gives a scattered photon. If the vibration occurs at the same frequency as an incident light (i.e., only electron clouds' distortion is involved), then such a process is called elastic scattering (also known as Rayleigh scattering). The Rayleigh scattering is the dominant

process. During elastic scattering the kinetic energy of an incident photon is conserved and, thus, the wavelength of the incident light will not be changed. If the vibration of an induced dipole involves atomic movements, it causes the vibrational frequency to change, and such a process is called inelastic scattering (or Raman scattering). In contrast to elastic scattering, the kinetic energy of the resulting inelastically scattered photon can be either lower or higher than that of the incident photon due to interactions with the medium. Thus, the wavelength of the incident light will be altered. The Raman scattering is a weak process. In fact, only one in every 10^6 - 10^8 scattered photons is inelastically scattered (Smith and Dent, 2005).

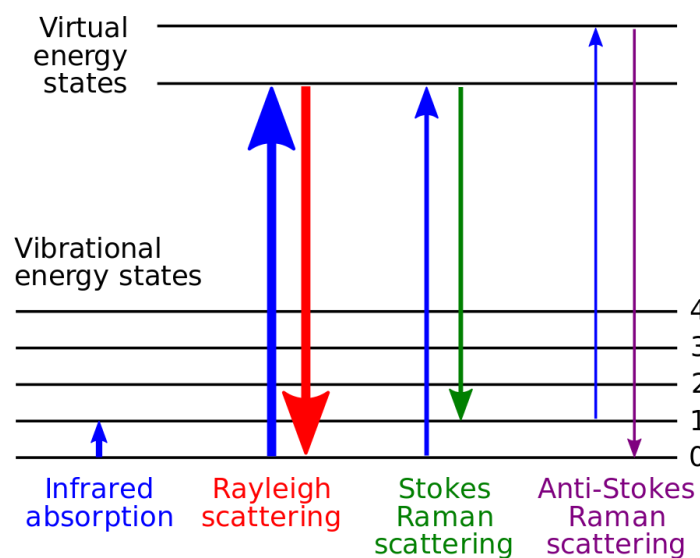


Figure II.7. A diagram of energy states involved in Raman scattering (from Wikimedia Commons).

Let's consider a situation when most structural motifs are present in the ground vibrational state (denoted "0" in Figure II.7). Under the interaction with light, an oscillating polarization in these motifs occurs. This polarization creates a short-lived state called a "virtual energy state". This state is not stable and the system quickly returns to the vibrational states. Most of the time it returns to the ground vibrational state. In such case, Rayleigh scattering will be observed. However, the system can return to a vibrational state of higher energy (state "1") producing a scattered photon possessing lower energy (longer wavelength). Such event is called Stokes Raman scattering. At the same time, some of the structural motifs can already be present in a higher energy state "1". If the system now comes to a "virtual state" and returns to the ground state it will produce a scattered photon possessing higher energy (shorter wavelength). Such event is called anti-Stokes Raman

scattering. Since at ambient conditions the population of the ground vibrational state is overwhelming, the intensity of Stokes scattering is much higher than that of anti-Stokes. Thereby, all our spectra represent Stokes Raman scattering. Raman shifts ($\Delta\omega$) are typically reported in wavenumbers and are given as

$$\Delta\omega = \frac{1}{\lambda_0} - \frac{1}{\lambda_i}$$

where λ_0 is the excitation wavelength and λ_i is the Raman spectrum wavelength.

6.2. Limitations

Even though Raman spectroscopy has many advantages (e.g., no or little need in specific sample preparation) it has also some limitations. For example, a phenomenon of fluorescence can arise during measurements of a Raman spectrum of glass. This phenomenon can at some cases severely interfere with the Raman signal, making it very hard to analyse Raman spectra. To eliminate or at least reduce the fluorescence the photobleaching or another excitation source are recommended. Hopefully, no fluorescence was observed during our measurements.

6.3. Experimental details

Unpolarized Raman spectra were recorded at room temperature using a T64000 Jobin-Yvon® triple Raman spectrometer equipped with a confocal system, a CCD cooled by liquid nitrogen and an optical microscope. A Coherent® 70-C5 argon laser with a wavelength of 488.01 nm and with a power of 0.85 W was used as the excitation source. All spectra were acquired in backscattering geometry between 20 and 1400 cm^{-1} with an acquisition time of 300 s and 3 repetitions per spectral window. No special sample preparations were made in advance. Before the deconvolution of the high-frequency region, all spectra were baseline corrected and normalized in such a manner that the total area under a spectrum was equal to one. Then the high-frequency region of the spectra was deconvoluted using the Fityk software (Wojdyr, 2010). All parameters, such as band's frequency, width and intensity were not constrained during the deconvolution procedure.

7. Nuclear magnetic resonance spectroscopy

The organization of the studied glasses at the short-range scale was investigated by means of the solid-state Nuclear Magnetic Resonance (NMR) spectroscopy (or for short just NMR). It is an element-specific technique that probes the chemical environment of atoms and gives information on their coordination number.

7.1. Method's description

To observe an NMR signal several conditions must be met:

- The nucleus under study has a non-zero spin;
- A constant magnetic field is applied to the sample in order to polarize nuclear spins;
- The alignment of spins is perturbed by employing a radio frequency (RF) pulse.

The nuclear spin, I , is an intrinsic property of a nucleus. It is a highly abstract concept and its description is far beyond the scope of the manuscript (those who are eager to understand the subject are invited to read, for example, [\(Levitt, 2008\)](#)). The important thing to know is that not all the isotopes are NMR active. Only nuclei with an odd number of protons and/or neutrons (e.g., ^{17}O , ^{27}Al , ^{29}Si etc.) possess a non-zero spin and, therefore, can give an NMR signal. All nuclei with a non-zero spin have a magnetic moment, μ , given by

$$\mu = \gamma I$$

where γ is the gyromagnetic ratio specific to each nucleus. In other words, nuclei behave as small magnets. In the absence of an external magnetic field (B_0), the magnetic moments of nuclei are oriented randomly in the space and there is no energetic difference for any particular orientation. When the nuclei are exposed to an external magnetic field, a splitting between the nuclear spin levels (also called the Zeeman splitting, [\(Zeeman, 1897\)](#)) occurs. In the case of nuclei of ^{29}Si ($I = \frac{1}{2}$), for example, it means that the magnetic moments of the silicon nuclei align themselves either parallel or antiparallel to B_0 (Figure II.8).

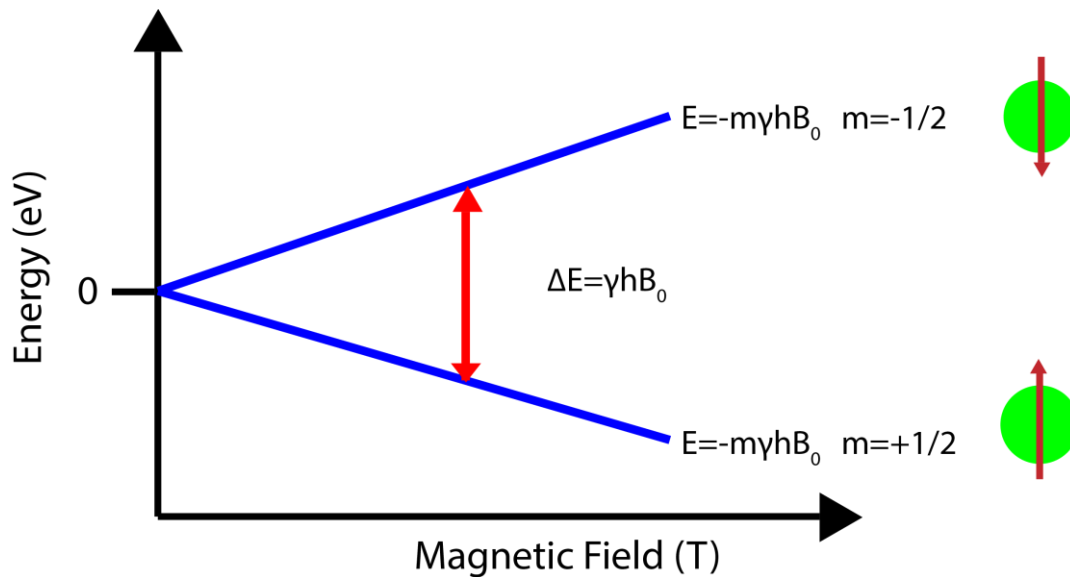


Figure II.8. Zeeman splitting for a nucleus with $I = \frac{1}{2}$ (from Wikimedia Commons).

The difference between the energy levels, ΔE , is proportional to the magnitude of the external magnetic field and to the gyromagnetic ratio:

$$\Delta E = \hbar\gamma B_0$$

where \hbar is the reduced Planck constant. In this condition of the Zeeman, splitting nuclei become able to absorb radio-frequency radiation of the exact energy equal to the ΔE . This causes spins to “flip” or, in other words, excites the transition of some nuclear spins to the high energy level. With time, the excited spins return to the ground state due to relaxation processes and release energy into the lattice. The two types of relaxation are spin-lattice (longitudinal) relaxation and spin-spin (transversal, energy conserving) relaxation. However, the magnetic moments being in B_0 are not perfectly aligned with it. They precess around the axis of B_0 with a frequency specific for each isotope called the Larmor frequency. This frequency of precession is proportional to the external magnetic field and equal to

$$\omega = -\gamma B_0$$

And it is this frequency that the excitation radio frequency should be matched to. Otherwise, the NMR phenomenon will not be observed.

Nevertheless, nuclei of a given nature (e.g., ^{27}Al , ^{29}Si etc.) do not resonate all at the same frequency. Due to the magnetic shielding effect of the electrons, the nuclei with different chemical environments will experience different local magnetic fields and hence

give signals at different frequencies. Any influence on this local magnetic field, caused by variations of the chemical bonding scheme (interactions with nucleus' neighbours in the first and the second coordination spheres) will slightly change the ΔE . The small change in the energy levels causes the change in the frequency required for the transition of nuclei from one energy level to a higher one. In this way, different degree of nuclear shielding gives different peaks in an NMR spectrum. For convenience' sake, a concept of a chemical shift has been introduced to the NMR spectroscopy. The chemical shift, δ , is the resonant frequency of a nucleus relative to a standard, defined as

$$\delta = \frac{\omega_s - \omega_{ref}}{\omega_{ref}}$$

where ω_s is the Larmor frequency of a particular nucleus and ω_{ref} is the Larmor frequency of the same isotope in a reference substance.

A quadrupolar nucleus is a nucleus with a spin quantum number greater than $\frac{1}{2}$. For example, nuclei ^{17}O and ^{27}Al have spin $5/2$. Unlike the nucleus with the spin $\frac{1}{2}$ (e.g., ^1H and ^{29}Si), the Zeeman splitting for such nuclei gives more than 2 energy levels. NMR signals of such nuclei are typically complicated due to strong quadrupolar interactions causing complex line broadening as well as the appearance of several lines arising from the various allowed energy transitions.

In the Solid-State NMR spectroscopy lines are broad due to anisotropic nuclear spin interactions. They are much broader than in the Liquid- or Solution-State NMR. In liquids, these interactions are averaged out because of the rapid motion of the particles constituting a compound. To improve the spectral resolution by narrowing the NMR lines, the Magic Angle Spinning (MAS) technique is used ([Andrew et al., 1958](#); [Lowe, 1959](#)). This technique involves spinning of a sample at the "magic angle" of approximately 54.7° with respect to the magnetic field B_0 (Figure II.9). Such spinning removes dipolar interactions and averages chemical shift anisotropy and the first order quadrupolar interactions (for nuclei with $I > \frac{1}{2}$). It improves the quality of a spectrum and permits analysis and quantification of NMR lines.

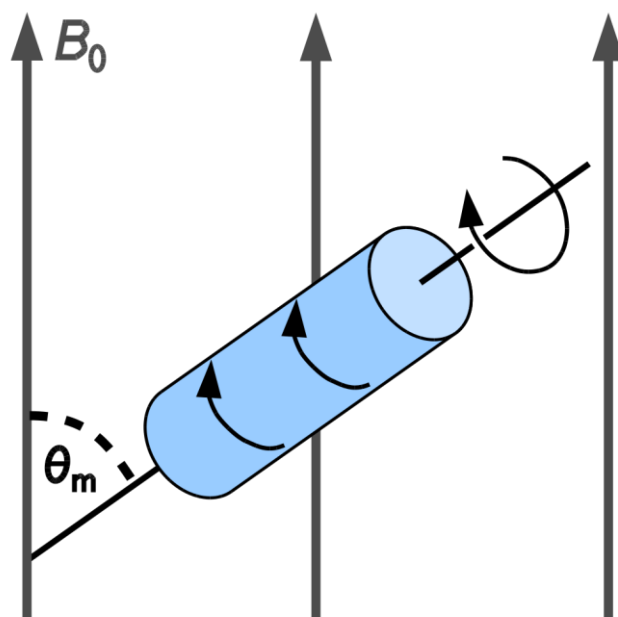


Figure II.9. Illustration of the Magic Angle Spinning (MAS) principle. A sample is rotating in the magnetic field (B_0) at the angle $\theta_m = 57.4^\circ$ between the axis of rotation and the B_0 (from Wikimedia Commons).

7.2. Limitations

NMR spectroscopy is an element specific method and it can be considered as both, an advantage and a disadvantage at the same time. It is possible to look on the incorporation of specific atoms into different structural units within the network, but it is not possible to see the overall structure of a material at once. NMR is a low-sensitive technique meaning that the difference in populations of two energy levels (case of $I = \frac{1}{2}$) is miserable. For instance, in the magnetic field of 18.8 Tesla, having 1 million atoms on the upper level, on the lower level there are only 1 million plus 128 atoms (James, 1998). If one considers the characteristic time scales, NMR is a relatively slow method. It produces an averaged spectrum and the amount of information is greatly reduced upon fast phenomena.

Some NMR active nuclei have a very low natural abundance. For example, natural abundance of ^{27}Al is 100 % that means that all aluminium atoms in a sample give the NMR signal. On the other hand, ^{29}Si is only 4.7 % and ^{17}O is even less – about 0.04% of all isotopes. This means that the NMR signal of samples with a natural abundance of these isotopes will be weak only because of a small fraction of atoms giving a contribution to the NMR signal. To obtain NMR spectra of such nuclei either long acquisitions (days or weeks) or isotope enrichment are required.

7.3. Experimental details

A. ^{27}Al MAS NMR

Quantitative 1 pulse ^{27}Al MAS NMR experiments were performed on an Avance III Bruker 850 MHz (20.0 T) spectrometer working at an ^{27}Al frequency of 221.5 MHz. Chemical shifts for ^{27}Al are referenced to a 1 M aqueous $\text{Al}(\text{NO}_3)_3$ solution. Magic Angle Spinning (MAS) experiments were performed at a spinning speed of 30 kHz in aluminium-free zirconia rotors of 2.5 mm diameter. All spectra were obtained using a single-pulse (“Bloch-decay”) sequence using a radio-frequency field $\nu_{\text{rf}} = 62.5$ kHz and applying a pulse of 0.4 μs (i.e. less than $\pi/18$ to ensure quantitative irradiation). Four thousand scans were accumulated for each composition with a recycling time of 0.15 s (spin-lattice relaxation times found in the range 1-5 s), using a spectral window of 2 MHz to avoid folding of the spinning sidebands manifold. The decomposition of the spectra was obtained using the dmfit software (Massiot et al., 2002), taking into account the spinning sidebands of the external transitions. This allows extracting the populations of the various components appearing on the central transition, their mean isotropic chemical shifts δ_{iso} , their distributions of isotropic chemical shift $\Delta\delta_{\text{iso}}$ and their mean quadrupolar coupling constants C_Q within the framework of the so-called “Czjzek” or “GIM” model (Le Caër and Brand, 1998).

B. HT ^{27}Al NMR

High-temperature ^{27}Al NMR experiments were carried out on an Avance I Bruker 400 MHz (9.4 T) spectrometer working at an ^{27}Al frequency of 104.3 MHz. Chemical shifts for ^{27}Al are referenced to a 1 M aqueous $\text{Al}(\text{NO}_3)_3$ solution in a quartz tube placed at the position of levitated samples. All spectra were acquired with a $\pi/2$ pulse of 50 μs , the spectral width of 25 kHz and the recycled delay of 1 ms. Each measurement is a set of 512 individual NMR spectra. The experimental setup followed previous laboratory-designed ones (Florian et al., 1995; Massiot et al., 1995) and was performed such as a spherical glass sample of 2.5-2.7 mm in diameter was put into a convergent-divergent nozzle (Figure II.10) made of aluminium and heated from the top and bottom by two CO_2 lasers while levitating. The samples were rapidly heated up to the temperature above their liquidus maintained at this temperature for 1-2 s and then cooled down by switching off the laser power. At the

same time, acquisition of the pyrometer's signal together with NMR acquisition was triggered taking a one-scan spectrum each 9 ms. The total experiment's duration, including heating of the sample with consequent cooling and the NMR acquisition, was less than 10 s. Such short exposures allowed reducing weight loss due to volatilization of the components of the melts down to 1-2 %. The background signal from the aluminium nozzle did not interfere with the main signal. However, the replacement of the boron nitride nozzle by the aluminium one allowed using air as levitating gas without fear of nozzle's decomposition at high temperatures and represents a significant difference with the previous settings used in the laboratory.

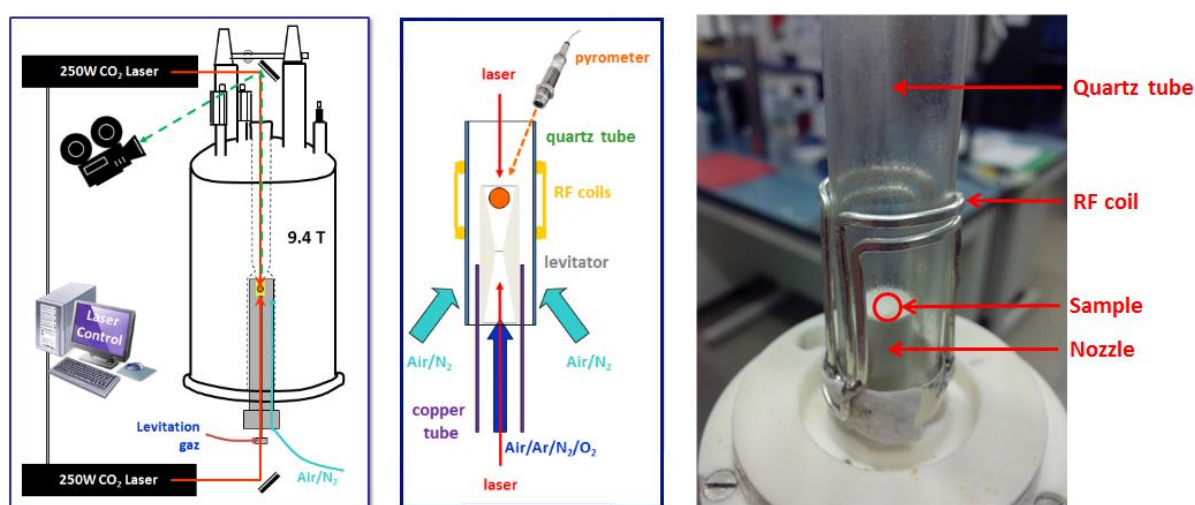


Figure II.10. *Left*: schematic representation of the HT NMR setup. *Centre*: schematic representation of the HT NMR probe. *Right*: the upper part of the HT NMR probe. The protective quartz tube and the RF coil are visible with the levitator's nozzle inside.

The temperature of the sample during the experiments was monitored with an IMPAC IN 140/5-H pyrometer ($\lambda = 5.14 \mu\text{m}$) allowing measurements from 500 to 2500 °C. The pyrometer was focused on the reflection of the sample in the top mirror. However, the area monitored by the pyrometer was greater than the sample's reflection. A temperature calibration (Figure II.11) was made against the observed recalescence of the compounds with known crystallization temperature (Al_2O_3 , SrSiO_3 , $\text{CaMgSi}_2\text{O}_6$, Li_2SiO_3). Spheres of different diameters were used for each compound and several crystallization events were registered and averaged for each sphere.

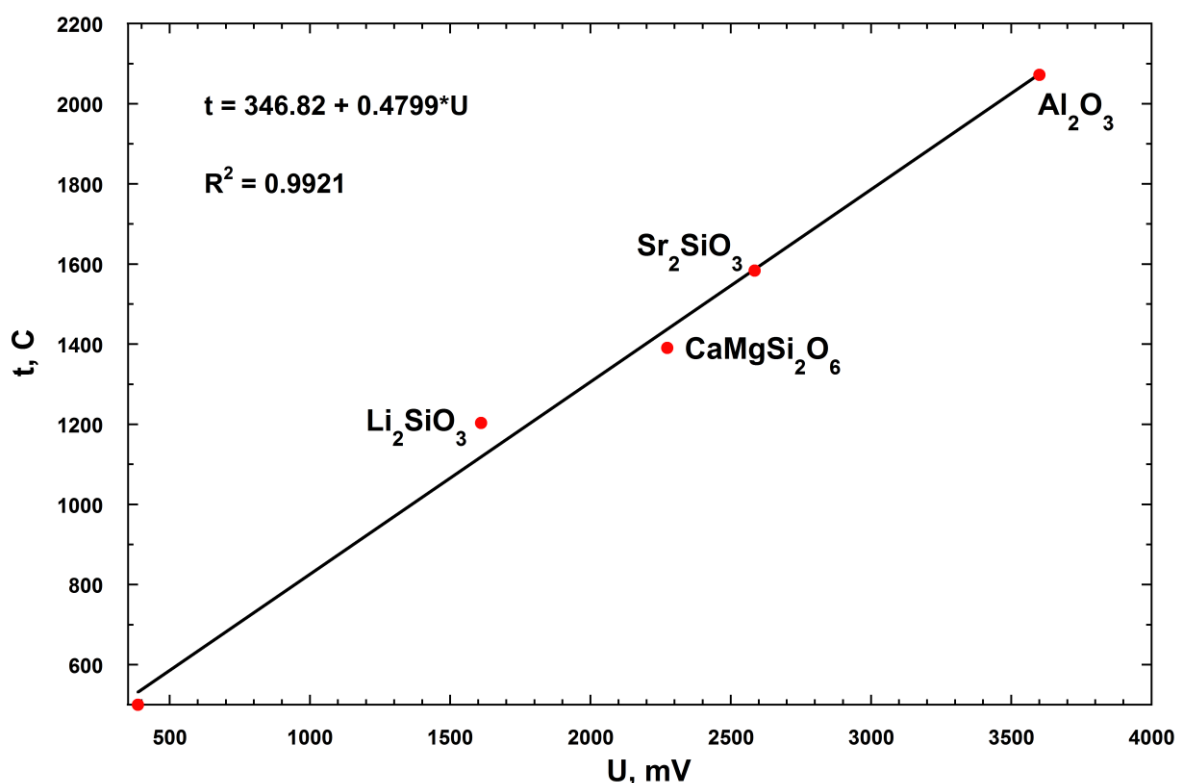


Figure II.11. Temperature calibration curve used in HT NMR experiments.

C. ^{29}Si NMR

^{29}Si MAS NMR experiments were performed on an Avance III Bruker 400 MHz (9.4 T) spectrometer working at a ^{29}Si frequency of 79.5 MHz. Chemical shifts for ^{29}Si are referenced to tetramethylsilane (TMS). Magic Angle Spinning (MAS) experiments were performed at a spinning rate of 14 kHz in zirconia rotors of 4.0 mm diameter. All spectra were obtained using the Carr-Purcell-Meiboom-Gill (CPMG) echo train acquisition (Carr and Purcell, 1954; Meiboom and Gill, 1958) with 250 echoes in each train and the recycle delay of 300 s.

8. Neutron diffraction

Neutron diffraction (ND) allows describing the structure of disordered materials through the pair distribution function (PDF). The PDF is related to the probability of finding an atom at the distance r away from another atom taken as a zero point and thus describe the distribution of distances between pairs of atoms composing the material.

8.1. Method's description

The diffraction is an elastic scattering process, meaning that scattered photons/particles have the same energy as the incoming ones but their direction is modified and depends on the atomic organisation of the sample. In the case of ordered crystalline solids the diffraction can be described using the Wulff-Bragg's condition:

$$2d \sin \theta = n\lambda$$

where λ is the wavelength of the incident wave, d is the distance between crystal planes, θ is the angle of the scattered wave, n is the so-called order of the diffracted beam taking positive integer values. However, for disordered systems, such as glasses and melts, the Bragg peaks are absent in diffraction, because there is no long range order (LRO), i.e. no regular lattice, in these systems. Typically, in diffraction experiments on disordered systems the static structure factor, $S(q)$, is measured:

$$S(q) = \frac{1}{N} \sum_{j=1}^N \sum_{k=1}^N e^{-iq(r_j - r_k)}$$

where N is the total number of atoms, i is the imaginary unit, r_j and r_k are the positions of j and k atoms, q is the scattering vector defining the direction of any scattered wave and defined as

$$q = \frac{4\pi}{\lambda} \sin \theta$$

where λ is the wavelength of the incident wave and θ is half of the angle between the incident and scattered beams. The obtained static structure factor, $S(q)$, is further Fourier transformed providing the pair distribution function, $g(r)$:

$$g(r) - 1 = \frac{1}{2\pi\rho r} \int_0^{\infty} [S(q) - 1] \sin(qr) dq$$

where ρ is the average number density of particles. As shown in Figure II.12 the position of each peak of $g(r)$ corresponds to an interatomic distance.

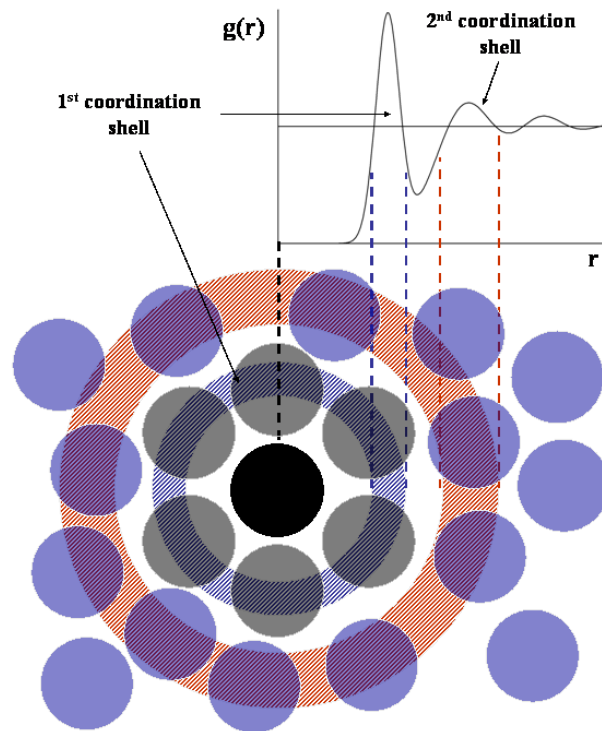


Figure II.12. Illustration of the concept of pair distribution function (from Wikimedia Commons).

Coordination numbers (CN) of the atoms can be found by fitting the radial distribution function (RDF). However, for the convenience' sake, $g(r)$ is transformed into the total correlation function, $T(r)$:

$$T(r) = \frac{RDF(r)}{r} = 4\pi\rho r \cdot g(r)$$

The advantage of using the $T(r)$ for the CNs determination is that the peaks become symmetric and they can be fitted with Gaussian bands. Hence, the CN is calculated as the area under a particular peak:

$$CN = r_i \int_{r_1}^{r_2} T(r) dr$$

where r_i is the position of a particular peak of the $T(r)$.

8.2. Limitations

The PDF (as well as the static structure factor) is a weighted sum of contributions of all pairs of atoms. Therefore, a possible large overlapping of the peaks in $g(r)$ is a common

issue for ND measurements performed on aluminosilicate glasses. This overlapping tangles the analysis, i.e. the extraction of bond lengths and coordination numbers. Another feature of ND experiments is, typically, quite long acquisitions that are required even with modern high-flux neutron sources.

8.3. Experimental details

ND experiments on Sr aluminosilicate glasses and one BAS composition (BA50.25) were carried out at the D4c instrument (Figure II.13) at the Institut Laue-Langevin (Grenoble, France). The neutron source produces an intense continuous neutron flux ($1.5 \cdot 10^{15}$ neutrons per cm^2 per second) with the top thermal power of 58.3 MW. An overview of the instrument can be found elsewhere (Fischer et al., 2002). A neutron wavelength (λ) of 0.4985 \AA were selected for the measurements. Glass samples were placed into a vacuum chamber that was pumped down to low pressure (10^{-4} mbar) before each run. It was done in order to have a reproducible background, essential for further data analysis. The samples were glass spheres of 2.5-2.7 mm in diameter. The total duration of each run was about 3 hours, including the displacement of the detector.

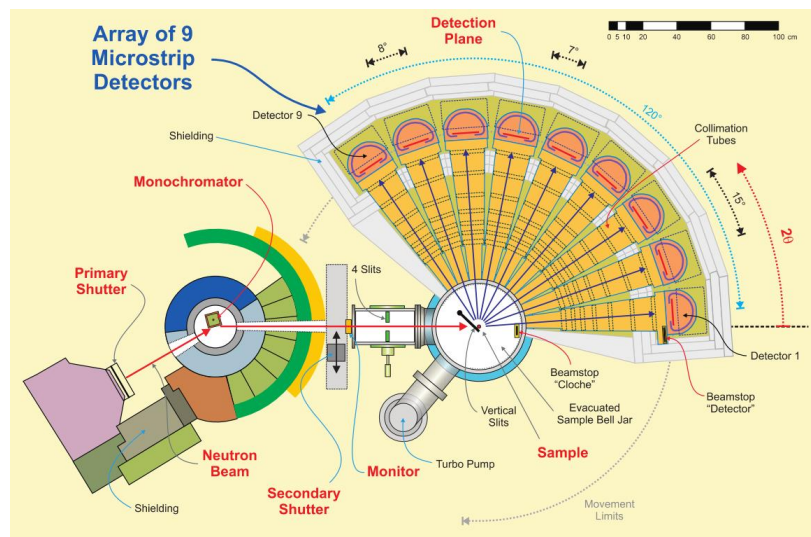


Figure II.13. Top-view schematic of the D4c neutron diffractometer (from (Fischer et al., 2002)).

ND experiments on Ba and Zn aluminosilicates were carried out at the 7C2 diffractometer at the Laboratoire Léon Brillouin (Gif-sur-Yvette, France). The neutron source maximal thermal flux is $3 \cdot 10^{14}$ neutrons per cm^2 per second with the top thermal power of 14 MW. An overview of the instrument can be found elsewhere (Cuello et al., 2016). A neutron wavelength of 0.723 \AA and 0.586 \AA was used for BAS and ZAS compositions,

respectively. Samples used for the measurements were either glass cylinders or packed shards of glass. They were put in cylindrical vanadium containers into a vacuum chamber that was then evacuated to low pressure. The total duration of runs varied from 7 to 18 hours, depending on the quantity of a sample.

Bibliography

- Amosse, J., Allibert, M., Fischer, W., Piboule, M., 1990. Experimental study of the solubility of platinum and iridium in basic silicate melts—Implications for the differentiation of platinum-group elements during magmatic processes. *Chem. Geol.* 81, 45–53. doi:10.1016/0009-2541(90)90038-9
- Andrew, E.R., Bradbury, A., Eades, R.G., 1958. Nuclear Magnetic Resonance Spectra from a Crystal rotated at High Speed. *Nature* 182, 1659–1659. doi:10.1038/1821659a0
- Carr, H.Y., Purcell, E.M., 1954. Effects of Diffusion on Free Precession in Nuclear Magnetic Resonance Experiments. *Phys. Rev.* 94, 630–638. doi:10.1103/PhysRev.94.630
- Coté, B., Massiot, D., Taulelle, F., Coutures, J.-P., 1992. ²⁷Al NMR spectroscopy of aluminosilicate melts and glasses. *Chem. Geol.* 96, 367–370. doi:10.1016/0009-2541(92)90065-D
- Cuello, G.J., Darpentigny, J., Hennet, L., Cormier, L., Dupont, J., Homatter, B., Beuneu, B., 2016. 7C2, the new neutron diffractometer for liquids and disordered materials at LLB. *J. Phys. Conf. Ser.* 746, 12020. doi:10.1088/1742-6596/746/1/012020
- Farges, F., Neuville, D.R., Brown, G.E., 1999. Structural investigation of platinum solubility in silicate glasses. *Am. Mineral.* 84, 1562–1568. doi:10.2138/am-1999-1009
- Fischer, H.E., Cuello, G.J., Palleau, P., Feltin, D., Barnes, A.C., Badyal, Y.S., Simonson, J.M., 2002. D4c: A very high precision diffractometer for disordered materials. *Appl. Phys. A Mater. Sci. Process.* 74, s160–s162. doi:10.1007/s003390101087
- Florian, P., Massiot, D., Poe, B., Farnan, I., Coutures, J.-P., 1995. A time resolved ²⁷Al NMR study of the cooling process of liquid alumina from 2450 °C to crystallisation. *Solid State Nucl. Magn. Reson.* 5, 233–238. doi:10.1016/0926-2040(95)01188-X
- Ginther, R.J., 1971. The contamination of glass by platinum. *J. Non. Cryst. Solids* 6, 294–306. doi:10.1016/0022-3093(71)90021-4
- Hennet, L., Pozdnyakova, I., Bytchkov, A., Cristiglio, V., Palleau, P., Fischer, H.E., Cuello, G.J., Johnson, M., Melin, P., Zanghi, D., Brassamin, S., Brun, J.-F., Price, D.L., Saboungi, M.-L.,

2006. Levitation apparatus for neutron diffraction investigations on high temperature liquids. *Rev. Sci. Instrum.* 77, 53903. doi:10.1063/1.2200756
- James, T.L., 1998. *Fundamentals of NMR*. pp. 1–31.
- Landsberg, G., Mandelstam, L., 1928. Eine neue Erscheinung bei der Lichtzerstreuung in Krystallen. *Naturwissenschaften* 16, 557–558. doi:10.1007/BF01506807
- Le Caër, G., Brand, R.A., 1998. General models for the distributions of electric field gradients in disordered solids. *J. Phys. Condens. Matter* 10, 10715–10774. doi:10.1088/0953-8984/10/47/020
- Le Losq, C., 2012. *Rôle Des Eléments Alcalins Et De l'Eau Sur Les Propriétés Et La Structure Des Aluminosilicates Fondus Et Vitreux: Implications Volcanologiques*. Université Paris Diderot (Paris 7).
- Levitt, M.H., 2008. *Spin dynamics: Basics of nuclear magnetic resonance*, 2nd edition. John Wiley & Sons, Ltd.
- Lowe, I.J., 1959. Free Induction Decays of Rotating Solids. *Phys. Rev. Lett.* 2, 285–287. doi:10.1103/PhysRevLett.2.285
- Massiot, D., Fayon, F., Capron, M., King, I., Le Calvé, S., Alonso, B., Durand, J.-O., Bujoli, B., Gan, Z., Hoatson, G., 2002. Modelling one- and two-dimensional solid-state NMR spectra. *Magn. Reson. Chem.* 40, 70–76. doi:10.1002/mrc.984
- Massiot, D., Trumeau, D., Touzo, B., Farnan, I., Rifflet, J.-C., Douy, A., Coutures, J.-P., 1995. Structure and Dynamics of CaAl₂O₄ from Liquid to Glass: A High-Temperature ²⁷Al NMR Time-Resolved Study. *J. Phys. Chem.* 99, 16455–16459. doi:10.1021/j100044a038
- Meiboom, S., Gill, D., 1958. Modified Spin-Echo Method for Measuring Nuclear Relaxation Times. *Rev. Sci. Instrum.* 29, 688–691. doi:10.1063/1.1716296
- Neuvill, D.R., 2006. Viscosity, structure and mixing in (Ca, Na) silicate melts. *Chem. Geol.* 229, 28–41. doi:10.1016/j.chemgeo.2006.01.008
- Neuvill, D.R., 1992. *Etude des propriétés thermodynamiques et rhéologiques des silicates fondus*.

- Neuville, D.R., Cormier, L., Montouillout, V., Florian, P., Millot, F., Rifflet, J.-C., Massiot, D., 2008. Structure of Mg- and Mg/Ca aluminosilicate glasses: ^{27}Al NMR and Raman spectroscopy investigations. *Am. Mineral.* 93, 1721–1731. doi:10.2138/am.2008.2867
- Neuville, D.R., Florian, P., Le Losq, C., Massiot, D., 2010. Structure et propriété des verres et des liquides : le rôle de l'aluminium. *Matériaux Tech.* 98, 395–402. doi:10.1051/mattech/2011014
- Neuville, D.R., Richet, P., 1991. Viscosity and mixing in molten (Ca, Mg) pyroxenes and garnets. *Geochim. Cosmochim. Acta* 55, 1011–1019. doi:10.1016/0016-7037(91)90159-3
- Novikov, A.N., Neuville, D.R., Hennet, L., Gueguen, Y., Thiaudiere, D., Charpentier, T., Florian, P., 2017. Al and Sr environment in tectosilicate glasses and melts: Viscosity, Raman and NMR investigation. *Chem. Geol.* 461, 115–127. doi:10.1016/j.chemgeo.2016.11.023
- Raman, C. V., 1928. A new radiation. *Indian J. Phys.* 2, 387–398.
- Smith, E., Dent, G., 2005. *Modern Raman Spectroscopy - A Practical Approach*. John Wiley & Sons, Ltd, Chichester, UK. doi:10.1002/0470011831
- Wojdyr, M., 2010. Fityk: a general-purpose peak fitting program. *J. Appl. Crystallogr.* 43, 1126–1128. doi:10.1107/S0021889810030499
- Zeeman, P., 1897. The Effect of Magnetisation on the Nature of Light Emitted by a Substance. *Nature* 55, 347–347. doi:10.1038/055347a0

Chapter III

Strontium aluminosilicates (SAS)

In this chapter we will discuss results obtained for Sr aluminosilicate glasses and melts. The chapter is divided into several sections dedicated to particular domains of the ternary diagram (Figure III.1). In total, there are four domains that differ by the ratio $R = \text{SrO}/\text{Al}_2\text{O}_3$: a domain of silicates ($R = \infty$), a peralkaline join ($R = 3$), a tectosilicate or charge compensated join ($R = 1$) and a peraluminous domain ($R < 1$). Glass names are given as $\text{SA}_{xx.yy}$, where “S” stands for strontium, “A” – for aluminosilicate, xx is the fraction of SiO_2 (in mol%), yy is the fraction of Al_2O_3 (in mol%) and SrO content calculated as $(100-xx-yy)$.

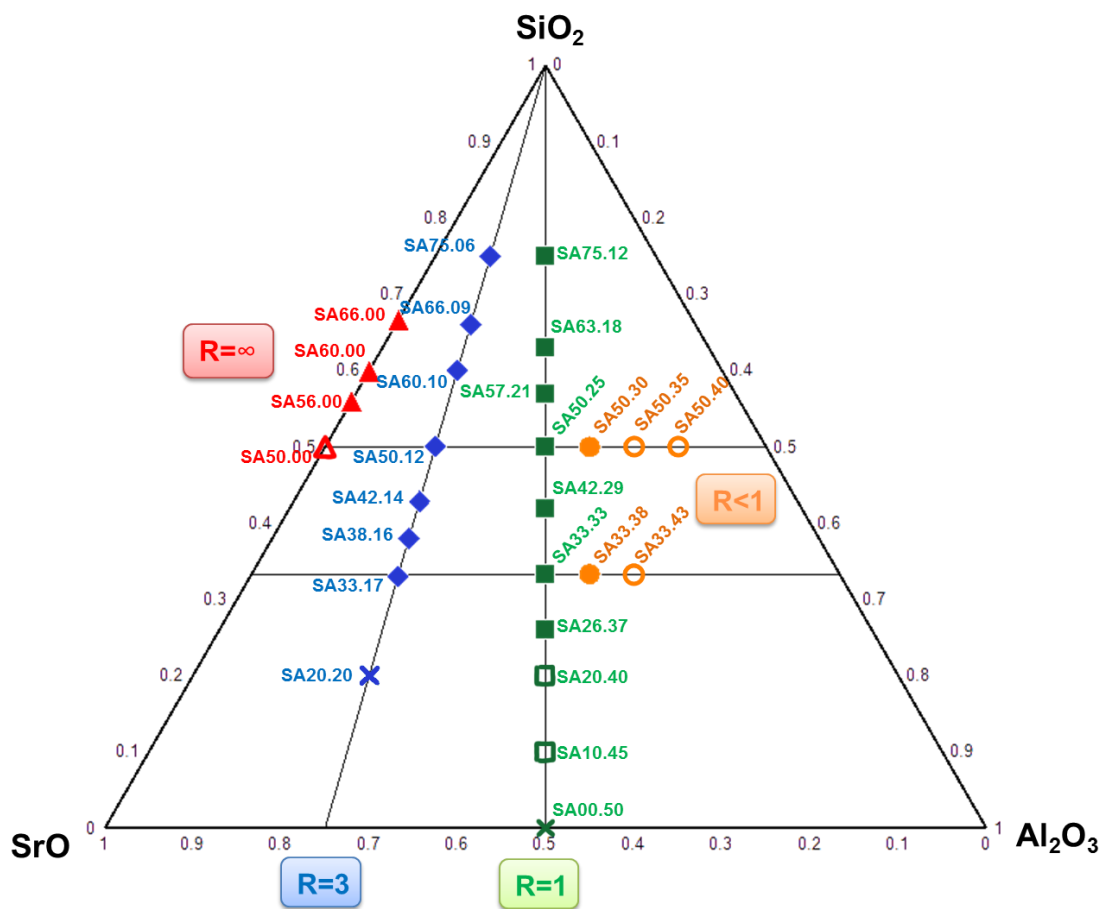


Figure III.1. Ternary plot for the SAS system (mole fractions) showing compositions studied. Glasses obtained by traditional quench are depicted as filled symbols. Glasses that could be obtained only by levitation quench are shown as open symbols. Crosses correspond to compositions for which no glass could be obtained by neither of two quench procedures. Color guide: red – silicate glasses, blue – peralkaline glasses, green – tectosilicate glasses, orange – peraluminous glasses. $R = \text{SrO}/\text{Al}_2\text{O}_3$.

We would like to start our discussion from the tectosilicate join ($R = 1$). Compositions lying on this join should, in theory, have a fully polymerized network composed of interconnected silicon and aluminium tetrahedra with metal cations proximal to the latter

ones and acting as charge compensators. Further, we will see that such structure description, being close enough to the verity, is still too simplified.

1. Tectosilicate join (R = 1)

This section we will begin with results published in an article in the Chemical Geology journal (Novikov et al., 2017). This will be a good departure point for our discussion of properties and structure of glasses in the SAS ternary system in general and on the tectosilicate join in particular. However, in order to keep the coherence and cohesion of the text, we invite the readers to find the article in Annex I. Further, we will highlight the main findings reported in the article.

- A small fraction of AlO_5 has been found in all studied glasses with a maximum of $\sim 4.5\%$ for compositions with 40-50 mol% of SiO_2 .
- XANES spectra of Sr tectosilicate glasses resemble that of a crystalline standard (strontianite) suggesting that the $CN(Sr-O) \approx 9$.
- The fraction of low-membered rings increases under the substitution of SiO_2 by $SrAl_2O_4$ as seen by Raman. The deconvolution of the high-frequency region of the Raman spectra revealed that the overwhelming majority (if not all) SiO_4 tetrahedra are in Q^4 species.
- The T_g curve possesses a minimum for the composition with 42 mol% of silica. An increase of glass transition temperature is observed for silica-poor compositions.

In addition to what has been already discussed in the article, we would like to report some more results of ^{29}Si MAS NMR and neutron diffraction experiments made on the same compositions. The discussion of the results is given below.

1.1. ^{29}Si NMR spectroscopy

^{29}Si NMR spectra of the glasses along the join R = 1 are presented in Figure III.2. Under the substitution of SiO_2 by $SrAl_2O_4$, the NMR signal moves to higher values of the chemical shift. The shift is caused by the Al-Si mixing, i.e. change of Q^n_m species' proportions (where n is the number of bridging oxygens and m is the number of Al attached to a silicon

tetrahedron (see Chapter I). Each of the species gives a signal with a characteristic chemical shift. In principle, the ^{29}Si NMR spectrum may potentially be a superposition of fifteen Q^n_m component peaks ($0 \leq m \leq n \leq 4$). Since the glasses are of tectosilicate composition the overwhelming majority of Q^n species is expected to be Q^4 . Therefore, the ^{29}Si NMR signal is a sum of Q^4_m contributions. Silica-rich SA75.12 glass should have Q^4_0 species as the major component while Q^4_4 species are expected for silica-poor SA10.45 glass.

A small wide feature at -110 ppm appears in the spectra of SA10.45 and SA20.40 with ~ 10 and 5 % of the overall intensity, respectively. Its position matches perfectly with that of vitreous silica and suggests the presence of Q^4_0 species in these glasses. Since such species are not statistically expected for silica-poor compositions (at least, in such amounts) and detachment of the line from the rest of the NMR signal, the existence of silica-like regions coexisting with the rest of the aluminosilicate network (i.e. phase separation) is suggested.

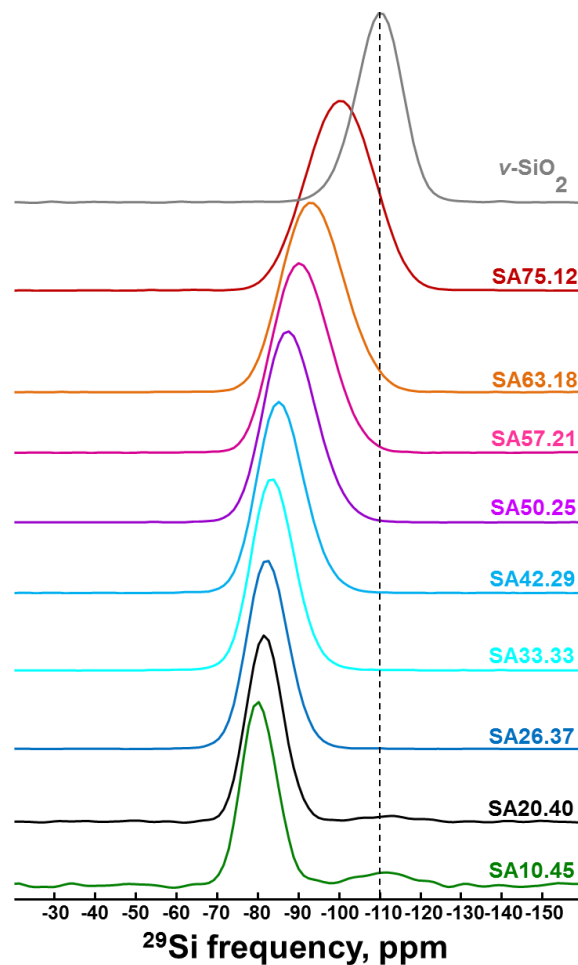


Figure III.2. ^{29}Si MAS NMR spectra of Sr tectosilicate glasses. Silica content decreases from top to bottom.

In addition to the variation of the barycentre's position, the line width significantly decreases from silica-rich to silica-poor compositions. Normally, the linewidth of a ^{29}Si NMR spectrum depends on the dispersion of δ_{iso} due to structural disorder (e.g., change in inter-tetrahedral and torsion angles) or substitution in the second coordination sphere (Si-Al exchange). Therefore, such decrease would imply local ordering around SiO_4 tetrahedra for silica-poor compositions and decrease of inter-tetrahedral angles, which is in agreement with lower values of Si-O-Al angles in comparison with Si-O-Si ones (Navrotsky et al., 1985; Neuville and Mysen, 1996; Seifert et al., 1982). However, the situation is more complex and it has been mentioned in the Chemical Geology paper that a small fraction of NBOs might exist for Sr glasses of the tectosilicate composition. The presence of < 10 % of NBOs and of three-coordinate oxygens (TBOs) was evidenced by MD simulations performed by Thibault Charpentier (personal communication). According to the simulations, TBOs are mostly connected to either 3 Al atoms or 2 Al and 1 Si and are preferentially bound to AlO_5 species. Thus the ^{29}Si NMR signal for the Sr tectosilicate glasses may contain contributions from other than just Q_m^4 units. Taking into account all aforesaid and the fact that the spectra do not possess any particular features (distinct inflection points, shoulders etc.), direct deconvolution of the ^{29}Si NMR data seems to be a very complex task.

When full ^{29}Si enrichment of the glasses can be performed, there is a way to extract the information on Q_m^n speciation. Figure III.3 presents an example of deconvolution of ^{29}Si NMR spectrum of SA50.25 glass based on the results of INADEQUATE experiments (Franck Fayon, personal communication). In this case, the deconvolution is obtained by recording the three "multiple-quantum" spectra corresponding to Si atoms linked to one, two or three other Si atoms which allow then the full reconstruction of the quantitative spectrum. We can see that for SA50.25 sample the majority (45 %) of Si has four aluminium atoms in their second coordination sphere (Q_4^4 units). The other units are Q_3^4 , Q_2^4 and Q_1^4 with their population decreasing in the same order. For analogous Ca composition (CA50.25 glass) it has been found almost the same Q_m^n species distribution (Hiet et al., 2009).

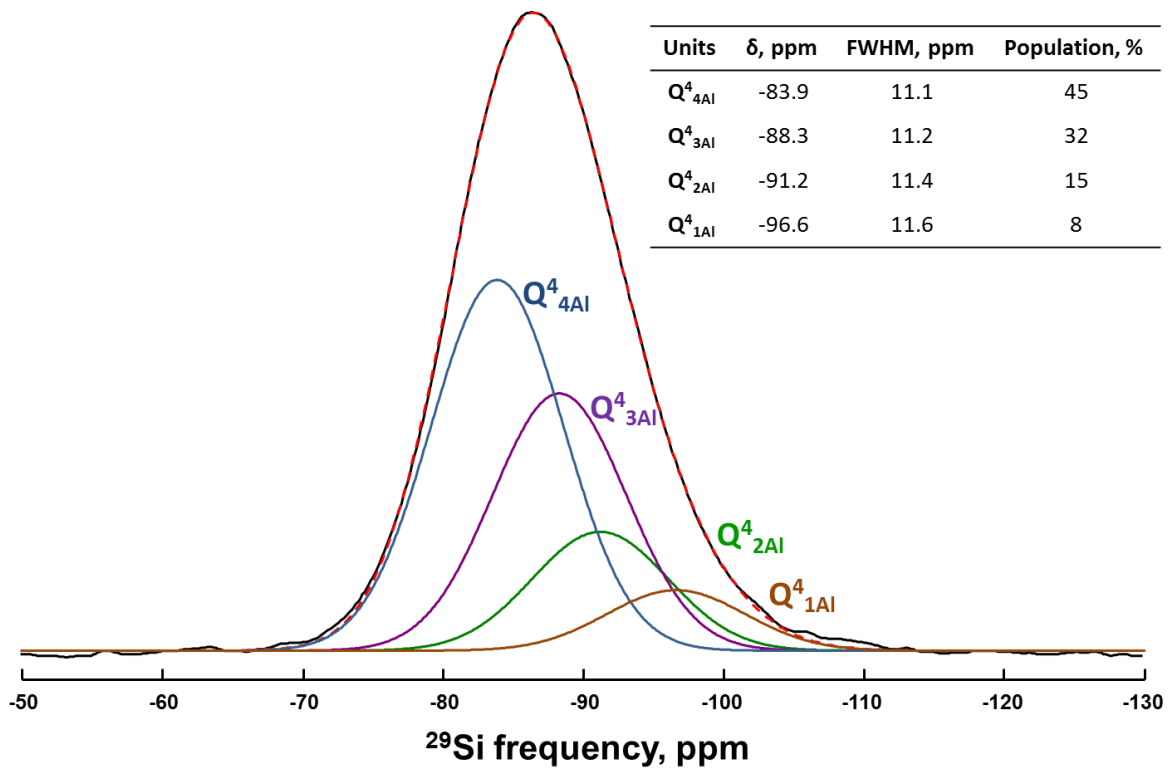


Figure III.3. Example of deconvolution of ^{29}Si MAS NMR spectrum of SA50.25 glass based on the results of INADEQUATE experiments (Franck Fayon, personal communication).

Based on the deconvolution of the SA50.25's spectrum (δ_{iso} and FWHM) and taking into account δ_{iso} for different Q^4_m lines found in crystalline counterparts of Sr tectosilicates (Al Saghir et al., 2015) we fitted our ^{29}Si NMR data. Values of δ_{iso} and FWHM were fixed during the deconvolution procedure and were let varying only when a satisfactory fit could not be obtained (Figure III.4).

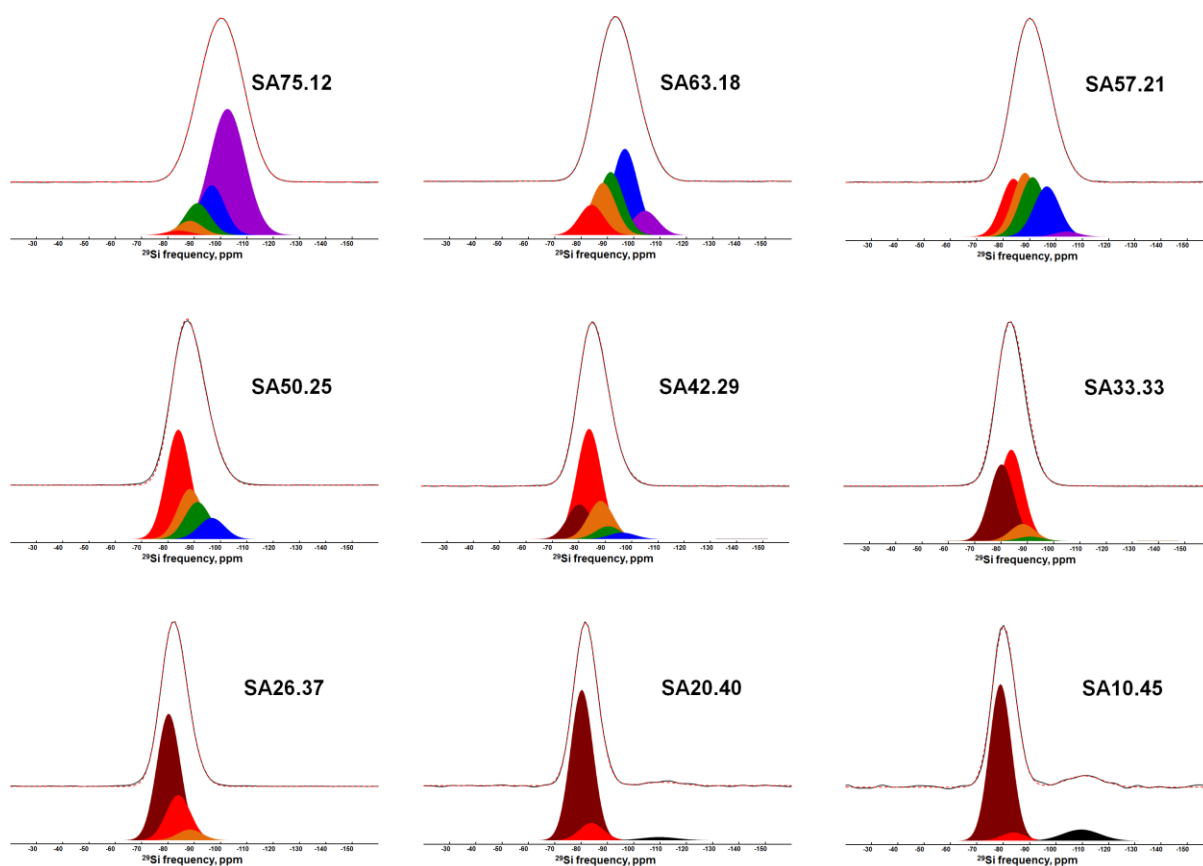


Figure III.4. Deconvolution of ^{29}Si MAS NMR spectra of Sr tectosilicate glasses. Colour guide: violet – Q^0 , blue – Q^1 , green – Q^2 , orange – Q^3 , light red – Q^4 , dark red – $\text{Q}^4(\text{Ba})$, black – Q^0 in the silica-like region.

Starting from SA42.29 composition, a new line appears at high values of the chemical shift. Based on the value of the δ_{iso} one could suggest the formation of Q^3_m units in the silica-poor glasses. However, this line becomes dominant and constitutes $\sim 90\%$ of the whole spectrum of SA10.45 composition. If the signal corresponds to Q^3_m units we would observe a huge drop in T_g which is not the case. Therefore, there should be another explanation for the line. This line has been observed for silica-poor crystalline Sr tectosilicates as well (Al Saghir et al., 2015). It has been demonstrated by coupled ^{29}Si NMR and DFT GIPAW computations (Fernández Carrión et al., submitted) that both lines at -80 and -84 ppm correspond to Q^4 sites. The difference between the sites is in the presence or absence of an extra Sr^{2+} in the second coordination sphere of Si. In simple words, the Q^4 Si sites giving a signal at -84 ppm have two Sr^{2+} nearby to charge compensate four AlO_4^- . The other Q^4 Si sites giving a signal at -80 ppm have an extra Sr^{2+} (three cations in sum) nearby the silicon tetrahedra (this site is denoted $\text{Q}^4(\text{Sr})$ in Figure III.5). Such a local uncompensated charge causes the difference in the chemical shift.

The Q_m^n distribution obtained from the deconvolution is presented in Figure III.5 and compared with that calculated with the assumption of random Al-Si mixing. It is clearly seen that two distributions do not match suggesting a certain degree of ordering in the system.

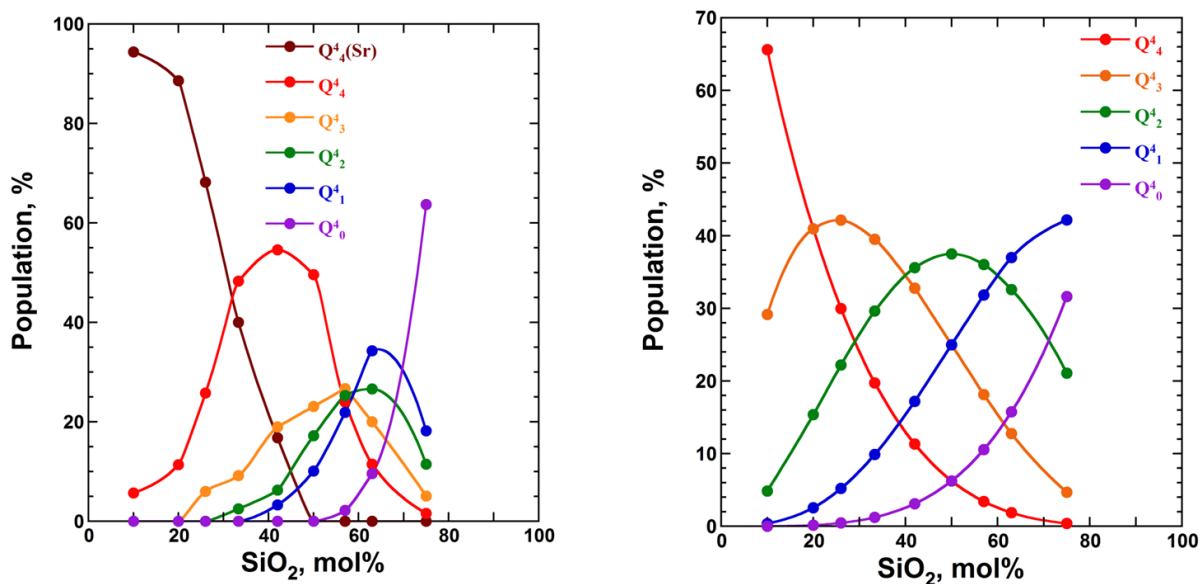


Figure III.5. The Q_m^n species distribution for Sr tectosilicate glasses obtained from experimental data (*left*) and calculated after (Moesgaard et al., 2010) assuming random Al-Si mixing (*right*).

Nevertheless, another deconvolution of the ^{29}Si MAS NMR spectra is possible. GIPAW calculations performed by Pierre Florian (personal communication) have shown that, in addition to different Q_m^4 units, depolymerized Q^n species together with TBOs are present in the structure of SA50.25 glass as well (Figure III.6). The Q_m^n distribution revealed by these calculations differs from that presented above. For example, a considerable amount of NBOs (18.7 %) was found to exist in the network of SA50.25 glass. This value is most likely overestimated but it points out to an important fact, that the possibility of the existence of NBOs in Sr tectosilicate glasses has been completely ignored. Moreover, the presence of NBOs has been already observed in Ca and Ba tectosilicate glasses (Lee and Stebbins, 2006, 2002; Thompson and Stebbins, 2012). MD simulations performed for Sr tectosilicate glasses by Thibault Charpentier (personal communication) on larger simulation boxes has also shown the presence of NBOs and TBOs in the structure, though in a lower amount (5-10 % for both).

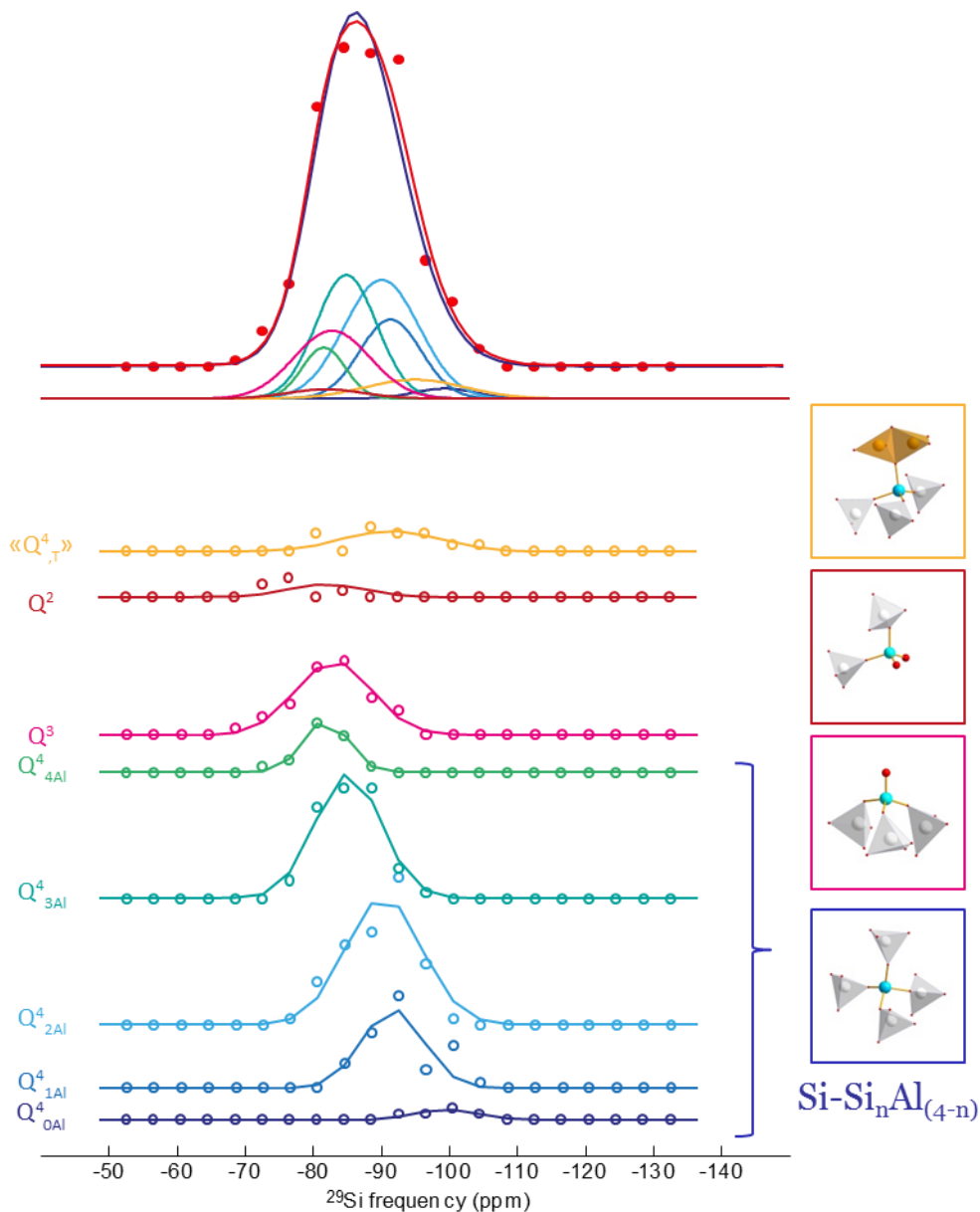


Figure III.6. Deconvolution of ^{29}Si MAS NMR spectrum of SA50.25 glass based on GIPAW calculations performed by Pierre Florian (personal communication).

Therefore, the overall picture of the Q_m^n species distribution should be more complex and not be limited only by Q_m^4 units. Further experiments are required to shed light on this question.

1.2. Neutron diffraction

The static structure factors, $S(q)$, for the glasses along the join $R = 1$ obtained from neutron diffraction measurements are plotted in Figure III.7. Under substitution of SiO_2 by SrAl_2O_4 , the first sharp diffraction peak (FSDP) moves to higher q values with a corresponding decrease in intensity. A similar behaviour of the FSDP has been already

observed for Ca aluminosilicate glasses of the tectosilicate composition (Hennet et al., 2016). It has been attributed to a decrease of the ring size from six- to four-membered with decreasing silica content (Neuville et al., 2004a). This change in ring statistics has been also observed in the Raman spectra reported in the Chemical Geology paper, where the introduction of SrAl_2O_4 and consequent augmentation of its content favoured formation of low-membered rings.

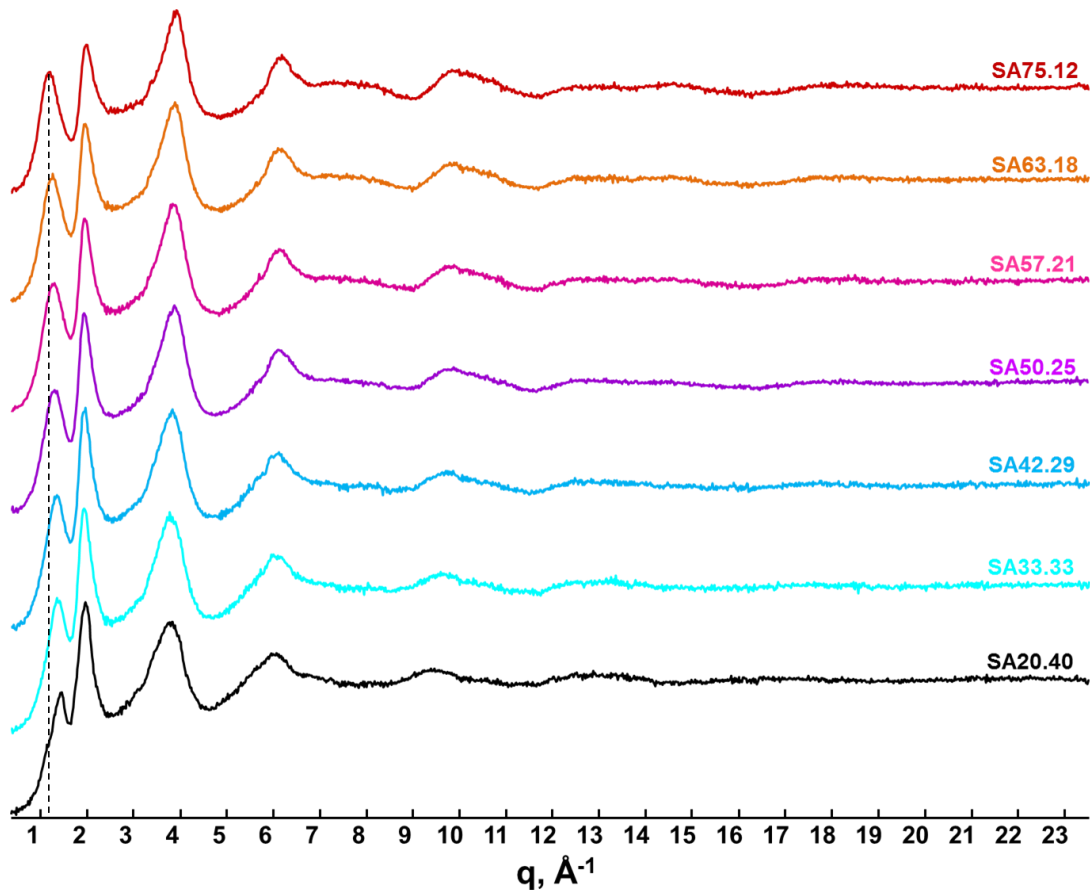


Figure III.7. Static structure factor, $S(q)$, of Sr tectosilicate glasses. Silica content decreases from top to bottom.

The pair distribution functions, $g(r)$, are dominated by four contributions marked in grey in Table III.1. These are O-O, Si-O, Al-O and Sr-O pairs. The contribution of other pairs is less than 5%. They are almost impossible to detect since they are hidden by the contribution of the four major pairs.

Table III.1. Normalized weighting factors (W_{ij}) of the atomic pairs for the compositions along the join R = 1.

Atomic pairs	SA75.12	SA63.18	SA57.21	SA50.25	SA42.29	SA33.33	SA20.40
Sr-Sr	0.0026	0.0060	0.0079	0.0105	0.0137	0.0176	0.0243
Sr-Al	0.0052	0.0118	0.0156	0.0206	0.0269	0.0346	0.0478
Sr-Si	0.0197	0.0241	0.0248	0.0247	0.0235	0.0208	0.0144
Sr-O	0.0724	0.1069	0.1217	0.1383	0.1564	0.1747	0.2011
Al-Al	0.0025	0.0058	0.0076	0.0101	0.0132	0.0170	0.0235
Al-Si	0.0193	0.0237	0.0244	0.0243	0.0231	0.0205	0.0141
Al-O	0.0712	0.1050	0.1196	0.1359	0.1536	0.1719	0.1976
Si-Si	0.0368	0.0242	0.0194	0.0146	0.0100	0.0061	0.0021
Si-O	0.2712	0.2151	0.1908	0.1635	0.1338	0.1032	0.0594
O-O	0.4990	0.4775	0.4681	0.4574	0.4457	0.4336	0.4156

The $g(r)$ for the glasses along the join R = 1 are plotted in Figure III.8. The first peak in $g(r)$ corresponds to contributions from Si-O and Al-O pairs, overlapping since the bond distances do not differ significantly. The position of the first peak changes almost linearly with composition. It shifts from $r \sim 1.62 \text{ \AA}$ for SA75.12 to $r \sim 1.72 \text{ \AA}$ for SA20.40 reflecting continuous Al-Si mixing. The second peak found at $r \sim 2.6\text{-}2.7 \text{ \AA}$ corresponds to overlapping contributions from Sr-O and O-O (belonging to SiO_4 and AlO_4 tetrahedra) pairs. The next peak at $r \sim 3.8 \text{ \AA}$, weakly probed, could correspond to the cation-cation correlations. Finally, the barely resolved peaks at $r \sim 4.3 \text{ \AA}$ and $r \sim 5.1 \text{ \AA}$ correspond to correlations Si-O(2) and Al-O(2) with the second oxygen neighbours.

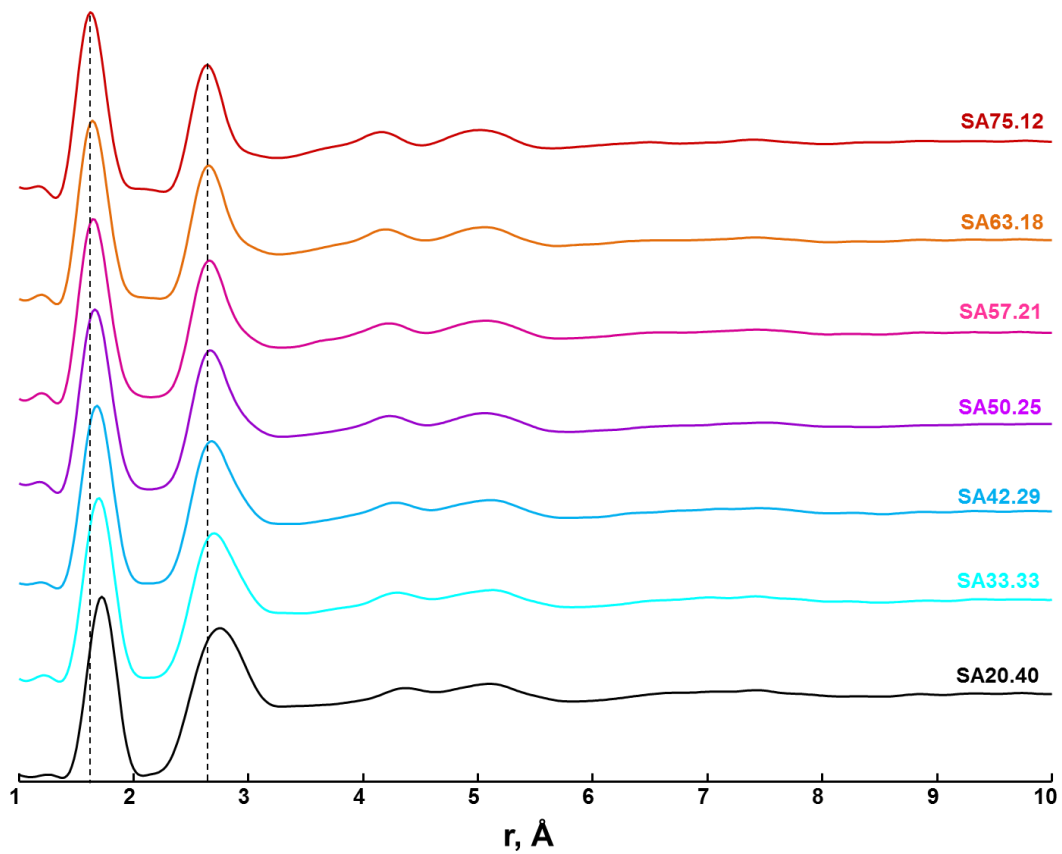


Figure III.8. Pair distribution function, $g(r)$, of Sr tectosilicate glasses. Silica content decreases from top to bottom.

Since direct deconvolution of the $g(r)$ (or rather the total correlation function, $T(r)$) is quite uncertain, the ND data were used for further MD simulations. Performed by Thibault Charpentier (personal communication) it allowed isolating partial contributions of different pairs. In Figure III.9 a comparison of the experimental and simulated static structure factors is presented. For the high silica content, there is a small difference of the peaks' positions and intensities, but the results still fit quite well.

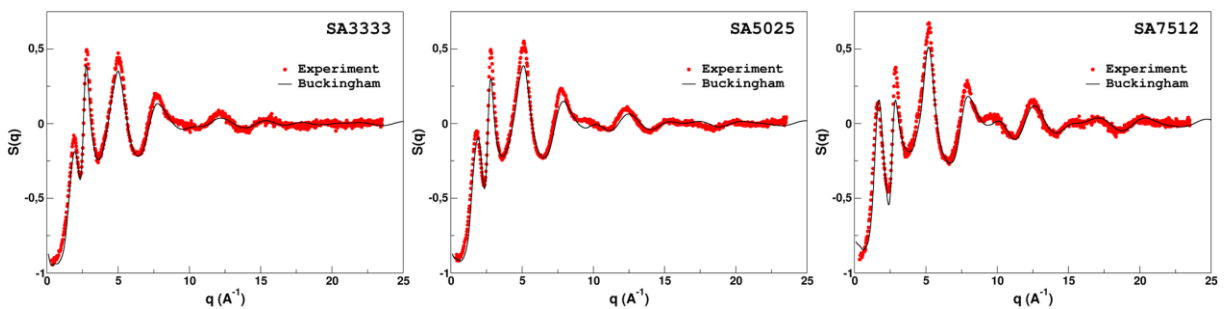


Figure III.9. Experimental $S(q)$ together with the results of MD simulations.

It was found that the first peak in the $g(r)$ is composed of the contributions of Si-O and Al-O pairs with average bond distances 1.58 and 1.76 Å, respectively (Figure III.10). The positions of Si-O and Al-O peaks do not change with composition, meaning that all the changes in the position of the first peak in the $g(r)$ are generated by the change of the Si/Al ratio. The second peak in the $g(r)$ located at around 2.6 Å results from O-O and Sr-O correlations centred at 2.60-2.68 and 2.56 Å, respectively. The MD simulations have shown that CN(Sr-O), varying from 6 to 10, has a maximum around 8-9. This is in agreement with CN \approx 9 stated in the Chemical Geology paper.

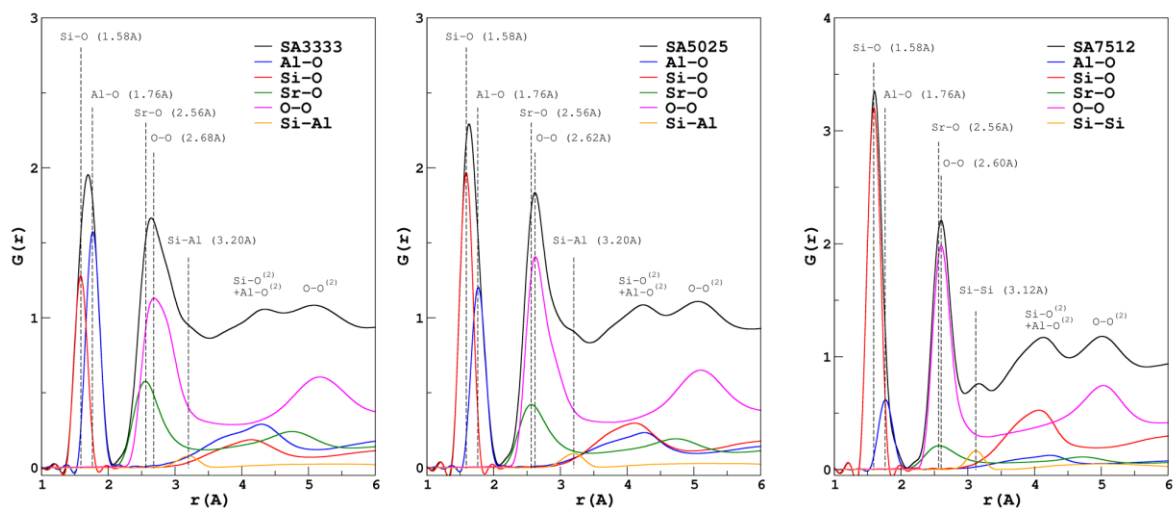


Figure III.10. Partial pair distribution functions $g_{ij}(r)$ calculated from the results of MD simulations together with experimental $g(r)$ for three Sr tectosilicate glasses.

Worth to notice, that for a Sr aluminosilicate glass of the tectosilicate composition (SA66.17 in our notation), the CN(Sr-O) has been found between 6 and 7 (Cormier et al., 1999; Creux et al., 1995). At the same time, in the crystalline strontium feldspar (SrAl₂Si₂O₈, SA50.25) Sr-O coordination number was found to be 7 or 9 depending on the model used (Chiari et al., 1975), with d(Sr-O) = 2.691 and 2.786 Å, respectively. Findings of the MD simulations and of XANES are in good agreement, therefore, we believe that the CN(Sr-O) for SA66.17 has been underestimated in the previous studies.

Section highlights

- AlO₅ species (\leq 4.5 %) are present in all Sr tectosilicate glasses as seen by ²⁷Al NMR.

- XANES experiments and MD simulations found that Sr is coordinated in average by 8-9 oxygens.
- Raman spectroscopy and ND showed a shift of the rings statistics towards the low-membered rings.
- Silicon tetrahedra were found in Q⁴ species by Raman and ²⁹Si NMR. However, a small fraction of NBOs still may exist in glasses on the join R = 1 as suggested by the simulations.
- Glass transition temperature increases noticeably for compositions in the silica-poor domain.

2. Silicates domain (R = ∞)

Contrary to tectosilicate compositions, silicates possess a network with a certain degree of depolymerization. Even a small fraction of modifying oxide introduced into the network of vitreous silica produces NBOs. Therefore, one expects the properties and structure of silicates to differ from those of the glasses along the charge compensated line. Here and further our discussion will be built as following: firstly, the glass structure from the short- to the medium-scale range will be described, and, secondly, macroscopic properties will be discussed.

2.1. ²⁹Si NMR spectroscopy

²⁹Si NMR spectra of the silicate glasses together with a spectrum of vitreous silica are presented in Figure III.11. For the silicate glasses the NMR signal is an asymmetric line whose width decreases under the introduction of SrO into the glass network. The spectra are shifted to higher values of chemical shift compared to that of silica glass.

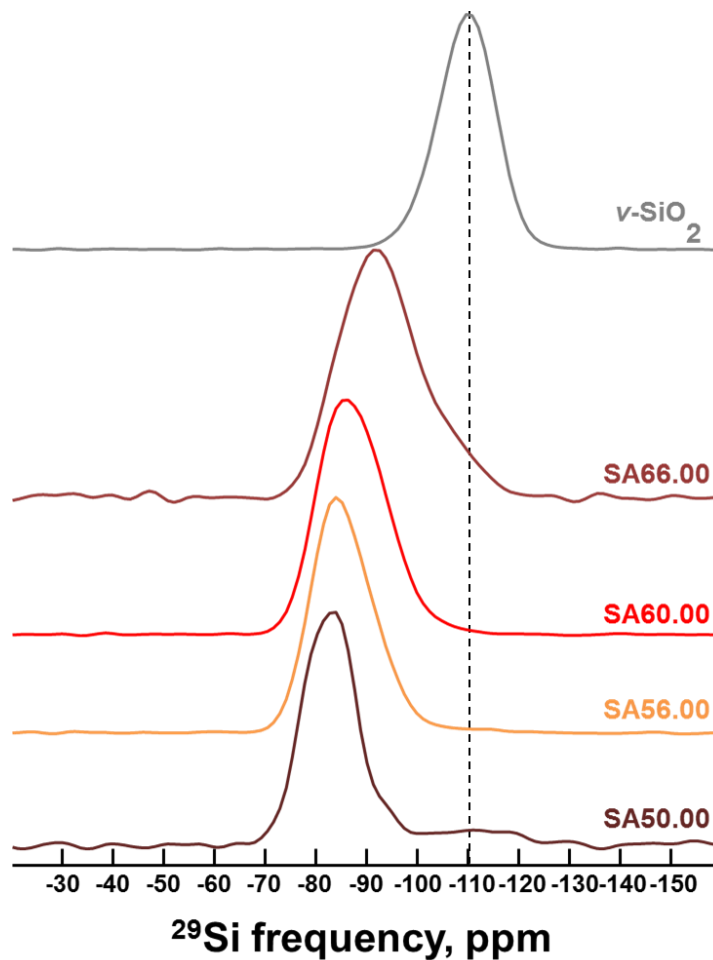


Figure III.11. ^{29}Si MAS NMR spectra of Sr silicate glasses. Silica content decreases from top to bottom.

In fact, the barycentre's position depends only on the interplay of signals coming from different Q^n species convoluted in the NMR signal. Therefore, we can conclude that only SA66.00 composition contains a significant fraction of Q^4 as indicated by the position of a shoulder to the right of the maximum. The maximum in the spectrum corresponds to the position of Q^3 species (Dupree et al., 1986; Lippmaa et al., 1980; Murdoch et al., 1985). The spectra of SA60.00 and SA56.00 are quite symmetric and absolutely featureless, making them difficult to deconvolute properly into different contributions. Nevertheless, the maximum position is shifted with respect to that of SA66.00 glass, suggesting Q^2 species to be responsible for its origin. In the spectrum of SA50.00 glass we observe the central contribution at the position of the Q^2 line found in crystalline SrSiO_3 (Smith et al., 1983), a shoulder to the left (probably a Q^1 line), a small shoulder to the right at the position of the Q^3 line and a wide separate line around -110 ppm. The last line is at the position of Q^4 one

found in vitreous silica. It leads us to a thought that the signal at -110 ppm (~ 10 % of overall intensity) might come from either a phase separated region or just a silica-like region coexisting with the rest of the network.

The deconvolution of the ^{29}Si NMR spectra for the silicate glasses is complicated by their almost featureless shape. Moreover, the range of the chemical shifts for each Q^n line reported in the literature is large (up to 20 ppm) making fits uncertain. However, in Figure III.12 we present results of direct deconvolution of the ^{29}Si NMR spectra.

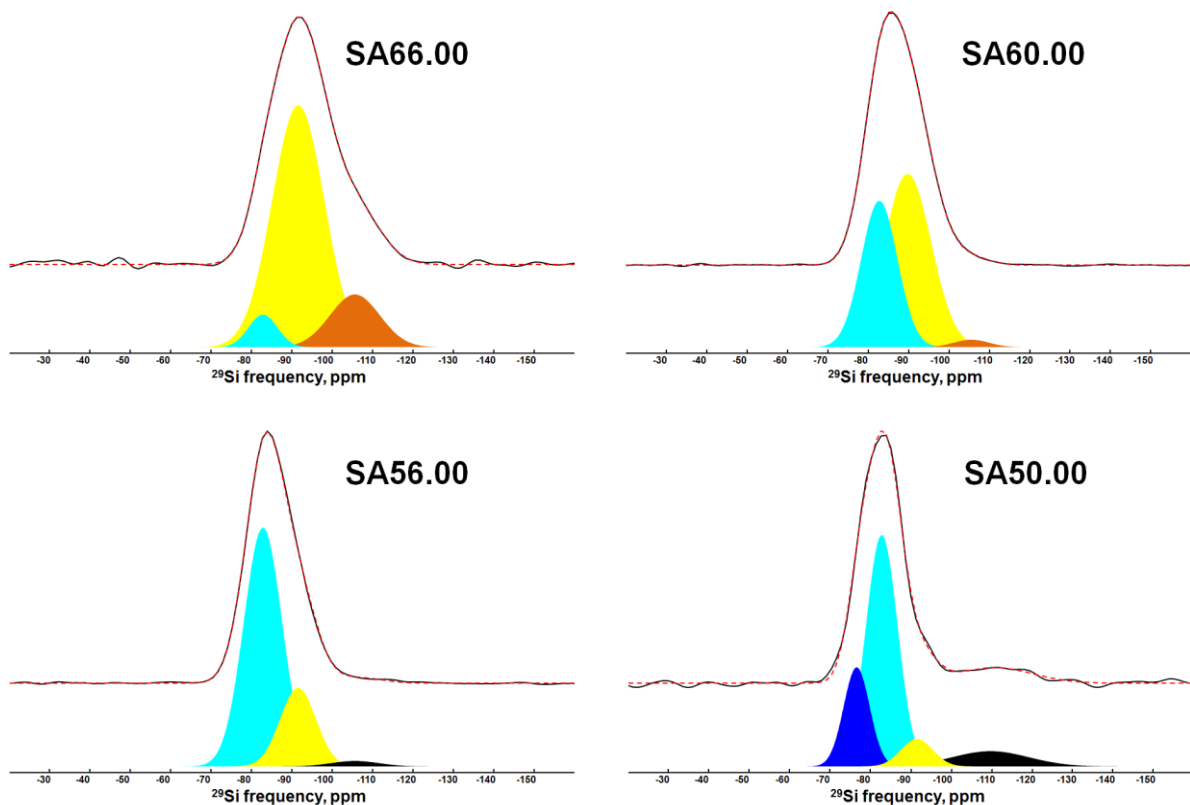


Figure III.12. Deconvolution of ^{29}Si MAS NMR spectra of Sr silicate glasses. Colour guide: orange – Q^4 , yellow – Q^3 , turquoise – Q^2 , blue – Q^1 , black – Q^4_0 in the silica-like region.

It was found that for two silica-rich glasses (SA66.00 & SA60.00) the network is composed of Q^4 to Q^2 species, Q^3 being the dominant ones. It is in agreement with findings of (Murdoch et al., 1985; Neuville, 2005) for these glasses. For the glass SA56.00, Q^2 dominates the network with Q^3 being minor entities. Finally, for the glass of the metasilicate composition (SA50.00), additionally to Q^2 and Q^3 species, Q^1 units appear. Despite the approximate nature of the deconvolution made here, our results are in a relatively good

agreement with the Q^n distribution found in other alkali and alkaline earth silicate systems (Figure III.13).

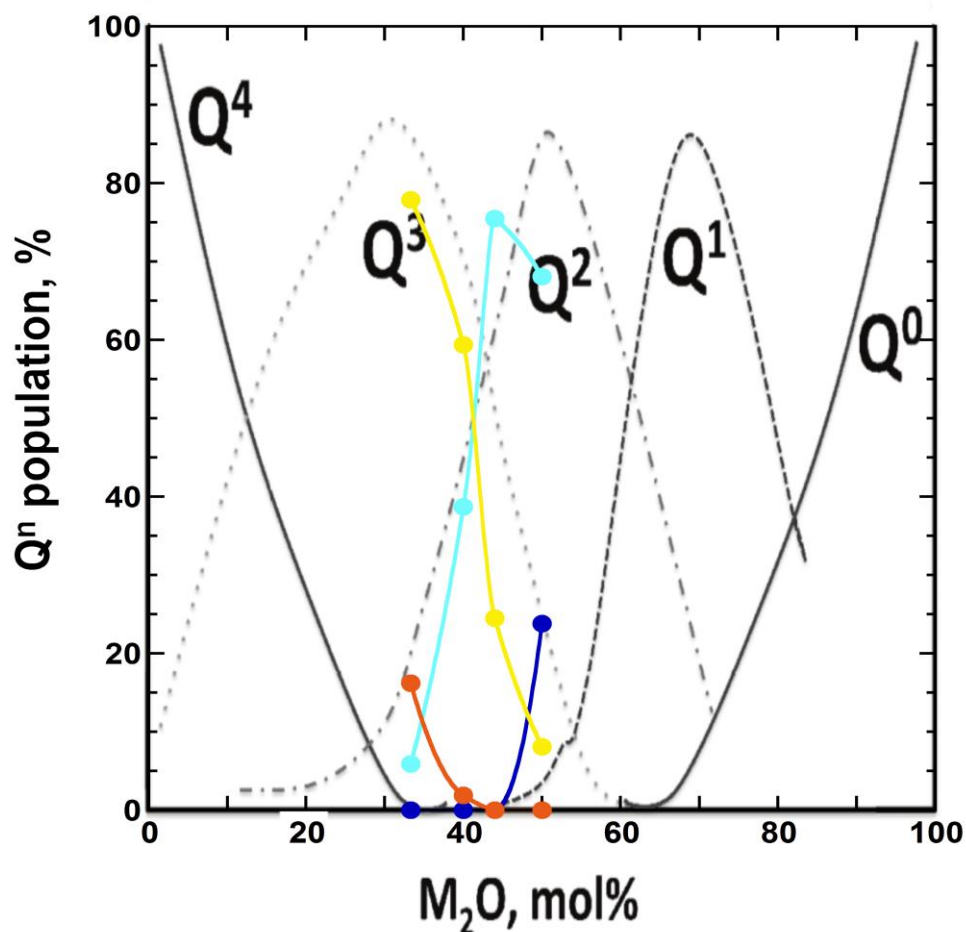


Figure III.13. Comparison of the Q^n distribution obtained from the deconvolution of the ^{29}Si MAS NMR spectra of Sr silicate glasses with the one typically found in alkali (Li, Na, K) and alkaline earth (Mg, Ca, Sr, Ba) silicate glasses (Neuvill et al., 2014). Colour guide: orange – Q^4 , yellow – Q^3 , turquoise – Q^2 , blue – Q^1 .

2.2. Raman spectroscopy

Raman spectra of the silicate glasses are presented in Figure III.14. The spectrum of SA66.00 possesses all the features already described in the Chemical Geology paper, except for a broad band of low-intensity around 334 cm^{-1} and a tiny bump around 220 cm^{-1} . The position of the former band seems not to be affected by the compositional change, while the latter one is observed only in the spectrum of SA50.00 glass. The band at 334 cm^{-1} becomes more intense with decreasing increasing SrO fraction, suggesting the involvement of Sr cations into the vibrations causing the band. Two bands in the same frequency region have been observed in depolarized (VH) Raman (Hehlen and Neuvill, 2015) and IR (De

Sousa Meneses et al., 2006) spectra of Na and Ca silicate and aluminosilicate glasses. The band at higher frequency has been attributed to cation-oxygen vibrations where cation acts as both a network modifier and a charge compensator. The other band has been attributed to cation-oxygen vibrations where cation acts solely as a network modifier. Since the bands in the low-frequency region of the spectra of Sr silicates are found at similar positions as those in the spectra of Na- and Ca-containing glasses, we suggest that they also originate from Sr-O vibrations.

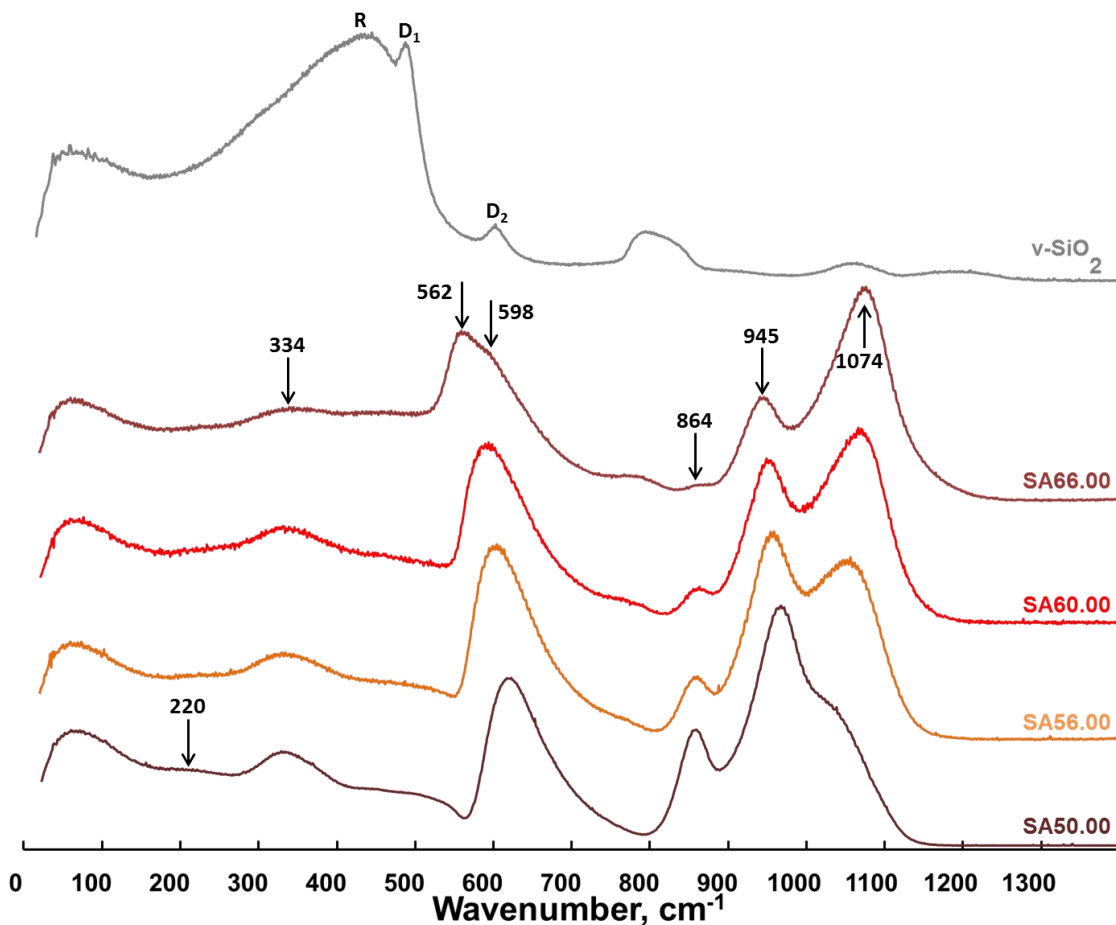


Figure III.14. Area normalized Raman spectra of Sr silicate glasses. Numbers correspond to the frequencies of observed bands maxima. Silica content decreases from top to bottom.

A band at $\sim 600 \text{ cm}^{-1}$ in the spectrum of SA66.00 glass possesses two distinct contributions: a maximum at 562 cm^{-1} and a shoulder at $\sim 598 \text{ cm}^{-1}$. The band shifts to higher wavenumbers as silica content drops down to 50 mol%. Its position is close to that of the D_2 band observed in the spectrum of vitreous silica, which has been attributed to breathing vibrations in three-membered tetrahedral rings (F. L. Galeener, 1982; Frank L.

Galeener, 1982; Kubicki and Sykes, 1993). Worth noticing, that the structure of crystalline Sr metasilicate (SA50.00) is also composed of three-membered tetrahedral rings (Machida et al., 1982). Several authors have suggested that the asymmetry of this band and its shift to higher frequency are caused by the incorporation of depolymerized Q^n units into three-membered tetrahedral rings (Dickinson et al., 1990; Matson et al., 1983; Micoulaut et al., 2005).

Concerning the high-frequency (HF) region of the spectra, following changes occur under augmentation of SrO content. The HF region of SA66.00 spectra possesses a tiny shoulder around 864 cm^{-1} and two peaks at 945 and 1074 cm^{-1} . With decreasing silica content, the peak at 864 cm^{-1} increases in intensity but stays at roughly the same position, while the peak at 945 cm^{-1} shifts slightly to higher wavenumbers and increases in intensity. At the same time, the third peak's intensity decreases and the peak shifts to a lower frequency. The three peaks described above (namely, their positions) correspond to vibrations of Q^3 , Q^2 and Q^0 species (see (Mysen et al., 1982) and references therein). The presence of Q^1 species is implied by the presence of both Q^2 and Q^0 species since the equilibrium $2Q^n \leftrightarrow Q^{n-1} + Q^{n+1}$ is expected to exist in a high-temperature melt from which the glass was quenched.

The barycentre of the high-frequency envelope rapidly shifts to lower wavenumbers when SrO substitutes for SiO_2 (Figure III.15). The shift is linear between the glasses SA66.00 and SA50.00. This suggests a continuous change in Q^n species distribution. The proximity of two curves for the silicate and tectosilicate glasses from 100 to 66.7 mol% of SiO_2 demonstrates that for silica-rich compositions the shift of the barycentre can be identical even if it is produced by different processes: change in Q^n distribution for silicate glasses and Al-Si mixing in the case of the tectosilicate glasses. Both curves have a slope of $2.2 \pm 0.1\text{ cm}^{-1}/\text{mol}\%$ of SiO_2 for the silica-rich compositions. At lower silica concentrations the curve for the silicates drops faster than the one for the tectosilicates with a slope of $4.4 \pm 0.1\text{ cm}^{-1}/\text{mol}\%$ of silica.

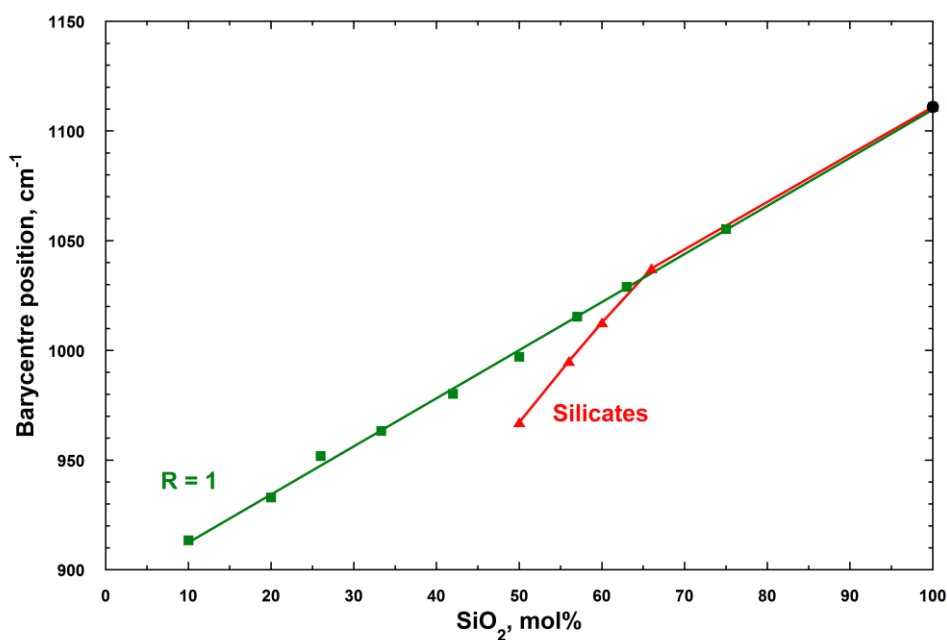


Figure III.15. Barycentre position of the high-frequency envelope of Raman spectra of Sr silicate (red) and tectosilicate (green) glasses. The lines are a guide to the eye.

Deconvolution of the HF envelope of the Raman spectra (Figure III.16) of the silicate glasses revealed the presence of Q^0 to Q^3 species in all the silicate glasses and Q^4 species in glasses with > 60 mol% of SiO_2 . With augmentation of SrO content Q^4 species disappear, the number of Q^3 species decreases and the number of Q^0 to Q^2 species grows.

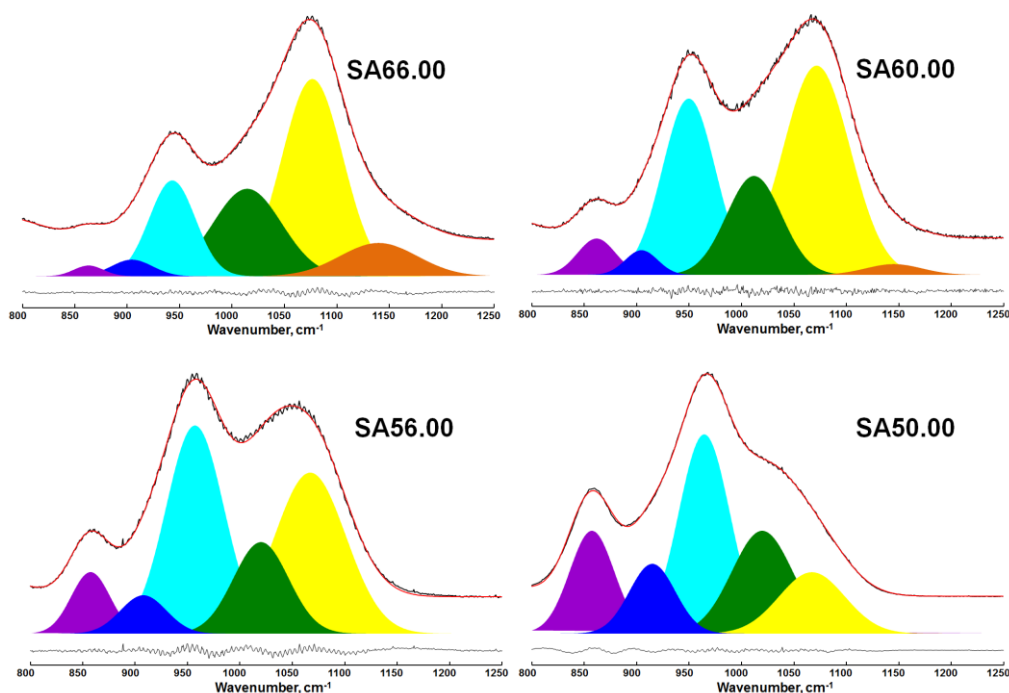


Figure III.16. Deconvolution of the HF region of the Raman spectra of Sr silicate glasses. Colour guide: orange – Q^4 , yellow – Q^3 , green – T_{25} , turquoise – Q^2 , blue – Q^1 , violet – Q^0 .

Presence of only one Q^4 band instead of two as in the case of the tectosilicate glasses suggests that the environment of Q^4 units becomes relatively homogeneous with unique angle distribution. Being a good estimation of the Q^n species distribution, the relative areas of the bands could not be, however, directly related to the concentration of each particular species (Smith and Dent, 2005). To correctly estimate the concentration, the Raman scattering cross section should be known and it varies for different Q^n units. For example, it has been concluded that the signal from Q^3 species is twice as much as from Q^4 ones for equal proportion in Na silicates (Furukawa et al., 1981). Nevertheless, the results of our deconvolution of the HF region of the Raman spectra resemble those obtained from ^{29}Si NMR (Figure III.17). The only exception is Q^0 species that has not been observed by NMR.

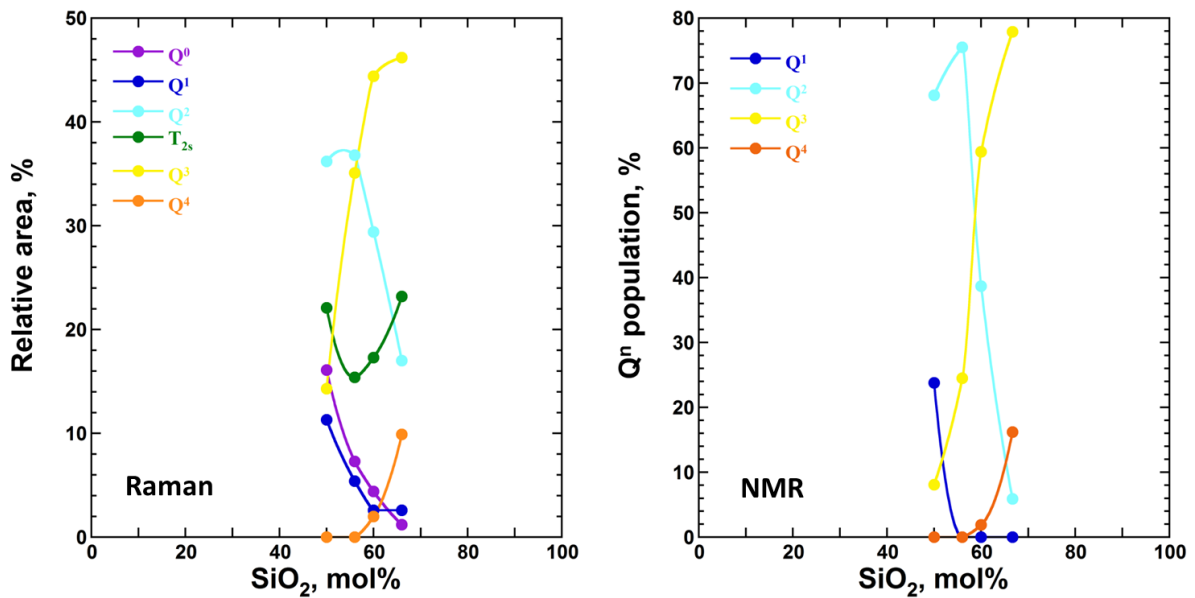


Figure III.17. *Left*: The relative area under the Gaussian bands obtained from deconvolution of the high-frequency region of the Raman spectra of Sr silicate glasses. *Right*: Population of Q^n species retrieved from ^{29}Si NMR.

2.3. Macroscopic properties

The density of the silicate glasses increases rapidly with increasing SrO fraction (Figure III.18). This increase is much steeper than in the case of tectosilicate compositions and is virtually linear. For the glasses on the join $R = 1$ density rises almost linearly in the whole range of concentration under the substitution of SiO_2 by SrAl_2O_4 . It is worth noticing, that the density reported by (Shinozaki et al., 2016) for the aluminate glass (SA00.50) breaks

out from the general trend, being less than for compositionally close glass with 10 mol% of silica.

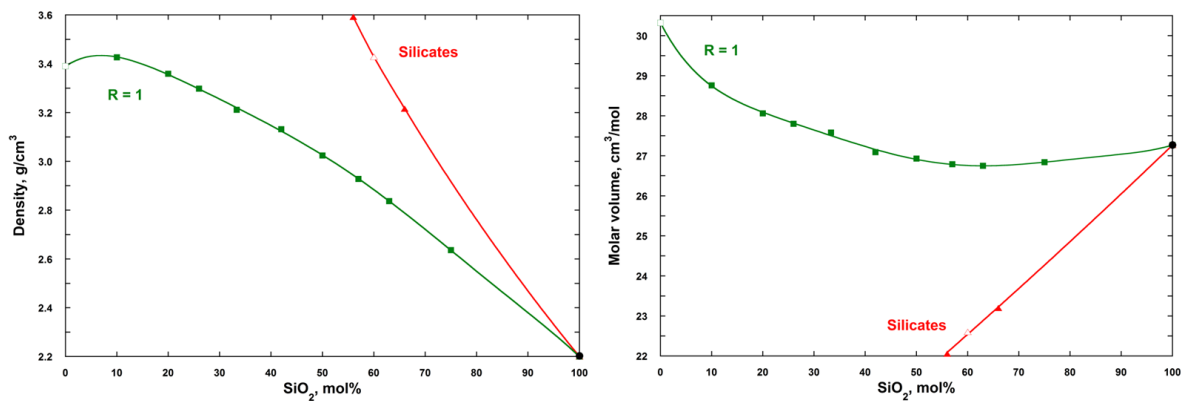


Figure III.18. Experimental densities (*left*) and calculated molar volumes (*right*) of Sr tectosilicate (green squares) and silicate (red triangles) glasses. The data for SA60.00 (the red open triangle) is from (Neuville, 2005) and the data for SA00.50 (the green open square) is from (Shinozaki et al., 2016). The black filled circle corresponds to the density of vitreous silica taken from (Brückner, 1970). Error bars are less than the symbol size. The lines are a guide to the eye.

Molar volume, V_m , was calculated as $V_m = d/M$, where d is glass density and M is its molar mass. The V_m for the silicate glasses reported in Figure III.18 decreases rapidly in a close-to-linear manner, suggesting a correlation with the depolymerisation degree. The silicate network becomes more and more compact with the introduction of SrO in comparison with SiO₂ glass. At the same time, for the tectosilicate glasses, molar volume drops down slightly from 100 to 63 mol% of SiO₂ and then rises continuously with acceleration for silica-poor compositions. This change in V_m is clearly connected to the introduction of aluminium into the network since for the silicate glasses only a decrease in the molar volume is observed.

For a mixed Sr-Na silicate glass (with 32 mol% of SrO and 6 mol% of Na₂O) the CN(Sr-O) was found to be 5-6 (Cormier et al., 1999; Creux et al., 1995) which is lower than both for Sr tectosilicate glasses (CN = 7-9) and crystalline SrSiO₃ (CN = 8, see (Machida et al., 1982)). Smaller CN(Sr-O) for silicates with respect to tectosilicate glasses suggests that Sr atoms are located in smaller sites. Indeed, (Creux et al., 1995) reported that in the Sr-Na silicate glass strontium is present in linked Sr-centred polyhedra. This explains lower molar volumes observed for the silicate glasses in comparison to the tectosilicate ones. Similar trends in V_m evolution have been reported for other alkali and alkaline earth silicates (Doweidar, 1999, 1996; Rabukhin, 1999). In all the binary systems except for silicates of heavy alkali elements

such as K and Rb (and, likely, Cs) with the rise of the depolymerisation degree the network becomes more compact.

The viscosity curves for the silicate glasses under study are very close to each other (Figure III.19). However, at low temperatures (right part of Figure III.19) they begin to differ. One observes an augmentation of viscosity for the composition with the lowest silica content (SA56.00) over two others. The viscosity of SA60.00 is also above that of SA66.00 but the difference is not great.

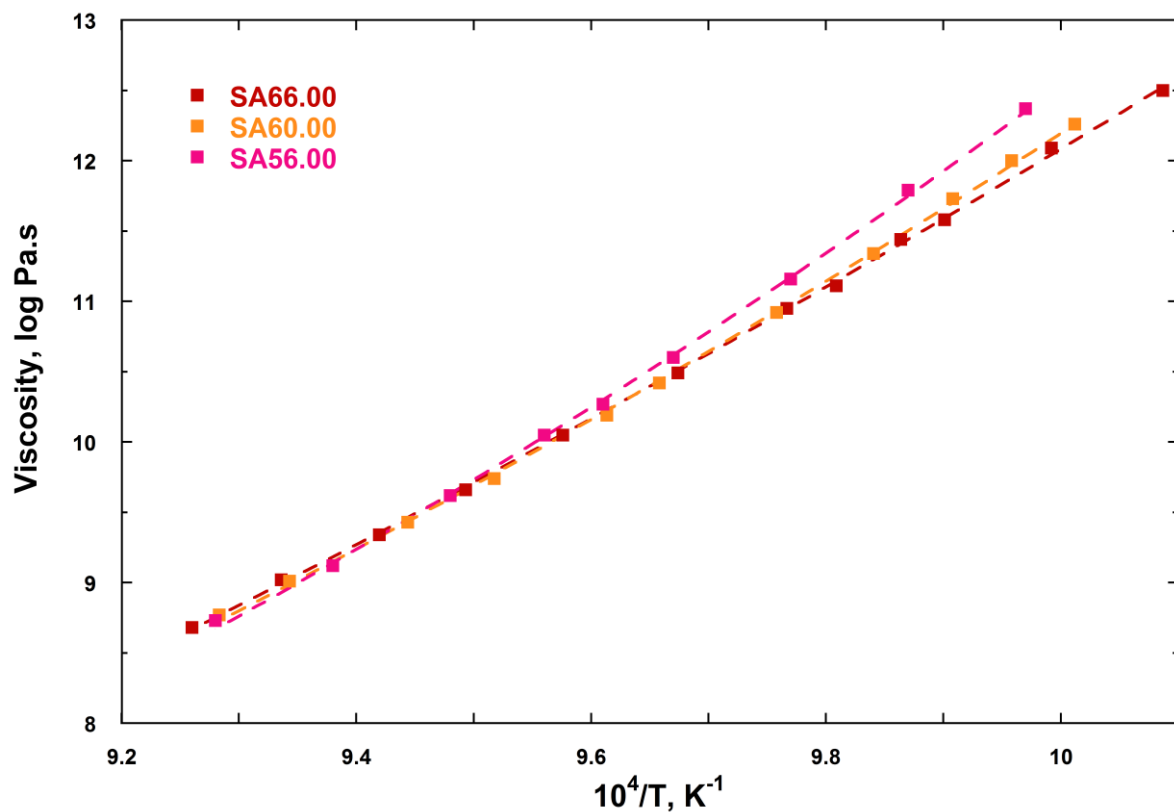


Figure III.19. High-viscosity curves for Sr silicate glasses. The data for SA60.00 are from (Neuville, 2005). Error bars are less than the symbol size. The dashed lines are corresponding VFTH fits.

Fitting the experimental data with the VFTH equation (*vide supra*) allowed extracting values of the glass transition temperatures. Figure III.20 clearly shows that with decreasing silica content the T_g increases. This increase is nonlinear, being slow for the compositions with 56-66.7 mol% of SiO_2 with a rapid rise to 50 mol%. Such behaviour of T_g has been reported by (Shelby, 1979) for Ca and Sr silicate glasses. He observed a threshold in T_g curves around 54 and 60% of SiO_2 for Ca and Sr silicate glasses, respectively. For silica-rich compositions the glass transition temperatures are very close. After the threshold, further

addition of modifying oxide leads to an increase of the T_g . For Ca silicate glasses several authors (see (De Sousa Meneses et al., 2006) and references therein) proposed a rearrangement of the silicate network at the threshold. They suggested that at high silica content the network resembles that described by Zachariasen and Warren (see Chapter I) with Ca cations acting as network modifiers. However, with addition of CaO (at the threshold and after) an ordering of the network occurs with clustering of CaO_6 polyhedra and appearance of other Ca sites. It has been proposed that when CaO exceeds a certain amount, Ca^{2+} starts participating in the network linkage. We can assume that in the case of Sr silicates an analogous phenomenon takes place.

Despite the increase of T_g of the silicates with decreasing SiO_2 content, it is still somewhat 100-150 K lower than those of the tectosilicate glasses, reflecting a higher degree of polymerization of the latter ones.

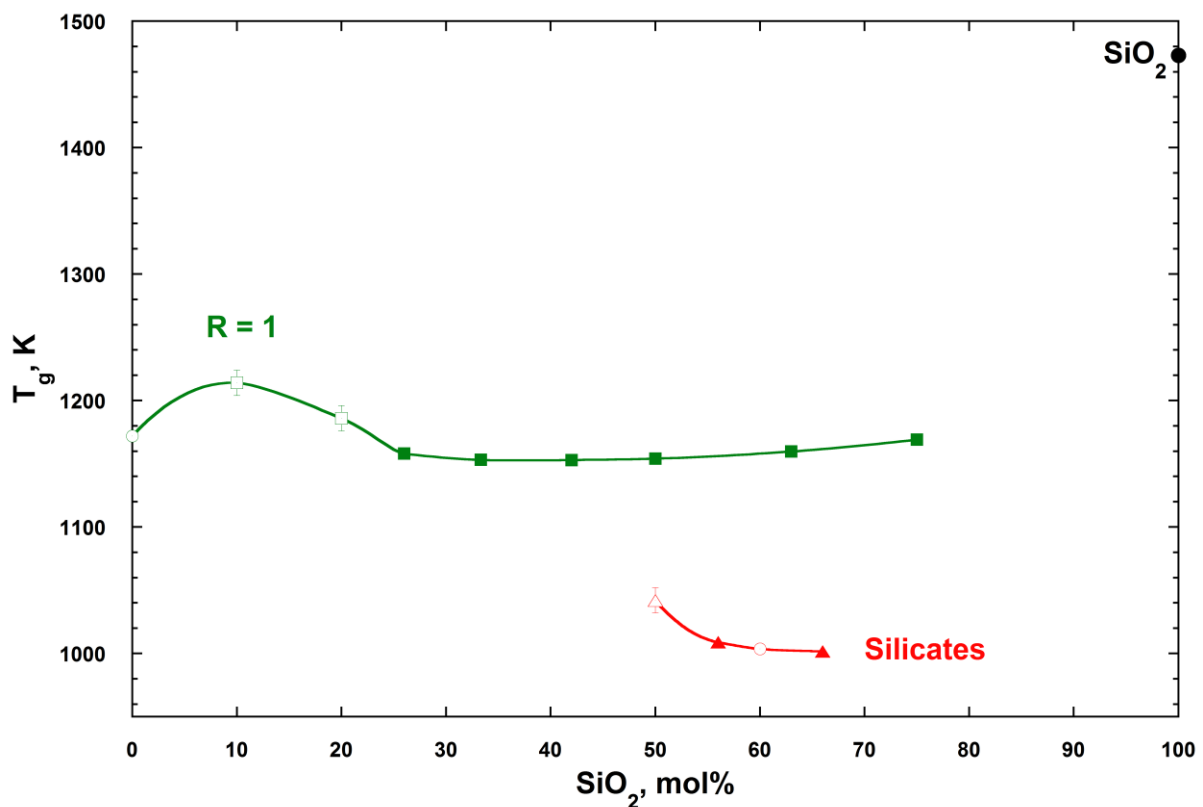


Figure III.20. Glass transition temperatures for Sr tectosilicate (green) and silicate (red) glasses. Filled symbols are T_g values extracted from viscosity data, open symbols are T_g values from DSC measurements. The data for SA60.00 (red open circle) is from (Neuvill, 2005). The data for SA00.50 (the green open circle) is from (Shinozaki et al., 2016). The glass transition temperature of vitreous silica (black filled circle) is given for comparison (Mackenzie, 1963). If not visible error bars are less than the size of symbols. The lines are a guide to the eye.

Let us make few comments on the T_g curve of the tectosilicates. A data point added for Sr aluminate glass (SA00.50) after (Shinozaki et al., 2016) has a value lower than one would expect from a simple interpolation of the experimental data. Moreover, available data on analogous Ca aluminosilicate glasses (Cormier et al., 2005; Neuville et al., 2004a) suggests that the T_g value for the aluminate glass on the join $R = 1$ should be higher than those of silica-poor aluminosilicates. Such behaviour with a maximum of T_g at low silica content has been observed only for Ca aluminosilicate glasses in the peralkaline region ($R > 1$). In that region, the decrease of the glass transition temperature has been attributed to the creation of NBOs connected to aluminium tetrahedra. In other words, AlO_4 cannot longer charge compensate an excess of alkaline earth cations and the alumina sub-network starts depolymerizing.

Section highlights

- Si tetrahedra are present in different mostly depolymerized Q^n species organized preferentially in three-membered rings as in the case of crystalline SA50.00 composition (Machida et al., 1982).
- In the low-frequency region of the Raman spectra two bands are observed. Their origin is unknown but likely caused by Sr-O vibrations.
- Molar volume of Sr silicates decreases with decreasing silica content suggesting compacting of the network. At the same time, T_g rises under the augmentation of SrO content. This increase could be connected with clustering of SrO_x polyhedra and participation of Sr^{2+} in the network linkage.

3. Peralkaline domain (R = 3)

In the previous section we have shown how macroscopic properties and structure evolve along the tectosilicate join ($R = 1$) with changing the Si/Al ratio. That join is considered as a fully polymerized where Sr cations play the role of charge compensators in the vicinity of negatively charged AlO_4 tetrahedra. On the join $R = 3$, to which we are going to switch now, for each aluminium tetrahedron there are three Sr^{2+} present, each SiO_2 is substituted by $Sr_3Al_2O_6$. This means that the excess of Sr cations participates in depolymerisation of the glass network, creating NBOs. The number of non-bridging oxygens

and the type of Q^n species involved depends on the Si/Al ratio. Thus, strontium plays a double role for the compositions on the join R = 3: it acts as a charge compensator and a network modifier.

3.1. ^{27}Al and ^{29}Si NMR spectroscopy

^{27}Al NMR spectra for the glasses along the join R = 3 shown in Figure III.21 resemble those of the tectosilicate ones. The main difference is a better separation of the signals of Al in tetrahedral and pentahedral coordination. The NMR line shifts to higher values of the chemical shift with decreasing SiO_2 content which is the consequence of Al-Si exchange in the second coordination shell of Al atoms.

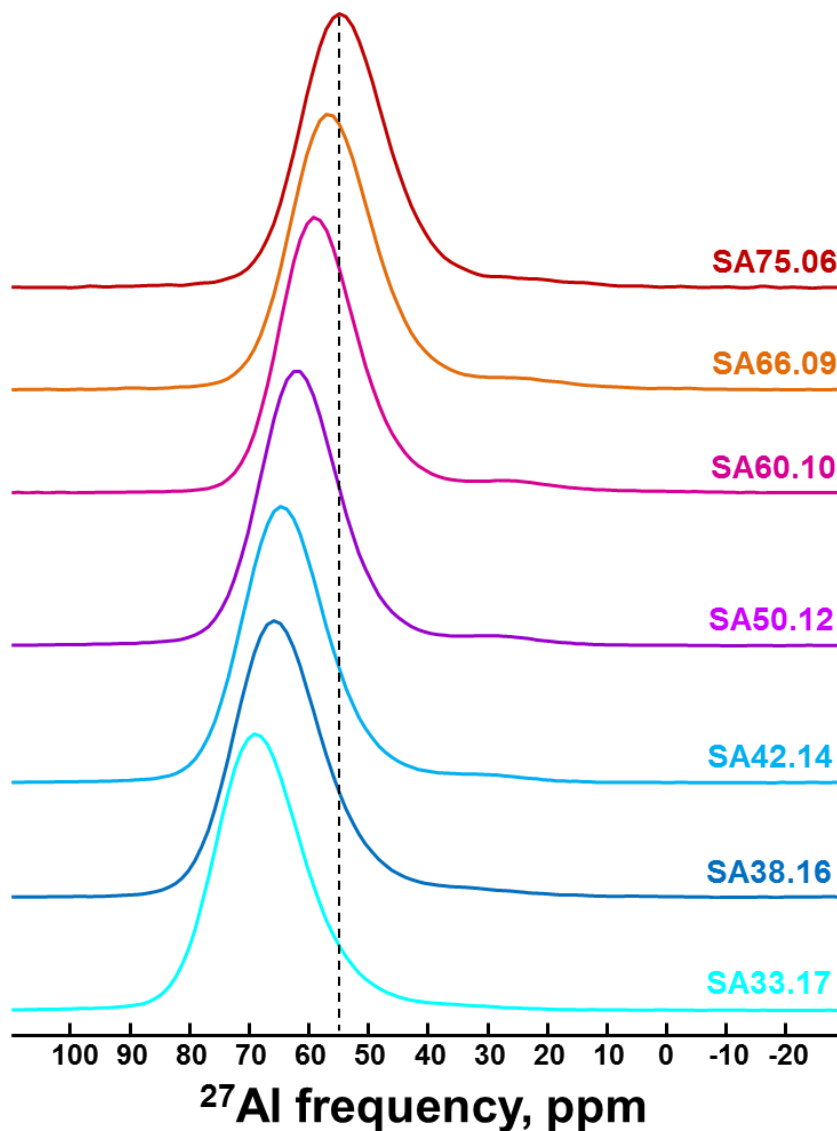


Figure III.21. ^{27}Al MAS NMR spectra of Sr peralkaline glasses. Silica content decreases from top to bottom.

Deconvolution of the ^{27}Al NMR spectra is given in Figure III.22.

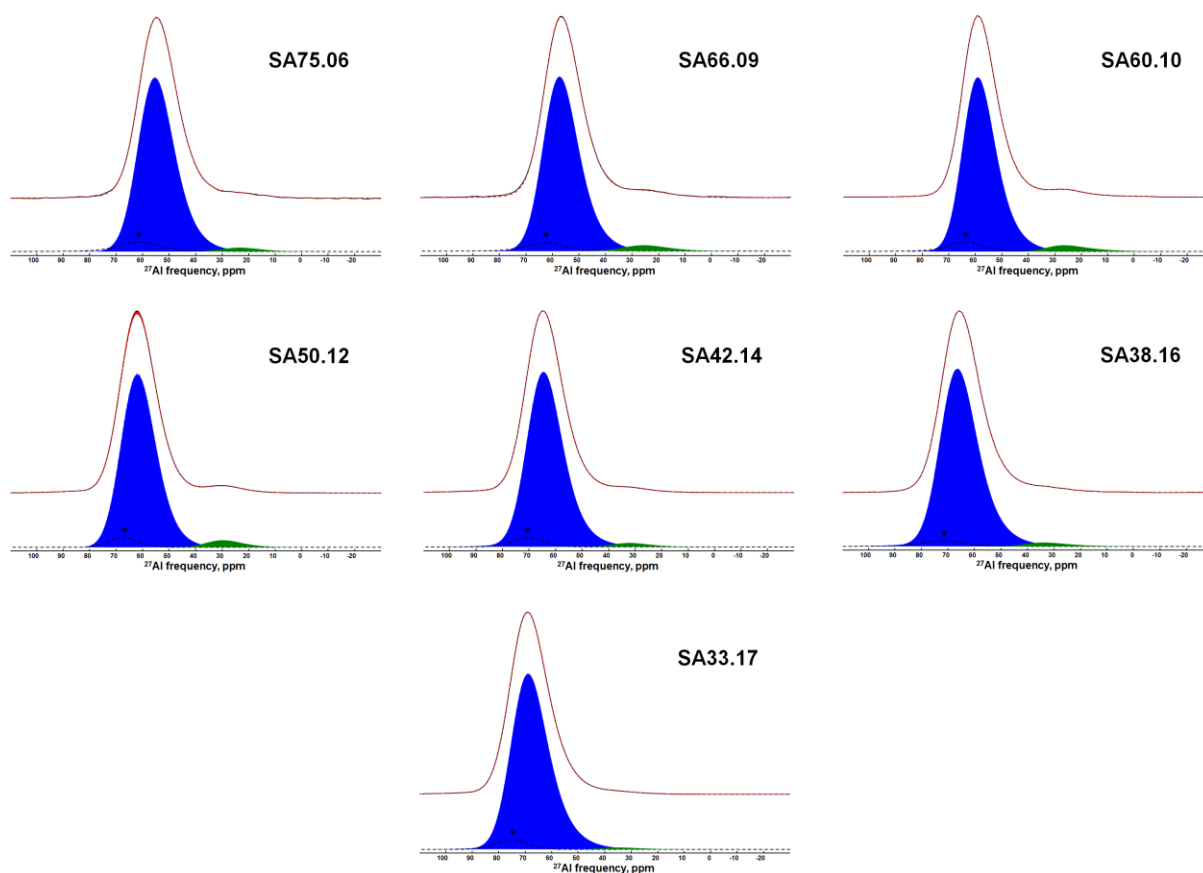


Figure III.22. Deconvolution of the ^{27}Al MAS NMR spectra of Sr peralkaline glasses. Colour guide: blue – AlO_4 , green – AlO_5 , black dashed lines with an asterisk – spinning sidebands.

The isotropic chemical shift of both sites changes almost linearly with silica content (Figure III.23). However, at low silica content, the values of the $\delta_{iso}(\text{AlO}_4)$ differ slightly for the peralkaline and tectosilicate glasses. This deviation from the linear trend potentially might be caused by the presence of depolymerized Q^n species with Al as a central atom. The existence of Al-NBO bonds for analogous silica-poor Ca aluminosilicate glasses has been suggested by (Allwardt et al., 2003; Neuville et al., 2006). Al-NBO bonds were also detected in highly polymerized rare-earth aluminosilicate glasses (Jaworski et al., 2016, 2015).

The population of AlO_5 sites in the glasses along the join R = 3 reaches 4-5 % that is similar to the AlO_5 fraction in the tectosilicate glasses. However, the maximum is shifted to silica-rich compositions with respect to the glasses along the join R = 1.

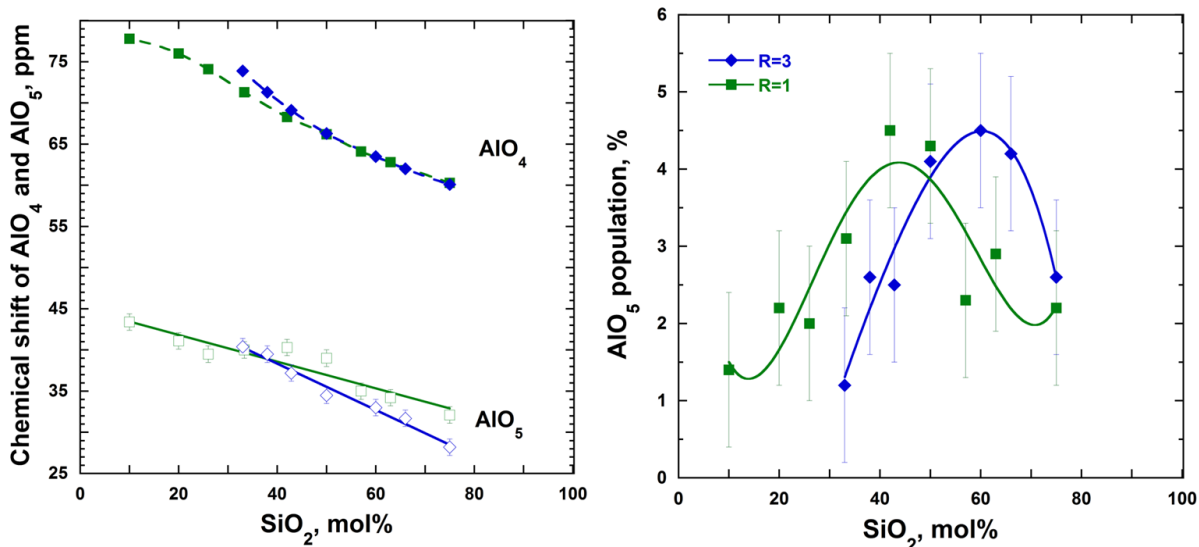


Figure III.23. *Left*: evolution of isotropic chemical shift (δ_{iso}) of AlO_4 and AlO_5 for Sr tectosilicate (green) and peralkaline (blue) glasses. If not visible, error bars are less than symbol's size. *Right*: AlO_5 population for Sr tectosilicate (green) and peralkaline (blue) glasses. The lines are a guide to the eye.

^{27}Al NMR clearly shows that the tetrahedral coordination dominates the Al speciation in the glasses along the join $R = 3$. Only a small fraction of five-coordinate aluminium, less than 5 %, is present. Its presence, however, is unexpected along the $\text{SiO}_2\text{-Sr}_3\text{Al}_2\text{O}_6$ join, since there is an excess of Sr cations to charge compensate all the AlO_4^- tetrahedra. Nevertheless, AlO_5 has been already reported for other alkaline earth aluminosilicate glasses in the peralkaline domain (see, for example, (Neuville et al., 2008, 2004b)).

^{29}Si NMR spectra of the peralkaline glasses show similar trends as it was already observed for the tectosilicate and silicate glasses. Namely, under the substitution of SiO_2 by $\text{Sr}_3\text{Al}_2\text{O}_6$ the line's barycentre position changes to higher values of the chemical shift (Figure III.24). At the same time, the linewidth decreases significantly from silica-rich to silica-poor compositions.

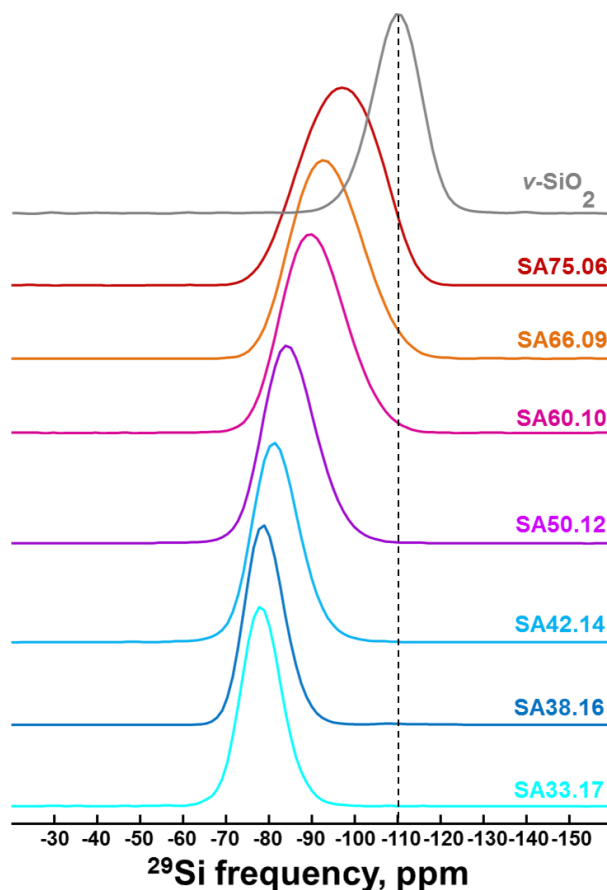


Figure III.24. ^{29}Si MAS NMR spectra of Sr peralkaline glasses. Silica content decreases from top to bottom.

In the case of the tectosilicate glasses the ^{29}Si NMR line is composed of the signals of Q_m^4 species and in the case of the silicate glasses it is composed of the signals of different Q^n species. For the peralkaline glasses the situation is more complex. The whole signal is a combination of the signals of the whole set of Q_m^n species. Since the contributions from Si-NBO and Si-O-Al give their own signals with particular line positions and the ranges of appearance of different Q_m^n species are not well-defined, large and overlapping, we believe that any attempt of direct deconvolution will result in an unreliable fit. Therefore, we have not deconvoluted the experimental ^{29}Si NMR data for the glasses along the join $R = 3$.

3.2. Neutron diffraction

As in the case of the tectosilicate glasses, the FSDP in $S(q)$ shifts to higher q values and its intensity decreases when $\text{Sr}_3\text{Al}_2\text{O}_6$ substitutes SiO_2 (Figure III.25). It suggests (as in the case of the tectosilicate glasses) a decrease of the size of tetrahedral rings.

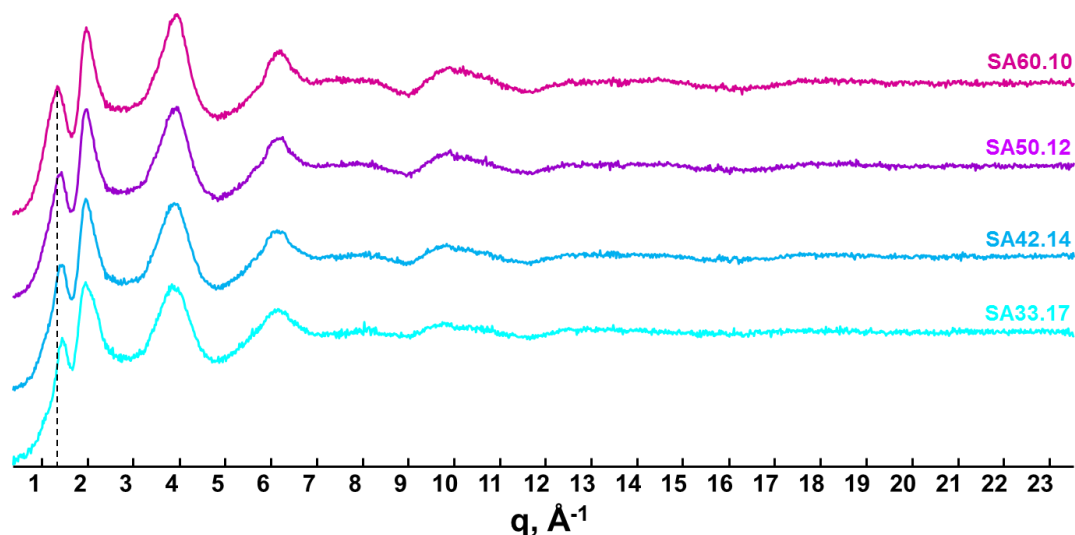


Figure III.25. Static structure factor, $S(q)$, of Sr peralkaline glasses. Silica content decreases from top to bottom.

The first peak in $g(r)$ shifts to higher r values as SiO_2 content decreases (Figure III.26). This change of the peak's position is due to the change of the Al/Si ratio since the signals convoluted in this peak correspond to contributions from Si-O and Al-O pairs. The second peak does not change its position for all the peralkaline glasses studied. This peak is composed of the contributions from Sr-O and O-O pairs as described previously.

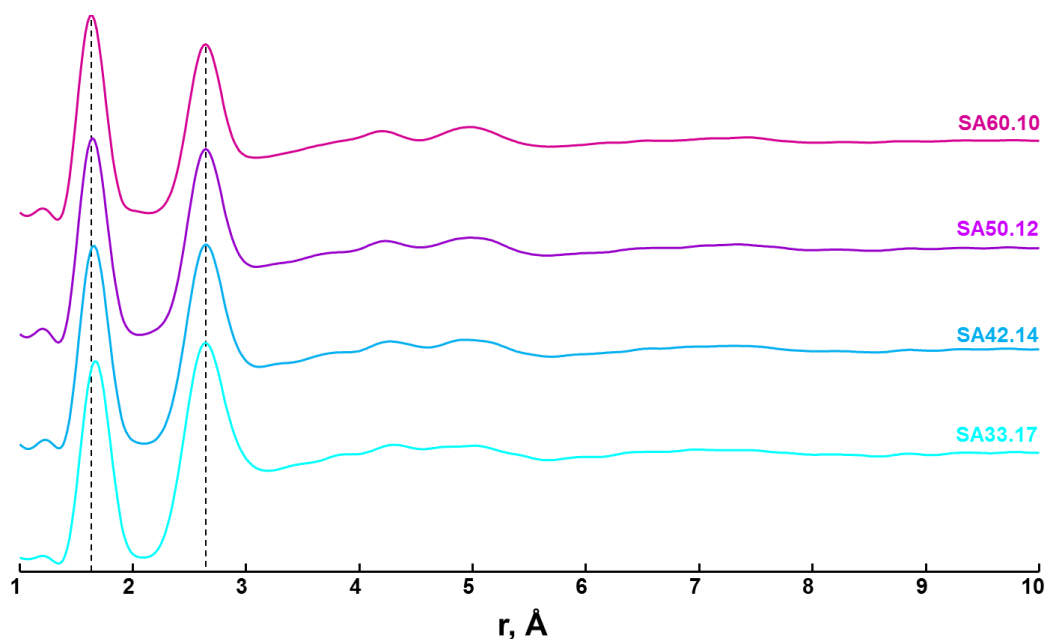


Figure III.26. Pair distribution function, $g(r)$, of Sr peralkaline glasses. Silica content decreases from top to bottom.

MD simulations performed by Thibault Charpentier (personal communication, Figure III.27) showed that in the case of glasses along the join $R = 3 \text{ CN}(\text{Sr-O})$ varies from 6 to 10 as for the tectosilicate glasses with maximum, however, being around 8 (8-9 for the tectosilicate glasses). Another difference between the two joins shown by the MD simulations is the number of NBOs and TBOs. In the case of Sr peralkaline glasses the fraction of non-bridging oxygens increases from $\sim 20\%$ for silica-rich compositions up to $\sim 40\%$ for silica-poor ones. At the same time, the number of three-coordinate oxygens is around zero while for the tectosilicate glasses it is about 5-10 %.

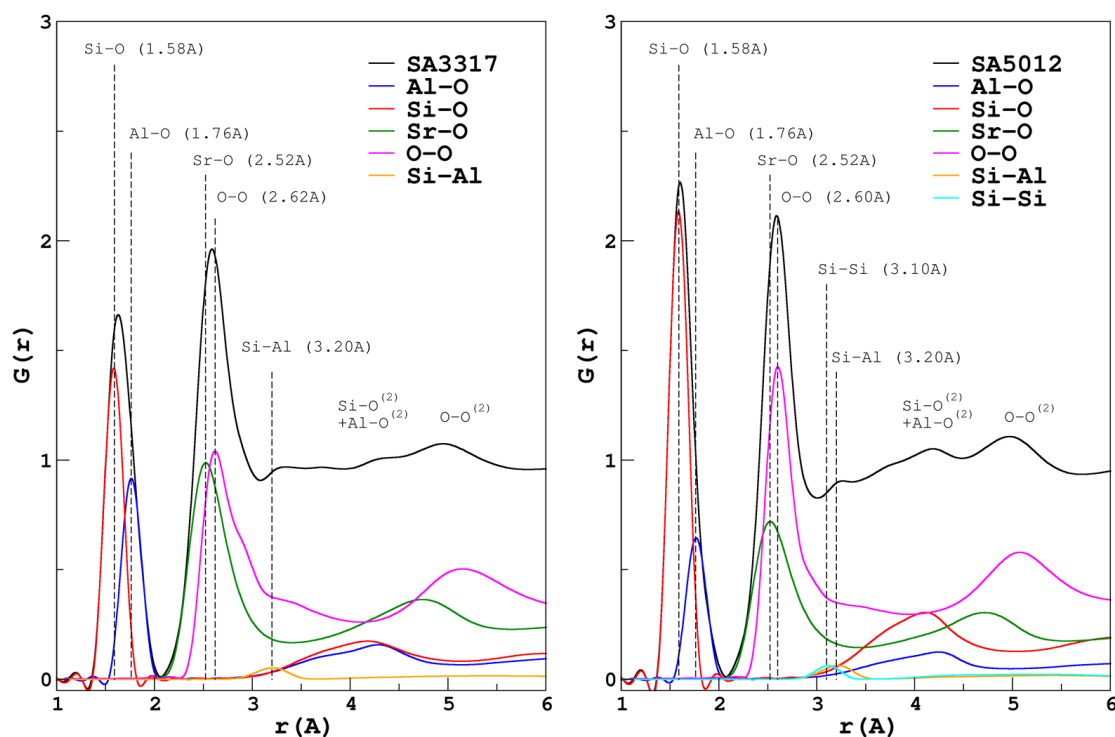


Figure III.27. Partial pair distribution functions $g_{ij}(r)$ calculated from the results of MD simulations together with experimental $g(r)$ for two Sr peralkaline glasses.

3.3. Raman spectroscopy

Raman spectra of the glasses along the $\text{SiO}_2\text{-Sr}_3\text{Al}_2\text{O}_6$ join, shown in Figure III.28, possess all the main features observed in the Raman spectra of the tectosilicate and silicate glasses. As in case of the tectosilicate glasses, two peaks located at ~ 500 and $\sim 570 \text{ cm}^{-1}$ are assigned to breathing motions in four- (D_1 band) and three-membered (D_2 band) rings. The D_2 band moves towards lower frequency under the substitution of SiO_2 by $\text{Sr}_3\text{Al}_2\text{O}_6$ implying incorporation of Al into three-membered rings (Le Losq, 2012). At the same time, their

intensities change. For SA75.06 glass the intensity of the D_1 band is higher than of the D_2 one and decreases with decreasing silica content. At the same time, the D_2 band grows in intensity. This change in the band's intensities suggests a change in ring statistics with composition and is in agreement with our ND data. There is a broad band of low intensity around $340\text{-}350\text{ cm}^{-1}$ in the spectra of all glasses except for the most silica-rich ones (SA66.09 and SA75.06). This band was already observed in the spectra of the silicate glasses and was assigned to Sr-O vibrations. In the low-frequency region, there is another band at $\sim 220\text{ cm}^{-1}$ that is clearly seen in the spectra of silica-poor glasses. This band was not observed in the spectra of the tectosilicate but was visible for one silicate glass. The band has been assigned to cation-oxygen vibration involving either NBOs or AlO_4^- units (Hehlen and Neville, 2015), involving cations playing both roles: of network modifier and charge compensator.

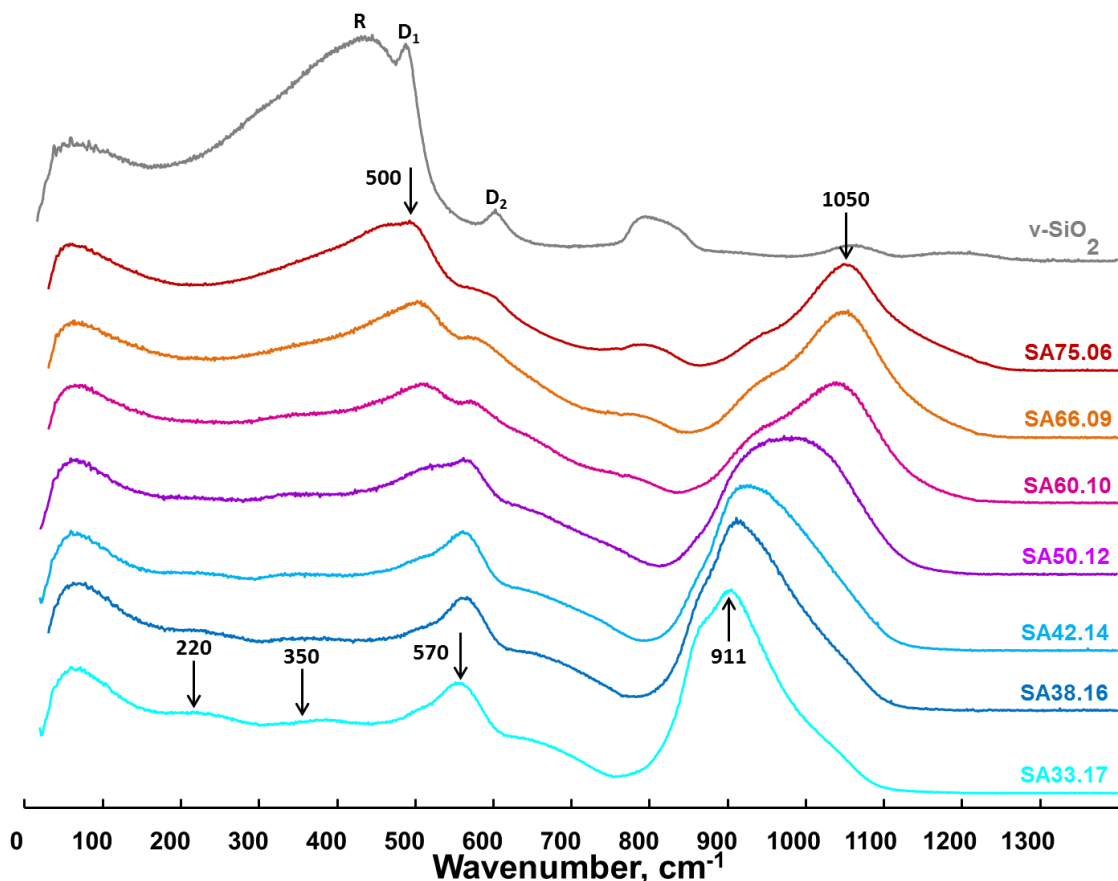


Figure III.28. Area normalized Raman spectra of Sr peralkaline glasses. Numbers correspond to the frequencies of observed bands maxima. Silica content decreases from top to bottom.

In the HF region of the Raman spectra a broad band caused by vibrations in different Q^n units shifts to lower wavenumber values with decreasing SiO_2 content, as in the case of two other series. The band's barycentre position is plotted in Figure III.29 as a function of composition. We can see that, once again, from 100 to 66 mol% of SiO_2 the barycentre shifts with the same slope ($2.3 \pm 0.1 \text{ cm}^{-1}/\text{mol}\%$ of SiO_2) as in the case of the silicate and tectosilicate glasses. With the further substitution of SiO_2 by $\text{Sr}_3\text{Al}_2\text{O}_6$ the slope changes to $3.5 \pm 0.1 \text{ cm}^{-1}/\text{mol}\%$ of SiO_2 ($4.4 \pm 0.1 \text{ cm}^{-1}/\text{mol}\%$ of SiO_2 for the silicate glasses). Therefore, the deviation of the barycentre's position from the straight line of the tectosilicate glasses can potentially be used as a measure of the network polymerization degree.

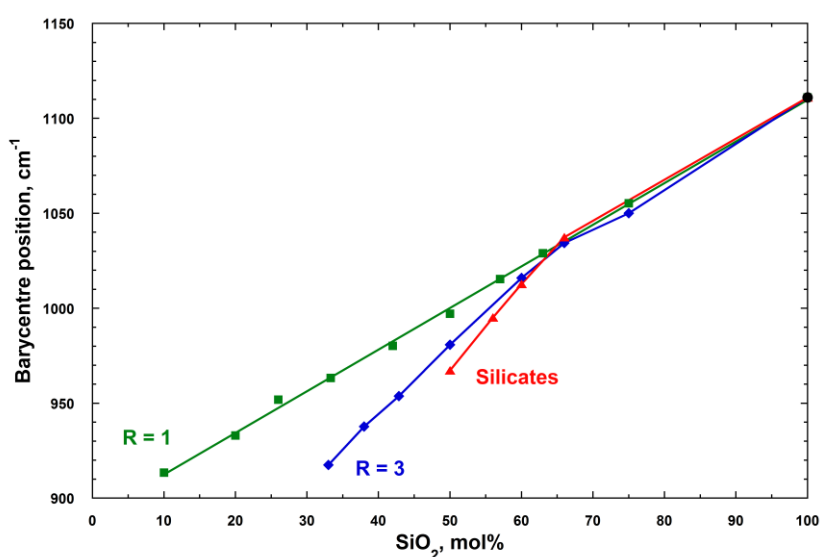


Figure III.29. Barycentre position of the high-frequency envelope of Raman spectra of Sr tectosilicate (green), peralkaline (blue) and silicate (red) glasses. The lines are a guide to the eye.

The HF region of the Raman spectra was deconvoluted with a set of Gaussian bands (Figure III.30). While for SA75.06 Q^2 to Q^4 species were found, for SA33.17 a set of Q^n species from Q^0 to Q^2 are present. In the spectrum of SA33.17 glass, an additional band at $\sim 800 \text{ cm}^{-1}$ is required to fit properly the low-frequency end of the HF envelope. The position of the band matches well with the position of the HF envelope in Raman spectra of Ca, Sr and Ba aluminate glasses (Licheron et al., 2011). This leads us to the conclusion that the band at $\sim 800 \text{ cm}^{-1}$ may arise from vibrations in depolymerized TO_4 tetrahedral units with $T = \text{Al}$. The fact that an additional band is required only in case of the most depolymerized SA33.17 glass correlates with our suggestion of the existence of Al-NBO bonds in this glass made from ^{27}Al NMR data.

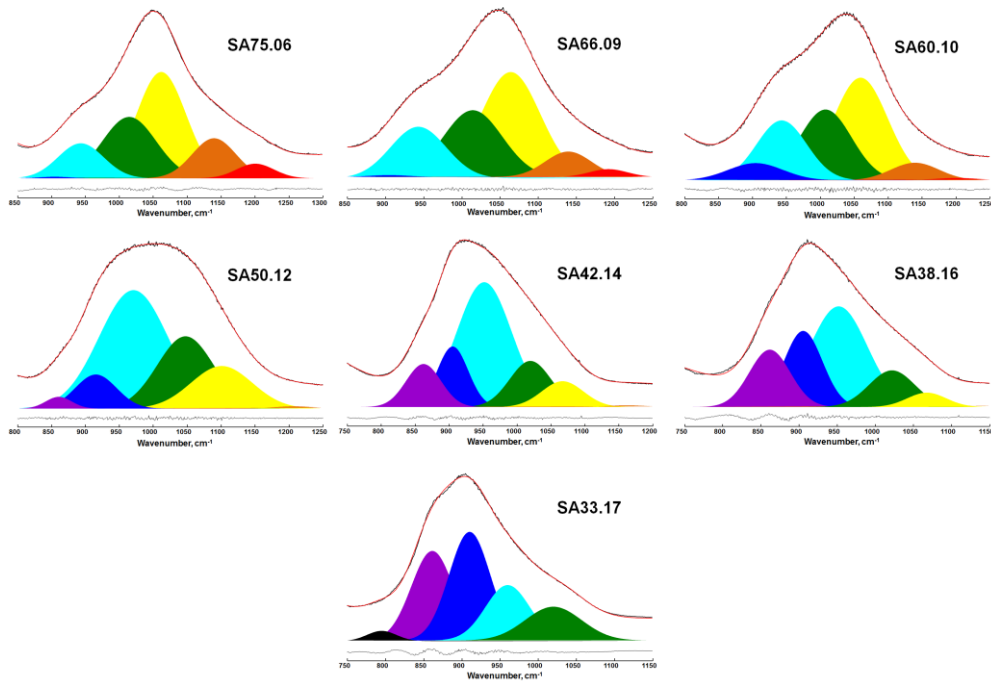


Figure III.30. Deconvolution of the HF region of the Raman spectra of Sr peralkaline glasses. Colour guide: red – $Q^{4,I}$, orange – $Q^{4,II}$, yellow – Q^3 , green – T_{2s} , turquoise – Q^2 , blue – Q^1 , violet – Q^0 , black – Al-NBO band.

The results of the deconvolution are presented in Figure III.31. In the same figure the population of Q^n species calculated assuming their random distribution is presented. The graph demonstrates why no glass could be obtained for composition with 20 mol% of SiO_2 (SA20.20). The reason for this is that the most part (if not 100 %) of Q^n species should be present in Q^0 species that are unable to create a continuous glass network.

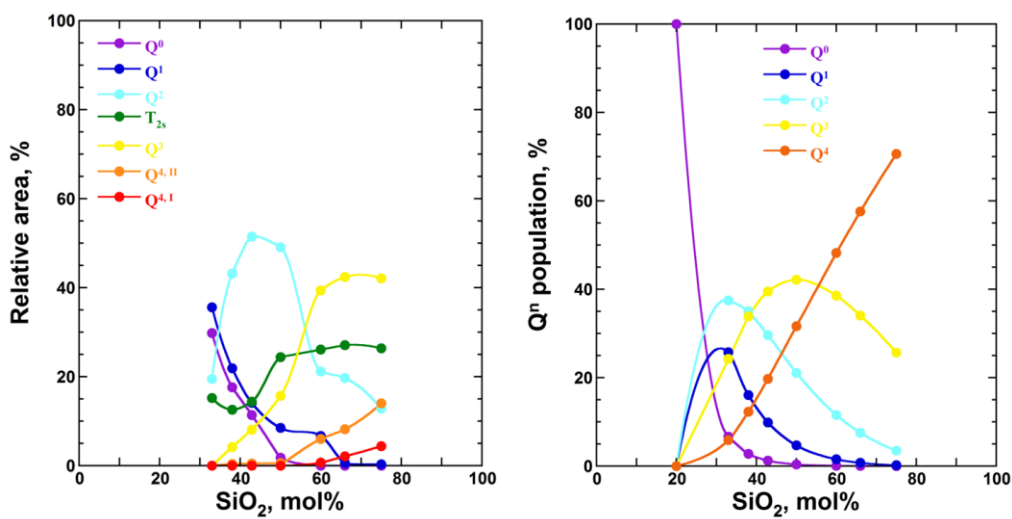


Figure III.31. *Left*: The relative area under the Gaussian bands obtained from deconvolution of the high-frequency region of the Raman spectra of Sr peralkaline glasses. *Right*: Population of Q^n species assuming their random distribution calculated after (Moesgaard et al., 2010).

3.4. Macroscopic properties

Both density and molar volume of the glasses on the join $R = 3$ lie in between those of the tectosilicates and silicates (Figure III.32). The density increases continuously under the substitution of SiO_2 by $\text{Sr}_3\text{Al}_2\text{O}_6$. Unlike the molar volume of the tectosilicate glasses, the V_m of compositions on the join $R = 3$ first drops fast when $\text{Sr}_3\text{Al}_2\text{O}_6$ is introduced into silica network, showing the behaviour close to that of the silicates. In the range of 33-50 mol% of SiO_2 it stays almost constant but with an overall trend to increase slowly until the aluminate composition.

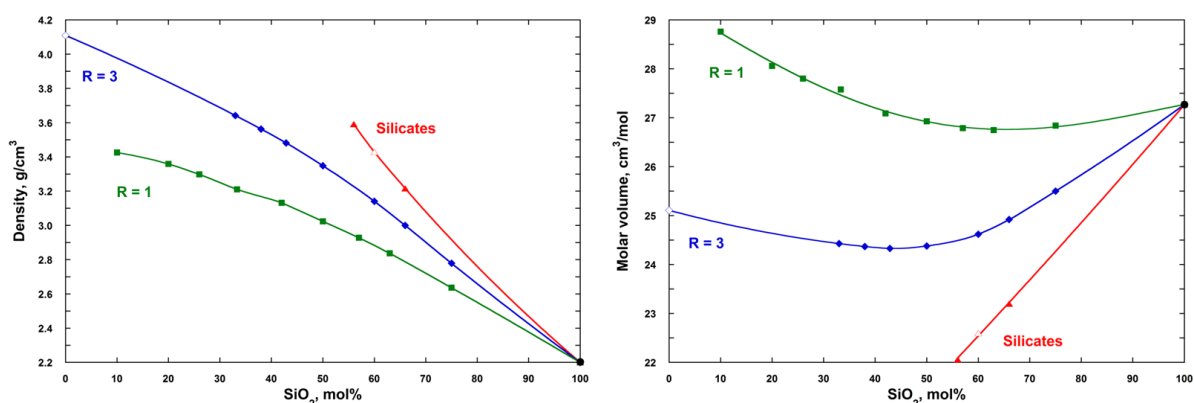


Figure III.32. Experimental densities (*left*) and calculated molar volumes (*right*) of Sr tectosilicate (green), peralkaline (blue) and silicate (red) glasses together with the literature data (blue open circle) for an aluminate glass (Alahraché et al., 2013). The black filled circle corresponds to the density of vitreous silica taken from (Brückner, 1970). Error bars are less than the symbol size. The lines are a guide to the eye.

Taking into account what was already discussed previously, we can suggest that, at first, when SiO_2 is substituted by $\text{Sr}_3\text{Al}_2\text{O}_6$, the V_m decreases due to the packing of the network caused by its depolymerization. Then the interplay between overall depolymerization and introduction of Al causes a slight increase of the molar volume.

Viscosity data for the glasses along the join $R = 3$ are plotted in Figure III.33. The first thing that catches the eye is a reverse order of the viscosity curves. We have already observed such behaviour for the silicate glasses but it was less pronounced since the compositional variation was small.

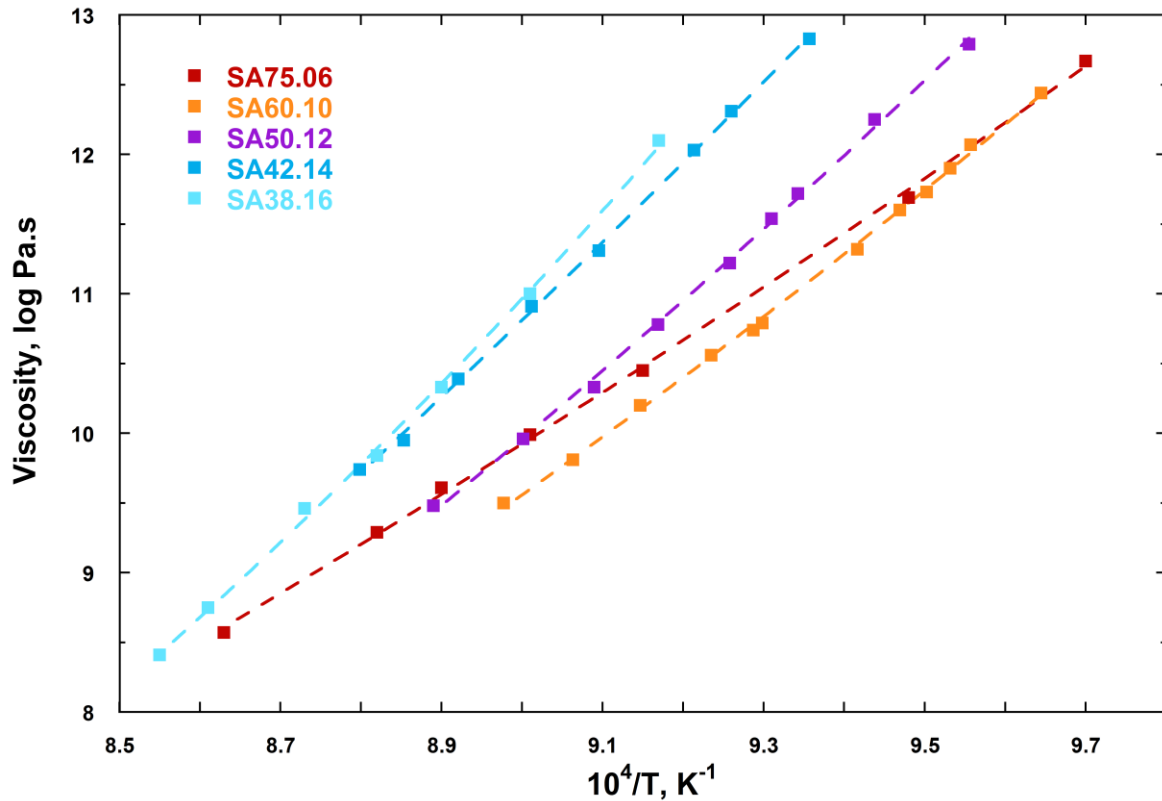


Figure III.33. Low-temperature viscosity curves for Sr peralkaline glasses. Error bars are less than the symbol size. The dashed lines are corresponding VFTH fits.

The T_g values for the glasses along the join $R = 3$ were extracted from the viscosity data by fitting the experimental data with the VFTH equation. As in the case of density and molar volume, the T_g curve of the peralkaline glasses is located between the curves for the tectosilicate and silicate glasses (Figure III.34). The T_g for silica-rich (60-75 mol% of SiO_2) peralkaline compositions do not differ much. With decreasing silica content the T_g curve rises until 33 mol% of SiO_2 . Again such behaviour is similar to that observed for the silicate glasses and might have a similar explanation. However, the whole picture must be more complex since Al is present in the glass network. A data point for $\text{Sr}_3\text{Al}_2\text{O}_6$ glass lies almost 150 K lower than for the closest silica-poor glass on the same join (SA33.17). Such behaviour with an increase and a following drop of T_g for glasses on the joins with $1 < R \leq 3$ has been already reported for Ca aluminosilicate glasses (Higby et al., 1990; Neuville et al., 2004a; Shelby, 1985).

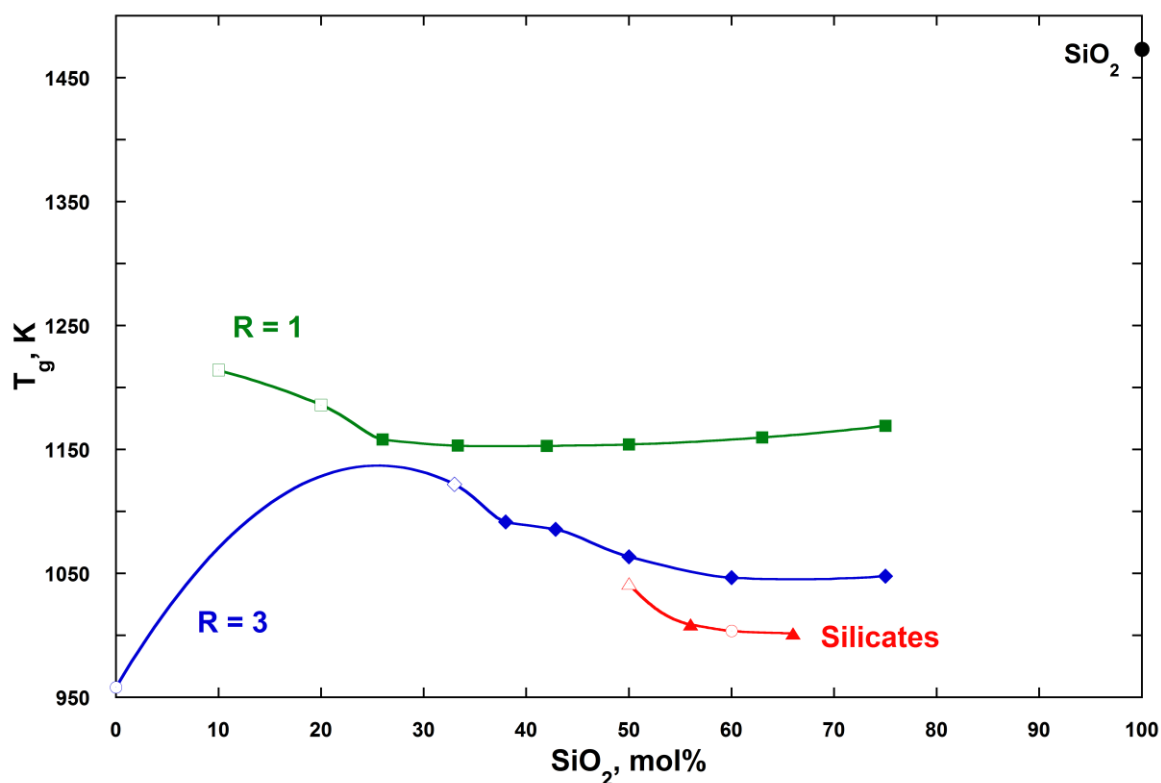


Figure III.34. Glass transition temperatures for Sr tectosilicate (green), peralkaline (blue) and silicate (red) glasses. Filled symbols are T_g values extracted from viscosity data, open symbols are T_g values from DSC measurements and open circles correspond to the literature data (Alahraché et al., 2013; Neuville, 2005). The glass transition temperature of vitreous silica (black filled circle) is given for comparison (Mackenzie, 1963). If not visible error bars are less than the size of symbols. The lines are a guide to the eye.

For peralkaline CAS glasses it has been suggested (Shelby, 1985) that Ca must change the role it plays in the glass network with decreasing SiO₂ content. If it continued acting only as a charge compensator or network modifier one would expect a continuous decrease in T_g from vitreous silica coupled with depolymerization of the network. Therefore, Ca must somehow participate in the network's linkage causing the augmentation of the T_g with decreasing silica content in this region. A similar idea has been proposed for Ca silicate glasses and discussed above (De Sousa Meneses et al., 2006). The increase of T_g should also be accompanied by the reorganization of the aluminosilicate network. Since Si-NBO bands are more energetically favourable than Al-NBO ones (Allwardt et al., 2003; Lee and Stebbins, 2006), then, under the substitution of SiO₂ by Sr₃Al₂O₆, Si should enter the most depolymerized Qⁿ units. Such depolymerized Qⁿ units would be distributed at the edge of the network leaving AlO₄ tetrahedra to gather into an ordered aluminate subnetwork (Higby et al., 1990). However, at some point, the aluminate subnetwork starts to depolymerize as

well with decreasing silica content. Al progressively enters depolymerized Q^n units and it causes a drop in T_g until it reaches a minimum for the aluminate glass composed of AlO_4 tetrahedra in different Q^n units. Since the behaviour of the T_g curve for Sr peralkaline glasses is very similar to that for the Ca ones, we believe that analogous explanation can be used.

Section highlights

- Si tetrahedra are present in different Q^n species while Al is in fully polymerized Q^4 units. The existence of Al-NBO bonds is suggested only for the most silica-poor composition. A small fraction of AlO_5 (4-5 %) is found in Sr peralkaline glasses as well.
- ND and Raman show changes in the ring statistics towards small-membered rings with decreasing SiO_2 content. In the low-frequency region of the Raman spectra of silica-poor compositions, two bands are clearly observed as in the case of the silicate glasses.
- Molar volume of the glasses on the join $R = 3$, being intermediate between those of tectosilicates and silicates, decreases under the substitution of SiO_2 by $Sr_3Al_2O_6$ down to 50 mol% of silica and then increases slightly.
- Glass transition temperature increases from 75 to 33 mol% of SiO_2 and then drops down for aluminate glass.

4. Peraluminous domain ($R < 1$)

In the peraluminous field, the network is expected to be highly polymerized as in the case of tectosilicate glasses. However, the excess of Al_2O_3 over SrO means that not all AlO_4^- tetrahedra can be charge compensated by Sr^{2+} . To cope with this situation other mechanisms of charge compensation such as the formation of high-coordinate AlO_x sites and three-coordinate oxygens will be involved. One would expect Al-O-Al bonds to form in high amounts in violation of the Loewenstein rule ([Loewenstein, 1954](#)).

In previous sections we demonstrated the influence of the Si/Al substitution along three different joins (silicate, peralkaline and tectosilicate compositions) on the glass structure and properties. In this section we would like to discuss the effect of aluminium at constant SiO_2 content, i.e. the effect caused by the Sr/Al substitution. To enlarge our discussion, we

will add some peraluminous glasses to already described ones and will follow two composition lines SA50.xx and SA33.xx.

4.1. ^{27}Al and ^{29}Si NMR spectroscopy

Figure III.35 presents ^{27}Al and ^{29}Si NMR spectra of the glasses in the SA50.xx series. There is a clear change in the distribution of Al in different AlO_x sites under the Sr/Al substitution. The fraction of AlO_5 increases significantly from 12.5 to 40 mol% of Al_2O_3 . One new contribution that was not observed in the spectra of the peralkaline and tectosilicate glasses is located at ~ 10 ppm. This peak originates from the aluminium atoms in six-coordinate sites (AlO_6). Its proportion is small, however, and does not exceed 6 % for the most peraluminous SA50.40 glass.

^{29}Si NMR line moves to lower values of the chemical shift when alumina is introduced into the glass network. At the same time, the linewidth increases significantly. We have seen in the first section of this chapter that the spectrum of SA50.25 glass was deconvoluted with four lines corresponding to Q^4_1 to Q^4_4 units. One would expect a reduction of the lines' number caused by augmentation of Al_2O_3 and, as consequence, the increased number of Al neighbours in the second coordination shell of Si atoms. The broadening of the signal can also be caused by the increase of inter-tetrahedral angles in the network. Nevertheless, an overall increase of the disorder in the system (increase in high-coordinate Al sites proportion) should also contribute to this broadening. It is well correlated with broadening of the signal of different Al sites (namely, their C_Q) as seen by ^{27}Al NMR. Therefore, both sets of spectra show an overall increase of disorder in the system under the Sr/Al substitution.

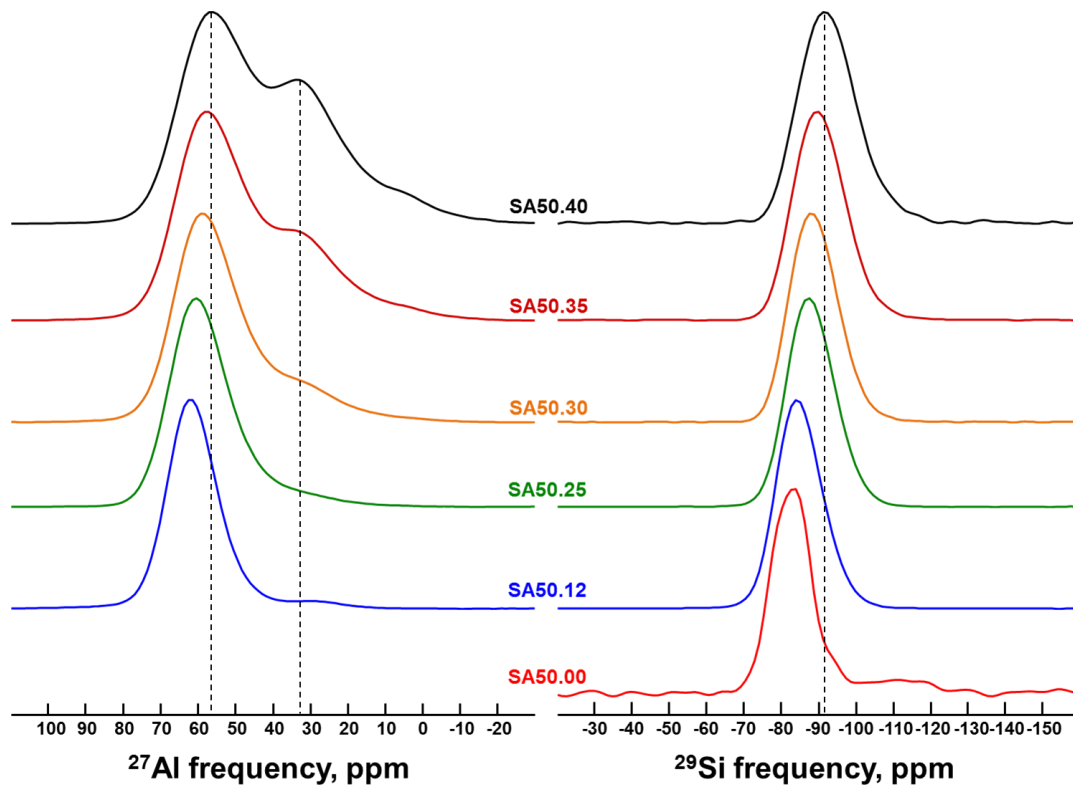


Figure III.35. ^{27}Al (*left*) and ^{29}Si (*right*) MAS NMR spectra of glasses in the SA50.xx series. Alumina content decreases from top to bottom.

For the glasses in the SA33.xx series the trends seen in the ^{27}Al and ^{29}Si NMR spectra (Figure III.36) are very similar to those observed for the glasses in the SA50.xx series.

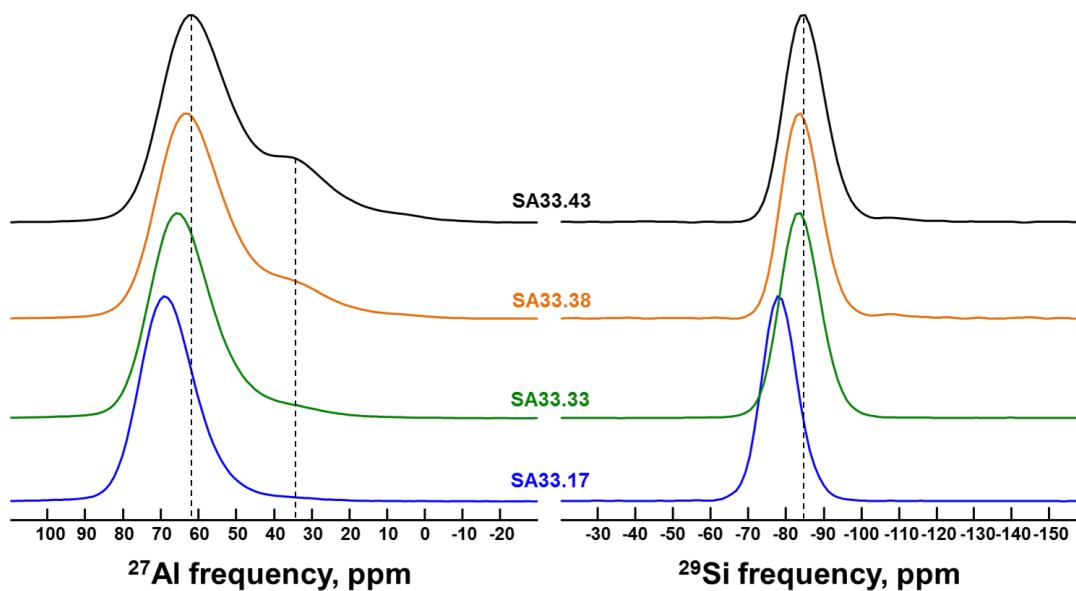


Figure III.36. ^{27}Al (*left*) and ^{29}Si (*right*) MAS NMR spectra of glasses in the SA33.xx series. Alumina content decreases from top to bottom.

The deconvolution of ^{27}Al NMR spectra of Sr peraluminous glasses is shown in Figure III.37.

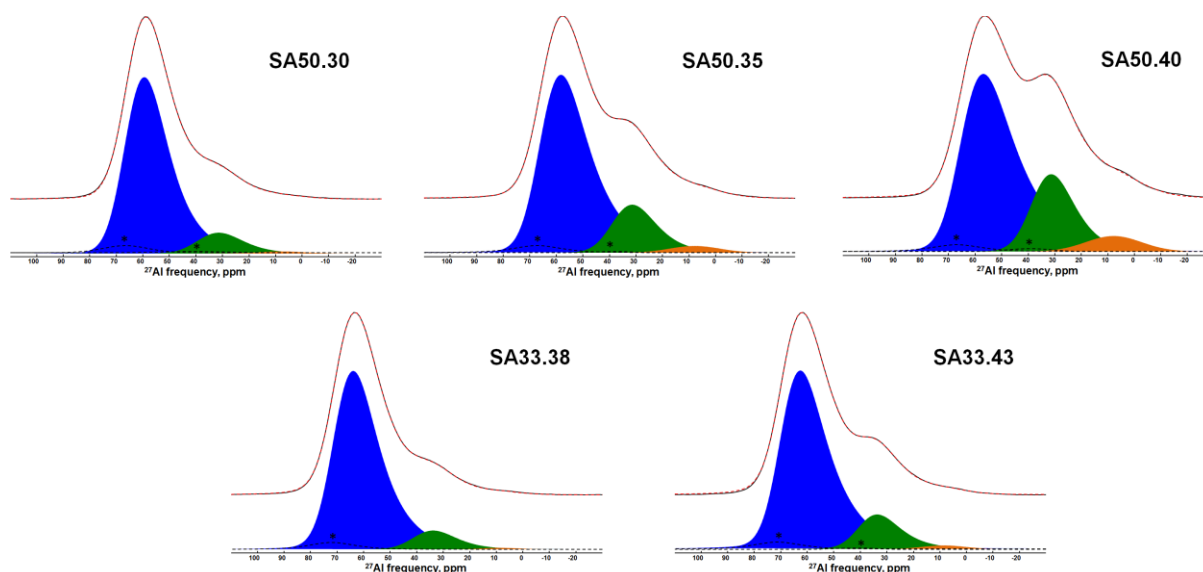


Figure III.37. Deconvolution of the ^{27}Al MAS NMR spectra of Sr peraluminous glasses. Colour guide: blue – AlO_4 , green – AlO_5 , orange – AlO_6 , black dashed lines with an asterisk – spinning sidebands.

The isotropic chemical shifts for three AlO_x sites are plotted in Figure III.38. The δ_{iso} does not vary significantly within each series with augmentation of alumina content, suggesting slight to no changes occurring in the second coordination shell of Al atoms under Sr/Al substitution. This reflects the fact that for all compositions the aluminium environments are solely made of Q_4^4 units (i.e. linked to four silicon atoms) and that no significant fraction of NBOs is on Al atoms. The deviation observed for $\delta_{iso}(\text{AlO}_5)$ of SA50.12 glass can be explained by the difficulty to unambiguously define the position of low-abundant AlO_5 sites. Another deviation to higher values of $\delta_{iso}(\text{AlO}_4)$ for SA33.17 glass can be connected to the formation of a small fraction of NBOs connected to Al as discussed previously.

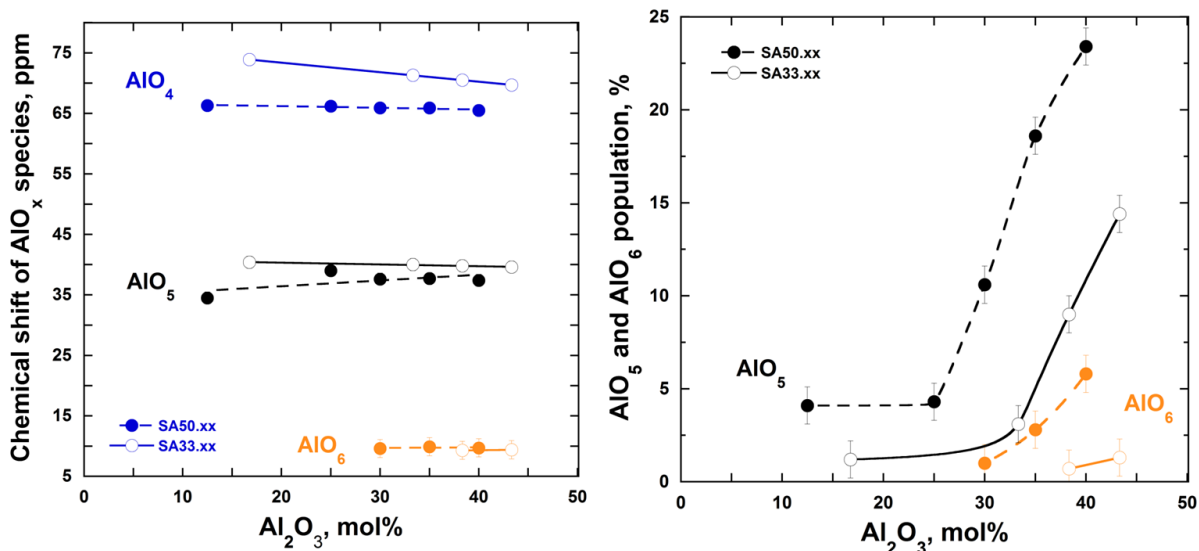


Figure III.38. *Left*: evolution of isotropic chemical shift (δ_{iso}) of AlO_4 (blue), AlO_5 (black) and AlO_6 (orange) sites for glasses in the SA50.xx (filled circles) and SA33.xx (open circles) series. *Right*: AlO_5 and AlO_6 population for glasses in the SA50.xx (filled circles) and SA33.xx (open circles) series. The lines are a guide to the eye.

The fraction of high-coordinate Al species does not change much from the peralkaline to tectosilicate compositions and after its increase is proportional to alumina content.

4.2. Raman spectroscopy

Raman spectra of the glasses in the SA50.xx series are presented in Figure III.39. Following changes occur in the spectra under the Sr/Al substitution. In the low-frequency region we can see two bands in the spectrum of SA50.00 corresponding to Sr-O vibrations. They become less pronounced with the introduction of 12.5 mol% of Al_2O_3 and then vanish from the spectra of glasses with more alumina. In the medium-frequency region, we observe an intense band in the spectrum of the silicate glass corresponding to vibrations in three-membered rings (D_2 band). This band shifts to lower frequencies since the tetrahedral rings start to incorporate not only three Si tetrahedra but also a combination of $\text{SiO}_4\text{-AlO}_4\text{-SiO}_4$ and $\text{AlO}_4\text{-SiO}_4\text{-AlO}_4$ threesomes (perhaps, even rings composed of three Al tetrahedra). At the same time, this band becomes less intense suggesting a decrease in the fraction of three-membered rings. Another band at lower frequency appears under the Sr/Al substitution as well, corresponding to vibrations in four-membered rings (D_1 band). This band becomes of low intensity in the spectra of the peraluminous glasses, and, at the same time, the frequency region between the Boson peak and the D_1 band becomes more

intense. Such increase might be caused by the augmentation of the fraction of high-membered rings.

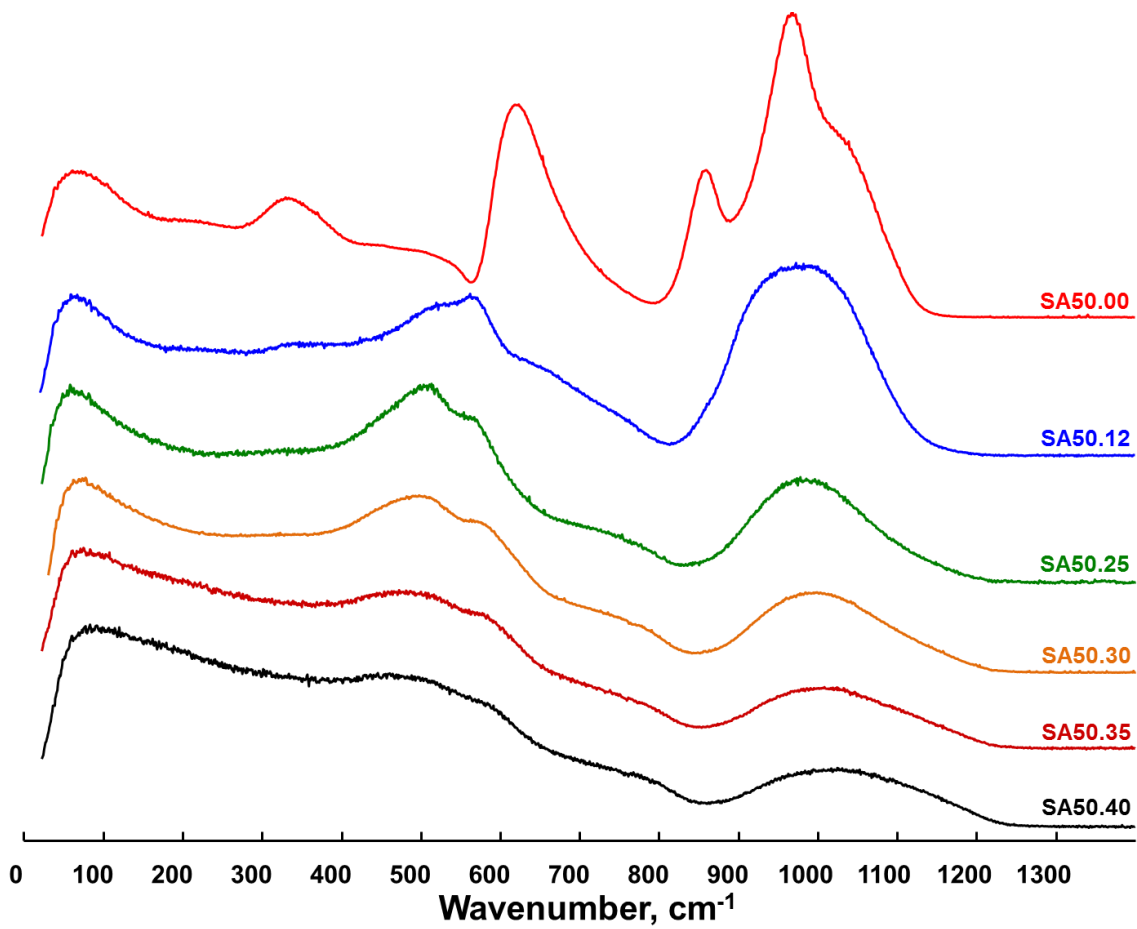


Figure III.39. Area normalized Raman spectra of glasses in the SA50.xx series. Alumina content increases from top to bottom.

For the series of SA33.xx glasses the same comments are true on the changes in their Raman spectra (Figure III.40).

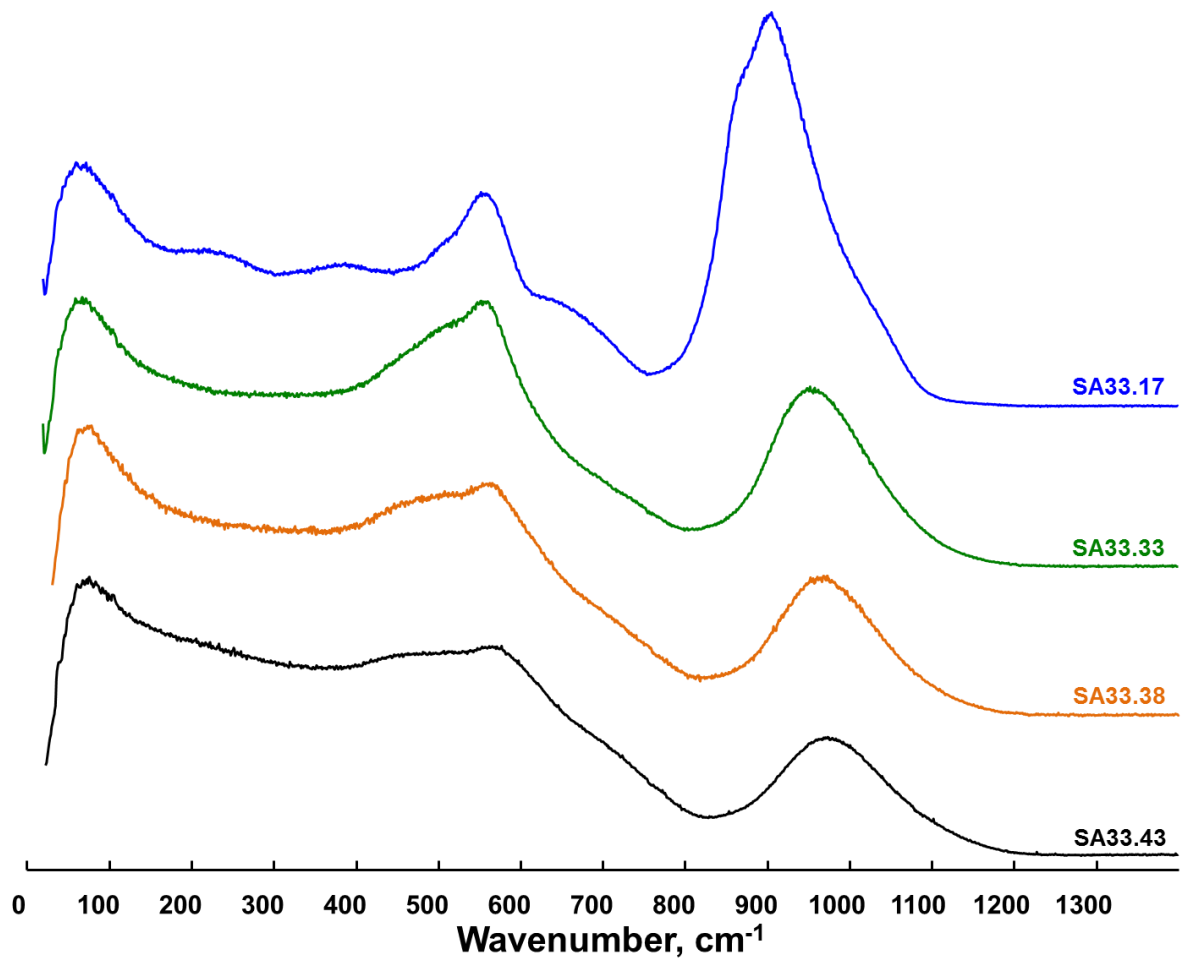


Figure III.40. Area normalized Raman spectra of glasses in the SA33.xx series. Alumina content increases from top to bottom.

Deconvolution of the HF envelope of the Raman spectra of the peraluminous glasses (Figure III.41) showed that, as in the case of the tectosilicate glasses, only Q^4 units are present in the glass network. Due to the increase of the fraction of $Q^{4,1}$ units (those with higher T-O-T angles, where T = Si or Al) the whole HF envelope shifts to higher frequencies. This observation is in good agreement with the broadening of the ^{29}Si NMR bands for the peraluminous glasses, confirming that it can be caused by the increase of inter-tetrahedral angles.

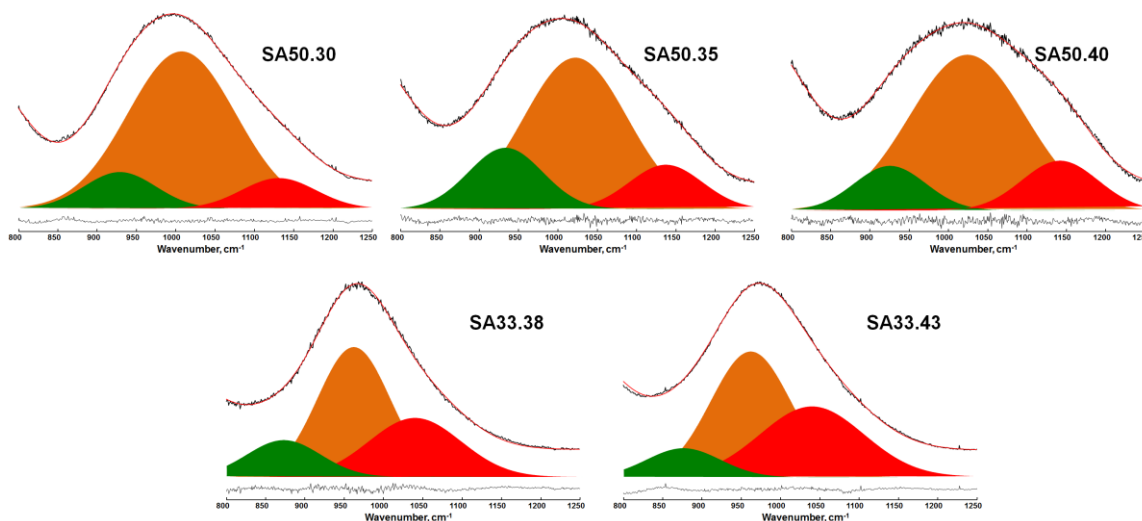


Figure III.41. Deconvolution of the HF region of the Raman spectra of Sr peraluminous glasses. Colour guide: red – $Q^{4,I}$, orange – $Q^{4,II}$, green – T_{2s} .

4.3. Macroscopic properties

The effect of Sr/Al substitution at constant silica content is clearly seen in Figure III.42. For both series density diminishes with the addition of Al_2O_3 into the glass network, while molar volume rises.

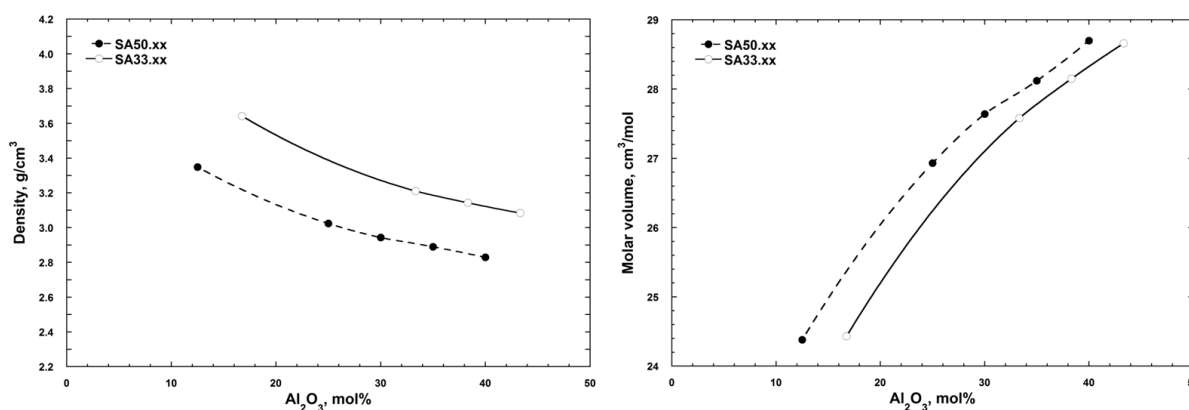


Figure III.42. Experimental densities (*left*) and calculated molar volumes (*right*) of glasses in the SA50.xx (filled circles) and SA33.xx (open circles) series. The lines are a guide to the eye.

The increase of the V_m with increasing alumina content correlates well with an overall rise in the system's disorder. Raman spectra show a change in ring statistics from three-membered rings for the silicate glasses to (potentially) high-membered (≥ 5) rings for the peraluminous glasses. NMR data indicates augmentation of high-coordinate Al sites.

Section highlights

- The fraction of high-coordinate AlO_x species increases significantly under Sr/Al substitution. ^{27}Al and ^{29}Si NMR show a rise of disorder in the system with increasing Al_2O_3 content.
- Raman and ^{29}Si NMR indicate an overall increase of T-O-T (T = Si or Al) angles. Changes in the ring statistics towards high-membered rings are inferred.
- Molar volume increases continuously from alumina-poor to alumina-rich compositions.

5. High-temperature melts

In this section we are going to discuss structure and properties of liquid Sr aluminosilicates at high temperatures ($> 1600\text{ }^\circ\text{C}$).

5.1. High-temperature ^{27}Al NMR spectroscopy

One of the techniques to probe the local structure in aluminosilicate melts is high-temperature ^{27}Al NMR. It allows characterizing melts dynamics as well as following changes in AlO_x speciation during the cooling of the samples from temperature well above $2000\text{ }^\circ\text{C}$. By recording one spectrum each 9 ms during free cooling of melt we were able to collect a great number of data points at different temperatures until disappearance of the signal (below $1600\text{ }^\circ\text{C}$). Each dataset for an individual composition consists of 100 to 200 individual spectra, simultaneous treating of which allows extracting temperature dependent line's position δ and FWHM. Each individual spectrum is a Lorentzian-shaped line, whose intensity decreases and linewidth increases under the cooling of the melt (Figure III.43). The line's position is the averaged chemical shift arising from all of the aluminium species (AlO_4 , AlO_5 and AlO_6) weighted by their abundance, or in other words, the line's position mostly measures the average coordination number of Al. Changes in the width reflect evolutions in the correlation times of the movements responsible for the NMR relaxation and FWHM increase is related to a slowing down of those movements often directly linked to changes in viscosity.

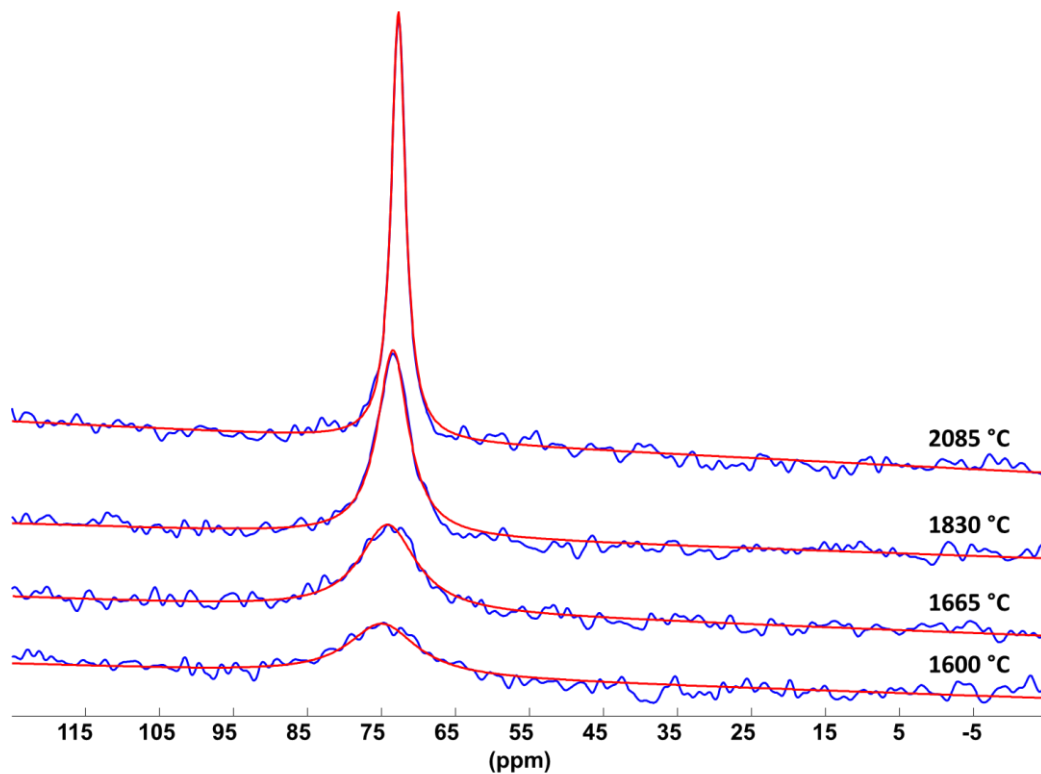


Figure III.43. One-scan HT ^{27}Al NMR spectra (blue lines) of SA10.45 melt at different temperatures during the melt's cooling. Temperature decreases from top to bottom. The red lines are fits of the NMR signal with Lorentzian function.

Figure III.44 demonstrates how line's position changes with temperature. The δ evolves linearly under the cooling but with varying slopes for different compositions. Such variation of the slope has been previously observed in different aluminate and aluminosilicate systems (Capron et al., 2001; Florian et al., 2007; Massiot et al., 1995). Here we present also results on liquid Al_2O_3 and SrAl_2O_4 (SA00.50). The range of the chemical shifts reported here is comparable with those known from the literature. The slope, $\Delta\delta/\Delta T$, for liquid alumina measured in our experiments equal 1.6 ppm/1000 °C, which is comparable with the value of 2.5 ppm/1000 °C reported in (Florian et al., 1995) and lower than the value of 5.2 ppm/1000 °C found in (Florian et al., 2007). There is an increase of $\Delta\delta/\Delta T$ from SA10.45 to SA63.18. Moreover, the placement of the experimental points indicates a progressive increase of the chemical shift with decreasing SiO_2 content. This is most likely caused by the increase of Al neighbours, which is in agreement with observations made for the glasses. In Figure III.44 we also put the barycentre's positions of ^{27}Al NMR lines of corresponding glasses. Since the glass structure should freeze at the glass transition temperature and below this temperature it should not evolve much, we placed the barycentre's positions at

the corresponding T_g . The extrapolation of HT data to T_g does not meet the point for glass as it does, for example, in case of CaAl_2O_4 (Massiot et al., 1995). However, the similar deviation has been observed for aluminosilicates of rare-earth metals (Florian et al., 2007) suggesting that it could be a feature of aluminosilicates, in general. The position derived from the glass being systematically higher than the one extrapolated from the high-temperature evolution. More experiments are required in order to clarify this behaviour.

As in the case of corresponding glasses, the fraction of high-coordinate aluminium increases from the peralkaline to peraluminous compositions in the SA50.xx series as suggested by the average chemical shifts.

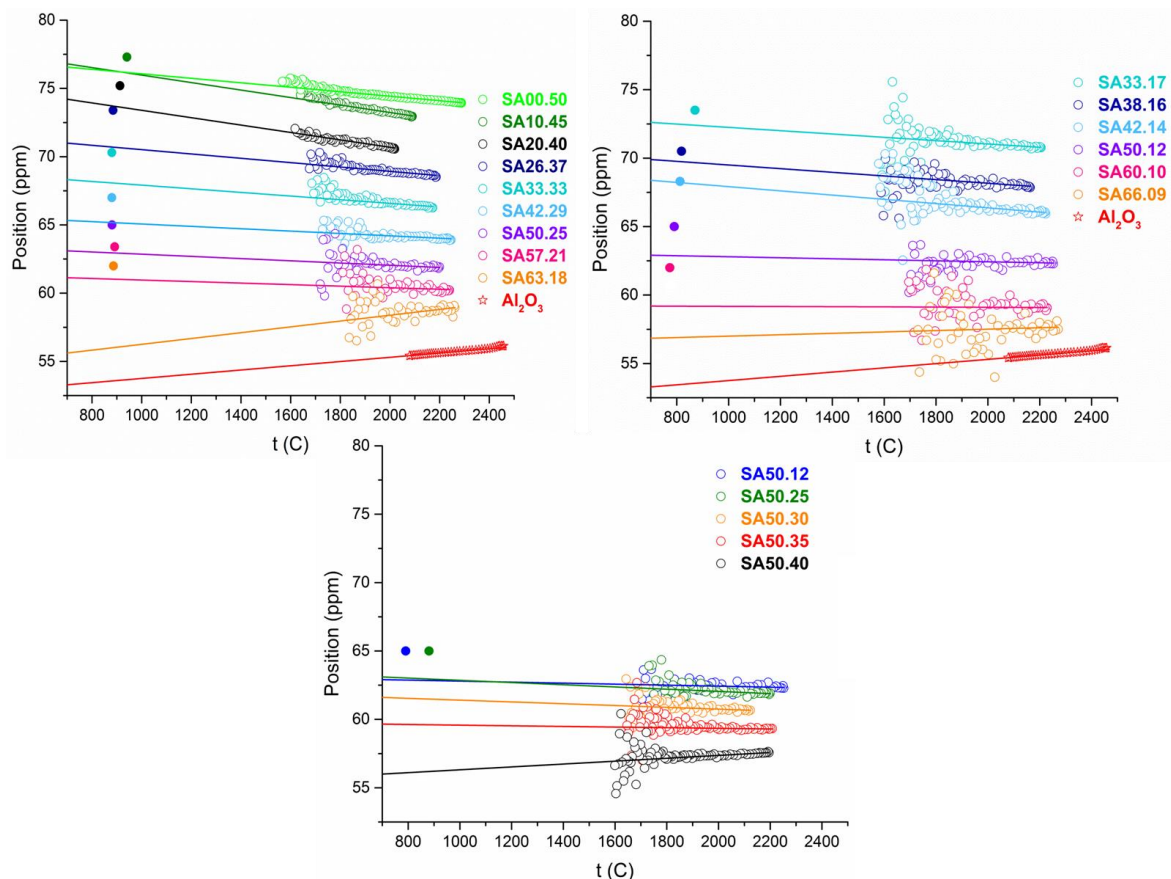


Figure III.44. Evolution of the NMR line's position with temperature for the melts along the joins $R = 1$ (top left) and $R = 3$ (top right), and in the series SA50.xx (bottom). Filled symbols correspond to the related NMR line's barycentre for glasses at r.t. (see text). The lines are linear fits of the HT data.

For the tectosilicate compositions the FWHM varies greatly from composition to composition (Figure III.45). For silica-poor SA10.45 it changes from ~ 250 to 1500 Hz in the temperature interval from 2100 to 1600 °C, while for silica-rich SA63.18 – from ~ 750 to 2250 Hz (2300 to 1900 °C). The effect of line's broadening is connected to the melt's

viscosity, at least well above T_g or for compositions with low SiO_2 contents for which oxygen's diffusion (viscosity) occurs on the same time scale as thermal vibrations (NMR relaxation). For the peralkaline melts the FWHM does not vary significantly and spans the region of ~ 500 - 2250 Hz in the temperature range from 2250 to 1600 °C. Greater scatter of the experimental points for the peralkaline compositions is caused by low aluminium content and, hence, by low signal-to-noise ratio. In the case of peraluminous compositions, due to high alumina content, the scatter of the data points is low and we can see that the FWHM practically does not change with composition. It evolves from ~ 250 to 3500 Hz in the temperature range from 2250 to 1600 °C.

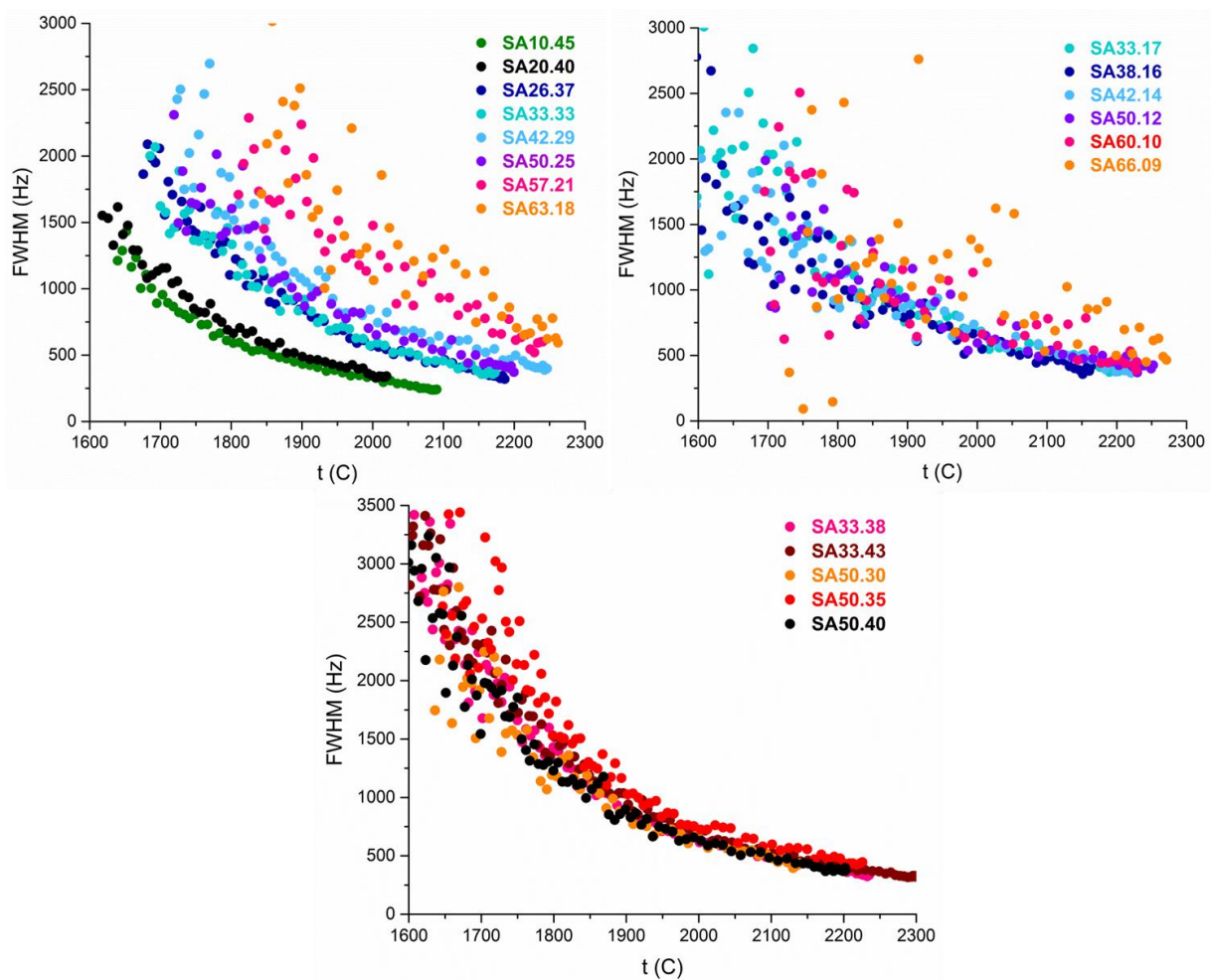


Figure III.45. Evolution of the line's FWHM with temperature for the melts along the joins $R = 1$ (top left), $R = 3$ (top right) and $R < 1$ (bottom).

The FWHM is related to the spin-lattice relaxation time T_1 by the following equation:

$$T_1 = \frac{1}{\pi \cdot FWHM}$$

However, this relation is true only if the fully average motional regime has been reached in the melt, i.e. the movements and/or exchange of the various Al species occur much faster than the NMR time scale (Florian et al., 2007). For this, we measured relaxation times T_1 and T_2 and made sure that the condition when $\text{FWHM} \sim T_1 \sim T_2$ is respected. If we further assume that the quadrupolar interaction is the main interaction contributing to the relaxation than T_1 can be calculated as

$$\frac{1}{T_1} = \frac{3}{10} \pi^2 \frac{2I + 3}{I^2(2I - 1)} \tilde{C}_{Q\eta}^2 \tau_c$$

where τ_c is correlation time of the fluctuation of the quadrupolar interaction, I is nuclear spin (5/2 in case of ^{27}Al) and $\tilde{C}_{Q\eta}$ is time-averaged dynamic quadrupolar product of the aluminium sites calculated as

$$\tilde{C}_{Q\eta} = \tilde{C}_Q \sqrt{1 + \frac{\tilde{\eta}_Q^2}{3}}$$

where \tilde{C}_Q is equal to the average quadrupolar coupling constant C_Q measured at room temperature and $\tilde{\eta}_Q$ is asymmetry of the quadrupolar interaction tensor that equal 0.6 as in the GIM model (Le Caër and Brand, 1998). Using these equations one can calculate the τ_c from the FWHM of the NMR line.

The decimal logarithm of the correlation time is plotted in Figure III.46 as a function of $10000/T$. As we can see for the tectosilicates, the τ_c increases from silica-poor to silica-rich compositions and changes linearly with temperature. The composition difference of τ_c for the peralkaline compositions is somewhat less pronounced reflecting the presence of NBOs in the melt. In the SA50.xx series the τ_c decreases with increasing Al_2O_3 content.

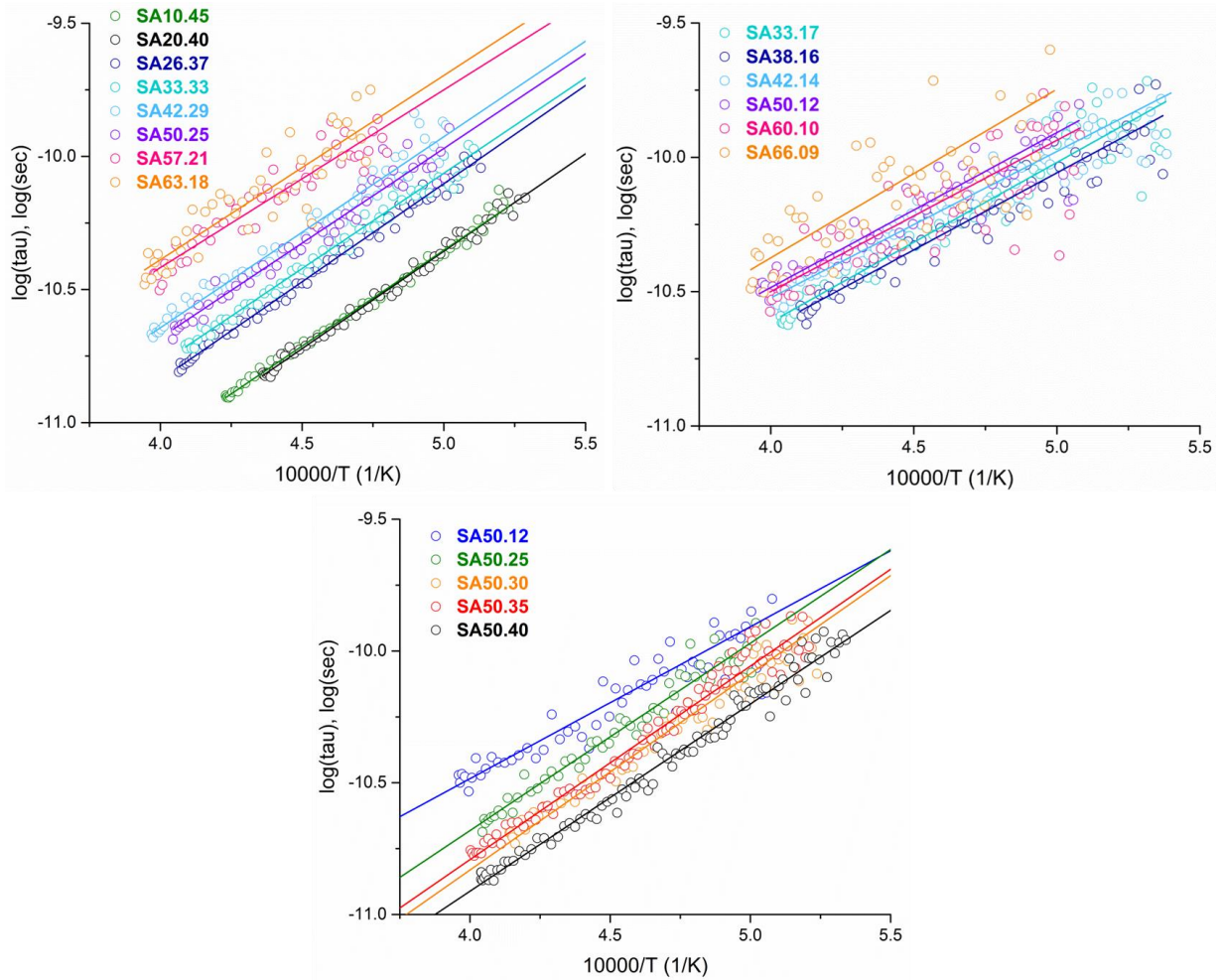


Figure III.46. $\log_{10}(\tau_c)$ as a function of reciprocal temperature for the melts along the joins $R = 1$ (top left) and $R = 3$ (top right), and in the series SA50.xx (bottom). The lines are linear fits of the experimental data.

Calculated values of the correlation times can be compared with the relaxation time for viscous flow τ_η related to viscosity η through the Maxwell equation:

$$\tau_\eta = \frac{\eta}{G_\infty}$$

where G_∞ is shear modulus at an infinite frequency equal $10^{10 \pm 0.5}$ Pa. The τ_η for two tectosilicate compositions were calculated according to this equation and plotted together with the corresponding τ_c in Figure III.47. Taking into account the uncertainties in G_∞ and $\tilde{C}_{Q\eta}$, introducing a constant offset in $\log_{10}(\tau_c)$, we can state that the relaxation times obtained by two methods are comparable. This implies that the movements responsible for the NMR relaxation of aluminium in the high-temperature liquid are correlated with the movements responsible for the macroscopic shear viscosity. It indicates that an oxygen

exchange mechanism involving the formation of AlO_5 intermediate species may play an important role in oxygen diffusion and the viscous flow process in aluminosilicate melts in analogy with what has been proposed for aluminate ones (Capron et al., 2001; Massiot et al., 1995; Poe et al., 1994).

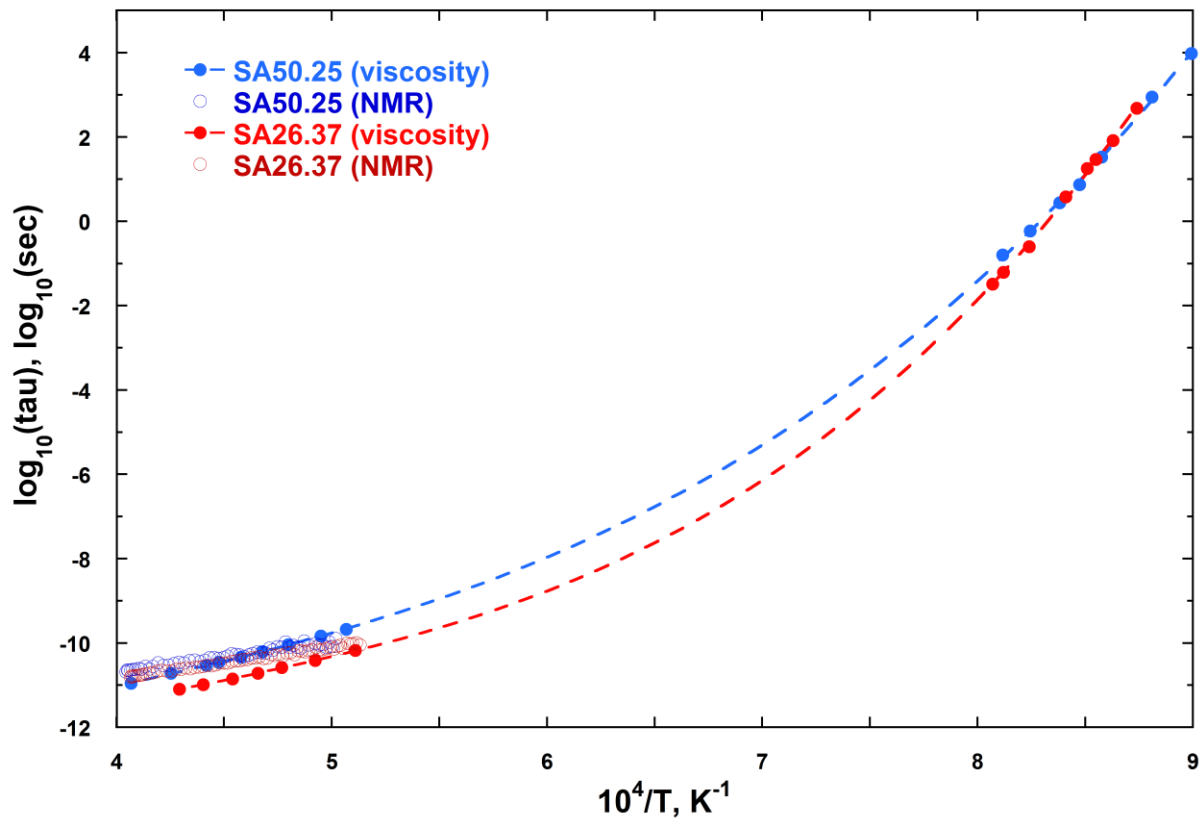


Figure III.47. Comparison of NMR correlation times with relaxation times for viscous flow for two tectosilicate compositions (SA26.37 and SA50.25). HT viscosity data are from (Urbain et al., 1982). The lines are a guide to the eye.

The NMR correlation time is related to the Arrhenius activation energy, E_{act} , as

$$\tau_c = \tau_0 \cdot e^{\frac{E_{act}}{RT}}$$

where τ_0 is pre-exponential factor and R is universal gas constant. The E_{act} were extracted from the slopes of the curves plotted in Figure III.46. None to negligible effect of composition on the activation energy along one join was evidenced. The Arrhenius activation energies for the compositions in two series (SA50.xx and SA33.xx) are plotted in Figure III.48. We see that from the peralkaline to tectosilicate compositions the E_{act} increases significantly and this rise continues for slightly peraluminous compositions. Further augmentation of Al_2O_3 (moving deeper into the peraluminous domain) causes a

decrease of the E_{act} . A similar trend has been observed for HT viscosities of Na and Ca aluminosilicate melts (Toplis et al., 1997; Toplis and Dingwell, 2004). Such displacement of the maximum to the peraluminous field has been correlated to the existence of three-coordinate oxygens in addition to high-coordinate Al in the melts.

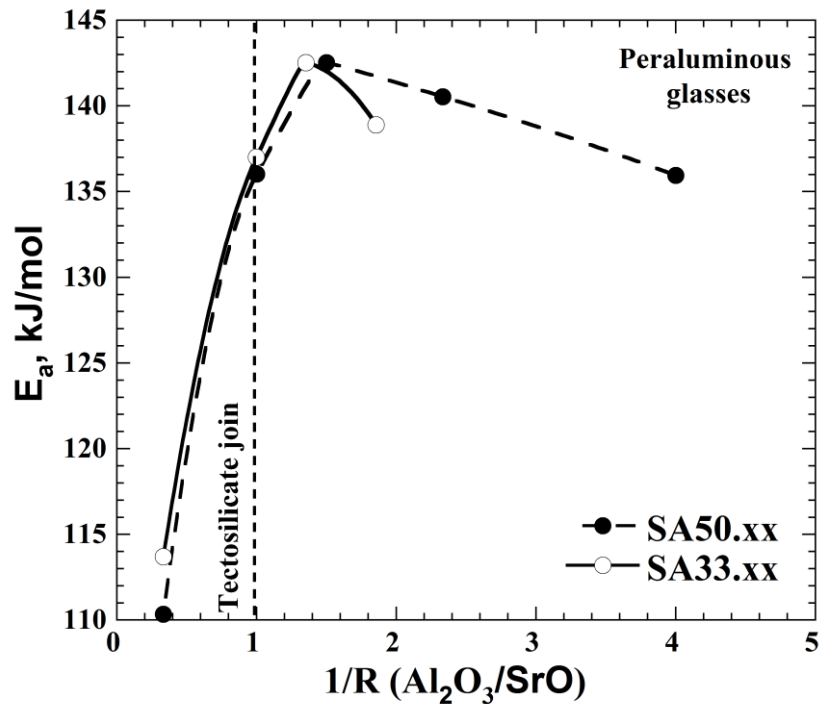


Figure III.48. Arrhenius activation energies (E_{act}) as a function of the $\text{Al}_2\text{O}_3/\text{SrO}$ ratio. The vertical dashed line corresponds to the tectosilicate compositions. Other lines are a guide to the eye.

It is interesting to compare the E_{act} for the ^{27}Al relaxation and for the viscosity. For two tectosilicate compositions, SA50.25 and SA26.37, $E_{act}(\text{viscosity})$ are 244 and 215 kJ/mol, while $E_{act}(\text{NMR})$ are 136 and 141 kJ/mol, respectively. The values of E_{act} calculated from the viscosity data and from the NMR relaxation are in a reasonable agreement taking into account possible errors in viscosity measurements as well as in the determination of the NMR correlation time.

5.2. Neutron diffraction from melts

Due to volatilization of SiO_2 under levitation conditions for silica-rich compositions, the high-temperature ND data only for compositions with up to 42 mol% (join $R = 1$) and 33 mol% (join $R = 3$) of silica are presented here. Compared to the glasses, all liquid structure factors are noisier (Figure III.49), notably due to the smaller sample volume

exposed to the beam. The FSDP is almost at the same position, but its intensity is much lower than that for the glass. This is a signature of a less ordered system.

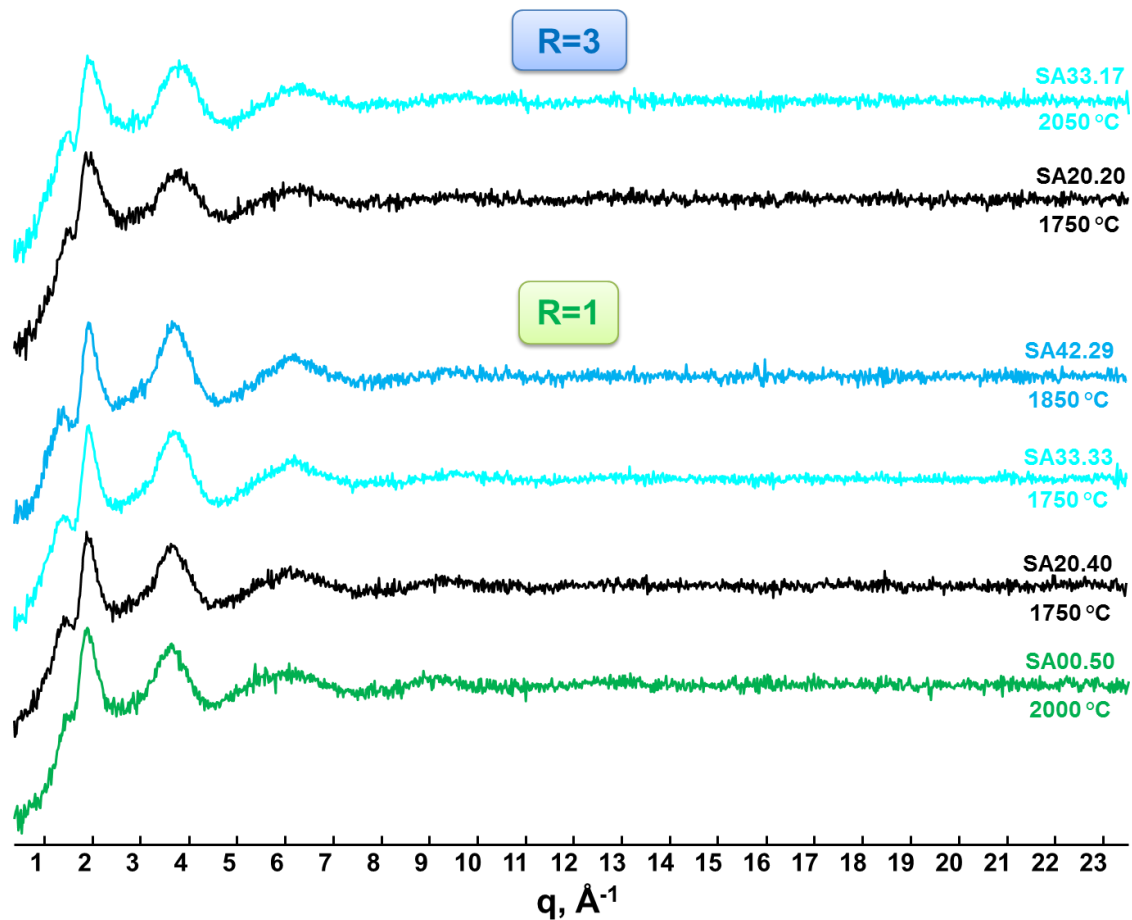


Figure III.49. Static structure factor, $S(q)$, of the melts along the joins R = 3 (top) and R = 1 (bottom).

This increase in the structural disorder in the melts is also detected in the pair distribution functions presented in Figure III.50 where broader peaks are observed. For Sr aluminate (SA00.50), Al-O correlations are found at a slightly higher distance than in glass, around 1.78 \AA instead of 1.76 \AA . This suggests an increase of the number of AlO_5 units in the melt as observed with some Ca aluminates (Hennet et al., 2016) and is in agreement with high-temperature ^{27}Al NMR evidencing formation of high-coordinate Al units in melts.

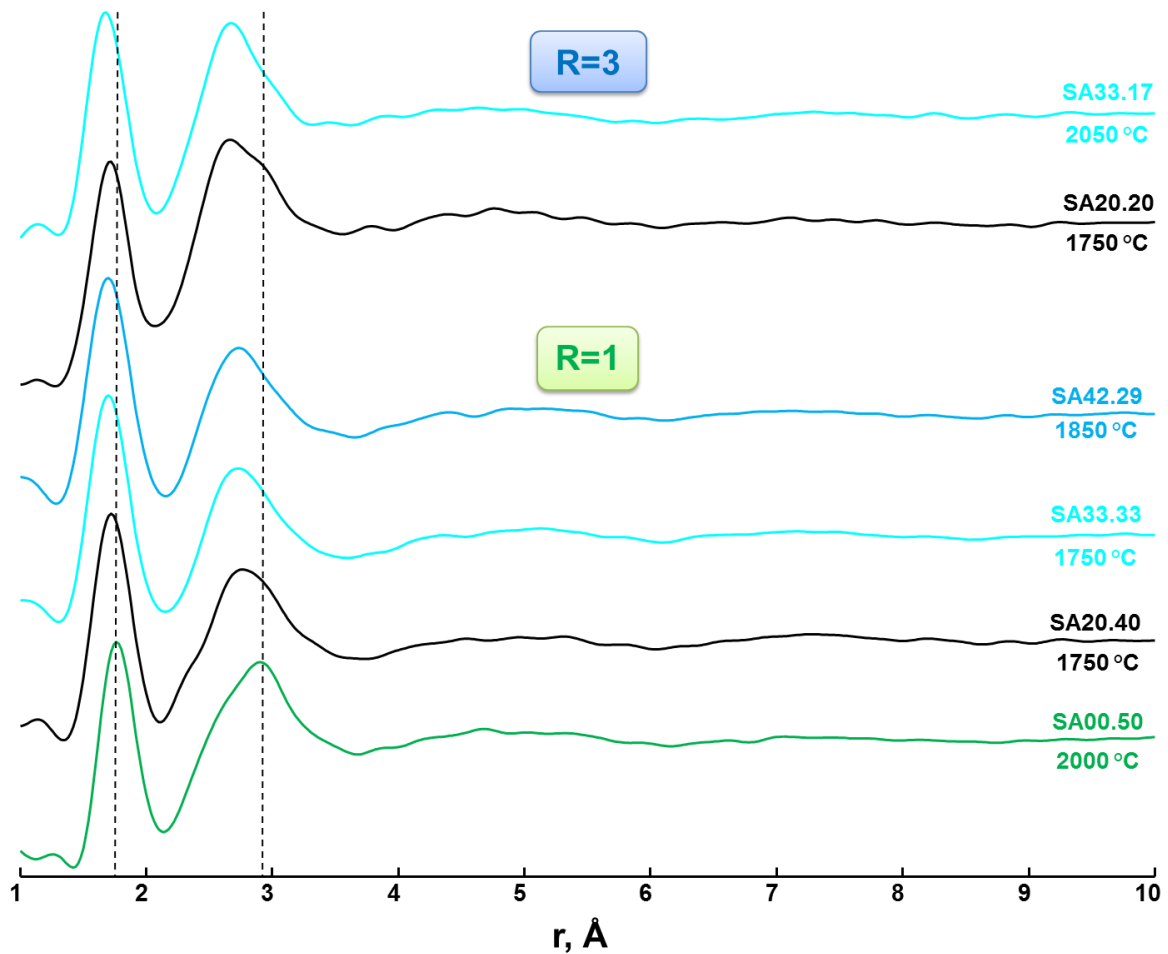


Figure III.50. Pair distribution function, $g(r)$, of the melts along the joins R = 3 (*top*) and R = 1 (*bottom*).

The short range order around Sr seems to be largely modified and shows a complex configuration. A first Sr-O contribution is present at distances shorter than 2.53 Å, meaning that Sr-O with coordination lower than 6 should be present. All pair distribution functions exhibit also a peak at about 3 Å corresponding to O-O distances in SrO₈ polyhedra. Finally, some correlations observed between 3 and 3.6 Å could be attributed to O-O bonds for 7-fold coordinated Sr. In general, the first coordination sphere of Sr becomes less defined in the melts.

Section highlights

- A good agreement was found between NMR correlation time and relaxation time for viscous flow for compositions on the join R = 1.

- Arrhenius activation energy increases with decreasing Sr/Al ratio and seems to possess a maximum for compositions in a slightly peraluminous domain. Such behaviour suggests the existence of three-coordinate oxygens in the melts.
- Sr environment becomes less defined in melts compared to glasses with a larger distribution of SrO_x polyhedra.

6. Conclusion

Four domains with various ratio $R = \text{SrO}/\text{Al}_2\text{O}_3$ in the SAS system were studied and the results of different measurements are presented in the chapter. Regions of glass formation were explored and reported. New glasses were prepared on the join $R = 3$ and in the peraluminous domain ($R < 1$). All glasses were studied using a multi-technique approach and following conclusions can be made.

The network of Sr silicate glasses consists of SiO₄ tetrahedra present in different Qⁿ units assembled on the medium-range scale into tetrahedral rings with a predominance of small three-membered ones. With augmentation of SrO content the network becomes more compact with a concurrent increase in T_g , that could be explained in terms of involvement of Sr cations in the network linkage.

The introduction of Al₂O₃ into the silicate network improves its interconnection. Al enters preferentially fully polymerized Q⁴ units while Si is distributed in different Qⁿ species. This increase in the polymerization degree of the glass network causes elevated T_g in comparison to analogous silicate compositions. The coordination number of Sr is higher and the network is less compact compared to the network of the silicate glasses. A small fraction of AlO₅ is present even though it was expected all Al atoms to be in AlO₄⁻ species, charge compensating Sr²⁺. As in the case of the silicate glasses, an increase in T_g is observed with decreasing SiO₂ content that could be explained by the reorganisation of the network.

With the further decrease of SrO/Al₂O₃ ratio (glasses on the join $R = 1$) the network polymerization increases even more in comparison with the silicate and peralkaline glasses. The overwhelming majority of Si and Al atoms are included in Q⁴ units differing by the number of Al or Si neighbours in the second coordination sphere (Q⁴_m species). However, a

small fraction of AlO_5 is found in the tectosilicate glasses and NBOs are expected to be present in the structure. The coordination number of Sr is 8-9 and higher than in the silicate and peralkaline glasses. Due to their almost completely polymerized network, tectosilicates possess elevated glass transition temperatures compared to compositions with $R > 1$. The T_g curve of the glasses on the join $R = 1$ increases in the silica-poor domain.

Glasses in the peraluminous domain possess an elevated degree of disorder in comparison to the glasses in other three domains as seen from values of V_m and line widths of ^{27}Al and ^{29}Si NMR spectra. This is caused by a higher fraction of high-coordinate AlO_x species and higher values of inter-tetrahedral angles.

Bibliography

- Alahraché, S., Al Saghir, K., Chenu, S., Véron, E., De Sousa Meneses, D., Becerro, A.I., Ocaña, M., Moretti, F., Patton, G., Dujardin, C., Cussó, F., Guin, J.-P., Nivard, M., Sangleboeuf, J.-C., Matzen, G., Allix, M., 2013. Perfectly Transparent Sr₃Al₂O₆ Polycrystalline Ceramic Elaborated from Glass Crystallization. *Chem. Mater.* 25, 4017–4024. doi:10.1021/cm401953d
- Al Saghir, K., Chenu, S., Veron, E., Fayon, F., Suchomel, M., Genevois, C., Porcher, F., Matzen, G., Massiot, D., Allix, M., 2015. Transparency through Structural Disorder: A New Concept for Innovative Transparent Ceramics. *Chem. Mater.* 27, 508–514. doi:10.1021/cm5037106
- Allwardt, J., Lee, S.K., Stebbins, J.F., 2003. Bonding preferences of non-bridging O atoms: Evidence from ¹⁷O MAS and ³QMAS NMR on calcium aluminate and low-silica Ca-aluminosilicate glasses. *Am. Mineral.* 88, 949–954.
- Brückner, R., 1970. Properties and structure of vitreous silica. I. *J. Non. Cryst. Solids* 5, 123–175. doi:10.1016/0022-3093(70)90190-0
- Capron, M., Florian, P., Fayon, F., Trumeau, D., Hennet, L., Gaihlanou, M., Thiaudière, D., Landron, C., Douy, A., Massiot, D., 2001. Local structure and dynamics of high temperature SrO–Al₂O₃ liquids studied by ²⁷Al NMR and Sr K-edge XAS spectroscopy. *J. Non. Cryst. Solids* 293–295, 496–501. doi:10.1016/S0022-3093(01)00762-1
- Chiari, G., Calleri, M., Bruno, E., Ribbe, P.H., 1975. The structure of partially disordered, synthetic strontium feldspar. *Am. Mineral.* 60, 111–119.
- Cormier, L., Calas, G., Creux, S., Gaskell, P., Bouchet-Fabre, B., Hannon, A., 1999. Environment around strontium in silicate and aluminosilicate glasses. *Phys. Rev. B* 59, 13517–13520. doi:10.1103/PhysRevB.59.13517
- Cormier, L., Neuville, D.R., Calas, G., 2005. Relationship Between Structure and Glass Transition Temperature in Low-silica Calcium Aluminosilicate Glasses: the Origin of the Anomaly at Low Silica Content. *J. Am. Ceram. Soc.* 88, 2292–2299. doi:10.1111/j.1551-2916.2005.00428.x

- Creux, S., Bouchet-Fabre, B., Gaskell, P.H., 1995. Anomalous wide angle X-ray scattering study of strontium silicate and aluminosilicate glasses. *J. Non. Cryst. Solids* 192 & 193, 360–363.
- De Sousa Meneses, D., Malki, M., Echegut, P., 2006. Optical and structural properties of calcium silicate glasses. *J. Non. Cryst. Solids* 352, 5301–5308.
doi:10.1016/j.jnoncrysol.2006.08.022
- Dickinson, J.E., Scarfe, C.M., McMillan, P., 1990. Physical properties and structure of $K_2Si_4O_9$ melt quenched from pressures up to 2.4 GPa. *J. Geophys. Res.* 95, 15675.
doi:10.1029/JB095iB10p15675
- Doweidar, H., 1999. Density-structure correlations in silicate glasses. *J. Non. Cryst. Solids* 249, 194–200. doi:10.1016/S0022-3093(99)00310-5
- Doweidar, H., 1996. The density of alkali silicate glasses in relation to the microstructure. *J. Non. Cryst. Solids* 194, 155–162. doi:10.1016/0022-3093(95)00489-0
- Dupree, R., Holland, D., Williams, D.S., 1986. The structure of binary alkali silicate glasses. *J. Non. Cryst. Solids* 81, 185–200. doi:10.1016/0022-3093(86)90269-3
- Florian, P., Massiot, D., Poe, B., Farnan, I., Coutures, J.-P., 1995. A time resolved ^{27}Al NMR study of the cooling process of liquid alumina from 2450 °C to crystallisation. *Solid State Nucl. Magn. Reson.* 5, 233–238. doi:10.1016/0926-2040(95)01188-X
- Florian, P., Sadiki, N., Massiot, D., Coutures, J.P., 2007. ^{27}Al NMR Study of the Structure of Lanthanum- and Yttrium-Based Aluminosilicate Glasses and Melts. *J. Phys. Chem. B* 111, 9747–9757. doi:10.1021/jp072061q
- Furukawa, T., Fox, K.E., White, W.B., 1981. Raman spectroscopic investigation of the structure of silicate glasses. III. Raman intensities and structural units in sodium silicate glasses. *J. Chem. Phys.* 75, 3226. doi:10.1063/1.442472
- Galeener, F.L., 1982. Planar rings in glasses. *Solid State Commun.* 44, 1037–1040.
doi:10.1016/0038-1098(82)90329-5
- Galeener, F.L., 1982. Planar rings in vitreous silica. *J. Non. Cryst. Solids* 49, 53–62.

doi:10.1016/0022-3093(82)90108-9

- Hehlen, B., Neuville, D.R., 2015. Raman Response of Network Modifier Cations in Aluminosilicate Glasses. *J. Phys. Chem. B* 119, 4093–4098. doi:10.1021/jp5116299
- Hennet, L., Drewitt, J.W.E., Neuville, D.R., Cristiglio, V., Kozaily, J., Brassamin, S., Zanghi, D., Fischer, H.E., 2016. Neutron diffraction of calcium aluminosilicate glasses and melts. *J. Non. Cryst. Solids* 451, 89–93. doi:10.1016/j.jnoncrysol.2016.05.018
- Hiet, J., Deschamps, M., Pellerin, N., Fayon, F., Massiot, D., 2009. Probing chemical disorder in glasses using silicon-29 NMR spectral editing. *Phys. Chem. Chem. Phys.* 11, 6935. doi:10.1039/b906399d
- Higby, P.L., Ginther, R.J., Aggarwal, I.D., Friebele, E.J., 1990. Glass formation and thermal properties of low-silica calcium aluminosilicate glasses. *J. Non. Cryst. Solids* 126, 209–215. doi:10.1016/0022-3093(90)90821-3
- Jaworski, A., Stevansson, B., Edén, M., 2016. The Bearings from Rare-Earth (RE = La, Lu, Sc, Y) Cations on the Oxygen Environments in Aluminosilicate Glasses: A Study by Solid-State ¹⁷O NMR, Molecular Dynamics Simulations, and DFT Calculations. *J. Phys. Chem. C* 120, 13181–13198. doi:10.1021/acs.jpcc.6b02032
- Jaworski, A., Stevansson, B., Edén, M., 2015. Direct ¹⁷O NMR experimental evidence for Al–NBO bonds in Si-rich and highly polymerized aluminosilicate glasses. *Phys. Chem. Chem. Phys.* 17, 18269–18272. doi:10.1039/C5CP02985F
- Kubicki, J.D., Sykes, D., 1993. Molecular orbital calculations of vibrations in three-membered aluminosilicate rings. *Phys. Chem. Miner.* 19, 381–391. doi:10.1007/BF00202975
- Le Caër, G., Brand, R.A., 1998. General models for the distributions of electric field gradients in disordered solids. *J. Phys. Condens. Matter* 10, 10715–10774. doi:10.1088/0953-8984/10/47/020
- Le Losq, C., 2012. Rôle Des Eléments Alcalins Et De l'Eau Sur Les Propriétés Et La Structure Des Aluminosilicates Fondus Et Vitreux: Implications Volcanologiques. Université Paris Diderot (Paris 7).

- Lee, S.K., Stebbins, J.F., 2006. Disorder and the extent of polymerization in calcium silicate and aluminosilicate glasses: O-17 NMR results and quantum chemical molecular orbital calculations. *Geochim. Cosmochim. Acta* 70, 4275–4286.
doi:10.1016/j.gca.2006.06.1550
- Lee, S.K., Stebbins, J.F., 2002. Extent of intermixing among framework units in silicate glasses and melts. *Geochim. Cosmochim. Acta* 66, 303–309. doi:10.1016/S0016-7037(01)00775-X
- Licheron, M., Montouillout, V., Millot, F., Neuville, D.R., 2011. Raman and ²⁷Al NMR structure investigations of aluminate glasses: (1-x)Al₂O₃-x MO, with M=Ca, Sr, Ba and 0.5<x<0.75). *J. Non. Cryst. Solids* 357, 2796–2801.
doi:10.1016/j.jnoncrysol.2011.03.001
- Lippmaa, E., Maegi, M., Samoson, A., Engelhardt, G., Grimmer, A.-R., 1980. Structural studies of silicates by solid-state high-resolution silicon-29 NMR. *J. Am. Chem. Soc.* 102, 4889–4893. doi:10.1021/ja00535a008
- Loewenstein, W., 1954. The distribution of aluminum in the tetrahedra of silicates and aluminates. *Am. Mineral.* 39, 92–96.
- Machida, K.I., Adachi, G.Y., Shiokawa, J., Shimada, M., Koizumi, M., 1982. Structure and high-pressure polymorphism of strontium metasilicate. *Acta Crystallogr. Sect. B Struct. Crystallogr. Cryst. Chem.* 38, 386–389. doi:10.1107/S0567740882003045
- Mackenzie, J.D., 1963. High-Pressure Effects on Oxide Glasses: II, Subsequent Heat Treatment. *J. Am. Ceram. Soc.* 46, 470–476. doi:10.1111/j.1151-2916.1963.tb13777.x
- Massiot, D., Trumeau, D., Touzo, B., Farnan, I., Rifflet, J.-C., Douy, A., Coutures, J.-P., 1995. Structure and Dynamics of CaAl₂O₄ from Liquid to Glass: A High-Temperature ²⁷Al NMR Time-Resolved Study. *J. Phys. Chem.* 99, 16455–16459. doi:10.1021/j100044a038
- Matson, D.W., Sharma, S.K., Philpotts, J.A., 1983. The structure of high-silica alkali-silicate glasses. A Raman spectroscopic investigation. *J. Non. Cryst. Solids* 58, 323–352.
doi:10.1016/0022-3093(83)90032-7

- Micoulaut, M., Malki, M., Simon, P., Canizares, A., 2005. On the rigid to floppy transitions in calcium silicate glasses from Raman scattering and cluster constraint analysis. *Philos. Mag.* 85, 3357–3378. doi:10.1080/14786430500157029
- Moesgaard, M., Keding, R., Skibsted, J., Yue, Y., 2010. Evidence of Intermediate-Range Order Heterogeneity in Calcium Aluminosilicate Glasses. *Chem. Mater.* 22, 4471–4483. doi:10.1021/cm1011795
- Murdoch, J.B., Stebbins, J.F., Carmichael, I.S.E., 1985. High-resolution ²⁹Si NMR study of silicate and aluminosilicate glasses: the effect of network-modifying cations. *Am. Mineral.* 70, 332–343.
- Mysen, B.O., Finger, L.W., Virgo, D., Seifert, F.A., 1982. Curve-fitting of Raman spectra of silicate glasses. *Am. Mineral.* 67, 686–695.
- Navrotsky, A., Geisinger, K.L., McMillan, P., Gibbs, G. V., 1985. The tetrahedral framework in glasses and melts - inferences from molecular orbital calculations and implications for structure, thermodynamics, and physical properties. *Phys. Chem. Miner.* 11, 284–298. doi:10.1007/BF00307406
- Neuvill, D.R., 2005. Structure and properties in (Sr, Na) silicate glasses and melts. *Phys. Chem. Glas.* 46, 112–118.
- Neuvill, D.R., Cormier, L., Flank, A.-M., Briois, V., Massiot, D., 2004a. Al speciation and Ca environment in calcium aluminosilicate glasses and crystals by Al and Ca K-edge X-ray absorption spectroscopy. *Chem. Geol.* 213, 153–163. doi:10.1016/j.chemgeo.2004.08.039
- Neuvill, D.R., Cormier, L., Massiot, D., 2006. Al coordination and speciation in calcium aluminosilicate glasses: Effects of composition determined by ²⁷Al MQ-MAS NMR and Raman spectroscopy. *Chem. Geol.* 229, 173–185. doi:10.1016/j.chemgeo.2006.01.019
- Neuvill, D.R., Cormier, L., Massiot, D., 2004b. Al environment in tectosilicate and peraluminous glasses: A ²⁷Al MQ-MAS NMR, Raman, and XANES investigation. *Geochim. Cosmochim. Acta* 68, 5071–5079. doi:10.1016/j.gca.2004.05.048

- Neuvill, D.R., Cormier, L., Montouillout, V., Florian, P., Millot, F., Rifflet, J.-C., Massiot, D., 2008. Structure of Mg- and Mg/Ca aluminosilicate glasses: ^{27}Al NMR and Raman spectroscopy investigations. *Am. Mineral.* 93, 1721–1731. doi:10.2138/am.2008.2867
- Neuvill, D.R., de Ligny, D., Henderson, G.S., 2014. Advances in Raman Spectroscopy Applied to Earth and Material Sciences. *Rev. Mineral. Geochemistry* 78, 509–541. doi:10.2138/rmg.2013.78.13
- Neuvill, D.R., Mysen, B.O., 1996. Role of aluminium in the silicate network: In situ, high-temperature study of glasses and melts on the join $\text{SiO}_2\text{-NaAlO}_2$. *Geochim. Cosmochim. Acta* 60, 1727–1737. doi:10.1016/0016-7037(96)00049-X
- Novikov, A.N., Neuvill, D.R., Hennem, L., Gueguen, Y., Thiaudiere, D., Charpentier, T., Florian, P., 2017. Al and Sr environment in tectosilicate glasses and melts: Viscosity, Raman and NMR investigation. *Chem. Geol.* 461, 115–127. doi:10.1016/j.chemgeo.2016.11.023
- Poe, B.T., McMillan, P.F., Cote, B., Massiot, D., Coutures, J.-P., 1994. Structure and Dynamics in Calcium Aluminate Liquids: High-Temperature ^{27}Al NMR and Raman Spectroscopy. *J. Am. Ceram. Soc.* 77, 1832–1838. doi:10.1111/j.1151-2916.1994.tb07058.x
- Rabukhin, A.I., 1999. Structural interpretation of concentration dependences of molar volume of glasses in $\text{R}_2\text{O-SiO}_2$ and RO-SiO_2 systems. *Glas. Ceram.* 56, 339–342. doi:10.1007/BF02681337
- Seifert, F.A., Mysen, B.O., Virgo, D., 1982. Three-dimensional network structure of quenched melts (glass) in the systems $\text{SiO}_2\text{-NaAlO}_2$, $\text{SiO}_2\text{-CaAl}_2\text{O}_4$ and $\text{SiO}_2\text{-MgAl}_2\text{O}_4$. *Am. Mineral.* 67, 696–717.
- Shelby, J.E., 1985. Formation and Properties of Calcium Aluminosilicate Glasses. *J. Am. Ceram. Soc.* 68, 155–158. doi:10.1111/j.1151-2916.1985.tb09656.x
- Shelby, J.E., 1979. Effect of morphology on the properties of alkaline earth silicate glasses. *J. Appl. Phys.* 50, 8010–8015. doi:10.1063/1.325986
- Shinozaki, K., Honma, T., Affatigato, M., Komatsu, T., 2016. Long afterglow in hexagonal

- SrAl₂O₄:Eu²⁺, Dy³⁺ synthesized by crystallization of glass and solidification of supercooled melts. *J. Lumin.* 177, 286–289. doi:10.1016/j.jlumin.2016.05.013
- Smith, E., Dent, G., 2005. *Modern Raman Spectroscopy - A Practical Approach*. John Wiley & Sons, Ltd, Chichester, UK. doi:10.1002/0470011831
- Smith, K.A., Kirkpatrick, R.J., Oldfield, E., Henderson, D.M., 1983. High-resolution silicon-29 nuclear magnetic resonance spectroscopic study of rock-forming silicates. *Am. Mineral.* 68, 1206–1215.
- Thompson, L.M., Stebbins, J.F., 2012. Non-stoichiometric non-bridging oxygens and five-coordinated aluminum in alkaline earth aluminosilicate glasses: Effect of modifier cation size. *J. Non. Cryst. Solids* 358, 1783–1789. doi:10.1016/j.jnoncrysol.2012.05.022
- Toplis, M.J., Dingwell, D.B., 2004. Shear viscosities of CaO-Al₂O₃-SiO₂ and MgO-Al₂O₃-SiO₂ liquids: Implications for the structural role of aluminium and the degree of polymerisation of synthetic and natural aluminosilicate melts. *Geochim. Cosmochim. Acta* 68, 5169–5188. doi:10.1016/j.gca.2004.05.041
- Toplis, M.J., Dingwell, D.B., Lenci, T., 1997. Peraluminous viscosity maxima in Na₂O-Al₂O₃-SiO₂ liquids: The role of triclusters in tectosilicate melts. *Geochim. Cosmochim. Acta* 61, 2605–2612. doi:10.1016/S0016-7037(97)00126-9
- Urbain, G., Bottinga, Y., Richet, P., 1982. Viscosity of liquid silica, silicates and aluminosilicates. *Geochim. Cosmochim. Acta* 46, 1061–1072. doi:10.1016/0016-7037(82)90059-X

Chapter IV

Barium aluminosilicates (BAS)

This chapter is devoted to Ba aluminosilicates (BAS), namely to their structure and properties. As in the previous chapter dealing with the SAS system, four domains will be discussed here: silicate ($R = \infty$), peralkaline ($R = 3$), tectosilicate ($R = 1$) and peraluminous ($R < 1$) glasses (Figure IV.1).

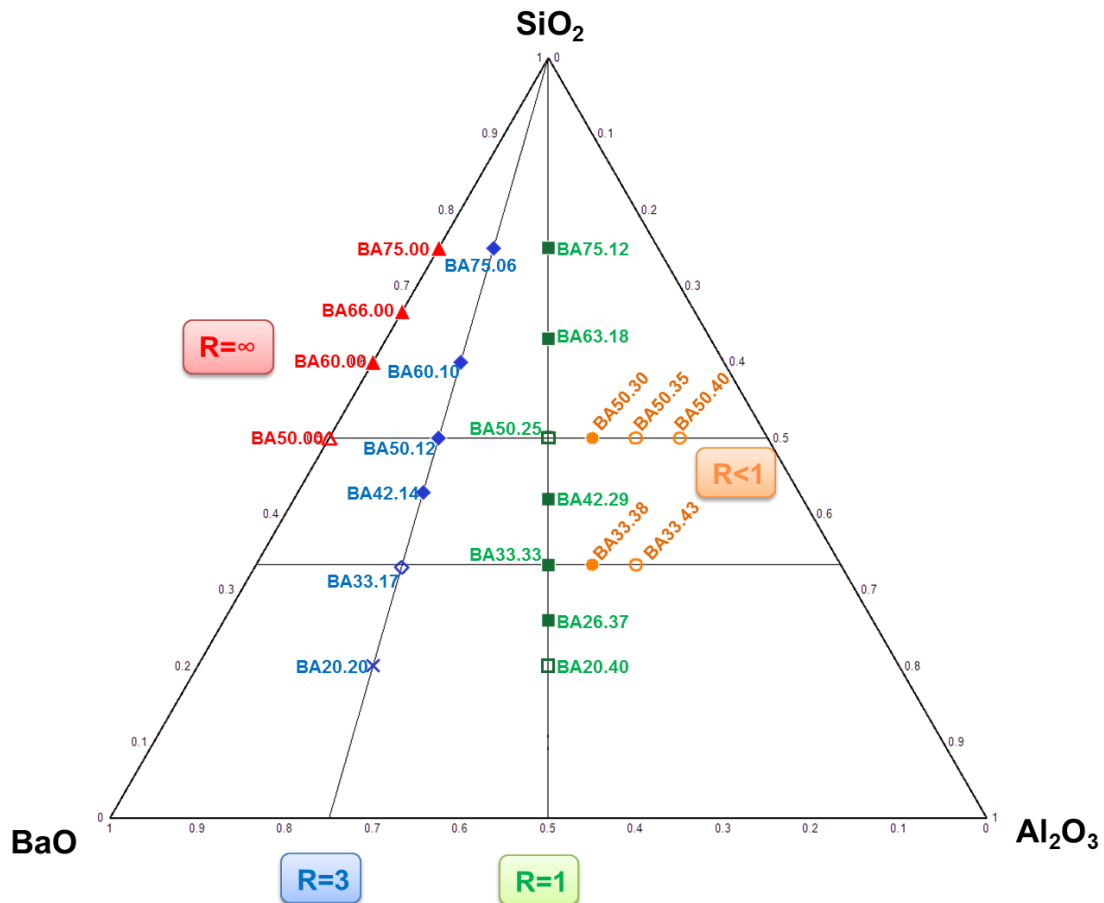


Figure IV.1. Ternary plot for the BAS system (mole fractions) showing compositions studied. Glasses obtained by traditional quench are depicted as filled symbols. Glasses that could be obtained only by levitation quench are shown as open symbols. Crosses correspond to compositions for which no glass could be obtained by neither of two quench procedures. Color guide: red – silicate glasses, blue – peralkaline glasses, green – tectosilicate glasses, orange – peraluminous glasses.
 $R = \text{BaO}/\text{Al}_2\text{O}_3$.

A general discussion on the structure and properties of the BAS glasses will begin from the tectosilicate compositions. Then we continue with silicate glasses possessing, unlike the tectosilicates, depolymerized network and, therefore, structure and properties different from the glasses on the join $R = 1$. After the silicates, we will move to the join $R = 3$ to see how the introduction of Al_2O_3 will change the network and macroscopic properties of the glasses on this join. A particular feature of the peralkaline join is that introduced alumina

helps to polymerize the glass network but its quantity is insufficient to fully charge compensate all Ba^{2+} present. Thus, peralkaline glasses are intermediate between silicate and tectosilicate ones in terms of properties and structure with Ba^{2+} playing a role of network modifier and charge compensator. The discussion on glasses will be finished with the peraluminous domain. To improve our understanding of the evolution of structure and properties of glasses we will follow two composition lines with constant SiO_2 content: BA50.xx and BA33.xx series. Consideration of glasses along these lines demonstrates in the more lucid way the role of Al in the network and its influence on their properties and structure. Finally, some ^{27}Al HT NMR results on BAS melts will be presented to complete the chapter from the side of melt's structure and dynamics.

1. Tectosilicate join (R = 1)

This section of the chapter will be presented as a manuscript of an article that is for submission to the Journal of Non-Crystalline Solids. A full-text version can be found in Annex II and below we provide some results reported in the manuscript.

- AlO_5 is present in all the studied glasses, though its content does not exceed $\sim 2.5\%$. The maximum in the fraction of five-coordinate Al for Ba tectosilicate glasses is lower than that found for Sr-containing ones ($\sim 4.5\%$).
- Replacement of SiO_2 by BaAl_2O_4 favours formation of four- and three-membered tetrahedral rings similarly to what has been observed for Sr counterparts. The overwhelming majority (if not all) SiO_4 tetrahedra are present in Q^4 species.
- The T_g increases for silica-poor Ba tectosilicate compositions as in the case of Sr-containing glasses on the join $R = 1$.

Further, we provide some additional results on Ba tectosilicate glasses that are not included in the manuscript, namely ^{29}Si NMR and neutron diffraction data.

1.1. ^{29}Si NMR spectroscopy

Figure IV.2 presents ^{29}Si NMR spectra of the tectosilicate glasses. When BaAl_2O_4 substitutes for SiO_2 , the NMR signal shifts to higher values of the chemical shift, reflecting a change of the number of Al neighbours in the second coordination sphere of Si atoms. As it

was demonstrated in Chapter III, signals from different Q^4_m species are convoluted in the spectra. The narrowing of the NMR signal from silica-rich to silica-poor compositions suggests a narrowing of the range of Q^4_m species present in the network.

A broad feature at around -110 ppm is observed in the spectra of two silica-poor compositions BA26.37 and BA20.40 with ~ 4 and 8% of overall intensity, respectively. The origin of this feature has been discussed before.

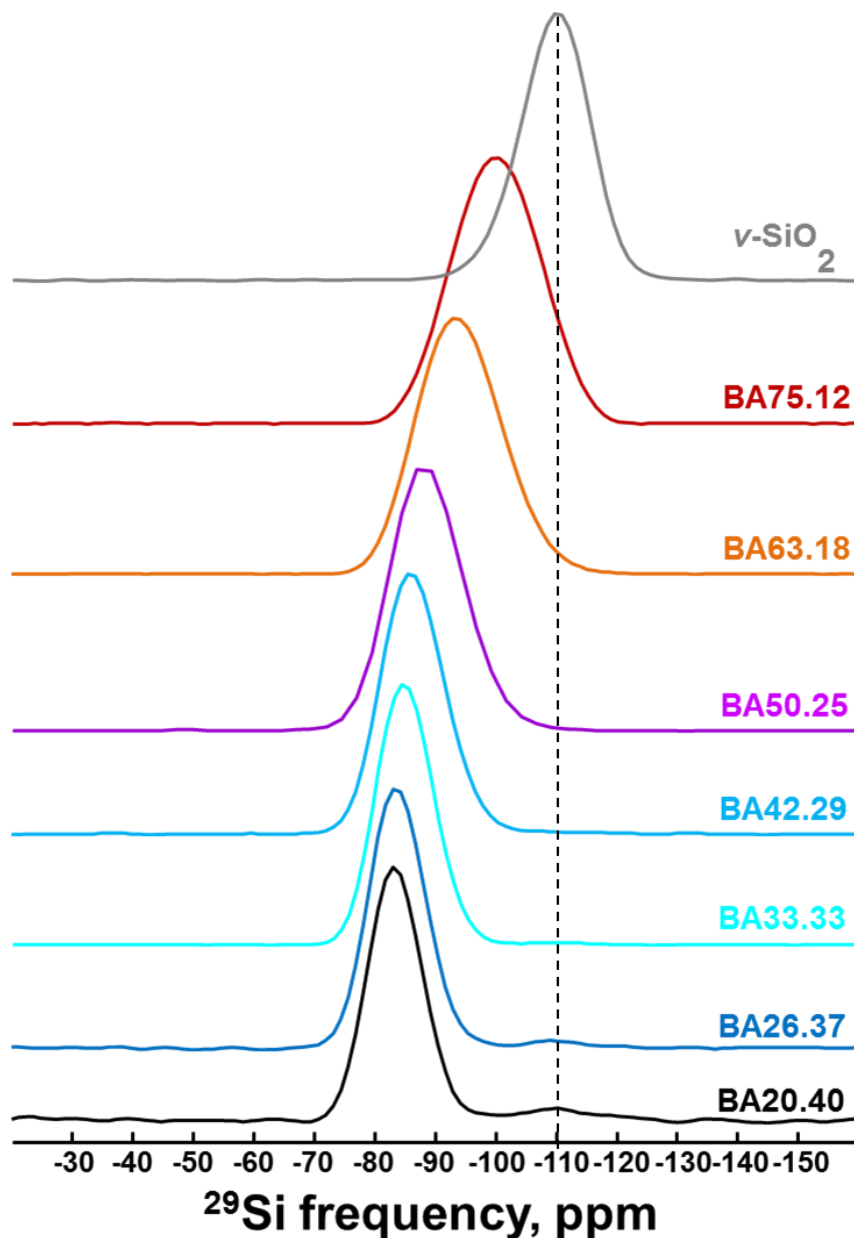


Figure IV.2. ^{29}Si MAS NMR spectra of Ba tectosilicate glasses. Silica content decreases from top to bottom.

As for Sr tectosilicates, we attempted to deconvolute the ^{29}Si NMR spectra of the analogous BAS glasses by fixing position and FWHM of the Gaussian lines corresponding to different Q_m^4 species. Considering the lack of the data on the lines' parameters for the BAS tectosilicates, we used those obtained for the SAS ones. However, the first attempt of the deconvolution was unsuccessful. We reduced the FWHM for all the lines and repeated the deconvolution keeping all parameters but the intensity fixed. This time it gave quite a reasonable result resembling that obtained for Sr tectosilicates (Figure IV.3).

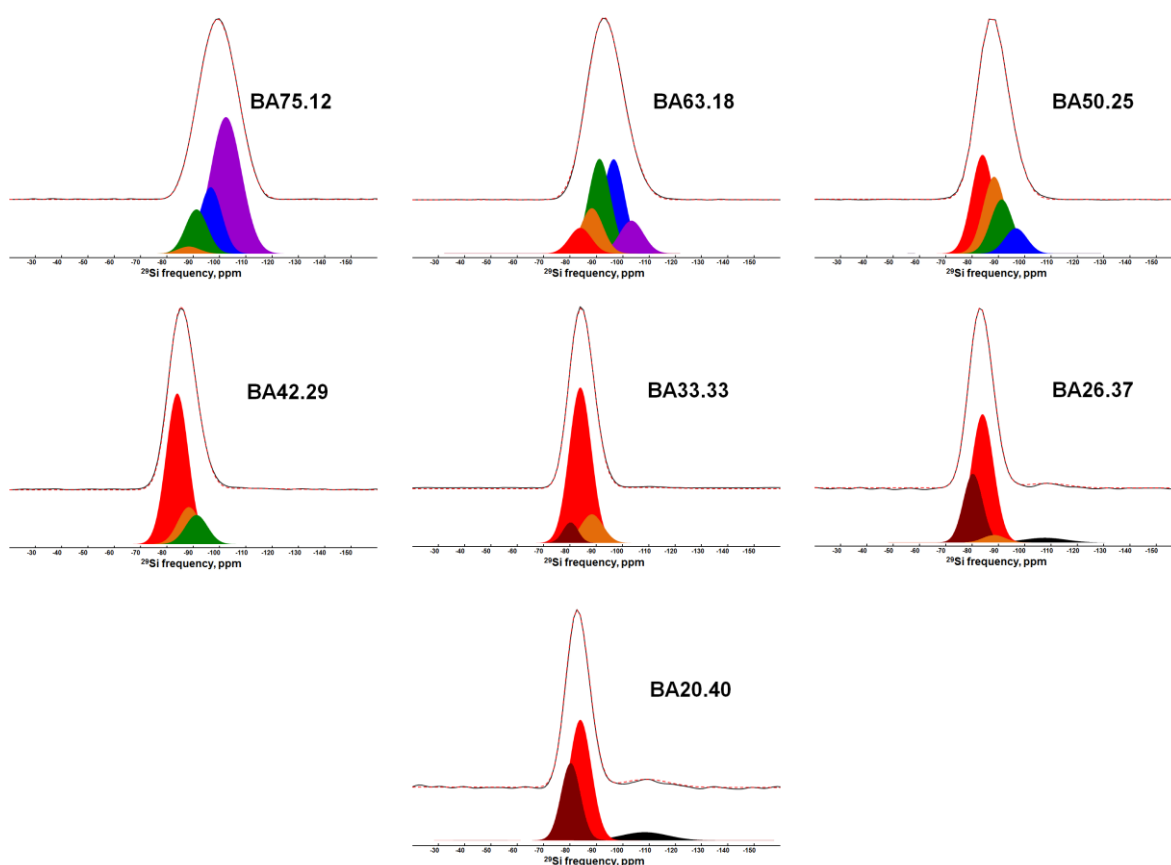


Figure IV.3. Deconvolution of ^{29}Si MAS NMR spectra of Ba tectosilicate glasses. Colour guide: violet – Q_0^4 , blue – Q_1^4 , green – Q_2^4 , orange – Q_3^4 , light red – Q_4^4 , dark red – $Q_4^4(\text{Ba})$, black – Q_0^4 in the silica-like region.

The results on the Q_m^4 species distribution is shown in Figure IV.4. It has been shown in Chapter III that the Q_m^4 distribution for Sr tectosilicates deviates significantly from the random Al-Si mixing model. This is the case for Ba tectosilicates as well since the Q_m^4 distribution in two systems is nearly identical. The main difference between the SAS and BAS systems is in the distribution of Q_4^4 units. For silica-poor Ba tectosilicates an additional line at lower values of the chemical shift is required as in the case of Sr tectosilicate glasses. Following the same logic as discussed previously, the line was attributed to Q_4^4 units with an

extra Ba^{2+} in the second coordination sphere of Si. Interestingly, $\text{Q}_4^4(\text{Ba})$ units do not become dominant in the compositional range studied as it was observed for $\text{Q}_4^4(\text{Sr})$ in the SAS system. It could be explained in terms of a steric factor considering a greater size of Ba cations in comparison to Sr^{2+} . Therefore, it is geometrically more difficult to put an extra Ba^{2+} in the neighbourhood of a Si atom.

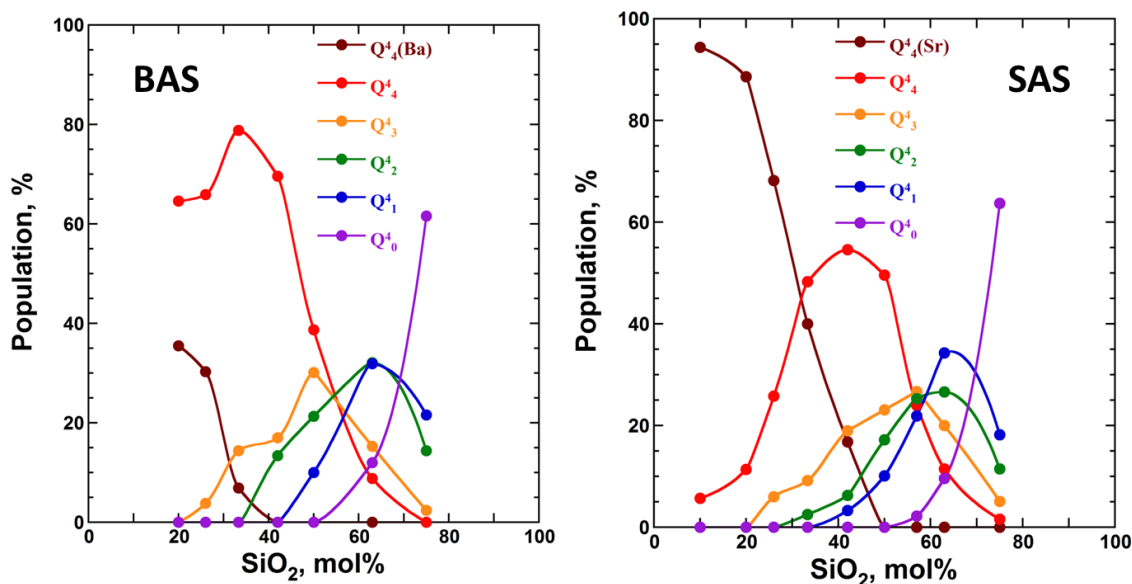


Figure IV.4. Distribution of Q_m^4 species in Ba (left) and Sr (right) tectosilicate glasses obtained from ^{29}Si NMR data.

Even though these results are in quite good agreement with those obtained in the SAS system, one should, nevertheless, keep in mind all the assumptions that were made in order to deconvolute the ^{29}Si NMR spectra. Firstly, we assumed that the line's positions for each Q_m^4 unit in the spectra of the Ba tectosilicate glasses are identical to those obtained for analogous SAS glasses. Secondly, the values of the FWHM were chosen empirically and could eventually be different. Thirdly, we assumed that no NBOs are present for the compositions on the join $R = 1$. However, (Thompson and Stebbins, 2012) have shown that a small fraction of non-bridging oxygens exists for BAS glasses with $R \approx 1$ (even in a slightly peraluminous domain). The presence of NBOs has been also suggested for tectosilicate glasses in the SAS (Chapter III) and CAS (Lee and Stebbins, 2006, 2002) system. Additionally, MD simulations performed by Thibault Charpentier (personal communication) have indicated the presence of 5 to 10% of NBOs and TBOs. All this suggests that the Q_m^n distribution in Ba tectosilicate glasses presented above might differ from the real one and is definitely more complex.

1.2. Neutron diffraction

The static structure factors, $S(q)$, for the glasses along the join R = 1 are plotted in Figure IV.5. The FSDP in the $S(q)$ shifts to higher values of q with a simultaneous drop in intensity when BaAl_2O_4 substitutes for SiO_2 . Similar changes were observed for Sr (Chapter III) and Ca tectosilicate glasses (Hennet et al., 2016) and were connected to the changes in ring statistics (Neuville et al., 2004). The reduction of the fraction of high-membered rings in favour of low-membered ones has been also seen by Raman spectroscopy (see the manuscript for JNCS in Annex II).

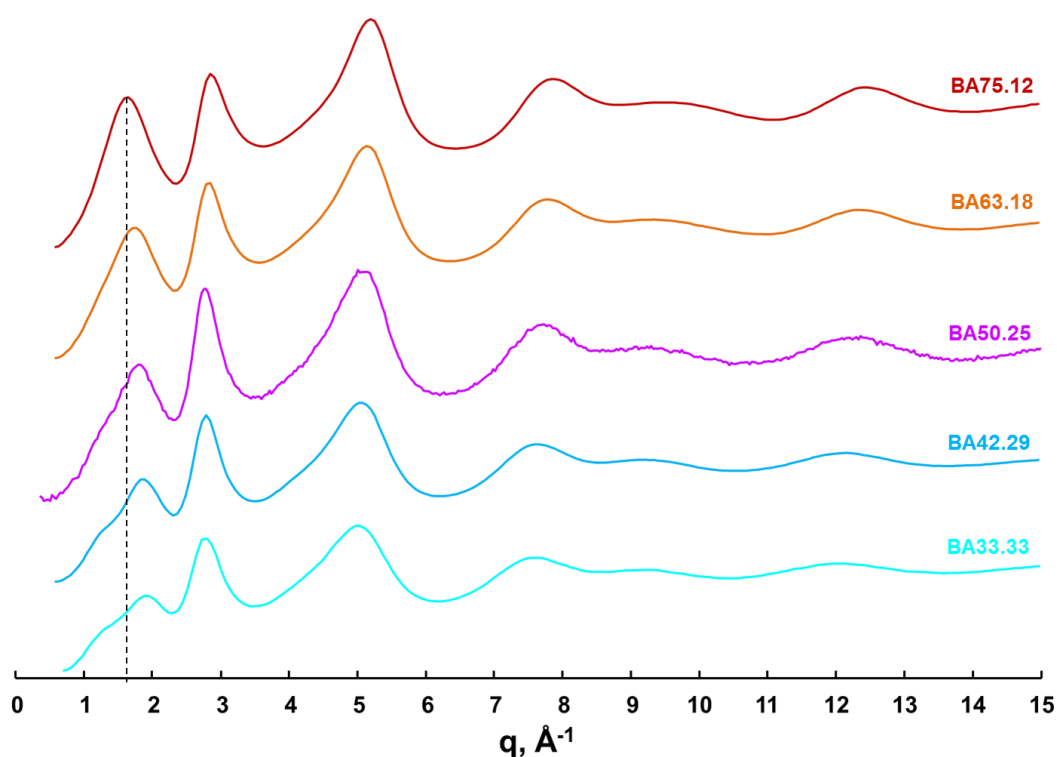


Figure IV.5. Static structure factor, $S(q)$, of Ba tectosilicate glasses. Silica content decreases from top to bottom.

The pair distribution functions, $g(r)$, for the glasses along the join R = 1 are dominated by contributions of O-O, Si-O, Al-O and Ba-O pairs (Figure IV.6). The first peak corresponding to contributions from Si-O and Al-O pairs shifts from 1.62 Å for BA75.12 to 1.69 Å for BA33.33. The second peak in $g(r)$ situated at around 2.7-2.8 Å corresponds to O-O and Ba-O pairs. This peak is shifted to higher values of r compared to corresponding Sr tectosilicates which is likely caused by a longer average Ba-O interatomic distance.

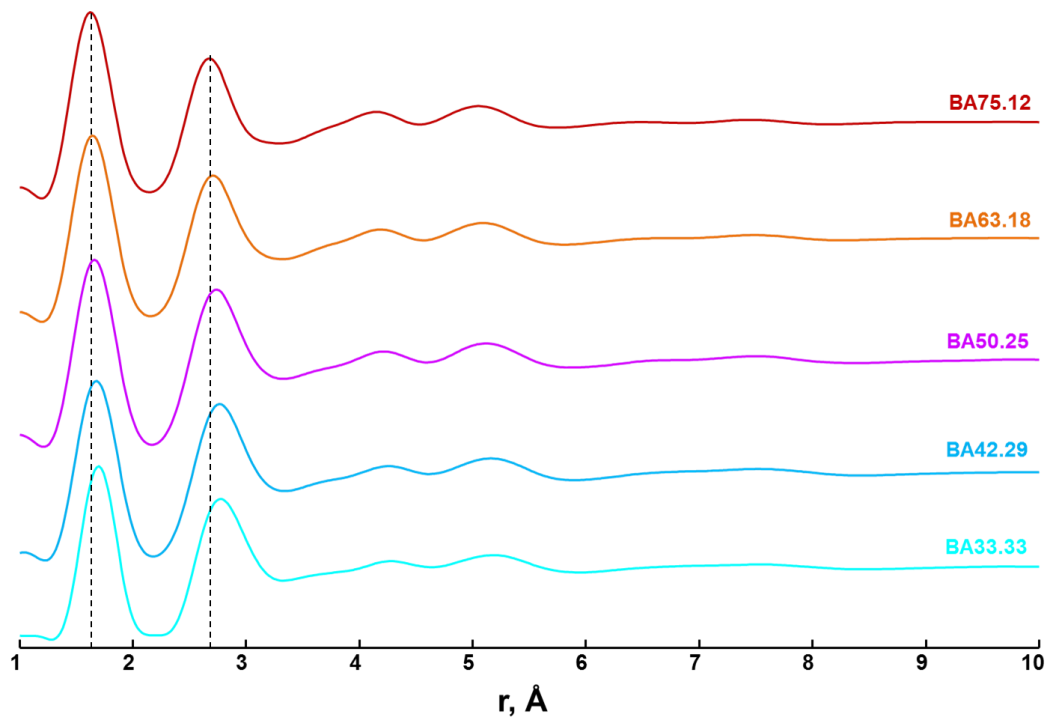


Figure IV.6. Pair distribution function, $g(r)$, of Ba tectosilicate glasses. Silica content decreases from top to bottom.

As for the Sr tectosilicate glasses, MD simulations were performed by Thibault Charpentier (personal communication) in order to retrieve partial pair distribution functions, $g_{ij}(r)$, for different pairs (Figure IV.7). It was found that Si-O and Al-O distances are constant in the whole compositional range and equal 1.58 and 1.76 Å, respectively. The average O-O distance is centred at ~ 2.6 Å and corresponds to oxygen atoms incorporated in tetrahedra. The average Ba-O distance is centred at around 2.8 Å, which is longer than for BA66.00 silicate glass reported by (Hasegawa and Yasui, 1987). The CN(Ba-O) was found to be close to 10, which is higher than CN(Sr-O) = 9 found in corresponding tectosilicate glasses (Chapter III). It is also higher than for BA00.50 aluminate glass of tectosilicate composition for which the CN(Ba-O) has been reported to be 9 (Skinner et al., 2006). For the crystalline BA50.25 tectosilicate (celsian) the CN(Ba-O) has been found to be 7 or 9 depending on the model used (Griffen and Ribbe, 1976), while for two crystalline silicates, BA60.00 and BA66.00, it has been reported 8 and 9-10, respectively (Hesse and Liebau, 1980a, 1980b).

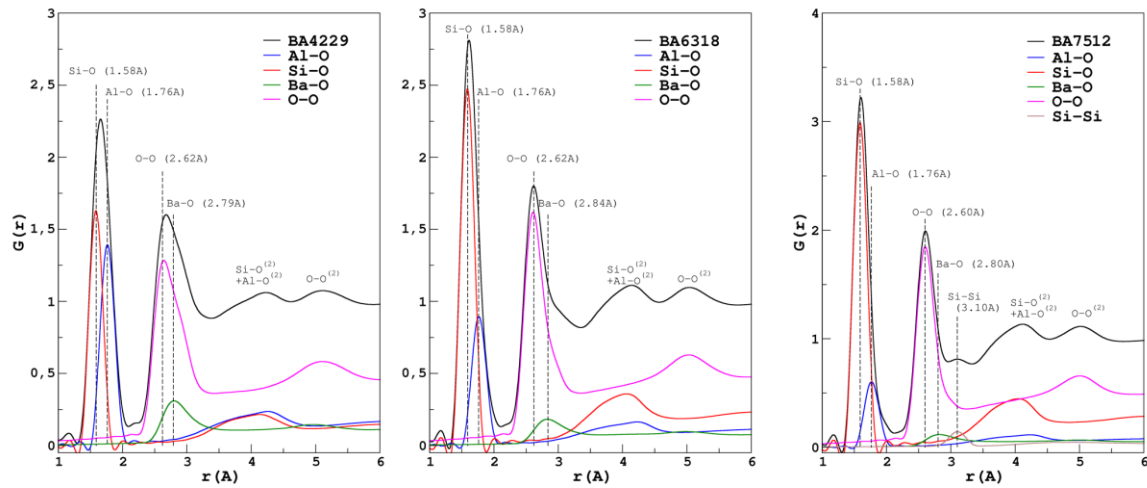


Figure IV.7. Partial pair distribution functions $g_{ij}(r)$ calculated from the results of MD simulations together with experimental $g(r)$ for three Ba tectosilicate glasses.

Section highlights

- ^{27}Al NMR revealed the presence of AlO_5 species ($\leq 2.5\%$) in all Ba tectosilicate glasses. This number is slightly lower than for corresponding SAS compositions.
- The average $\text{CN}(\text{Ba-O})$ found by MD simulations is around 10 which is higher than the average $\text{CN}(\text{Sr-O}) = 8-9$ found for analogous Sr tectosilicates.
- Raman spectroscopy and ND showed a shift of the rings statistics towards the low-membered rings similarly to what was observed in the SAS system.
- Silicon tetrahedra were found in Q^4 species by Raman and ^{29}Si NMR. However, MD simulations indicate the presence of NBOs and TBOs (5-10 % of both).
- As for Sr tectosilicate glasses, T_g increases for BAS compositions in the silica-poor domain.

2. Silicates domain ($R = \infty$)

2.1. ^{29}Si NMR spectroscopy

^{29}Si NMR spectra of the silicate glasses are presented in Figure IV.8. With increasing BaO content the NMR signal shifts to higher values of the δ_{iso} , reflecting changes in the Q^n species distribution. The spectrum of BA75.00 possesses a shoulder at the position of Q^4 units and the main peak at the position of Q^3 ones. The barycentre's position suggests that the majority of Q^n species should be represented by Q^3 ones (Dupree et al., 1986; Lippmaa

et al., 1980; Murdoch et al., 1985). The spectra of two other silicates are more symmetric and quite featureless. Nevertheless, the barycentre's positions of the spectra of the glasses match with the positions of the NMR lines found in crystalline counterparts (Murdoch et al., 1985; Smith et al., 1983). Therefore, for BA66.00 and BA50.00 glasses one expects the dominant Q^n species to be Q^3 and Q^2 , respectively. The spectrum of BA50.00 glass also possesses a wide feature at around -110 ppm with $\sim 2\%$ of the total intensity. The origin of the line has been discussed in the previous chapter.

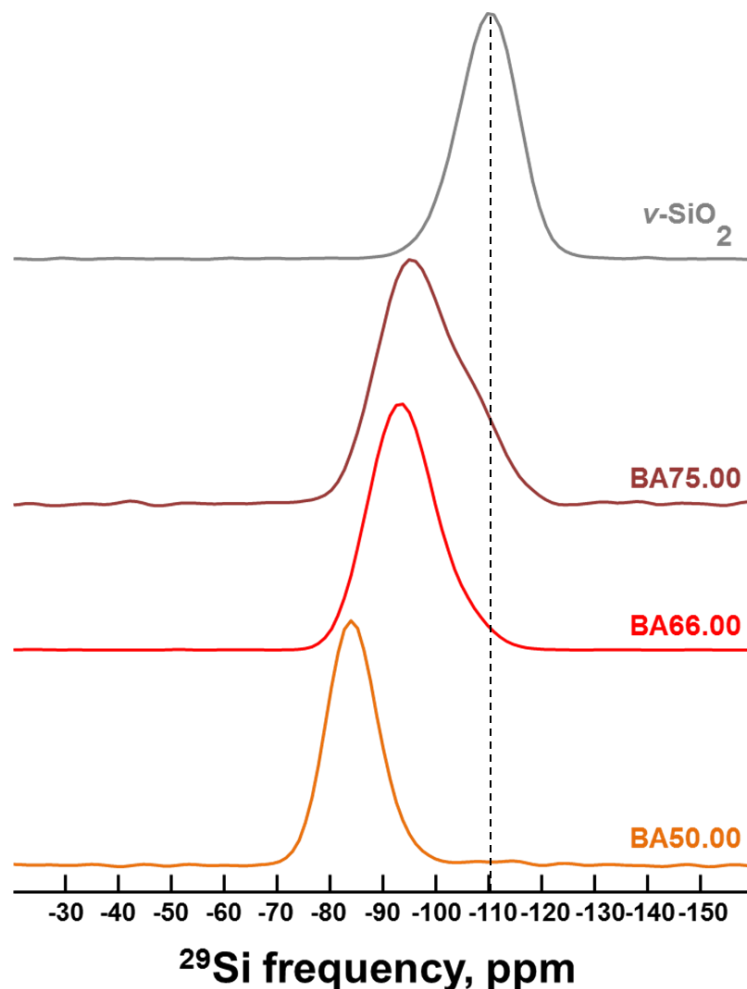


Figure IV.8. ^{29}Si MAS NMR spectra of Ba silicate glasses. Silica content decreases from top to bottom.

As for the tectosilicate glasses, to deconvolute the ^{29}Si NMR spectra of Ba silicate ones we took positions of Q^n lines for Sr silicates as a departure point. By fixing them and letting varying all the other parameters, we deconvoluted the ^{29}Si NMR spectra. The results are presented in Figure IV.9.

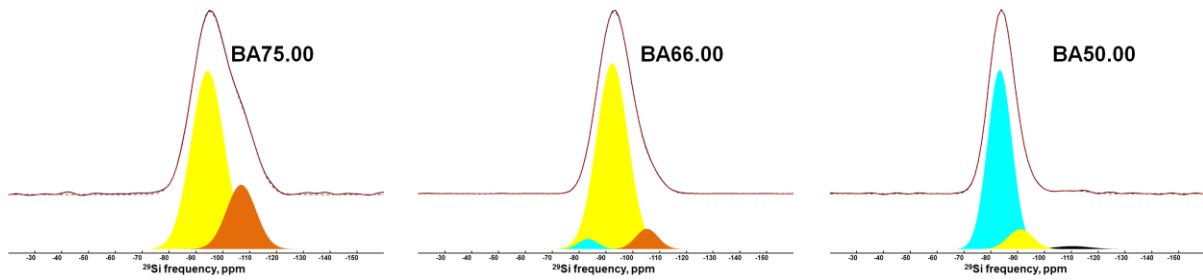


Figure IV.9. Deconvolution of ^{29}Si MAS NMR spectra of Ba silicate glasses. Colour guide: orange – Q^4 , yellow – Q^3 , turquoise – Q^2 , black – Q^0 in the silica-like region.

According to the deconvolution, the network of BA75.00 glass is mainly composed of Q^3 units with approximately 25 % of Q^4 ones. The addition of BaO, as expected, depolymerizes the network favouring formation of NBOs. Thus, for BA66.00 we still observe the majority of Q^3 units but with the rest incorporated in Q^2 and Q^4 ones. For the most depolymerized BA50.00 glass the network is dominated by Q^2 units with a minor fraction of Q^3 ones. Our results are in good agreement with those reported for BA66.00 glass by (Murdoch et al., 1985; Schlenz et al., 2002; Schneider et al., 2003). It has been found the presence of Q^2 , Q^3 and Q^4 units with a relative abundance of 24 ± 7 , 62 ± 5 and 14 ± 5 %, respectively. Slight deviations in the population of Q^n species obtained from our deconvolution could be explained by the fact that the authors (Schneider et al., 2003) used different δ_{iso} values for Q^n lines and fixed the FWHM for all the lines at 11 ± 1 ppm. In general, the Q^n species distribution obtained from our deconvolution is in rather good agreement with the one found in other alkali and alkaline earth silicate systems (Figure IV.10).

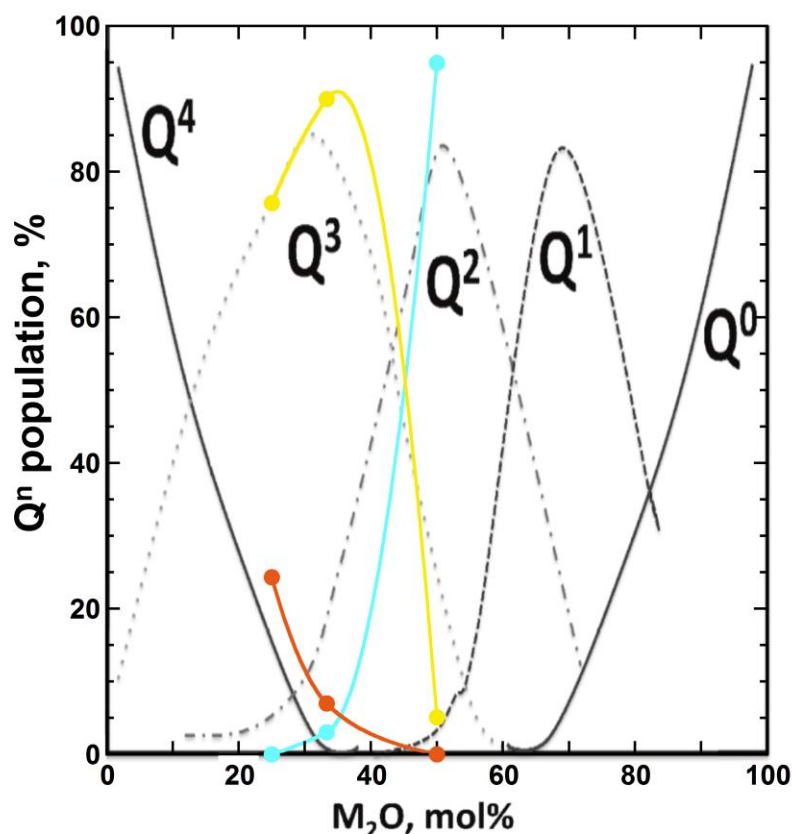


Figure IV.10. Comparison of the Q^n distribution obtained from the deconvolution of the ^{29}Si MAS NMR spectra of Ba silicate glasses with the one typically found in alkali (Li, Na, K) and alkaline earth (Mg, Ca, Sr, Ba) silicate glasses (Neuville et al., 2014). Colour guide: orange – Q^4 , yellow – Q^3 , turquoise – Q^2 .

Worth noticing, that the NMR spectra of Ba silicate glasses are narrower than of Sr ones. That has been already seen for silicate glasses with 66.7 mol% of silica by (Murdoch et al., 1985). They pointed out that network-modifying cations with an elevated polarizing power (i.e. cation field strength) disturb the silicate structure more by creating a broader range of Q^n species. If we assume the coordination number of both Sr and Ba is 6 in silicate glasses, the cation field strength will be 1.37 and 0.96, respectively. These values of the CFS were calculated using ionic radii from (Whittaker and Muntus, 1970). Therefore, the Q^n species distribution obtained from the deconvolution of ^{29}Si NMR spectra is in agreement with the CFS influence. For example, the network of SA50.00 glass consists of Q^0 to Q^3 units, while the one of BA50.00 is composed of Q^1 and Q^2 species only.

2.2. Raman spectroscopy

Raman spectra of Ba silicates presented in Figure IV.11 resemble the ones of corresponding Sr silicates. In the low-frequency region, they have two broad bands at 180-

190 and 300-310 cm^{-1} that could be attributed to the Ba-O vibrations as discussed in Chapter III. These bands are shifted to lower frequencies in comparison to analogous bands of Sr-O vibrations in the spectra of Sr silicates due to the higher atomic weight of Ba compared to Sr. In the spectrum of BA75.00, we observe a peak at 538 cm^{-1} and a shoulder at $\sim 593 \text{ cm}^{-1}$. These two peaks merge into one with increasing BaO content and appear as an asymmetric peak around 600 cm^{-1} for the compositions with less than 60 mol% of SiO_2 . This band was previously attributed to vibrations in three-membered rings composed of different Q^n species. In the high-frequency region, two peaks at 936 and 1075 cm^{-1} are found in the spectrum of BA75.00 glass. The intensity of the first peak increases and of the latter one decreases under the substitution of SiO_2 by BaO. At the same time, a new peak appears at $\sim 850 \text{ cm}^{-1}$ and grows in intensity. These peaks, as discussed previously, are characteristic for vibrations in Q^0 (850 cm^{-1}), Q^2 (950 cm^{-1}) and Q^3 (1070 cm^{-1}) units.

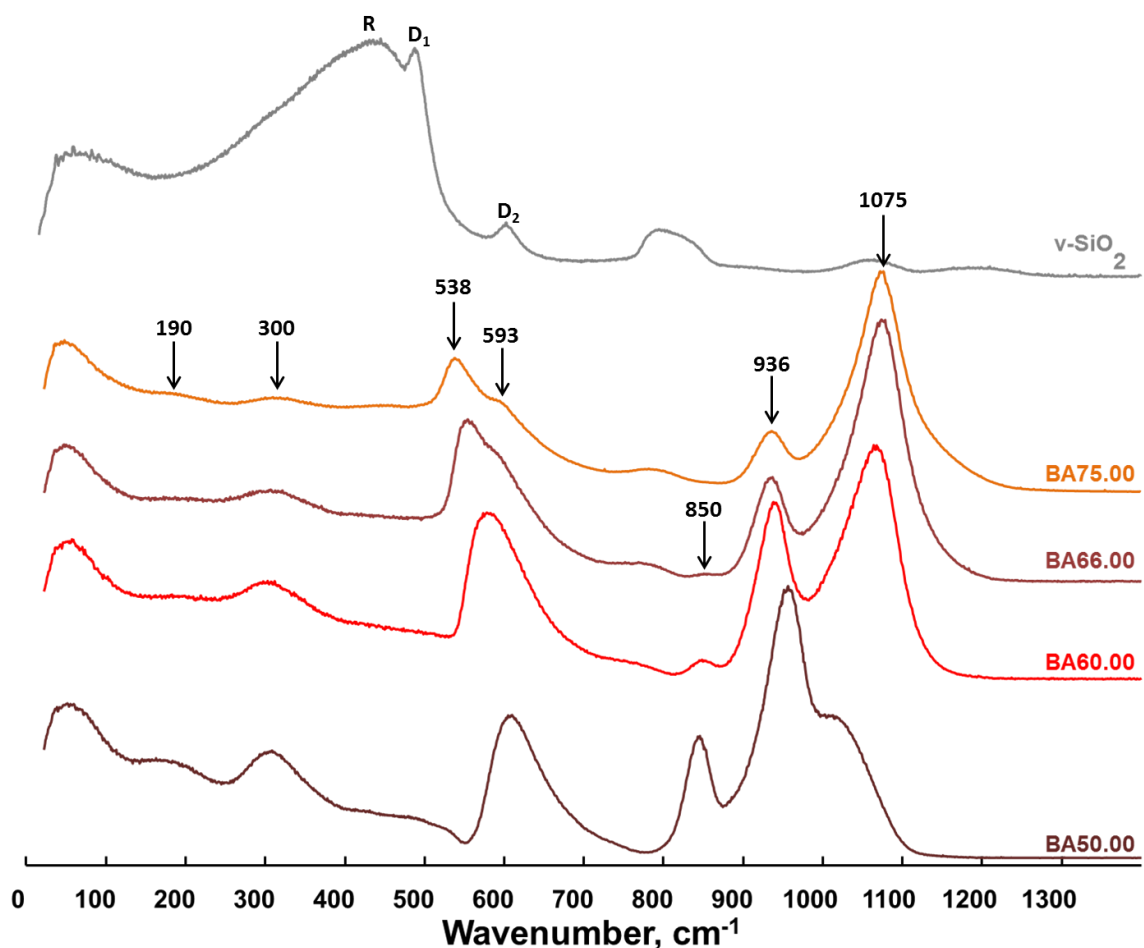


Figure IV.11. Area normalized Raman spectra of Ba silicate glasses. Numbers correspond to the frequencies of observed bands maxima. Silica content decreases from top to bottom.

The barycentre's position of the Raman spectra is plotted in Figure IV.12 as a function of silica content. For the silicate and tectosilicate glasses, the slope of both curves from 100 to 66.7 mol% of SiO_2 is equal $2.2 \pm 0.1 \text{ cm}^{-1}/\text{mol}\%$ of SiO_2 . While for the tectosilicate glasses the slope is constant in the whole range of silica content, for the silicate ones it changes to $5.3 \pm 0.1 \text{ cm}^{-1}/\text{mol}\%$ of SiO_2 at 66.7 mol% of silica.

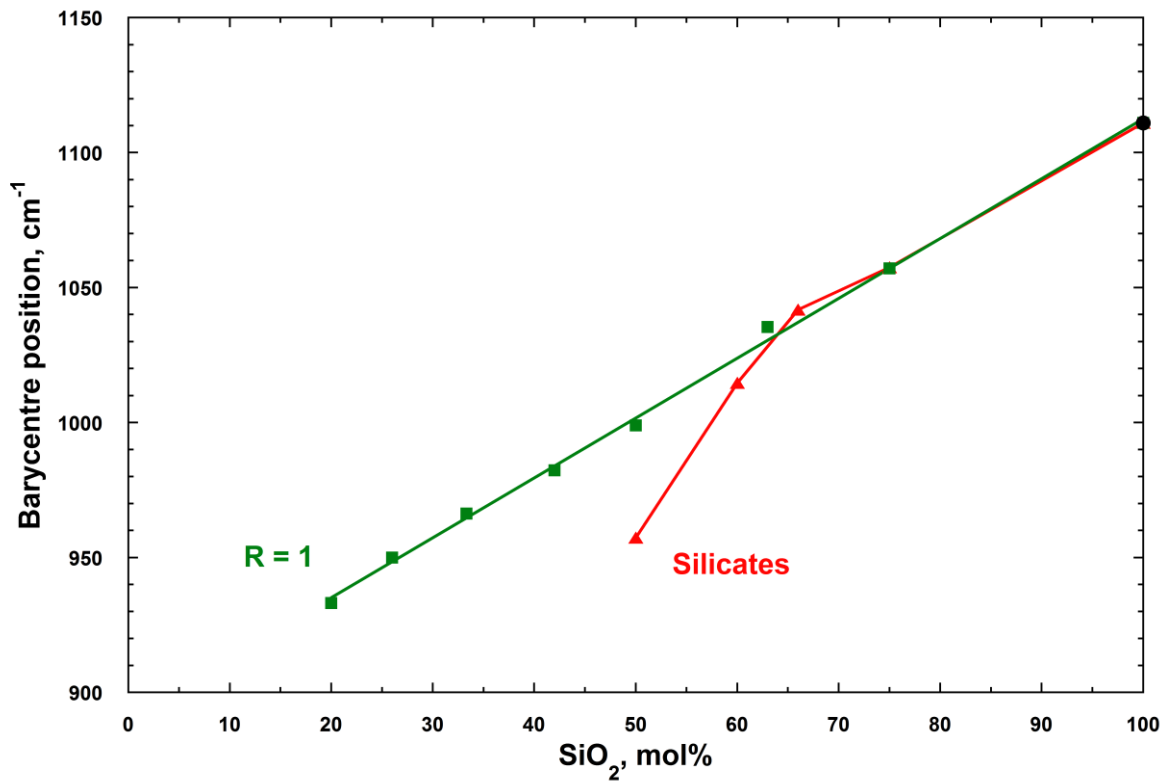


Figure IV.12. Barycentre position of the high-frequency envelope of Raman spectra of Ba silicate (red) and tectosilicate (green) glasses. The lines are a guide to the eye.

The results of the deconvolution of the HF region of the spectra are presented in Figure IV.13. For BA75.00 glass all possible Q^n species were detected with the Q^3 band being the dominant one. Even though the relative area of the band is not directly correlated to the content of Q^n species it still remains a good estimate of the evolution of the Q^n species distribution. Therefore, we can state that with further increasing BaO content the number of Q^4 and Q^3 units dramatically decreases in favour of more depolymerized Q^2 , Q^1 and Q^0 units.

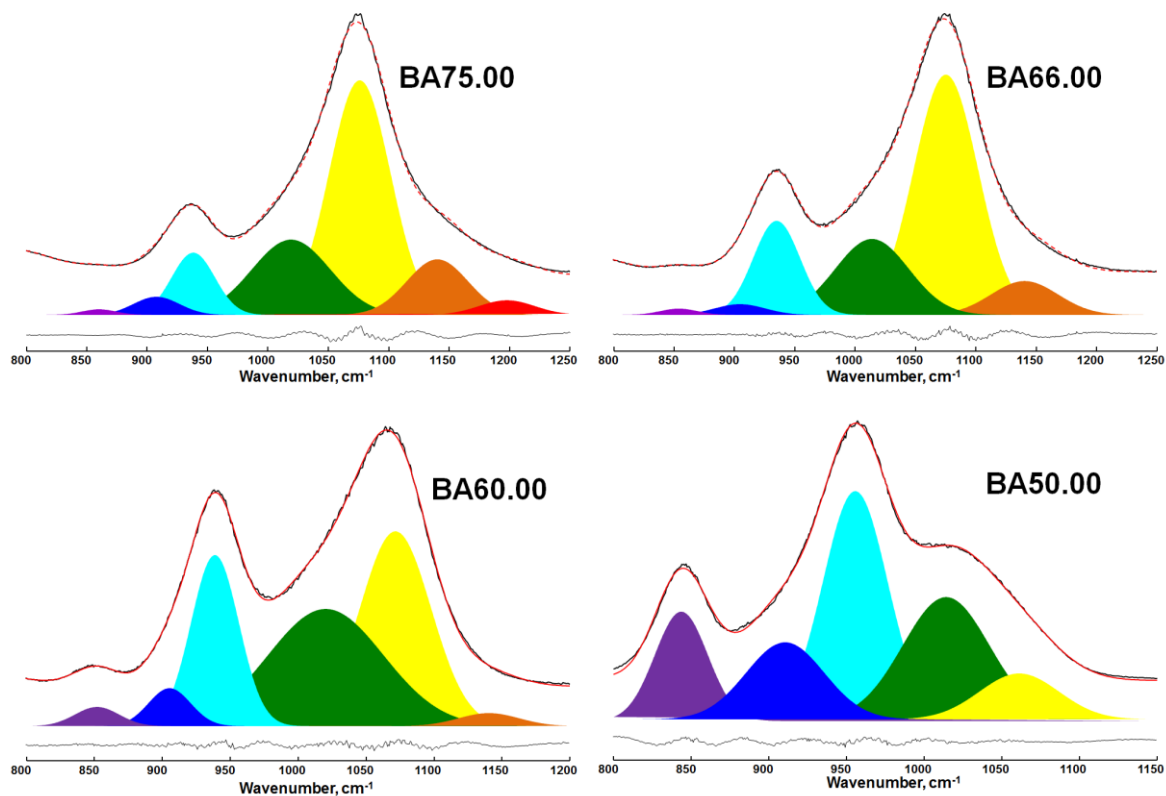


Figure IV.13. Deconvolution of the HF region of the Raman spectra of Ba silicate glasses. Colour guide: red – $Q^{4,I}$, orange – $Q^{4,II}$, yellow – Q^3 , green – T_{2s} , turquoise – Q^2 , blue – Q^1 , violet – Q^0 .

Several authors have reported deconvolution of the HF envelope of the Raman spectrum of BA66.00 glass. (Schlenz et al., 2002) found Q^1 to Q^4 units in the structure of BA66.00 glass, with 20.0 ± 1.7 % of Q^2 and 77.7 ± 5.3 % of Q^3 units, Q^1 and Q^4 species being at 1-2 % level. On the other hand, (Lenoir et al., 2008) reported only Q^2 to Q^4 units for the same glass: 11.89, 48.88 and 16.48 % of the relative area, respectively. The results of our deconvolution lie somewhere in between the reported ones. In general, there is no universal agreement on how to fit the Raman spectra of silicate or aluminosilicate glasses. Therefore, there is a discrepancy between reported data, since the HF region of a Raman spectrum can be successfully deconvoluted in a way to fit one's theory. In our case, the Q^n species distribution (or rather relative areas) seen by Raman for Ba silicate glasses resembles the one obtained from ^{29}Si NMR (Figure IV.14). Therefore, we believe that the deconvolution we made is rather reasonable.

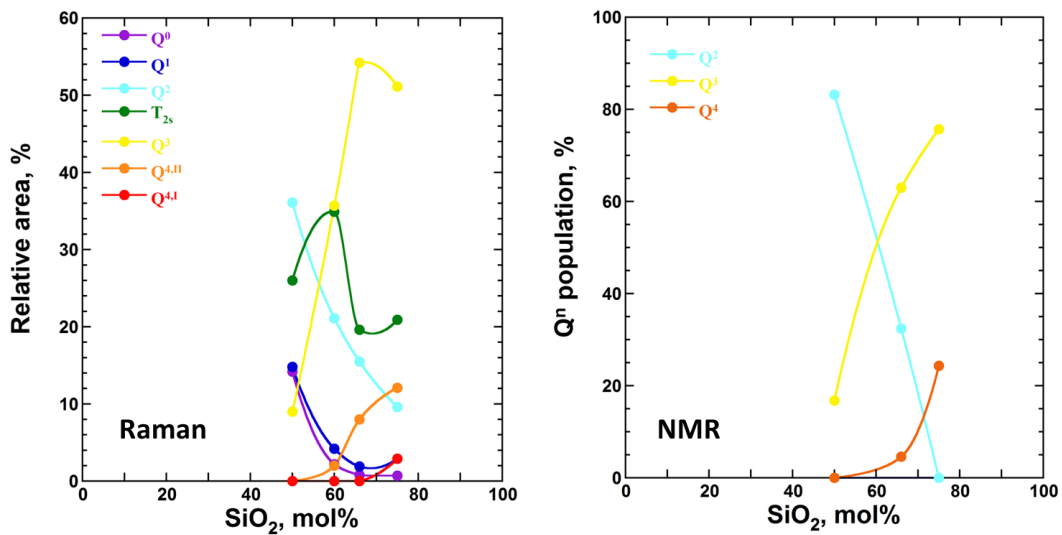


Figure IV.14. *Left*: The relative area under the Gaussian bands obtained from deconvolution of the high-frequency region of the Raman spectra of Ba silicate glasses. *Right*: Population of Qⁿ species retrieved from ²⁹Si NMR.

2.3. Macroscopic properties

Densities of the silicate and tectosilicate glasses are reported in Figure IV.15. With decreasing SiO₂ content density increases on the both joins. This increase is much greater in the case of the silicate glasses as it has been already seen in the SAS system. The density of BA00.50 reported here (Skinner et al., 2006) fits quite well the overall trend. We made a comment in Chapter I that this glass might be of different composition. Nevertheless, if it is true the shift in the composition is not great, which is well seen from the density plot.

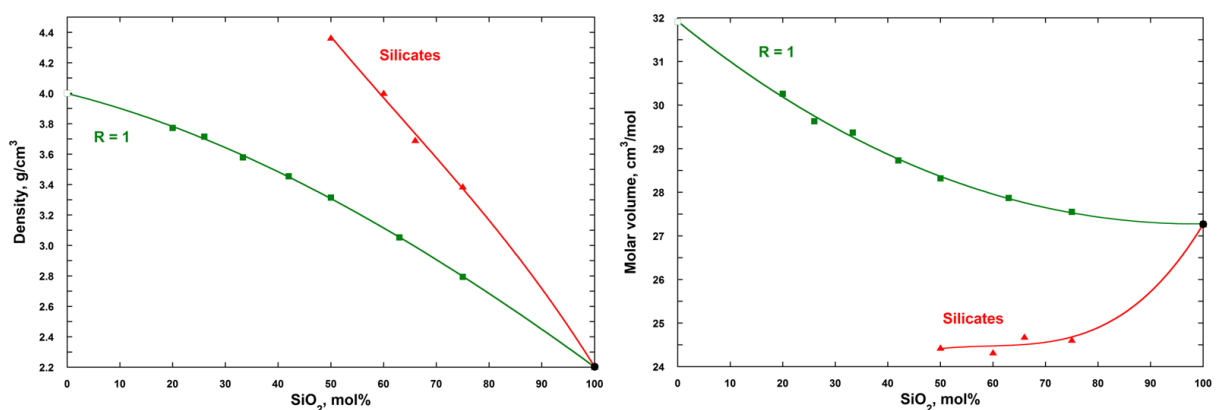


Figure IV.15. Experimental densities (*left*) and calculated molar volumes (*right*) of Ba tectosilicate (green squares) and silicate (red triangles) glasses. The data for BA00.50 (green open square) is from (Skinner et al., 2006). The black filled circle corresponds to the density of vitreous silica taken from (Brückner, 1970). Error bars are less than the symbol size. The lines are a guide to the eye.

On the join R = 1, molar volume increases gradually under the substitution of SiO₂ by BaAl₂O₄. Unlike the V_m of Sr tectosilicate glasses, there is no minimum in the V_m curve. Molar volume of the silicate glasses drops from vitreous silica to BA75.00 and then does not vary significantly with further decrease of SiO₂ content. Taking into account that the network polymerization declines with increasing BaO content (as seen by ²⁹Si NMR and Raman), this implies that the network does not collapse but rather holds constant V_m . A similar trend in the evolution of V_m has been already observed for Ba silicates by (Doweidar, 1999; Rabukhin, 1999). It seems that a threshold in network's packing was already achieved for silica-rich Ba silicates and further substitution of SiO₂ by BaO does not affect the V_m of the system significantly. This behaviour is opposite to the one observed for Sr silicate glasses, for which the augmentation of SrO content lowers molar volume continuously. However, there are examples in literature when V_m increases with increasing depolymerization of glass network (Doweidar, 1996; Rabukhin, 1999). These examples concern silicate glasses with huge K and Cs cations. In this sense, Ba silicates are intermediate in their behaviour.

Higher values of V_m for the tectosilicate glasses are in agreement with higher CN(Ba-O) \approx 10. For vitreous BA66.00 silicate CN(Ba-O) = 6.76 \pm 0.12 according to (Schlenz et al., 2002), reflecting the fact that the silicate network is packed denser.

Figure IV.16 shows the evolution of T_g for the silicate and tectosilicate glasses. Glass transition temperature of the silicates rises with decreasing silica content as for Sr silicate glasses. Such behaviour of the T_g curve has been observed by (Shelby, 1979) for Ca and Sr silicate glasses but not for ones containing Ba. However, the author did not study Ba silicates with less than 60 mol% of SiO₂. Recalling discussion from Chapter III on the T_g curve of Sr silicates, we suppose that Ba cations can also participate in the network linkage after reaching a certain concentration threshold. This participation, nevertheless, is weaker than in the case of Sr silicates, since the gap between the T_g curves of Ba silicates and tectosilicates is higher (200-250 K) than in the SAS system (100-150 K). In the row Ca – Sr – Ba, the CFS decreases as well as the glass transition temperature of corresponding silicate glasses. Therefore, low CFS of Ba²⁺ reduces its ability to participate in the network linkage, whereas for smaller cations this ability is higher. Interestingly, for Na and K silicate glasses the T_g is lower than for alkaline earth counterparts and it decreases gradually under the

introduction of alkali cations (Le Losq and Neuville, 2017; MacDonald et al., 1985). It brings to mind the idea of (Bockris et al., 1955) that in silicate melts doubly-charged cations obstruct the viscous flow while cations with a single positive charge do not, making former melts more viscous.

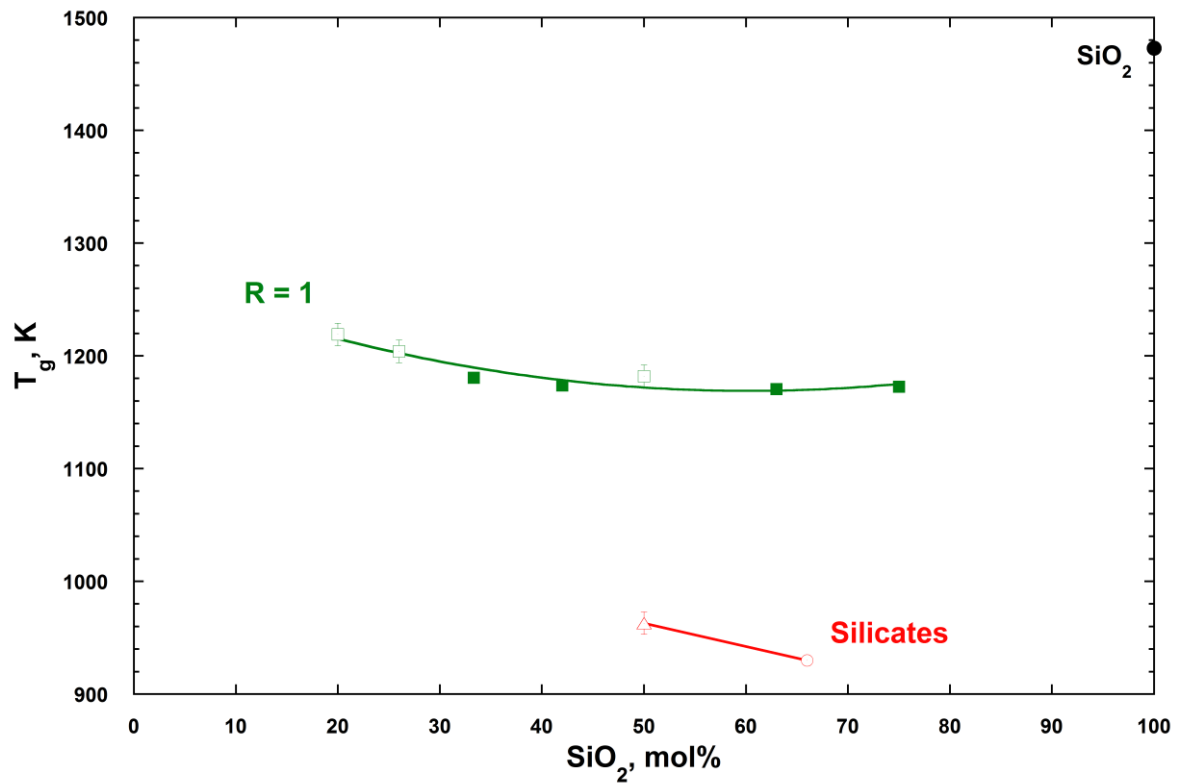


Figure IV.16. Glass transition temperatures for Ba tectosilicate (green) and silicate (red) glasses. Filled symbols are T_g values extracted from viscosity data, open symbols are T_g values from DSC measurements. The data for BA66.00 (red open circle) is from (Lenoir et al., 2008). The glass transition temperature of vitreous silica (black filled circle) is given for comparison (Mackenzie, 1963). If not visible error bars are less than the size of symbols. The lines are a guide to the eye.

Section highlights

- The network of silicate glasses consists of different Q^n species as seen by Raman and ^{29}Si NMR. These species form tetrahedral rings that are predominantly the three-membered ones.
- Two bands are observed in the low-frequency region of the Raman spectra and were attributed to Ba-O vibrations in analogy with the SAS system.
- Molar volume of Ba silicates does not evolve much with decreasing silica content dissimilarly to what was observed for Sr silicate glasses. However, T_g

increases under the substitution of SiO₂ by BaO suggesting the participation of Ba cations in the network linkage.

3. Peralkaline domain (R = 3)

3.1. ²⁷Al and ²⁹Si NMR spectroscopy

²⁷Al NMR spectra of the glasses along the join R = 3 are presented in Figure IV.17. The spectra consist of the main contribution at 60-70 ppm corresponding to Al atoms in the tetrahedral environment and a barely visible bump at 30-40 ppm corresponding to five-coordinate Al. Due to Al-Si exchange in the second coordination sphere of Al atoms, the NMR line shifts to higher δ_{iso} values under the substitution of SiO₂ by Ba₃Al₂O₆.

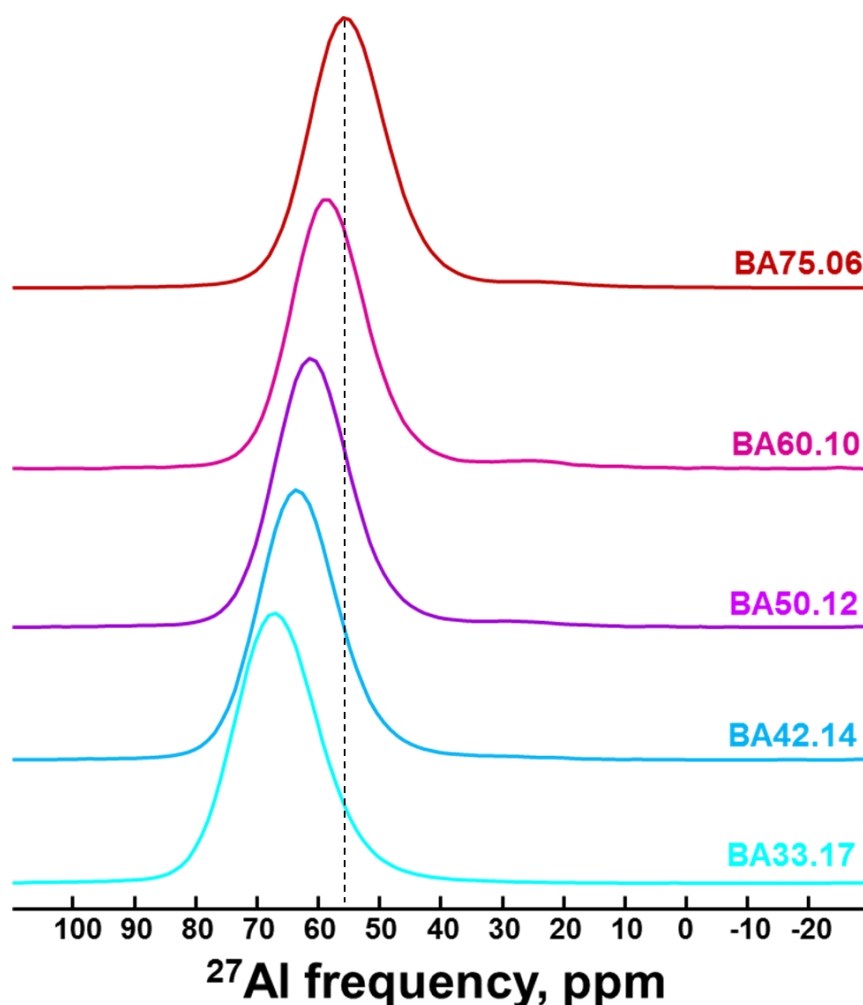


Figure IV.17. ²⁷Al MAS NMR spectra of Ba peralkaline glasses. Silica content decreases from top to bottom.

The NMR spectra were deconvoluted and the results are presented in Figure IV.18.

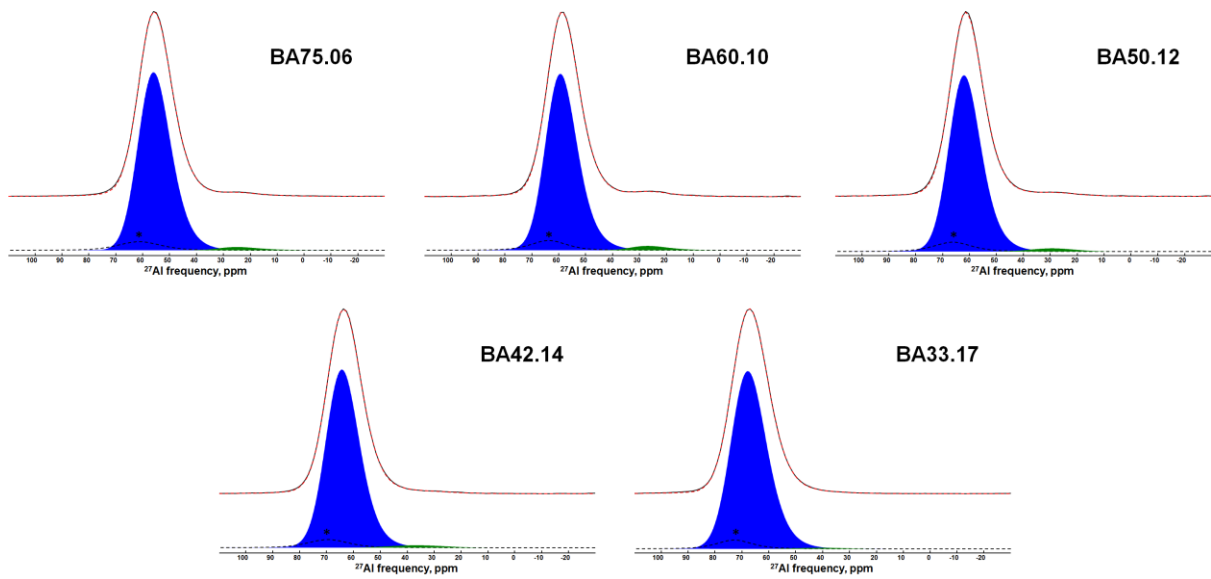


Figure IV.18. Deconvolution of the ^{27}Al MAS NMR spectra of Ba peralkaline glasses. Colour guide: blue – AlO_4 , green – AlO_5 , black dashed lines with an asterisk – spinning sidebands.

The chemical shift of both AlO_4 and AlO_5 sites changes almost linearly with composition (Figure IV.19). For silica-poor BA33.17 glass, the value of $\delta_{\text{iso}}(\text{AlO}_4)$ is slightly higher than for the tectosilicate counterpart. We suggest that, as in the case of SA33.17 glass, one possible explanation of such deviation can be the presence of Al-NBO bonds.

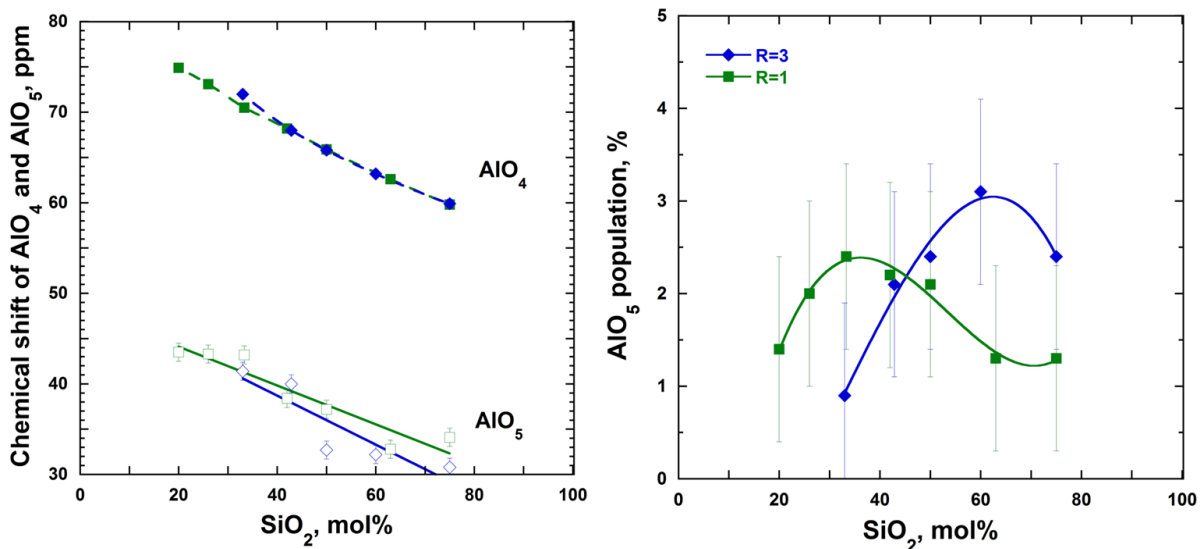


Figure IV.19. *Left*: evolution of isotropic chemical shift (δ_{iso}) of AlO_4 and AlO_5 for Ba tectosilicate (green) and peralkaline (blue) glasses. If not visible, error bars are less than symbol's size. *Right*: AlO_5 population for Ba tectosilicate (green) and peralkaline (blue) glasses. The lines are a guide to the eye.

A small fraction $\sim 3\%$ of AlO_5 presents in the peralkaline glasses. This finding is in agreement with (Thompson and Stebbins, 2012) who has shown the presence of AlO_5 even in the peralkaline domain of the BAS system. The maximum is shifted to the silica-rich domain with respect to the tectosilicate compositions as in the SAS system. The AlO_5 population in Ba tectosilicate and peralkaline glasses is lower than in Sr, Ca and Mg ones (Neuville et al., 2008, 2006; Novikov et al., 2017). Thus, together with previous data on different alkali, alkaline earth and rare earth aluminosilicate glasses, we confirmed that the CFS directly correlates to an AlO_5 fraction (Allwardt et al., 2005; Florian et al., 2007; Iftekhar et al., 2011; Thompson and Stebbins, 2012).

Figure IV.20 shows ^{29}Si NMR spectra of the peralkaline glasses. With decreasing SiO_2 content the NMR signal shifts to higher δ_{iso} values with a concurrent narrowing.

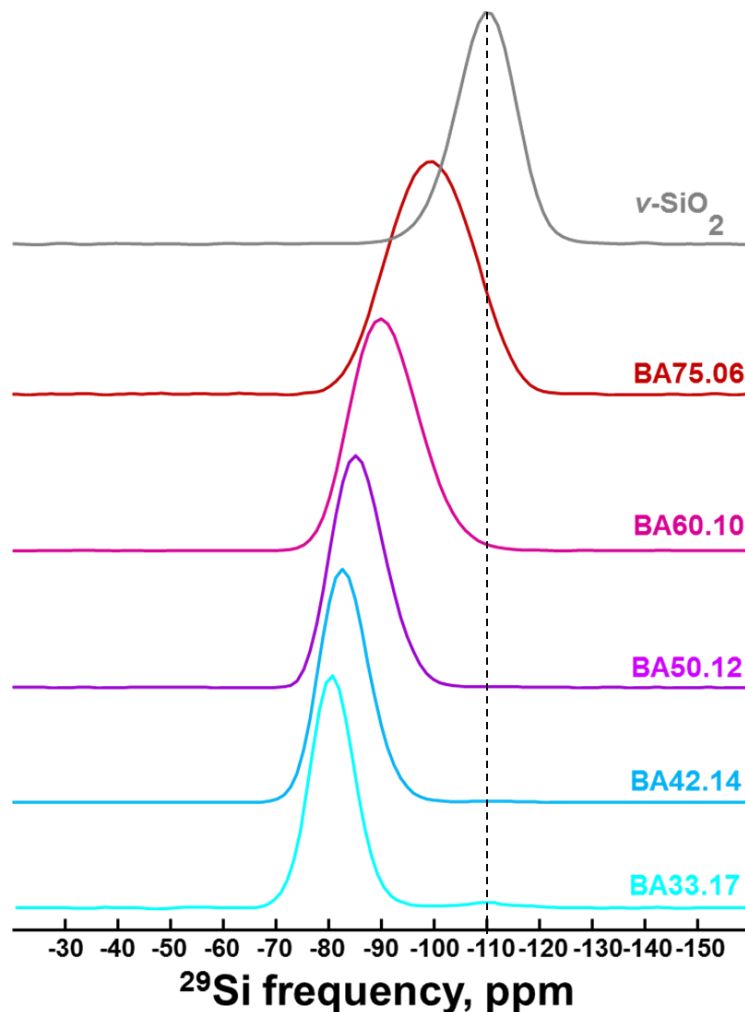


Figure IV.20. ^{29}Si MAS NMR spectra of Ba peralkaline glasses. Silica content decreases from top to bottom.

As discussed previously, the ^{29}Si NMR spectra of peralkaline glasses are a sum of the signals of different Q_m^n species. Direct deconvolution of such spectra is a complex task likely resulting in unreliable fits. Therefore, we do not present here any deconvolution of the ^{29}Si NMR spectra of Ba peralkaline glasses.

3.2. Neutron diffraction

The static structure factor $S(q)$ of the peralkaline glasses is shown in Figure IV.21. The FSDP shifts to higher q values and becomes less intense with decreasing SiO_2 content, suggesting a change in the ring statistics with the introduction of $\text{Ba}_3\text{Al}_2\text{O}_6$ towards low-membered rings as discussed before.

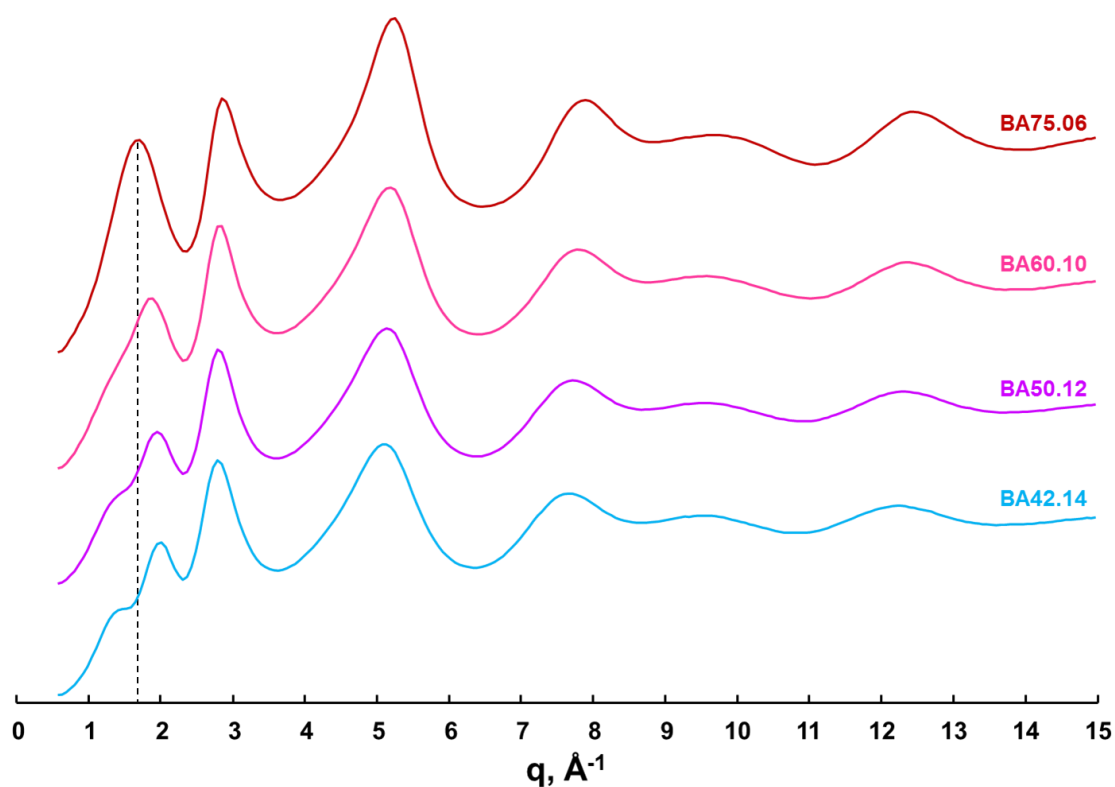


Figure IV.21. Static structure factor, $S(q)$, of Ba peralkaline glasses. Silica content decreases from top to bottom.

Changes in the $g(r)$ observed for Ba peralkaline glasses are similar to ones on the other joins in the BAS and SAS systems (Figure IV.22). Namely, the first peak in $g(r)$, corresponding to Si-O and Al-O contributions, shifts to higher r values as well as the second peak corresponding to O-O and Ba-O contributions.

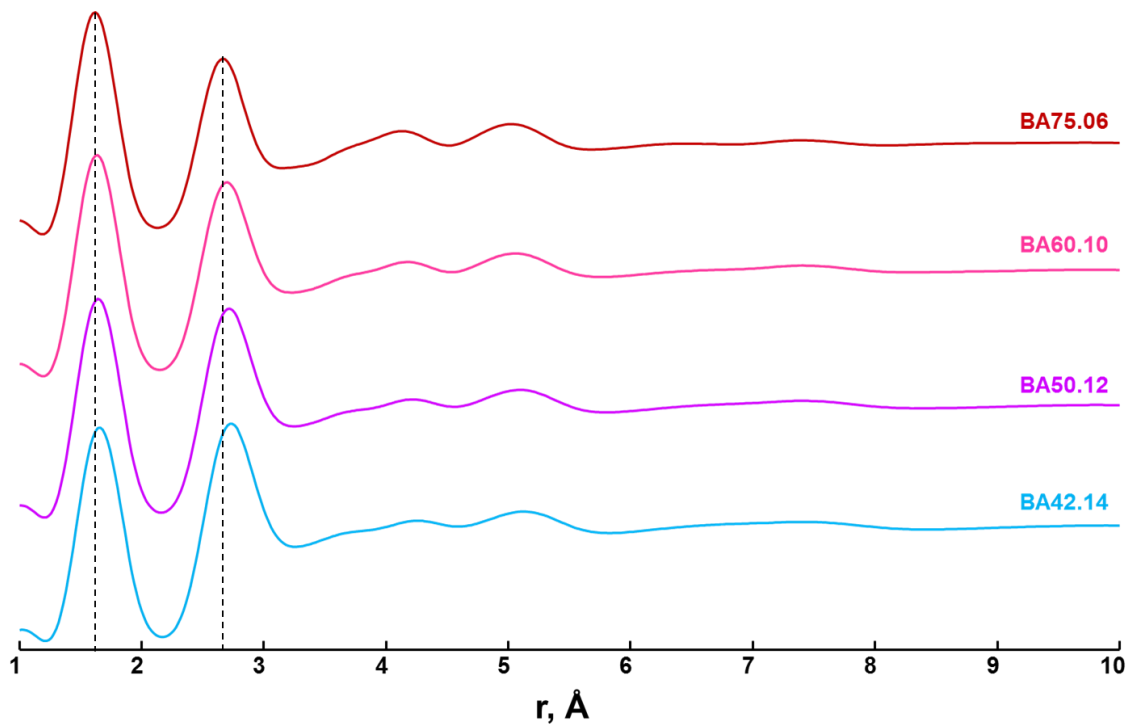


Figure IV.22. Pair distribution function, $g(r)$, of Ba peralkaline glasses. Silica content decreases from top to bottom.

MD simulations performed by Thibault Charpentier (personal communication), based on the ND data, demonstrated that Si-O and Al-O distances remain unchanged from one composition to another and whatever join ($R = 1$ or 3) or system (SAS or BAS) are concerned. The Ba-O distance shortens from 2.80 \AA for silica-rich to 2.76 \AA for silica-poor compositions (Figure IV.23). The MD simulations revealed that $\text{CN}(\text{Ba-O})$ is around 9 for the compositions studied. This coordination number is lower than for Ba tectosilicate compositions ($\text{CN} \approx 10$) and higher than for corresponding Sr peralkaline glasses ($\text{CN} \approx 8$) also found from MD simulations.

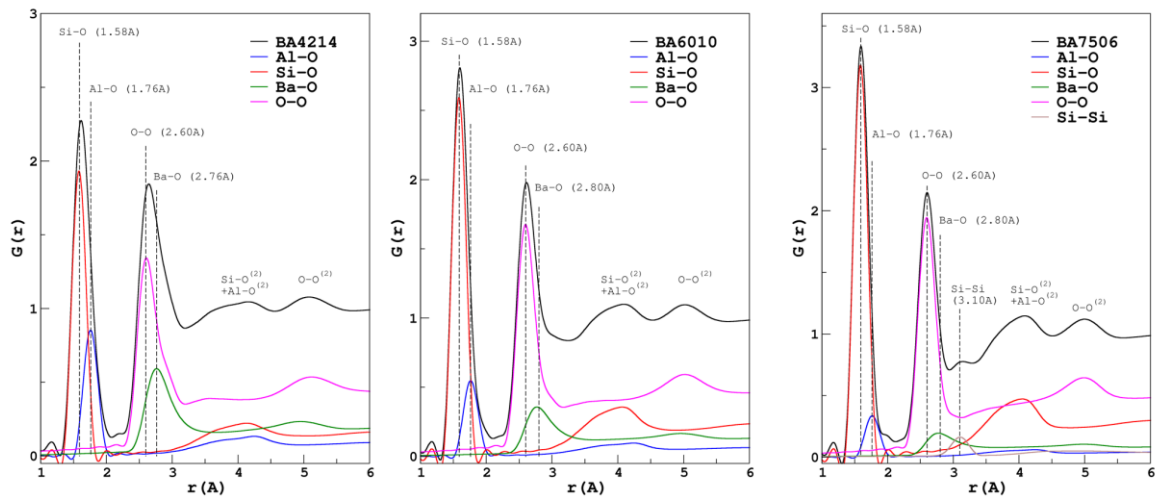


Figure IV.23. Partial pair distribution functions $g_{ij}(r)$ calculated from the results of MD simulations together with experimental $g(r)$ for three Ba peralkaline glasses.

3.3. Raman spectroscopy

Raman spectra of Ba peralkaline glasses are shown in Figure IV.24. In general, they resemble those of Sr peralkaline glasses, but most of the peaks are better resolved in the spectra of Ba ones. Under the substitution of SiO_2 by $\text{Ba}_3\text{Al}_2\text{O}_6$, the bands at ~ 180 and $\sim 315 \text{ cm}^{-1}$ caused by Ba-O vibrations (as discussed previously) become more pronounced. These bands are shifted to lower frequencies with respect to Sr counterparts. This shift is in agreement with the fact that Ba cations are heavier than Sr ones. Additionally to these two bands, in the spectrum of BA33.17 a new contribution becomes visible at around 370 cm^{-1} . It might be present in the other spectra but is hidden by more intense signals. The origin of this band is unknown and requires additional studies.

Two bands, appearing in the spectrum of BA75.06 at 476 and 575 cm^{-1} and assigned as D_1 and D_2 bands, shift towards each other with decreasing SiO_2 content. The former one becomes less intense and the latter one gains in intensity from 75 to 33 mol% of silica. Thus, small three-membered rings become more favourable than larger ones under the substitution of SiO_2 by $\text{Ba}_3\text{Al}_2\text{O}_6$. This is in agreement with observations made on the FSDP position in $S(q)$ of the ND data.

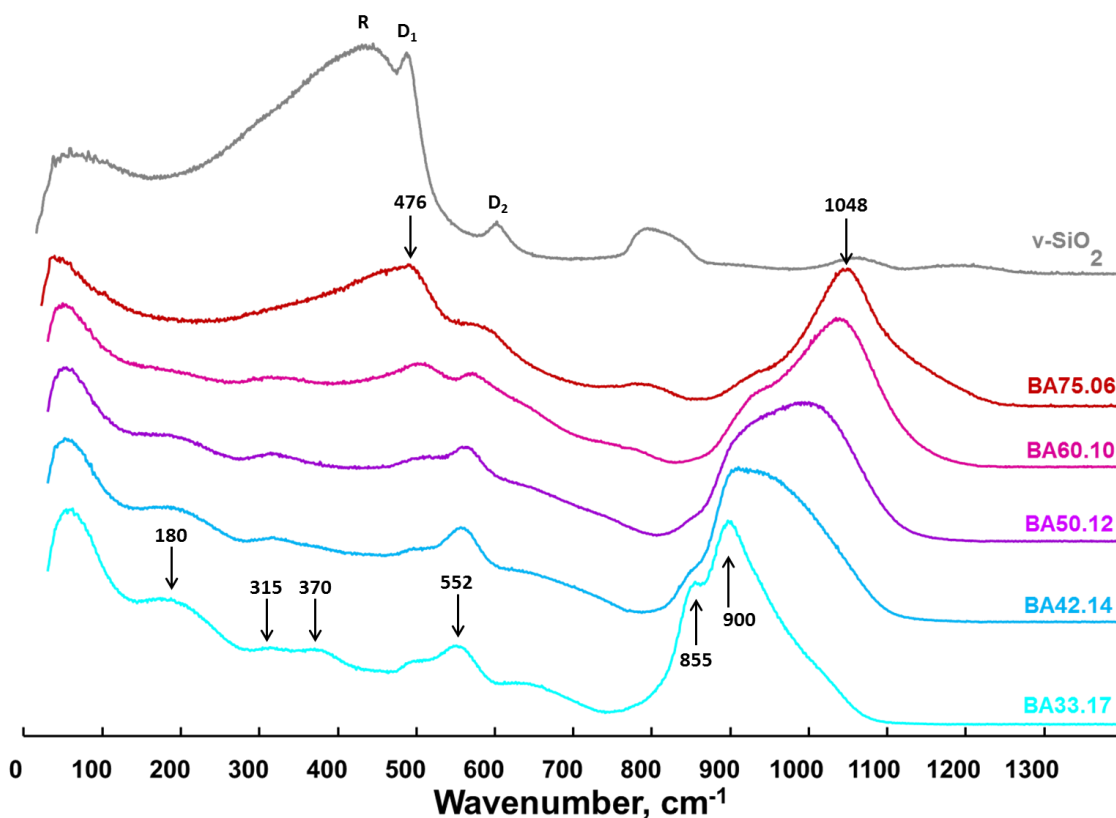


Figure IV.24. Area normalized Raman spectra of Ba peralkaline glasses. Numbers correspond to the frequencies of observed bands maxima. Silica content decreases from top to bottom.

The barycentre of the HF envelope of the Raman spectra of the peralkaline glasses is plotted in Figure IV.25 as a function of composition. In the range of SiO_2 content from 100 to 60 mol% the slope is constant and equal to $2.4 \pm 0.1 \text{ cm}^{-1}/\text{mol}\%$ of SiO_2 . It differs from $2.2 \pm 0.1 \text{ cm}^{-1}/\text{mol}\%$ of SiO_2 observed for the silicate and tectosilicate glasses but not significantly. Considering the lack of the data on BA66.09 composition, the one where we observed the inflection point, we can assume that the slopes of all the glasses in the SAS and BAS systems in the range of silica concentrations from 100 to 66.7 mol% are identical. After the inflection point at 60 mol% of SiO_2 the slope of the curve for Ba peralkaline glasses changes to $3.9 \pm 0.1 \text{ cm}^{-1}/\text{mol}\%$ of SiO_2 .

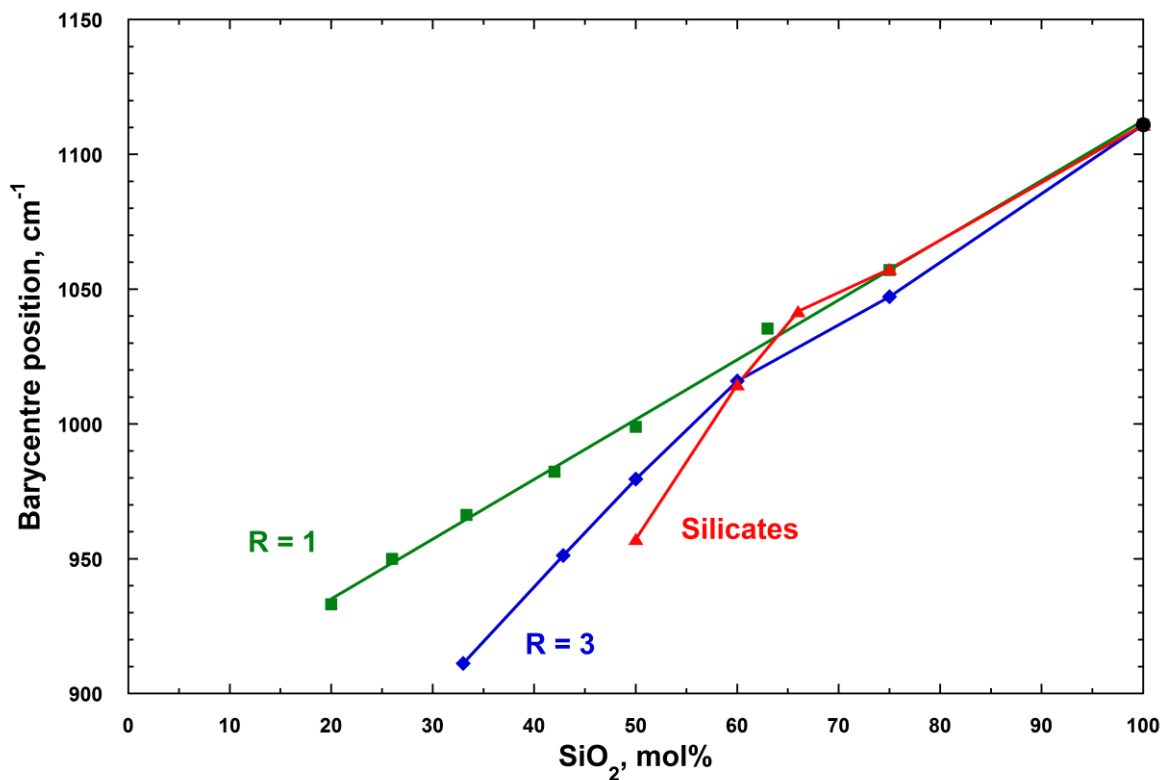


Figure IV.25. Barycentre position of the high-frequency envelope of Raman spectra of Ba tectosilicate (green), peralkaline (blue) and silicate (red) glasses. The lines are a guide to the eye.

Deconvolution of the HF region of the Raman spectra is given in Figure IV.26 and the Q^n species distribution is presented in Figure IV.27.

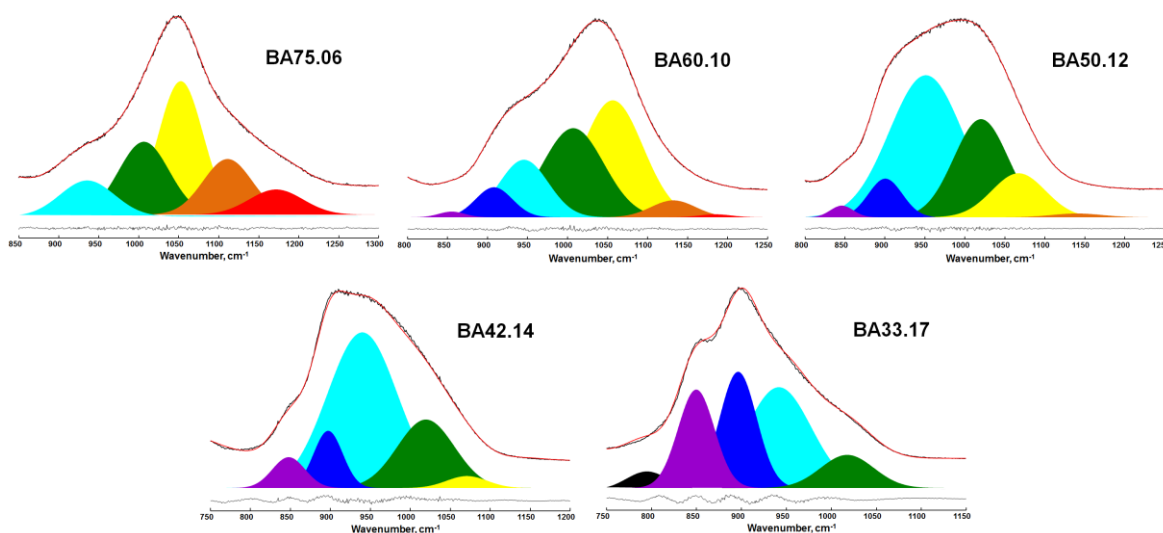


Figure IV.26. Deconvolution of the HF region of the Raman spectra of Ba peralkaline glasses. Colour guide: red – $Q^{4,1}$, orange – $Q^{4,II}$, yellow – Q^3 , green – T_{2s} , turquoise – Q^2 , blue – Q^1 , violet – Q^0 , black – Al-NBO band.

We see changes in the Q^n species distribution from Q^2 - Q^4 species for BA75.06 to Q^0 - Q^2 ones for BA33.17 glass. A similar distribution has been seen for Sr peralkaline glasses (Figure IV.27). To fit properly the HF envelope of BA33.17 glass we needed to add an extra band at $\sim 800\text{ cm}^{-1}$ as for analogous SA33.17 glass. On the one hand, the position of the HF envelope in Raman spectra of alkaline earth aluminate glasses is located at nearly the same frequency (Licheron et al., 2011). On the other hand, ^{27}Al NMR data showed that $\delta_{iso}(\text{AlO}_4)$ of BA33.17 glass deviates from the overall trend, suggesting the presence of Al-NBO bonds. Therefore, the band at $\sim 800\text{ cm}^{-1}$ in the Raman spectrum of BA33.17 glass is likely caused by vibrations of AlO_4 units containing NBOs.

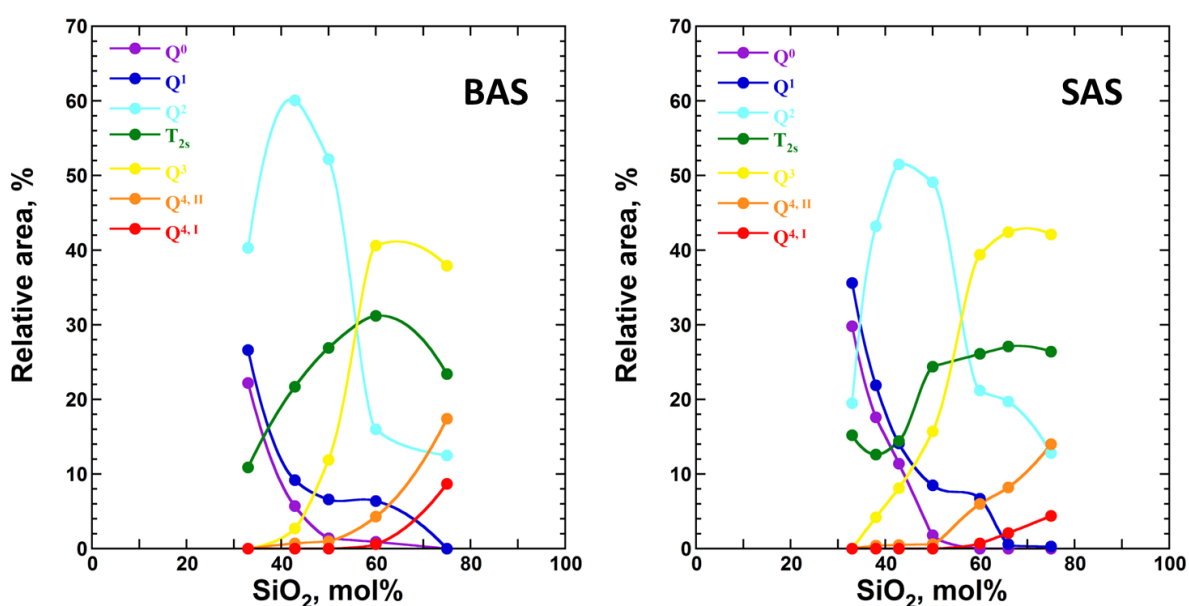


Figure IV.27. The relative area under the Gaussian bands obtained from deconvolution of the high-frequency region of the Raman spectra of Ba (*left*) and Sr (*right*) glasses along the join R = 3.

3.4. Macroscopic properties

Glasses on the join R = 3 possess density and molar volume that are intermediate between those for the silicate and tectosilicate glasses (Figure IV.28). The density of the peralkaline glasses increases almost linearly with decreasing SiO_2 content. For the V_m more complex compositional dependence is observed. Firstly, the molar volume drops down under the substitution of silica by $\text{Ba}_3\text{Al}_2\text{O}_6$, reaching a plateau at 50-60 mol% of SiO_2 , and then increases under further substitution.

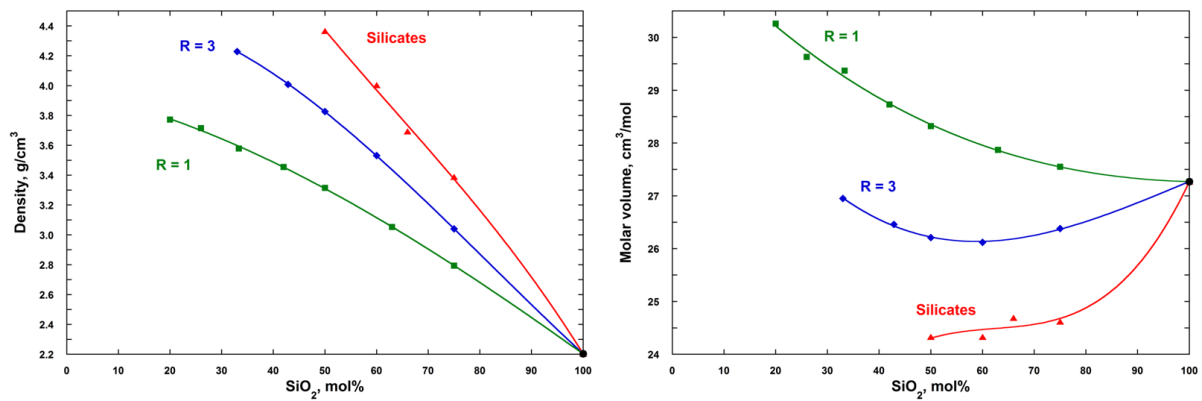


Figure IV.28. Experimental densities (*left*) and calculated molar volumes (*right*) of Ba tectosilicate (green), peralkaline (blue) and silicate (red) glasses. The black filled circle corresponds to the density of vitreous silica taken from (Brückner, 1970). Error bars are less than the symbol size. The lines are a guide to the eye.

A similar trend in the V_m evolution has been already observed in the SAS system. However, for Sr peralkaline glasses molar volume stays nearly constant in the silica-poor domain. Previously we assigned such behaviour to the interplay between packing of the silicate network causing the decrease of V_m and introduction of Al into the network acting in the opposite way. Since in the case of Ba silicate glasses we do not observe a continuous packing of the glass network under decreasing SiO_2 content, we can suggest that the increase of the molar volume of the silica-poor Ba peralkaline glasses caused, once again, by the interplay of the two factors described above.

Figure IV.29 shows the evolution of glass transition temperature of the glasses on the join R = 3 together with the silicate and tectosilicate compositions. The T_g curve of the peralkaline glasses rises under the substitution of SiO_2 by $\text{Ba}_3\text{Al}_2\text{O}_6$ and resembles the curves of Sr (Chapter III) and Ca (Neuville et al., 2004) peralkaline glasses. Since the behaviour in three systems is very similar, we believe that an explanation given in Chapter III should be applicable here as well. Namely, the increase in T_g should be caused by the reorganization of the network and participation of the cation in the network linkage.

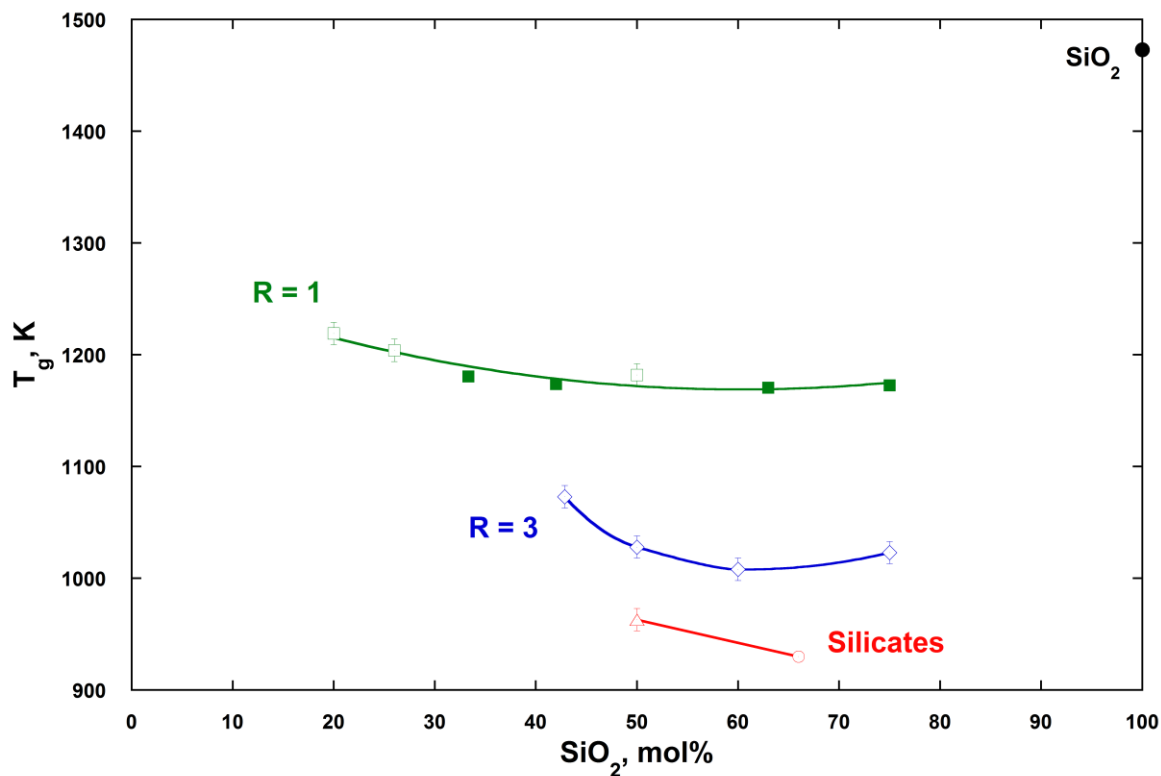


Figure IV.29. Glass transition temperatures for Ba tectosilicate (green), peralkaline (blue) and silicate (red) glasses. Filled symbols are T_g values extracted from viscosity data, open symbols are T_g values from DSC measurements. The data for BA66.00 (red open circle) is from (Lenoir et al., 2008). The glass transition temperature of vitreous silica (black filled circle) is given for comparison (Mackenzie, 1963). If not visible error bars are less than the size of symbols. The lines are a guide to the eye.

Section highlights

- AlO_5 is present in Ba peralkaline glasses in a small amount ($\leq 3\%$).
- The existence of Al-NBO bonds is suggested by ^{27}Al NMR and Raman data for the composition with the lowest silica content.
- ND and Raman indicate changes in the ring statistics towards small-membered rings with decreasing SiO_2 content. In the low-frequency region of the Raman spectra, two bands are clearly observed as in the case of Sr-containing counterparts. A band of unknown origin is observed around 370 cm^{-1} in the spectrum of the composition with the lowest SiO_2 content.
- V_m and T_g curves of Ba peralkaline glasses follow a trend very similar to the one observed for analogous SAS glasses. Namely, molar volume decreases first under the substitution of SiO_2 by $\text{Ba}_3\text{Al}_2\text{O}_6$ and then start increasing in the silica-poor domain; glass transition temperature rises from silica-rich to silica-poor compositions.

4. Peraluminous domain ($R < 1$)

4.1. ^{27}Al and ^{29}Si NMR spectroscopy

^{27}Al and ^{29}Si NMR spectra of the glasses in the BA50.xx and BA33.xx series are presented in Figure IV.30 and Figure IV.31, respectively. In both series under the Ba/Al substitution, the fraction of high-coordinate AlO_x sites increases significantly. A contribution at around 10 ppm characteristic for AlO_6 sites is visible in the spectra of highly peraluminous glasses, especially in the BA50.xx series. The fraction of AlO_6 is small and reaches a maximum of 3-4 % for BA50.40 glass.

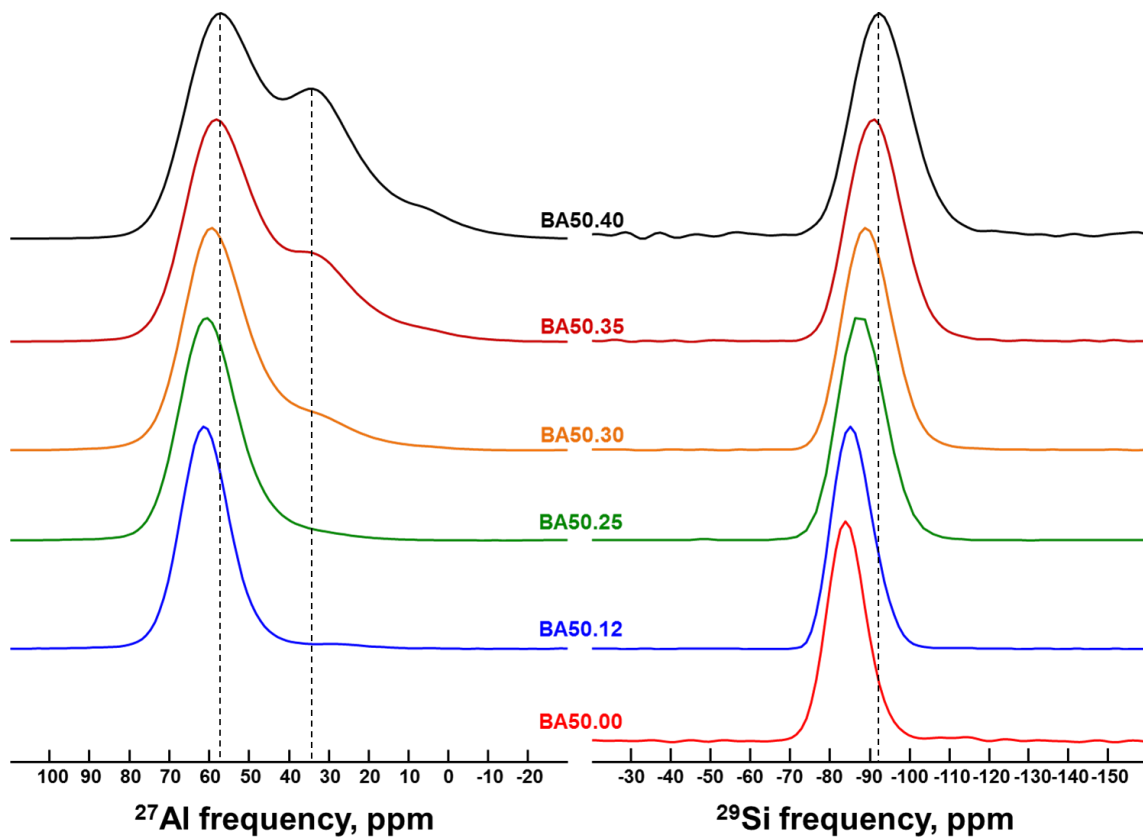


Figure IV.30. ^{27}Al (left) and ^{29}Si (right) MAS NMR spectra of glasses in the BA50.xx series. Alumina content decreases from top to bottom.

The barycentre of the ^{29}Si NMR line shifts to lower δ_{iso} values and the line broadens with increasing Al_2O_3 content. Such broadening of the signal can be caused by the increase of inter-tetrahedral angles as well as by an overall increase of the disorder in the system. Worth noticing, that even in the peraluminous domain of the BAS system a small fraction of NBOs exists at has been demonstrated by (Thompson and Stebbins, 2012). In the case of the

^{27}Al NMR spectra, we also observe line's broadening under the Ba/Al substitution showing also increasing disorder. In both cases of ^{27}Al and ^{29}Si NMR, the broadening is more pronounced in the BA50.xx series.

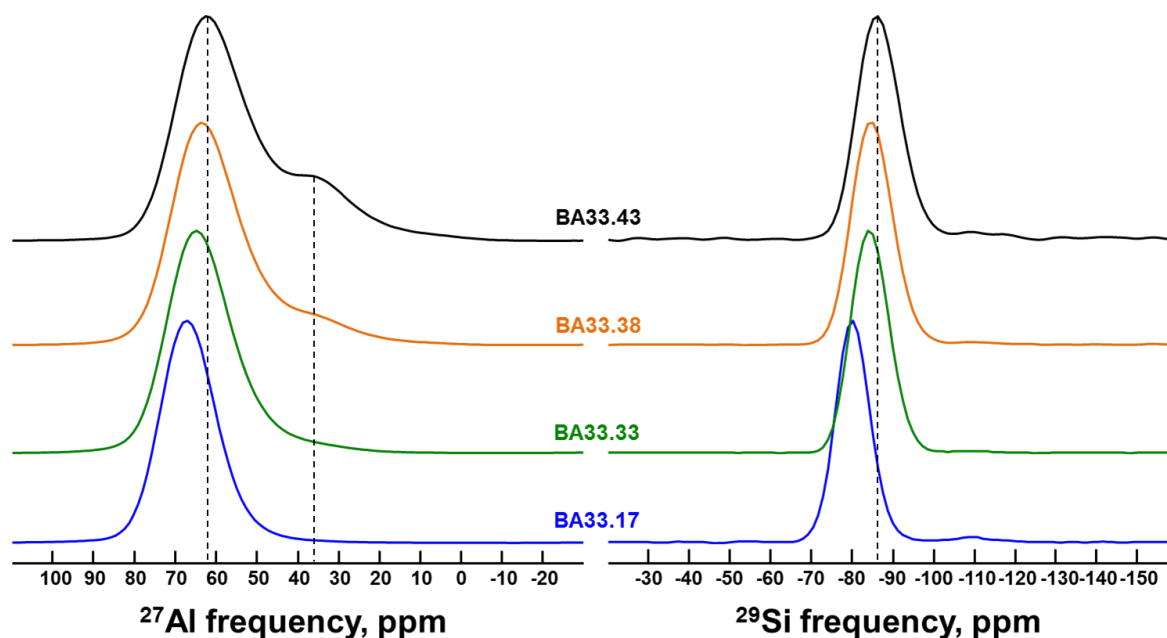


Figure IV.31. ^{27}Al (*left*) and ^{29}Si (*right*) MAS NMR spectra of glasses in the BA33.xx series. Alumina content decreases from top to bottom.

The deconvolution of the ^{27}Al NMR spectra of the peraluminous glasses is shown in Figure IV.32.

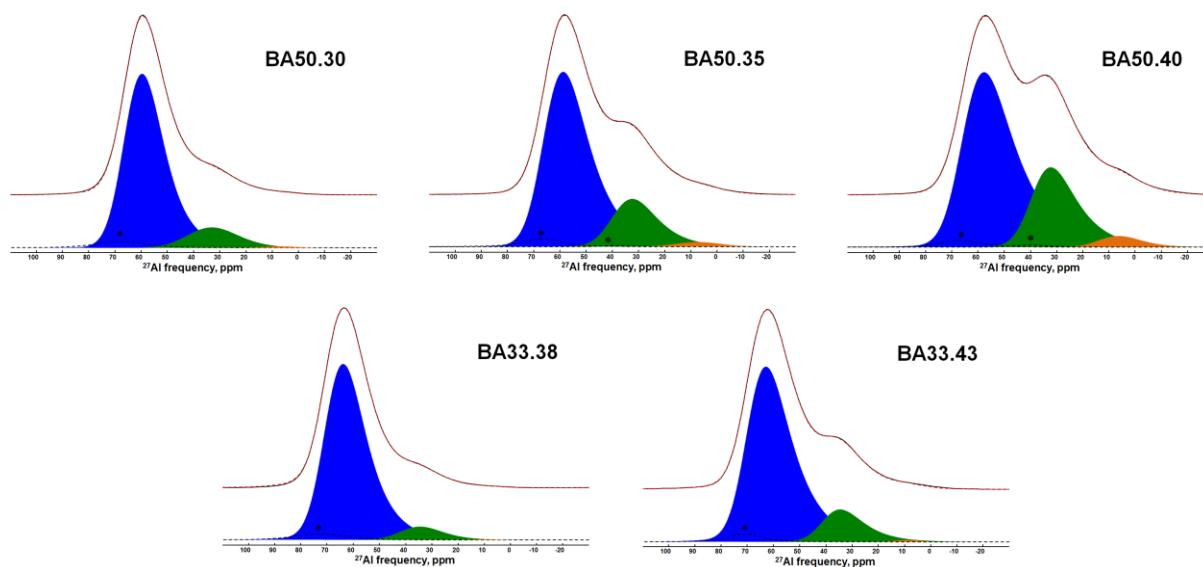


Figure IV.32. Deconvolution of the ^{27}Al MAS NMR spectra of Ba peraluminous glasses. Colour guide: blue – AlO_4 , green – AlO_5 , orange – AlO_6 , black dashed lines with an asterisk – spinning sidebands.

The evolution of the δ_{iso} for AlO_x sites and their population is plotted in Figure IV.33. The chemical shift of all three sites does not change significantly under Ba/Al substitution. Any disagreements with the previous statement concerning AlO_5 and AlO_6 can be explained by the difficulty to unambiguously define the position of low-abundant sites. Nevertheless, in the case of AlO_4 sites, any deviation from the constant value should signify something. As it was explained before, a higher $\delta_{iso}(\text{AlO}_4)$ of BA33.17 composition with respect to other compositions in the BA33.xx series implies the existence of Al-NBO bonds in the glass network.

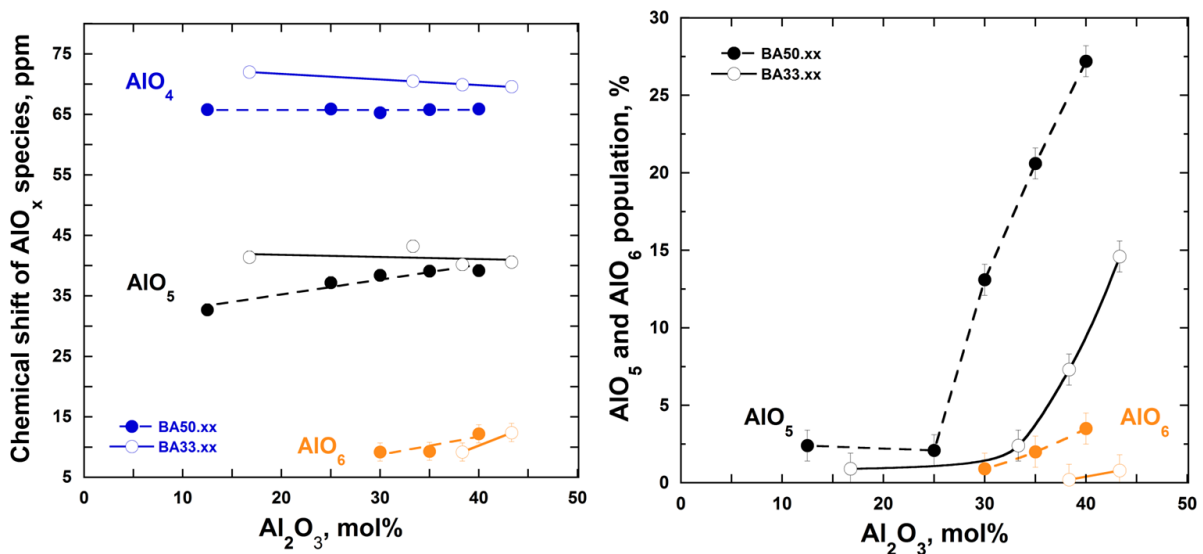


Figure IV.33. *Left*: evolution of isotropic chemical shift (δ_{iso}) of AlO_4 (blue), AlO_5 (black) and AlO_6 (orange) sites for glasses in the BA50.xx (filled circles) and BA33.xx (open circles) series. *Right*: AlO_5 and AlO_6 population for glasses in the BA50.xx (filled circles) and BA33.xx (open circles) series. The lines are a guide to the eye.

As in the case of the SAS system, the fraction of AlO_5 is nearly constant from the peralkaline to tectosilicate compositions and then increases almost linearly with increasing Al_2O_3 content. Similar trends in AlO_5 evolution with Al_2O_3 content has been also observed in the MAS and CAS systems (Neuvill et al., 2008, 2006).

4.2. Raman spectroscopy

Raman spectra of the glasses in the BA50.xx and BA33.xx series are presented in Figure IV.34 and Figure IV.35, respectively.

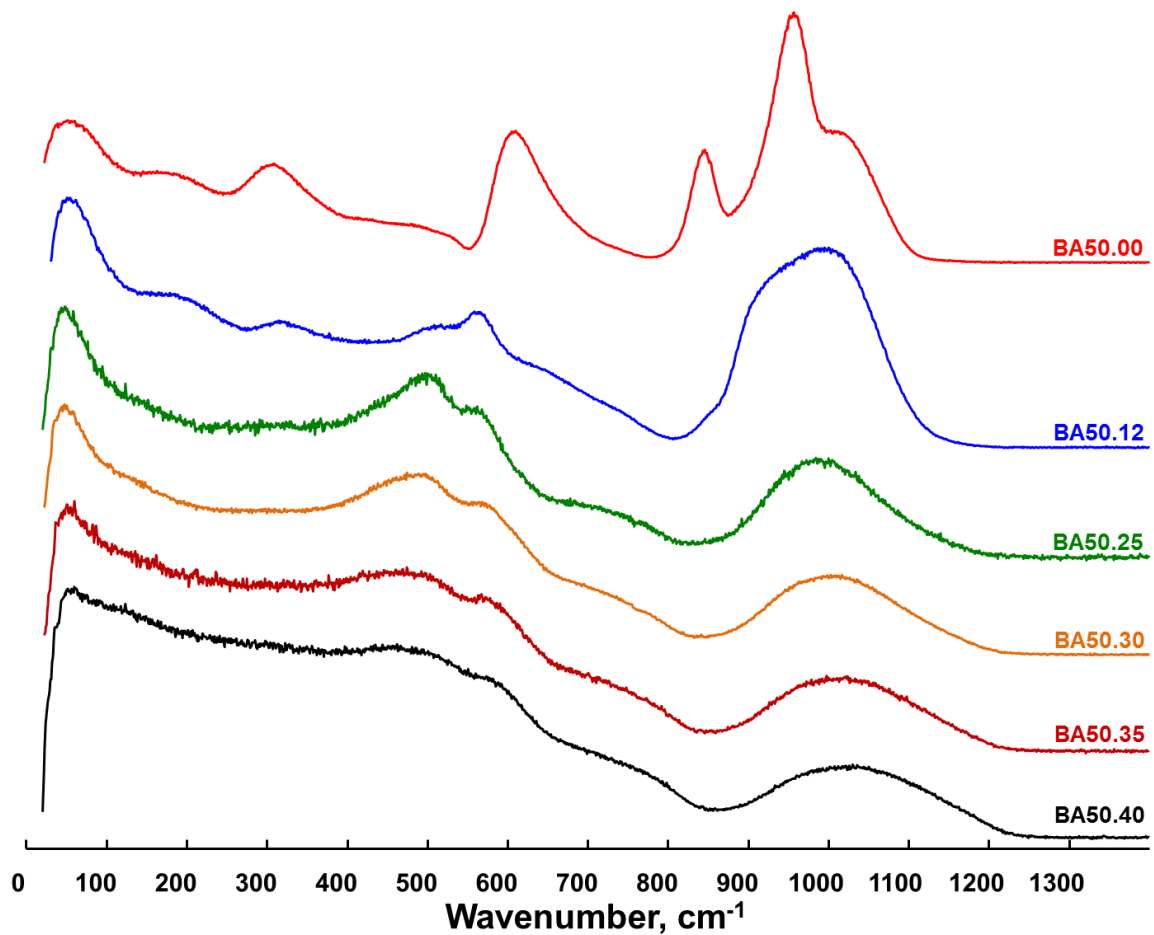


Figure IV.34. Area normalized Raman spectra of the BA50.xx series of glasses. Alumina content increases from top to bottom.

With increasing Al_2O_3 content the spectra lose literally all the main features in the low- to intermediate-frequency regions. Two bands assigned to cation-oxygen vibrations are not seen already in the spectra of the tectosilicate glasses. The D_2 band assigned to vibrations in three-membered rings decreases in intensity from the peralkaline to peraluminous glasses. At the same time, the D_1 band reaches maximum intensity for the tectosilicate compositions and then the intensity drops down and the band broadens significantly for the peraluminous compositions. The broadening is thought to be caused by changes in ring statistics, namely, the formation of high-membered rings.

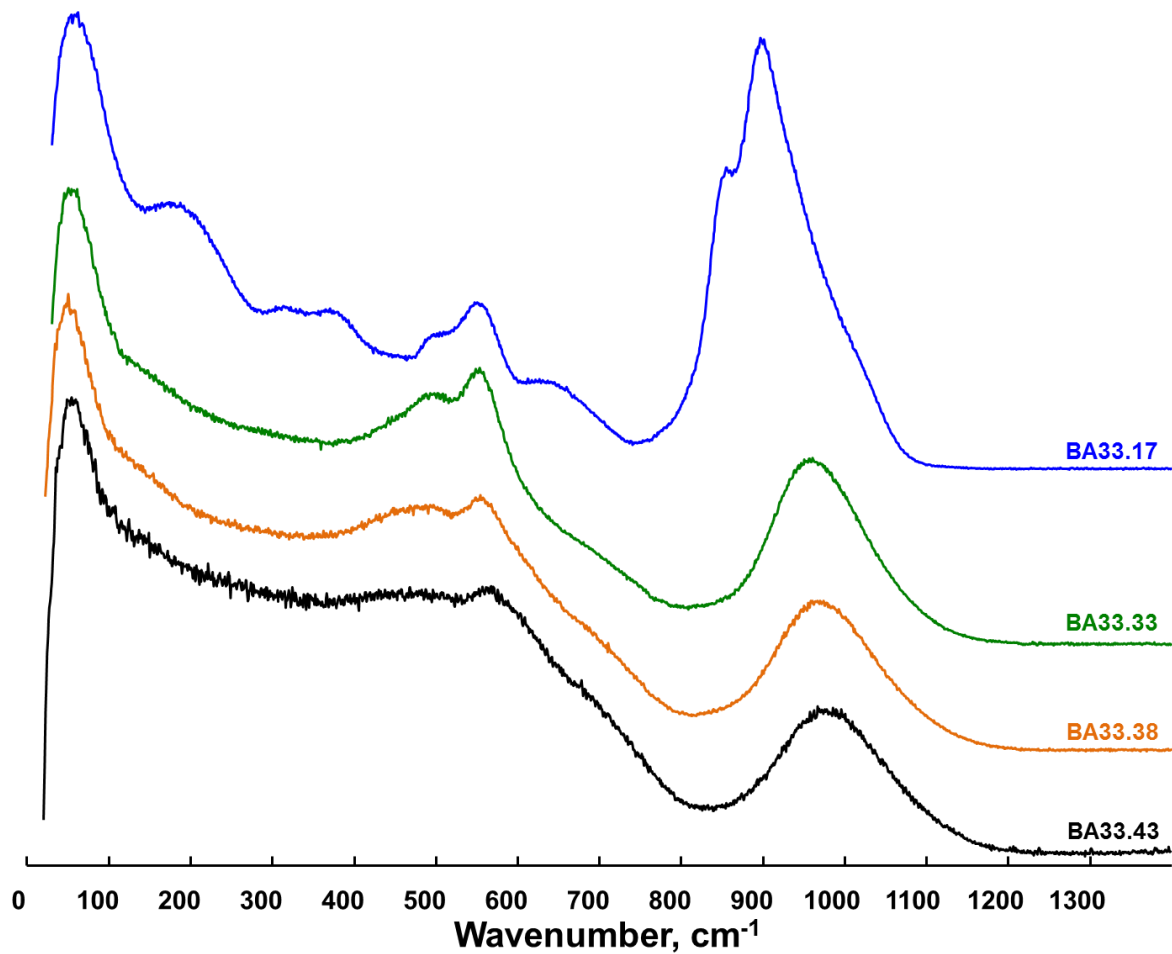


Figure IV.35. Area normalized Raman spectra of glasses in the BA33.xx series. Alumina content increases from top to bottom.

The HF envelope of the Raman spectra shifts to higher frequency under the Ba/Al substitution. Its deconvolution (Figure IV.36) revealed that in the peraluminous domain the structure of glasses is composed of Q^4 units only. The fraction of $Q^{4,l}$ units possessing greater inter-tetrahedral angles is higher than in the case of the tectosilicate glasses. This is in good agreement with the broadening of the ^{29}Si NMR bands of the peraluminous glasses, confirming that it can be caused by the increase of inter-tetrahedral angles.

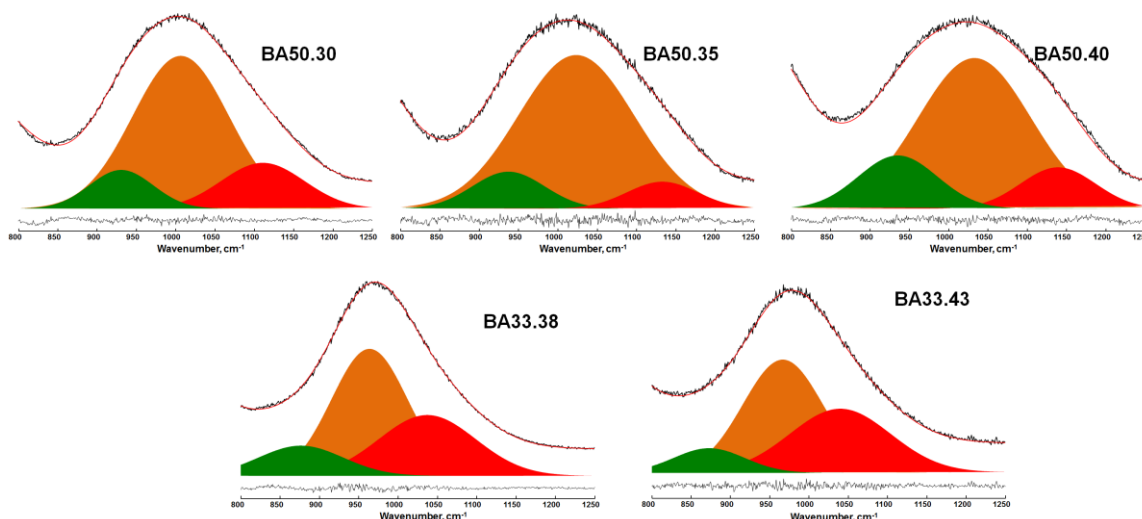


Figure IV.36. Deconvolution of the HF region of the Raman spectra of Ba peraluminous glasses. Colour guide: red – $Q^{4,I}$, orange – $Q^{4,II}$, green – T_{2s} .

4.3. Macroscopic properties

Figure IV.37 demonstrates the effect of Ba/Al exchange on the density and molar volume of glasses in the BA50.xx and BA33.xx series. In both series, density decreases with augmentation of alumina content. On the other hand, the V_m increases and seems to reach a plateau in the peralkaline domain in both series. This effect is better seen in the BA50.xx series. Such plateaus have not been observed for peraluminous glasses in the SAS system. At the same time, another interesting feature distinguishes the BAS system from the SAS one. In the SAS system the V_m curve of the SA50.xx glasses is above of the curve of the SA33.xx ones for any Al_2O_3 content. In the BAS system, two curves coincide with each other at low alumina content and with entering the peraluminous domain the V_m curve of BA33.xx glasses surpasses the one of BA50.xx glasses.

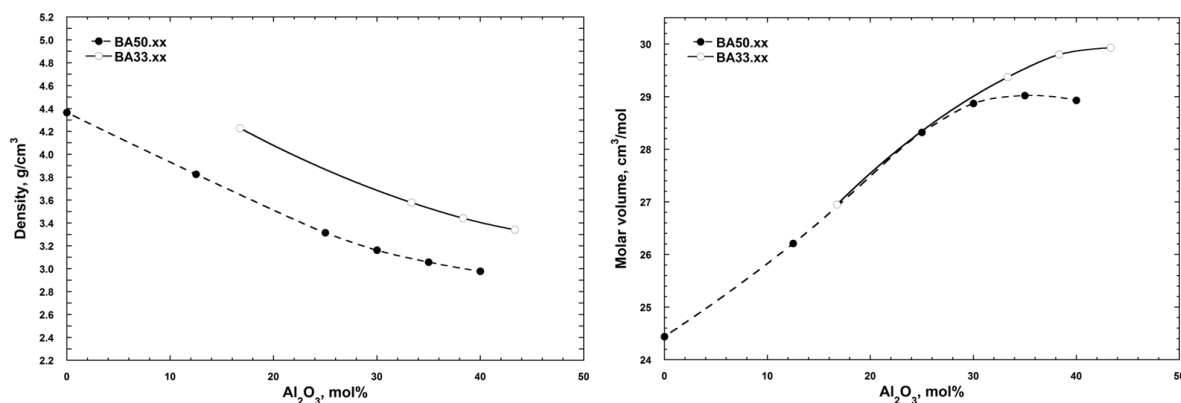


Figure IV.37. Experimental densities (*left*) and calculated molar volumes (*right*) of glasses in the BA50.xx (filled circles) and BA33.xx (open circles) series. The lines are a guide to the eye.

Under the substitution of BaO by Al₂O₃ at constant SiO₂ content following structural changes occur. The number of high-coordinate AlO_x species increases as well as the fraction of high-membered rings. At the same time, the rise of an overall disorder of the system occurs. All this produces the increase of the V_m in two series with increasing alumina content.

Section highlights

- The fraction of high-coordinate AlO_x species increases significantly when Al₂O₃ substitutes for BaO. ²⁷Al and ²⁹Si NMR show a rise of disorder in the system with increasing Al₂O₃ content.
- Raman and ²⁹Si NMR indicate an overall increase of T-O-T (T = Si or Al) angles. Changes in the ring statistics towards high-membered rings are inferred.
- The structural changes mentioned above produce the increase of the V_m in two series with increasing alumina content.

5. High-temperature melts

As it has been demonstrated by (Urbain et al., 1982), viscosities of Ba aluminosilicate melts are higher than those of Sr ones. This means that at any given temperature aluminosilicate melts in the BAS system will be more viscous than compositionally similar ones in the SAS system. Therefore, the signal-to-noise ratio for NMR spectra of the BAS melts will be worse than in the case of Sr aluminosilicates. This fact causes all the measurements and calculations made on the BAS melts to be less accurate.

High-temperature ²⁷Al NMR spectroscopy

The evolution of line's position with temperature is given in Figure IV.38. As in the case of Sr aluminosilicates (Chapter III) or other aluminate and aluminosilicate systems (Capron et al., 2001; Florian et al., 2007; Massiot et al., 1995) the chemical shift changes linearly with decreasing temperature (in the temperature range explored here). The slope, $\Delta\delta/\Delta T$, decreases with decreasing silica content, reflecting the tendency to increase the fragile behaviour (i.e. the speed of structural changes with temperature, (Massiot et al., 2008)) upon increasing SiO₂ content. The position curves shift to higher δ_{iso} values with decreasing SiO₂ content on the joins R = 1 and R = 3. This observation reflects the fact that the number

of Al atoms in the second coordination sphere increases as in the case of corresponding glasses. In the BA50.xx series the difference in the placement of the position curves is rather caused by the averaging of δ_{iso} of different aluminium sites present in the melt. Since an elevated amount of high-coordinate Al sites is expected for the peraluminous compositions, that is why their position curves are shifted to lower chemical shift values.

Once again, extrapolation of the HT data down to T_g does not meet the average δ_{iso} of the corresponding glasses (except for some compositions on the join R = 1). A similar situation has been previously observed for the Sr (Chapter III) and rare-earth aluminosilicates (Florian et al., 2007).

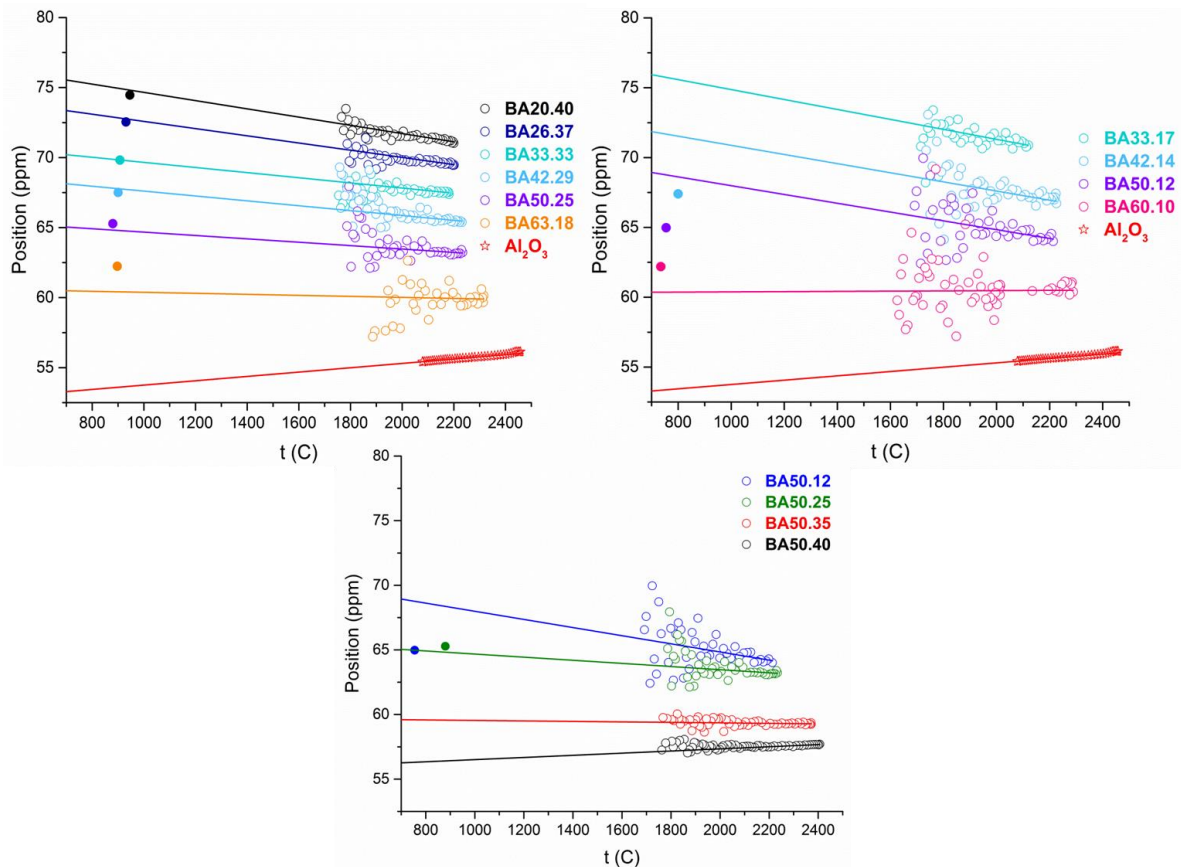


Figure IV.38. Evolution of the NMR line's position with temperature for the melts along the joins R = 1 (*top left*) and R = 3 (*top right*), and in the BA50.xx series (*bottom*). Filled symbols correspond to the related NMR line's barycentre for glasses at r.t. (see text). The lines are linear fits of the HT data.

Calculated from the FWHM of the NMR lines, the correlation time, τ_c , is shown in Figure IV.39. Similarly to Sr tectosilicates, the τ_c decreases with decreasing SiO₂ content for Ba ones as well. For compositions on the join R = 3, the evolution of the correlation time with composition is not obvious. As it was mentioned at the beginning of this section, the

signal-to-noise ratio for the compositions in the BAS system is lower than in the SAS one. Together with low alumina content for the peralkaline compositions, it leads to huge scattering of data points, producing illogical deviations from expected trends as observed for BA60.10, for example. In general, the data for the peralkaline compositions is so scattered that its use may lead to some contradictions when compared with other data. In the BA50.xx series the τ_c decreases with increasing Al_2O_3 content.

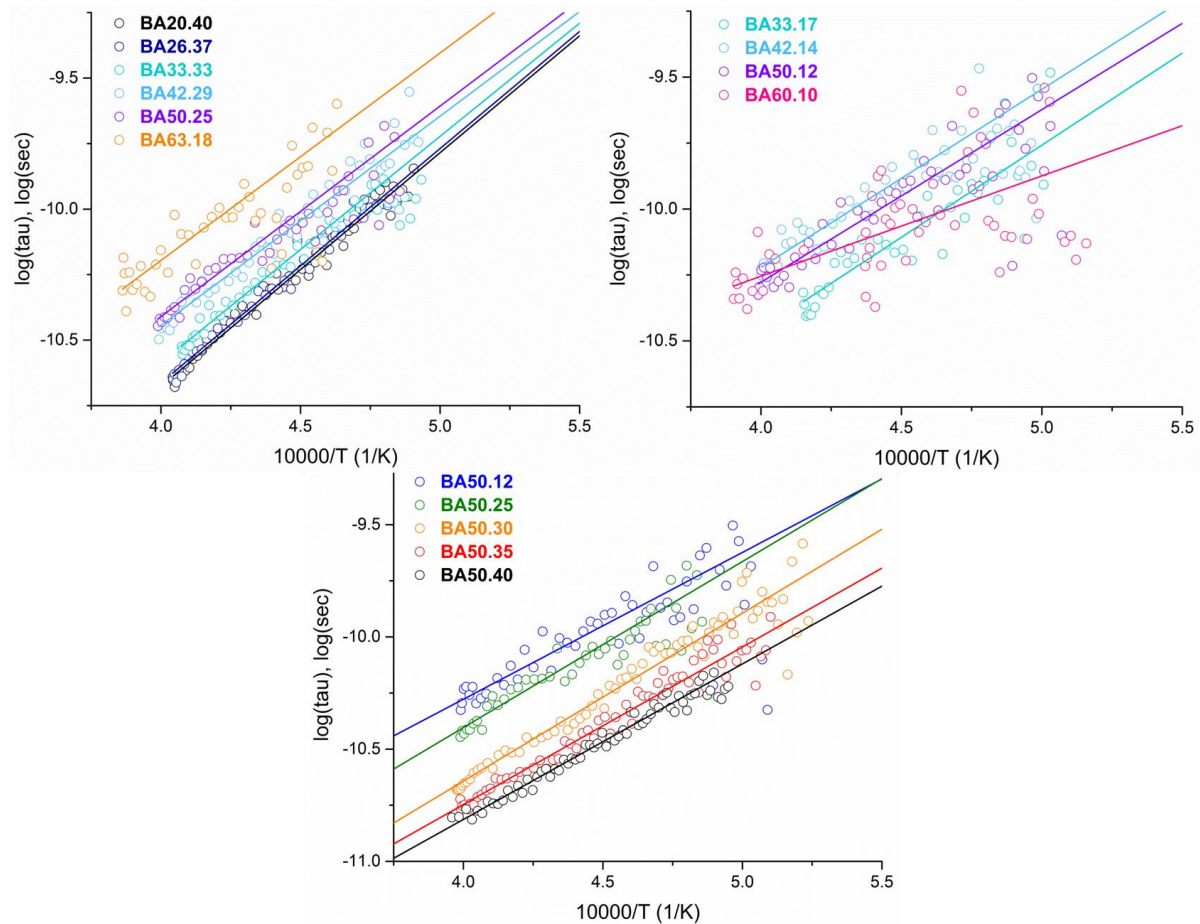


Figure IV.39. $\log_{10}(\tau_c)$ as a function of reciprocal temperature for the melts along the joins $R = 1$ (top left) and $R = 3$ (top right), and in the BA50.xx series (bottom). The lines are linear fits of the experimental data.

The slopes of the τ_c curves were used for the calculation of the Arrhenius activation energy as described in Chapter III. We compared the E_{act} calculated from our HT NMR data and from HT viscosity data from (Urbain et al., 1982). For two Ba tectosilicate compositions, namely BA50.25 and BA26.37, $E_{act}(\text{viscosity})$ are 291 and 238 kJ/mol, while $E_{act}(\text{NMR})$ are 141 and 165 kJ/mol, respectively. The values of the E_{act} extracted from the viscosity data are slightly higher than ones obtained from the HT NMR data. This is due to the fact that

²⁷Al NMR relaxation relies on thermal vibrations while viscosity is related to the oxygen diffusivity D through Si-O bond-breaking mechanisms. The oxygen diffusivity is defined as

$$D = \frac{kT}{\eta a}$$

where η is the viscosity and a is the diffusive jump length. Both mechanisms couple when oxygen diffusion and oxygen jumps occur on the same timescale, i.e. only in most fragile liquids at $T_g/T \sim 2$ or in all liquids at very high temperature. Differences in activation energies reflect the intrinsic different nature of the two mechanisms, even when correlation times meet: oxygen jumps is driven by the enthalpy for migration which can be different from the activation energy for diffusion.

The E_{act} for the compositions in the BA50.xx and BA33.xx series are plotted in Figure IV.40. As in the SAS system, the maximum in the E_{act} is displaced into the peraluminous domain in both series. The difference between the Arrhenius activation energies of the tectosilicate and peraluminous compositions is, however, less than for analogous SAS compositions. It was discussed previously that such behaviour with the maximum of the E_{act} in the peraluminous domain might be connected with the formation of three-coordinate oxygens in the melts as suggested by HT viscosity data in NAS and CAS systems (Toplis et al., 1997; Toplis and Dingwell, 2004).

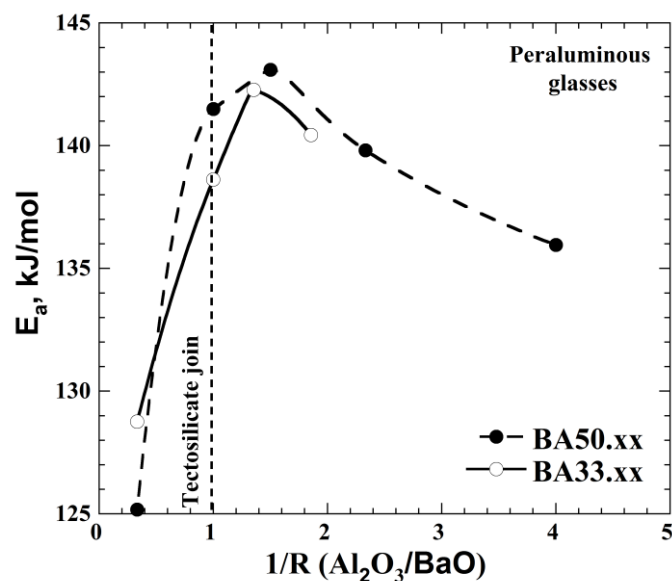


Figure IV.40. Arrhenius activation energies (E_{act}) as a function of the $\text{Al}_2\text{O}_3/\text{BaO}$ ratio. The vertical dashed line corresponds to the tectosilicate compositions. Other lines are a guide to the eye.

Section highlights

- Arrhenius activation energy found from HT NMR data possesses a maximum for slightly peraluminous compositions similarly to the SAS system, suggesting the existence of three-coordinate oxygens in the melts.

6. Conclusion

In general, glasses in the BAS system have structure and properties very close to Sr ones. Different cation's size or the cation field strength, however, introduces some differences between the systems. Below we present a short summary of these differences.

It has not been discussed anywhere before but worth noticing here, that glasses in the BAS system generally require higher temperatures for their elaboration. For example, it is not possible to obtain a melt of BA50.25 composition even at 1750 °C, while for SA50.25 composition this temperature is sufficient.

On the tectosilicate join, there are less Q_4 units with an extra cation in the second coordination sphere of Si atoms in the BAS system than in the SAS one. This difference is most likely caused by steric factors since Ba^{2+} is larger than Sr^{2+} . At the same time, a fraction of five-coordinate Al is lower as well. $CN(Ba-O) \approx 10$ is higher than $CN(Sr-O) \approx 8-9$ for analogous tectosilicate compositions.

Sr and Ba silicates show similar trends in T_g evolution: with augmentation of modifying cation content the glass transition temperature increases. However, T_g of Sr silicates is higher than for Ba ones, which is a consequence of lower Ba CFS, preventing it from effective participation in the silicate network linkage. This effect could not be compensated by an overall less degree of disorder observed for Ba silicates. $CN(Ba-O) \approx 6-7$ in silicate glasses which is slightly higher than $CN(Sr-O) \approx 5-6$.

In both systems, glasses on the join $R = 3$ have structure and properties intermediate between those of silicate and tectosilicate glasses. The fraction of five-coordinate Al is lower for Ba peralkaline glasses due to lower CFS of Ba comparing to Sr. $CN(Ba-O) \approx 9$ is higher than $CN(Sr-O) \approx 8$.

In the peraluminous field, glasses in both systems are quite similar. The main difference is the behaviour of the V_m curves. The curves of Sr peraluminous glasses rise under the augmentation of Al_2O_3 content, while the ones of Ba peraluminous glasses reach a plateau.

The high-temperature melts demonstrate analogous patterns in their structure and dynamics. Nevertheless, Ba containing melts are more viscous than Sr ones. In both systems, a maximum in E_{act} is shifted to a slightly peraluminous domain.

Bibliography

- Allwardt, J.R., Stebbins, J.F., Schmidt, B.C., Frost, D.J., Withers, A.C., Hirschmann, M.M., 2005. Aluminum coordination and the densification of high-pressure aluminosilicate glasses. *Am. Mineral.* 90, 1218–1222. doi:10.2138/am.2005.1836
- Bockris, J.O., Mackenzie, J.D., Kitchener, J.A., 1955. Viscous flow in silica and binary liquid silicates. *Trans. Faraday Soc.* 51, 1734–1748. doi:10.1039/TF9555101734
- Brückner, R., 1970. Properties and structure of vitreous silica. I. *J. Non. Cryst. Solids* 5, 123–175. doi:10.1016/0022-3093(70)90190-0
- Capron, M., Florian, P., Fayon, F., Trumeau, D., Hennet, L., Gaihlhanou, M., Thiaudière, D., Landron, C., Douy, A., Massiot, D., 2001. Local structure and dynamics of high temperature SrO–Al₂O₃ liquids studied by ²⁷Al NMR and Sr K-edge XAS spectroscopy. *J. Non. Cryst. Solids* 293–295, 496–501. doi:10.1016/S0022-3093(01)00762-1
- Cormier, L., Calas, G., Creux, S., Gaskell, P., Bouchet-Fabre, B., Hannon, A., 1999. Environment around strontium in silicate and aluminosilicate glasses. *Phys. Rev. B* 59, 13517–13520. doi:10.1103/PhysRevB.59.13517
- Creux, S., Bouchet-Fabre, B., Gaskell, P.H., 1995. Anomalous wide angle X-ray scattering study of strontium silicate and aluminosilicate glasses. *J. Non. Cryst. Solids* 192 & 193, 360–363.
- Doweidar, H., 1999. Density-structure correlations in silicate glasses. *J. Non. Cryst. Solids* 249, 194–200. doi:10.1016/S0022-3093(99)00310-5
- Doweidar, H., 1996. The density of alkali silicate glasses in relation to the microstructure. *J. Non. Cryst. Solids* 194, 155–162. doi:10.1016/0022-3093(95)00489-0
- Dupree, R., Holland, D., Williams, D.S., 1986. The structure of binary alkali silicate glasses. *J. Non. Cryst. Solids* 81, 185–200. doi:10.1016/0022-3093(86)90269-3
- Florian, P., Sadiki, N., Massiot, D., Coutures, J.P., 2007. ²⁷Al NMR Study of the Structure of Lanthanum- and Yttrium-Based Aluminosilicate Glasses and Melts. *J. Phys. Chem. B* 111, 9747–9757. doi:10.1021/jp072061q

- Greaves, G.N., 1985. EXAFS and the structure of glass. *J. Non. Cryst. Solids* 71, 203–217.
doi:10.1016/0022-3093(85)90289-3
- Griffen, D.T., Ribbe, P., 1976. Refinement of the crystal structure of celsian. *Am. Mineral.* 61, 414–418.
- Hasegawa, H., Yasui, I., 1987. X-ray and neutron diffraction analyses of barium silicate glass. *J. Non. Cryst. Solids* 95–96, 201–208. doi:10.1016/S0022-3093(87)80111-4
- Hehlen, B., Neuville, D.R., 2015. Raman Response of Network Modifier Cations in Alumino-Silicate Glasses. *J. Phys. Chem. B* 119, 4093–4098. doi:10.1021/jp5116299
- Hennet, L., Drewitt, J.W.E., Neuville, D.R., Cristiglio, V., Kozaily, J., Brassamin, S., Zanghi, D., Fischer, H.E., 2016. Neutron diffraction of calcium aluminosilicate glasses and melts. *J. Non. Cryst. Solids* 451, 89–93. doi:10.1016/j.jnoncrysol.2016.05.018
- Hesse, K.-F., Liebau, F., 1980a. Crystal chemistry of silica-rich Barium silicates. *Zeitschrift für Krist. - Cryst. Mater.* 153, 33–41. doi:10.1524/zkri.1980.0002
- Hesse, K.-F., Liebau, F., 1980b. Crystal chemistry of silica-rich Barium silicates. *Zeitschrift für Krist. - Cryst. Mater.* 153, 33–41. doi:10.1524/zkri.1980.0004
- Iftekhar, S., Grins, J., Gunawidjaja, P.N., Edén, M., 2011. Glass Formation and Structure-Property-Composition Relations of the RE₂O₃-Al₂O₃-SiO₂ (RE=La, Y, Lu, Sc) Systems. *J. Am. Ceram. Soc.* 94, 2429–2435. doi:10.1111/j.1551-2916.2011.04548.x
- Le Losq, C., Neuville, D.R., 2017. Molecular structure, configurational entropy and viscosity of silicate melts: Link through the Adam and Gibbs theory of viscous flow. *J. Non. Cryst. Solids* 463, 175–188. doi:10.1016/j.jnoncrysol.2017.02.010
- Lee, S.K., Stebbins, J.F., 2006. Disorder and the extent of polymerization in calcium silicate and aluminosilicate glasses: O-17 NMR results and quantum chemical molecular orbital calculations. *Geochim. Cosmochim. Acta* 70, 4275–4286.
doi:10.1016/j.gca.2006.06.1550
- Lee, S.K., Stebbins, J.F., 2002. Extent of intermixing among framework units in silicate glasses and melts. *Geochim. Cosmochim. Acta* 66, 303–309. doi:10.1016/S0016-

7037(01)00775-X

- Lenoir, M., Grandjean, A., Linard, Y., Cochain, B., Neuville, D.R., 2008. The influence of Si,B substitution and of the nature of network-modifying cations on the properties and structure of borosilicate glasses and melts. *Chem. Geol.* 256, 316–325. doi:10.1016/j.chemgeo.2008.07.002
- Licheron, M., Montouillout, V., Millot, F., Neuville, D.R., 2011. Raman and ^{27}Al NMR structure investigations of aluminate glasses: $(1-x)\text{Al}_2\text{O}_3-x\text{MO}$, with $\text{M}=\text{Ca}, \text{Sr}, \text{Ba}$ and $0.5 < x < 0.75$. *J. Non. Cryst. Solids* 357, 2796–2801. doi:10.1016/j.jnoncrysol.2011.03.001
- Lippmaa, E., Maegi, M., Samoson, A., Engelhardt, G., Grimmer, A.-R., 1980. Structural studies of silicates by solid-state high-resolution silicon-29 NMR. *J. Am. Chem. Soc.* 102, 4889–4893. doi:10.1021/ja00535a008
- MacDonald, W.M., Anderson, A.C., Schroeder, J., 1985. Low-temperature behavior of potassium and sodium silicate glasses. *Phys. Rev. B* 31, 1090–1101. doi:10.1103/PhysRevB.31.1090
- Machida, K.I., Adachi, G.Y., Shiokawa, J., Shimada, M., Koizumi, M., 1982. Structure and high-pressure polymorphism of strontium metasilicate. *Acta Crystallogr. Sect. B Struct. Crystallogr. Cryst. Chem.* 38, 386–389. doi:10.1107/S0567740882003045
- Mackenzie, J.D., 1963. High-Pressure Effects on Oxide Glasses: II, Subsequent Heat Treatment. *J. Am. Ceram. Soc.* 46, 470–476. doi:10.1111/j.1151-2916.1963.tb13777.x
- Massiot, D., Fayon, F., Montouillout, V., Pellerin, N., Hiet, J., Roiland, C., Florian, P., Coutures, J.-P., Cormier, L., Neuville, D.R., 2008. Structure and dynamics of oxide melts and glasses: A view from multinuclear and high temperature NMR. *J. Non. Cryst. Solids* 354, 249–254. doi:10.1016/j.jnoncrysol.2007.06.097
- Massiot, D., Trumeau, D., Touzo, B., Farnan, I., Rifflet, J.-C., Douy, A., Coutures, J.-P., 1995. Structure and Dynamics of CaAl_2O_4 from Liquid to Glass: A High-Temperature ^{27}Al NMR Time-Resolved Study. *J. Phys. Chem.* 99, 16455–16459. doi:10.1021/j100044a038

- Meyer, A., Horbach, J., Kob, W., Kargl, F., Schober, H., 2004. Channel Formation and Intermediate Range Order in Sodium Silicate Melts and Glasses. *Phys. Rev. Lett.* 93, 27801. doi:10.1103/PhysRevLett.93.027801
- Murdoch, J.B., Stebbins, J.F., Carmichael, I.S.E., 1985. High-resolution ²⁹Si NMR study of silicate and aluminosilicate glasses: the effect of network-modifying cations. *Am. Mineral.* 70, 332–343.
- Neuvill, D.R., Cormier, L., Flank, A.-M., Briois, V., Massiot, D., 2004. Al speciation and Ca environment in calcium aluminosilicate glasses and crystals by Al and Ca K-edge X-ray absorption spectroscopy. *Chem. Geol.* 213, 153–163.
doi:10.1016/j.chemgeo.2004.08.039
- Neuvill, D.R., Cormier, L., Massiot, D., 2006. Al coordination and speciation in calcium aluminosilicate glasses: Effects of composition determined by ²⁷Al MQ-MAS NMR and Raman spectroscopy. *Chem. Geol.* 229, 173–185. doi:10.1016/j.chemgeo.2006.01.019
- Neuvill, D.R., Cormier, L., Montouillout, V., Florian, P., Millot, F., Rifflet, J.-C., Massiot, D., 2008. Structure of Mg- and Mg/Ca aluminosilicate glasses: ²⁷Al NMR and Raman spectroscopy investigations. *Am. Mineral.* 93, 1721–1731. doi:10.2138/am.2008.2867
- Neuvill, D.R., de Ligny, D., Henderson, G.S., 2014. Advances in Raman Spectroscopy Applied to Earth and Material Sciences. *Rev. Mineral. Geochemistry* 78, 509–541.
doi:10.2138/rmg.2013.78.13
- Novikov, A.N., Neuvill, D.R., Hennet, L., Gueguen, Y., Thiaudiere, D., Charpentier, T., Florian, P., 2017. Al and Sr environment in tectosilicate glasses and melts: Viscosity, Raman and NMR investigation. *Chem. Geol.* 461, 115–127.
doi:10.1016/j.chemgeo.2016.11.023
- Rabukhin, A.I., 1999. Structural interpretation of concentration dependences of molar volume of glasses in R₂O-SiO₂ and RO-SiO₂ systems. *Glas. Ceram.* 56, 339–342.
doi:10.1007/BF02681337
- Schlenz, H., Kirfel, A., Schulmeister, K., Wartner, N., Mader, W., Raberg, W., Wandelt, K., Oligschleger, C., Bender, S., Franke, R., Hormes, J., Hoffbauer, W., Lansmann, V.,

- Jansen, M., Zotov, N., Marian, C., Putz, H., Neuefeind, J., 2002. Structure analyses of Ba-silicate glasses. *J. Non. Cryst. Solids* 297, 37–54. doi:10.1016/S0022-3093(01)00922-X
- Schneider, J., Mastelaro, V.R., Zanotto, E.D., Shakhmatkin, B.A., Vedishcheva, N.M., Wright, A.C., Panepucci, H., 2003. Qn distribution in stoichiometric silicate glasses: thermodynamic calculations and ²⁹Si high resolution NMR measurements. *J. Non. Cryst. Solids* 325, 164–178. doi:10.1016/S0022-3093(03)00332-6
- Shelby, J.E., 1979. Effect of morphology on the properties of alkaline earth silicate glasses. *J. Appl. Phys.* 50, 8010–8015. doi:10.1063/1.325986
- Skinner, L.B., Barnes, A.C., Crichton, W., 2006. Novel behaviour and structure of new glasses of the type Ba–Al–O and Ba–Al–Ti–O produced by aerodynamic levitation and laser heating. *J. Phys. Condens. Matter* 18, L407–L414. doi:10.1088/0953-8984/18/32/L01
- Smith, K.A., Kirkpatrick, R.J., Oldfield, E., Henderson, D.M., 1983. High-resolution silicon-29 nuclear magnetic resonance spectroscopic study of rock-forming silicates. *Am. Mineral.* 68, 1206–1215.
- Thompson, L.M., Stebbins, J.F., 2012. Non-stoichiometric non-bridging oxygens and five-coordinated aluminum in alkaline earth aluminosilicate glasses: Effect of modifier cation size. *J. Non. Cryst. Solids* 358, 1783–1789. doi:10.1016/j.jnoncrysol.2012.05.022
- Toplis, M.J., Dingwell, D.B., 2004. Shear viscosities of CaO–Al₂O₃–SiO₂ and MgO–Al₂O₃–SiO₂ liquids: Implications for the structural role of aluminium and the degree of polymerisation of synthetic and natural aluminosilicate melts. *Geochim. Cosmochim. Acta* 68, 5169–5188. doi:10.1016/j.gca.2004.05.041
- Toplis, M.J., Dingwell, D.B., Lenci, T., 1997. Peraluminous viscosity maxima in Na₂O–Al₂O₃–SiO₂ liquids: The role of triclusters in tectosilicate melts. *Geochim. Cosmochim. Acta* 61, 2605–2612. doi:10.1016/S0016-7037(97)00126-9
- Urbain, G., Bottinga, Y., Richet, P., 1982. Viscosity of liquid silica, silicates and aluminosilicates. *Geochim. Cosmochim. Acta* 46, 1061–1072. doi:10.1016/0016-7037(82)90059-X

Whittaker, E.J.W., Muntus, R., 1970. Ionic radii for use in geochemistry. *Geochim. Cosmochim. Acta* 34, 945–956. doi:10.1016/0016-7037(70)90077-3

Chapter V

Zinc aluminosilicates (ZAS)

Zinc aluminosilicates are interesting because of the intermediate role of Zn in the glass network, where Zn^{2+} can adopt configurations from tetrahedral to octahedral (Calas et al., 2002; Rosenthal and Garofalini, 1987; Xiang et al., 2013). The tetrahedral configuration is typical of a glass network-former, whereas the octahedral one is typical of a network-modifier. Therefore the structural role of Zn^{2+} appears to be somewhat different from that of other transition metals or alkaline earth cations despite the equality of charge (2+) and similarity of ionic radius ($\sim 0.6 \text{ \AA}$) to Mg^{2+} and Fe^{2+} in particular. As a result, zinc has a tendency to follow iron during geochemical processes. Such behaviour is exploited by the $\text{Zn}^{2+}/\text{Fe}^{2+}$ ratio in basaltic rocks, where, in the absence of ferric iron, $\text{Zn}^{2+}/\text{Fe}^{2+}$ should remain constant during mantle melting. Variations in the $\text{Zn}^{2+}/\text{Fe}^{2+}$ ratio in basalts are used to infer changes in the oxidation state of the Earth's mantle (Lee et al., 2010). The similarity in Zn^{2+} and Fe^{2+} partitioning behaviour is quantified by the $K_D^{\text{Zn-Mg}}$ olivine-melt $\frac{(\text{Zn}^{2+}/\text{Mg}^{2+})_{\text{Olivine}}}{(\text{Zn}^{2+}/\text{Mg}^{2+})_{\text{Melt}}}$ exchange coefficient with respect to that for iron, where, in both cases, $K_D \approx 0.3$ is found in basaltic melts, but they depart strongly from one another as the melts become more silicic, implying a change in coordination (Kohn and Schofield, 1994). A possible reason is that Zn^{2+} differs from Fe^{2+} by having a fully-occupied 3d10 valence shell, meaning that it exists overwhelmingly in tetrahedral coordination in silicate minerals (Neumann, 1949), as compared to predominantly VI-fold for Fe^{2+} . Despite its geochemical importance, information on Zn coordination in natural silicate melts is entirely lacking. Knowledge of its bonding environment is crucial in modelling geochemical processes, including stable isotope fractionation, which arises due to differences in Zn bonding environment between two phases.

In addition to fundamental and geochemical interest, glasses obtained in the ZAS system are attractive for industrial applications due to their high glass transition temperature, low thermal expansion coefficient, low electrical conductivity, high chemical stability and good mechanical properties (Ehrt et al., 2008; Shimbo, 1987). Transparent glass-ceramics and high modulus glass fibers have been obtained in the ZAS system (Duan et al., 2003; Wallenberger et al., 1993; Yoo et al., 2003, 2002), while Zn containing glasses and glass-ceramics has been used as a sealant in solid oxide fuel cell (Arora et al., 2011) and in bioactive glasses (Goel et al., 2013; Kaur et al., 2012).

In this chapter we are going to briefly discuss glass forming ability of Zn aluminosilicate compositions considering only two joins: $R = 1$ and $R = 3$ (Figure V.1). The chapter begins with the tectosilicate section and will show what changes aluminosilicate glasses will experience when cations with different CFS (Z/r^2) are accommodated in the network. One should keep in mind during our discussion that the CFS decreases in the row $Mg^{2+} \approx Zn^{2+} > Ca^{2+} > Sr^{2+} > Ba^{2+}$. After discussing structure and properties of tectosilicate glasses, we will move to the join $R = 3$ to see how the glass network evolve at different SiO_2 content and with various cations incorporated, and how it affects macroscopic properties.

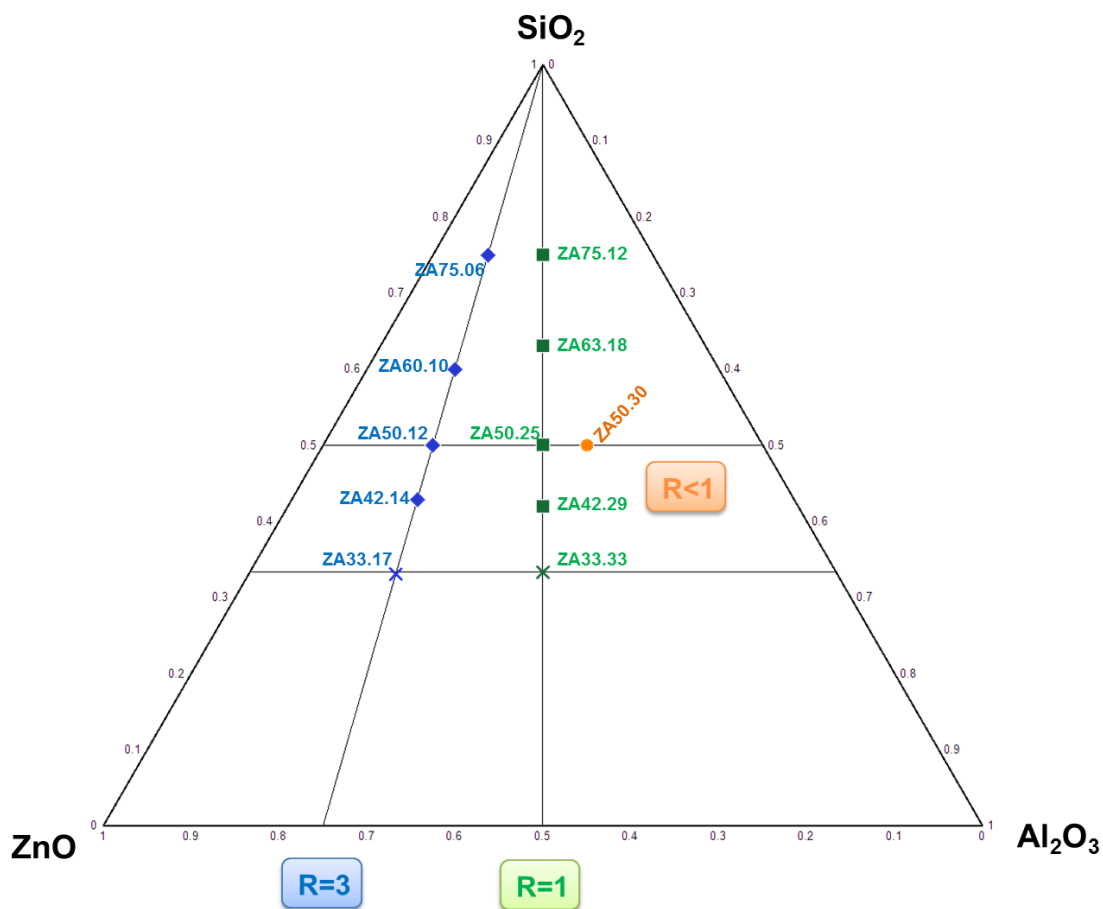


Figure V.1. Ternary plot for the ZAS system (mole fractions) showing compositions studied. Glasses obtained by traditional quench are depicted as filled symbols. Crosses correspond to compositions for which no glass could be obtained by neither of two quench procedures. Color guide: blue – peralkaline glasses, green – tectosilicate glasses, orange – peraluminous glasses. $R = ZnO/Al_2O_3$.

The domain of vitrification in the ZAS system is quite limited when compared to CAS, SAS and BAS systems and resembles the MAS one for which no silica-poor glasses has been reported so far. If compositions with 50 mol% of SiO_2 (ZA50.25 and ZA50.12) are easy to vitrify, traditional quench of ZA42.29 melt, for example, produces glass abundantly covered

with a thick white crystalline layer. Attempts to produce glasses with lower silica content (ZA33.33 and ZA33.17) resulted in completely crystalline solids. The use of the levitation setup proved to be inefficient since under the laser radiation samples start volatilizing long before becoming liquid. It is also true for high-temperature melts. During the melting stage we observed some fumes. On the one hand, the electron microprobe analysis has not shown significant deviations of the compositions from theoretical. On the other hand, the volatilization of samples has made impossible the use of high-temperature NMR setup. That is why no such data on Zn aluminosilicate melts will be presented here. The only peraluminous composition ZA50.30 has been obtained to demonstrate the possibility of producing a small quantity of the glass by the traditional quench, though no studies were carried out on this composition.

Additionally to a restricted domain of vitrification, a phenomenon of phase separation occurs in the ZAS system. The most obvious phase separation occurs for silica-rich Zn aluminosilicates as it will be demonstrated further by different methods. For example, on the join R = 3 two silica-rich compositions, namely ZA75.06 and ZA60.10, appeared as opalescent glasses (Figure V.2), which is a typical feature of phase separated systems.

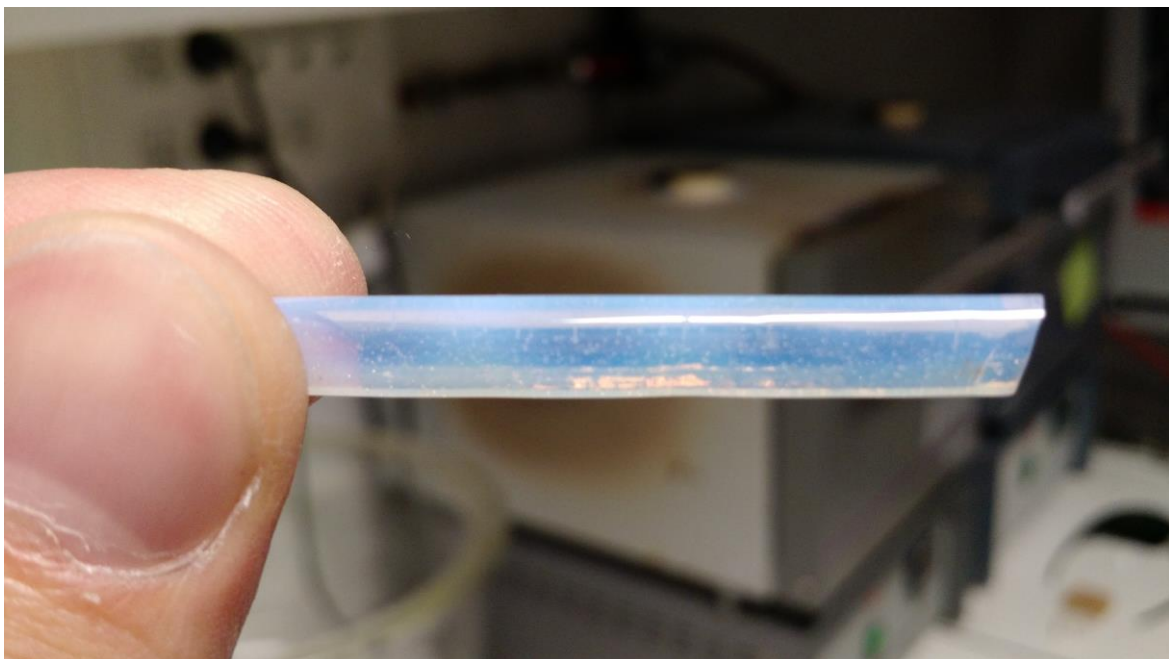


Figure V.2. Visible to the naked eye phase separation in ZA75.06 composition appearing as opalescent glass. Identical phenomenon is observed for ZA60.10 glass as well.

To confirm our guess we analysed ZA75.06 and ZA60.10 glasses by means of transmission electron microscopy (Figure V.3). Both samples were found to be phase-separated. In the case of ZA75.06 a severe phase separation of “spinodal decomposition” type is observed, while a moderate one of “nucleation and growth” type is present for ZA60.10 sample. Even though we did not check the other compositions, there is information in literature that phase separation in the ZAS system occurs down to 50 mol% of silica for compositions with $R = \text{ZnO}/\text{Al}_2\text{O}_3 = 4$ and 3.5, respectively (Ehrt et al., 2008). The authors have not reported any phase separation for glasses with 45 mol% of SiO_2 and $R = 3.4$ and 2.7.

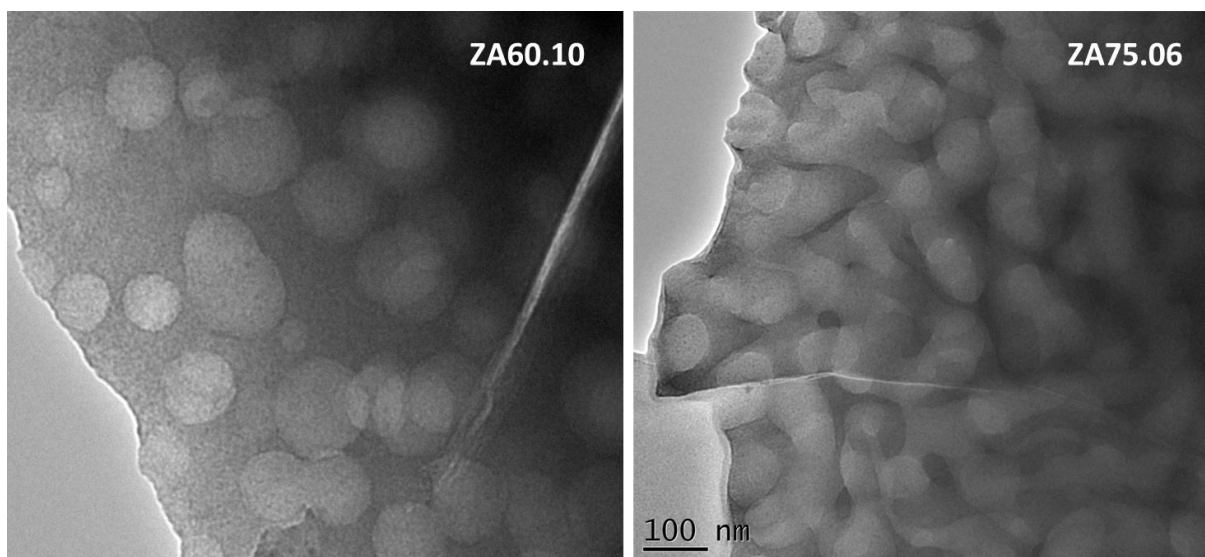


Figure V.3. TEM images of phase separated ZA60.10 (*left*) and ZA75.06 (*right*) glasses. The phase separation of “nucleation and growth” type is observed for the former one and of “spinodal decomposition” type for the latter one. Bright regions are rich in SiO_2 .

Before going to the first section, some important remarks must be stated here. The ZAS system is the most recent one for which we elaborated and analysed glasses. The phenomenon of phase separation in our glasses was discovered only lately and could not be properly investigated in view of the lack of time. Most of the experiments were carried out only once without a proper sampling (e.g., one Raman spectrum was measured for one piece of glass only). Further, even with the knowledge of phase separation, we treated the data of biphasic glasses as for homogeneous ones. This was made in order to have at least a preliminary data on the phase-separated compositions required for further investigations. For a proper study of the phenomenon of phase separation it is required (at least) to study small and big pieces of one glass separately, investigate the influence of the quench rate on

degree of phase separation, carry out measurements on glass annealed above its T_g and so on.

Therefore, additional studies in the ZAS system are required to shed light on the mechanisms of the observed phenomenon, and especially to investigate potential phase separations happening on a smaller scale than the one producing visual opalescence.

1. Tectosilicate join (R = 1)

1.1. ^{27}Al and ^{29}Si NMR spectroscopy

Unlike ^{27}Al NMR spectra of corresponding Sr and Ba tectosilicate glasses, the spectra of glasses on the join R = 1 in the ZAS system are much broader and possess three distinguished maxima (Figure V.4). These maxima are characteristic of Al atoms in four-, five- and six-fold coordination. Already by examining the raw data we can conclude that the width of an NMR line as well as intensity of AlO_x contributions decreases in the row Zn – Sr – Ba, in accordance with reducing CFS and findings of (Mizoguchi et al., 1982) made on Sr, Ba and Zn aluminosilicate melts. The line width of the NMR signal reflects the degree of structural disorder in the system, a measure of which is given by the ^{27}Al “average” C_Q obtained by simulating the spectra in the context of the GIM model (Le Caër and Brand, 1998) as well as the ^{29}Si NMR line widths. Therefore, among tectosilicate glasses studied here the Zn-containing ones possess the highest degree of disorder, in agreement with the idea that cations with high CFS increase disorder in the network (Lee and Stebbins, 2002, 2000; Murdoch et al., 1985; Mysen et al., 1982; Navrotsky et al., 1985).

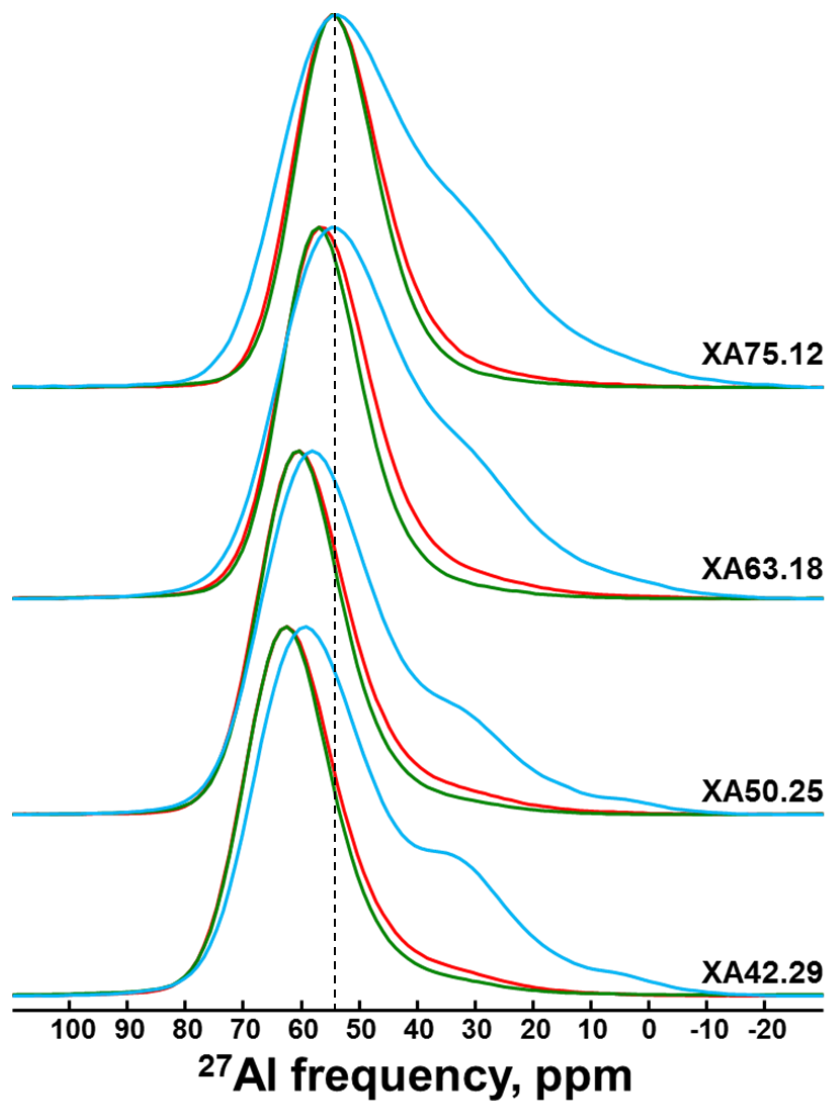


Figure V.4. ^{27}Al MAS NMR spectra of Zn (blue, X = Z), Sr (red, X = S) and Ba (green, X = B) tectosilicate glasses. Silica content decreases from top to bottom.

The deconvolution of all ^{27}Al NMR spectra of Zn tectosilicate glasses was made assuming the presence of only one phase (Figure V.5); however one should keep in mind the discussion given above on phase separation occurring in silica-rich compositions.

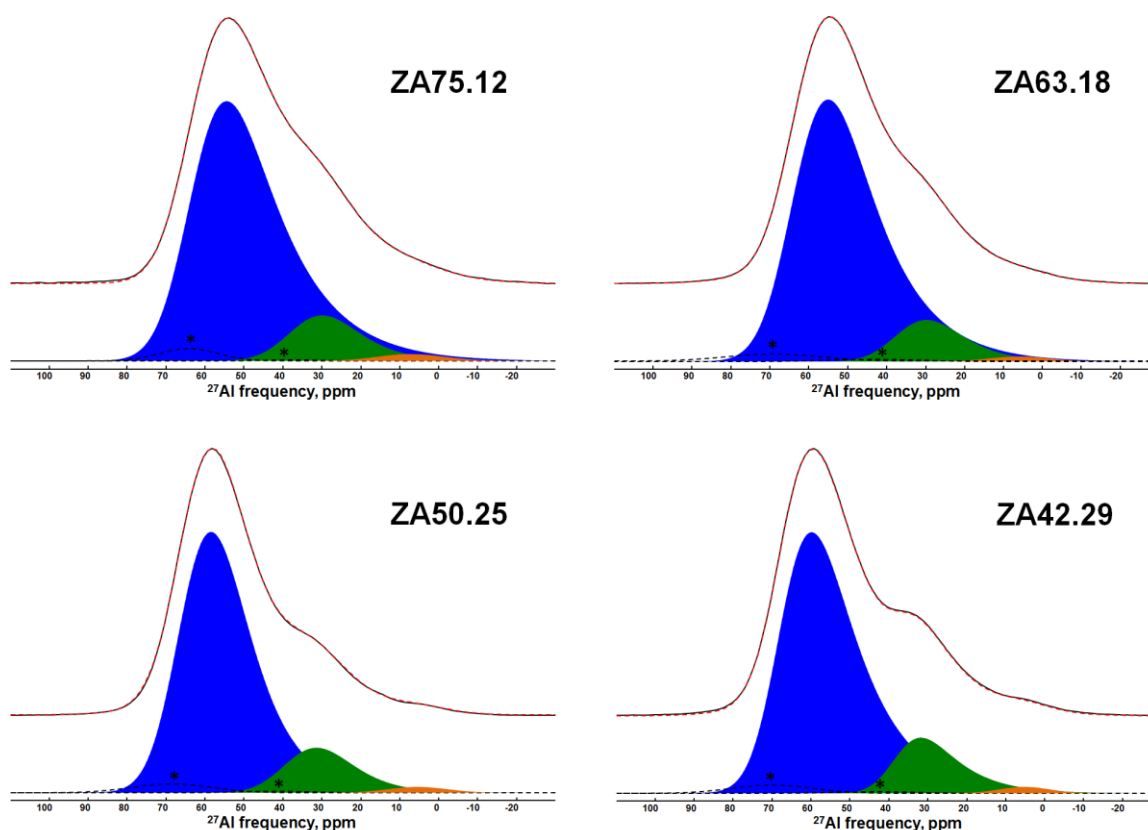


Figure V.5. Deconvolution of the ^{27}Al MAS NMR spectra of Zn tectosilicate glasses. Colour guide: blue – AlO_4 , green – AlO_5 , orange – AlO_6 , black dashed lines with an asterisk – spinning sidebands.

Figure V.6 presents the results of the deconvolution for Zn tectosilicates together with the data reported on alkaline earth counterparts. We can see that $\delta_{iso}(\text{AlO}_4)$ changes almost linearly only for Ca, Sr and Ba tectosilicate glasses. In the case of glasses containing cations with high CFS (Mg and Zn), there is a clear deviation from the general trend at high silica content. The reason for such deviation is a various AlO_4 environments, in the ZAS and MAS systems compared to the others, caused by the presence of two phases (at least in the ZAS system). This indicates a possible phase separation in silica-rich Mg tectosilicates as well. Less well-defined but still evident, $\delta_{iso}(\text{AlO}_5)$ for Zn and Mg tectosilicates differs from the others as well for silica-rich compositions.

The fraction of five-coordinate Al rises with increasing the CFS, from Ba to Mg and Zn (Figure V.6). An identical trend has been estimated by (Mizoguchi et al., 1982) for aluminosilicate melts. They have shown that the fraction of high-coordinate AlO_x species in melt increases in the row Ba – Sr – Ca – Mg – Zn. Their findings are in excellent agreement with results obtained for the tectosilicate glasses. Similar dependence of AlO_5 content on the cation field strength has been reported many times by different authors investigating

aluminosilicate glasses containing alkali, alkaline earth and rare-earth elements as non-network formers (Allwardt et al., 2005; Florian et al., 2007; Iftekhar et al., 2011; Neuville et al., 2008, 2006, 2004b; Novikov et al., 2017; Thompson and Stebbins, 2012). The maximum of five-fold aluminium observed for Zn and Mg tectosilicates is comparable and about 14 and 13 %, respectively. However, the AlO_5 curves do not change in the same manner which could be a consequence of the different nature of the two cations: Mg being an alkaline earth element, while Zn is a transition one. In any case, in both systems Mg and Zn tectosilicate glasses are characterized by an elevated disorder as indicated by high C_Q values around 9-10 MHz (see Annex III) when compared with other systems.

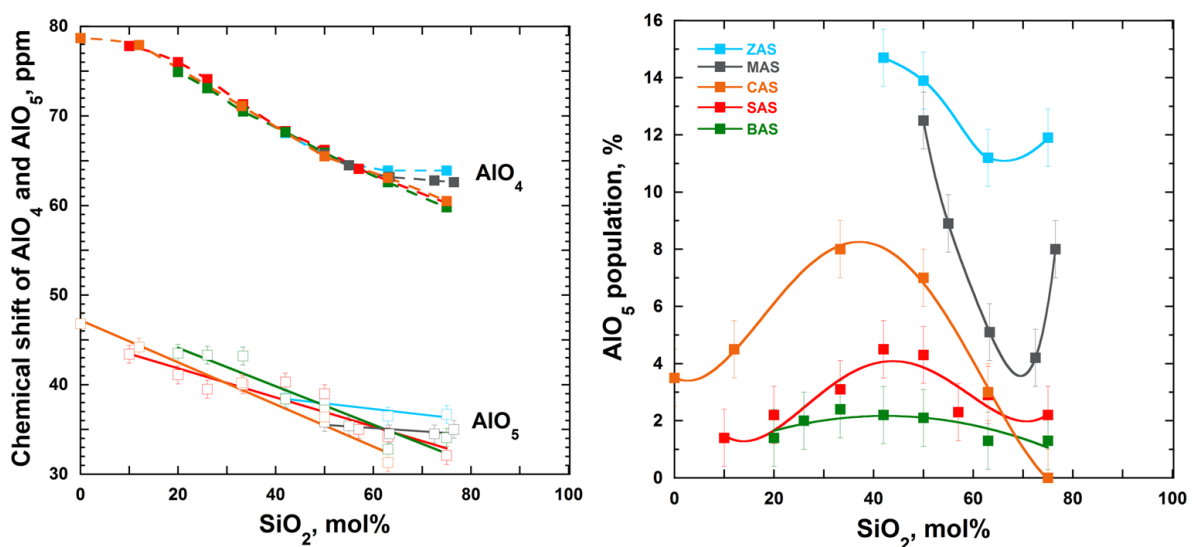


Figure V.6. *Left*: evolution of the isotropic chemical shift (δ_{iso}) of AlO_4 and AlO_5 for tectosilicate glasses in the ZAS, MAS, CAS, SAS and BAS systems. If not visible, error bars are less than symbol's size. *Right*: AlO_5 population for glasses along the join R = 1. The lines are a guide to the eye. Color guide: blue – ZAS, grey – MAS, orange – CAS, red – SAS, green – BAS. Data for the MAS and CAS systems are from (Neuville et al., 2008, 2006, 2004b).

^{29}Si NMR spectra of Zn tectosilicate glasses are much broader and their maxima are shifted to lower values of δ_{iso} relative to the spectra of corresponding Sr and Ba tectosilicates (Figure V.7). This as has been mentioned before is a consequence of the increased disorder introduced in the aluminosilicate network by Zn possessing a high CFS. The NMR line width decreases with decreasing the cation field strength in the row Zn – Sr – Ba. While all the ^{29}Si NMR spectra of Sr and Ba tectosilicates are quite symmetric and featureless, this is not the case of the spectra of silica-rich Zn compositions. The most remarkable case is the spectrum of ZA75.12 glass. It has a maximum that matches the

position of Q^4_0 units, as inferred from the spectrum of vitreous SiO_2 , and a shoulder at higher δ_{iso} values. For SA75.12 and BA75.12 most of the Q^4_m species were found in Q^4_0 . However, the spectra of these two glasses differ a lot from the spectrum of ZA75.12. This fact and the fact that the spectrum of ZA75.12 glass resembles more that of vitreous silica proves that for silica-rich Zn tectosilicates a phase separation occurs with a silica-like phase. In fact, phase separation in silica-rich Zn aluminosilicate and silicate glasses has been already reported (Ehrt et al., 2008; Van Tran et al., 2017). The separated phases were typically SiO_2 -rich droplets and a matrix enriched in Zn and Al which is in agreement with our previous statement.

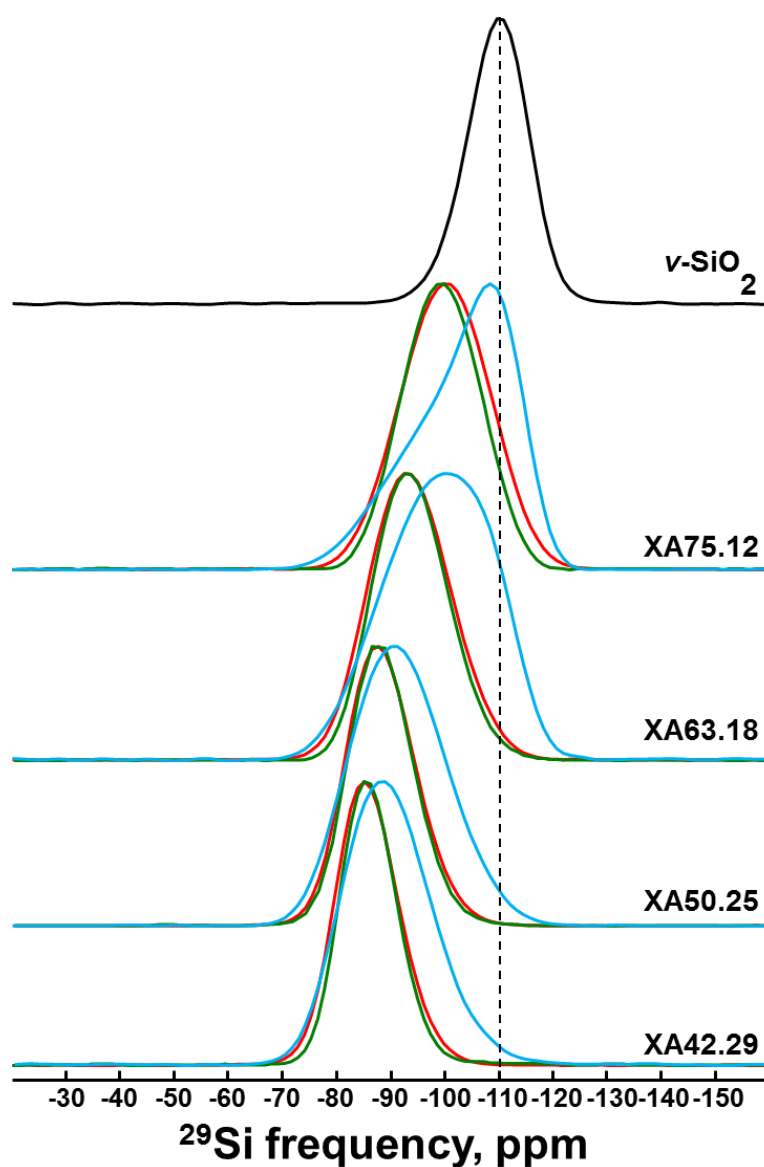


Figure V.7. ^{29}Si MAS NMR spectra of Zn (blue, X = Z), Sr (red, X = S) and Ba (green, X = B) tectosilicate glasses. Silica content decreases from top to bottom.

At the same time, MD simulations performed for ZA50.25 composition (Thibault Charpentier, personal communication) revealed presence of $\sim 21\%$ of three-coordinate oxygens and $\sim 13\%$ of NBOs. A considerable fraction of TBOs together with edge-sharing polyhedra and high-coordinate silicon species has been also revealed in Zn silicate glasses by other MD simulations (Rosenthal and Garofalini, 1987, 1986). Their simulations showed that, even though Zn acts as a network former, it disrupts the silica network a lot by creating a considerable fraction of edge-sharing ZnO_x units, TBOs and SiO_5 species. In fact, partial incorporation of Zn into edge-sharing units seems to be quite common. For example, Zn were found in edge-sharing configuration also in borate and halide glasses (Lou et al., 2015; Swansbury and Mountjoy, 2017). For high-pressure CAS glasses, it has been demonstrated that an increase in Al coordination is accompanied by the compression of CaO_x sites (Allwardt et al., 2005), i.e. creation of edge-sharing polyhedra. Therefore, the high fraction of five-coordinate Al in Zn tectosilicate glasses could be explained by the presence of ZnO_x polyhedra sharing edges.

Our findings indicate the presence of non-negligible amount of depolymerized Q_m^n units (where $n < 4$), TBOs and, on top of it, of phase separation in Zn tectosilicates. All this makes the deconvolution of the ^{29}Si NMR spectra extremely uncertain and, therefore, will not be presented here.

1.2. Neutron diffraction

Figure V.8 presents the static structure factors, $S(q)$, of Zn tectosilicate glasses. The FSDP shifts to higher q values and becomes less intense with decreasing SiO_2 content. Such a shift, typical for alkaline earth aluminosilicates as well, has been attributed to changes in ring statistics, namely to the reduction of their size (Neuville et al., 2004a).

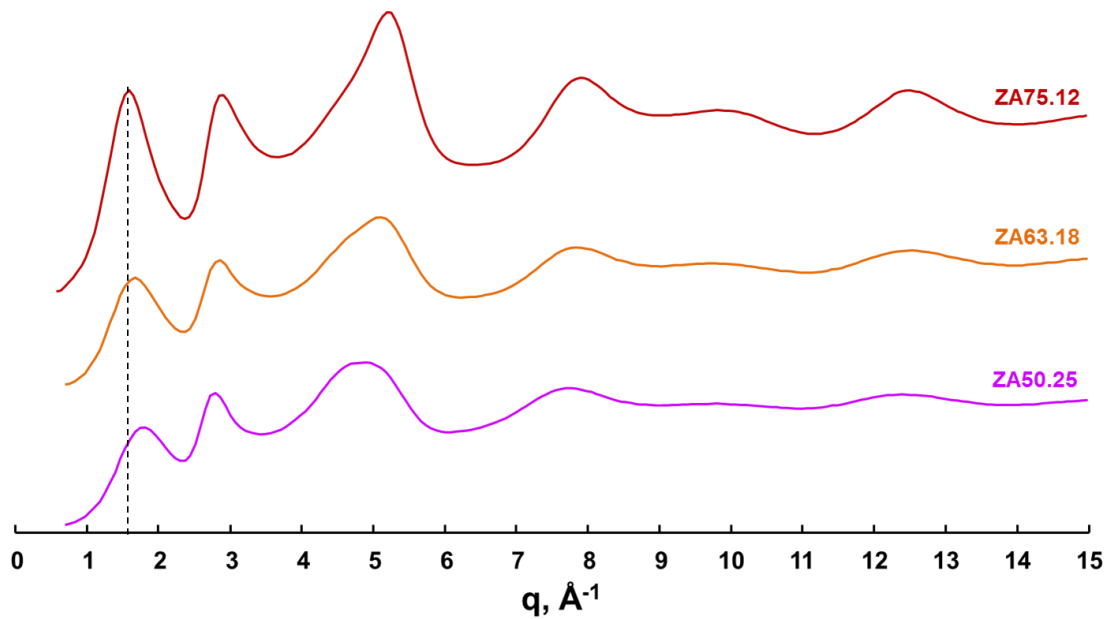


Figure V.8. Static structure factor, $S(q)$, of Zn tectosilicate glasses. Silica content decreases from top to bottom.

The first peak in the $g(r)$ corresponding to Si-O and Al-O contributions shifts to higher r values like in the case of analogous Sr and Ba glasses (Figure V.9). Nevertheless, unlike Sr and Ba tectosilicates, the peak possesses a high- r shoulder. This shoulder corresponds to Zn-O contribution and should be in principle easy to fit since the Si-O and Al-O contributions possess well-defined positions and coordination numbers.

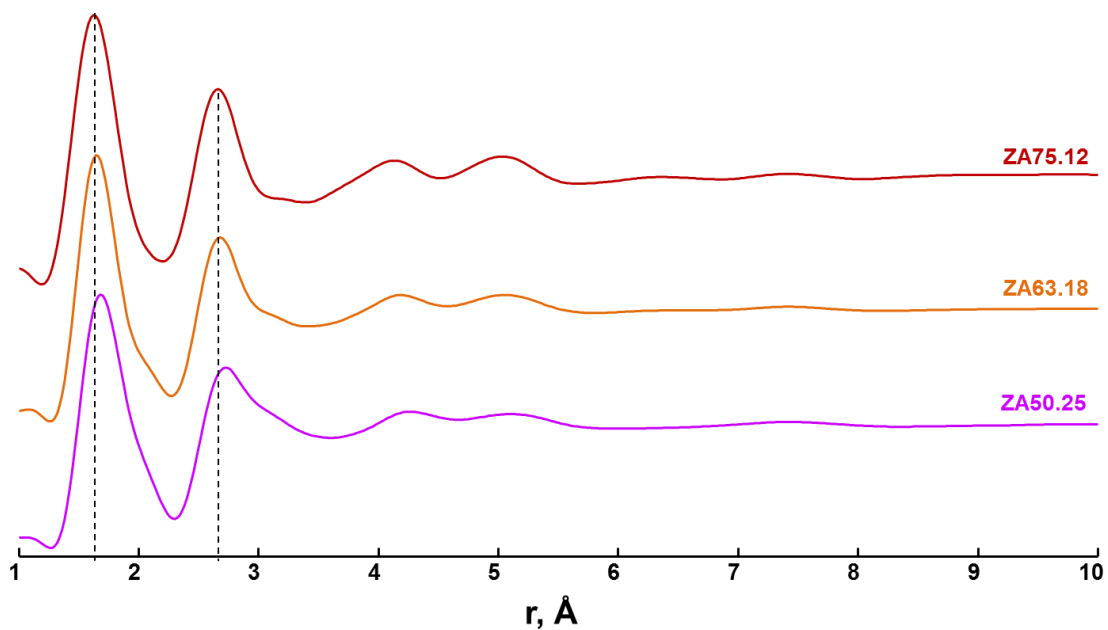


Figure V.9. Pair distribution function, $g(r)$, of Zn tectosilicate glasses. Silica content decreases from top to bottom.

By fixing Si-O distance around 1.62 Å and CN(Si-O) = 4, we deconvoluted the total distribution function, $T(r)$, of Zn tectosilicate glasses as shown in Figure V.10. The information on the Zn-O distances and CN(Zn-O) is presented in Table V.1. It appears that the coordination number of Zn increases from 4.4 to 5.3 for ZA75.12 and ZA50.25 glass, respectively. However, this change is within the error bars. It is also interesting to compare our results with coordination number of magnesium in compositionally analogous glasses. (Guignard and Cormier, 2008) have reported the CN(Mg-O) for two tectosilicate glasses MA76.12 and MA50.25 equal to 4.75 ± 0.1 and 5.06 ± 0.1 Å, respectively. These values are comparable with our findings for the CN(Zn-O) and also show a trend of increasing coordination number of cation with decreasing SiO₂ content.

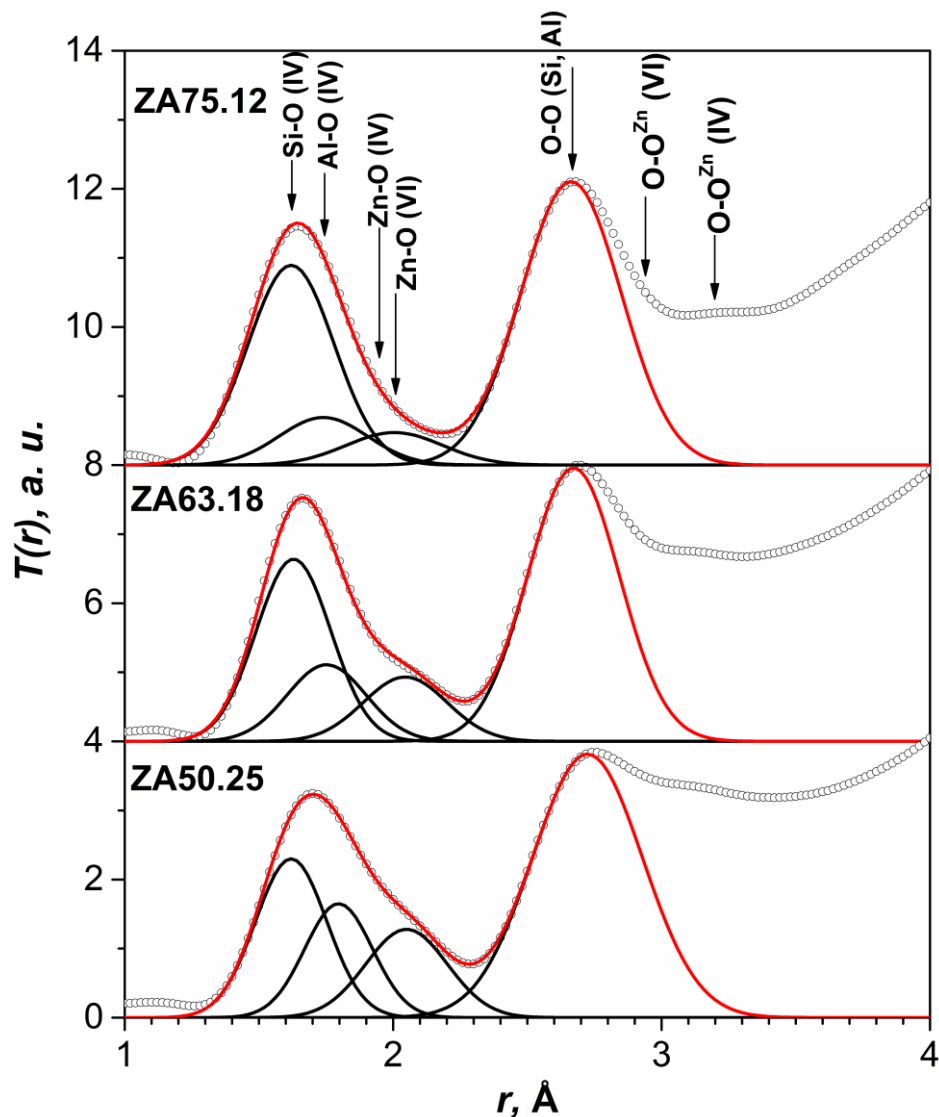


Figure V.10. Deconvolution of the first peak in $T(r)$ of three Zn tectosilicate glasses. Points are the experimental data, black lines are partial fits and red line is the total fit.

According to the MD simulations performed on ZA50.25 composition by Thibault Charpentier (personal communication) the average Si-O, Al-O and Zn-O distances are equal 1.65 ± 0.06 , 1.85 ± 0.11 and 2.12 ± 0.22 Å, respectively, with Zn found predominantly in ZnO₄ (56 %) and ZnO₅ (31 %) polyhedra (with a small fraction of ZnO₆). Such distribution of ZnO_x species is in good agreement with our findings.

Table V.1. Average Zn-O interatomic distances (r , in Å) and coordination number (CN) obtained from the deconvolution of the ND data for Zn tectosilicate glasses.

	ZA75.12	ZA63.18	ZA50.25
$r(\pm 0.02)$	2.01	2.05	2.05
CN(± 0.5)	4.4	5.1	5.3

Another way to look at the data is to trace changes in the position of O-O contributions coming from ZnO₄ and ZnO₆ (Figure V.10). The position of O-O contribution moves to lower r values under the substitution of SiO₂ by ZnAl₂O₄, implying a change in CN(Zn-O) from 4 to 6 (since $r(\text{O-O})$ in tetrahedra is higher than the one in octahedral environment). Hence, considering this observation and the results of deconvolution, we can conclude that on the join R = 1 the coordination number of Zn increases with decreasing silica content. Identical trend in the CN(Zn-O) evolution has been found for silica-rich Zn silicates by [Rosenthal and Garofalini, 1987, 1986](#)), who have found that the coordination number of Zn increases from 4 to 6 with decreasing SiO₂ content.

1.3. Raman spectroscopy

When ZnAl₂O₄ substitutes for SiO₂ in the tectosilicate network, it produces striking changes in corresponding Raman spectra (Figure V.11). In the spectrum of ZA75.12 glass one can distinguish all the main features characteristic for the spectrum of vitreous silica. There is a broad band of low intensity in the HF region, an asymmetric band around 800 cm⁻¹, the D₁ and D₂ bands etc. Already in the spectrum of ZA63.18 glass all these features (except for the HF envelope) become almost indistinguishable and vanish with further decrease of silica content. It is, therefore, difficult to assume what changes in ring statistics are induced under the substitution of SiO₂ in Zn tectosilicate glasses since intensities of all bands in the low-frequency region decrease simultaneously. Nevertheless, the results of ND (namely, the FSDP's shift) suggest that the ring statistics change towards low-membered rings.

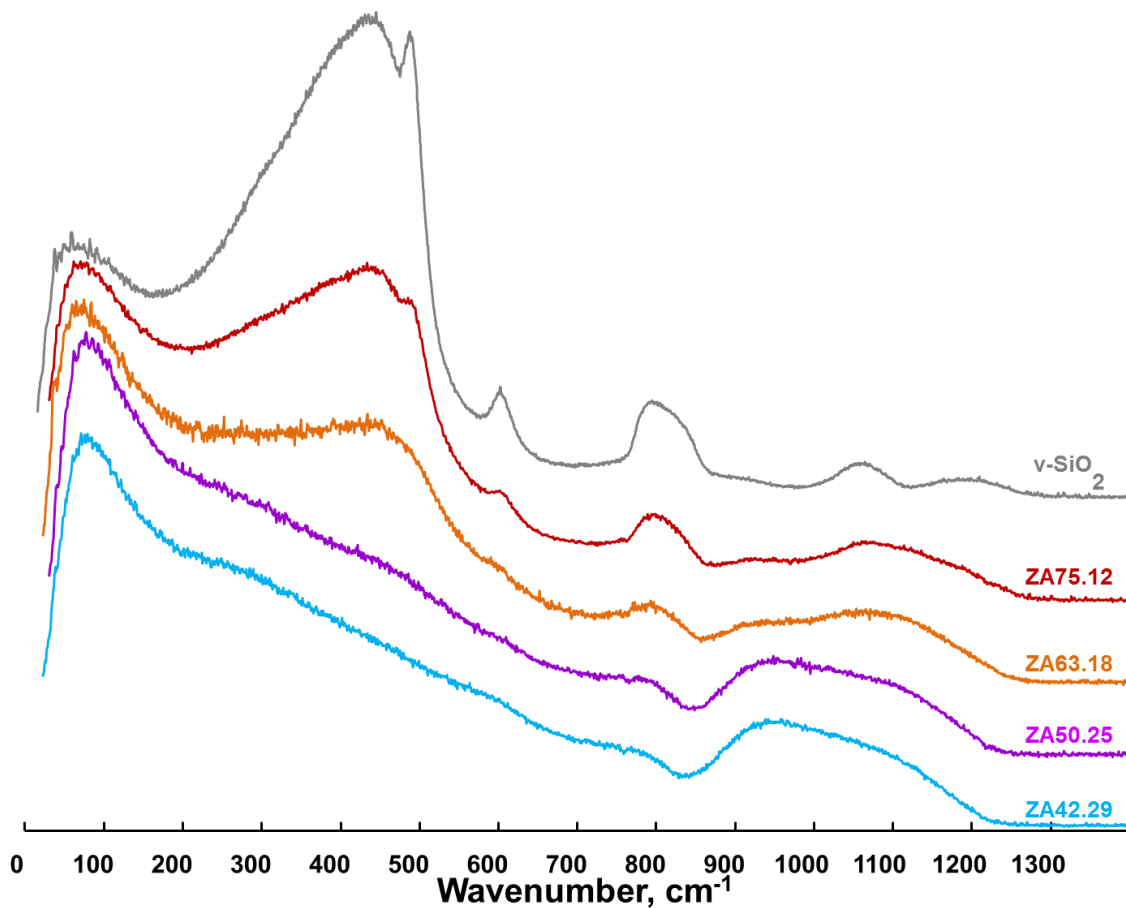


Figure V.11. Area normalized Raman spectra of Zn tectosilicate glasses. Silica content decreases from top to bottom.

It has been stated in previous sections that ZA75.12 glass is phase separated and the other glasses have NBOs and, possibly, TBOs in their structure. To strengthen these statements we deconvoluted the HF envelope of the Raman spectra of Zn tectosilicates using only three Gaussian bands as it has been implemented for corresponding Sr and Ba aluminosilicate glasses (Figure V.12). The deconvolution revealed that, firstly, the position of the three Gaussian bands does not change linearly with composition as it has been found for Na, Mg, Ca, Sr and Ba tectosilicate glasses (Neuville et al., 2008, 2004b; Neuville and Mysen, 1996; Novikov et al., 2017; Seifert et al., 1982); secondly, the low-frequency band is found at too low wavenumbers that are normally expected for compositions with ≥ 42 mol% of SiO_2 ($910\text{-}920\text{ cm}^{-1}$ instead of typical $930\text{-}990\text{ cm}^{-1}$). At such wavenumbers one usually finds bands corresponding to vibrations in highly depolymerized species (according to our previous deconvolutions in the SAS and BAS systems). Moreover, the relative area of the band increases progressively with decreasing SiO_2 content. Therefore, we suspect that this

band is caused by vibrations in depolymerized Q^n units, which supports the idea that Zn tectosilicate glasses are less polymerized than the alkaline earth ones.

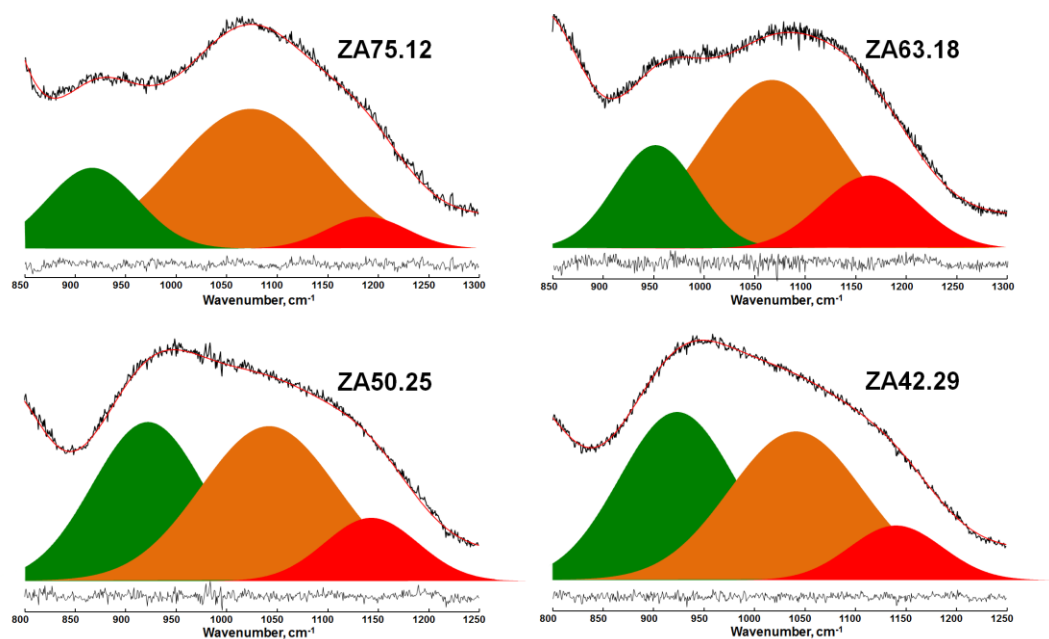


Figure V.12. Deconvolution of the HF region of the Raman spectra of Zn tectosilicate glasses. Colour guide: red – $Q^{4,I}$, orange – $Q^{4,II}$, green – T_{2s} .

Nevertheless, one should be aware that the deconvolution we made is not quantitative since, when a phase separation occurs, the Raman spectra are a combination of spectra of two phases. Obviously, additional experiments are required in order to investigate the phases separately.

1.4. Macroscopic properties

In the group of alkaline earth tectosilicate glasses, both density and molar volume increases concurrently with decreasing the CFS, i.e. from Mg to Ba (Figure V.13). Interestingly, the density and V_m curves of Mg tectosilicates follow a linear trend while for Ca, Sr and Ba containing glasses their behaviour is more complex. For example, the V_m curve of Ca tectosilicates decreases rapidly from 100 to 75 mol% of SiO_2 as in the case of Mg, then this decrease slows down and after approximately 50 mol% of silica one observes a rise of the molar volume. For Sr tectosilicates the V_m curve drops slightly from 100 to 63 mol% of SiO_2 and then increases with acceleration for silica-poor compositions. In the case of Ba containing glasses, we do not observe a drop of the V_m curve for silica-rich compositions at all. There is only a continuous increase for the whole range of compositions. Concerning ZAS

glasses along the join $R = 1$, the behaviour of density and molar volume clearly indicates phase separation in the silica-rich domain. The V_m curve of Zn tectosilicates do not change from 100 to 75 mol% of silica, then drops fast down to 50 mol% of SiO_2 with following increase. The fact that the molar volume of ZA75.12 glass is practically identical to that of vitreous silica supports the idea that for this composition a phase separation occurs. This could be also the case of ZA63.18 glass but to a lesser degree.

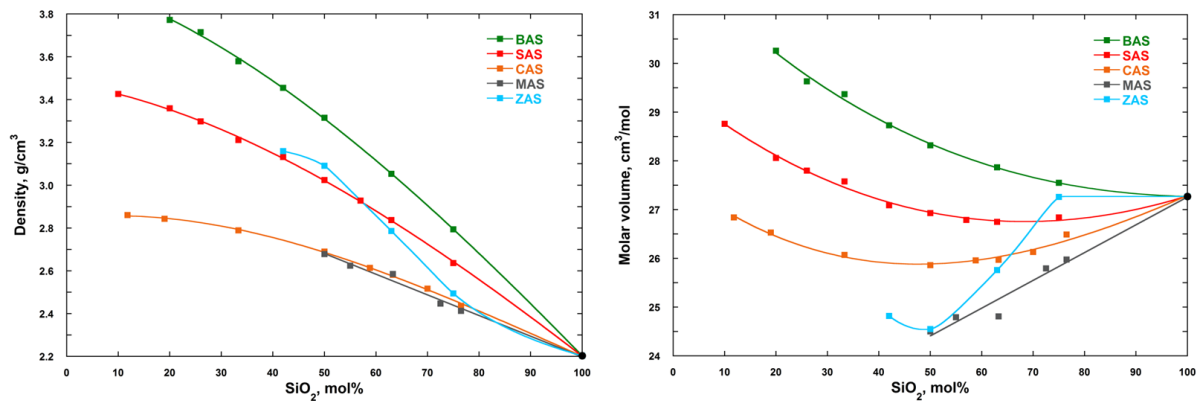


Figure V.13. Experimental densities (*left*) and calculated molar volumes (*right*) of tectosilicate glasses in the ZAS, MAS, CAS, SAS and BAS systems. Data for the MAS and CAS systems are from (Neuvill, 1992; Neuvill et al., 2004b). The black filled circle corresponds to the density of vitreous silica taken from (Brückner, 1970). Error bars are less than the symbol size. The lines are a guide to the eye.

It is interesting to trace how the introduction of cations possessing different CFS is adopted with or without changing much the initial glass structure in each system. For Mg tectosilicates the introduction of MgAl_2O_4 into silica network produces a linear decrease of the V_m suggesting that Mg^{2+} is easily accommodated in the voids of the aluminosilicate network. This is in agreement with Mg atoms occupying small four- to six-fold sites (Guignard and Cormier, 2008). For larger cations such as Ca and Sr, the aluminosilicate network can accommodate only a limited amount of cations without significant reorganization. This reorganization is accompanied by changes in the ring statistics, namely rise of the fraction of low-membered rings at the expense of high-membered ones (Cormier et al., 2003; Neuvill et al., 2004b). Ba cations are so huge that even a small amount of them cannot be incorporated in the aluminosilicate network without inducing important structural changes. It has been shown that in case of large alkali cations such as K and Rb the V_m of tectosilicate and silicate glasses also increases even for silica-rich compositions (Le Losq, 2012; Rabukhin, 1999). Worth noticing, that the coordination number of the cations increases from Mg (CN \approx 5) to Ba (CN \approx 10). At the same time, the fraction of AlO_5

(improving the packing of the network) decreases in the row Mg – Ca – Sr – Ba. These and probably some other factors are responsible for the difference in observed molar volumes between the alkaline earth systems.

In Figure V.14 we summarized the evolution of the glass transition temperature as a function of SiO₂ content for alkaline earth and Zn tectosilicate glasses. It is clearly seen that the T_g curves of glasses along the join R = 1 descend to lower values in the following order: BAS – SAS – CAS – MAS – ZAS. The only exception is observed for compositions with 75-76 mol% of SiO₂, where T_g of MA76.12 composition is much higher than for analogous Ca, Sr and Ba containing glasses. Such deviation is consistent with the idea of phase separation as suggested by the departure of $\delta_{iso}(AlO_4)$ from a linear trend and by the shape of AlO₅ curve for silica-rich Mg tectosilicates (Figure V.6). The deviation might also be caused by something else since one does not observe any deviations in the V_m curve for this composition as for ZA75.12, for example. Additionally, one does not observe a deviation in glass transition temperature for the phase-separated ZA75.12 glass. The latter fact can be explained by the difference of the methods used for T_g determination. In the case of MA76.12 glass T_g has been extracted from viscosity measurements, while for ZA75.12 compositions T_g were determined from DSC. It is very likely that a part of the silica-rich Zn tectosilicate used for DSC measurements was not phase-separated as the one used for recording the ²⁹Si NMR spectrum, for example. This emphasizes again the necessity of the systematic approach for studying phase-separated glasses.

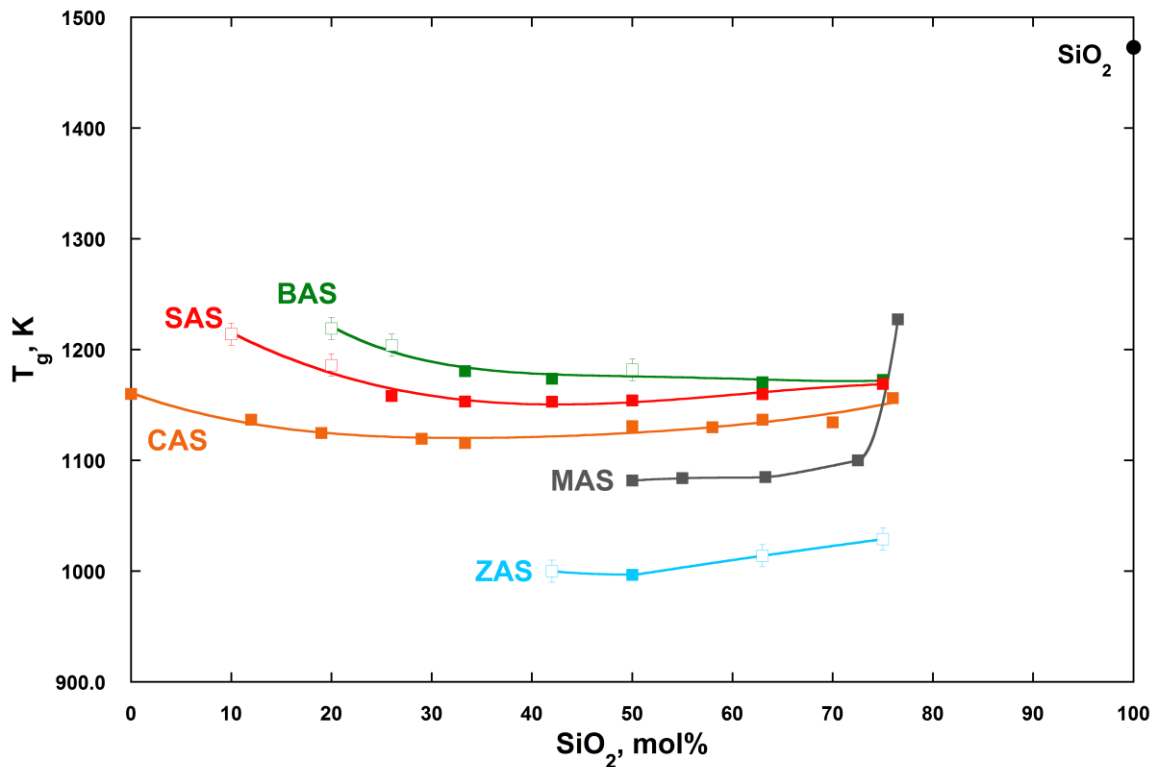


Figure V.14. Glass transition temperatures of tectosilicate glasses in the ZAS, MAS, CAS, SAS and BAS systems. Filled symbols are T_g values extracted from viscosity data, open symbols are T_g values from DSC measurements. Data for the MAS and CAS systems are from (Cormier et al., 2005; Neuville, 1992; Neuville et al., 2004a). The glass transition temperature of vitreous silica (black filled circle) is given for comparison (Mackenzie, 1963). If not visible error bars are less than the size of symbols. The lines are a guide to the eye.

Comparing the curves of Ca, Sr and Ba tectosilicate glasses we can conclude that the augmentation of T_g in the silica-poor domain is a common phenomenon occurring for alkaline earth aluminosilicates. It appears that the following rule is applicable: the larger the cation the more pronounced the rise of T_g , with the latter rise starting at higher silica content.

It has been shown that viscosity and glass transition temperature in alkali aluminosilicates increases from Na- to K-containing ones (Le Losq, 2012), i.e. also with increasing the size of the cation. Recent findings (Le Losq et al., submitted) suggest that such dependence of T_g on the cation's size may be connected with the existence of percolation channels in the glass network. According to (McMillan et al., 1998) who studied Rb and Cs aluminosilicate glasses along the join $R=1$, large cations require formation of large cages/rings in the glass structure to be incorporated into the network. The formation of large rings provokes simultaneous formation of low-membered rings to improve the

network's connectivity. It is easy to imagine that under further substitution of SiO_2 cages/rings can merge to create percolation channels filled with cations as in Compensated Continuous Random Network of (Greaves and Ngai, 1995). For K tectosilicate glasses (Le Losq, 2012) has demonstrated that the fraction of three- and four-membered rings increases significantly with decreasing SiO_2 content for K tectosilicate glasses. Similar observation has been made for Ca, Sr and Ba tectosilicate compositions. Therefore, the creation of percolation channels accompanied by the formation of small-membered tetrahedral rings could be responsible for the difference in glass transition temperatures between alkaline earth systems and for the increase of T_g at low SiO_2 content. Nevertheless, there could be a more sophisticated explanation of the observed trends involving the presence or absence of high-coordinate Al species, NBOs and TBOs etc.

To demonstrate the effect of the cation's nature on the glass transition temperature, we represented T_g as a function of the cation field strength in Figure V.15. For this we calculated the values of CFS from ionic radii (Whittaker and Muntus, 1970) assuming that Zn and Mg are five-coordinate (Guignard and Cormier, 2008), Ca is in seven-fold coordination (Neuvillie et al., 2004a) and coordination numbers of Sr and Ba are 9 and 10, respectively (see Chapter III and Chapter IV). It is clearly seen that in the alkaline earth group T_g decreases with increasing the cation field strength (for the deviation of the point for MA76.12 composition see discussion above). In addition, the slope of the curves presented in Figure V.15 changes from silica-rich to silica-poor compositions reflecting the fact that the difference in T_g is lower in the case of XA75.12 glass than in the case of XA20.40 one. The T_g values for Zn tectosilicate glasses are lower than for any of the alkaline earth ones (as it has been also demonstrated by Figure V.14). This demonstrates that glasses are likely organized differently when Zn is incorporated into the aluminosilicate network in comparison to alkaline earth tectosilicates. The tendency of Zn to form edge-sharing units (as discussed above) together with high fractions of NBOs and AlO_5 , and a phase separation on top of it result in such low values of glass transition temperature.

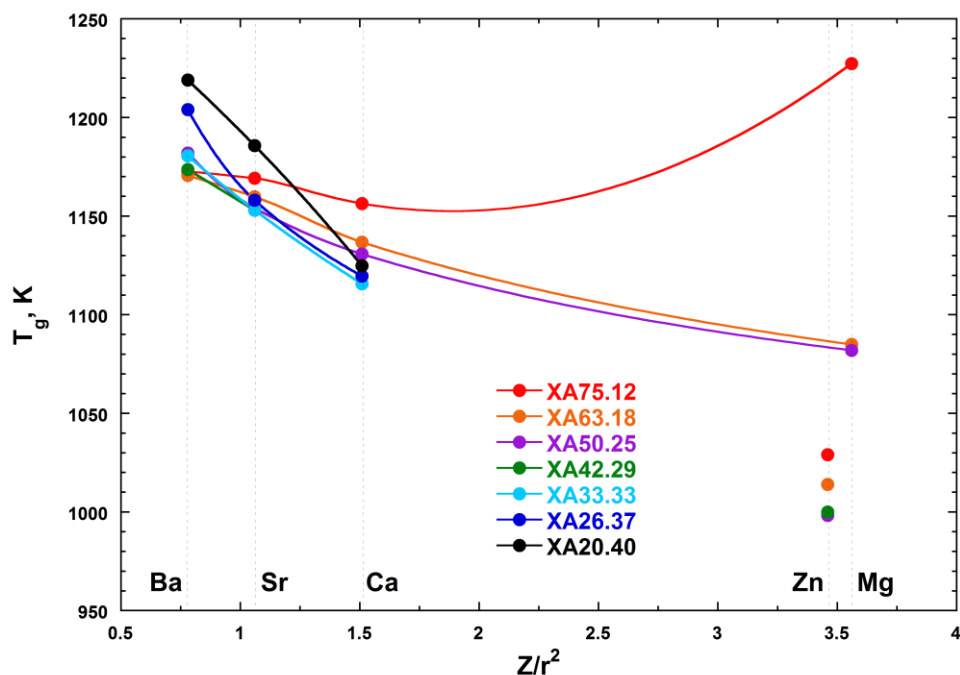


Figure V.15. Glass transition temperature as a function of the cation field strength (Z/r^2) for tectosilicate glasses in the ZAS ($X = Z$), MAS ($X = M$), CAS ($X = C$), SAS ($X = S$) and BAS ($X = B$) systems. Data for the MAS and CAS systems are from (Neuvill, 1992; Neuvill et al., 2004a). The lines connect alkaline earth compositions only and are a guide to the eye.

Section highlights

- Phase separation occurs in ZA75.12 glass and probably other silica-rich compositions.
- The fraction of five-coordinate Al species is higher in the ZAS tectosilicate glasses than in the alkaline earth ones. Such elevated amount of AlO_5 can be explained by the presence of Zn in edge-sharing configurations.
- Zn coordination in the tectosilicate glasses is around 5 and shows a slight tendency to increase under the substitution of SiO_2 by $ZnAl_2O_4$. The CN(cation-oxygen) increases in the following row: $Zn \approx Mg < Ca < Sr < Ba$.
- Depolymerized Q^n species are present even in theoretically fully polymerized tectosilicate glasses in the ZAS system. The low-frequency region of the Raman spectra diminishes significantly with decreasing SiO_2 content and becomes featureless.
- Glass transition temperatures of Zn tectosilicate glasses are lower than for corresponding alkaline earth ones, reflecting different organisation of the network of these glasses and the presence of high amount of NBOs, TBOs and

AlO_5 . For alkaline earth tectosilicates T_g drops down with increasing CFS as $\text{Ba} > \text{Sr} > \text{Ca} > \text{Mg}$. This rise in T_g can be due to the formation of percolation channels within the glass network.

2. Peralkaline domain (R = 3)

2.1. ^{27}Al and ^{29}Si NMR spectroscopy

As in the case of tectosilicate glasses, the ^{27}Al NMR spectra of Zn glasses along the join R = 3 differ from those of alkaline earth counterparts significantly (Figure V.16). The difference appears in the line width, population of high-coordinate Al and the maximum position of the main peak. All this indicates an increased disorder and different Al environment in the ZAS system in comparison to the SAS and BAS ones. The degree of disorder decreases in the row Zn – Sr – Ba demonstrating a correlation with the cation field strength as discussed before.

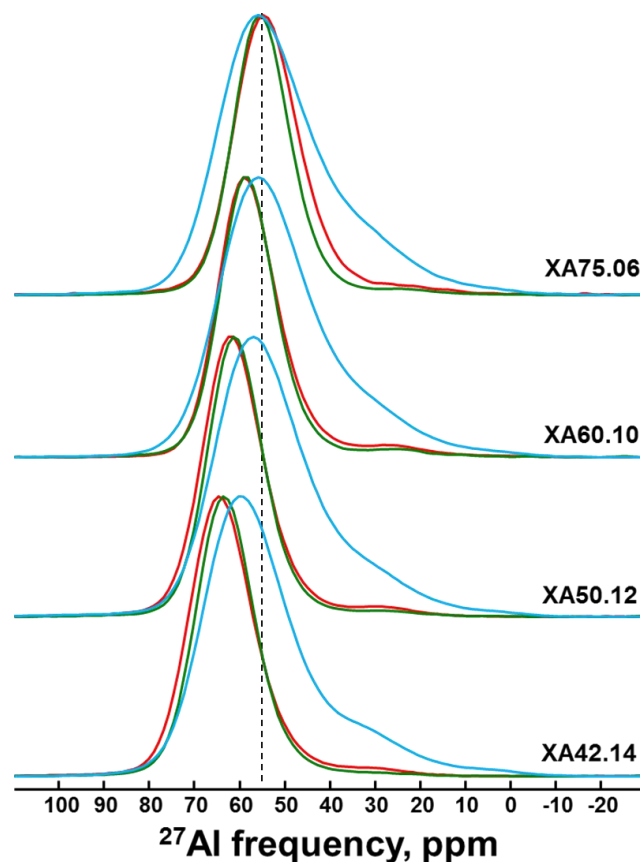


Figure V.16. ^{27}Al MAS NMR spectra of Zn (blue, X = Z), Sr (red, X = S) and Ba (green, X = B) glasses along the join R = 3. Silica content decreases from top to bottom.

The deconvolution of ^{27}Al NMR spectra of ZAS glasses on the join R = 3 is shown in Figure V.17. As in the case of NMR spectra of Zn tectosilicate glasses, it was made with assumption that the samples were homogeneous, even though it was demonstrated earlier that the silica-rich compositions are clearly biphasic. Actually, the spectra of phase-separated samples are the sum of the two spectra arising from each phase and hence it is very difficult – if not impossible on a 1D spectrum – to separate the two contributions.

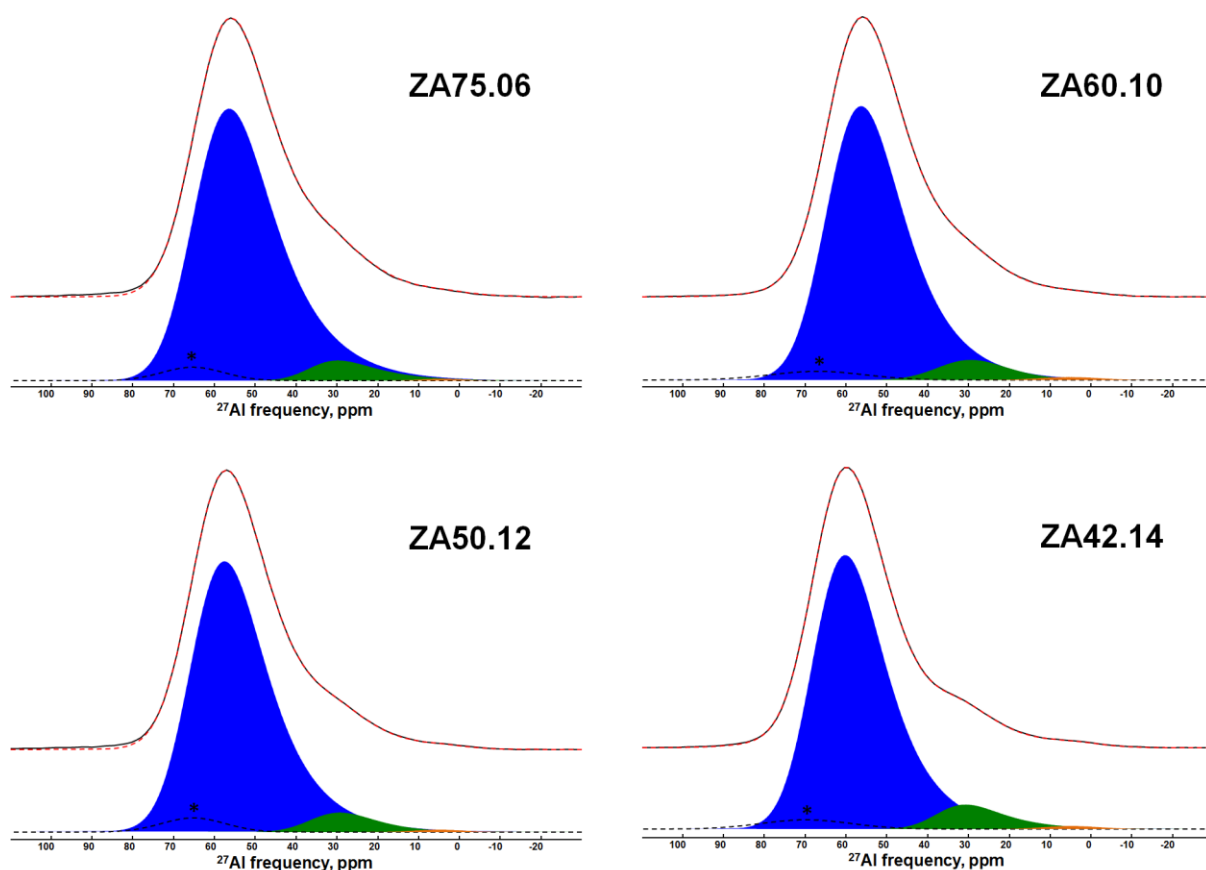


Figure V.17. Deconvolution of the ^{27}Al MAS NMR spectra of ZAS glasses along the join R = 3. Colour guide: blue – AlO_4 , green – AlO_5 , orange – AlO_6 , black dashed lines with an asterisk – spinning sidebands.

The chemical shift of four- and five-fold Al sites increases with decreasing SiO_2 content reflecting the Si/Al exchange in the second coordination sphere of aluminium atoms (Figure V.18). The $\delta_{iso}(\text{AlO}_4)$ changes almost linearly for Mg, Ca, Sr and Ba peralkaline glasses, while for glasses containing Zn a deviation at high SiO_2 content occurs. Similar deviation has been observed for silica-rich Zn compositions and was attributed to a phase separation (see Figure V.2). Interestingly, there is no such deviation for ZA60.10 composition that is also phase separated but in less than ZA75.06 degree. It could be caused by the use

of the least opalescent pieces of ZA60.10 glass for the NMR measurements. This indicates once again that for studying phase-separated glasses a more systematic approach is required.

Concerning the AlO_5 population, it increases from Ba to Mg according to increasing CFS. The exception is silica-rich Mg peralkaline glasses for which the fraction of five-coordinate Al reaches values comparable to those for other peralkaline glasses. For Zn glasses along the join $R = 3$, AlO_5 content stays around 6 % for compositions with 75 to 50 mol% of SiO_2 and increases slightly up to 7.6 % for ZA42.14 composition. At lower silica content (≤ 50 mol% of SiO_2) the fraction of AlO_5 is lower for Zn containing compositions than for analogous Mg ones. This demonstrates again, that for Zn and Mg cations comparable in size and CFS, the structure of host aluminosilicate matrix can be, nevertheless, different.

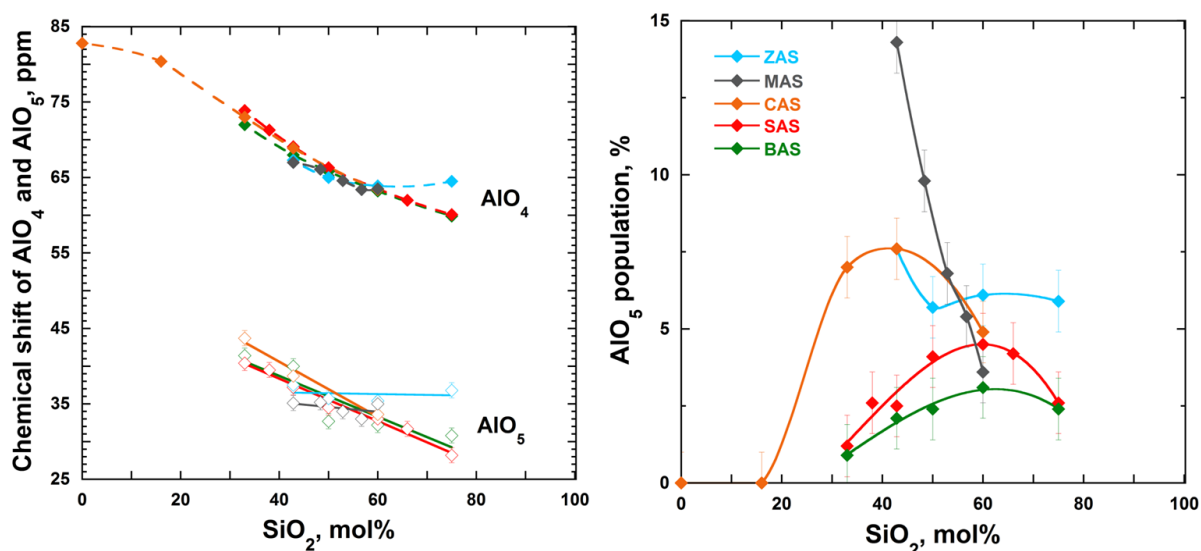


Figure V.18. *Left*: evolution of isotropic chemical shift (δ_{iso}) of AlO_4 and AlO_5 for glasses along the join $R = 3$ in the ZAS, MAS, CAS, SAS and BAS systems. If not visible, error bars are less than symbol's size. *Right*: AlO_5 population for glasses along the join $R = 3$. The lines are a guide to the eye. Color guide: blue – ZAS, grey – MAS, orange – CAS, red – SAS, green – BAS. Data for the MAS and CAS systems is from (Neuvillle et al., 2008, 2006, 2004b).

The phase separation observed for ZA75.06 and ZA60.10 glasses is clearly seen in their ^{29}Si NMR spectra (Figure V.19). In the spectrum of ZA75.06 glass two distinct peaks are observed. The one at lower δ_{iso} values is at the position of Q^4_0 units found in vitreous silica and possesses a similar shape. This is in agreement with TEM findings showed the presence of SiO_2 -like phase. Less pronounced in the spectrum of ZA60.10 glass, this phase is still present as indicated by a shoulder at the low δ_{iso} side. In general, the spectra of Zn

containing glasses are broader than those of Sr and Ba peralkaline glasses. This indicates a wider Q_m^n species distribution in these glasses in accordance with a higher degree of disorder expected in compositions with cations possessing elevated CFS. The line width of the spectra of glasses on the join $R = 3$ decreases in the row Zn – Sr – Ba. For the reason already discussed in previous chapters and taking into account phase separation occurring for at least half of ZAS compositions, no attempts to deconvolute the ^{29}Si NMR spectra of Zn aluminosilicate glasses along the join $R = 3$ were undertaken.

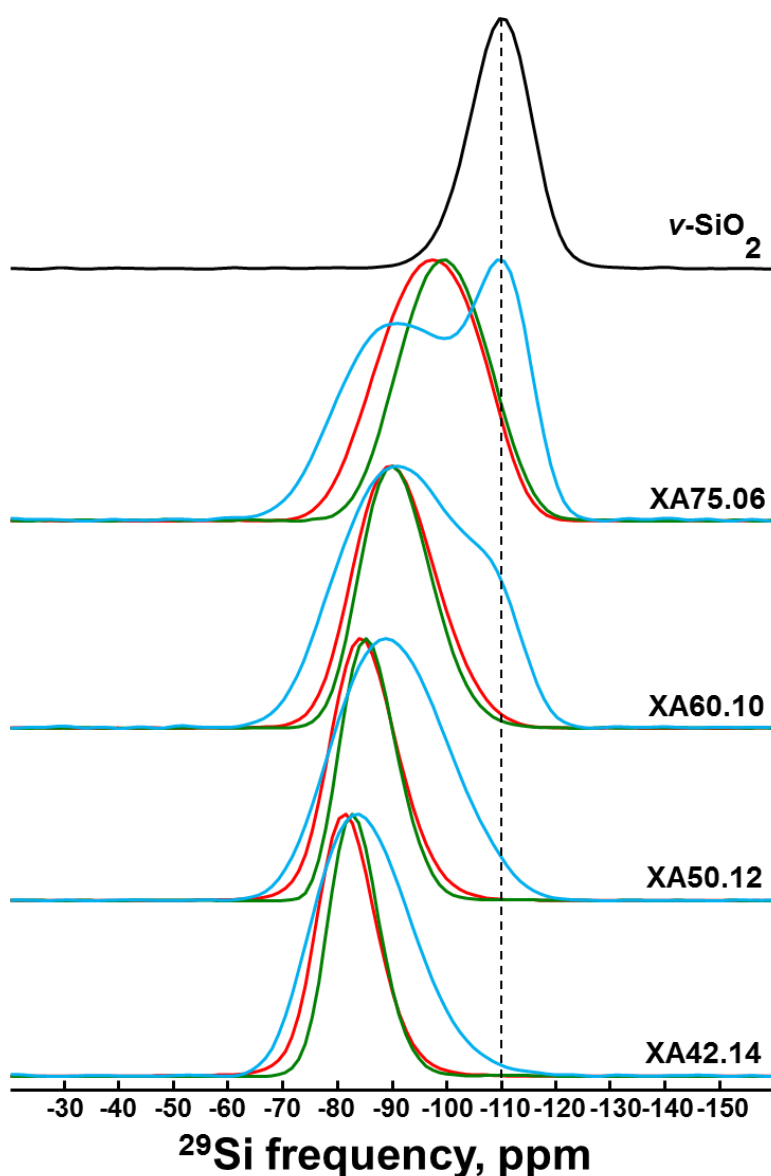


Figure V.19. ^{29}Si MAS NMR spectra of Zn (blue, X = Z), Sr (red, X = S) and Ba (green, X = B) peralkaline glasses. Silica content decreases from top to bottom.

2.2. Neutron diffraction

The first sharp diffraction peak in $S(q)$ shifts to higher q values and its intensity diminishes from ZA75.06 to ZA42.14 glass (Figure V.20). It has been discussed in previous section and in Chapter III and Chapter IV that such behaviour of the FSDP typically correlates with changes in rings statistics as seen by Raman spectroscopy.

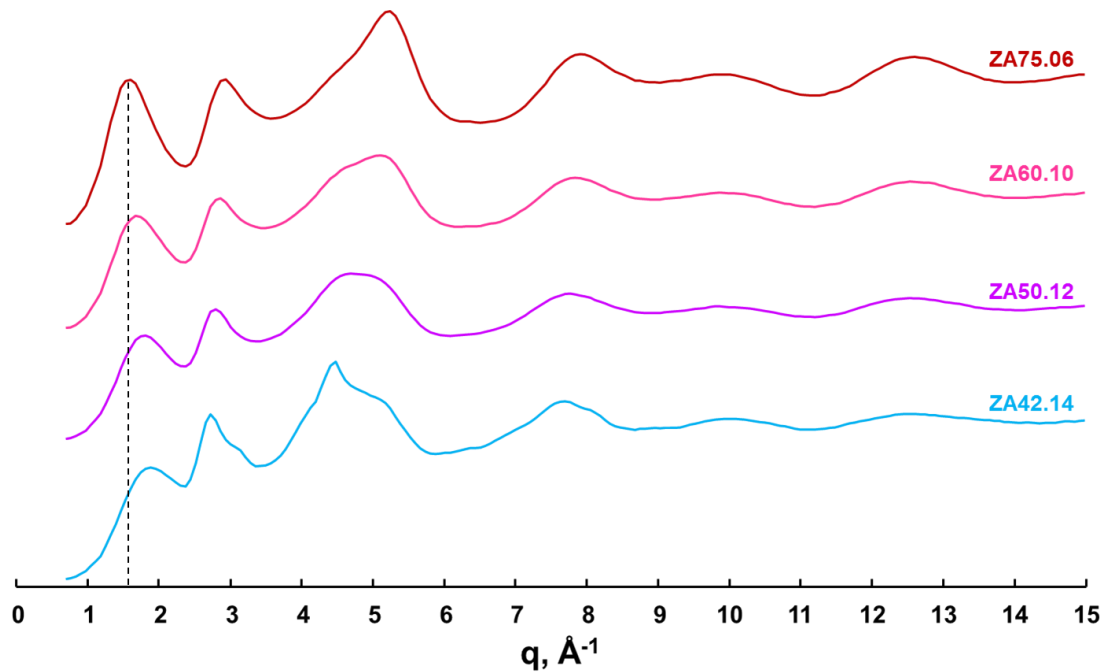


Figure V.20. Static structure factor, $S(q)$, of ZAS glasses along the join R = 3. Silica content decreases from top to bottom.

The first peak in the $g(r)$ moves to higher r values under the substitution of SiO_2 by $\text{Zn}_3\text{Al}_2\text{O}_6$ (Figure V.21). At the same time, a shoulder appearing at the high r side of the peak increases in intensity. As it has been shown in the previous section, while the main peak arises from Si-O and Al-O contributions, the shoulder is due to the Zn-O one.

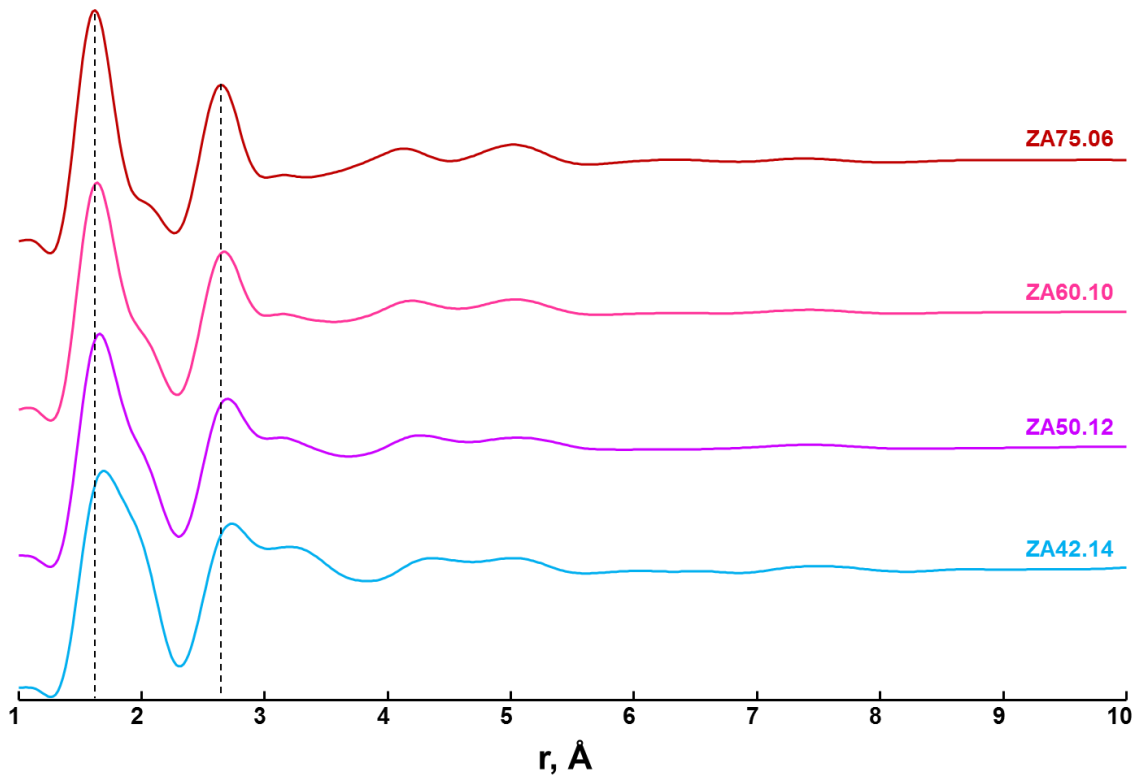


Figure V.21. Pair distribution function, $g(r)$, of ZAS glasses along the join $R = 3$. Silica content decreases from top to bottom.

Transforming $g(r)$ to $T(r)$ we deconvoluted the latter one as for Zn tectosilicate glasses. The results of the deconvolution are presented in Figure V.22. The average interatomic Zn-O distance and coordination number of Zn do not vary much with composition as seen from Table V.2 (all variations are within the error bars).

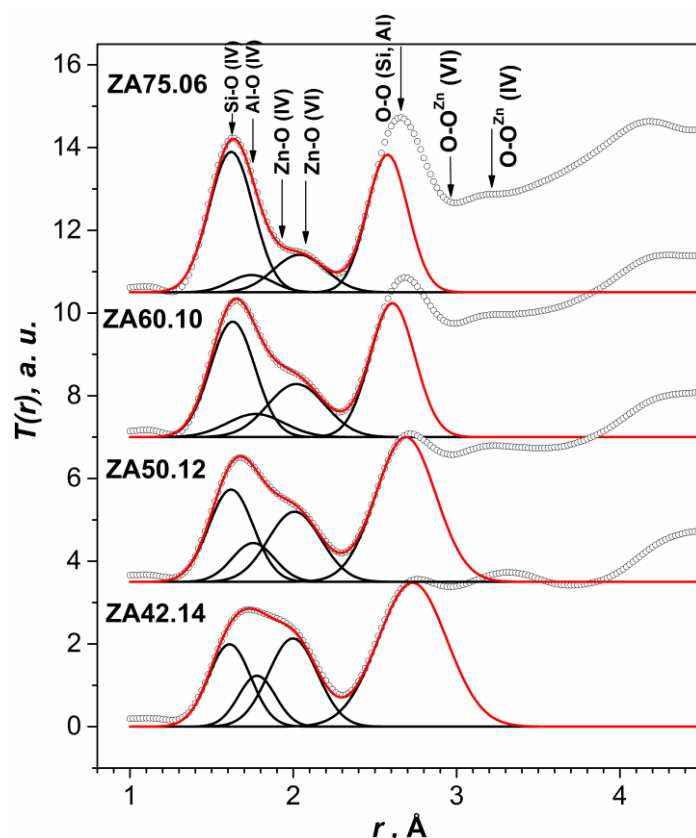


Figure V.22. Deconvolution of the first peak in $T(r)$ of four Zn aluminosilicate glasses along the join $R = 3$. Points are the experimental data, black lines are partial fits and red line is the total fit.

It has been reported for Mg peralkaline glass MA42.14 that the majority of magnesium atoms are in MgO_6 sites (Shimoda et al., 2007). Such octahedral coordination usually implies a network modifier role that cation plays in the glass network. However, (Guignard and Cormier, 2008) found the average coordination number of Mg around 5 in MA50.xx glasses (glasses with constant silica content, 50 mol%). The coordination number of Mg in peralkaline glasses is, therefore, comparable with that of Zn in analogous compositions.

Table V.2. Average Zn-O interatomic distances (r , in Å) and coordination number (CN) obtained from the deconvolution of the ND data for ZAS glasses along the join $R = 3$.

	ZA75.06	ZA60.10	ZA50.12	ZA42.14
$r(\pm 0.02)$	2.04	2.02	2.01	2.00
CN(± 0.5)	4.8	4.7	4.5	4.4

Interestingly, a peak corresponding to the O-O contributions in tetrahedral and octahedral Zn environment shifts slightly to higher r values with decreasing SiO_2 content (Figure V.22). This shift towards the O-O contribution in ZnO_4 sites reflects an overall

tendency of Zn glasses along the join R = 3 to form four-coordinate Zn with decreasing SiO₂ content. However, one should keep in mind the phase separation observed for silica-rich Zn compositions.

2.3. Raman spectroscopy

Raman spectra of ZAS glasses on the join R = 3 behave, in general, like the spectra of Zn tectosilicates under the substitution of SiO₂ (Figure V.23). The intensity of the low-frequency region drops down rapidly from ZA75.06 to ZA42.14 glass leaving it almost featureless. Here we also present a Raman spectrum of ZA33.17 composition that was completely crystallized except for some small pieces of glass-ceramic that were sufficiently big to record their individual spectrum. We cannot say that the glassy part is of theoretical composition but it seems that its spectrum fits well the overall trend so we present it here for comparison. In the spectrum of ZA50.12 glass one observes a broad band of low intensity at 230-250 cm⁻¹. All in all, as in the case of Zn tectosilicates, Raman spectra of ZAS glasses on the join R = 3 do not allow extracting qualitative information on the ring statistics. The only hint on the changes in the ring statistics comes from the ND data, where the shift of the FSDP in $S(q)$ suggests a decrease of the rings size.

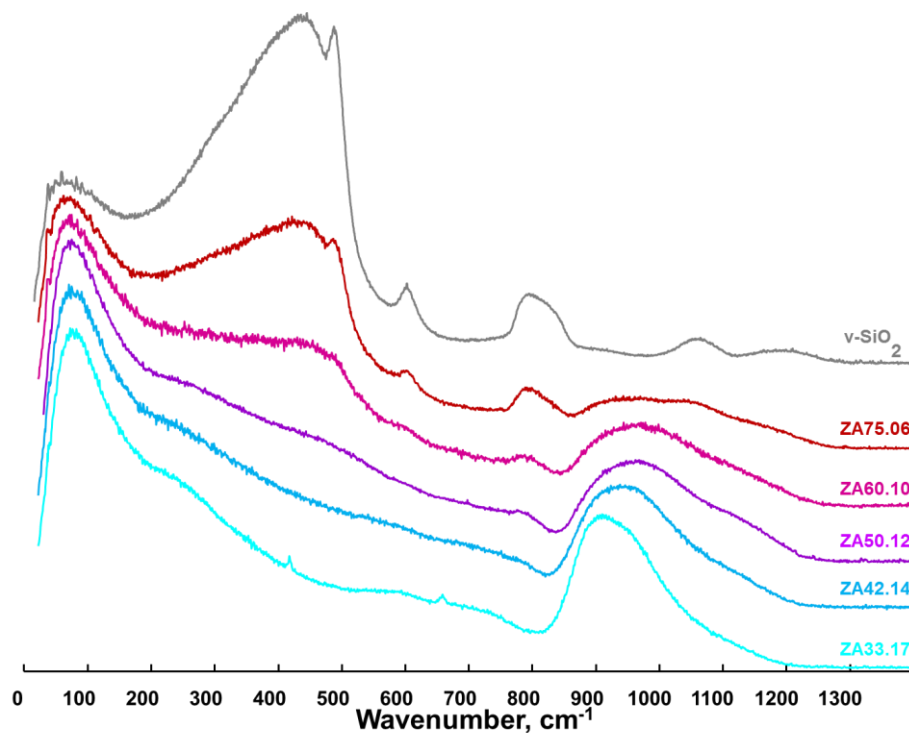


Figure V.23. Area normalized Raman spectra of ZAS glasses along the join R = 3. Silica content decreases from top to bottom.

The HF region of the Raman spectra is very wide with a long “tail” spreading to high-frequency end. This reflects the fact that ZA75.06 and ZA60.10 glasses are clearly phase-separated and the others could be too. We will not present here any deconvolution of the HF region since it will not be reliable due to the phase separation observed for ZAS glasses on the join $R = 3$.

2.4. Macroscopic properties

The density and molar volume curves for alkaline earth and Zn glasses along the join $R = 3$ behave in a similar way as those of the tectosilicate glasses (Figure V.24). Namely, both density and V_m increase with decreasing the CFS in the row Mg – Ca – Sr – Ba. For Ba peralkaline glasses we observe a slight drop in the V_m from 100 to 60 mol% of SiO_2 with further continuous rise of the curve at lower silica content. For Ca and Sr glasses along the join $R = 3$ a more important decrease of V_m occurs upon the substitution of SiO_2 . In both systems a plateau is reached at low silica content. However, the plateau in the SAS system occurs already at 50 mol% of SiO_2 , while in the CAS system it is around 40 mol% of SiO_2 . With further decreasing silica content the V_m in both systems does not change significantly. For Mg peralkaline glasses as well as for Zn containing ones the V_m decreases in a close-to-linear manner in the whole range of composition. Surprisingly, we do not observe any important deviations of the V_m of phase separated ZA75.06 and ZA60.10 compositions, like we did, for example, in the case of ZA75.12 glass. This means that molar volume is not very sensitive to a phenomenon such as a phase separation.

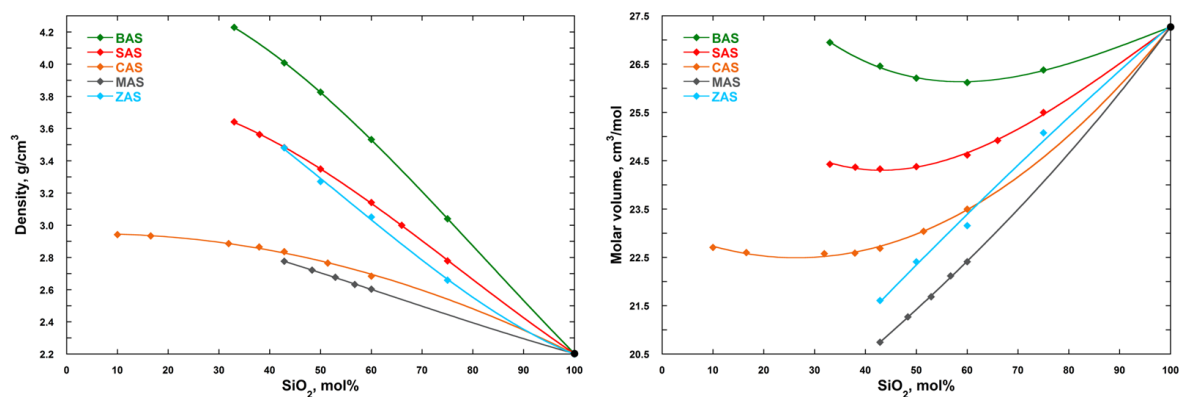


Figure V.24. Experimental densities (*left*) and calculated molar volumes (*right*) of glasses along the join $R = 3$ in the ZAS, MAS, CAS, SAS and BAS systems. Data for the MAS and CAS systems are from (Neuvill, 1992). The black filled circle corresponds to the density of vitreous silica taken from (Brückner, 1970). Error bars are less than the symbol size. The lines are a guide to the eye.

The drop of V_m observed in the silica-rich domain reflects the packing of the structure with introduction of $X_3Al_2O_6$ ($X = Zn, Mg, Ca, Sr$ or Ba) due to depolymerization of the glass network. For small Mg and Zn cations such packing continues with further substitution of SiO_2 since they can be easily accommodated by the glass network into the free volume available. For larger cations such as Ca, Sr and Ba the glass network adjusts itself depending on the cation that is introduced. As suggested by different slopes of the V_m curves in the silica-rich domain the ease of cation's accommodation falls down from Mg to Ba . Finally, at low silica content the structure of CAS and SAS glasses along the join $R = 3$ does not evolve much and introduction of $Ca_3Al_2O_6$ or $Sr_3Al_2O_6$ is not accompanied by significant changes in the glass network (only a minor increase in V_m is observed). For Ba peralkaline glasses, on the other hand, the network cannot accommodate huge barium cations without reorganizing itself. The increase of V_m in the row $Mg - Ca - Sr - Ba$ is in agreement with the increase of the coordination number from Mg to Ba .

The evolution of T_g for Zn and alkaline earth glasses on the join $R = 3$ is shown in Figure V.25. It seems that two different trends are observed for peralkaline glasses before and after 60 mol% of SiO_2 . At higher silica content glass transition temperature decreases in the row $Mg - Ca - Sr - Ba$ (if one extrapolates the curves of Mg and Ca to the silica-rich domain). At silica content lower than 60 mol% T_g decreases from Ba to Mg (if one extrapolates the curve of Ba to the silica-poor domain). Moreover, the T_g curve for Mg peralkaline glasses decreases continuously under the substitution of SiO_2 , while for the glasses in the CAS, SAS and BAS systems the curves start increasing with decreasing silica content. Furthermore, the slope of T_g curves increases in absolute value in the row $Ca - Sr - Ba$, implying that introduction of a larger cation causes greater changes of the glass network. The interpretation of this data for glasses on the join $R = 3$ is somewhat non-trivial since many factors must be taken into account: changes in the fraction of NBOs, presence of high-coordinate Al species, compacting of the glass network. One (but not the only) possible explanation for the observed T_g evolution could be the idea of percolation channels proposed above and suggesting that bigger cations would create larger channels producing a more pronounced increase in glass transition temperature in accordance with observations made in KAS and NAS systems (Le Losq et al., submitted).

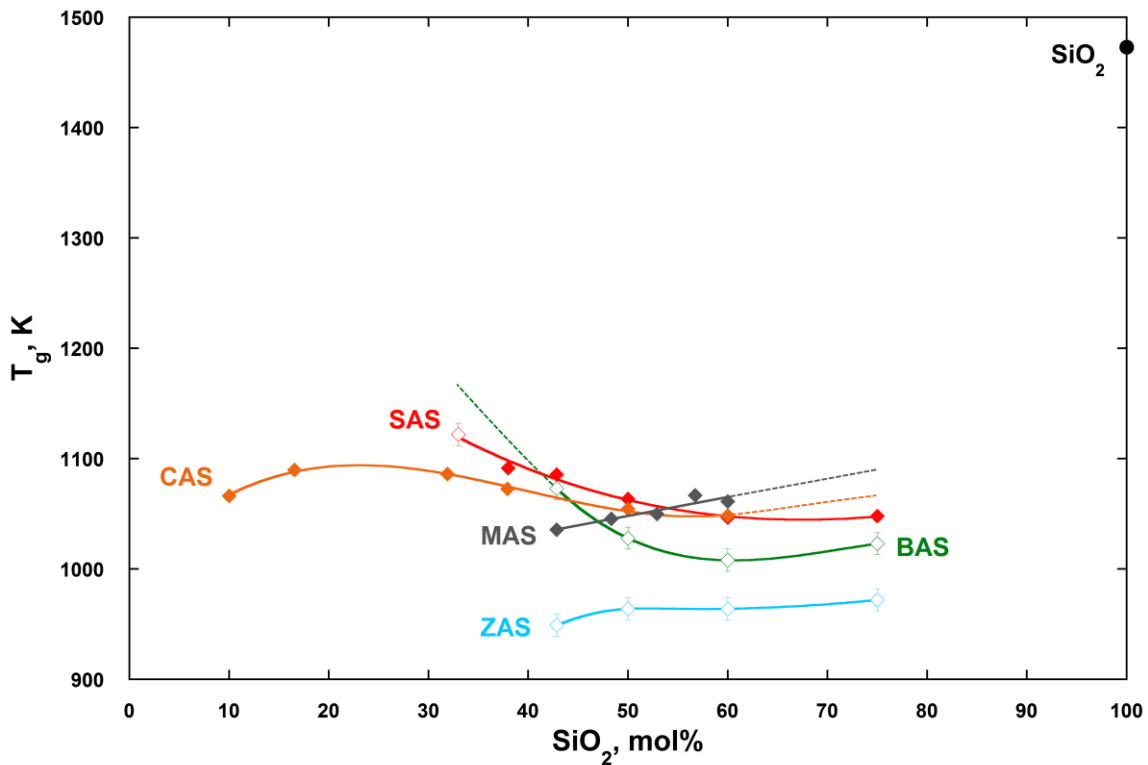


Figure V.25. Glass transition temperatures of the compositions along the join R = 3 in the ZAS, MAS, CAS, SAS and BAS systems. Filled symbols are T_g values extracted from viscosity data, open symbols are T_g values from DSC measurements. Data for the MAS and CAS systems are from (Neuville, 1992; Neuville et al., 2004a). The glass transition temperature of vitreous silica (black filled circle) is given for comparison (Mackenzie, 1963). If not visible error bars are less than the size of symbols. The dashed lines are extrapolation of the experimental data, the solid lines are a guide to the eye.

In Figure V.26 we plotted glass transition temperature of above discussed glasses as a function of the cation field strength. The estimation of the CFS we based on coordination numbers of the cations (available either from literature or from our own measurements) and using ionic radii from (Whittaker and Muntus, 1970), assuming that Zn and Mg are five-coordinate (Guignard and Cormier, 2008), Ca is in seven-fold coordination (Neuville et al., 2004a) and the coordination number of Sr and Ba are 8 and 9, respectively. Figure V.26 clearly demonstrates how the difference in glass transition temperature (ΔT_g) evolves in different series. For example, while T_g of CA60.10 is comparable to that of SA60.10 glass, with decreasing SiO₂ content glass transition temperature of Sr peralkaline glasses becomes higher and the ΔT_g for the two systems becomes more and more significant. At the same time, ΔT_g between Sr and Ba peralkaline glasses becomes less and less and might become comparable or even higher for BAS glasses at low silica content. Once again the T_g values for Zn containing glasses on the join R = 3 do not fit the overall trend indicating the structural

difference of these glasses compared to alkaline earth counterparts. This also probably points to the idea that the CFS is a notion too crude to fully account for the structural origins of such complex systems where many structural elements are at play (Al in various CN, Zn and Mg in various CN, presence of NBOs and TBOs, phase separation etc.).

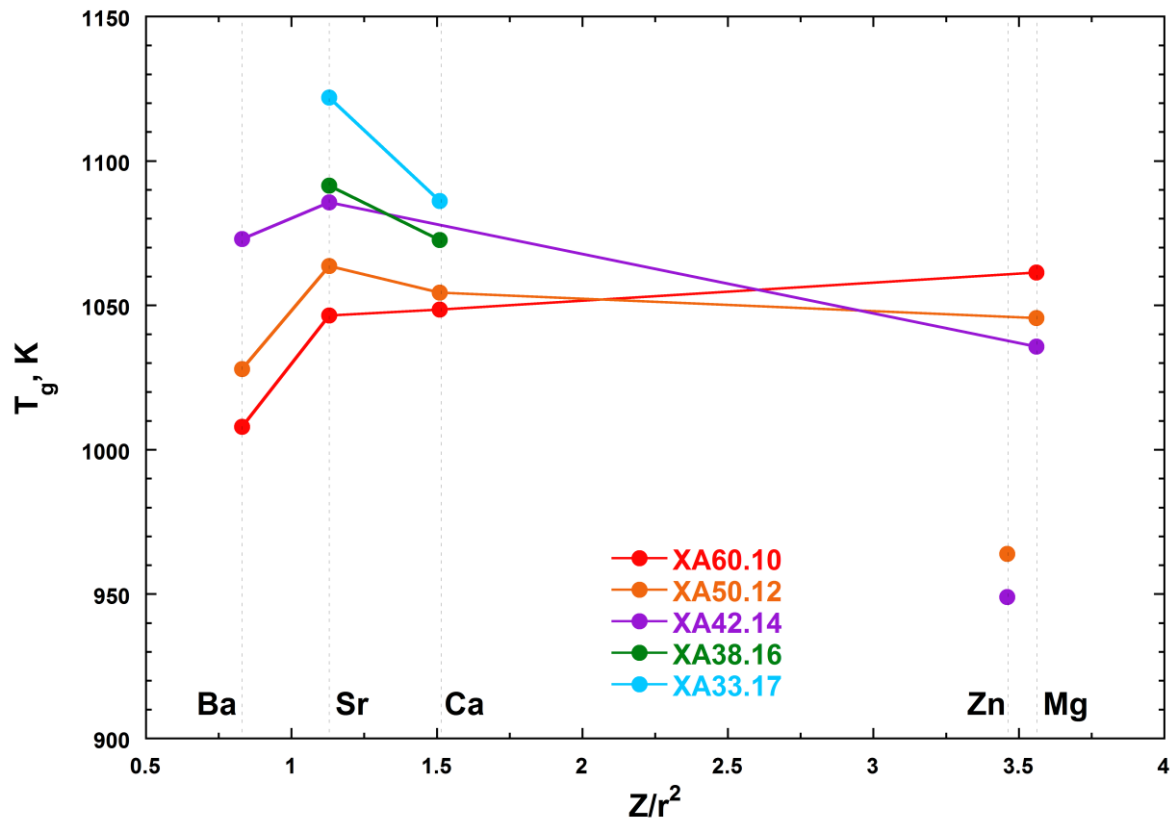


Figure V.26. Glass transition temperature as a function of the cation field strength (Z/r^2) for glasses along the join $R = 3$ in the ZAS ($X = Z$), MAS ($X = M$), CAS ($X = C$), SAS ($X = S$) and BAS ($X = B$) systems. Data for the MAS and CAS systems are from (Neuvill, 1992; Neuvill et al., 2004a). The lines connect alkaline earth compositions only and are a guide to the eye.

Section highlights

- Phase separation is present in at least two silica-rich ZAS glasses on the join $R = 3$, ZA75.06 and ZA60.10.
- The average coordination number of Zn in glasses on the join $R = 3$ is 5 and similar to the CN(Zn-O) in tectosilicate compositions. The CN(cation-oxygen) increases in the following row: $Zn \approx Mg < Ca < Sr < Ba$.
- The low-frequency region of the Raman spectra diminishes significantly with decreasing SiO_2 content as in the case of tectosilicate glasses.

- Glass transition temperatures of ZAS glasses on the join R = 3 are lower than for corresponding alkaline earth ones. For compositions with more than 60 mol% of SiO₂ T_g changes as following: Mg > Ca > Sr > Ba > Zn. At lower silica content T_g decreases as for tectosilicate glasses, i.e. Ba > Sr > Ca > Mg > Zn.
- Molar volume increases in the row Mg < Ca < Sr < Ba concurrently with a rise of coordination number of the cations.

3. Conclusion

In this chapter we presented results of studies carried out on Zn aluminosilicate glasses along two joins R = 1 and 3. Our results were compared with the data obtained on aluminosilicate glasses of alkaline earth elements. Our findings showed that the structure and macroscopic properties of aluminosilicate glasses with M²⁺ cations are dependent on several factors. They are Al/Si ratio, ratio R = MO/Al₂O₃ (where M = Zn, Mg, Ca, Sr or Ba) and the nature of non-network forming cation. The last factor was chosen for the discussion as affecting the aluminosilicate network the most.

For compositionally identical alkaline earth aluminosilicates the degree of disorder increases with increasing the CFS as inferred from the ²⁷Al and ²⁹Si NMR line width analysis. This increase of disorder is caused by the appearance of elevated fraction of high-coordinate AlO_x species as well as larger distribution of Q_mⁿ species. At the same time, density and molar volume decrease in the row Ba – Sr – Ca – Mg following a more compact packing of the network caused by the drop of the CN(cation-oxygen). On the tectosilicate join (R = 1) T_g of alkaline earth aluminosilicates decreases with increasing the CFS. On the peralkaline join (R = 3), however, T_g decreases from Mg to Ba for silica-rich (> 60 mol% of SiO₂) glasses and inverts for silica-poor compositions following a trend observed for glasses on the join R = 1.

For both tectosilicate and peralkaline glasses of Ca, Sr and Ba we observed an augmentation glass transition temperature with decreasing silica content. This augmentation was correlated to formation of large cages and/or percolation channels accompanied by the formation of low-membered rings as suggested by Raman data.

Zn-containing aluminosilicate glasses are a particular case. Firstly, silica-rich ZAS glasses are clearly phase-separated which also finds support in literature. Secondly, although Zn^{2+} is comparable with Mg^{2+} (both possess high CFS and low coordination numbers), ZAS glasses, nevertheless, are likely organized in a different way. It was proposed that Zn cations could be partially incorporated in edge-sharing units provoking the formation of AlO_5 species.

Bibliography

- Allwardt, J.R., Stebbins, J.F., Schmidt, B.C., Frost, D.J., Withers, A.C., Hirschmann, M.M., 2005. Aluminum coordination and the densification of high-pressure aluminosilicate glasses. *Am. Mineral.* 90, 1218–1222. doi:10.2138/am.2005.1836
- Arora, A., Singh, K., Pandey, O.P., 2011. Thermal, structural and crystallization kinetics of SiO₂–BaO–ZnO–B₂O₃–Al₂O₃ glass samples as a sealant for SOFC. *Int. J. Hydrogen Energy* 36, 14948–14955. doi:10.1016/j.ijhydene.2011.03.036
- Brückner, R., 1970. Properties and structure of vitreous silica. I. *J. Non. Cryst. Solids* 5, 123–175. doi:10.1016/0022-3093(70)90190-0
- Calas, G., Cormier, L., Galois, L., Jollivet, P., 2002. Structure–property relationships in multicomponent oxide glasses. *Comptes Rendus Chim.* 5, 831–843. doi:10.1016/S1631-0748(02)01459-5
- Cormier, L., Ghaleb, D., Neuville, D.R., Delaye, J.-M., Calas, G., 2003. Chemical dependence of network topology of calcium aluminosilicate glasses: a computer simulation study. *J. Non. Cryst. Solids* 332, 255–270. doi:10.1016/j.jnoncrysol.2003.09.012
- Cormier, L., Neuville, D.R., Calas, G., 2005. Relationship Between Structure and Glass Transition Temperature in Low-silica Calcium Aluminosilicate Glasses: the Origin of the Anomaly at Low Silica Content. *J. Am. Ceram. Soc.* 88, 2292–2299. doi:10.1111/j.1551-2916.2005.00428.x
- Duan, X.L., Yuan, D.R., Xu, D., Lu, M.K., Wang, X.Q., Sun, Z.H., Wang, Z.M., Sun, H.Q., Lu, Y.Q., 2003. Preparation and characterization of Co²⁺-doped ZnO–Al₂O₃–SiO₂ glass-ceramics by the sol–gel method. *Mater. Res. Bull.* 38, 705–711. doi:10.1016/S0025-5408(03)00009-6
- Ehrt, D., Vu, H.T., Herrmann, A., Volksch, G., 2008. Luminescent ZnO–Al₂O₃–SiO₂ Glasses and Glass Ceramics. *Adv. Mater. Res.* 39–40, 231–236. doi:10.4028/www.scientific.net/AMR.39-40.231
- Florian, P., Sadiki, N., Massiot, D., Coutures, J.P., 2007. ²⁷Al NMR Study of the Structure of

- Lanthanum- and Yttrium-Based Aluminosilicate Glasses and Melts. *J. Phys. Chem. B* 111, 9747–9757. doi:10.1021/jp072061q
- Goel, A., Kapoor, S., Tilocca, A., Rajagopal, R.R., Ferreira, J.M.F., 2013. Structural role of zinc in biodegradation of alkali-free bioactive glasses. *J. Mater. Chem. B* 1, 3073. doi:10.1039/c3tb20163e
- Greaves, G.N., Ngai, K.L., 1995. Reconciling ionic-transport properties with atomic structure in oxide glasses. *Phys. Rev. B* 52, 6358–6380. doi:10.1103/PhysRevB.52.6358
- Guignard, M., Cormier, L., 2008. Environments of Mg and Al in MgO–Al₂O₃–SiO₂ glasses: A study coupling neutron and X-ray diffraction and Reverse Monte Carlo modeling. *Chem. Geol.* 256, 111–118. doi:10.1016/j.chemgeo.2008.06.008
- Iftekhhar, S., Grins, J., Gunawidjaja, P.N., Edén, M., 2011. Glass Formation and Structure-Property-Composition Relations of the RE₂O₃-Al₂O₃-SiO₂ (RE=La, Y, Lu, Sc) Systems. *J. Am. Ceram. Soc.* 94, 2429–2435. doi:10.1111/j.1551-2916.2011.04548.x
- Kaur, G., Sharma, P., Kumar, V., Singh, K., 2012. Assessment of in vitro bioactivity of SiO₂-BaO-ZnO-B₂O₃-Al₂O₃ glasses: An optico-analytical approach. *Mater. Sci. Eng. C* 32, 1941–1947. doi:10.1016/j.msec.2012.05.034
- Kohn, S.C., Schofield, P.F., 1994. The importance of melt composition in controlling trace-element behaviour: an experimental study of Mn and Zn partitioning between forsterite and silicate melts. *Chem. Geol.* 117, 73–87. doi:10.1016/0009-2541(94)90122-8
- Le Caër, G., Brand, R.A., 1998. General models for the distributions of electric field gradients in disordered solids. *J. Phys. Condens. Matter* 10, 10715–10774. doi:10.1088/0953-8984/10/47/020
- Le Losq, C., 2012. Rôle Des Éléments Alcalins Et De l'Eau Sur Les Propriétés Et La Structure Des Aluminosilicates Fondus Et Vitreux: Implications Volcanologiques. Université Paris Diderot (Paris 7).
- Lee, C.-T. a, Luffi, P., Le Roux, V., Dasgupta, R., Albarède, F., Leeman, W.P., 2010. The redox

- state of arc mantle using Zn/Fe systematics. *Nature* 468, 681–685.
doi:10.1038/nature09617
- Lee, S.K., Stebbins, J.F., 2002. Extent of intermixing among framework units in silicate glasses and melts. *Geochim. Cosmochim. Acta* 66, 303–309. doi:10.1016/S0016-7037(01)00775-X
- Lee, S.K., Stebbins, J.F., 2000. Al–O–Al and Si–O–Si sites in framework aluminosilicate glasses with Si/Al=1: quantification of framework disorder. *J. Non. Cryst. Solids* 270, 260–264. doi:10.1016/S0022-3093(00)00089-2
- Lou, Y., Li, D., Li, Z., Jin, S., Chen, X., 2015. Unidirectional thermal expansion in edge-sharing BO₄ tetrahedra contained KZnB₃O₆. *Sci. Rep.* 5, 10996. doi:10.1038/srep10996
- Mackenzie, J.D., 1963. High-Pressure Effects on Oxide Glasses: II, Subsequent Heat Treatment. *J. Am. Ceram. Soc.* 46, 470–476. doi:10.1111/j.1151-2916.1963.tb13777.x
- McMillan, P.F., Grzechnik, A., Chotalla, H., 1998. Structural characterization of SiO₂–CsAlO₂ and SiO₂–RbAlO₂ glasses. *J. Non. Cryst. Solids* 226, 239–248. doi:10.1016/S0022-3093(98)00416-5
- Mizoguchi, K., Okamoto, K., Suginozawa, Y., 1982. Oxygen Coordination of Al³⁺ Ion in Several Silicate Melts Studied by Viscosity Measurements. *J. Japan Inst. Met.* 46, 1055–1060.
- Murdoch, J.B., Stebbins, J.F., Carmichael, I.S.E., 1985. High-resolution ²⁹Si NMR study of silicate and aluminosilicate glasses: the effect of network-modifying cations. *Am. Mineral.* 70, 332–343.
- Mysen, B.O., Virgo, D., Seifert, F.A., 1982. The structure of silicate melts: Implications for chemical and physical properties of natural magma. *Rev. Geophys. Sp. Phys.* 20, 353. doi:10.1029/RG020i003p00353
- Navrotsky, A., Geisinger, K.L., McMillan, P., Gibbs, G. V., 1985. The tetrahedral framework in glasses and melts - inferences from molecular orbital calculations and implications for structure, thermodynamics, and physical properties. *Phys. Chem. Miner.* 11, 284–298. doi:10.1007/BF00307406

- Neumann, H., 1949. Notes on the mineralogy and geochemistry of zinc. *Mineral. Mag.* 28, 575–581.
- Neuvill, D.R., 1992. Etude des propriétés thermodynamiques et rhéologiques des silicates fondus.
- Neuvill, D.R., Cormier, L., Flank, A.-M., Briois, V., Massiot, D., 2004a. Al speciation and Ca environment in calcium aluminosilicate glasses and crystals by Al and Ca K-edge X-ray absorption spectroscopy. *Chem. Geol.* 213, 153–163.
doi:10.1016/j.chemgeo.2004.08.039
- Neuvill, D.R., Cormier, L., Massiot, D., 2006. Al coordination and speciation in calcium aluminosilicate glasses: Effects of composition determined by ²⁷Al MQ-MAS NMR and Raman spectroscopy. *Chem. Geol.* 229, 173–185. doi:10.1016/j.chemgeo.2006.01.019
- Neuvill, D.R., Cormier, L., Massiot, D., 2004b. Al environment in tectosilicate and peraluminous glasses: A ²⁷Al MQ-MAS NMR, Raman, and XANES investigation. *Geochim. Cosmochim. Acta* 68, 5071–5079. doi:10.1016/j.gca.2004.05.048
- Neuvill, D.R., Cormier, L., Montouillout, V., Florian, P., Millot, F., Rifflet, J.-C., Massiot, D., 2008. Structure of Mg- and Mg/Ca aluminosilicate glasses: ²⁷Al NMR and Raman spectroscopy investigations. *Am. Mineral.* 93, 1721–1731. doi:10.2138/am.2008.2867
- Neuvill, D.R., Mysen, B.O., 1996. Role of aluminium in the silicate network: In situ, high-temperature study of glasses and melts on the join SiO₂-NaAlO₂. *Geochim. Cosmochim. Acta* 60, 1727–1737. doi:10.1016/0016-7037(96)00049-X
- Novikov, A.N., Neuvill, D.R., Hennem, L., Gueguen, Y., Thiaudiere, D., Charpentier, T., Florian, P., 2017. Al and Sr environment in tectosilicate glasses and melts: Viscosity, Raman and NMR investigation. *Chem. Geol.* 461, 115–127.
doi:10.1016/j.chemgeo.2016.11.023
- Rabukhin, A.I., 1999. Structural interpretation of concentration dependences of molar volume of glasses in R₂O-SiO₂ and RO-SiO₂ systems. *Glas. Ceram.* 56, 339–342.
doi:10.1007/BF02681337

- Rosenthal, A.B., Garofalini, S.H., 1987. Structural Role of Zinc Oxide in Silica and Soda-Silica Glasses. *J. Am. Ceram. Soc.* 70, 821–826. doi:10.1111/j.1151-2916.1987.tb05634.x
- Rosenthal, A.B., Garofalini, S.H., 1986. Molecular dynamics simulation of amorphous zinc silicate. *J. Non. Cryst. Solids* 87, 254–262. doi:10.1016/S0022-3093(86)80081-3
- Seifert, F.A., Mysen, B.O., Virgo, D., 1982. Three-dimensional network structure of quenched melts (glass) in the systems SiO₂-NaAlO₂, SiO₂-CaAl₂O₄ and SiO₂-MgAl₂O₄. *Am. Mineral.* 67, 696–717.
- Shimbo, M., 1987. Thermal Stability and Acid Resistivity of Glasses Based on ZnO-Al₂O₃-SiO₂. *J. Am. Ceram. Soc.* 70, C-101-C-102. doi:10.1111/j.1151-2916.1987.tb05013.x
- Shimoda, K., Tobu, Y., Hatakeyama, M., Nemoto, T., Saito, K., 2007. Structural investigation of Mg local environments in silicate glasses by ultra-high field 25Mg 3QMAS NMR spectroscopy. *Am. Mineral.* 92, 695–698. doi:10.2138/am.2007.2535
- Swansbury, L.A., Mountjoy, G., 2017. A fully tetrahedral and highly corner-sharing network model of ZnCl₂ glass and its comparison to SiO₂ glass. *J. Chem. Phys.* 147, 44502. doi:10.1063/1.4995248
- Thompson, L.M., Stebbins, J.F., 2012. Non-stoichiometric non-bridging oxygens and five-coordinated aluminum in alkaline earth aluminosilicate glasses: Effect of modifier cation size. *J. Non. Cryst. Solids* 358, 1783–1789. doi:10.1016/j.jnoncrysol.2012.05.022
- Van Tran, T.T., Dung Cao, T.M., Lam, Q.V., Le, V.H., 2017. Emission of Eu³⁺ in SiO₂-ZnO glass and SiO₂-SnO₂ glass-ceramic: Correlation between structure and optical properties of Eu³⁺ ions. *J. Non. Cryst. Solids* 459, 57–62. doi:10.1016/j.jnoncrysol.2016.12.040
- Wallenberger, F.T., Brown, S.D., Onoda, G.Y., 1993. ZnO-modified high modulus glass fibers. *J. Non. Cryst. Solids* 152, 279–283. doi:10.1016/0022-3093(93)90263-W
- Whittaker, E.J.W., Muntus, R., 1970. Ionic radii for use in geochemistry. *Geochim. Cosmochim. Acta* 34, 945–956. doi:10.1016/0016-7037(70)90077-3
- Xiang, Y., Du, J., Skinner, L.B., Benmore, C.J., Wren, A.W., Boyd, D.J., Towler, M.R., 2013. Structure and diffusion of ZnO–SrO–CaO–Na₂O–SiO₂ bioactive glasses: a combined

high energy X-ray diffraction and molecular dynamics simulations study. RSC Adv. 3, 5966. doi:10.1039/c3ra23231j

Yoo, S., Paek, U.-C., Han, W.-T., 2003. Development of a glass optical fiber containing ZnO–Al₂O₃–SiO₂ glass-ceramics doped with Co²⁺ and its optical absorption characteristics. J. Non. Cryst. Solids 315, 180–186. doi:10.1016/S0022-3093(02)01425-4

Yoo, S., Paek, U.-C., Han, W.-T., 2002. Optical properties of the optical fiber containing Co²⁺ doped ZnO–Al₂O₃–SiO₂ glass-ceramics. J. Non. Cryst. Solids 303, 291–295. doi:10.1016/S0022-3093(02)01041-4

General conclusion and perspectives

Three ternary systems (SAS, BAS and ZAS) have been investigated during this PhD thesis. The main goals were the elaboration and characterization of previously poorly studied Sr, Ba and Zn aluminosilicate glasses. A systematic study has been carried out on glasses and in some cases on melts with various MO/Al_2O_3 ($M = Sr, Ba, Zn$) and SiO_2/Al_2O_3 ratios. The compositions studied here cover a significant part of the ternary diagrams (from silicates to peraluminous glasses, from silica-poor to silica-rich compositions) and allowed expanding our knowledge of the vitrification domains in these systems. In the ZAS system, for example, a phase separation has been clearly evidenced for silica-rich compositions. This phenomenon requires further thorough investigation. Our preliminary results made in this system are, on the one hand, only a superficial touch allowing us seeing the directions for further experiments. On the other hand, one of these directions may lead to new materials taking advantage of the phase separation.

In order to obtain information on the structure and macroscopic properties of SAS, BAS and ZAS glasses, a multi-technique approach has been implemented. Such approach allows having a broad (everything is relative!) view on the systems and finding nano- to microscopic origins of macroscopic properties. The techniques used during this thesis probe short- (NMR, ND) to medium-range (Raman) scale and among the properties studied were density, viscosity and glass transition temperature. Some valuable hints have also come from the side of MD simulations performed by our collaborators.

Our studies have shown the complexity of the systems, a strong departure from the “theoretical” structure of the glass network. For example, for tectosilicate compositions, one would expect a fully polymerized aluminosilicate network with corner-sharing tetrahedral units in the whole range of silica contents. However, our findings indicate the presence of AlO_5 species (its fraction rises with increasing the cation field strength) and the simulations suggest the existence of non-bridging and three-coordinate oxygens. For Zn aluminosilicate glasses, the edge-sharing ZnO_x species were suspected to produce the observed elevated fraction of high-coordinate AlO_x species. Therefore, the whole picture is more complex than it would be anticipated.

The data resulting from this thesis provides a better understanding of the changes in the structure and macroscopic properties of the aluminosilicate glasses produced by

variations in $\text{MO}/\text{Al}_2\text{O}_3$ or $\text{SiO}_2/\text{Al}_2\text{O}_3$, or by the nature of non-network forming cation. Nevertheless, this work cannot answer all the questions raised by the present study. For this, further investigations, more focused on something particular are definitely required. Among the things to do as we can see it now, there are:

- Treatment of already acquired XRD and XAS data (Sr K-edge) for glasses and melts to have a deeper understanding of what happens on the atomic scale. Additionally, to shed light on the local environment of Ba and Zn in the corresponding glasses and melts, it is necessary to carry out XAS experiments at the edges of these elements. This would help to see if the distribution of non-network forming cations is heterogeneous, whether the edge-sharing occurs for cations polyhedra etc.
- Preparation of glass samples enriched in ^{29}Si and/or ^{17}O for NMR experiments. It would allow performing some experiments sensitive for isotopic abundance. For example, to see the correlations between Al and Si atoms or connecting preferences of non-bridging oxygens and so on. Such isotopic enrichment is particularly interesting for high-temperature NMR measurements that can access melts dynamics and the average speciation of probed atoms.
- A powerful combination would be the use of two complementary methods – VV/VH Raman and infrared spectroscopy – to observe and make sense of active or inactive in each method bands. This combination would be very useful for a proper assessment of two bands in the low-frequency region of the Raman spectra of Sr/Ba silicate and peralkaline glasses.
- A thorough investigation of the phase separation phenomenon occurring in the ZAS system. It would be really nice, first of all, check all the available compositions for phase separation and identify the phases. Secondly, to study the effect of different factors (such as quenching rate, for instance) on the degree of phase separation, on the size of phase-separated domains etc. Thirdly, to try to crystallize phase-separated glasses under the controlled conditions. It might lead to some new materials with interesting properties (e.g., transparent ceramics) or to the discovery of new solid solutions in the system. Our preliminary DSC and HT XRD data indicate a set of crystallization events

occurring under the heating of ZAS glasses. Thus, controlling the annealing temperature we will be able to obtain various ceramics/glass-ceramics.

Annex I

Sr tectosilicate glasses (Chemical Geology)



Al and Sr environment in tectosilicate glasses and melts: Viscosity, Raman and NMR investigation

Alexey N. Novikov^{a,b,*}, Daniel R. Neuville^{b,**}, Louis Hennem^a, Yann Gueguen^c, Dominique Thiaudière^d, Thibault Charpentier^e, Pierre Florian^a

^a CEMHTI UPR3079 CNRS, Univ. Orléans, F-45071 Orléans, France

^b IPGP UMR7154 CNRS, Géomatériaux, Paris Sorbonne Cité, 75005 Paris, France

^c IPR UMR UR1-CNRS 6251, Université de Rennes 1, 35042 Rennes, France

^d Synchrotron SOLEIL, 91192 Gif-sur-Yvette, France

^e NIMBE, CEA, CNRS, Université Paris-Saclay, CEA Saclay, 91191 Gif-sur-Yvette cedex, France

ARTICLE INFO

Article history:

Received 3 March 2016

Received in revised form 20 October 2016

Accepted 16 November 2016

Available online 20 November 2016

Keywords:

Strontium glasses

Aluminosilicates

Viscosity

Configurational entropy

Five-fold aluminium

Structure

ABSTRACT

Structure and properties of SrO-Al₂O₃-SiO₂ glasses and melts were investigated along the tectosilicate join (SrO/Al₂O₃ = 1), varying the amount of silica. The structure of the glasses was studied by means of various spectroscopic techniques: Raman, ²⁷Al NMR and XAS at the Sr K-edge. Raman spectroscopy revealed that the fraction of high-membered tetrahedral rings diminishes upon substitution of SiO₂ by SrAl₂O₄ favouring the formation of low-membered rings. Sr K-edge XANES shows that the strontium coordination number is around 9, based on the spectrum similarity with the one obtained for crystalline strontianite. ²⁷Al NMR spectroscopy indicates the presence of four- and five-coordinated aluminium the latter being found in small quantities (<5%), i.e. smaller than for analogous Mg- and Ca-based aluminosilicate glasses. A minimum in *T_g* is found when the AlO₅ content is maximum, both in Sr and Ca aluminosilicates. This fact indicates the importance of minor species such as five-fold aluminium in activating viscous flow, similarly to what has been proposed for five-fold silicon by Farnan and Stebbins (1994). Increase of *T_g* at low silica content was correlated to a decrease in AlO₅ content as well as to a decrease of a number of different structural units and, as a consequence, an ordering of the system.

© 2016 Elsevier B.V. All rights reserved.

1. Introduction

Strontium is an element whose abundance in Earth's crust is at the level of 300–400 ppm (Turekian and Kulp, 1956; Turekian and Wedepohl, 1961; Taylor, 1964; Rudnick and Gao, 2003). In earth science, strontium can be used as a Sr/Rb geochronometer, for studying the petrogenesis of igneous rocks and for tracing weathering processes (Moorbath et al., 1977; Capo et al., 1998). It is possible to date rocks formation by measuring the ratio of non-radiogenic ⁸⁶Sr to radiogenic ⁸⁷Sr (resulting from the radioactive decay of ⁸⁷Rb). But Sr and Rb follow different behaviour during fractional crystallization: the former goes preferentially in early-formed calcic plagioclase while the latter concentrates in the residual magma and enters later potassium minerals (Faure and Powell, 1972; DePaolo, 1981). In material sciences, Sr aluminosilicate glasses, glass-ceramics and ceramics have shown applications as transparent ceramics (Al Saghir et al., 2015), high-temperature

sealants (Sharma et al., 2012) and refractory materials (Hyatt and Bansal, 1996; Bansal, 1998; Beall, 2009).

To better understand natural and industrial processes, it is important to link macroscopic properties (density, viscosity, glass transition temperature etc.) of the glasses/ceramics with the structure of the corresponding melts. Some investigations in this field have been already made for Na-based (Furukawa et al., 1981; Seifert et al., 1982; Fukumi et al., 1990; Mysen, 1990; Merzbacher and White, 1991; Mysen and Frantz, 1993; Mysen and Frantz, 1994; Mysen, 1999; Allwardt et al., 2005a, 2005b; Le Losq et al., 2014), Mg-based (Seifert et al., 1982; Merzbacher and White, 1991; Neuville et al., 2008a) and Ca-based aluminosilicates (Seifert et al., 1982; Frantz and Mysen, 1995; Allwardt et al., 2005b; Kanehashi and Stebbins, 2007; Neuville et al., 2004a, 2004b, 2006, 2008b, 2010; Drewitt et al., 2012; Jakse et al., 2012; Hennem et al., 2016) using a multi-technique approach. The SrO-Al₂O₃-SiO₂ (SAS) ternary system is, on the other hand, poorly studied. There are only a handful of studies in this system and most of them concentrate only on specific properties and have used only few techniques (see for example Bockris et al., 1955; Chiari et al., 1975; Magaritz and Hofmann, 1978; Creux et al., 1995; Neuville, 2005; Licheron et al., 2011; Abel et al., 2013).

* Correspondence to: A.N. Novikov, CEMHTI UPR3079 CNRS, Univ. Orléans, F-45071 Orléans, France.

** Corresponding author.

E-mail addresses: alexey.novikov@cnrs-orleans.fr (A.N. Novikov), neuville@ipgp.fr (D.R. Neuville).

In order to connect structural features with macroscopic properties of Sr aluminosilicates we intend to apply a multi-technique approach for studying tectosilicate compositions. This approach consists of measuring density and viscosity as well as using various spectroscopic techniques such as Raman, NMR and X-ray absorption spectroscopy. We also intend to compare the effect of Sr on the aluminosilicate network with the well-studied ones of Mg and Ca, recalling that strontium is a heavier element possessing a bigger radius than the two latter cations. Those differences are expected to affect the properties and structure of the melts and corresponding glasses/ceramics like potassium does, i.e. by greatly disturbing the network and increasing its topological and chemical disorder (Le Losq and Neuville, 2013; Le Losq et al., 2016).

2. Experimental methods

2.1. Starting materials

Strontium aluminosilicate samples were made by a traditional melting-quenching procedure described in Neuville (2006). For this, powders of Rectapur reagents from Merck were pre-dried at 1000 °C (SiO₂, Al₂O₃) and 550 °C (SrCO₃) before being mixed at a stoichiometric amount and crushed together in an agate mortar under ethanol for 1 h. Then the mixture was slowly heated in a platinum crucible up to 1100–1250 °C in an electric muffle furnace and held at that temperature for several hours to decompose the carbonate. After the decarbonation step, mixtures were melted at 1600 °C and quenched either by dipping the bottom of the crucible in water if the viscosity of the melt was high or by pouring the melt on a large copper plate if the viscosity was low. The grinding, melting, quenching procedures were repeated three more times to ensure the homogeneity of the final product. Compositions were maintained at a temperature above their melting points for several hours to produce bubble-free samples for further viscosity measurements. In the cases when glass samples could not be obtained by traditional quenching (i.e. SA10.45, SA20.40, SA50.25 and SA57.21 samples), ceramic compositions were prepared following the above described procedure and an aerodynamic levitation device coupled with two CO₂ lasers was used to prepare small glass spheres (Hennet et al., 2006; Neuville et al., 2006, 2008a, 2014). To be sure that those two quenching procedures did not affect the properties and structure of the glasses, two samples of a SAS glass obtained by traditional and “levitation” quench were studied. ²⁷Al NMR and Raman spectroscopies as well as density measurements did not reveal any differences in the samples. So, we assume further that for the studied samples the quenching method did not cause significant differences in the structure and properties.

All samples were checked to be free of a crystalline phase. For this, several pieces of each composition were studied microscopically and by means of Raman spectroscopy. Densities measured with the Archimedeian method using toluene as the immersion liquid of those pieces were also measured and are found to be approximately identical for each composition. Chemical compositions (Table 1) were measured using a Cameca SX100 electron probe microanalyser with a 10 nA current, accelerating voltage of 15 kV and 90 s counting time. Each composition is an average of 5–10 measurements. The names of the glasses are given by SAxx.yy, where xx is the SiO₂ content in mol%, yy is the Al₂O₃ content in mol%, the remaining being the content of SrO.

2.2. Viscosity measurements

Creep apparatus: The viscosity measurements at low temperatures were performed using a creep apparatus (Neuville and Richet, 1991; Neuville, 2006) permitting measurements in the temperature interval of 700–1200 K and the viscosity range of 10⁸–10¹² Pa·s. Samples used for the measurements were glass cylinders of 5–7 mm in diameter and 10–15 mm in length with two polished parallel faces. The cylinders were held in a furnace at 600–800 °C for 1 day to remove internal stress before the measurements. To ensure minimal temperature gradient during the measurements a silver cylinder was placed around the sample. This allowed reducing the gradient between the top and the bottom parts of the sample to <0.3 K. The thermal gradients along the sample were checked using two Pt–PtRh10% thermocouples. The reported viscosity values at one temperature are the result of an average of 20–40 measurements at different applied stresses. The viscosity uncertainty and reproducibility is <0.03 log units with this technique (Neuville, 2006).

Micro-penetration: Glass spheres obtained using the levitation device were too small to use the creep apparatus. Therefore, the viscosity measurements were performed on a homemade micro-indenter. The samples were polished to obtain two parallel faces at least 1 mm in diameter. These surfaces were polished using SiC paper and diamond suspension (1/4-micron particle size). The apparatus is a depth-sensing indentation device, permitting viscosity measurements between 293 and 1373 K with a thermal gradient of ± 1 K. The method used to measure the load/penetration and to determine the viscosity from the indentation creep tests is described elsewhere (Bernard et al., 2010; Gueguen et al., 2011). The indenter used was a sphere made of silicon carbide of 2 mm in diameter. The penetration depth has never exceeded 50 μm. The viscosity uncertainty of this method is 0.1 log units.

2.3. DTA measurements

Glass transition temperatures (T_g) of two samples – SA10.45 and SA20.40 – were measured using Setaram® L96 Evo TGA-DTA/DSC apparatus in DTA mode with the heating rate of 5 K/min. T_g was determined as an inflection point of the heat flow curve and a correction of 22 K was then applied to the values to have T_g comparable to those obtained from the viscosity curves at $\log \eta = 12$ Pa·s. This correction value was calibrated by measuring samples with known glass transition temperatures under the same conditions.

2.4. Raman spectroscopy

Unpolarized Raman spectra were recorded at room temperature using a T64000 Jobin-Yvon® triple Raman spectrometer equipped with a confocal system, a 1024 Charge-Coupled Detector cooled by liquid nitrogen and an Olympus® microscope. A Coherent® 70-C5 argon laser with a wavelength of 488.01 nm was used as the excitation source. All spectra were acquired between 20 and 1400 cm⁻¹ with acquisition time of 300 s and with 3 repetitions. Before the deconvolution of the high-frequency region, all spectra were corrected for temperature and excitation line effects using the method of Long (Long, 1977; Neuville and Mysen, 1996). Corrected spectra were normalized to the peak of maximum intensity and then the high-frequency region of the spectra

Table 1
Chemical composition (in wt%)^a and density (in g/cm³) of studied glasses.

	SA75.12	SA63.18	SA57.21	SA50.25	SA42.29	SA33.33	SA26.37	SA20.40	SA10.45
SiO ₂	62.54(16)	48.59(21)	42.73(9)	36.15(3)	29.72(11)	22.55(15)	16.35(1)	12.96(10)	7.00(4)
Al ₂ O ₃	18.01(9)	24.68(5)	27.36(10)	30.35(4)	33.37(3)	36.88(22)	39.67(8)	41.25(25)	46.08(10)
SrO	19.45(12)	26.73(26)	29.91(19)	33.49(2)	36.91(8)	40.57(37)	43.98(7)	45.78(30)	46.92(29)
Density	2.636(1)	2.837(3)	2.928(12)	3.024(1)	3.132(3)	3.211(2)	3.298(1)	3.359(2)	3.426(2)

^a Average of 5–10 analyses made with a Cameca SX100 electron microprobe for each glass at 15 kV and 10 nA with 90 s counting time.

Table 2Viscosity measurements performed on Sr aluminosilicate glasses. Viscosity is in $\log(\text{Pa} \cdot \text{s})$ and temperature is in K.

SA75.12		SA63.18		SA50.25 ^a		SA42.29		SA33.33		SA26.37	
T	η	T	η	T	η	T	η	T	η	T	η
1153.1	12.51	1148.9	12.42	1112.0	13.98	1137.0	12.72	1144.8	12.44	1144.2	12.68
1169.5	11.98	1158.9	12.01	1135.0	12.95	1145.3	12.35	1151.1	12.09	1159.2	11.92
1186.3	11.50	1161.3	11.94	1166.0	11.52	1152.6	12.01	1156.4	11.90	1169.2	11.47
1196.4	11.23	1181.4	11.24	1180.0	10.87	1161.3	11.64	1160.6	11.61	1175.2	11.25
1206.7	10.95	1186.6	11.04	1193.0	10.44	1168.5	11.38	1165.7	11.39	1189.2	10.58
1221.4	10.53	1191.3	10.90	1213.0	9.77	1177.3	11.00	1170.8	11.22	1214.2	9.40
1231.3	10.33	1196.2	10.72	1232.0	9.20	1183.3	10.75	1175.9	10.97	1231.2	8.79
1237.7	10.14	1204.8	10.37			1185.6	10.66	1186.9	10.50	1239.2	8.51
1247.1	9.99	1209.2	10.19			1192.9	10.40	1192.0	10.31		
		1219.5	9.92			1201.7	10.09	1206.9	9.81		
		1228.5	9.69			1209.4	9.82	2000.0 ^b	-0.20 ^b		
		2000.0 ^b	0.92 ^b			2000.0 ^b	0.01 ^b	2050.0 ^b	-0.36 ^b		
		2050.0 ^b	0.70 ^b			2050.0 ^b	-0.17 ^b	2100.0 ^b	-0.50 ^b		
		2100.0 ^b	0.51 ^b			2100.0 ^b	-0.33 ^b	2200.0 ^b	-0.76 ^b		
		2200.0 ^b	0.18 ^b			2200.0 ^b	-0.60 ^b				

^a Measured using a micro-penetration technique.^b Interpolated values.

was deconvoluted. All parameters, such as band's frequency, width and intensity were not constrained during the deconvolution procedure.

2.5. Nuclear magnetic resonance spectroscopy

²⁷Al NMR experiments were performed on an Avance III Bruker 850 MHz (20.0 T) spectrometer working at an ²⁷Al frequency of 195.5 MHz. Chemical shifts for ²⁷Al are referenced to a 1 M aqueous Al(NO₃)₃ solution. Magic Angle Spinning (MAS) experiments were performed at a spinning speed of 30 kHz in aluminium-free zirconia rotors of 2.5 mm diameter. All spectra were obtained using a single-pulse ("Bloch-decay") sequence using a radio-frequency field $\nu_{rf} = 62.5$ kHz and applying a pulse of 0.4 μ s (i.e. less than $\pi/18$ to ensure quantitative irradiation). Four thousand scans were accumulated for each composition with a recycling time of 0.15 s (spin-lattice relaxation times found in the range 1–5 s), using a spectral window of 2 MHz to avoid folding of the spinning-sideband's manifold. The decomposition of the spectra was obtained using the dmfit software (Massiot et al., 2002), taking

into account the spinning sidebands of the external transitions. This allows extracting the populations of the various components appearing on the central transition, their mean isotropic chemical shifts δ_{iso} , their distributions of isotropic chemical shift $\Delta\delta_{iso}$ and their mean quadrupolar coupling constants C_Q within the framework of the so-called "Czjzek" or "GIM" model (Le Caër and Brand, 1998).

2.6. X-ray absorption spectroscopy

X-ray absorption experiments at the Sr K-edge (16,105 eV) were performed at the DIFFABS beamline at the SOLEIL synchrotron (Gif-sur-Yvette, France). This storage ring has energy of 2.75 GeV and was operating in a top up mode with an average electron current of 450 mA. The beamline optics consist of a double Si[111] crystal monochromator surrounded by 2 rhodium coated mirrors. The X-ray beam is focused onto the sample horizontally and vertically by bending the second crystal and the second mirror respectively. The final beam size at the sample position was about 300 μ m (H) \times 250 μ m (V). The actual

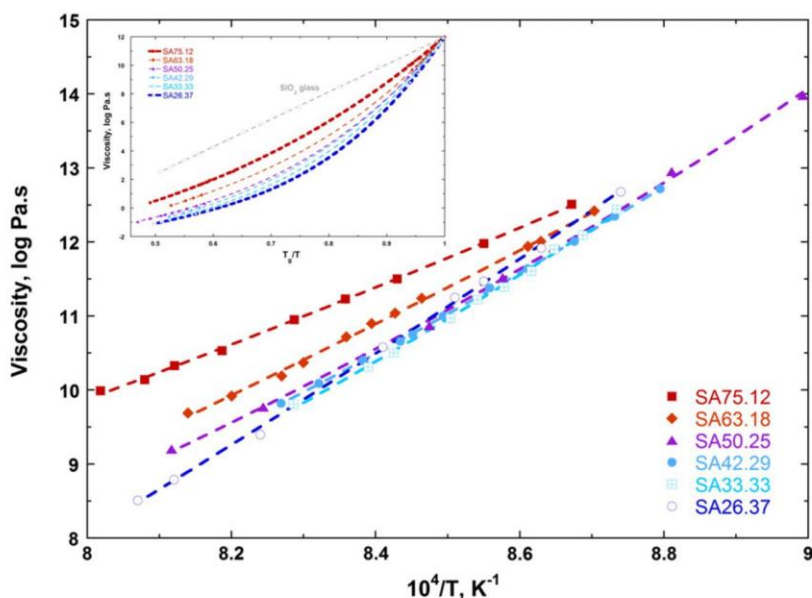


Fig. 1. Viscosity curves of studied glasses as a function of reciprocal temperature. Lines are VFTH fits. Error bars are less than symbols' size. *Inset:* viscosity data for Sr aluminosilicates plotted versus T_g/T , representing melt's fragility. High-temperature data for SA75.12, SA50.25 and SA26.37 are reproduced from Urbain et al. (1982) and viscosities for the intermediate compositions were estimated linearly from the end-members. Lines are only guide for the eye.

Table 3

T_g and VFTH parameters (A, B, T_1) retrieved from the fitting of low-temperature viscosity data. m is fragility of melts. $C_{p,g}$, $C_{p,l}$, C_p^{conf} and Adam-Gibbs parameters ($A_e, B_e, S^{conf}(T_g)$) determined from the viscosity data presented in Fig. 1. See explanation in the text on how the values of $C_{p,g}$ and $C_{p,l}$ were obtained. T_g, T_1, T_0 are in K; $C_{p,g}, C_{p,l}, C_p^{conf}, B_e$ are in J/mol; A_e is in $\log(\text{Pa} \cdot \text{s})$, $S^{conf}(T_g)$ is in $\text{J}/(\text{mol} \cdot \text{K})$.

	SA75.12	SA63.18	SA50.25	SA42.29	SA33.33	SA26.37	SA20.40	SA10.45
T_g	1169.2	1159.8	1154.1	1153.0	1153.1	1158.1	1185.8 ^a	1214.0 ^a
A	-5.7944	-14.0710	-5.8682	-8.1320	-9.8495	-20.3770	-	-
B	10,614.0	18,048.0	7390.1	9314.8	10,226.0	21,514.0	-	-
T_1	572.7	467.5	740.5	690.3	685.1	493.6	-	-
m	34.9	43.7	49.9	50.2	53.8	56.4	-	-
$C_{p,g}$	77.21	79.58	82.18	83.80	85.56	87.11	88.59	90.91
$C_{p,l}$	88.97	92.46	96.22	98.57	101.14	103.49	106.32	110.64
C_p^{conf}	11.77	12.88	14.04	14.77	15.58	16.38	17.73	19.73
A_e	-2.6425	-2.6278	-3.1003	-3.4952	-3.4188	-3.1614	-	-
$10^5 B_e$	1.9656	2.2416	3.0132	3.8054	3.9249	3.6818	-	-
$S^{conf}(T_g)$	11.48	13.21	17.29	21.30	22.06	20.96	-	-
T_0	384	647	699	690	742	806	-	-

^a T_g value was obtained from DTA measurements.

energy of the monochromator was calibrated at the Y K-edge (17,038 eV) using an yttrium calibration foil. The experiments were performed in a transmission mode. The incident and transmitted intensity were measured with two ionization chambers operating with a nitrogen flux at atmospheric pressure as absorbing gas. All studied samples were crushed to a fine powder. An appropriate quantity to provide an absorbance jump of 1 at the edge was ground with boron nitride (BN) and pressed into pellets with a thickness of about 250 μm . Each spectrum is an average of 3 measurements performed with a step of 2 eV which was reduced to 1 eV around the absorption edge. The data reduction was performed using the Athena software (Ravel and Newville, 2005).

3. Results

3.1. Viscosity

The viscosity measurements are presented in Table 2 and plotted in Fig. 1 as a function of reciprocal temperature. When considering the two extreme compositions – SA75.12 and SA26.37, a difference of about 15 K at constant viscosity of $10^{12} \text{ Pa} \cdot \text{s}$ and almost an order of magnitude in the viscosities at $T = 1169 \text{ K}$ (T_g of SA75.12) are observed. Low-

temperature viscosity data were fitted by using the Vogel–Fulcher–Tammann–Hesse (VFTH) equation:

$$\log \eta = A + \frac{B}{T - T_1} \quad (1)$$

where η is the viscosity in $\text{Pa} \cdot \text{s}$, T is the temperature in K and A, B, T_1 are adjustable parameters given in Table 3. The glass transition temperatures T_g were obtained from the fitting of the experimental data and are summarized in Table 3 and shown in Fig. 2 (along with the data derived from DTA measurements). The inset in Fig. 1 represents the viscosity of the melts plotted as a function of T_g/T and illustrates the evolution of the melts' fragilities (m) (Angell, 1991), i.e. the gradient of the viscosity curve at the glass transition temperature on a reduced temperature scale (Plazek and Ngai, 1991; Böhmer and Angell, 1992). It can be calculated by the following equation:

$$m = \left. \frac{d(\log_{10} \eta)}{d\left(\frac{T_g}{T}\right)} \right|_{T=T_g} = \frac{B}{T_g(1 - T_1/T_g)^2} \quad (2)$$

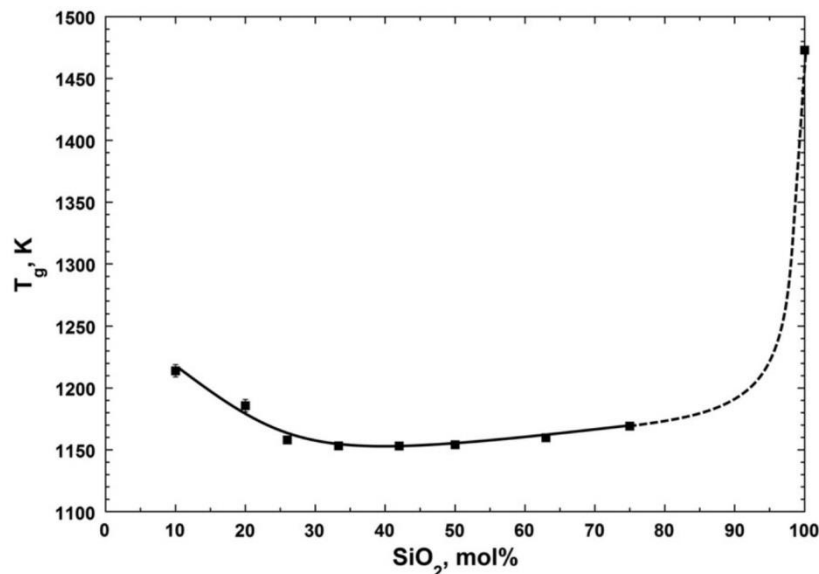


Fig. 2. T_g versus silica content. Points for SA10.45 and SA20.40 compositions were obtained using DTA. Error bars are less than the size of symbols except for SA10.45 and SA20.40 for which they were reasonably set at $\pm 5 \text{ K}$ level. Line is a guide for the eye. A dashed part of the line shows expected behaviour of T_g curve in the region of 75–100 mol% of SiO_2 (no experimental data available for the SAS system). T_g of 1473 K for vitreous silica is from Bruckner (1970).

where B and T_1 are recovered from the Eq. (1). The calculated fragilities are listed in the Table 3.

From the inset in Fig. 1 one can see that the melts become more fragile upon decreasing the silica content. The viscosity of melts can also be connected to their entropy of configuration through the Adam and Gibbs theory (Adam and Gibbs, 1965; Urbain, 1974; Richet, 1984; Scherer, 1984; Neuville and Richet, 1991):

$$\log \eta = A_e + \frac{B_e}{T \cdot S^{conf}(T)} \quad (3)$$

where η is the viscosity in $\text{Pa} \cdot \text{s}$, T is the temperature in K, A_e is a pre-exponential factor, B_e is a constant proportional to the potential barrier opposed to the cooperative rearrangement of the liquid's structure and $S^{conf}(T)$ is the melt's configurational entropy. $S^{conf}(T)$ can be calculated

from the following equation:

$$S^{conf}(T) = S^{conf}(T_g) + \int_{T_g}^T C_p^{conf} / T dT \quad (4)$$

where $S^{conf}(T_g)$ is the configurational entropy of the melt at T_g , C_p^{conf} is the configurational heat capacity calculated as a difference of heat capacities of the glass at T_g , $C_{p,g}(T_g)$, and the heat capacity of the liquid, $C_{p,l}$, determined from Richet and Bottinga (1985). Partial molar heat capacities of SiO_2 and Al_2O_3 for the calculations of $C_{p,g}(T_g)$ were taken from Richet (1987) and the value of partial molar heat capacity of crystalline SrO was taken from Robie et al. (1978), following previous calculations by Neuville (2006). Combining Eqs. (3) and (4), parameters such as $S^{conf}(T_g)$, A_e and B_e can be estimated (Table 3).

In Fig. 2 the glass transition temperatures T_g of the studied glasses derived from viscosity and DTA measurements are plotted as a function of silica content. T_g decreases rapidly with the addition of even a small

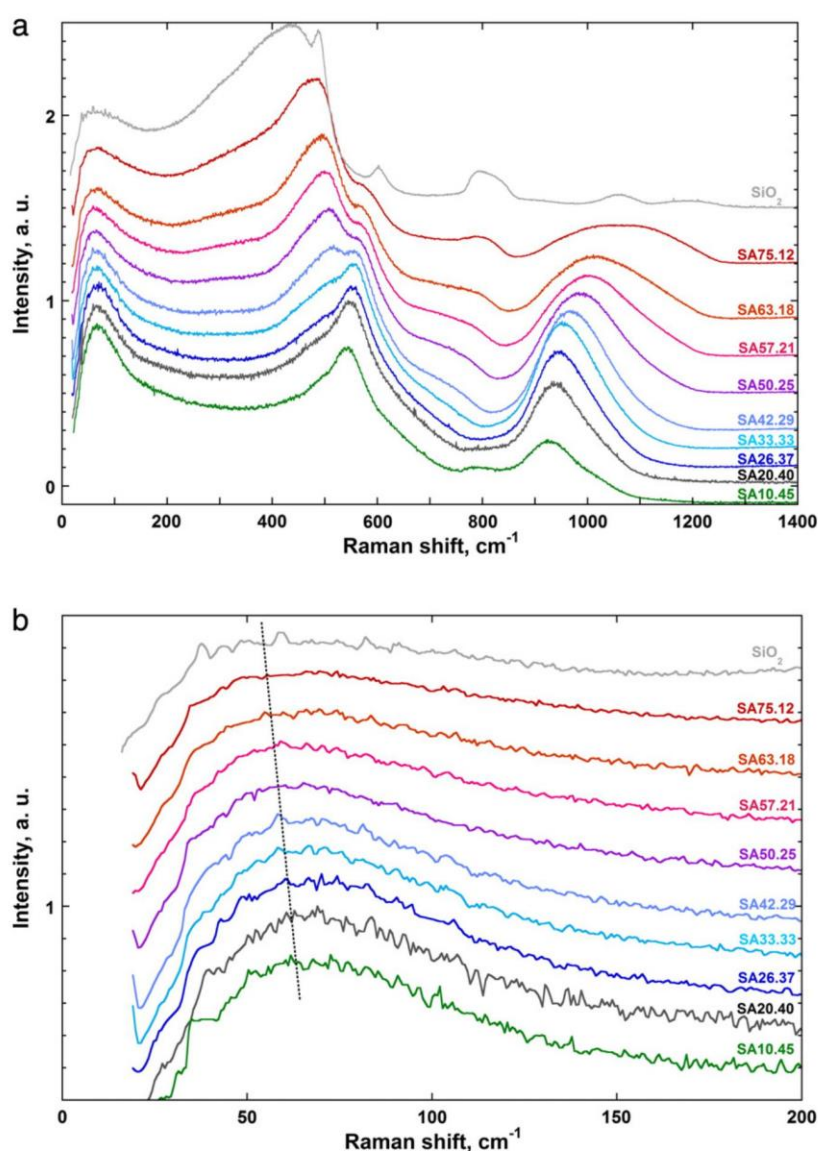
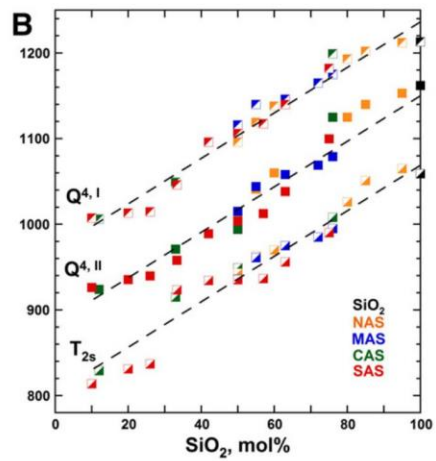
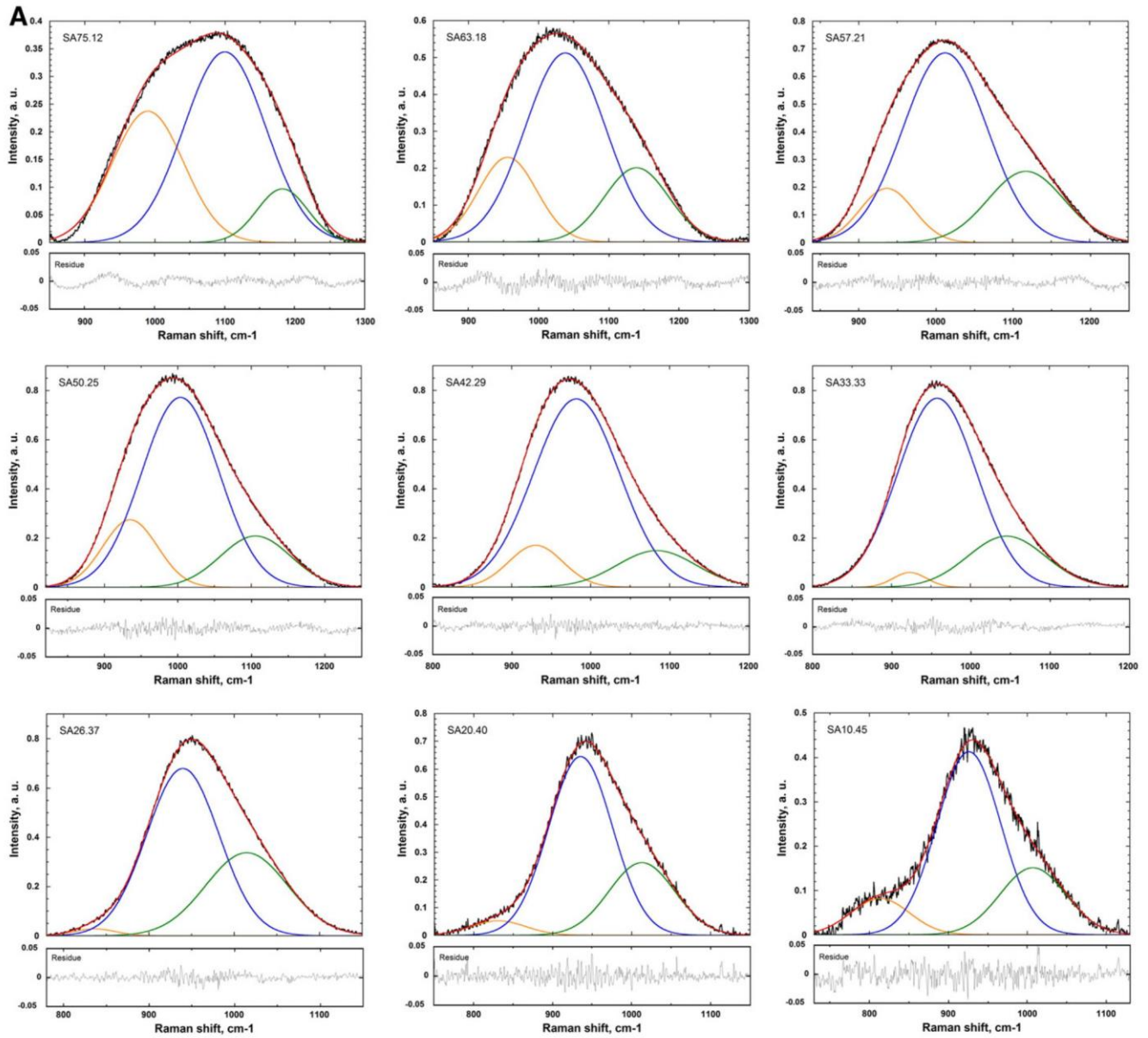


Fig. 3. a. Uncorrected normalized Raman spectra of Sr tectosilicate glasses. SiO_2 spectrum corresponds to one of INF302 silica glass. b. Boson peaks of uncorrected spectra of SAS glasses. The line shows a trend in the evolution of a Boson peak with changing composition.



quantities of SrAl₂O₄ to the silica glass. After this, a slight decrease in T_g is observed upon changing the composition from SA75.12 to SA42.29. The latter has the minimal T_g and with further addition of SrAl₂O₄ the glass transition temperature starts to increase again, similarly to observations made on the tectosilicate join of the CaO–Al₂O₃–SiO₂ system (Neuvillle et al., 2004b).

3.2. Raman spectroscopy

Fig. 3a presents unpolarised raw spectra of SAS glasses. The Raman spectra can be divided into four regions: the Boson region (20–250 cm⁻¹), the low frequency region (250–700 cm⁻¹), the intermediate region (700–850 cm⁻¹), and the high frequency region (850–1300 cm⁻¹).

3.2.1. The boson region (20–250 cm⁻¹)

The origin of the boson peak has been attributed to rotational motions of interconnected tetrahedral units (Buchenu et al., 1986; Hehlen et al., 2000, 2002; Courtens et al., 2001). It becomes more pronounced and shows a shift of approximately 1 cm⁻¹ each 10% of silica added to SrAl₂O₄ (Fig. 3b). This decrease can be extrapolated up to Sr aluminate and is in agreement with previous measurements (Licheron et al., 2011). This variation in frequency as a function of composition is found to be a linear combination of that of the pure SiO₂ and SrAl₂O₄ compounds.

3.2.2. The low frequency region (250–700 cm⁻¹)

In the Raman spectrum of SiO₂ three bands are clearly observed at 600, 490, and 435 cm⁻¹. These bands are well known and attributed to 3-, 4- and higher-membered rings of SiO₄ tetrahedra, respectively (Sharma et al., 1981; Galeener, 1982a, 1982b; Galeener et al., 1984; McMillan et al., 1994; Pasquarello and Car, 1998; Umari and Pasquarello, 2002; Rahmani et al., 2003; Kalampounias et al., 2006). The band at 500 cm⁻¹ decreases in intensity and shifts strongly to a higher frequency when SiO₂ is substituted by SrAl₂O₄ and becomes a shoulder for the compositions with SiO₂ content <42 mol%. A new band appears at 560 cm⁻¹, increases in intensity and moves a little to lower frequency upon decreasing silica content. It is observed as a shoulder for the compositions with SiO₂ content above 42 mol%. These two bands are usually assigned to vibrations of three- (~560 cm⁻¹) and four-membered (~500 cm⁻¹) rings of tetrahedra present in the aluminosilicate network (McMillan, 1984).

3.2.3. The intermediate frequency region (700–850 cm⁻¹)

A band at 800 cm⁻¹ is observed for SiO₂. This band is usually attributed to the threefold degenerate “rigid cage” vibrational mode of TO₂ units (Galeener, 1979), to the motion of the Si atom in its oxygen cage (Mysen et al., 1982) or to Si–O stretching involving oxygen motions in the Si–O–Si plane (McMillan et al., 1994). It decreases in intensity rapidly with decreasing silica content and moves to lower frequency. A band appearing in this region again for SA20.40 and more visibly for SA10.45 has a different nature and could possibly be related to a shift of the entire high-frequency envelope to lower frequency under substitution of SiO₂ by SrAl₂O₄.

3.2.4. The high frequency region (850–1300 cm⁻¹)

For SiO₂ glass in the high frequency region two broad bands are observed. They merge into a single band for SA75.12, and this band becomes narrower and shifts to lower frequency with decreasing silica

content, similarly to what has been observed for MAS and CAS tectosilicate glasses (Neuvillle et al., 2006, 2008a). Several studies pointed out that different peaks are convoluted in this band, arising from the T–O stretching (T=Si, Al) in different Qⁿ tetrahedral units, where n is the number of bridging oxygens and Q is the four-fold coordinated cation (McMillan, 1984; Mysen, 1999).

3.2.5. Spectra deconvolution

Before treating the high frequency region, the Raman spectra of the SAS glasses were corrected for temperature and excitation line effects (Long, 1977). The spectra were then simulated following Mysen (1999) using three Gaussian bands as proposed by several authors (Seifert et al., 1982; Neuvillle and Mysen, 1996 (Fig. 4a)). These three bands have been observed in silica glass as well as in alkali and alkaline earth tectosilicate glasses (Mysen et al., 1982; Neuvillle and Mysen, 1996; Neuvillle et al., 2004a, 2008a; Le Losq et al., 2014). Bands' parameters are reported in Table 4 and the bands' frequencies are plotted as a function of silica content in Fig. 4b together with data for sodium, magnesium and calcium tectosilicates. All three bands shift to lower frequencies with decreasing silica content, changing from 990, 1100 and 1182 cm⁻¹ for SA75.12 to 814, 926 and 1007 cm⁻¹ for SA10.45. The two higher frequency bands have been attributed to two Q⁴ units in two different structural environment presenting a T-O-T angle difference of about 5–10° (Seifert et al., 1982). The band at the highest frequency, called Q⁴ⁱ, arises from Q⁴ units with larger T-O-T angles than the band at lower frequency, called Q⁴ⁱⁱ, having smaller T-O-T angles. The lowest frequency band has been reported in spectra of vitreous silica, alkali and alkaline earth silicate and aluminosilicate glasses and melts (Mysen et al., 1982; McMillan, 1984; Neuvillle and Mysen, 1996). It has been suggested by Le Losq and Neuvillle (2013) that this band can arise from a stretching T_{2s} vibrational mode of TO₄ tetrahedra.

3.3. NMR spectroscopy

The ²⁷Al quantitative 1 pulse MAS NMR spectra of the investigated SAS glasses are shown in Fig. 5. The NMR bands consist of the main contribution which maximum shifts from approximately 55 to 78 ppm with decreasing SiO₂ content, positions characteristic of four-fold coordinated aluminium, Al^{IV}. A small shoulder around 30–45 ppm is also visible for almost all compositions and is ascribed to the presence of aluminium in five-fold coordination, Al^V (MacKenzie and Smith, 2002; Massiot et al., 2002; Neuvillle et al., 2004a) and similar contributions have also been observed for MAS and CAS glasses (Neuvillle et al., 2004a, 2006, 2007, 2008a). These spectra are very satisfactorily simulated using fully random distribution of quadrupolar and isotropic chemical shift interactions as expressed within the GIM model (Le Caër and Brand, 1998). The retrieved average isotropic chemical shift δ_{iso} , mean quadrupolar coupling constant C_Q and population of each site are given in Table 5. The average isotropic chemical shift, δ_{iso} , for Al^{IV} increases linearly with increasing SiO₂ content (Fig. 6a) in a manner very similar to the one observed for the MAS and CAS systems on the same joins, independent of the XO/Al₂O₃ ratio (X = Sr, Ca, or Mg). This suggests similar chemical AlO₄ environments in these three systems, the δ_{iso} being mainly controlled by the progressive substitution of Al by Si in the first coordination sphere of Al (Florian et al., 2012). Less precisely defined because of much lower intensity, the average isotropic chemical shift of the Al^V species also follows an overall linear decrease with increasing SiO₂ content, in agreement with previous observations for Mg- and Ca-based systems. The average quadrupolar coupling constant C_Q

Fig. 4. a. Deconvolution of the high-frequency region of corrected and normalized Raman spectra of SAS glasses. Orange bands are related to T_{2s} vibrational mode, blue and green ones – to vibrations of Q⁴ⁱⁱ and Q⁴ⁱ species, respectively. b. Dependence of Raman shift of Gaussian bands on silica content obtained from fitting of the high-frequency region of Raman spectra. ■ – T_{2s} vibrational mode, ■ – vibrations of Q⁴ⁱⁱ species, ■ – vibrations of Q⁴ⁱ species. Information on vitreous SiO₂ (black symbols) is from Mysen et al. (1982). Orange symbols correspond to Na tectosilicates (Neuvillle and Mysen, 1996), blue symbols correspond to Mg tectosilicates (Neuvillle et al., 2008a) and green symbols correspond to Ca tectosilicates (Neuvillle et al., 2004a). New data on Sr aluminosilicates are represented by red symbols. Lines are only guide for the eye.)

Table 4Gaussian bands' positions (V_i , cm^{-1}) and areas (A_i , a.u.) obtained from the deconvolution of the high-frequency region of the Raman spectra.

	SA75.12	SA63.18	SA57.21	SA50.25	SA42.29	SA33.33	SA26.37	SA20.40	SA10.45
V_1	990.1	956.0	936.5	935.2	934.2	923.4	836.9	831.1	813.7
V_2	1099.7	1038.3	1012.5	1003.7	988.9	958.0	939.7	935.4	926.2
V_3	1181.9	1139.8	1117.4	1106.0	1096.0	1046.0	1014.6	1013.1	1007.3
A_1	30.4	23.9	17.2	25.6	22.5	3.2	1.6	4.6	7.6
A_2	50.3	73.5	93.6	102.0	101.9	96.2	72.2	65.5	42.0
A_3	8.8	23.2	31.8	25.0	13.3	25.7	40.8	27.6	15.8

for $\text{Al}^{[4]}$ is found between 7.0 MHz and 8.1 MHz, i.e. close to typical values found for Ca-based glasses (5.9 MHz to 9.3 MHz; Neuville et al., 2006) and slightly below those obtained on Mg-based systems (7.6 MHz to 10.0 MHz; Neuville et al., 2008a).

The maximum in $\text{Al}^{[5]}$ population for SAS glasses (see Fig. 6b) corresponds to 4.5% and is found for the compositions in the middle of the ternary system, i.e. close to the ones found in MAS and CAS systems (Neuville et al., 2006, 2008a).

3.4. X-ray absorption spectroscopy at Sr K-edge

Normalized spectra of SAS glasses together with a crystalline standard (strontianite, SrCO_3) are presented in Fig. 7. The position of the white line is around 16,105 eV for all compositions investigated and for the crystalline standard, which confirms that strontium is in the oxidation state +2. The XANES Sr K-edge spectra of all glasses are almost similar to that of the strontianite. This may imply that Sr in SAS glasses has a coordination number similar to the one found in SrCO_3 . Coordination number has been reported by different authors to be 9 for strontianite (De Villiers, 1971; Antao and Hassan, 2009; Ye et al., 2012). This value is higher than those proposed by McKeown et al. (2003) for Sr borosilicates and also higher than the 6–7 coordination number found for Ca aluminosilicate glasses with analogous compositions

(Neuville et al., 2004b). A precise data analysis is underway, in order to confirm these fingerprint observations.

4. Discussion

4.1. Structural changes along the SiO_2 - SrAl_2O_4 join

The knowledge of the aluminosilicate glasses and melts structure is a key to understand the variation of macroscopic properties such as viscosity and glass transition temperature. This key may be lifted by coupling NMR and XANES studies, giving information about the short-range order, coordination number and speciation, and Raman spectroscopy which brings knowledge about the ring organization and polymerization of the glass and melt. Finally, both approaches provide information about the glasses and melts' structure and can be directly correlated to the viscosity through the configurational entropy variation as shown by Neuville and Mysen (1996).

Common wisdom dictates that the tectosilicate glass network at both high and low silica content is fully polymerized and consists solely of corner sharing tetrahedral units TO_4 ($\text{T}=\text{Si}, \text{Al}$). In other words, in all compositions being on the charge compensation line, Al and Si are expected to stay as Q^4 species, i.e. only a very small amount of NBOs are expected to be present (Faman et al., 1992; Allwardt and Stebbins, 2004; Thompson and Stebbins, 2012). SiO_2 glass is the simplest model of a

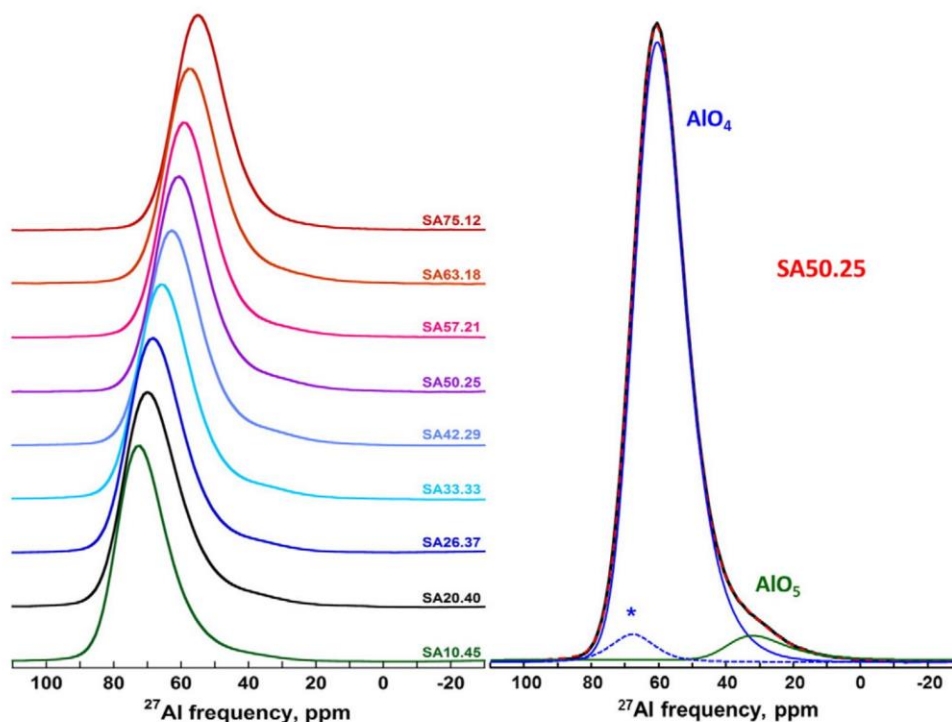


Fig. 5. Left: 1D ^{27}Al Quantitative 1 pulse MAS NMR of studied glasses. A shift to higher values of δ_{iso} is clearly visible. Right: Deconvolution of the ^{27}Al NMR spectrum for SA50.25 using the GIM model (Massiot et al., 2002). Black solid line is the original spectrum, red dashed line is the sum, blue solid line – the signal from AlO_4 sites, blue dashed line with asterisk – a spinning side band, green solid line – the signal from AlO_5 sites.

Table 5

²⁷Al MAS NMR parameters obtained from the deconvolution of the spectra using a Cjzek model. δ_{iso} is isotropic chemical shift (in ppm) and C_Q is quadrupolar coupling constant (in MHz). Population is in %.

	SA75.12	SA63.18	SA57.21	SA50.25	SA42.29	SA33.33	SA26.37	SA20.40	SA10.45
δ_{iso}									
AlO ₄	60.3	62.8	64.1	66.2	68.3	71.3	74.1	76.0	77.8
AlO ₅	32.1	34.2	35.0	39.0	40.3	40.0	39.5	41.1	43.4
C_Q									
AlO ₄	7.31	7.29	7.00	7.32	7.41	7.45	7.81	8.11	7.53
AlO ₅	7.82	7.83	7.13	8.65	8.67	7.62	6.39	6.93	6.81
Population									
AlO ₄	97.8	97.1	97.7	95.7	95.5	96.9	98.0	97.8	98.6
AlO ₅	2.2	2.9	2.3	4.3	4.5	3.1	2.0	2.2	1.4

fully polymerized glass structure and can be approximated by using the central-force model (Sen and Thorpe, 1977; Galeener, 1979), used by Seifert et al. (1982) to propose that SiO₂ is composed of two different coexisting structures with different inter-tetrahedral angles: $Q^{4,I}$ and $Q^{4,II}$. These two interconnected structures in vitreous SiO₂ have subsequently been found in alkali and alkaline earth aluminosilicates by a range of Raman studies (Seifert et al., 1982; Neuvill and Mysen, 1996; Neuvill et al., 2004a, 2004b, 2006, 2008a; Le Losq and Neuvill, 2013). It should nevertheless be noted that no other techniques have yet evidenced such a bimodal distribution of Si-O-Si inter-tetrahedral angles.

For glasses along the SiO₂-SrAl₂O₄ join, the Raman spectra exhibit changes in the low and high frequency regions. In the silica's spectrum, in the low frequency region, signals from 3-, 4- and higher-membered rings are observed (with a significant fraction of high-membered rings; see Fig. 3a). With introduction of SrAl₂O₄ (e.g., SA75.12) the fraction of high-membered rings decreases and further addition of SrAl₂O₄ favours formation of low-membered rings (e.g., SA10.45). In the high frequency regions Raman spectra exhibit a continuous shift of the band frequencies as a function of the Al/(Al + Si) ratio as already seen in the NAS, MAS and CAS systems. The high frequency envelope of the Raman spectra of glasses along this join was simulated (Fig. 4a) using three bands associated with two Q^4 units and the T_{25} band (Seifert et al., 1982; Neuvill and Mysen, 1996; Neuvill et al., 2004a; Le Losq et al., 2014; Neuvill et al., 2014). In Fig. 4b, the wavenumbers of the three bands after deconvolution are plotted as a function of SiO₂ content showing no evidence for the appearance of new bands with decreasing silica content. The negative frequency change with increasing Al₂O₃ content is consistent with aluminium substitution for Si in these units (Neuvill and Mysen, 1996; Mysen, 1999). This substitution produces a linear shift in the Raman frequency (Neuvill and Mysen, 1996; Neuvill et al., 2006, 2008a). The Raman spectra of SAS glasses follow a similar trend as the one observed for the glasses in CAS (Seifert et al., 1982; Neuvill et al., 2006), MAS (Neuvill et al., 2008a) and NAS (Seifert et al., 1982; Neuvill and Mysen, 1996) systems. This is in good agreement with Merzbacher and White (1991) who have shown that the substitution of alkaline earth element produces a very small effect on the Raman spectra. This indicates that, on the tectosilicate join, Si/Al substitution has larger influence on the aluminosilicate network than the nature of a cation, which plays the role of a charge compensator. Nevertheless, Raman spectroscopy probing the medium range order is not able to investigate the short range order and detect minor species such as, for example, aluminium in the five-fold coordination state (Neuvill et al., 2004a, 2006, 2008a). This is the reason why NMR spectroscopy was used to investigate aluminium environment.

²⁷Al NMR data indicate that the majority (at least 95%) of aluminium atoms are in four-fold coordination. Fig. 6a shows significant changes in δ_{iso} for Al^[4] sites as a function of silica content, where, in agreement with previous values for MAS and CAS systems (Neuvill et al., 2004a, 2006, 2008a), the δ_{iso} goes from 62 up to 79 ppm respectively for 76 and 0 mol% of SiO₂. This linear decrease of δ_{iso} results from a purely random

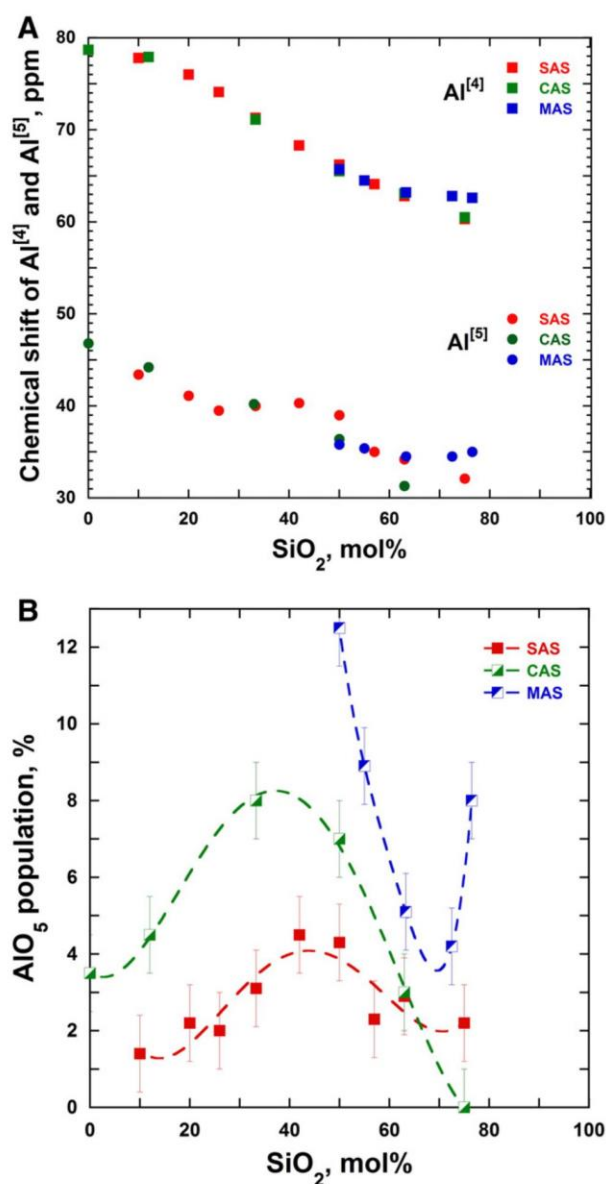


Fig. 6. a. Evolution of isotropic chemical shift δ_{iso} of Al^[4] and Al^[5] for SAS (red), CAS (green, Neuvill et al., 2004a) and MAS (blue, Neuvill et al., 2008a) glasses. Error bars are less than symbols' size. b. Population of Al^[5] in SAS (red), CAS (green, Neuvill et al., 2004a) and MAS (blue, Neuvill et al., 2008a) glasses. Lines are only guide for the eye.

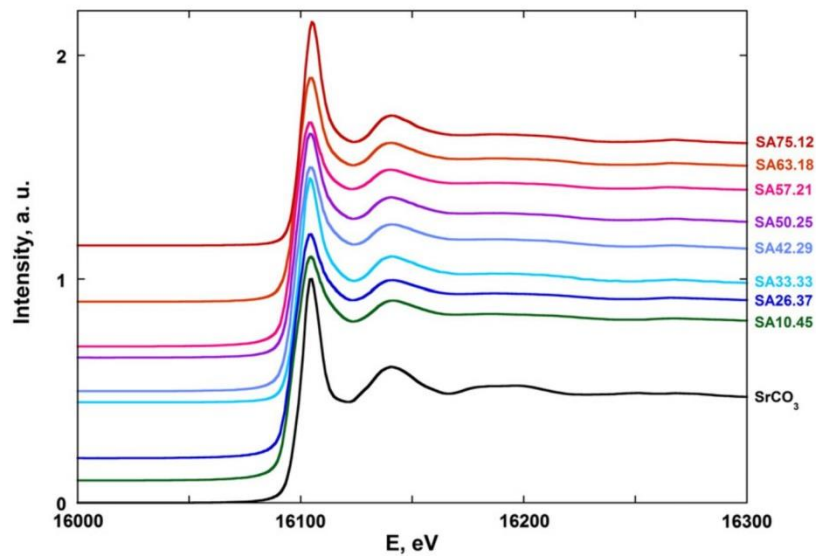


Fig. 7. XANES spectra at the Sr K-edge for Sr tectosilicate glasses with a crystalline standard (SrCO_3).

substitution of Si by Al in the second coordination sphere of aluminium, which produces an approximate -3 ppm shift per substitution (Florian et al., 2012) and is to be related to the bands' shifts also observed in the high frequency regions of the Raman spectra (vide supra). The evolution of the $\text{Al}^{[5]}$ population as a function of silica content (Fig. 6b) for SAS glasses possesses a maximum ($\sim 4.5\%$ of five-fold aluminium) that is clearly observed between 42 and 50 mol% of SiO_2 . This maximum is shifted to lower silica content (33–42 mol%) for the CAS system, while for the MAS system it is difficult to assume the same trend since no data are available in the low-silica region.

In the SAS system, the proportion of $\text{Al}^{[5]}$ is lower than that observed in MAS and CAS glasses which is in a good agreement with previous studies on alkali, earth alkaline and rare earth aluminosilicates which show that the increase of the cation field strength directly correlates with an increase of the $\text{Al}^{[5]}$ population (Allwardt et al., 2005b; Florian et al., 2007; Iftekhhar et al., 2011; Thompson and Stebbins, 2012). In

this respect, the $\text{SrO-Al}_2\text{O}_3\text{-SiO}_2$ system has a behaviour similar to sodium aluminosilicate glasses which have a small to non-detectable amount of high coordinated Al species (Stebbins et al., 1992; Allwardt et al., 2005a, 2005b). Contrarily to MAS and CAS systems, $\text{Al}^{[6]}$ is not detected in $\text{SrO-Al}_2\text{O}_3\text{-SiO}_2$ glasses apart from a couple of compositions for which it represents $<0.5\%$ of the total intensity.

4.2. Influence of structural changes on macroscopic properties

It is well known that the SiO_2 glass network consists only of SiO_4 tetrahedra forming low- and high-membered rings (Fig. 3a) hence $S^{\text{conf}}(T_g)$ is minimal in this case (Fig. 8) and consists of a pure topological contribution (Richet and Neuville, 1992). Under substitution of SiO_2 by SrAl_2O_4 the following changes take place. The number of particles in the system increases (two AlO_4^- units for one Sr^{2+} cation), additional structural units (AlO_4 , AlO_5) appear in the system and tetrahedral

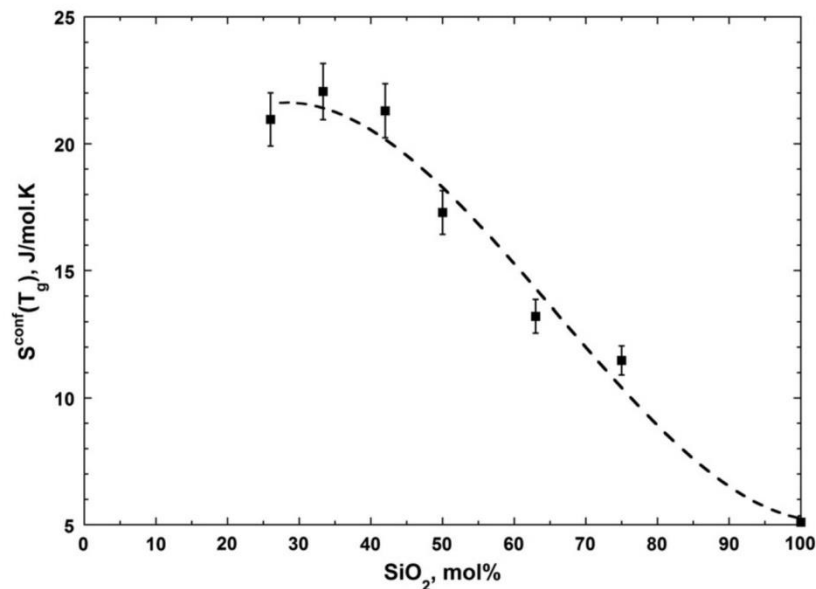


Fig. 8. $S^{\text{conf}}(T_g)$ as a function of SiO_2 content. Line is a guide for the eye. Error bars was set as $\pm 5\%$ after Neuville and Richet (1991).

rings start to include not only SiO_4 but also AlO_4 . As expected, the fragility (inset of Fig. 1) increases with decreasing SiO_2 content. This proves that, when Al goes in tetrahedral position and substitutes Si, it produces Al-O-Al linkages which are weaker than Si-O-Si ones. In agreement with Angell (1991), the increase in fragility also well correlates with the increase in the $C_{p,l}/C_{p,g}$ from 1.1 up to 1.2 where $C_{p,l}$ values were calculated from the partial heat capacity of the liquid from Richet and Bottinga (1985) and $C_{p,g}$ values were calculated from partial heat capacity of the glass for SiO_2 and Al_2O_3 from Richet (1987) and for SrO from Robie et al. (1978). Starting from a pure topological contributions to the configurational entropy (5 J/mol·K for SiO_2 glass), some new topological and chemical contributions are added upon addition of SrAl_2O_4 into SiO_2 leading to an increase of $S^{\text{conf}}(T_g)$ (Fig. 8) and to a rapid drop in T_g under introduction of small quantities of SrAl_2O_4 into SiO_4 -based network. Going from 75 to 42 mol% of silica T_g decreases gradually (Fig. 2) as a consequence of an increasing melts fragility, increasing disorder in the system and increasing fraction of AlO_5 (reaching a maximum of 4.5% at 42–50 mol% of SiO_2 ; see Fig. 6b). Below 42 mol% of silica the melts' fragility continues to increase while the fraction of low-membered rings prevails and the AlO_5 content decreases down to 1.4%. $S^{\text{conf}}(T_g)$ seems to reach a plateau around 21 J/mol·K in this region (Fig. 8) and it is likely that different contributions to the configurational entropy start to compensate each other in this low-silica content region. For example, the number of particles continues to increase with addition of SrAl_2O_4 , but at the same time the number of different structural units decreases (less SiO_4 and AlO_5). Considering the lack of the viscosity data (and hence values of $S^{\text{conf}}(T_g)$) for the compositions SA20.40, SA10.45 we can only assume that the observed increase in T_g with further decrease in SiO_2 content is due to a progressive ordering of the system.

A similar behaviour has been already observed in the $\text{CaO-Al}_2\text{O}_3\text{-SiO}_2$ system, where the viscosities and glass transition temperatures first decrease with SiO_2 content decreasing down to 30 mol% and then increase with further decreasing SiO_2 (Neuvill, 1992; Neuvill et al., 2004b). It is worth noticing that the maximum in $\text{Al}^{[5]}$ content (Fig. 6b), observed for the composition SA42.29, corresponds to the minimum in T_g (Fig. 2). The same trend has been seen for the Ca tectosilicates where a maximum in $\text{Al}^{[5]}$ and a minimum in T_g are observed for the composition CA33.33 (Neuvill et al., 2004a, 2004b, 2006). Thus, five-fold coordinated Al can be seen as having a similar role as $\text{Si}^{[5]}$ species in promoting the viscous flow (Farnan and Stebbins, 1994). Such a participation of the AlO_5 units in the network mobility has been proposed by Poe et al. (1994) for aluminated melts and more recently by Le Losq et al. (2014) for aluminosilicate melts. In other words, since in both systems, SAS and CAS, the minimum in T_g matches with the maximum in AlO_5 content we can conclude that minor species such as AlO_5 should significantly influence the transport mechanisms for the tectosilicate compositions (Neuvill et al., 2008b).

5. Conclusion

Spectroscopic investigations of $\text{SrO-Al}_2\text{O}_3\text{-SiO}_2$ glasses were made using Raman, NMR and X-ray absorption spectroscopy in order to obtain information on short and medium range order on glass structure and correlate those to viscosity measurements close to the glass transition temperature. All these experiments give a better knowledge on this ternary system, in particular:

- $\text{Al}^{[5]}$ is present in all studied glasses, though in quantities less than for Mg and Ca aluminosilicates with similar compositions. A maximum of approximately 4.5% of five-fold aluminium environments has been found for the compositions around 40–50 mol% of SiO_2 .
- X-ray absorption spectroscopy indicates that the first coordination shell of strontium in tectosilicate glasses is close to that found in strontianite. This suggests a coordination number of Sr close to 9, which is higher than that of Mg and Ca for analogous compositions

in MAS and CAS systems. A detailed analysis is underway and should allow us to shed light on Sr coordination in these compounds.

- Aluminium randomly replaces silicon in tetrahedral units when SrAl_2O_4 added to silica leading to a linear shift of the high frequency Raman bands as well as of the average chemical shifts of $\text{Al}^{[4]}$ and $\text{Al}^{[5]}$. Such linear trends and negative correlation between ^{27}Al NMR and Raman has been previously observed for Mg and Ca aluminosilicates.
- Viscosity and DTA measurements show the presence of a minimum in T_g for the composition with 42 mol% of silica. With further addition of SrAl_2O_4 T_g increases slightly. Similar observations have been made for Ca tectosilicates. Calculated values of $S^{\text{conf}}(T_g)$ increases gradually while SiO_2 content decreases pointing to an increase of disorder in the system while replacing Si by Al in the glass network.

Acknowledgments

The authors would like to thank Lilian Latapie for help in viscosity measurements. Franck Fayon is acknowledged for helping with NMR experiments. Thanks are due to the OXYMORE funding from Île-de-France region for supporting the purchase of a Multi HT96 LINE TGA-DTA/DSC Setaram®. This research was conducted under funding from the ANR DyStrAS project (ANR-13-BS08-0012). We also acknowledge an anonymous reviewer whose explicit comments helped to improve the quality of the paper.

References

- Adam, G., Gibbs, J.H., 1965. On the temperature dependence of cooperative relaxation properties in glass-forming liquids. *J. Chem. Phys.* 43:139–146. <http://dx.doi.org/10.1063/1.1696442>.
- Abel, B.M., Morgan, J.M., Mauro, J.C., Smedskjaer, M.M., 2013. Liquidus temperature of $\text{SrO-Al}_2\text{O}_3\text{-SiO}_2$ glass-forming compositions. *Int. J. Appl. Glas. Sci.* 4:225–230. <http://dx.doi.org/10.1111/ijag.12017>.
- Allwardt, J.R., Stebbins, J.F., 2004. Ca-Mg and K-Mg mixing around non-bridging O atoms in silicate glasses: An investigation using ^{17}O MAS and $^3\text{QMAS}$ NMR. *Am. Mineral.* 89: 777–784. <http://dx.doi.org/10.2138/am-2004-5-611>.
- Allwardt, J.R., Poe, B.T., Stebbins, J.F., 2005a. The effect of fictive temperature on Al coordination in high-pressure (10 GPa) sodium aluminosilicate glasses. *Am. Mineral.* 90: 1453–1457. <http://dx.doi.org/10.2138/am.2005.1736>.
- Allwardt, J.R., Stebbins, J.F., Schmidt, B.C., Frost, D.J., Withers, A.C., Hirschmann, M.M., 2005b. Aluminum coordination and the densification of high-pressure aluminosilicate glasses. *Am. Mineral.* 90:1218–1222. <http://dx.doi.org/10.2138/am.2005.1836>.
- Al Saghir, K., Chenu, S., Veron, E., Fayon, F., Suchomel, M., Genevois, C., Porcher, F., Matzen, G., Massiot, D., Allix, M., 2015. Transparency through structural disorder: a new concept for innovative transparent ceramics. *Chem. Mater.* 27:508–514. <http://dx.doi.org/10.1021/cm5037106>.
- Angell, C.A., 1991. Relaxation in liquids, polymers and plastic crystals - strong/fragile patterns and problems. *J. Non-Cryst. Solids* 131–133:13–31. [http://dx.doi.org/10.1016/0022-3093\(91\)90266-9](http://dx.doi.org/10.1016/0022-3093(91)90266-9).
- Antao, M.S., Hassan, I., 2009. The orthorhombic structure of CaCO_3 , SrCO_3 , PbCO_3 and BaCO_3 : linear structural trends. *Can. Mineral.* 47:1245–1255. <http://dx.doi.org/10.3749/canmin.47.5.1245>.
- Bansal, N.P., 1998. Solid state synthesis and properties of monoclinic celsian. *J. Mater. Sci.* 33:4711–4715. <http://dx.doi.org/10.1023/A:1004484903436>.
- Beall, G.H., 2009. Refractory glass-ceramics based on alkaline earth aluminosilicates. *J. Eur. Ceram. Soc.* 29:1211–1219. <http://dx.doi.org/10.1016/j.jeurceramsoc.2008.08.010>.
- Bernard, C., Keryvin, V., Sangleboeuf, J.-C., Rouxel, T., 2010. Indentation creep of window glass around glass transition. *Mech. Mater.* 42:196–206. <http://dx.doi.org/10.1016/j.mechmat.2009.11.008>.
- Bockris, J.O., MacKenzie, J.D., Kitchener, J.A., 1955. Viscous flow in silica and binary liquid silicates. *Trans. Faraday Soc.* 51:1734–1748. <http://dx.doi.org/10.1039/TF955101734>.
- Böhmer, R., Angell, C.A., 1992. Correlations of the nonexponentiality and state dependence of mechanical relaxations with bond connectivity in Ge-As-Se supercooled liquids. *Phys. Rev. B* 45:10091–10094. <http://dx.doi.org/10.1103/PhysRevB.45.10091>.
- Bruckner, R., 1970. Properties and structure of vitreous silica. *I. J. Non-Cryst. Solids* 5: 123–175. [http://dx.doi.org/10.1016/0022-3093\(70\)90190-0](http://dx.doi.org/10.1016/0022-3093(70)90190-0).
- Buchenau, U., Prager, M., Nucker, N., Dianoux, A.J., Ahmad, N., Phillips, W.A., 1986. Low-frequency modes in vitreous silica. *Phys. Rev. B* 34:5665–5673. <http://dx.doi.org/10.1103/PhysRevB.34.5665>.
- Capo, R.C., Stewart, B.W., Chadwick, O.A., 1998. Strontium isotopes as tracers of ecosystem processes: theory and methods. *Geoderma* 82:197–225. [http://dx.doi.org/10.1016/S0016-7061\(97\)00102-X](http://dx.doi.org/10.1016/S0016-7061(97)00102-X).
- Chiari, G., Calleri, M., Bruno, E., Ribbe, P.H., 1975. The structure of partially disordered, synthetic strontium feldspar. *Am. Mineral.* 60, 111–119.
- Courtens, E., Foret, M., Hehlen, B., Vacher, R., 2001. Vibrational modes of glasses. *Solid State Commun.* 117:187–200. [http://dx.doi.org/10.1016/S0038-1098\(00\)00434-8](http://dx.doi.org/10.1016/S0038-1098(00)00434-8).

- Creux, S., Bouchet-Fabre, B., Gaskell, P.H., 1995. Anomalous wide angle X-ray scattering study of strontium silicate and aluminosilicate glasses. *J. Non-Cryst. Solids* 192–193: 360–363. [http://dx.doi.org/10.1016/0022-3093\(95\)00377-0](http://dx.doi.org/10.1016/0022-3093(95)00377-0).
- DePaolo, D.J., 1981. Trace element and isotopic effects of combined wallrock assimilation and fractional crystallization. *Earth Planet. Sci. Lett.* 53:189–202. [http://dx.doi.org/10.1016/0012-821X\(81\)90153-9](http://dx.doi.org/10.1016/0012-821X(81)90153-9).
- De Villiers, J.P.R., 1971. Crystal structures of aragonite, strontianite, and witherite. *Am. Mineral.* 56, 758–767.
- Drewitt, J.W.E., Hennet, L., Zeidler, A., Jahn, S., Salmon, P.S., Neuville, D.R., Fischer, H.E., 2012. Structural transformations on vitrification in the fragile glass-forming system CaAl_2O_4 . *Phys. Rev. Lett.* 109:235501. <http://dx.doi.org/10.1103/PhysRevLett.109.235501>.
- Farnan, I., Stebbins, J.F., 1994. The nature of the glass transition in a silica-rich oxide melt. *Science* 265:1206–1209. <http://dx.doi.org/10.1126/science.265.5176.1206>.
- Farnan, I., Grandinetti, P.J., Baltisberger, J.H., Stebbins, J.F., Werner, U., Eastman, M.A., Pines, A., 1992. Quantification of the disorder in network-modified silicate glasses. *Nature* 358:31–35. <http://dx.doi.org/10.1038/358031a0>.
- Faure, G., Powell, J.L., 1972. *Strontium Isotope Geology*. Springer Berlin Heidelberg, Berlin, Heidelberg. <http://dx.doi.org/10.1007/978-3-642-65367-4>.
- Florian, P., Sadiki, N., Massiot, D., Coutures, J.P., 2007. ^{27}Al NMR study of the structure of lanthanum- and yttrium-based aluminosilicate glasses and melts. *J. Phys. Chem. B* 111:9747–9757. <http://dx.doi.org/10.1021/jp072061q>.
- Florian, P., Veron, E., Green, T.F.G., Yates, J.R., Massiot, D., 2012. Elucidation of the Al/Si ordering in gehlenite $\text{Ca}_2\text{Al}_2\text{SiO}_7$ by combined ^{29}Si and ^{27}Al NMR spectroscopy/quantum chemical calculations. *Chem. Mater.* 24:4068–4079. <http://dx.doi.org/10.1021/cm3016935>.
- Frantz, J.D., Mysen, B.O., 1995. Raman spectra and structure of BaO-SiO_2 , SrO-SiO_2 and CaO-SiO_2 melts to 1600 °C. *Chem. Geol.* 121:155–176. [http://dx.doi.org/10.1016/0009-2541\(94\)00127-T](http://dx.doi.org/10.1016/0009-2541(94)00127-T).
- Fukumi, K., Hayakawa, J., Komiyama, T., 1990. Intensity of Raman band in silicate glasses. *J. Non-Cryst. Solids* 119:297–302. [http://dx.doi.org/10.1016/0022-3093\(90\)90302-3](http://dx.doi.org/10.1016/0022-3093(90)90302-3).
- Furukawa, T., Fox, K., White, W., 1981. Raman spectroscopic investigation of the structure of silicate glasses. III. Raman intensities and structural units in sodium silicate glasses. *J. Chem. Phys.* 75:3226–3237. <http://dx.doi.org/10.1063/1.442472>.
- Galeener, F.L., 1979. Band limits and the vibrational spectra of tetrahedral glasses. *Phys. Rev. B* 19:4292–4297. <http://dx.doi.org/10.1103/PhysRevB.19.4292>.
- Galeener, F.L., 1982a. Planar rings in vitreous silica. *J. Non-Cryst. Solids* 49:53–62. [http://dx.doi.org/10.1016/0022-3093\(82\)90108-9](http://dx.doi.org/10.1016/0022-3093(82)90108-9).
- Galeener, F.L., 1982b. Planar rings in glasses. *Solid State Commun.* 44:1037–1040. [http://dx.doi.org/10.1016/0038-1098\(82\)90329-5](http://dx.doi.org/10.1016/0038-1098(82)90329-5).
- Galeener, F.L., Barrio, R.A., Martinez, E., Elliott, R.J., 1984. Vibrational decoupling of rings in amorphous solids. *Phys. Rev. Lett.* 53:2429–2432. <http://dx.doi.org/10.1103/PhysRevLett.53.2429>.
- Gueguen, Y., Rouxel, T., Gadaud, P., Bernard, C., Keryvin, V., Sangleboeuf, J.C., 2011. High-temperature elasticity and viscosity of $\text{Ge}_2\text{Se}_{1-x}$ glasses in the transition range. *Phys. Rev. B: Condens. Matter Mater. Phys.* 84:1–10. <http://dx.doi.org/10.1103/PhysRevB.84.064201>.
- Hehlen, B., Courtens, E., Vacher, R., Yamanaka, A., Kataoka, M., Inoue, K., 2000. Hyper-Raman scattering observation of the boson peak in vitreous silica. *Phys. Rev. Lett.* 84:5355–5358. <http://dx.doi.org/10.1103/PhysRevLett.84.5355>.
- Hehlen, B., Courtens, E., Yamanaka, A., Inoue, K., 2002. Nature of the boson peak of silica glasses from hyper-Raman scattering. *J. Non-Cryst. Solids* 307–310:87–91. [http://dx.doi.org/10.1016/S0022-3093\(02\)01444-8](http://dx.doi.org/10.1016/S0022-3093(02)01444-8).
- Hennet, L., Pozdnyakova, I., Bytchkov, A., Cristiglio, V., Palleau, P., Fischer, H.E., Cuello, G.J., Johnson, M., Melin, P., Zanghi, D., Brassamin, S., Brun, J.F., Price, D.L., Saboungi, M.L., 2006. Levitation apparatus for neutron diffraction investigations on high temperature liquids. *Rev. Sci. Instrum.* 77:053903. <http://dx.doi.org/10.1063/1.2200756>.
- Hennet, L., Drewitt, J.W.E., Neuville, D.R., Cristiglio, V., Kozaily, J., Brassamin, S., Zanghi, D., Fischer, H.E., 2016. Neutron diffraction of calcium aluminosilicate glasses and melts. *J. Non-Cryst. Solids* 451:89–93. <http://dx.doi.org/10.1016/j.jnoncrysol.2016.05.018>.
- Hyatt, M.J., Bansal, N.P., 1996. Crystal growth kinetics in $\text{BaOAl}_2\text{O}_3\text{2SiO}_2$ and $\text{SrOAl}_2\text{O}_3\text{2SiO}_2$ glasses. *J. Mater. Sci.* 31:172–184. <http://dx.doi.org/10.1007/BF00355142>.
- Iftikhar, S., Grins, J., Gunawidjaja, P.N., Edén, M., 2011. Glass formation and structure-property-composition relations of the $\text{RE}_2\text{O}_3\text{-Al}_2\text{O}_3\text{-SiO}_2$ (RE = La, Y, Lu, Sc) systems. *J. Am. Ceram. Soc.* 94:2429–2435. <http://dx.doi.org/10.1111/j.1551-2916.2011.04548.x>.
- Jakse, N., Bouhadja, M., Kozaily, J., Drewitt, J.W.E., Hennet, L., Neuville, D.R., Fischer, H.E., Cristiglio, V., Pasturel, A., 2012. Interplay between non-bridging oxygen, triclusters, and fivefold Al coordination in low silica content calcium aluminosilicate melts. *Appl. Phys. Lett.* 101. <http://dx.doi.org/10.1063/1.4766920>.
- Kalamponias, A.G., Yannopoulos, S.N., Papatheodorou, G.N., 2006. Temperature-induced structural changes in glassy, supercooled, and molten silica from 77 to 2150 K. *J. Chem. Phys.* 124:014504. <http://dx.doi.org/10.1063/1.213687>.
- Kanehashi, K., Stebbins, J.F., 2007. In situ high temperature ^{27}Al NMR study of structure and dynamics in a calcium aluminosilicate glass and melt. *J. Non-Cryst. Solids* 353: 4001–4010. <http://dx.doi.org/10.1016/j.jnoncrysol.2007.06.030>.
- Le Caër, G., Brand, R.A., 1998. General models for the distributions of electric field gradients in disordered solids. *J. Phys. Condens. Matter* 10:10715–10774. <http://dx.doi.org/10.1088/0953-8984/10/47/020>.
- Le Losq, C., Neuville, D.R., 2013. Effect of the Na/K mixing on the structure and the rheology of tectosilicate silica-rich melts. *Chem. Geol.* 346:57–71. <http://dx.doi.org/10.1016/j.chemgeo.2012.09.009>.
- Le Losq, C., Neuville, D.R., Florian, P., Henderson, G.S., Massiot, D., 2014. The role of Al^{3+} on rheology and structural changes in sodium silicate and aluminosilicate glasses and melts. *Geochim. Cosmochim. Acta* 126:495–517. <http://dx.doi.org/10.1016/j.gca.2013.11.010>.
- Le Losq, C., Neuville, D.R., Florian, P., Massiot, D., Zhou, Z., Chen, W., Greaves, N., 2016. Percolation channels: a universal idea to describe the atomic structure of glasses and melts. *Nat. Commun.* (submitted).
- Licheron, M., Montouillout, V., Millot, F., Neuville, D.R., 2011. Raman and ^{27}Al NMR structure investigations of aluminate glasses: $(1-x)\text{Al}_2\text{O}_3-x\text{MO}$, with $\text{M} = \text{Ca}, \text{Sr}, \text{Ba}$ and $0.5 < x < 0.75$. *J. Non-Cryst. Solids* 357:2796–2801. <http://dx.doi.org/10.1016/j.jnoncrysol.2011.03.001>.
- Long, D.A., 1977. *Raman Spectroscopy*. McGraw Hill, New York.
- MacKenzie, K.J.D., Smith, M.E., 2002. *Multinuclear Solid State NMR of Inorganic Materials*. Pergamon.
- Magaritz, M., Hofmann, A.W., 1978. Diffusion of Sr, Ba and Na in obsidian. *Geochim. Cosmochim. Acta* 42:595–605. [http://dx.doi.org/10.1016/0016-7037\(78\)90004-2](http://dx.doi.org/10.1016/0016-7037(78)90004-2).
- Massiot, D., Fayon, F., Capron, M., King, I., Le Calvé, S., Alonso, B., Durand, J.O., Bujoli, B., Gan, Z., Hoatson, G., 2002. Modelling one- and two-dimensional solid-state NMR spectra. *Magn. Reson. Chem.* 40:70–76. <http://dx.doi.org/10.1002/mrc.984>.
- McKeown, D.A., Kot, W.K., Gan, H., Pegg, I.L., 2003. X-ray absorption studies of local strontium environments in borosilicate waste glasses. *J. Non-Cryst. Solids* 317:290–300. [http://dx.doi.org/10.1016/S0022-3093\(03\)00482-4](http://dx.doi.org/10.1016/S0022-3093(03)00482-4).
- McMillan, P., 1984. Structural studies of silicate glasses and melts-applications and limitations of Raman spectroscopy. *Am. Mineral.* 69, 622–644.
- McMillan, P.F., Poe, B.T., Gillet, P.H., Reynard, B., 1994. A study of SiO_2 glass and supercooled liquid to 1950 K via high-temperature Raman spectroscopy. *Geochim. Cosmochim. Acta* 58:3653–3664. [http://dx.doi.org/10.1016/0016-7037\(94\)90156-2](http://dx.doi.org/10.1016/0016-7037(94)90156-2).
- Merzbacher, C.I., White, W.B., 1991. The structure of alkaline earth aluminosilicate glasses as determined by vibrational spectroscopy. *J. Non-Cryst. Solids* 130:18–34. [http://dx.doi.org/10.1016/0022-3093\(91\)90152-V](http://dx.doi.org/10.1016/0022-3093(91)90152-V).
- Moorbath, S., Allaart, J.H., Bridgwater, D., McGregor, V.R., 1977. Rb-Sr ages of early Archaean supracrustal rocks and Amitsoq gneisses at Isua. *Nature* 270:43–45. <http://dx.doi.org/10.1038/270043a0>.
- Mysen, B.O., 1990. Role of Al in depolymerized, peralkaline aluminosilicate melts in the systems $\text{Li}_2\text{O-Al}_2\text{O}_3\text{-SiO}_2$, $\text{Na}_2\text{O-Al}_2\text{O}_3\text{-SiO}_2$, and $\text{K}_2\text{O-Al}_2\text{O}_3\text{-SiO}_2$. *Am. Mineral.* 75, 120–134.
- Mysen, B.O., 1999. Structure and properties of magmatic liquids: From haplobasalt to haploandesite. *Geochim. Cosmochim. Acta* 63:95–112. [http://dx.doi.org/10.1016/S0016-7037\(98\)00273-7](http://dx.doi.org/10.1016/S0016-7037(98)00273-7).
- Mysen, B.O., Frantz, J.D., 1993. Structure and properties of alkali silicate melts at magmatic temperatures. *Eur. J. Mineral.* 5:393–407. <http://dx.doi.org/10.1127/ejm/5/3/0393>.
- Mysen, B.O., Frantz, J.D., 1994. Silicate melts at magmatic temperatures: in-situ structure determination to 1651 °C and effect of temperature and bulk composition on the mixing behaviour of structural units. *Contrib. Mineral. Petrol.* 117:1–14. <http://dx.doi.org/10.1007/BF00307725>.
- Mysen, B.O., Finger, L.W., Virgo, D., Seifert, F.A., 1982. Curve-fitting of Raman spectra of silicate glasses. *Am. Mineral.* 67, 686–695.
- Neuville, D.R., 1992. *Etude des Propriétés Thermodynamiques et Rhéologiques des Silicates Fondus*. Thèse de l'Université de Paris VII, spécialité Géochimie Fondamentale.
- Neuville, D.R., 2005. Structure and properties in (Sr, Na) silicate glasses and melts. *Phys. Chem. Glasses* 46, 112–118.
- Neuville, D.R., 2006. Viscosity, structure and mixing in (Ca, Na) silicate melts. *Chem. Geol.* 229:28–41. <http://dx.doi.org/10.1016/j.chemgeo.2006.01.008>.
- Neuville, D.R., Richet, P., 1991. Viscosity and mixing in molten (Ca, Mg) pyroxenes and garnets. *Geochim. Cosmochim. Acta* 55:1011–1019. [http://dx.doi.org/10.1016/0016-7037\(91\)90159-3](http://dx.doi.org/10.1016/0016-7037(91)90159-3).
- Neuville, D.R., Mysen, B.O., 1996. Role of aluminium in the silicate network: in situ, high-temperature study of glasses and melts on the join $\text{SiO}_2\text{-NaAlO}_2$. *Geochim. Cosmochim. Acta* 60:1727–1737. [http://dx.doi.org/10.1016/0016-7037\(96\)00049-X0](http://dx.doi.org/10.1016/0016-7037(96)00049-X0).
- Neuville, D.R., Cormier, L., Massiot, D., 2004a. Al environment in tectosilicate and peraluminous glasses: a ^{27}Al MQ-MAS NMR, Raman, and XANES investigation. *Geochim. Cosmochim. Acta* 68:5071–5079. <http://dx.doi.org/10.1016/j.gca.2004.05.048>.
- Neuville, D.R., Cormier, L., Flank, A.M., Brioso, V., Massiot, D., 2004b. Al speciation and Ca environment in calcium aluminosilicate glasses and crystals by Al and Ca K-edge X-ray absorption spectroscopy. *Chem. Geol.* 213:153–163. <http://dx.doi.org/10.1016/j.chemgeo.2004.08.039>.
- Neuville, D.R., Cormier, L., Massiot, D., 2006. Al coordination and speciation in calcium aluminosilicate glasses: effects of composition determined by ^{27}Al MQ-MAS NMR and Raman spectroscopy. *Chem. Geol.* 229:173–185. <http://dx.doi.org/10.1016/j.chemgeo.2006.01.019>.
- Neuville, D.R., Cormier, L., Montouillout, V., Massiot, D., 2007. Local Al site distribution in aluminosilicate glasses by ^{27}Al MQMAS NMR. *J. Non-Cryst. Solids* 353:180–184. <http://dx.doi.org/10.1016/j.jnoncrysol.2006.09.035>.
- Neuville, D.R., Cormier, L., Montouillout, V., Florian, P., Millot, F., Rifflet, J.-C., Massiot, D., 2008a. Structure of Mg- and Mg/Ca aluminosilicate glasses: ^{27}Al NMR and Raman spectroscopy investigations. *Am. Mineral.* 93:1721–1731. <http://dx.doi.org/10.2138/am.2008.2867>.
- Neuville, D.R., Cormier, L., De Ligny, D., Roux, J., Flank, A.M., Lagarde, P., 2008b. Environments around Al, Si, and Ca in aluminate and aluminosilicate melts by X-ray absorption spectroscopy at high temperature. *Am. Mineral.* 93:228–234. <http://dx.doi.org/10.2138/am.2008.2646>.
- Neuville, D.R., Henderson, G.S., Cormier, L., Massiot, D., 2010. The structure of crystals, glasses, and melts along the $\text{CaO-Al}_2\text{O}_3$ join: Results from Raman, Al L- and K-edge X-ray absorption, and ^{27}Al NMR spectroscopy. *Am. Mineral.* 95:1580–1589. <http://dx.doi.org/10.2138/am.2010.3465>.
- Neuville, D.R., de Ligny, D., Henderson, G.S., 2014. Advances in Raman spectroscopy applied to Earth and material sciences. *Rev. Mineral. Geochem.* 78:509–541. <http://dx.doi.org/10.2138/rmg.2013.78.13>.

- Pasquarello, A., Car, R., 1998. Identification of Raman defect lines as signatures of ring structures in vitreous silica. *Phys. Rev. Lett.* 80:5145–5147. <http://dx.doi.org/10.1103/PhysRevLett.80.5145>.
- Plazek, D.J., Ngai, K.L., 1991. Correlation of polymer segmental chain dynamics with temperature-dependent time-scale shifts. *Macromolecules* 24:1222–1224. <http://dx.doi.org/10.1021/ma00005a044>.
- Poe, B.T., McMillan, P.F., Cote, B., Massiot, D., Coutures, J.-P., 1994. Structure and dynamics in calcium aluminate liquids: High-temperature ^{27}Al NMR and Raman spectroscopy. *J. Am. Ceram. Soc.* 77:1832–1838. <http://dx.doi.org/10.1111/j.1151-2916.1994.tb07058.x>.
- Rahmani, A., Benoit, M., Benoit, C., 2003. Signature of small rings in the Raman spectra of normal and compressed amorphous silica: A combined classical and ab initio study. *Phys. Rev. B* 68:21. <http://dx.doi.org/10.1103/PhysRevB.68.184202>.
- Ravel, B., Newville, M., 2005. Athena, artemis, hephaestus: data analysis for X-ray absorption spectroscopy using IFEFFIT. *J. Synchrotron Radiat.* 12:537–541. <http://dx.doi.org/10.1107/S0909049505012719>.
- Richet, P., 1984. Viscosity and configurational entropy of silicate melts. *Geochim. Cosmochim. Acta* 48:471–483. [http://dx.doi.org/10.1016/0016-7037\(84\)90275-8](http://dx.doi.org/10.1016/0016-7037(84)90275-8).
- Richet, P., 1987. Heat capacity of silicate glasses. *Chem. Geol.* 62:111–124. [http://dx.doi.org/10.1016/0009-2541\(87\)90062-3](http://dx.doi.org/10.1016/0009-2541(87)90062-3).
- Richet, P., Bottinga, Y., 1985. Heat capacity of aluminum-free liquid silicates. *Geochim. Cosmochim. Acta* 49:471–486. [http://dx.doi.org/10.1016/0016-7037\(85\)90039-0](http://dx.doi.org/10.1016/0016-7037(85)90039-0).
- Richet, P., Neuville, D.R., 1992. Thermodynamics of silicate melts: configurational properties. *Thermodynamic Data*: pp. 133–161 http://dx.doi.org/10.1007/978-1-4612-2842-4_5.
- Robie, R.A., Hemingway, B.S., Fisher, J.R., 1978. Thermodynamic properties of minerals and related substances at 298.15 K and 1 bar pressure and at higher temperatures. *US Geological Survey Bulletin* 1452.
- Rudnick, R.L., Gao, S., 2003. Composition of the Continental Crust. *Treatise on Geochemistry*. Elsevier: pp. 1–64 <http://dx.doi.org/10.1016/B0-08-043751-6/03016-4>.
- Scherer, G.W., 1984. Use of the Adam-Gibbs equation in the analysis of structural relaxation. *J. Am. Ceram. Soc.* 67:504–511. <http://dx.doi.org/10.1111/j.1151-2916.1984.tb19643.x>.
- Seifert, F.A., Mysen, B.O., Virgo, D., 1982. Three-dimensional network structure of quenched melts (glass) in the systems $\text{SiO}_2\text{-NaAlO}_2$, $\text{SiO}_2\text{-CaAl}_2\text{O}_4$ and $\text{SiO}_2\text{-MgAl}_2\text{O}_4$. *Am. Mineral.* 67, 696–717.
- Sen, P.N., Thorpe, M.F., 1977. Phonons in AX_2 glasses: From molecular to band-like modes. *Phys. Rev. B* 15:4030–4038. <http://dx.doi.org/10.1103/PhysRevB.15.4030>.
- Sharma, S.K., Mammone, J.F., Nicol, M.F., 1981. Raman investigation of ring configurations in vitreous silica. *Nature* <http://dx.doi.org/10.1038/292140a0>.
- Sharma, K., Kothiyal, G.P., Montagne, L., Méar, F.O., Revel, B., 2012. A new formulation of barium-strontium silicate glasses and glass-ceramics for high-temperature sealant. *Int. J. Hydrog. Energy* 37:11360–11369. <http://dx.doi.org/10.1016/j.ijhydene.2012.04.142>.
- Stebbins, J.F., Farnan, I., Xue, X., 1992. The structure and dynamics of alkali silicate liquids: A view from NMR spectroscopy. *Chem. Geol.* 96:371–385. [http://dx.doi.org/10.1016/0009-2541\(92\)90066-E](http://dx.doi.org/10.1016/0009-2541(92)90066-E).
- Taylor, S.R., 1964. Abundance of chemical elements in the continental crust: a new table. *Geochim. Cosmochim. Acta* 28:1273–1285. [http://dx.doi.org/10.1016/0016-7037\(64\)90129-2](http://dx.doi.org/10.1016/0016-7037(64)90129-2).
- Thompson, L.M., Stebbins, J.F., 2012. Non-stoichiometric non-bridging oxygens and five-coordinated aluminum in alkaline earth aluminosilicate glasses: effect of modifier cation size. *J. Non-Cryst. Solids* 358:1783–1789. <http://dx.doi.org/10.1016/j.jnoncrysol.2012.05.022>.
- Turekian, K.K., Kulp, J.L., 1956. The geochemistry of strontium. *Geochim. Cosmochim. Acta* 10:245–296. [http://dx.doi.org/10.1016/0016-7037\(56\)90015-1](http://dx.doi.org/10.1016/0016-7037(56)90015-1).
- Turekian, K.K., Wedepohl, K.H., 1961. Distribution of the elements in some major units of the Earth's crust. *Geol. Soc. Am. Bull.* 72:175–192. [http://dx.doi.org/10.1130/0016-7606\(1961\)72\[175:DOTEIS\]2.0.CO;2](http://dx.doi.org/10.1130/0016-7606(1961)72[175:DOTEIS]2.0.CO;2).
- Umari, P., Pasquarello, A., 2002. Modeling of the Raman spectrum of vitreous silica: concentration of small ring structures. *Phys. B Condens. Matter* 316-317:572–574. [http://dx.doi.org/10.1016/S0921-4526\(02\)00576-8](http://dx.doi.org/10.1016/S0921-4526(02)00576-8).
- Urbain, G., 1974. Viscosité et structure de silicoalumineux liquides. I. Méthode de mesure et résultats expérimentaux. *Rev. Intl. Hautes Temp. Réfract.* 11, 133–145.
- Urbain, G., Bottinga, Y., Richet, P., 1982. Viscosity of liquid silica, silicates and aluminosilicates. *Geochim. Cosmochim. Acta* 46:1061–1072. [http://dx.doi.org/10.1016/0016-7037\(82\)90059-X](http://dx.doi.org/10.1016/0016-7037(82)90059-X).
- Ye, Y., Smyth, J.R., Boni, P., 2012. Crystal structure and thermal expansion of aragonite-group carbonates by single-crystal X-ray diffraction. *Am. Mineral.* 97:707–712. <http://dx.doi.org/10.2138/am.2012.3923>.

Annex II

Ba tectosilicate glasses (Journal of Non-Crystalline Solids)

1 **Structure-property relationships in Ba tectosilicate glasses**

2 Alexey N. Novikov^{a,b*}, Pierre Florian^a, Louis Hennet^a and Daniel R. Neuville^b

3 ^a CEMHTI UPR3079 CNRS, Univ. Orléans, F-45071 Orléans, France

4 ^b IPGP UMR7154 CNRS, Géomatériaux, Paris Sorbonne Cité, 75005 Paris, France

5 * alexey.novikov@cnrs-orleans.fr

6

7 **Abstract**

8 Seven glasses in the BaO-Al₂O₃-SiO₂ ternary system with BaO/Al₂O₃ = 1 and silica content
9 varying from 75 to 20 mol% were investigated. The structure of the glasses was studied by
10 ²⁷Al NMR and Raman spectroscopy. A small fraction (< 2.5 %) of AlO₅ “defects” is present in
11 the network. Replacement of SiO₂ by BaAl₂O₄ favours formation of four- and three-
12 membered tetrahedral rings. The *T_g* curve obtained from viscosity measurements possesses
13 a minimum for the compositions with 42-63 mol%. This minimum is found for the
14 compositions with the highest concentration of five-coordinate aluminium. In general,
15 barium aluminosilicate glasses of tectosilicate composition have structure and properties
16 very close to those of analogous strontium containing glasses studied in our previous work.

17 **Keywords:** barium aluminosilicate glasses; viscosity; Raman; Al-27 NMR

18

19 **1. Introduction**

20 Alkali and alkaline earth aluminosilicates are of great importance in geoscience and
21 materials science as well as in industrial processes of glass/ceramics production. However,
22 barium aluminosilicates (BAS) are of rare occurrence in the Earth's crust and have attracted
23 only few attention of researchers before the second half of the 20th century [1,2]. Extensive
24 exploration of the BaO-Al₂O₃-SiO₂ phase diagram later in the 1950s [3,4] has aroused an
25 interest in the system. In particular, the crystalline phase of BaAl₂Si₂O₈ composition (known
26 as "celsian") has practical applications due to its high melting point, low coefficient of
27 thermal expansion, good oxidation and reduction resistance, resistance to alkali attack, low
28 values of dielectric constant and loss tangent [5–9]. Nowadays, BAS-based compositions
29 have a broad spectrum of applications, such as: crown optical glasses [10], glass-ceramic
30 sealants for solid oxide fuel cells [11–17] or for oxygen transport membranes [18], glass-
31 ceramic composites with high energy storage efficiency [19], high energy density dielectric
32 glasses [20–22], transparent ceramics [23], bioactive glasses [24], glasses with good
33 radiation shielding properties [25], matrices for photoactive glasses and glass ceramics [26],
34 and radio-transparent ceramic materials [27].

35 The BaO-Al₂O₃-SiO₂ ternary system has been investigated by many authors but those
36 studies have been concentrated mainly on particular compositions (e.g., celsian, Ba silicates
37 or aluminates). And most of the studies have concentrated either on macroscopic properties
38 [1,28–35] or on the structure of BAS [6,7,36–47]. Only several studies have used a multi-
39 technique approach to study Ba aluminosilicates [23,48–52] but not always for describing
40 their structure/properties relationship. In the present work, we aim at correlating short and
41 medium range order of BAS glasses on the tectosilicate join by means of ²⁷Al MAS NMR and
42 Raman spectroscopy along with measurements of macroscopic properties (density and
43 viscosity). All the studied glasses have the BaO/Al₂O₃ ratio equal to one, i. e. Ba²⁺ cations are
44 expected to be charge compensators proximal to AlO₄⁻ tetrahedra.

45 **2. Materials and methods**

46 *2.1 Synthesis of glasses in the BaO-Al₂O₃-SiO₂ system*

47 Homogeneous glass/ceramic samples of barium aluminosilicates were prepared by a
48 classic melting-quenching procedure. Dry powders of SiO₂, Al₂O₃ and BaCO₃ (all reagents

49 were Rectapur[®] from Merck) were mixed in a stoichiometric amount to make 100 g batches.
50 The powders were crushed together in an agate mortar under ethanol for 1 h and then
51 decarbonated in a platinum crucible at temperatures up to 1200 °C in an electric muffle
52 furnace for at least two hours. After this, the mixtures were melted at 1600 °C and
53 quenched either by dipping the bottom of the crucible in water or by pouring the melt on a
54 large copper plate. Quenching method depended on the viscosity of a melt. The grinding,
55 melting, quenching procedures were repeated three more times to ensure the homogeneity
56 of the final product. At the final stage, the products were maintained at a temperature
57 above their melting points for several hours to produce bubble-free samples for further
58 viscosity measurements. If glass samples could not be obtained directly by traditional
59 quenching (case of BA20.40, BA26.37 and BA50.25 compositions), ceramic samples were
60 prepared following the above-described procedure and an aerodynamic levitation device
61 coupled with two CO₂ lasers was used to prepare small glass spheres [53]. In our previous
62 study [54] some samples of equivalent strontium glasses obtained by different quenching
63 methods have been examined. It has been found that different quenching rates do not
64 cause any significant structural difference in the samples (namely, no difference in density,
65 Raman and NMR spectra). So, further in this paper, we will be assuming that for the BAS
66 glasses any differences in properties and the structure are caused by changes in
67 composition and not by the quenching methods.

68 All glasses were transparent and visually free of a crystalline phase. Density
69 measurements of several pieces of each composition didn't reveal any macroscopic
70 inhomogeneities as well. The densities were measured using the Archimedean method with
71 toluene as the immersion liquid and listed in Table together with chemical compositions of
72 glasses. The names of the glasses are given as BAxx.yy, where xx is the SiO₂ content in mol%,
73 yy is the Al₂O₃ content in mol%, the remaining being the content of BaO.

74 2.2 Viscosity measurements

75 The viscosity measurements at low temperatures were performed using a creep
76 apparatus described elsewhere [55,56]. Samples used for the measurements were glass
77 cylinders with height to diameter ratio $H/D \approx 2$ ($H = 10-15$ mm, $D = 5-7$ mm). The cylinders
78 were polished from two sides in order to have parallel faces. Before the viscosity
79 measurements, the cylinders were held in a furnace at 600-800 °C for 1 day to remove

80 internal stress. The reported viscosity values at one temperature are the result of an
81 average of 20-40 measurements at different applied stresses.

82 *2.3 DSC measurements*

83 Glass transition temperatures (T_g) of BA50.25, BA26.37 and BA20.40 glass samples were
84 measured using Setaram® L96 Evo TGA-DTA/DSC apparatus with the heating rate of
85 5 K/min. T_g was determined as an inflection point of the heat flow curve and a correction of
86 22 K was then applied to the values to have T_g comparable to those obtained from the
87 viscosity curves at $\log\eta = 12$ Pa·s. This correction value was calibrated by measuring samples
88 with known glass transition temperatures under the same conditions.

89 *2.4 Raman spectroscopy*

90 Unpolarized Raman spectra were recorded at room temperature using a T64000 Jobin-
91 Yvon® triple Raman spectrometer. A Coherent® 70-C5 argon laser with a wavelength of
92 488.01 nm and with a power of 0.85 W was used as the excitation source. All spectra were
93 acquired in backscattering geometry between 20 and 1400 cm^{-1} with an acquisition time of
94 300 s and 3 repetitions per spectral window. No special sample preparations were made in
95 advance. Before the deconvolution of the high-frequency region, all spectra were baseline
96 corrected and normalized in such a manner that the total area under a spectrum was equal
97 one. Then the high-frequency region of the spectra was deconvoluted using the Fityk
98 software [57]. All parameters, such as band's frequency, width and intensity were not
99 constrained during the deconvolution procedure.

100 *2.5 Nuclear magnetic resonance spectroscopy*

101 Quantitative 1 pulse ^{27}Al MAS NMR experiments were performed on an Avance III
102 Bruker 850 MHz (20.0 T) spectrometer working at an ^{27}Al frequency of 221.5 MHz. Chemical
103 shifts for ^{27}Al were referenced to a 1 M aqueous $\text{Al}(\text{NO}_3)_3$ solution. Magic Angle Spinning
104 (MAS) experiments were performed at a spinning speed of 30 kHz in aluminium-free
105 zirconia rotors of 2.5 mm diameter. All spectra were obtained using a single-pulse ("Bloch-
106 decay") sequence using a radio-frequency field $\nu_{\text{rf}} = 62.5$ kHz and applying a pulse of 0.4 μs
107 (i.e. less than $\pi/18$ to ensure quantitative irradiation). Four thousand scans were
108 accumulated for each composition with a recycling time of 0.15 s (spin-lattice relaxation
109 times found in the range 1-5 s), using a spectral window of 2 MHz to avoid folding of the

110 spinning sidebands manifold. The decomposition of the spectra was obtained using the
111 dmfit software [58], taking into account the spinning sidebands of the external transitions.
112 This allows extracting the populations of the various components appearing on the central
113 transition, their mean isotropic chemical shifts δ_{iso} , their distributions of isotropic chemical
114 shift $\Delta\delta_{iso}$ and their mean quadrupolar coupling constants C_Q within the framework of the
115 so-called “Czjzek” or “GIM” model [59].

116 3. Results

117 3.1 Viscosity, fragility and T_g

118 **Figure** represents viscosity curves plotted as a function of reciprocal temperature (data
119 are presented in **Table**). It can be seen that at temperatures above T_g (left part of the
120 figure) viscosities at a fixed temperature follow a general rule for tectosilicate compositions
121 – the higher SiO_2 content the higher viscosity. But this rule is violated approaching lower
122 temperatures (right part of the figure), where one can see that viscosity of the composition
123 with 33.33 mol% of silica (BA33.33) is higher than that of the one with 75 mol% of silica
124 (BA75.12). The viscosity data were fitted with the Vogel–Fulcher–Tammann–Hesse (VFTH)
125 equation:

$$126 \quad \log\eta = A + \frac{B}{T-T_1}, \quad (1)$$

127 where η is the viscosity in Pa·s, T is the temperature in K and A , B , T_1 are adjustable
128 parameters given in **Table**. The glass transition temperatures were derived from the fits as
129 the temperature at which viscosity is 10^{12} Pa·s (**Table**). Starting from pure silica glass, T_g
130 decreases rapidly with the addition of BaAl_2O_4 and the difference between vitreous SiO_2 and
131 BA75.12 is around 300 K (**Figure**). From BA75.12, a slight decrease in T_g is observed upon
132 changing the composition with a minimum somewhere in between 42 and 63 mol% of SiO_2 .
133 Starting from the composition BA42.29, further addition of BaAl_2O_4 causes an increase in
134 the glass transition temperature. Similar observations have been made on Ca and Sr
135 tectosilicate glasses [54,60].

136 In **Figure** the viscosity data for glasses and melts are plotted in the so-called Angell plot
137 [61,62]. Such a plot illustrates how fast kinetic arrest happens under a small decrease in

138 temperature, i.e. the evolution of the melt's fragility (m). It is well seen that with the
 139 substitution of SiO₂ by BaAl₂O₄ (going from silica glass to the BA33.33 composition) the
 140 melts become more fragile. The fragility can be calculated by the following equation:

$$141 \quad m = \left. \frac{d(\log_{10}\eta)}{d\left(\frac{T}{T_g}\right)} \right|_{T=T_g} = \frac{B}{T_g(1-T_1/T_g)^2}, \quad (2)$$

142 where B and T_1 are the coefficients obtained from the VFTH equation (1). The calculated
 143 fragilities m are listed in [Table](#) .

144 The viscosity of melts can be connected with thermodynamic properties, such as
 145 entropy of configuration, through the Adam and Gibbs theory [63,64] and following the
 146 equation:

$$147 \quad \log \eta = A_e + \frac{B_e}{T \cdot S^{conf}(T)}, \quad (3)$$

148 where η is the viscosity in Pa·s, T is the temperature in K, A_e is a pre-exponential factor,
 149 B_e is a constant proportional to the potential barrier opposed to the cooperative
 150 rearrangement of the liquid's structure and $S^{conf}(T)$ is the melt's configurational entropy.
 151 $S^{conf}(T)$ can be calculated from the following equation:

$$152 \quad S^{conf}(T) = S^{conf}(T_g) + \int_{T_g}^T \frac{C_p^{conf}}{T} dT, \quad (4)$$

153 where $S^{conf}(T_g)$ is the configurational entropy of the melt at T_g , C_p^{conf} is the
 154 configurational heat capacity calculated as a difference of heat capacities of the glass at T_g ,
 155 $C_{p,g}(T_g)$, and the heat capacity of the liquid, $C_{p,l}$, determined from [65]. Partial molar heat
 156 capacities of SiO₂ and Al₂O₃ for the calculations of $C_{p,g}(T_g)$ were taken from [66] and the
 157 value of partial molar heat capacity of crystalline BaO was taken from [67], following
 158 previous calculations by Neuville [56] for the Na₂O-CaO-SiO₂ system and by Novikov et al.
 159 [54] for the SrO-Al₂O₃-SiO₂ system. Combining equations (3) and (4), parameters such as
 160 $S^{conf}(T_g)$, A_e and B_e can be estimated ([Table](#)). Dependence of the configurational entropy at
 161 T_g from SiO₂ content is plotted in [Figure](#) . It is clearly seen that with decreasing of silica
 162 fraction (increasing of BaAl₂O₄) $S^{conf}(T_g)$ goes up.

163 3.2 Raman spectroscopy

164 **Figure** presents a stack plot of area normalized Raman spectra of the BAS glasses. In
165 the region spanning 20-250 cm^{-1} the Boson peak occurs. It becomes narrower and more
166 pronounced with the substitution of SiO_2 by BaAl_2O_4 . It also shifts from 45 to 55 cm^{-1} for
167 BA75.12 and BA20.40, respectively. In the low-frequency region (250-750 cm^{-1}) important
168 changes occur in the peak distribution. If the spectrum of silica glass possesses three bands
169 at 435, 490, and 606 cm^{-1} , there are only two bands at 478 and 575 cm^{-1} (the latter one
170 appearing as a shoulder) in the spectrum of BA75.12 in this region. Under substitution of
171 SiO_2 by BaAl_2O_4 , the first peak decreases in intensity and stays almost at the same position
172 (487 cm^{-1} for BA20.40), while the second peak shifts to a lower frequency and its intensity
173 increases (543 cm^{-1} for BA20.40). These two bands are usually assigned to vibrations of
174 three- and four-membered rings of tetrahedra present in the aluminosilicate network [68–
175 71]. A broad asymmetrical band around 800 cm^{-1} is observed for SiO_2 in the intermediate
176 frequency range (700-850 cm^{-1}). It shifts to a lower frequency and its intensity rapidly goes
177 down with decreasing silica content. This band is usually attributed to the threefold
178 degenerate “rigid cage” vibrational mode of TO_2 units [72], to the motion of the Si atom in
179 its oxygen cage [73] or to Si–O stretching involving oxygen motions in the Si–O–Si plane [74].
180 In the high-frequency region (850-1300 cm^{-1}) two broad bands are observed in the spectrum
181 of vitreous silica. For BA75.12 glass only a single broad band is observed and it becomes
182 narrower and shifts to lower frequency with decreasing silica content, similarly to what has
183 been observed for Mg, Ca and Sr tectosilicate glasses (further MAS, CAS and SAS,
184 respectively) [54,75,76]. Several studies pointed out that different peaks are convoluted in
185 this band, arising from the T–O stretching (T = Si, Al) in different Q^n tetrahedral units, where
186 n is the number of bridging oxygens and Q is the four-fold coordinated cation [77,78].

187 3.3 ^{27}Al NMR spectroscopy

188 **Figure** shows ^{27}Al NMR spectra of the studied glasses. The NMR bands appear as broad
189 asymmetric lines possessing a single maximum. The position of this maximum changes from
190 60 to 73 ppm as SiO_2 is substituted by BaAl_2O_4 . Deconvolution of the spectra reveals the
191 presence of the second component at 35-47 ppm. The two contributions to an NMR signal
192 are attributed to aluminium in four-fold ($\text{Al}^{[4]}$) or five-fold coordination ($\text{Al}^{[5]}$), respectively.
193 The parameters obtained from the deconvolution, such as average isotropic chemical shift

194 δ_{iso} , mean quadrupolar coupling constant C_Q and population of each site are given in [Table](#) .
195 The average isotropic chemical shift of Al^[4] sites increases linearly with the substitution of
196 SiO₂ by BaAl₂O₄ ([Figure](#)). The very similar trend has been observed for the CAS and SAS
197 systems on the same join [\[54,79\]](#). Less precisely defined because of much lower intensity,
198 the average isotropic chemical shift of the Al^[5] sites also follows an overall linear increase
199 with decreasing SiO₂ content.

200 **4. Discussion**

201 *4.1 Changes along the SiO₂-BaAl₂O₄ join: structural considerations*

202 Silica glass is the simplest model of a fully polymerized glass. Its network consists of
203 corner-sharing SiO₄ tetrahedra forming rings of different size. Unlike quartz composed of
204 solely six-membered rings, the structure of amorphous silica includes a set of rings from
205 small three-membered to larger ones [\[68,69,74,80–85\]](#). With the addition of BaAl₂O₄ into
206 silica, one does not expect depolymerisation of the network since each Ba²⁺ cation is charge
207 compensated by two negatively charged AlO₄⁻ tetrahedra. Thus, common wisdom suggests
208 that the network should stay fully polymerized both at high and low silica content,
209 composed solely of corner sharing tetrahedral units TO₄ (T = Si, Al). However, it has been
210 shown previously that a small amount of different “defects” can be present in the
211 aluminosilicate network even for compositions on the charge compensation line. Among
212 them are five- and six-coordinate aluminium, non-bridging oxygens (NBOs) and oxygen
213 triclusters (for examples see [\[46,86–89\]](#)). In addition to these features, tectosilicate glasses
214 are also expected to display various medium range organisation, i.e. rings of different sizes
215 (three-membered to larger ones).

216 We characterized the short range order (SRO) and the medium range order (MRO) in
217 this work with ²⁷Al NMR probing local environment around aluminium atoms and Raman
218 spectroscopy giving information on ring statistics and Qⁿ species distributions. In the Raman
219 spectrum of SiO₂ glass three bands at 606, 490, and 435 cm⁻¹ are observed and they have
220 been assigned to vibrations occurring in three-, four- and higher-membered tetrahedral
221 rings, respectively [\[68,69,74,80–85\]](#). For glasses along the SiO₂-BaAl₂O₄ join, the Raman
222 spectra exhibit changes in ring statistics with the introduction of the barium aluminate
223 ([Figure](#)): the fraction of high-membered rings decreases with the introduction of BaAl₂O₄

224 and four- and three-membered rings become dominant. This is in contrast with the calcium
225 tectosilicate glasses for which the fraction of four-membered rings becomes dominant with
226 decreasing SiO₂ content [75,90]. For analogous BAS glasses with decreasing SiO₂ content the
227 band attributed to three-membered rings becomes more intense while the band attributed
228 to four-membered rings diminishes. Similar situation with the favoured formation of small
229 three-membered rings has been seen for the SAS tectosilicate glasses [54].

230 In the high-frequency region Raman spectra exhibit a continuous shift of the band
231 frequencies as a function of the Al/(Al+Si) ratio as has already been seen for other alkali and
232 alkaline earth tectosilicate systems. The high-frequency envelope of the Raman spectra of
233 glasses along this join was deconvoluted using three bands assigned to two Q⁴ units (Q^{4,I} and
234 Q^{4,II}) and the T_{2s} vibrational mode as it has been implemented by other authors before
235 [54,75,91–94]. There is no evidence of the appearance of any other Qⁿ species except for Q⁴
236 under the substitution of SiO₂ by BaAl₂O₄. In Figure , the positions of the three bands after
237 deconvolution are plotted as a function of SiO₂ content together with the data available on
238 other tectosilicates. The negative linear frequency shift with increasing Al₂O₃ content is
239 consistent with the aluminium substitution for Si in these units [78,92]. The three bands
240 follow a similar trend for Na, Mg, Ca, Sr and Ba tectosilicate glasses. This is in good
241 agreement with Merzbacher and White [95] who have shown that the substitution of
242 alkaline earth element produces a very small effect on the Raman spectra. This indicates
243 that, on the tectosilicate join, Si/Al substitution has a larger influence on the aluminosilicate
244 network than the nature of a cation, which plays the role of a charge compensator.

245 Similar linear trend under the Si/Al exchange can be seen in δ_{iso} for Al^[4] and Al^[5] sites
246 for the MAS, CAS, SAS and BAS tectosilicate glasses. Chemical shifts for the two aluminium
247 sites are plotted in Figure versus SiO₂ content. This similar change of δ_{iso} in the four systems
248 suggests a close-to-random substitution of Si by Al in the second coordination sphere of
249 aluminium, independent of the modifier nature and which produces an approximate 3 ppm
250 shift for each 10 mol% of SiO₂. This is in agreement with 3 ppm and 5 ppm shift per
251 substitution reported respectively by other authors [96,97]. Interestingly, this linear
252 behaviour does not hold for the compositions with high silica content. This could suggest
253 some kind of local structural heterogeneities or phase separation for those compositions.

254 The Al^[5] population curve (Figure) for BAS glasses does not exceed ~2.5 % of five-fold
255 aluminium. The proportion of Al^[5] in the BAS glasses is lower than that observed in MAS,

256 CAS and SAS counterparts. This is in a good agreement with previous studies on alkali, earth
257 alkaline and rare earth aluminosilicates that have shown that the increase of the cation field
258 strength directly correlates with an increase of the Al^[5] population [46,98–100]. In this
259 respect, the BaO-Al₂O₃-SiO₂ system has a behaviour similar to sodium aluminosilicate
260 glasses which have a small to non-detectable amount of high coordinated Al species
261 [98,101,102].

262 4.2 Changes along the SiO₂-BaAl₂O₄ join: macroscopic properties

263 Configurational entropy at the glass transition temperature, $S^{conf}(T_g)$, for silica glass is
264 minimal when compared with any aluminosilicate glasses because it consists of only a pure
265 topological contribution [103]. The introduction of even small amounts of BaAl₂O₄ into the
266 silica network, adds some new topological and chemical contributions to $S^{conf}(T_g)$. Firstly,
267 additional structural units (AlO₄, AlO₅, potential NBOs and three-coordinate oxygens)
268 appear; and secondly, tetrahedral rings start to include not only SiO₄ but also AlO₄. All this
269 leads to an increase of $S^{conf}(T_g)$ (Figure) and to a rapid drop in T_g (Figure). Al substitutes Si in
270 SiO₄ which causes the fragility to increase (Figure) under continuous introduction of BaAl₂O₄
271 since the Al-O bonds are weaker than the Si-O ones. From 75 mol% of silica T_g decreases
272 gradually (Figure) as a consequence of an increasing fragility, increasing disorder in the
273 system and increasing fraction of AlO₅. Below 42 mol% of silica the melts' fragility continues
274 to increase while the fraction of low-membered rings prevails and the number of different
275 structural units decreases (less SiO₄ and AlO₅). Considering the lack of the viscosity data (and
276 hence values of $S^{conf}(T_g)$) for the compositions with less than 33 mol% of silica we can only
277 assume that the observed increase in T_g with further decrease in SiO₂ content is due to a
278 progressive ordering of the system.

279 It is worth noticing that the maximum in Al^[5] content (Figure), observed for the
280 composition range 33-50 mol% of SiO₂, corresponds to the minimum in T_g (Figure). The
281 same trend has been seen for Ca and Sr tectosilicates where a maximum in Al^[5] corresponds
282 to a minimum in T_g [54,60,79]. Thus, five-fold coordinated Al can be considered as having a
283 similar role as Si^[5] species in promoting the viscous flow [104]. Such a participation of the
284 AlO₅ units in the network mobility has been proposed by Poe et al. [105] for aluminate melts
285 and more recently by Le Losq et al. [93] for aluminosilicate melts. Nevertheless, the
286 presence of AlO₅ units might be not enough to explain the observed variation in viscosity

287 and T_g . Even though the deconvolution of Raman spectra did not show the presence of
288 NBOs (only Q^4 species), they might play a significant role even in small quantities affecting
289 macroscopic properties. For example, Thompson et al. [46] have shown existence of $\sim 5\%$ of
290 NBOs for BAS glasses with low silica content ($\sim 30\%$ mol%) and $BaO/Al_2O_3 \approx 1$, while Skinner et
291 al. [52] have indicated the presence of a huge fraction ($\sim 21\%$) of oxygen triclusters in a Ba
292 aluminate glass (though not on the tectosilicate join). Other authors have demonstrated an
293 important role of minor aluminium species and even of small quantities of NBOs and oxygen
294 triclusters in changing properties of glasses in the CAS system [88,89,106].

295 Thompson and Stebbins [107] have shown that for tectosilicates in the CAS system the
296 proportion of NBOs increases with decreasing SiO_2 content up to a maximum of $\sim 6\%$ for
297 the CA30.35 (using our notation) composition. Nevertheless, there is no information on
298 NBOs content for compositions with SiO_2 content lower than 30% mol% for which we observe
299 an increase in T_g (Figure). Iuga et al. [108] have reported for $CaAl_2O_4$ (CA00.50) a proportion
300 of NBOs of $\sim 5\%$. This lower proportion of NBOs together with the lower amount of AlO_5
301 (Figure) and the expected decrease in S^{conf} (less possible configurations in the aluminate
302 than in aluminosilicates) could explain the increased T_g for this aluminate composition and
303 hence could also be the origin of the increase of T_g at low silica content. Thompson and
304 Stebbins [46,107] have also shown by comparing glasses in KAS, CAS and BAS systems that it
305 is the cation's charge and not the size that defines NBOs content. They have demonstrated
306 that the amount of NBOs increases from KAS to CAS system but is identical for BAS and CAS
307 glasses. Hence, we can assume equal proportions of NBOs in the two systems for our
308 compositions and this excludes the influence of NBOs on the glass transition temperature.

309 At the same time, the proportion of five-coordinate aluminium in the CAS system is
310 almost 4 times higher than in the BAS one (Figure). This is in agreement with observations
311 of the dependence of the $Al^{[5]}$ proportion on the cation field strength (CFS)
312 [46,107,109,110]. The CFS decreases in the row Mg-Ca-Sr-Ba and the fraction of AlO_5
313 diminishes concurrently (Figure). At the same time, T_g curves (Figure) have an opposite
314 trend: tectosilicates of Ba possess the highest values of the glass transition temperatures
315 while the curve for the CAS glasses lies below with the SAS curve being in between. This
316 points toward the existence of a link between the $Al^{[5]}$ content and the difference in T_g
317 between the systems as well as the minimum on the T_g curves as seen above.

318 Therefore, we can conclude that even in small amounts such minor species could
319 influence S^{conf} and as a consequence T_g . One should nevertheless keep in mind that we are
320 not considering the presence of three-coordinate oxygens since we have currently no means
321 to observe them. Their presence is supposed to have a great impact on the viscosity of
322 aluminosilicate melts [86,111].

323 5. Conclusions

324 Short and medium range order of BaO-Al₂O₃-SiO₂ glasses was investigated by Raman
325 and ²⁷Al NMR spectroscopies. The obtained information on the structure was correlated
326 with viscosity measurements around T_g . It was found that five-coordinate aluminium is
327 present in all the studied glasses, though its content does not exceed ~2.5 %. The highest
328 concentration of Al^[5] is observed for the compositions with 40-50 mol% of SiO₂. Ring
329 statistics are changing with replacing silica by BaAl₂O₄. The fraction of large rings diminishes
330 under the substitution and at low SiO₂ content four- and three-membered rings are
331 dominant. Mixing between aluminium and silicon in TO₄ is close to random for the
332 compositions with intermediate silica content as suggested by the linear shifts of $\delta_{iso}(Al^{[4]})$
333 and the high-frequency Raman bands. Viscosity measurements show the presence of a
334 minimum in T_g for the composition with 42 to 63 mol% of SiO₂. This minimum coincides with
335 the maximum in Al^[5] content but can be caused by a more complex nature of glass structure
336 (e.g., the presence of non-bridging oxygens, oxygen triclusters etc.). As a perspective for this
337 study, an ¹⁷O NMR, as well as MD simulations, would help to shed light on the NBOs and
338 triclusters content and their effect on viscosity and T_g .

339 Acknowledgments

340 This research was conducted under the ANR funding [ANR-13-BS08-0012].

341 References

- 342 [1] P. Eskola, The silicates of strontium and barium, Am. J. Sci. s5-4 (1922) 331–375.
343 doi:10.2475/ajs.s5-4.23.331.
- 344 [2] N.L. Bowen, Crystals of barium disilicate in optical glass, J. Washingt. Acad. Sci. VIII
345 (1918) 265–268.
- 346 [3] R.H. Thomas, Phase Equilibrium in a Portion of the Ternary System BaO-Al₂O₃-SiO₂, J.
347 Am. Ceram. Soc. 33 (1950) 35–44.

- 348 [4] N.A. Toropov, F.Y. Galakhov, I.A. Bondar, The Diagram of State of the Ternary System
349 BaO-Al₂O₃-SiO₂, Izvest. Akad. Nauk S.S.S.R., Otd. Khim. Nauk. (1954) 647–655.
- 350 [5] B. Hoghooghi, J. McKittrick, C. Butler, P. Desch, Synthesis of celsian ceramics from
351 zeolite precursors, *J. Non. Cryst. Solids*. 170 (1994) 303–307. doi:10.1016/0022-
352 3093(94)90061-2.
- 353 [6] M.J. Hyatt, N.P. Bansal, Crystal growth kinetics in BaOAl₂O₃SiO₂ and SrOAl₂O₃SiO₂
354 glasses, *J. Mater. Sci.* 31 (1996) 172–184. doi:10.1007/BF00355142.
- 355 [7] S.M. Allameh, K.H. Sandhage, Synthesis of Celsian (BaAl₂Si₂O₈) from Solid Ba-Al-
356 Al₂O₃-SiO₂ Precursors: I, XRD and SEM/EDX Analyses of Phase Evolution, *J. Am.*
357 *Ceram. Soc.* 80 (1997) 3109–3126. doi:10.1111/j.1151-2916.1997.tb03239.x.
- 358 [8] N.P. Bansal, Solid State Synthesis and Properties of Monoclinic Celsian, *J. Mater. Sci.*
359 33 (1998) 4711–4715. doi:10.1023/A:1004484903436.
- 360 [9] S. Bošković, Đ. Kosanović, D. Bahloul-Hourlier, P. Thomas, S.J. Kiss, Formation of
361 celsian from mechanically activated BaCO₃-Al₂O₃-SiO₂ mixtures, *J. Alloys Compd.*
362 290 (1999) 230–235. doi:10.1016/S0925-8388(99)00091-2.
- 363 [10] W.A. Fraser, L.O. Upton, Barium Crown Optical Glass, 2523362, 1950.
- 364 [11] A. Arora, K. Singh, O.P. Pandey, Thermal, structural and crystallization kinetics of
365 SiO₂-BaO-ZnO-B₂O₃-Al₂O₃ glass samples as a sealant for SOFC, *Int. J. Hydrogen*
366 *Energy*. 36 (2011) 14948–14955. doi:10.1016/j.ijhydene.2011.03.036.
- 367 [12] S.E. Lin, Y.R. Cheng, W.C.J. Wei, BaO-B₂O₃-SiO₂-Al₂O₃ sealing glass for intermediate
368 temperature solid oxide fuel cell, *J. Non. Cryst. Solids*. 358 (2012) 174–181.
369 doi:10.1016/j.jnoncrysol.2011.09.013.
- 370 [13] K. Sharma, G.P. Kothiyal, L. Montagne, F.O. Méar, B. Revel, A new formulation of
371 barium-strontium silicate glasses and glass-ceramics for high-temperature sealant,
372 *Int. J. Hydrogen Energy*. 37 (2012) 11360–11369. doi:10.1016/j.ijhydene.2012.04.142.
- 373 [14] F. Heydari, A. Maghsoudipour, Z. Hamnabard, S. Farhangdoust, Evaluation on
374 Properties of CaO-BaO-B₂O₃-Al₂O₃-SiO₂ Glass-Ceramic Sealants for Intermediate
375 Temperature Solid Oxide Fuel Cells, *J. Mater. Sci. Technol.* 29 (2013) 49–54.
376 doi:10.1016/j.jmst.2012.11.011.
- 377 [15] J. Tong, M. Han, S.C. Singhal, Y. Gong, Influence of Al₂O₃ addition on the properties
378 of Bi₂O₃-BaO-SiO₂-R_xO_y (R=K, Zn, etc.) glass sealant, *J. Non. Cryst. Solids*. 358
379 (2012) 1038–1043. doi:10.1016/j.jnoncrysol.2012.01.044.
- 380 [16] L. Luo, Y. Lin, Z. Huang, Y. Wu, L. Sun, L. Cheng, J. Shi, Application of BaO-CaO-Al₂O₃-
381 B₂O₃-SiO₂ glass-ceramic seals in large size planar IT-SOFC, *Ceram. Int.* 41 (2015)
382 9239–9243. doi:10.1016/j.ceramint.2015.01.091.
- 383 [17] M.J. Da Silva, J.F. Bartolomé, A.H. De Aza, S. Mello-Castanho, Glass ceramic sealants
384 belonging to BAS (BaO-Al₂O₃-SiO₂) ternary system modified with B₂O₃ addition: A
385 different approach to access the SOFC seal issue, *J. Eur. Ceram. Soc.* 36 (2016) 631–

- 386 644. doi:10.1016/j.jeurceramsoc.2015.10.005.
- 387 [18] A.I. Borhan, M. Gromada, G.G. Nedelcu, L. Leontie, Influence of (CoO, CaO, B₂O₃)
388 additives on thermal and dielectric properties of BaO–Al₂O₃–SiO₂ glass–ceramic
389 sealant for OTM applications, *Ceram. Int.* 42 (2016) 10459–10468.
390 doi:10.1016/j.ceramint.2016.03.199.
- 391 [19] S. Xiao, S. Xiu, W. Zhang, B. Shen, J. Zhai, Y. Zhang, Effects of Ba_xSr_{1-x}TiO₃ ceramics
392 additives on structure and energy storage properties of Ba_{0.4}Sr_{0.6}TiO₃–BaO–B₂O₃–
393 Al₂O₃–SiO₂ glass-ceramic, *J. Alloys Compd.* 675 (2016) 15–21.
394 doi:10.1016/j.jallcom.2016.03.105.
- 395 [20] N.J. Smith, B. Rangarajan, M.T. Lanagan, C.G. Pantano, Alkali-free glass as a high
396 energy density dielectric material, *Mater. Lett.* 63 (2009) 1245–1248.
397 doi:10.1016/j.matlet.2009.02.047.
- 398 [21] H. Lee, N.J. Smith, C.G. Pantano, E. Furman, M.T. Lanagan, Dielectric Breakdown of
399 Thinned BaO–Al₂O₃–B₂O₃–SiO₂ Glass, *J. Am. Ceram. Soc.* 93 (2010) 2346–2351.
400 doi:10.1111/j.1551-2916.2010.03749.x.
- 401 [22] P. Dash, E. Furman, C.G. Pantano, M.T. Lanagan, Activation energy for alkaline-earth
402 ion transport in low alkali aluminoborosilicate glasses, *Appl. Phys. Lett.* 102 (2013)
403 82904. doi:10.1063/1.4794174.
- 404 [23] M. Boyer, S. Alahraché, C. Genevois, M. Licheron, F.-X. Lefevre, C. Castro, G.
405 Bonnefont, G. Patton, F. Moretti, C. Dujardin, G. Matzen, M. Allix, Enhanced
406 Transparency through Second Phase Crystallization in BaAl₄O₇ Scintillating Ceramics,
407 *Cryst. Growth Des.* 16 (2016) 386–395. doi:10.1021/acs.cgd.5b01374.
- 408 [24] G. Kaur, P. Sharma, V. Kumar, K. Singh, Assessment of in vitro bioactivity of SiO₂–BaO–
409 ZnO–B₂O₃–Al₂O₃ glasses: An optico-analytical approach, *Mater. Sci. Eng. C.* 32 (2012)
410 1941–1947. doi:10.1016/j.msec.2012.05.034.
- 411 [25] S. Kaewjaeng, J. Kaewkhao, P. Limsuwan, U. Maghanemi, Effect of BaO on Optical,
412 Physical and Radiation Shielding Properties of SiO₂–B₂O₃–Al₂O₃–CaO–Na₂O Glasses
413 System, *Procedia Eng.* 32 (2012) 1080–1086. doi:10.1016/j.proeng.2012.02.058.
- 414 [26] D. Ehrhart, Photoactive glasses and glass ceramics, *IOP Conf. Ser. Mater. Sci. Eng.* 21
415 (2011) 12001. doi:10.1088/1757-899X/21/1/012001.
- 416 [27] G. V. Lisachuk, R. V. Kryvobok, E.Y. Fedorenko, A. V Zakharov, Ceramic
417 radiotransparent materials on the basis of BaO–Al₂O₃–SiO₂ and SrO–Al₂O₃–SiO₂
418 systems, *Epa. - J. Silic. Based Compos. Mater.* 67 (2015) 20–23.
419 doi:10.14382/epitoanyag-jsbcm.2015.4.
- 420 [28] J.O. Bockris, J.D. Mackenzie, J.A. Kitchener, Viscous flow in silica and binary liquid
421 silicates, *Trans. Faraday Soc.* 51 (1955) 1734–1748. doi:10.1039/TF9555101734.
- 422 [29] J.W. Tomlinson, M.S.R. Heynes, J.O. Bockris, The structure of liquid silicates. Part 2.—
423 Molar volumes and expansivities, *Trans. Faraday Soc.* 54 (1958) 1822–1833.
424 doi:10.1039/TF9585401822.

- 425 [30] K. Mizoguchi, K. Okamoto, Y. Suginozawa, Oxygen Coordination of Al³⁺ Ion in Several
426 Silicate Melts Studied by Viscosity Measurements, *J. Japan Inst. Met.* 46 (1982) 1055–
427 1060.
- 428 [31] G. Urbain, Y. Bottinga, P. Richet, Viscosity of liquid silica, silicates and alumino-
429 silicates, *Geochim. Cosmochim. Acta.* 46 (1982) 1061–1072. doi:10.1016/0016-
430 7037(82)90059-X.
- 431 [32] S. Webb, R. Knoche, The glass-transition, structural relaxation and shear viscosity of
432 silicate melts, *Chem. Geol.* 128 (1996) 165–183. doi:10.1016/0009-2541(95)00171-9.
- 433 [33] A.I. Rabukhin, Structural interpretation of the concentration dependence of molar
434 volume in ternary aluminosilicate glasses containing oxides of the first and second
435 groups of the periodic system, *Glas. Ceram.* 57 (2000) 154–157.
436 doi:10.1007/BF02681263.
- 437 [34] N.F. Richet, Boson peak of alkali and alkaline earth silicate glasses: Influence of the
438 nature and size of the network-modifying cation, *J. Chem. Phys.* 136 (2012) 34703.
439 doi:10.1063/1.3677194.
- 440 [35] X. Xia, I. Dutta, J.C. Mauro, B.G. Aitken, K.F. Kelton, Temperature dependence of
441 crystal nucleation in BaO·2SiO₂ and 5BaO·8SiO₂ glasses using differential thermal
442 analysis, *J. Non. Cryst. Solids.* 459 (2017) 45–50.
443 doi:10.1016/j.jnoncrysol.2016.12.032.
- 444 [36] M. Czank, P.R. Buseck, Crystal chemistry of silica-rich barium silicates, *Zeitschrift Für*
445 *Krist. - Cryst. Mater.* 153 (1980) 33–41. doi:10.1524/zkri.1980.0003.
- 446 [37] K.-F. Hesse, F. Liebau, Crystal chemistry of silica-rich Barium silicates, *Zeitschrift Für*
447 *Krist. - Cryst. Mater.* 153 (1980) 33–41. doi:10.1524/zkri.1980.0002.
- 448 [38] K.-F. Hesse, F. Liebau, Crystal chemistry of silica-rich Barium silicates, *Zeitschrift Für*
449 *Krist. - Cryst. Mater.* 153 (1980) 33–41. doi:10.1524/zkri.1980.0004.
- 450 [39] J.B. Murdoch, J.F. Stebbins, High-resolution ²⁹Si NMR study of silicate and
451 aluminosilicate glasses: the effect of network-modifying cations, *Am. Mineral.* 70
452 (1985) 332–343. http://www.minsocam.org/ammin/AM70/AM70_332.pdf.
- 453 [40] H. Hasegawa, I. Yasui, X-ray and neutron diffraction analyses of barium silicate glass,
454 *J. Non. Cryst. Solids.* 95–96 (1987) 201–208. doi:10.1016/S0022-3093(87)80111-4.
- 455 [41] B.O. Mysen, J.D. Frantz, Structure of silicate melts at high temperature: In-situ
456 measurements in the system BaO-SiO₂ to 1669 C, *Am. Mineral.* 78 (1993) 699–709.
- 457 [42] J.D. Frantz, B.O. Mysen, Raman spectra and structure of BaO-SiO₂, SrO-SiO₂ and CaO-
458 SiO₂ melts to 1600C, *Chem. Geol.* 121 (1995) 155–176.
- 459 [43] J.F. Stebbins, J. V. Oglesby, Z. Xu, Disorder among network-modifier in silicate
460 glasses : cations New constraints from triple-quantum ¹⁷O NMR, *Am. Mineral.* 82
461 (1997) 1116–1124.
- 462 [44] L. Cormier, P.H. Gaskell, S. Creux, Comparison of the low-Q features in diffraction

- 463 data for silicate glasses and crystals containing Sr or Ba, *J. Non. Cryst. Solids*. 248
464 (1999) 84–91. doi:10.1016/S0022-3093(99)00102-7.
- 465 [45] L.B. Skinner, A.C. Barnes, W. Crichton, Novel behaviour and structure of new glasses
466 of the type Ba–Al–O and Ba–Al–Ti–O produced by aerodynamic levitation and laser
467 heating, *J. Phys. Condens. Matter*. 18 (2006) L407–L414. doi:10.1088/0953-
468 8984/18/32/L01.
- 469 [46] L.M. Thompson, J.F. Stebbins, Non-stoichiometric non-bridging oxygens and five-
470 coordinated aluminum in alkaline earth aluminosilicate glasses: Effect of modifier
471 cation size, *J. Non. Cryst. Solids*. 358 (2012) 1783–1789.
472 doi:10.1016/j.jnoncrysol.2012.05.022.
- 473 [47] L.M. Thompson, R.J. McCarty, J.F. Stebbins, Estimating accuracy of ^{17}O NMR
474 measurements in oxide glasses: Constraints and evidence from crystalline and glassy
475 calcium and barium silicates, *J. Non. Cryst. Solids*. 358 (2012) 2999–3006.
476 doi:10.1016/j.jnoncrysol.2012.07.032.
- 477 [48] H. Schlenz, A. Kirfel, K. Schulmeister, N. Wartner, W. Mader, W. Raberg, K. Wandelt,
478 C. Oligschleger, S. Bender, R. Franke, J. Hormes, W. Hoffbauer, V. Lansmann, M.
479 Jansen, N. Zotov, C. Marian, H. Putz, J. Neufeind, Structure analyses of Ba-silicate
480 glasses, *J. Non. Cryst. Solids*. 297 (2002) 37–54. doi:10.1016/S0022-3093(01)00922-X.
- 481 [49] A. Kremenovic, P. Colomban, B. Piriou, D. Massiot, P. Florian, Structural and
482 spectroscopic characterization of the quenched hexacelsian, *J. Phys. Chem. Solids*. 64
483 (2003) 2253–2268. doi:10.1016/S0022-3697(03)00252-X.
- 484 [50] J. Schneider, V.R. Mastelaro, E.D. Zanotto, B.A. Shakhmatkin, N.M. Vedishcheva, A.C.
485 Wright, H. Panepucci, Qn distribution in stoichiometric silicate glasses:
486 thermodynamic calculations and ^{29}Si high resolution NMR measurements, *J. Non.*
487 *Cryst. Solids*. 325 (2003) 164–178. doi:10.1016/S0022-3093(03)00332-6.
- 488 [51] M. Licheron, V. Montouillout, F. Millot, D.R. Neuville, Raman and ^{27}Al NMR structure
489 investigations of aluminate glasses: $(1-x)\text{Al}_2\text{O}_3-x\text{MO}$, with $\text{M}=\text{Ca}, \text{Sr}, \text{Ba}$ and
490 $0.5 < x < 0.75$), *J. Non. Cryst. Solids*. 357 (2011) 2796–2801.
491 doi:10.1016/j.jnoncrysol.2011.03.001.
- 492 [52] L.B. Skinner, A.C. Barnes, P.S. Salmon, H.E. Fischer, J.W.E. Drewitt, V. Honkimäki,
493 Structure and triclustering in Ba–Al–O glass, *Phys. Rev. B*. 85 (2012) 64201.
494 doi:10.1103/PhysRevB.85.064201.
- 495 [53] L. Hennet, I. Pozdnyakova, A. Bytchkov, V. Cristiglio, P. Palleau, H.E. Fischer, G.J.
496 Cuello, M. Johnson, P. Melin, D. Zanghi, S. Brassamin, J.-F. Brun, D.L. Price, M.-L.
497 Saboungi, Levitation apparatus for neutron diffraction investigations on high
498 temperature liquids, *Rev. Sci. Instrum.* 77 (2006) 53903. doi:10.1063/1.2200756.
- 499 [54] A.N. Novikov, D.R. Neuville, L. Hennet, Y. Gueguen, D. Thiaudière, T. Charpentier, P.
500 Florian, Al and Sr environment in tectosilicate glasses and melts: Viscosity, Raman and
501 NMR investigation, *Chem. Geol.* (2016). doi:10.1016/j.chemgeo.2016.11.023.
- 502 [55] D.R. Neuville, P. Richet, Viscosity and mixing in molten (Ca, Mg) pyroxenes and

- 503 garnets, *Geochim. Cosmochim. Acta.* 55 (1991) 1011–1019. doi:10.1016/0016-
504 7037(91)90159-3.
- 505 [56] D.R. Neuville, Viscosity, structure and mixing in (Ca, Na) silicate melts, *Chem. Geol.*
506 229 (2006) 28–41. doi:10.1016/j.chemgeo.2006.01.008.
- 507 [57] M. Wojdyr, Fityk: a general-purpose peak fitting program, *J. Appl. Crystallogr.* 43
508 (2010) 1126–1128. doi:10.1107/S0021889810030499.
- 509 [58] D. Massiot, F. Fayon, M. Capron, I. King, S. Le Calvé, B. Alonso, J.-O. Durand, B. Bujoli,
510 Z. Gan, G. Hoatson, Modelling one- and two-dimensional solid-state NMR spectra,
511 *Magn. Reson. Chem.* 40 (2002) 70–76. doi:10.1002/mrc.984.
- 512 [59] G. Le Caër, R.A. Brand, General models for the distributions of electric field gradients
513 in disordered solids, *J. Phys. Condens. Matter.* 10 (1998) 10715–10774.
514 doi:10.1088/0953-8984/10/47/020.
- 515 [60] D.R. Neuville, L. Cormier, A.-M. Flank, V. Briois, D. Massiot, Al speciation and Ca
516 environment in calcium aluminosilicate glasses and crystals by Al and Ca K-edge X-ray
517 absorption spectroscopy, *Chem. Geol.* 213 (2004) 153–163.
518 doi:10.1016/j.chemgeo.2004.08.039.
- 519 [61] C.A. Angell, Relaxation in liquids, polymers and plastic crystals — strong/fragile
520 patterns and problems, *J. Non. Cryst. Solids.* 131–133 (1991) 13–31.
521 doi:10.1016/0022-3093(91)90266-9.
- 522 [62] C.A. Angell, Formation of Glasses from Liquids and Biopolymers, *Science* (80-.). 267
523 (1995) 1924–1935. doi:10.1126/science.267.5206.1924.
- 524 [63] G. Adam, J.H. Gibbs, On the Temperature Dependence of Cooperative Relaxation
525 Properties in Glass-Forming Liquids, *J. Chem. Phys.* 43 (1965) 139.
526 doi:10.1063/1.1696442.
- 527 [64] P. Richet, Viscosity and configurational entropy of silicate melts, *Geochim.*
528 *Cosmochim. Acta.* 48 (1984) 471–483. doi:10.1016/0016-7037(84)90275-8.
- 529 [65] P. Richet, Y. Bottinga, Heat capacity of aluminum-free liquid silicates, *Geochim.*
530 *Cosmochim. Acta.* 49 (1985) 471–486.
- 531 [66] P. Richet, Heat capacity of silicate glasses, *Chem. Geol.* 62 (1987) 111–124.
532 doi:10.1016/0009-2541(87)90062-3.
- 533 [67] R. Robie, B.S. Hemingway, J. Fisher, *Thermodynamic Properties of Minerals and*
534 *Related Substances at 298.15K and 1bar Pressure and at Higher Temperatures*, 1978.
- 535 [68] F.L. Galeener, Planar rings in vitreous silica, *J. Non. Cryst. Solids.* 49 (1982) 53–62.
536 doi:10.1016/0022-3093(82)90108-9.
- 537 [69] F.L. Galeener, Planar rings in glasses, *Solid State Commun.* 44 (1982) 1037–1040.
538 doi:10.1016/0038-1098(82)90329-5.
- 539 [70] J.D. Kubicki, D. Sykes, Molecular orbital calculations of vibrations in three-membered

- 540 aluminosilicate rings, *Phys. Chem. Miner.* 19 (1993) 381–391.
541 doi:10.1007/BF00202975.
- 542 [71] D. Sykes, J.D. Kubicki, Four-membered rings in silica and aluminosilicate glasses, *Am.*
543 *Mineral.* 81 (1996) 265–272. doi:10.2138/am-1996-3-401.
- 544 [72] F.L. Galeener, Band limits and the vibrational spectra of tetrahedral glasses, *Phys.*
545 *Rev. B.* 19 (1979) 4292–4297. doi:10.1103/PhysRevB.19.4292.
- 546 [73] B.O. Mysen, L.W. Finger, D. Virgo, F.A. Seifert, Curve-fitting of Raman spectra of
547 silicate glasses, *Am. Mineral.* 67 (1982) 686–695.
- 548 [74] P.F. McMillan, B.T. Poe, P.H. Gillet, B. Reynard, A study of SiO₂ glass and supercooled
549 liquid to 1950 K via high-temperature Raman spectroscopy, *Geochim. Cosmochim.*
550 *Acta.* 58 (1994) 3653–3664. doi:10.1016/0016-7037(94)90156-2.
- 551 [75] D.R. Neuville, L. Cormier, D. Massiot, Al environment in tectosilicate and
552 peraluminous glasses: A ²⁷Al MQ-MAS NMR, Raman, and XANES investigation,
553 *Geochim. Cosmochim. Acta.* 68 (2004) 5071–5079. doi:10.1016/j.gca.2004.05.048.
- 554 [76] D.R. Neuville, L. Cormier, V. Montouillout, P. Florian, F. Millot, J.-C. Rifflet, D. Massiot,
555 Structure of Mg- and Mg/Ca aluminosilicate glasses: ²⁷Al NMR and Raman
556 spectroscopy investigations, *Am. Mineral.* 93 (2008) 1721–1731.
557 doi:10.2138/am.2008.2867.
- 558 [77] P. McMillan, Structural studies of silicate glasses and melts-applications and
559 limitations of Raman spectroscopy, *Am. Mineral.* 69 (1984) 622–644.
- 560 [78] B.O. Mysen, Structure and properties of magmatic liquids: from haplobasalt to
561 haploandesite, *Geochim. Cosmochim. Acta.* 63 (1999) 95–112. doi:10.1016/S0016-
562 7037(98)00273-7.
- 563 [79] D.R. Neuville, L. Cormier, D. Massiot, Al coordination and speciation in calcium
564 aluminosilicate glasses: Effects of composition determined by ²⁷Al MQ-MAS NMR
565 and Raman spectroscopy, *Chem. Geol.* 229 (2006) 173–185.
566 doi:10.1016/j.chemgeo.2006.01.019.
- 567 [80] S.K. Sharma, J.F. Mammone, M.F. Nicol, Raman investigation of ring configurations in
568 vitreous silica, *Nature.* 292 (1981) 140–141. doi:10.1038/292140a0.
- 569 [81] F.L. Galeener, R.A. Barrio, E. Martinez, R.J. Elliott, Vibrational Decoupling of Rings in
570 Amorphous Solids, *Phys. Rev. Lett.* 53 (1984) 2429–2432.
571 doi:10.1103/PhysRevLett.53.2429.
- 572 [82] A. Pasquarello, R. Car, Identification of Raman Defect Lines as Signatures of Ring
573 Structures in Vitreous Silica, *Phys. Rev. Lett.* 80 (1998) 5145–5147.
574 doi:10.1103/PhysRevLett.80.5145.
- 575 [83] P. Umari, A. Pasquarello, Modeling of the Raman spectrum of vitreous silica:
576 concentration of small ring structures, *Phys. B Condens. Matter.* 316–317 (2002) 572–
577 574. doi:10.1016/S0921-4526(02)00576-8.

- 578 [84] A. Rahmani, M. Benoit, C. Benoit, Signature of small rings in the Raman spectra of
579 normal and compressed amorphous silica: A combined classical and ab initio study,
580 *Phys. Rev. B.* 68 (2003) 184202. doi:10.1103/PhysRevB.68.184202.
- 581 [85] A.G. Kalampounias, S.N. Yannopoulos, G.N. Papatheodorou, Temperature-induced
582 structural changes in glassy, supercooled, and molten silica from 77 to 2150 K, *J.*
583 *Chem. Phys.* 124 (2006) 14504. doi:10.1063/1.2136878.
- 584 [86] M.J. Toplis, D.B. Dingwell, T. Lenci, Peraluminous viscosity maxima in Na₂O-Al₂O₃-
585 SiO₂ liquids: The role of triclusters in tectosilicate melts, *Geochim. Cosmochim. Acta.*
586 61 (1997) 2605–2612. doi:10.1016/S0016-7037(97)00126-9.
- 587 [87] Y. Xiang, J. Du, M.M. Smedskjaer, J.C. Mauro, Structure and properties of sodium
588 aluminosilicate glasses from molecular dynamics simulations, *J. Chem. Phys.* 139
589 (2013) 44507. doi:10.1063/1.4816378.
- 590 [88] M. Bouhadja, N. Jakse, A. Pasturel, Striking role of non-bridging oxygen on glass
591 transition temperature of calcium aluminosilicate glass-formers, *J. Chem. Phys.* 140
592 (2014) 234507. doi:10.1063/1.4882283.
- 593 [89] N. Jakse, M. Bouhadja, J. Kozaily, J.W.E. Drewitt, L. Hennet, D.R. Neuville, H.E. Fischer,
594 V. Cristiglio, A. Pasturel, Interplay between non-bridging oxygen, triclusters, and
595 fivefold Al coordination in low silica content calcium aluminosilicate melts, *Appl. Phys.*
596 *Lett.* 101 (2012) 201903. doi:10.1063/1.4766920.
- 597 [90] L. Cormier, D. Ghaleb, D.R. Neuville, J.-M. Delaye, G. Calas, Chemical dependence of
598 network topology of calcium aluminosilicate glasses: a computer simulation study, *J.*
599 *Non. Cryst. Solids.* 332 (2003) 255–270. doi:10.1016/j.jnoncrysol.2003.09.012.
- 600 [91] F.A. Seifert, B.O. Mysen, D. Virgo, Three-dimensional network structure of quenched
601 melts (glass) in the systems SiO₂-NaAlO₂, SiO₂-CaAl₂O₄ and SiO₂-MgAl₂O₄., *Am.*
602 *Mineral.* 67 (1982) 696–717.
- 603 [92] D.R. Neuville, B.O. Mysen, Role of aluminium in the silicate network: In situ, high-
604 temperature study of glasses and melts on the join SiO₂-NaAlO₂, *Geochim.*
605 *Cosmochim. Acta.* 60 (1996) 1727–1737. doi:10.1016/0016-7037(96)00049-X.
- 606 [93] C. Le Losq, D.R. Neuville, P. Florian, G.S. Henderson, D. Massiot, The role of Al³⁺ on
607 rheology and structural changes in sodium silicate and aluminosilicate glasses and
608 melts, *Geochim. Cosmochim. Acta.* 126 (2014) 495–517.
609 doi:10.1016/j.gca.2013.11.010.
- 610 [94] D.R. Neuville, D. de Ligny, G.S. Henderson, Advances in Raman Spectroscopy Applied
611 to Earth and Material Sciences, *Rev. Mineral. Geochemistry.* 78 (2014) 509–541.
612 doi:10.2138/rmg.2013.78.13.
- 613 [95] C.I. Merzbacher, W.B. White, The structure of alkaline earth aluminosilicate glasses as
614 determined by vibrational spectroscopy, *J. Non. Cryst. Solids.* 130 (1991) 18–34.
615 doi:10.1016/0022-3093(91)90152-V.
- 616 [96] P. Florian, E. Veron, T.F.G. Green, J.R. Yates, D. Massiot, Elucidation of the Al/Si

- 617 Ordering in Gehlenite $\text{Ca}_2\text{Al}_2\text{SiO}_7$ by Combined ^{29}Si and ^{27}Al NMR
618 Spectroscopy/Quantum Chemical Calculations, *Chem. Mater.* 24 (2012) 4068–4079.
619 doi:10.1021/cm3016935.
- 620 [97] E. Gambuzzi, A. Pedone, M.C. Menziani, F. Angeli, D. Caurant, T. Charpentier, Probing
621 silicon and aluminium chemical environments in silicate and aluminosilicate glasses
622 by solid state NMR spectroscopy and accurate first-principles calculations, *Geochim.*
623 *Cosmochim. Acta.* 125 (2014) 170–185. doi:10.1016/j.gca.2013.10.025.
- 624 [98] J.R. Allwardt, J.F. Stebbins, B.C. Schmidt, D.J. Frost, A.C. Withers, M.M. Hirschmann,
625 Aluminum coordination and the densification of high-pressure aluminosilicate
626 glasses, *Am. Mineral.* 90 (2005) 1218–1222. doi:10.2138/am.2005.1836.
- 627 [99] P. Florian, N. Sadiki, D. Massiot, J.P. Coutures, ^{27}Al NMR Study of the Structure of
628 Lanthanum- and Yttrium-Based Aluminosilicate Glasses and Melts, *J. Phys. Chem. B.*
629 111 (2007) 9747–9757. doi:10.1021/jp072061q.
- 630 [100] S. Iftekhhar, J. Grins, P.N. Gunawidjaja, M. Edén, Glass Formation and Structure-
631 Property-Composition Relations of the $\text{RE}_2\text{O}_3\text{-Al}_2\text{O}_3\text{-SiO}_2$ (RE=La, Y, Lu, Sc) Systems,
632 *J. Am. Ceram. Soc.* 94 (2011) 2429–2435. doi:10.1111/j.1551-2916.2011.04548.x.
- 633 [101] T.K. Bechgaard, A. Goel, R.E. Youngman, J.C. Mauro, S.J. Rzoska, M. Bockowski, L.R.
634 Jensen, M.M. Smedskjaer, Structure and mechanical properties of compressed
635 sodium aluminosilicate glasses: Role of non-bridging oxygens, *J. Non. Cryst. Solids.*
636 441 (2016) 49–57. doi:10.1016/j.jnoncrysol.2016.03.011.
- 637 [102] J.R. Allwardt, B.T. Poe, J.F. Stebbins, The effect of fictive temperature on Al
638 coordination in high-pressure (10 GPa) sodium aluminosilicate glasses, *Am. Mineral.*
639 90 (2005) 1453–1457. doi:10.2138/am.2005.1736.
- 640 [103] P. Richet, D.R. Neuville, Thermodynamics of Silicate Melts: Configurational Properties,
641 in: 1992: pp. 132–161. doi:10.1007/978-1-4612-2842-4_5.
- 642 [104] I. Farnan, J.F. Stebbins, The Nature of the Glass Transition in a Silica-Rich Oxide Melt,
643 *Science* (80-.). 265 (1994) 1206–1209. doi:10.1126/science.265.5176.1206.
- 644 [105] B.T. Poe, P.F. McMillan, B. Cote, D. Massiot, J.-P. Coutures, Structure and Dynamics in
645 Calcium Aluminate Liquids: High-Temperature ^{27}Al NMR and Raman Spectroscopy, *J.*
646 *Am. Ceram. Soc.* 77 (1994) 1832–1838. doi:10.1111/j.1151-2916.1994.tb07058.x.
- 647 [106] J.F. Stebbins, E. V. Dubinsky, K. Kanehashi, K.E. Kelsey, Temperature effects on non-
648 bridging oxygen and aluminum coordination number in calcium aluminosilicate
649 glasses and melts, *Geochim. Cosmochim. Acta.* 72 (2008) 910–925.
650 doi:10.1016/j.gca.2007.11.018.
- 651 [107] L.M. Thompson, J.F. Stebbins, Non-bridging oxygen and high-coordinated aluminum
652 in metaluminous and peraluminous calcium and potassium aluminosilicate glasses:
653 High-resolution ^{17}O and ^{27}Al MAS NMR results, *Am. Mineral.* 96 (2011) 841–853.
654 doi:10.2138/am.2011.3680.
- 655 [108] D. Iuga, C. Morais, Z. Gan, D.R. Neuville, L. Cormier, D. Massiot, NMR Heteronuclear

- 656 Correlation between Quadrupolar Nuclei in Solids, *J. Am. Chem. Soc.* 127 (2005)
657 11540–11541. doi:10.1021/ja052452n.
- 658 [109] J. Wu, J.F. Stebbins, Effects of cation field strength on the structure of
659 aluminoborosilicate glasses: High-resolution ^{11}B , ^{27}Al and ^{23}Na MAS NMR, *J. Non.*
660 *Cryst. Solids.* 355 (2009) 556–562. doi:10.1016/j.jnoncrysol.2009.01.025.
- 661 [110] E.I. Morin, J. Wu, J.F. Stebbins, Modifier cation (Ba, Ca, La, Y) field strength effects on
662 aluminum and boron coordination in aluminoborosilicate glasses: the roles of fictive
663 temperature and boron content, *Appl. Phys. A.* 116 (2014) 479–490.
664 doi:10.1007/s00339-014-8369-4.
- 665 [111] M.J. Toplis, D.B. Dingwell, Shear viscosities of $\text{CaO-Al}_2\text{O}_3\text{-SiO}_2$ and $\text{MgO-Al}_2\text{O}_3\text{-SiO}_2$
666 liquids: Implications for the structural role of aluminium and the degree of
667 polymerisation of synthetic and natural aluminosilicate melts, *Geochim. Cosmochim.*
668 *Acta.* 68 (2004) 5169–5188. doi:10.1016/j.gca.2004.05.041.
- 669 [112] R. Bruckner, Properties and structure of vitreous silica. I, *J. Non. Cryst. Solids.* 5 (1970)
670 123–175. doi:10.1016/0022-3093(70)90190-0.
- 671

672 *Table 1. Chemical composition (in mol%)* and density (in g/cm³) of the studied glasses. The*
 673 *values in parentheses are the standard deviations.*

	BA75.12	BA63.18	BA50.25	BA42.29	BA33.33	BA26.37	BA20.40
SiO₂	74.80(7)	62.76(15)	48.73(38)	41.80(13)	33.12(17)	24.11(17)	20.26(11)
Al₂O₃	12.48(5)	18.46(7)	25.97(56)	28.89(6)	33.37(33)	37.48(18)	39.61(14)
BaO	12.72(7)	18.78(10)	25.29(21)	29.31(10)	33.51(22)	38.40(12)	40.13(9)
Density	2.794(1)	3.053(2)	3.315(5)	3.455(1)	3.579(1)	3.715(1)	3.772(3)

674 * Average of 10 analyses made with a Cameca SXFive electron microprobe for each glass at
 675 15 kV and 40 nA with 90 s counting time.

676

677 Table 2. Viscosity measurements performed on Ba aluminosilicate glasses. Viscosity is in
 678 $\log(\text{Pa}\cdot\text{s})$ and temperature is in K.

BA75.12		BA63.18		BA42.29		BA33.33	
T	η	T	η	T	η	T	η
1164	12.24	1162	12.29	1166	12.33	1175	12.23
1170	12.09	1172	11.95	1169	12.17	1180	12.03
1175	11.95	1182	11.61	1179	11.78	1190	11.61
1178	11.83	1186	11.48	1184	11.61	1200	11.11
1184	11.70	1210	10.71	1202	10.79	1223	10.17
1189	11.57	1220	10.49	1218	10.25	1233	9.83
1209	11.03	1235	10.02	1227	9.90	1258	8.92
1221	10.79	1245	9.77	1233	9.75	2073*	-
1226	10.67	1260	9.31	1244	9.38	2123*	0.22*
1235	10.42	2073*	0.96*	1253	9.04	2173*	-
1251	10.12	2123*	0.75*	2073*	0.02*	2223*	0.37*
1260	9.98	2173*	0.56*	2123*	-0.15*	2273*	-
		2223*	0.40*	2173*	-0.32*	2323*	0.52*
		2273*	0.23*	2223*	-0.44*	2373*	-
		2323*	0.08*	2273*	-0.60*		0.65*
		2373*	-0.08*	2323*	-0.71*		-
				2373*	-0.86*		0.78*
							-
							0.90*
							-
							1.06*

679 * Interpolated values.

680

681 Table 3. T_g and VFTH parameters (A , B , T_1) retrieved from the fitting of low-temperature
682 viscosity data. m is fragility of melts. $C_{p,g}$, $C_{p,l}$, C_p^{conf} and Adam-Gibbs parameters (A_e , B_e ,
683 $S^{conf}(T_g)$) determined from the viscosity data presented in Figure 1. See explanation in the
684 text on how the $C_{p,g}$ and $C_{p,l}$ values were obtained. T_g , T_1 , T_0 are in K; $C_{p,g}$, $C_{p,l}$, C_p^{conf} , B_e are in
685 J/mol; A_e is in $\log(\text{Pa}\cdot\text{s})$, $S^{conf}(T_g)$ is in J/(mol·K).

	BA75.12	BA63.18	BA50.25	BA42.29	BA33.33	BA26.37	BA20.40
T_g	1173	1171	1182*	1174	1181	1204*	1219*
A	-4.565	-12.765	-	-10.597	-11.588	-	-
B	10146	18418	-	11987	12157	-	-
T_1	560.2	426.9	-	643.2	665.2	-	-
m	31.7	39.0	-	50.0	54.0	-	-
$C_{p,g}$	77.37	79.87	82.69	84.29	86.17	87.93	89.33
$C_{p,l}$	88.24	91.51	95.34	97.34	99.95	102.82	105.12
C_p^{conf}	10.88	11.64	12.65	13.05	13.77	14.89	15.79
A_e	-3.1913	-2.8877	-	-3.2310	-3.2793	-	-
$10^5 B_e$	2.8402	3.0047	-	3.8366	4.0659	-	-
$S^{conf}(T_g)$	15.94	17.24	-	21.46	22.53	-	-
T_0	225	557	-	724	775	-	-

686 * T_g value obtained from DSC measurements

687

688 *Table 4. Gaussian bands' positions (V_i , cm^{-1}) and relative areas (A_i , %) obtained from the*
 689 *deconvolution of the high-frequency region of the Raman spectra.*

	BA75.12	BA63.18	BA50.25	BA42.29	BA33.33	BA26.37	BA20.40
V₁	980	964	943	931	836	833	827
V₂	1100	1057	1004	991	956	943	940
V₃	1182	1158	1122	1098	1045	1016	1012
A₁	40.0	28.6	16.2	23.3	2.5	7.8	14.7
A₂	53.4	66.2	76.6	67.4	76.4	63.0	57.9
A₃	6.7	5.1	7.2	9.2	21.1	29.2	27.4

690

691 Table 5. ^{27}Al MAS NMR parameters obtained from the deconvolution of the spectra using a
 692 Czjzek model. δ_{iso} is the isotropic chemical shift (in ppm) and C_{Q} is the quadrupolar coupling
 693 constant (in MHz). The population is in %.

	BA75.12	BA63.18	BA50.25	BA42.29	BA33.33	BA26.37	BA20.40
	δ_{iso}						
AlO₄	59.8	62.6	65.9	68.2	70.5	73.1	74.9
AlO₅	34.1	32.8	37.2	38.4	43.2	43.3	43.5
	C_{Q}						
AlO₄	6.47	6.70	6.84	6.99	6.97	7.27	7.32
AlO₅	7.93	6.49	7.15	7.18	7.81	8.06	7.19
	Population						
AlO₄	98.7	98.8	97.9	97.8	97.6	98.0	98.6
AlO₅	1.3	1.3	2.1	2.2	2.4	2.0	1.4

694

695

696 **Figure captions**

697 Figure 1. Viscosity curves of four studied glasses as a function of reciprocal temperature.
698 Lines are VFTH fits. Error bars are less than symbols' size.

699

700 Figure 2. T_g evolution as a function of composition for CAS (orange, [60]), SAS (red, [54]) and
701 BAS (green, this work) glasses. It is well seen that for silica-poor compositions T_g starts to
702 increase. Error bars for viscosity data are less than the size of symbols, for DSC
703 measurements they were reasonably set at ± 10 K level. Lines are only guide for the eyes. T_g
704 of vitreous silica (1473 K, black symbol) is from Bruckner [112] and is presented for
705 comparison reasons.

706

707 Figure 3. Viscosity data for the studied glasses (filled symbols) plotted versus T_g/T ,
708 representing melt's fragility. High-temperature data for BA75.12 (▣ symbols) are reproduced
709 from Urbain et al. [31] and low viscosities for the intermediate compositions (open symbols)
710 were interpolated from the data of Urbain et al. [31]. Lines are only guide for the eyes.

711

712 Figure 4. $S^{conf}(T_g)$ as a function of SiO₂ content for CAS (orange), SAS (red, [54]) and BAS
713 (green) glasses. The lines are guides for the eyes.

714

715 Figure 5. Area-normalized Raman spectra of the BAS tectosilicate glasses. Silica content
716 decreases from top to bottom.

717

718 Figure 6. Gaussian bands position obtained from fitting the high-frequency region of the
719 Raman spectra. ▣ – T_{2s} vibrational mode, ■ – vibrations of Q^{4,II} species, ▣ – vibrations of Q^{4,I}
720 species. Data on vitreous SiO₂ (black symbols) are from Mysen et al. [73]. Light blue symbols
721 correspond to Na tectosilicates [92], dark blue symbols correspond to Mg tectosilicates [76],
722 orange symbols correspond to Ca tectosilicates [75] and red symbols correspond to Sr
723 tectosilicates [54]. New data on the Ba aluminosilicates are represented by green symbols.
724 Lines are only guide for the eyes.

725

726 Figure 7. 1D ²⁷Al quantitative 1 pulse MAS NMR spectra of the studied glasses. A shift to
727 higher values of δ_{iso} with the substitution of SiO₂ by BaAl₂O₄ is clearly visible.

728

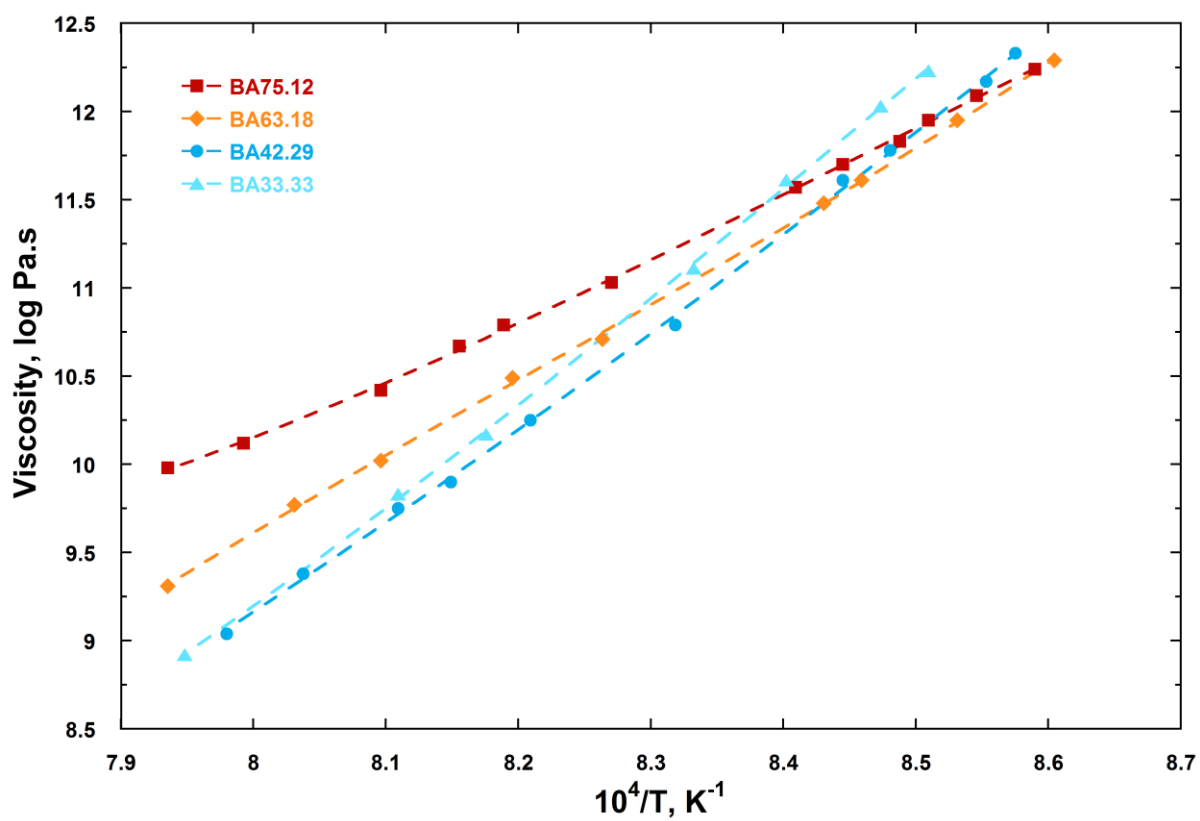
729 Figure 8. Evolution of δ_{iso} of AlO₄ (top) and AlO₅ (bottom) species as a function of
730 composition. Grey diamonds correspond to MAS glasses [76], orange triangles – to CAS
731 glasses [75], red squares – to SAS glasses [54], and green circles – to BAS glasses (present
732 study). The green solid line is a linear fit to the data points of BAS glasses with SiO₂ content
733 less than 63 mol%. The line was drawn to show the deviation from the linear trend of
734 $\delta_{iso}(AlO_4)$ for the compositions rich in silica.

735

736 Figure 9. AlO₅ population (in relative %) for Mg (grey, [76]), Ca (orange, [75]), Sr (red, [54])
737 and Ba (green) tectosilicate glasses. Error bars were reasonably set as ±1 %. Lines are only
738 guide for the eyes.

739

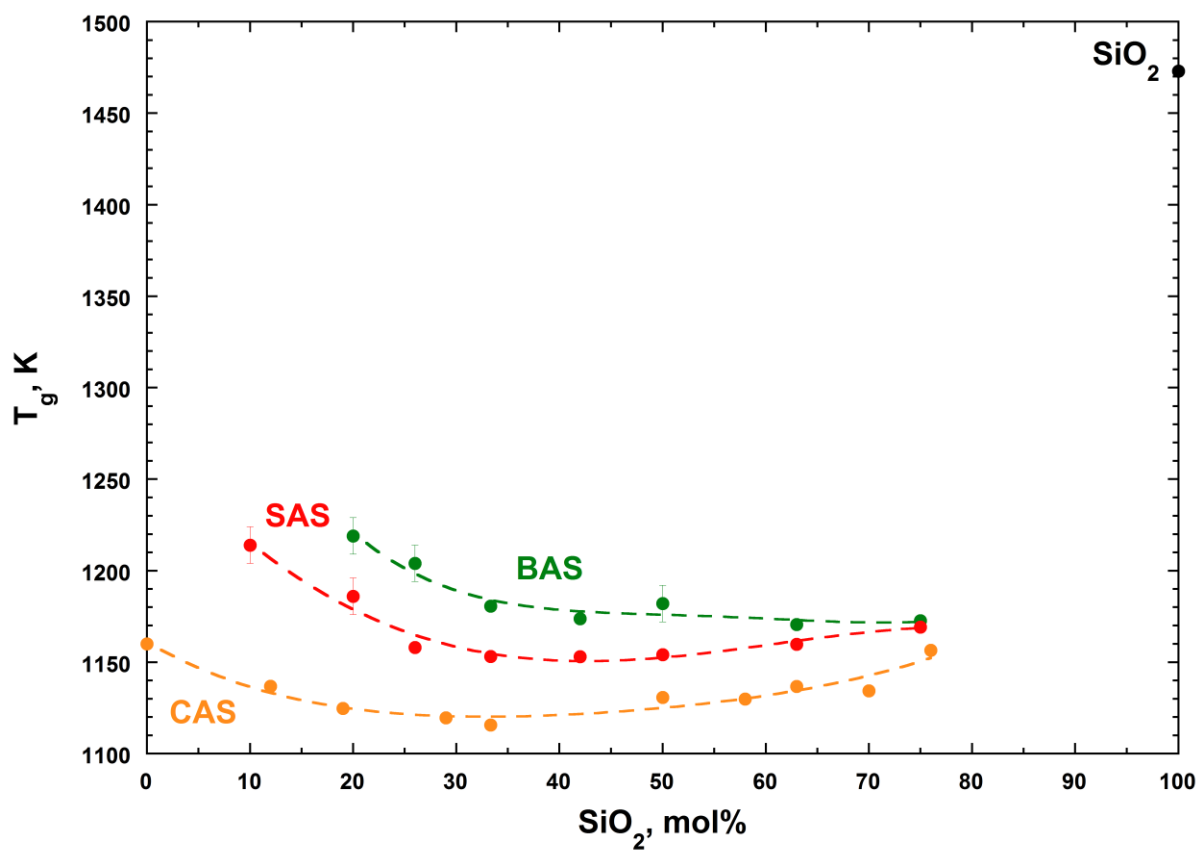
740 Figure 1



741

742

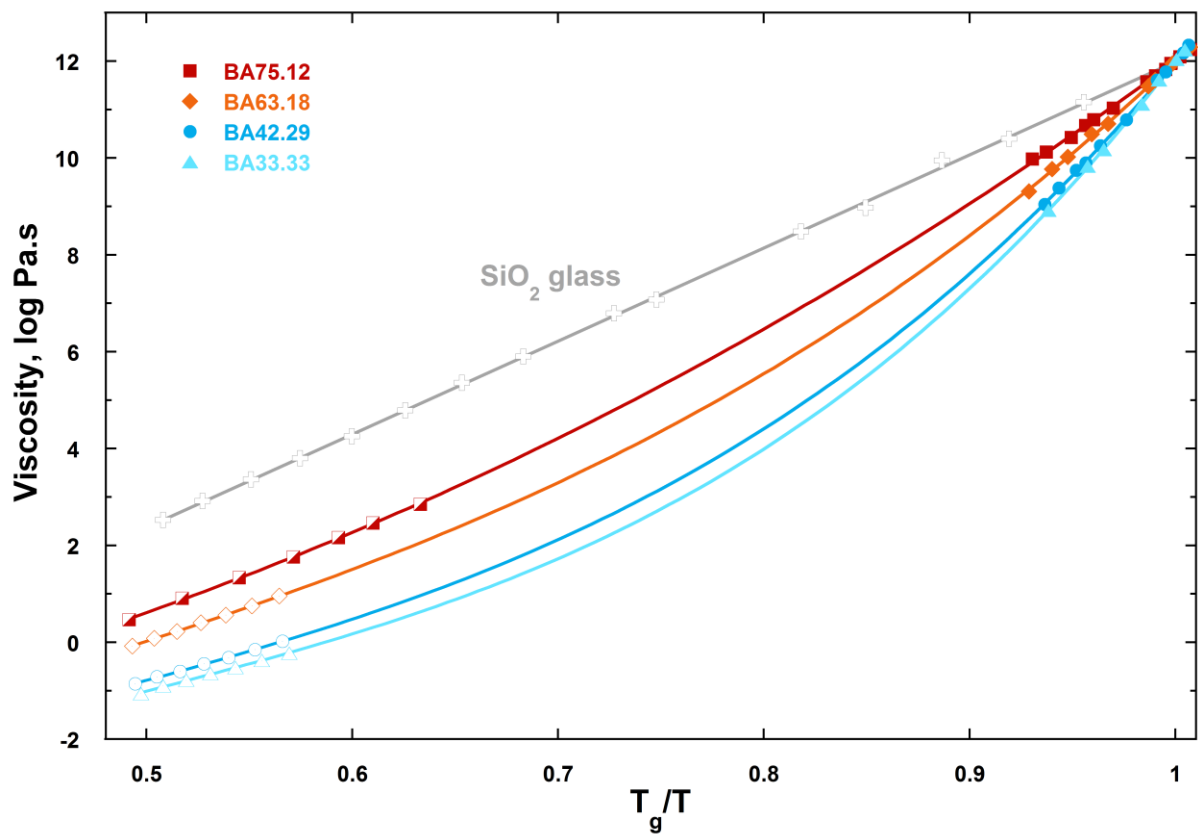
743 Figure 2



744

745

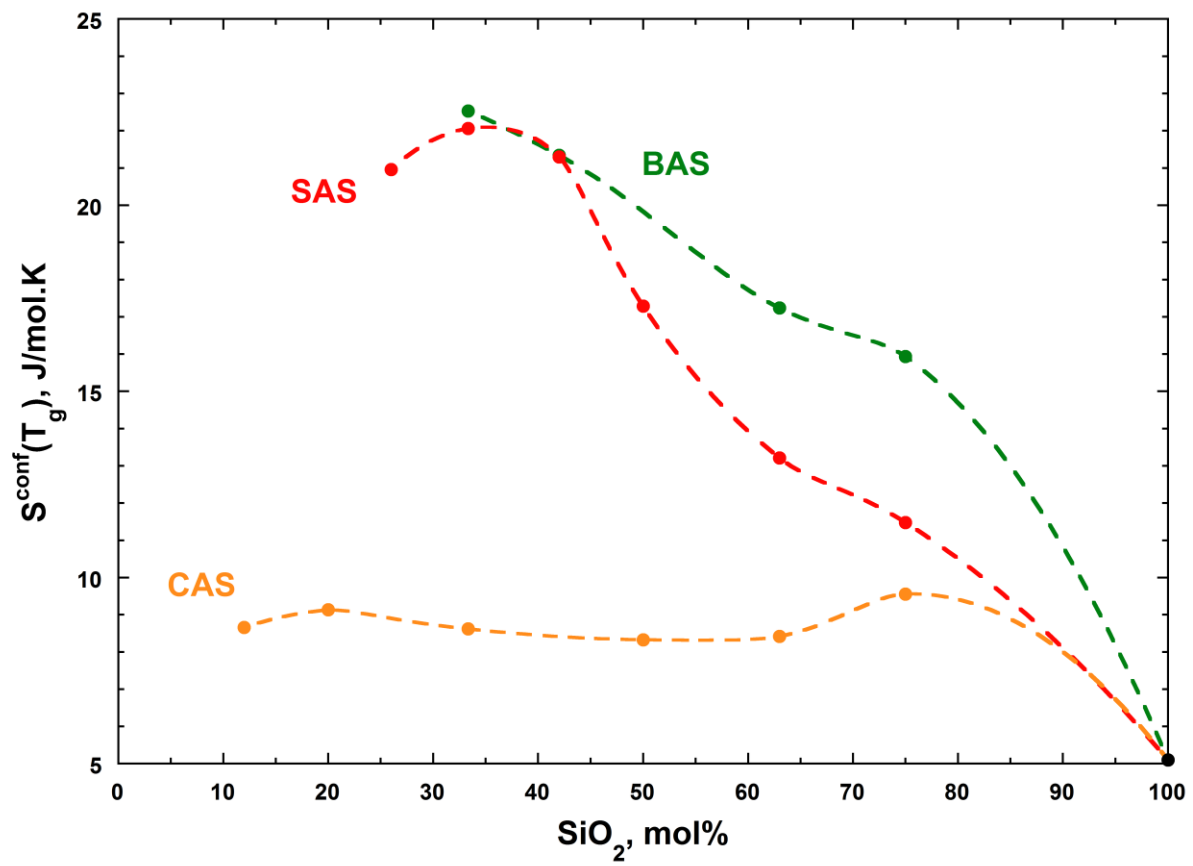
746 Figure 3



747

748

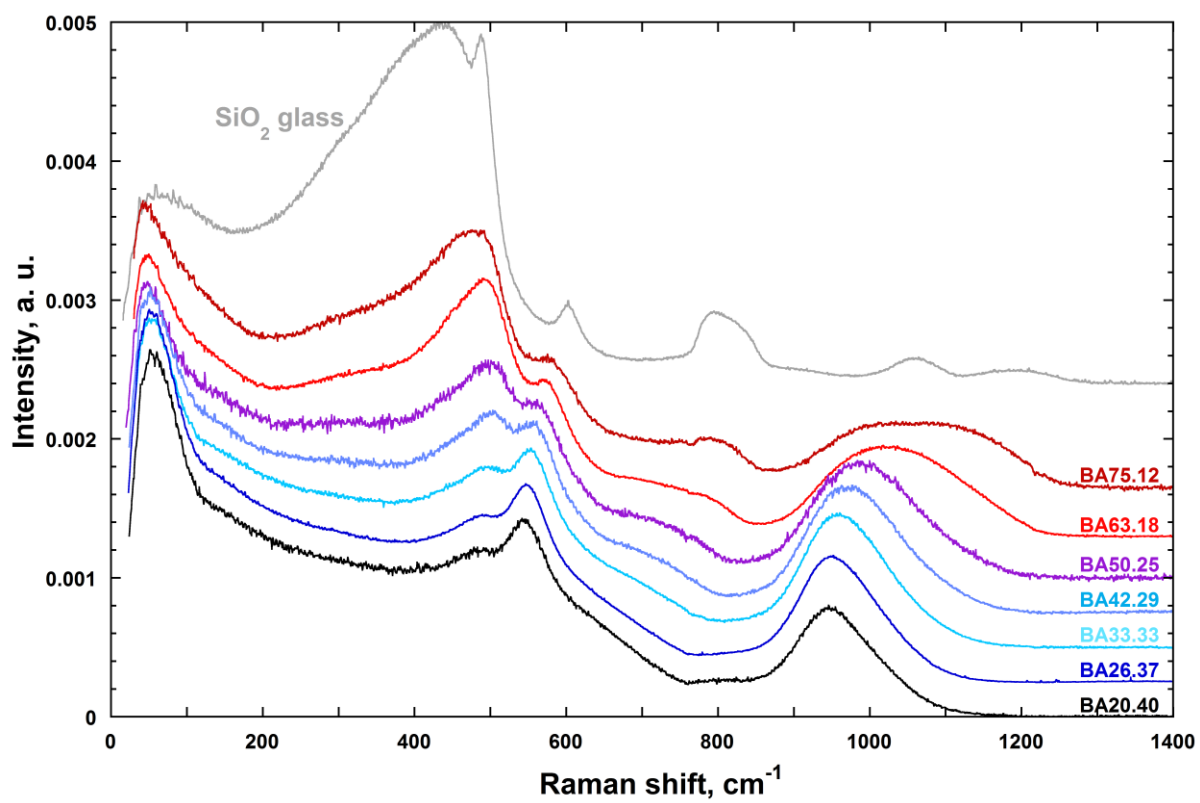
749 Figure 4



750

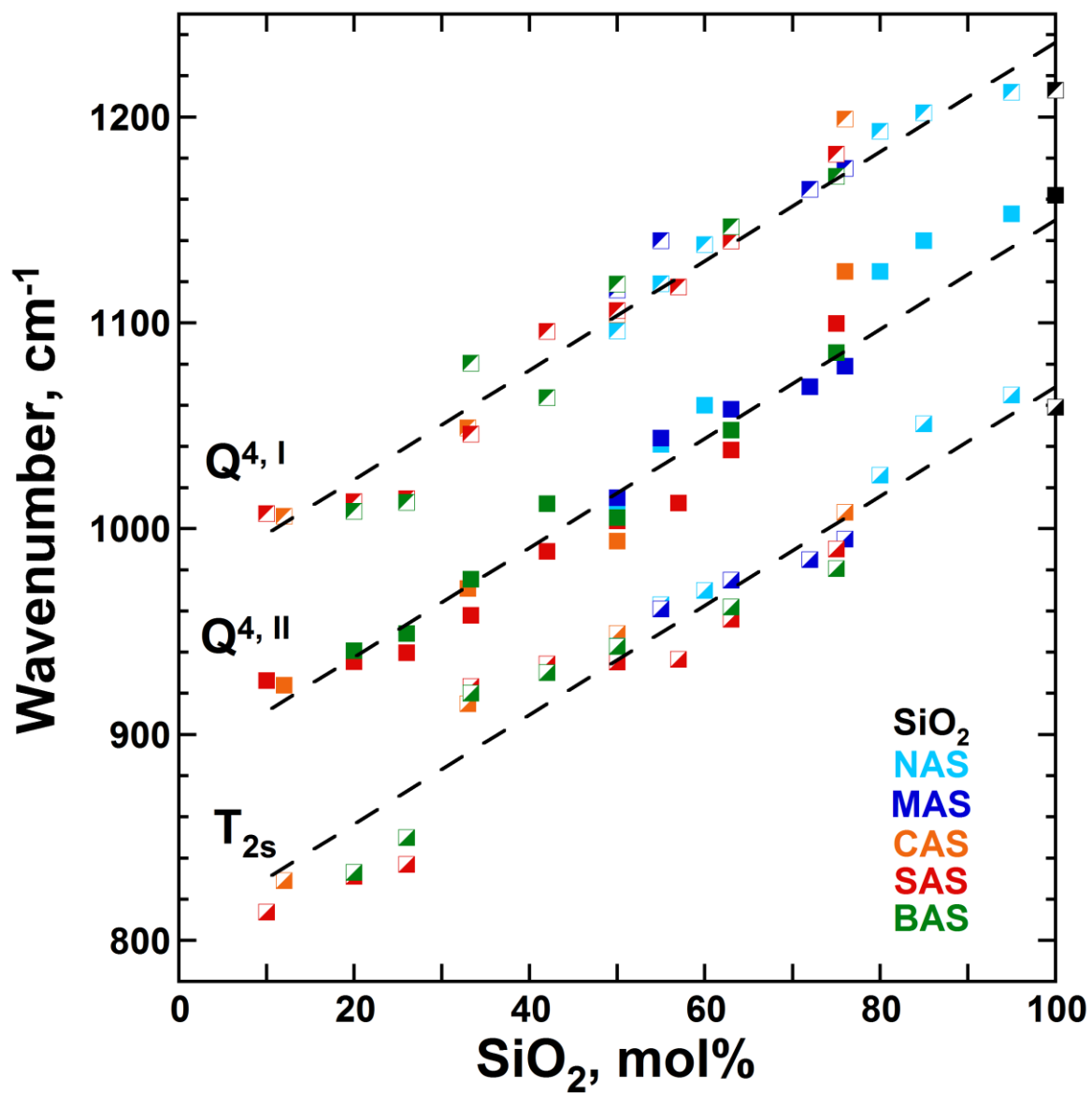
751

752 Figure 5



753

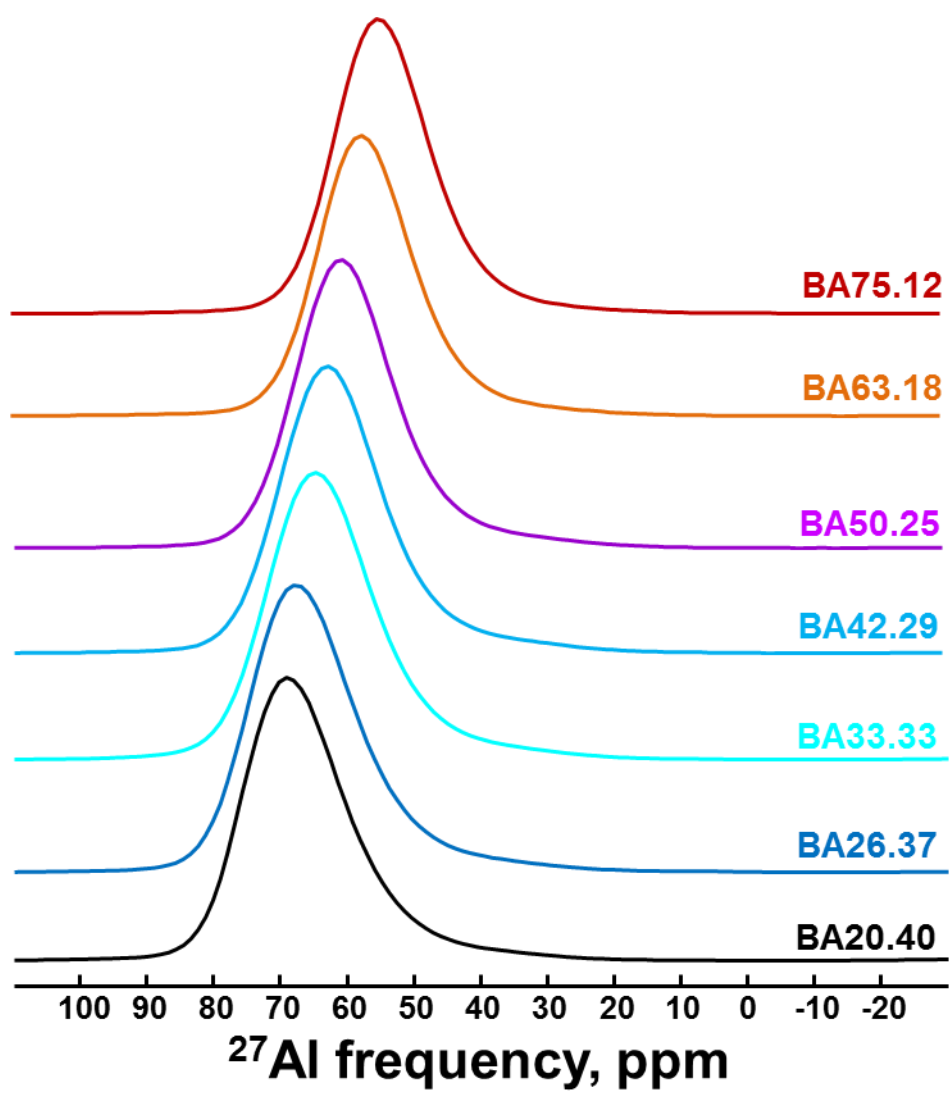
754



756

757

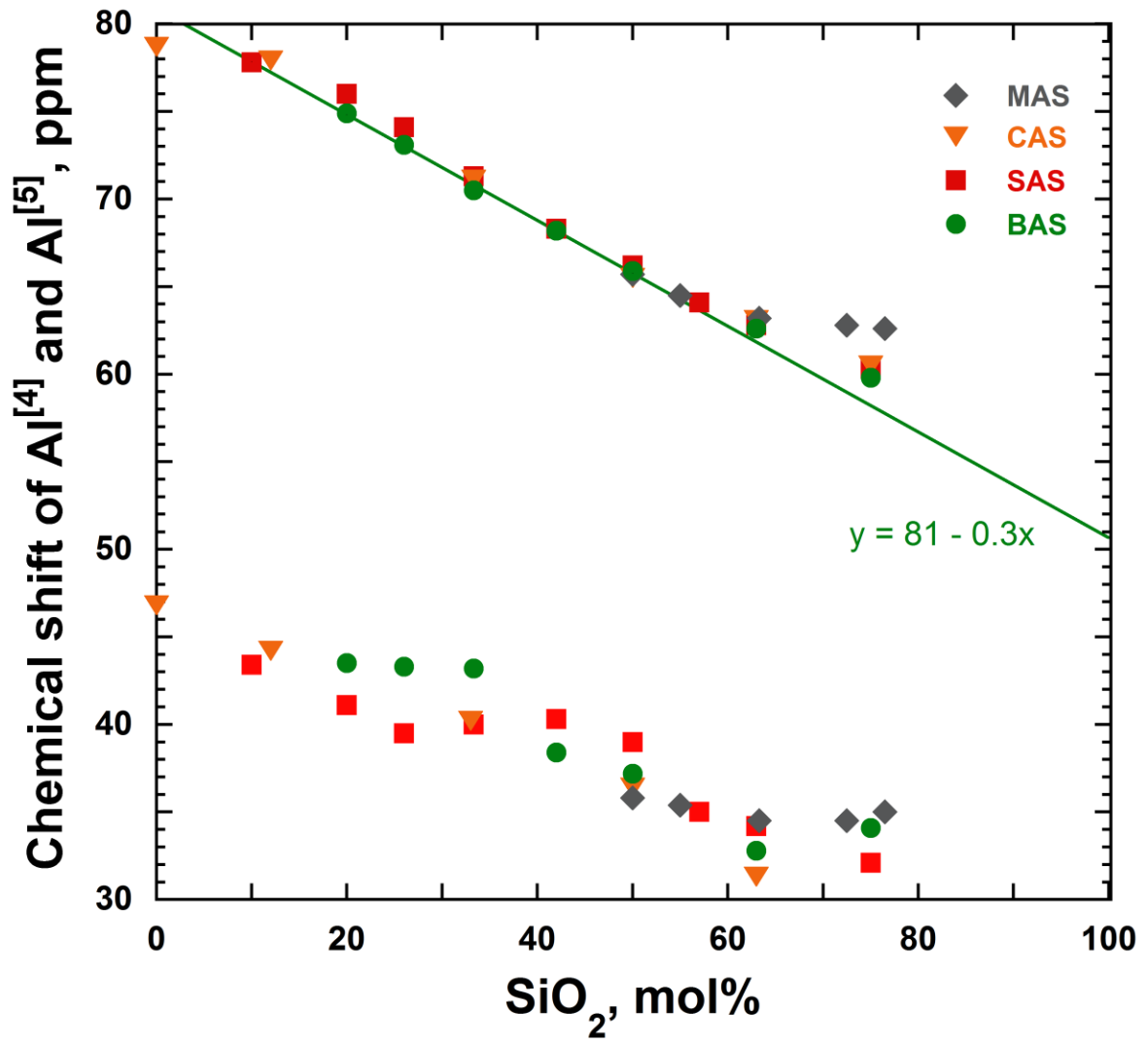
758 Figure 7



759

760

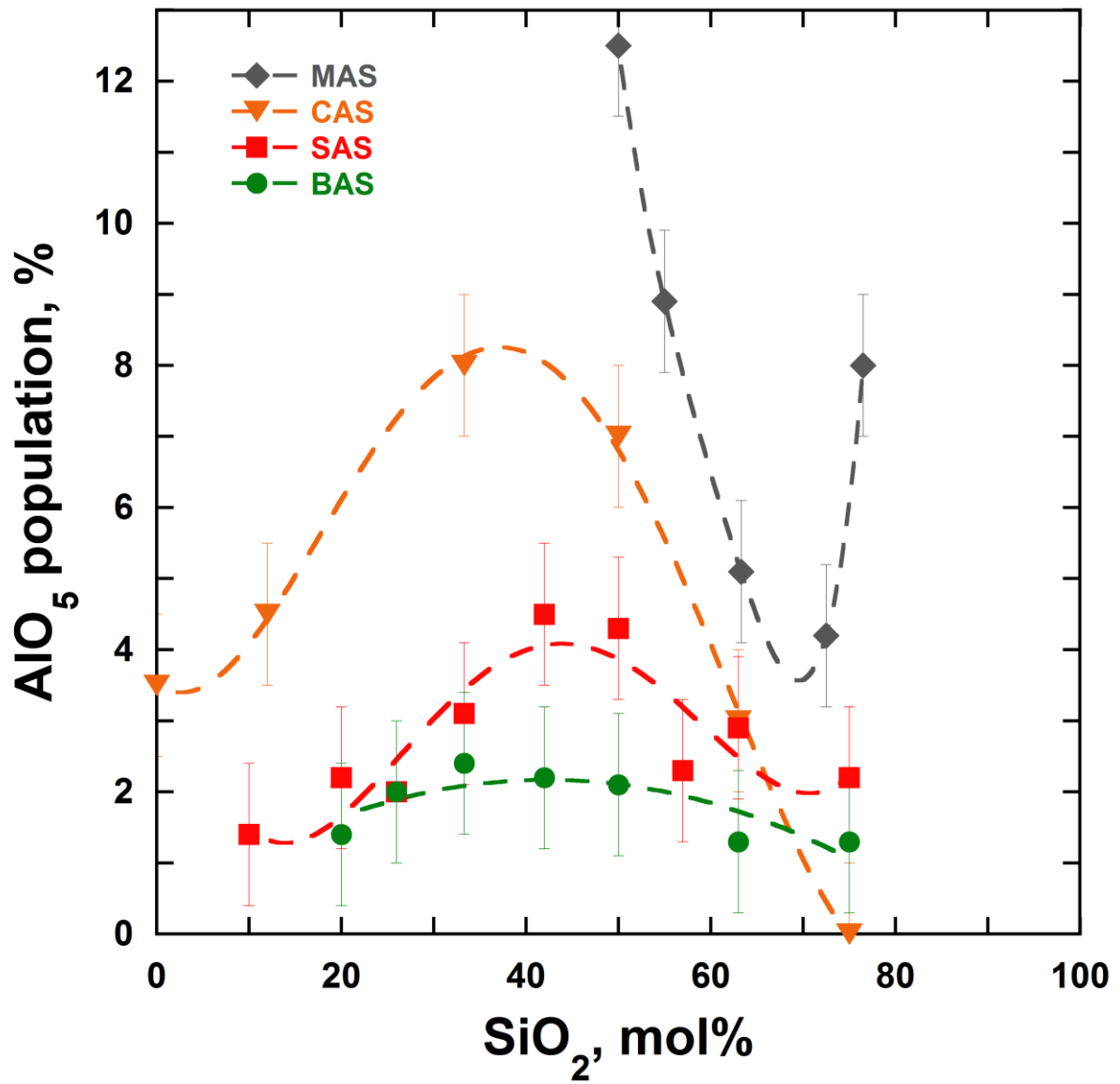
761 Figure 8



762

763

764 Figure 9



765

766

Annex III

Supplementary Information

1. Sr aluminosilicates (SAS)

1.1. Tectosilicate join ($R=1$)

^{27}Al NMR spectroscopy

Table 1. Deconvolution parameters obtained for ^{27}Al NMR spectra of Sr tectosilicate glasses. δ_{iso} is isotropic chemical shift (in ppm) and C_Q is quadrupolar coupling constant (in MHz). Population is in %.

	SA75.12	SA63.18	SA57.21	SA50.25	SA42.29	SA33.33	SA26.37	SA20.40	SA10.40
δ_{iso}									
AlO_4	60.3	62.8	64.1	66.2	68.3	71.3	74.1	76.0	77.8
AlO_5	32.1	34.2	35.0	39.0	40.3	40.0	39.5	41.1	43.4
C_Q									
AlO_4	7.3	7.3	7.0	7.3	7.4	7.5	7.8	8.1	7.5
AlO_5	7.8	7.8	7.1	8.7	8.7	7.6	6.4	6.9	6.8
Population									
AlO_4	97.8	97.1	97.7	95.7	95.5	96.9	98.0	97.8	98.6
AlO_5	2.2	2.9	2.3	4.3	4.5	3.1	2.0	2.2	1.4

^{29}Si NMR spectroscopy

Table 2. Barycentre position (in ppm), fitting parameters (in ppm) and population (in %) of Q_m^n species retrieved from the deconvolution of ^{29}Si NMR spectra of Sr tectosilicate glasses.

	SA75.12	SA63.18	SA57.21	SA50.25	SA42.29	SA33.33	SA26.37	SA20.40	SA10.40
Barycentre									
	-99.1	-92.9	-90.3	-87.5	-84.9	-83.0	-81.6	-80.7*	-79.4*
δ_{iso}									
Q_0^4	-102.6	-104.2	-104.2	-	-	-	-	-	-
Q_1^4	-96.6	-96.6	-96.6	-96.6	-96.6	-	-	-	-
Q_2^4	-91.2	-91.2	-91.2	-91.2	-91.2	-91.2	-	-	-
Q_3^4	-88.3	-88.3	-88.3	-88.3	-88.3	-88.3	-88.3	-	-
Q_4^4	-83.9	-83.9	-83.9	-83.9	-83.9	-83.9	-83.9	-83.9	-83.9
$\text{Q}_4^4(\text{Sr})$	-	-	-	-	-80.2	-80.2	-80.2	-80.2	-79.0

FWHM									
Q ⁴ ₀	16.1	11.5	10.9	-	-	-	-	-	-
Q ⁴ ₁	11.6	11.6	11.6	11.6	11.6	-	-	-	-
Q ⁴ ₂	11.4	11.4	11.4	11.4	11.4	11.4	-	-	-
Q ⁴ ₃	11.2	11.2	11.2	11.2	11.2	11.2	11.2	-	-
Q ⁴ ₄	11.1	11.1	11.1	11.1	11.1	11.1	11.1	11.1	11.1
Q ⁴ ₄ (Sr)	-	-	-	-	11.0	11.0	10.6	10.2	10.0
Population									
Q ⁴ ₀	63.7	9.6	2.2	0	0	0	0	0	0
Q ⁴ ₁	18.2	34.3	21.9	10.1	3.3	0	0	0	0
Q ⁴ ₂	11.5	26.6	25.3	17.2	6.3	2.5	0	0	0
Q ⁴ ₃	5.1	20.0	26.7	23.1	19.0	9.2	6.0	0	0
Q ⁴ ₄	1.6	11.5	24.0	45.0	54.6	48.3	25.8	11.4	5.7
Q ⁴ ₄ (Sr)	0	0	0	0	16.8	40.0	68.2	88.6	94.4

* a band at – 110 ppm was not taken into account to estimate the barycentre position

Neutron diffraction

Table 3. The position of the first sharp diffraction peak (in Å⁻¹) in $S(q)$ and positions of first two peaks in $g(r)$ (in Å) of Sr tectosilicate glasses.

	SA75.12	SA63.18	SA57.21	SA50.25	SA42.29	SA33.33	SA20.40
$S(q)$							
FSDP	1.64	1.73	1.78	1.80	1.89	1.94	2.03
$g(r)$							
1 st peak	1.62	1.64	1.64	1.66	1.68	1.69	1.72
2 nd peak	2.63	2.65	2.65	2.66	2.67	2.70	2.74

Raman spectroscopy

Table 4. Bands position (in cm^{-1}) observed in Raman spectra of Sr tectosilicate glasses.

	SA75.12	SA63.18	SA57.21	SA50.25	SA42.29	SA33.33	SA26.37	SA20.40	SA10.40
Boson	60	67	61	63	64	65	67	66	68
D ₁	487*	494	501	506	514	519*	506*	503*	497*
D ₂	572*	567*	564*	561*	556	555	552	547	542
T _{2b}	791	-	-	-	-	-	-	-	-
HF band ^a	1055	1029	1015	997	980	963	952	933	913

* observed as a shoulder

^a barycentre of a high-frequency envelope

Table 5. Gaussian bands positions (in cm^{-1}) and relative areas (in %) after the deconvolution of the high-frequency envelope of Raman spectra of Sr tectosilicate glasses.

	SA75.12	SA63.18	SA57.21	SA50.25	SA42.29	SA33.33	SA26.37	SA20.40	SA10.40
Wavenumber									
T _{2s}	990	956	937	935	934	923	837	83	814
Q ^{4,II}	1100	1038	1013	1004	989	958	940	935	926
Q ^{4,I}	1182	1140	1117	1106	1096	1046	1015	1013	1007
Relative area									
T _{2s}	27.0	17.0	11.4	16.8	16.3	2.6	1.4	4.7	11.6
Q ^{4,II}	65.2	66.5	67.5	66.8	74.0	76.9	63.0	67.0	64.2
Q ^{4,I}	7.8	16.5	21.1	16.4	9.7	20.5	35.6	28.2	24.2

Macroscopic properties

Table 6. Chemical composition (theoretical and analysed), density (in g/cm^3) and molar volume V_m (in cm^3/mol) of Sr tectosilicate glasses. The values in parentheses are standard deviation.

Glass		SiO ₂	Al ₂ O ₃	SrO	density	V_m
	mol% ¹	75.00	12.50	12.50		
SA75.12	wt% ²	63.68	18.01	18.30	2.636(1)	26.84(1)
	an wt% ³	61.21(48)	17.62(6)	19.03(8)		

	mol%	63.00	18.50	18.50		
SA63.18	wt%	49.88	24.86	25.26	2.837(3)	26.75(3)
	an wt%	48.68(1.04)	24.72(47)	26.77(20)		
	mol%	57.00	21.50	21.50		
SA57.21	wt%	43.66	27.94	28.40	2.928(1)	26.79(1)
	an wt%	42.73(59)	27.36(33)	29.92(66)		
	mol%	50.00	25.00	25.00		
SA50.25	wt%	36.89	31.30	31.81	3.024(1)	26.93(1)
	an wt%	35.86(29)	30.10(18)	33.22(26)		
	mol%	42.00	29.00	29.00		
SA42.29	wt%	29.74	34.85	35.41	3.132(3)	27.09(3)
	an wt%	29.42(1)	33.03(16)	36.53(23)		
	mol%	33.33	33.33	33.33		
SA33.33	wt%	22.61	38.38	39.00	3.211(2)	27.58(2)
	an wt%	22.28(5)	36.44(6)	40.09(55)		
	mol%	26.00	37.00	37.00		
SA26.37	wt%	17.04	41.15	41.82	3.298(1)	27.80(1)
	an wt%	16.65(2)	40.25(10)	42.01(13)		
	mol%	20.00	40.00	40.00		
SA20.40	wt%	12.75	43.27	43.98	3.359(2)	28.06(2)
	an wt%	12.43(13)	42.79(19)	44.04(32)		
	mol%	10.00	45.00	45.00		
SA10.45*	wt%	6.10	46.57	47.33	3.426(2)	28.76(2)
	an wt%	6.83(4)	44.97(10)	45.79(29)		

¹ theoretical content in mol%

² theoretical content in wt%

³ analysed content in wt%

* glass only with the levitation quench

Table 7. Experimental viscosity data for Sr tectosilicate glasses. Viscosity, η , is in log(Pa·s) and temperature, T , is in K.

SA75.12		SA63.18		SA50.25*		SA42.29		SA33.33		SA26.37	
T	η	T	η	T	η	T	η	T	η	T	η
1153.1	12.51	1148.9	12.42	1112.0	13.98	1137.0	12.72	1144.8	12.44	1144.2	12.68
1169.5	11.98	1158.9	12.01	1135.0	12.95	1145.3	12.35	1151.1	12.09	1159.2	11.92
1186.3	11.50	1161.3	11.94	1166.0	11.52	1152.6	12.01	1156.4	11.90	1169.2	11.47
1196.4	11.23	1181.4	11.24	1180.0	10.87	1161.3	11.64	1160.6	11.61	1175.2	11.25
1206.7	10.95	1186.6	11.04	1193.0	10.44	1168.5	11.38	1165.7	11.39	1189.2	10.58
1221.4	10.53	1191.3	10.90	1213.0	9.77	1177.3	11.00	1170.8	11.22	1214.2	9.40
1231.3	10.33	1196.2	10.72	1232.0	9.20	1183.3	10.75	1175.9	10.97	1231.2	8.79
1237.7	10.14	1204.8	10.37			1185.6	10.66	1186.9	10.50	1239.2	8.51
1247.1	9.99	1209.2	10.19			1192.9	10.40	1192.0	10.31		
		1219.5	9.92			1201.7	10.09	1206.9	9.81		
		1228.5	9.69			1209.4	9.82				

* measured using a micro-penetration technique

Table 8. T_g and VFTH parameters (A , B , T_1) retrieved from the fitting of the viscosity data for Sr tectosilicate glasses. m is melt's fragility. σ_{VFTH} is standard deviation of the VFTH fit from the experimental data. T_g and T_1 are in K.

	SA75.12	SA63.18	SA50.25	SA42.29	SA33.33	SA26.37	SA20.40	SA10.45
T_g	1169.2	1159.8	1154.1	1153.0	1153.1	1158.1	1186*	1214*
A	-5.7944	-14.0710	-6.3440	-8.1320	-9.8495	-20.3770	-	-
B	10614.0	18048.0	7771.7	9314.8	10226.0	21514.0	-	-
T_1	572.7	467.5	730.4	690.3	685.1	493.6	-	-
σ_{VFTH}	0.02	0.03	0.05	0.01	0.04	0.04	-	-
m	34.9	43.7	49.9	50.2	53.8	56.4	-	-

* T_g value is retrieved from DSC measurements

1.2. Silicates domain ($R = \infty$)

^{29}Si NMR spectroscopy

Table 9. Barycentre position (in ppm), fitting parameters (in ppm) and population (in %) of Q^n species retrieved from the deconvolution of ^{29}Si NMR spectra of Sr silicate glasses.

	SA66.00	SA60.00	SA56.00	SA50.00
	Barycentre			
	-93.4	-87.4	-85.2	-82.0*
	δ_{iso}			
Q^1	-	-	-	-76.6
Q^2	-82.8	-82.8	-82.8	-82.8
Q^3	-91.5	-89.8	-91.5	-91.5
Q^4	-106.9	-106.9	-	-
	FWHM			
Q^1	-	-	-	7.6
Q^2	8.4	10.6	11.2	9.3
Q^3	15.2	13.7	11.0	9.3
Q^4	14.5	10.4	-	-
	Population			
Q^1	-	-	-	23.8
Q^2	5.9	38.7	75.5	68.1
Q^3	77.9	59.4	24.5	8.1
Q^4	16.2	1.9	-	-

* a band at -110 ppm was not taken into account to estimate the barycentre position

Raman spectroscopy

Table 3. Bands position (in cm^{-1}) observed in Raman spectra of Sr silicate glasses.

	SA66.00	SA60.00	SA56.00	SA50.00
Boson	63	66	65	68
Sr-O band	343	334	334	334
D_2	562	593	604	620
T_{2b}	774*	770*	-	-
HF band ^a	1037	1013	995	967

* observed as a shoulder

^a barycentre of the high-frequency envelope

Table 11. Gaussian bands positions (in cm^{-1}) and relative areas (in %) after the deconvolution of the high-frequency envelope of Raman spectra of Sr silicate glasses.

	SA66.00	SA60.00	SA56.00	SA50.00
	Wavenumber			
Q ⁰	863	862	857	857
Q ¹	905	905	908	915
Q ²	943	950	957	965
T _{2s}	1014	1012	1020	1020
Q ³	1076	1072	1067	1067
Q ⁴	1140	1145	-	-
	Relative area			
Q ⁰	1.2	4.4	7.3	16.1
Q ¹	2.6	2.6	5.4	11.3
Q ²	17.0	29.4	36.8	36.2
T _{2s}	23.2	17.3	15.4	22.1
Q ³	46.2	44.4	35.1	14.3
Q ⁴	9.9	2.0	0	0

Macroscopic properties

Table 12. Chemical composition (theoretical and analysed), density (in g/cm^3) and molar volume V_m (in cm^3/mol) of Sr silicate glasses. The values in parentheses are standard deviation.

Glass		SiO₂	Al₂O₃	SrO	density	V_m
	mol% ¹	66.66	0.00	33.33		
SA66.00	wt% ²	53.69	0.00	46.30	3.216(3)	23.17(3)
	an wt% ³	51.84(18)	0.38(30)	45.64(62)		
	mol%	60.00	0.00	40.00		
SA60.00	wt%	46.52	0.00	53.48	3.429(1)	22.60(1)
	an wt%	47.11(43)	0.68(7)	50.60(56)		
	mol%	56.00	0.00	44.00		
SA56.00	wt%	42.46	0.00	57.54	3.592(2)	22.07(2)
	an wt%	40.00(42)	0.66(9)	57.79(96)		
	mol%	50.00	0.00	50.00		
SA50.00*	wt%	36.70	0.00	63.30	-	-
	an wt%	35.67(13)	0.01(1)	61.13(47)		

¹ theoretical content in mol%

² theoretical content in wt%

³ analysed content in wt%

* glass only with the levitation quench

Table 13. Experimental viscosity data for Sr silicate glasses. Viscosity, η , is in log(Pa·s) and temperature, T , is in K.

SA66.00		SA56.00	
T	η	T	η
991.4	12.50	1003.0	12.37
1000.8	12.09	1013.2	11.79
1010.0	11.58	1023.5	11.16
1013.8	11.44	1034.1	10.60
1019.5	11.11	1040.6	10.27
1023.9	10.95	1046.0	10.05
1033.7	10.49	1054.9	9.62
1044.3	10.05	1066.1	9.12
1053.4	9.66	1077.6	8.73
1061.6	9.34		
1071.1	9.02		
1079.9	8.68		

Table 14. T_g and VFTH parameters (A , B , T_1) retrieved from the fitting of the viscosity data for Sr silicate glasses. m is melt's fragility. σ_{VFTH} is standard deviation of the VFTH fit from the experimental data. T_g and T_1 are in K.

	SA66.00	SA56.00	SA50.00
T_g	1001.7	1008.9	1042*
A	-10.868	-6.8244	-
B	10489	7286	-
T_1	543.0	689.3	-
σ_{VFTH}	0.02	0.03	-
m	49.9	59.4	-

* T_g value is retrieved from DSC measurements

1.3. Peralkaline domain ($R = 3$)

^{27}Al NMR spectroscopy

Table 15. Deconvolution parameters obtained for ^{27}Al NMR spectra of Sr peralkaline glasses. δ_{iso} is isotropic chemical shift (in ppm) and C_Q is quadrupolar coupling constant (in MHz). Population is in %.

	SA75.06	SA66.09	SA60.10	SA50.12	SA42.14	SA38.16	SA33.17
	δ_{iso}						
AlO_4	60.1	62.0	63.5	66.3	69.1	71.3	73.9
AlO_5	28.2	31.7	33.0	34.5	37.2	39.5	40.4
	C_Q						
AlO_4	6.44	6.47	6.46	6.09	6.33	6.62	6.79
AlO_5	6.46	7.49	8.49	6.50	6.83	7.37	7.62
	Population						
AlO_4	97.4	95.8	95.5	95.9	97.5	97.4	98.8
AlO_5	2.6	4.2	4.5	4.1	2.5	2.6	1.2

Table 16. Barycentre position (in ppm) of ^{29}Si NMR spectra of Sr peralkaline glasses.

	SA75.06	SA66.09	SA60.10	SA50.12	SA42.14	SA38.16	SA33.17
Barycentre	-96.6	-92.9	-89.4	-83.8	-80.6	-78.5	-77.3

Neutron diffraction

Table 17. The position of the first sharp diffraction peak (in \AA^{-1}) in $S(q)$ and positions of first two peaks in $g(r)$ (in \AA) of Sr peralkaline glasses.

	SA60.10	SA50.12	SA42.14	SA33.17
	$S(q)$			
FSDP	1.87	1.96	1.99	2.03
	$g(r)$			
1 st peak	1.63	1.64	1.65	1.66
2 nd peak	2.64	2.64	2.64	2.64

Raman spectroscopy

Table 18. Bands position (in cm^{-1}) observed in Raman spectra of Sr peralkaline glasses.

	SA75.06	SA66.09	SA60.10	SA50.12	SA42.14	SA38.16	SA33.17
Boson	60	63	66	65	66	67	65
D ₁	491	503	508	531*	-	-	-
D ₂	560*	568*	570*	564	561	562	555
T _{2b}	789	772*	-	-	-	-	-
HF band ^a	1050	1034	1016	981	954	938	918

* observed as a shoulder

^a barycentre of a high-frequency envelope

Table 19. Gaussian bands positions (in cm^{-1}) and relative areas (in %) after the deconvolution of the high-frequency envelope of Raman spectra of Sr peralkaline glasses.

	SA75.06	SA66.09	SA60.10	SA50.12	SA42.14	SA38.16	SA33.17
Wavenumber							
Q ⁰	-	-	-	854	862	862	861
Q ¹	905	905	905	902	905	905	910
Q ²	943	943	943	952	952	952	960
T _{2s}	1014	1014	1008	1020	1020	1022	1020
Q ³	1062	1064	1059	1067	1067	1067	-
Q ^{4,II}	1140	1140	1140	1162	1162	1140	-
Q ^{4,I}	1200	1192	1201	-	-	-	-
Relative area							
Q ⁰	0	0	0	1.8	11.4	17.6	29.8
Q ¹	0.3	0.6	6.7	8.5	21.9	21.9	35.6
Q ²	12.8	19.7	21.2	49.1	51.2	43.2	19.5
T _{2s}	26.4	27.1	26.1	24.4	14.4	12.6	15.2
Q ³	42.1	42.4	39.4	15.7	8.1	4.2	0
Q ^{4,II}	14.0	8.2	6.0	0.6	0.5	0.4	0
Q ^{4,I}	4.4	2.1	0.7	0	0	0	0

Macroscopic properties

Table 20. Chemical composition (theoretical and analysed), density (in g/cm³) and molar volume V_m (in cm³/mol) of Sr peralkaline glasses. The values in parentheses are standard deviation.

Glass		SiO ₂	Al ₂ O ₃	SrO	density	V_m
SA75.06	mol% ¹	75.00	6.25	18.75		
	wt% ²	63.59	8.99	27.42	2.779(1)	25.50(1)
	an wt% ³	61.90(21)	10.80(23)	27.52(58)		
SA66.09	mol%	66.00	8.50	25.50		
	wt%	53.05	11.59	35.35	3.000(2)	24.92(2)
	an wt%	51.53(15)	13.16(28)	35.40(45)		
SA60.10	mol%	60.00	10.00	30.00		
	wt%	46.62	13.18	40.20	3.141(2)	24.62(2)
	an wt%	45.34(22)	12.75(5)	42.05(29)		
SA50.12	mol%	50.00	12.50	37.50		
	wt%	36.80	15.61	47.59	3.349(3)	24.38(3)
	an wt%	35.40(23)	15.25(8)	48.07(58)		
SA42.14	mol%	42.86	14.28	42.86		
	wt%	30.40	17.19	52.42	3.482(5)	24.33(5)
	an wt%	29.45(14)	16.56(19)	54.38(11)		
SA38.16	mol%	38.00	15.50	46.50		
	wt%	26.30	18.20	55.50	3.563(2)	24.37(2)
	an wt%	25.36(12)	18.94(40)	55.81(57)		
SA33.17*	mol%	33.00	16.75	50.25		
	wt%	22.28	19.19	58.52	3.642(1)	24.43(1)
	an wt%	21.43(13)	19.11(1.17)	59.05(1.80)		

¹ theoretical content in mol%

² theoretical content in wt%

³ analysed content in wt%

* glass only with the levitation quench

Table 21. Experimental viscosity data for Sr peralkaline glasses. Viscosity, η , is in log(Pa·s) and temperature, T , is in K.

SA75.06		SA60.10		SA50.12		SA42.14		SA38.16	
T	η								
1030.9	12.67	1036.8	12.44	1046.6	12.79	1068.8	12.83	1090.5	12.10
1054.9	11.69	1046.4	12.07	1059.5	12.25	1079.9	12.31	1109.9	11.00
1092.9	10.45	1049.2	11.90	1070.4	11.72	1085.4	12.03	1123.6	10.33
1109.9	9.99	1052.4	11.73	1074.1	11.54	1099.4	11.31	1133.8	9.84
1123.6	9.61	1056.1	11.60	1080.1	11.22	1109.6	10.91	1145.5	9.46
1133.8	9.29	1062.0	11.32	1090.7	10.78	1121.0	10.39	1161.4	8.75
1158.7	8.57	1075.5	10.79	1100.1	10.33	1129.5	9.95	1169.6	8.41
		1076.8	10.74	1111.0	9.96	1136.5	9.74		
		1082.8	10.56	1124.8	9.48				
		1093.3	10.20						
		1103.4	9.81						
		1113.9	9.50						

Table 22. T_g and VFTH parameters (A , B , T_1) retrieved from the fitting of the viscosity data for Sr peralkaline glasses. m is melt's fragility. σ_{VFTH} is standard deviation of the VFTH fit from the experimental data. T_g and T_1 are in K.

	SA75.06	SA60.10	SA50.12	SA42.14	SA38.16	SA33.17
T_g	1047.9	1046.6	1063.6	1085.7	1091.5	1122*
A	-9.4164	-8.2735	-11.346	-17.719	-8.2923	-
B	12622	9547	11576	18094	7391	-
T_1	458.5	575.7	567.8	476.9	727.3	-
σ_{VFTH}	0.04	0.03	0.04	0.03	0.04	-
m	38.1	45.1	50.1	53.0	60.8	-

* T_g value was obtained from DSC measurements

1.4. Peraluminous domain ($R < 1$)

^{27}Al NMR spectroscopy

Table 23. Deconvolution parameters obtained for ^{27}Al NMR spectra of Sr peraluminous glasses. δ_{iso} is isotropic chemical shift (in ppm) and C_Q is quadrupolar coupling constant (in MHz). Population is in %.

	SA50.30	SA50.35	SA50.40	SA33.38	SA33.43
δ_{iso}					
AlO_4	65.9	65.9	65.5	70.5	69.7
AlO_5	37.6	37.7	37.4	39.8	39.6
AlO_6	9.6	9.9	9.7	9.3	9.4
C_Q					
AlO_4	8.04	9.06	9.92	8.31	8.82
AlO_5	7.56	7.74	7.54	7.53	7.76
AlO_6	3.57	3.71	3.54	1.70	2.36
Population					
AlO_4	88.4	78.6	70.8	90.3	84.4
AlO_5	10.6	18.6	23.4	9.0	14.4
AlO_6	1.0	2.8	5.8	0.7	1.3

Table 24. Barycentre position (in ppm) of ^{29}Si NMR spectra of Sr peraluminous glasses.

	SA50.30	SA50.35	SA50.40	SA33.38	SA33.43
Barycentre	-88.09	-89.59	-91.70	-83.44	-84.47

Raman spectroscopy

Table 25. Bands position (in cm^{-1}) observed in Raman spectra of Sr peraluminous glasses.

	SA50.30	SA50.35	SA50.40	SA33.38	SA33.43
Boson	70	74	83	75	75
D_1	498	476*	461*	-	-
D_2	570*	574*	-	561	570*
T_{2b}	-	-	-	-	-
HF band ^a	1010	1017	1029	973	980

* observed as a shoulder

^a barycentre of a high-frequency envelope

Table 26. Gaussian bands positions (in cm^{-1}) and relative areas (in %) after the deconvolution of the high-frequency envelope of Raman spectra of Sr peraluminous glasses.

	SA50.30	SA50.35	SA50.40	SA33.38	SA33.43
	Position				
T _{2s}	929	933	925	877	877
Q ^{4,II}	1007	1022	1024	962	962
Q ^{4,I}	1131	1137	1142	1040	1040
	Relative area				
T _{2s}	12.0	19.3	12.7	17.2	10.1
Q ^{4,II}	77.5	66.8	72.1	52.5	51.9
Q ^{4,I}	10.4	13.9	15.2	30.3	37.9

Macroscopic properties

Table 27. Chemical composition (theoretical and analysed), density (in g/cm^3) and molar volume V_m (in cm^3/mol) of Sr peraluminous glasses. The values in parentheses are standard deviation.

Glass		SiO₂	Al₂O₃	SrO	density	V_m
SA50.30	mol% ¹	50.00	30.00	20.00		
	wt% ²	36.93	37.60	25.47	2.943(1)	27.64(1)
	an wt% ³	36.12(19)	35.55(62)	25.35(53)		
SA50.35*	mol%	50.00	35.00	15.00		
	wt%	36.97	43.91	19.12	2.890(3)	28.12(3)
	an wt%	35.48(70)	40.20(1.28)	19.30(38)		
SA50.40*	mol%	50.00	40.00	10.00		
	wt%	37.00	50.23	12.76	2.829(1)	28.70(1)
	an wt%	36.72(22)	45.10(48)	12.99(24)		
SA33.38	mol%	33.33	38.33	28.33		
	wt%	22.64	44.17	33.18	3.143(2)	28.15(2)
	an wt%	22.10(14)	39.99(42)	33.32(62)		
SA33.43*	mol%	33.33	43.33	23.23		
	wt%	22.66	49.98	27.35	3.084(2)	28.66(2)
	an wt%	23.42(13)	42.64(55)	28.18(47)		

¹ theoretical content in mol%

² theoretical content in wt%

³ analysed content in wt%

* glass only with the levitation quench

1.5. High-temperature melts

²⁷Al HT NMR spectroscopy

Table 28. The slopes, $\Delta\delta/\Delta T$, of the “line’s position vs temperature” curves (in ppm/1000 °C) and activation energy (in kJ/mol), E_{act} , of Sr tectosilicate melts.

	SA63.18	SA57.21	SA50.25	SA42.29	SA33.33	SA26.37	SA20.40	SA10.40	SA00.50
$\Delta\delta/\Delta T$	2.1	-0.5	-0.9	-0.9	-1.3	-1.6	-2.7	-2.7	-1.6
E_{act}	132	128	136	137	137	141	140	138	-

Table 29. The slopes, $\Delta\delta/\Delta T$, of the “line’s position vs temperature” curves (in ppm/1000 °C) and activation energy (in kJ/mol), E_{act} , of Sr peralkaline melts.

	SA66.09	SA60.10	SA50.12	SA42.14	SA38.16	SA33.17
$\Delta\delta/\Delta T$	0.5	-0.6	-0.4	-1.6	-1.3	-1.2
E_{act}	120	108	110	104	110	114

Table 30. The slopes, $\Delta\delta/\Delta T$, of the “line’s position vs temperature” curves (in ppm/1000 °C) and activation energy (in kJ/mol), E_{act} , of Sr peraluminous melts.

	SA50.30	SA50.35	SA50.40	SA33.38	SA33.43
$\Delta\delta/\Delta T$	-0.6	-0.2	1.0	-1.3	-0.9
E_{act}	143	141	136	143	139

HT neutron diffraction

Table 31. The position of the first sharp diffraction peak (in \AA^{-1}) in $S(q)$ and positions of first two peaks in $g(r)$ (in \AA) of Sr tectosilicate and peralkaline melts.

	SA42.29	SA33.33	SA20.40	SA00.50	SA33.17	SA20.20
S(q)						
FSDP	1.91	1.96	2.02	2.12	2.09	2.10
g(r)						
1 st peak	1.69	1.70	1.72	1.76	1.67	1.71
2 nd peak	2.73	2.72	2.76	2.90	2.67	2.65

2. Ba aluminosilicates (BAS)

2.1. Tectosilicate join ($R=1$)

^{27}Al NMR spectroscopy

Table 32. Deconvolution parameters obtained for ^{27}Al NMR spectra of Ba tectosilicate glasses. δ_{iso} is isotropic chemical shift (in ppm) and C_Q is quadrupolar coupling constant (in MHz). Population is in %.

	BA75.12	BA63.18	BA50.25	BA42.29	BA33.33	BA26.37	BA20.40
δ_{iso}							
AlO_4	59.8	62.6	65.9	68.2	70.5	73.1	74.9
AlO_5	34.1	32.8	37.2	38.4	43.2	43.3	43.5
C_Q							
AlO_4	6.5	6.7	6.8	7.0	7.0	7.3	7.3
AlO_5	7.9	6.5	7.2	7.2	7.8	8.1	7.2
Population							
AlO_4	98.7	98.8	97.9	97.8	97.6	98.0	98.6
AlO_5	1.3	1.3	2.1	2.2	2.4	2.0	1.4

^{29}Si NMR spectroscopy

Table 33. Barycentre position (in ppm), fitting parameters (in ppm) and population (in %) of Q_m^n species retrieved from the deconvolution of ^{29}Si NMR spectra of Ba tectosilicate glasses.

	BA75.12	BA63.18	BA50.25	BA42.29	BA33.33	BA26.37	BA20.40
Barycentre							
	-99.1	-93.4	-88.2	-85.9	-84.4	-83.1*	-82.8*
δ_{iso}							
Q_0^4	-102.4	-103.4	-	-	-	-	-
Q_1^4	-96.6	-96.6	-96.6	-	-	-	-
Q_2^4	-91.2	-91.2	-91.2	-91.2	-	-	-
Q_3^4	-88.3	-88.3	-88.3	-88.3	-88.3	-88.3	-88.3
Q_4^4	-	-83.9	-83.9	-83.9	-83.9	-83.9	-83.9
$Q_4^4(\text{Ba})$	-	-	-	-	-80.2	-80.2	-80.2

FWHM							
Q^4_0	13.6	10.8	-	-	-	-	-
Q^4_1	10	10	10	-	-	-	-
Q^4_2	10	10	10	10	-	-	-
Q^4_3	10	10	10	10	10	10	10
Q^4_4	-	10	10	10	10	10	10
$Q^4_4(\text{Ba})$	-	-	-	-	6.73	8.60	8.61
Population							
Q^4_0	61.6	12.0	0	0	0	0	0
Q^4_1	21.6	31.9	10.0	0	0	0	0
Q^4_2	14.4	32.1	21.3	13.4	0	0	0
Q^4_3	2.4	15.3	30.1	17.0	14.4	3.8	0
Q^4_4	0	8.8	38.7	69.6	78.8	65.9	64.6
$Q^4_4(\text{Ba})$	0	0	0	0	6.9	30.3	35.5

* a band at – 110 ppm was not taken into account to estimate the barycentre position

Neutron diffraction

Table 34. The position of the first sharp diffraction peak (in \AA^{-1}) in $S(q)$ and positions of first two peaks in $g(r)$ (in \AA) of Ba tectosilicate glasses.

	BA75.12	BA63.18	BA50.25	BA42.29	BA33.33
$S(q)$					
FSDP	1.64	1.74	1.81	1.85	1.92
$g(r)$					
1 st peak	1.62	1.64	1.66	1.67	1.69
2 nd peak	2.67	2.70	2.74	2.76	2.77

Raman spectroscopy

Table 35. Bands position (in cm^{-1}) observed in Raman spectra of Ba tectosilicate glasses.

	BA75.12	BA63.18	BA50.25	BA42.29	BA33.33	BA26.37	BA20.40
Boson	45	50	47	52	55	53	55
D ₁	490*	492	501	503	494*	489*	482*
D ₂	576*	570*	557*	557*	552	548	545
T _{2b}	789*	-	-	-	-	-	-
HF band ^a	1057	1035	999	982	966	950	933

* observed as a shoulder

^a barycentre of a high-frequency envelope

Table 36. Gaussian bands positions (in cm^{-1}) and relative areas (in %) after the deconvolution of the high-frequency envelope of Raman spectra of Ba tectosilicate glasses.

	BA75.12	BA63.18	BA50.25	BA42.29	BA33.33	BA26.37	BA20.40
Wavenumber							
T _{2s}	980	964	943	931	836	833	827
Q ^{4,II}	1100	1057	1004	991	956	943	940
Q ^{4,I}	1182	1158	1122	1098	1045	1016	1012
Relative area							
T _{2s}	40.0	28.6	16.2	23.3	2.5	7.8	14.7
Q ^{4,II}	53.4	66.2	76.6	67.4	76.4	63.0	57.9
Q ^{4,I}	6.7	5.1	7.2	9.2	21.1	29.2	27.4

Macroscopic properties

Table 37. Chemical composition (theoretical and analysed), density (in g/cm³) and molar volume V_m (in cm³/mol) of Ba tectosilicate glasses. The values in parentheses are standard deviation.

Glass		SiO ₂	Al ₂ O ₃	BaO	density	V_m
BA75.12	mol% ¹	75.00	12.50	12.50		
	wt% ²	58.54	16.56	24.90	2.794(1)	27.55(1)
	an wt% ³	57.97(29)	16.42(9)	25.16(17)		
BA63.18	mol%	63.00	18.50	18.50		
	wt%	44.49	22.17	33.34	3.053(2)	27.87(2)
	an wt%	44.07(31)	21.99(7)	33.65(10)		
BA50.25*	mol%	50.00	25.00	25.00		
	wt%	32.01	27.16	40.84	3.315(5)	28.32(5)
	an wt%	30.97(15)	28.01(85)	41.03(19)		
BA42.29	mol%	42.00	29.00	29.00		
	wt%	25.42	29.79	44.79	3.455(1)	28.73(1)
	an wt%	25.19(16)	29.54(10)	45.07(10)		
BA33.33	mol%	33.33	33.33	33.33		
	wt%	19.05	32.33	48.62	3.579(1)	29.37(1)
	an wt%	18.80(10)	32.14(51)	48.55(22)		
BA26.37*	mol%	26.00	37.00	37.00		
	wt%	14.19	34.27	51.54	3.715(1)	29.63(1)
	an wt%	12.82(10)	33.83(17)	52.12(20)		
BA20.40*	mol%	20.00	40.00	40.00		
	wt%	10.53	35.73	53.74	3.772(3)	30.26(3)
	an wt%	10.54(8)	34.98(17)	53.29(17)		

* glass only with the levitation quench

² theoretical content in wt%

³ analysed content in wt%

* glass only with the levitation quench

Table 38. Experimental viscosity data for Ba tectosilicate glasses. Viscosity, η , is in log(Pa·s) and temperature, T , is in K.

BA75.12		BA63.18		BA42.29		BA33.33	
T	η	T	η	T	η	T	η
1164.4	12.24	1161.8	12.29	1165.7	12.33	1175.2	12.23
1169.7	12.09	1172.0	11.95	1169.1	12.17	1180.4	12.03
1175.1	11.95	1182.3	11.61	1178.7	11.78	1190.4	11.61
1178.2	11.83	1186.4	11.48	1183.9	11.61	1199.9	11.11
1184.1	11.70	1209.9	10.71	1201.9	10.79	1223.4	10.17
1188.7	11.57	1220.2	10.49	1218.0	10.25	1233.1	9.83
1209.1	11.03	1235.0	10.02	1227.4	9.90	1257.7	8.92
1221.4	10.79	1245.4	9.77	1232.8	9.75		
1225.6	10.67	1259.7	9.31	1244.1	9.38		
1234.6	10.42			1253.4	9.04		
1250.6	10.12						
1260.2	9.98						

Table 39. T_g and VFTH parameters (A , B , T_1) retrieved from the fitting of the viscosity data for Ba tectosilicate glasses. m is melt's fragility. σ_{VFTH} is standard deviation of the VFTH fit from the experimental data. T_g and T_1 are in K.

	BA75.12	BA63.18	BA50.25	BA42.29	BA33.33	BA26.37	BA20.40
T_g	1172.7	1170.6	1182*	1173.7	1180.6	1204*	1219*
A	-4.565	-12.765	-	-10.597	-11.588	-	-
B	10146	18418	-	11987	12157	-	-
T_1	560.2	426.9	-	643.2	665.2	-	-
σ_{VFTH}	0.03	0.02	-	0.03	0.02	-	-
m	31.7	39.0	-	50.0	54.0	-	-

* T_g value is retrieved from DSC measurements

2.2. Silicates domain ($R = \infty$)

^{29}Si NMR spectroscopy

Table 40. Barycentre position (in ppm), fitting parameters (in ppm) and population (in %) of Q^n species retrieved from the deconvolution of ^{29}Si NMR spectra of Ba silicate glasses.

	BA75.00	BA66.00	BA50.00
Barycentre			
	-97.4	-93.2	-84.1*
Chemical shift			
Q^2	-	-83.5	-83.5
Q^3	-94.4	-92.5	-92.5
Q^4	-106.9	-105.4	-
FWHM			
Q^2	-	8.5	10.9
Q^3	14.6	13.8	8.3
Q^4	12.9	9.8	-
Population			
Q^2	0	3.0	94.9
Q^3	75.7	89.9	5.1
Q^4	24.3	7.0	0

* a band at -110 ppm was not taken into account to estimate the barycentre position

Raman spectroscopy

Table 41. Bands position (in cm^{-1}) observed in Raman spectra of Ba silicate glasses.

	BA75.00	BA66.00	BA60.00	BA50.00
Boson	49	50	54	53
Ba-O 1 st band	187*	190*	186*	179
Ba-O 2 nd band	313	307	302	308
D_1	538	555	-	-
D_2	593*	589*	581	609
T_{2b}	783*	772*	-	-
HF band ^a	1058	1042	1015	957

* observed as a shoulder

^a barycentre of the high-frequency envelope

Table 42. Gaussian bands positions (in cm^{-1}) and relative areas (in %) after the deconvolution of the high-frequency envelope of Raman spectra of Ba silicate glasses.

	BA75.00	BA66.00	BA60.00	BA50.00
Wavenumber				
Q ⁰	860	854	852	844
Q ¹	908	905	905	911
Q ²	938	935	939	956
T _{2s}	1019	1014	1020	1014
Q ³	1076	1075	1071	1061
Q ^{4,II}	1140	1140	1140	-
Q ^{4,I}	1197	-	-	-
Relative area				
Q ⁰	0.7	0.8	2.2	14.2
Q ¹	2.9	1.9	4.2	14.8
Q ²	9.6	15.5	21.1	36.1
T _{2s}	20.9	19.6	34.9	26.0
Q ³	51.1	54.2	35.7	9.0
Q ^{4,II}	12.1	8.0	2.0	0
Q ^{4,I}	2.9	0	0	0

Macroscopic properties

Table 43. Chemical composition (theoretical and analysed), density (in g/cm^3), molar volume V_m (in cm^3/mol) and T_g (in K) of Ba silicate glasses. The values in parentheses are standard deviation.

Glass		SiO₂	Al₂O₃	BaO	density	V_m	T_g
BA75.00	ol% ¹	75.00	0.00	25.00			
	wt% ²	54.03	0.00	45.97	3.388(4)	24.62(4)	-
	an wt% ³	49.23(27)	0.33(2)	49.48(23)			
BA66.00	mol%	66.66	0.00	33.33			
	wt%	43.94	0.00	56.06	3.693(2)	24.69(2)	-
	an wt%	44.07(32)	0.39(2)	54.45(20)			
BA60.00	mol%	60.00	0.00	40.00			
	wt%	37.02	0.00	62.98	4.003(2)	24.33(2)	-
	an wt%	36.59(40)	0.47(2)	61.80(35)			
BA50.00*	mol%	50.00	0.00	50.00			
	wt%	28.15	0.00	71.85	4.366(2)	24.44(2)	963**
	an wt%	27.58(13)	0.51(3)	70.26(18)			

¹ theoretical content in mol%

² theoretical content in wt%

³ analysed content in wt%

* glass only with the levitation quench

** T_g value retrieved from DSC measurements

2.3. Peralkaline domain ($R = 3$)

²⁷Al NMR spectroscopy

Table 44. Deconvolution parameters obtained for ²⁷Al NMR spectra of Ba peralkaline glasses. δ_{iso} is isotropic chemical shift (in ppm) and C_Q is quadrupolar coupling constant (in MHz). Population is in %.

	BA75.06	BA60.10	BA50.12	BA42.14	BA33.17
δ_{iso}					
AlO ₄	59.9	63.2	65.8	68.0	72.0
AlO ₅	30.8	32.2	32.7	40.0	41.4
C_Q					
AlO ₄	5.8	5.7	5.6	5.6	5.9
AlO ₅	7.5	7.2	5.0	4.3	2.0
Population					
AlO ₄	97.7	96.9	97.6	97.9	99.1
AlO ₅	2.4	3.1	2.4	2.1	0.9

Table 45. Barycentre position (in ppm) of ²⁹Si NMR spectra of Ba peralkaline glasses.

	BA75.06	BA60.10	BA50.12	BA42.14	BA33.17
Barycentre	-99.0	-90.7	-86.2	-82.9	-79.9

Neutron diffraction

Table 46. The position of the first sharp diffraction peak (in \AA^{-1}) in $S(q)$ and positions of first two peaks in $g(r)$ (in \AA) of Ba peralkaline glasses.

	BA75.06	BA60.10	BA50.12	BA42.14
$S(q)$				
FSDP	1.67	1.86	1.95	1.99
$g(r)$				
1 st peak	1.62	1.63	1.64	1.65
2 nd peak	2.66	2.69	2.71	2.73

Raman spectroscopy

Table 47. Bands position (in cm^{-1}) observed in Raman spectra of Ba peralkaline glasses.

	BA75.06	BA60.10	BA50.12	BA42.14	BA33.17
Boson	43	51	54	55	58
Ba-O 1 st band	-	-	179*	180*	176
Ba-O 2 nd band	-	318	314	316	314
D ₁	491	505	502*	495*	494*
D ₂	570*	570	562	557	551
T _{2b}	787	-	-	-	-
HF band ^a	1047	1016	980	951	911

* observed as a shoulder

^a barycentre of a high-frequency envelope

Table 48. Gaussian bands positions (in cm^{-1}) and relative areas (in %) after the deconvolution of the high-frequency envelope of Raman spectra of Ba peralkaline glasses.

	BA75.06	BA60.10	BA50.12	BA42.14	BA33.17
Wavenumber					
Q ⁰	-	855	846	848	850
Q ¹	-	908	900	897	896
Q ²	935	945	951	940	942
T _{2s}	1006	1007	1020	1020	1018
Q ³	1052	1057	1067	1071	-
Q ^{4,II}	1111	1132	1140	1140	-
Q ^{4,I}	1172	1185	-	-	-

	Relative area				
Q ⁰	0	0.9	1.4	5.7	22.2
Q ¹	0	6.4	6.6	9.2	26.6
Q ²	12.5	16.0	52.2	60.1	40.3
T _{2s}	23.4	31.2	26.9	21.7	10.9
Q ³	37.9	40.6	11.9	2.7	0
Q ^{4,II}	17.4	4.3	1.0	0.7	0
Q ^{4,I}	8.7	0.6	0	0	0

Macroscopic properties

Table 49. Chemical composition (theoretical and analysed), density (in g/cm³) and molar volume V_m (in cm³/mol) of Ba peralkaline glasses. The values in parentheses are standard deviation.

Glass		SiO ₂	Al ₂ O ₃	BaO	density	V_m	T_g
BA75.06	mol% ¹	75.00	6.25	18.75			
	wt% ²	56.20	7.95	35.85	3.040(1)	26.38(1)	1023**
	an wt% ³	55.42(26)	8.07(5)	35.98(10)			
BA60.10	mol%	60.00	10.00	30.00			
	wt%	39.08	11.05	49.87	3.532(1)	26.12(1)	1008**
	an wt%	38.07(12)	12.81(43)	49.68(28)			
BA50.12	mol%	50.00	12.50	37.50			
	wt%	29.96	12.71	57.34	3.826(1)	26.21(1)	1028**
	an wt%	29.26(17)	15.37(70)	56.95(17)			
BA42.14	mol%	42.86	14.28	42.86			
	wt%	24.29	13.73	61.98	4.008(3)	26.46(3)	1073**
	an wt%	23.71(12)	15.78(90)	61.44(25)			
BA33.17*	mol%	33.00	16.75	50.25			
	wt%	17.40	14.99	67.61	4.229(2)	26.95(2)	-
	an wt%	17.09(12)	18.22(54)	66.95(25)			

¹ theoretical content in mol%

² theoretical content in wt%

³ analysed content in wt%

* glass only with the levitation quench

** T_g value was obtained from DSC measurements

2.4. Peraluminous domain ($R < 1$)

^{27}Al NMR spectroscopy

Table 50. Deconvolution parameters obtained for ^{27}Al NMR spectra of Ba peraluminous glasses. δ_{iso} is isotropic chemical shift (in ppm) and C_Q is quadrupolar coupling constant (in MHz). Population is in %.

	BA50.30	BA50.35	BA50.40	BA33.38	BA33.43
δ_{iso}					
AlO_4	65.3	65.8	65.9	69.9	69.6
AlO_5	38.4	39.1	39.2	40.2	40.6
AlO_6	9.2	9.3	12.2	9.2	12.4
C_Q					
AlO_4	7.3	8.6	9.6	7.7	8.5
AlO_5	6.3	8.2	8.6	7.1	8.0
AlO_6	3.4	3.8	7.3	1.3	5.9
Population					
AlO_4	86.0	77.4	69.3	92.5	84.7
AlO_5	13.1	20.6	27.2	7.3	14.6
AlO_6	0.9	2.0	3.5	0.2	0.8

Table 51. Barycentre position (in ppm) of ^{29}Si NMR spectra of Ba peraluminous glasses.

	BA50.30	BA50.35	BA50.40	BA33.38	BA33.43
Barycentre	-89.5	-90.7	-92.3	-84.9	-85.7

Raman spectroscopy

Table 52. Bands position (in cm^{-1}) observed in Raman spectra of Ba peraluminous glasses.

	BA50.30	BA50.35	BA50.40	BA33.38	BA33.43
Boson	49	53	56	50	55
D_1	494	474*	471*	482*	-
D_2	567*	572	573	556	566
T_{2b}	-	-	-	-	-
HF band ^a	1011	1021	1027	975	983

* observed as a shoulder

^a barycentre of a high-frequency envelope

Table 53. Gaussian bands positions (in cm^{-1}) and relative areas (in %) after the deconvolution of the high-frequency envelope of Raman spectra of Ba peraluminous glasses.

	BA50.30	BA50.35	BA50.40	BA33.38	BA33.43
	Position				
T _{2s}	930	937	935	877	876
Q ^{4,II}	1006	1023	1033	964	967
Q ^{4,I}	1111	1133	1139	1037	1040
	Relative area				
T _{2s}	11.7	11.9	17.3	14.2	10.2
Q ^{4,II}	70.1	79.5	69.9	53.2	52.4
Q ^{4,I}	18.2	8.6	12.8	32.6	37.4

Macroscopic properties

Table 54. Chemical composition (theoretical and analysed), density (in g/cm^3) and molar volume V_m (in cm^3/mol) of Ba peraluminous glasses. The values in parentheses are standard deviation.

Glass		SiO₂	Al₂O₃	BaO	density	V_m
	mol% ¹	50.00	30.00	20.00		
BA50.30	wt% ²	32.91	33.50	33.59	3.162(1)	28.87(1)
	an wt% ³	32.70(22)	33.26(14)	33.56(21)		
	mol%	50.00	35.00	15.00		
BA50.35*	wt%	33.86	40.22	25.92	3.058(2)	29.02(2)
	an wt%	33.34(20)	39.62(13)	26.09(19)		
	mol%	50.00	40.00	10.00		
BA50.40*	wt%	34.87	47.34	17.80	2.978(5)	28.93(5)
	an wt%	30.17(16)	48.92(33)	18.55(18)		
	mol%	33.33	38.33	28.33		
BA33.38	wt%	19.53	38.11	42.36	3.442(3)	29.80(3)
	an wt%	19.37(16)	37.60(14)	42.24(17)		
	mol%	33.33	43.33	23.23		
BA33.43*	wt%	20.03	44.19	35.78	3.341(7)	29.93(7)
	an wt%	19.37(11)	42.79(20)	35.53(15)		

¹ theoretical content in mol%

² theoretical content in wt%

³ analysed content in wt%

* glass only with the levitation quench

2.5. High-temperature melts

²⁷Al HT NMR spectroscopy

Table 55. The slopes, $\Delta\delta/\Delta T$, of the “line’s position vs temperature” curves (in ppm/1000 °C) and activation energy (in kJ/mol), E_{act} , of Ba tectosilicate melts.

	BA63.18	BA50.25	BA42.29	BA33.33	BA26.37	BA20.40
$\Delta\delta/\Delta T$	-0.3	-1.2	-1.7	-1.8	-2.6	-2.9
E_{act}	152	141	153	139	165	171

Table 56. The slopes, $\Delta\delta/\Delta T$, of the “line’s position vs temperature” curves (in ppm/1000 °C) and activation energy (in kJ/mol), E_{act} , of Ba peralkaline melts.

	BA60.10	BA50.12	BA42.14	BA33.17
$\Delta\delta/\Delta T$	0.1	-3.2	-3.3	-3.6
E_{act}	73	125	129	129

Table 57. The slopes, $\Delta\delta/\Delta T$, of the “line’s position vs temperature” curves (in ppm/1000 °C) and activation energy (in kJ/mol), E_{act} , of Ba peraluminous melts.

	BA50.30	BA50.35	BA50.40	BA33.38	BA33.43
$\Delta\delta/\Delta T$	-1.3	-0.2	0.8	-1.7	-0.8
E_{act}	143	141	136	142	140

3.Zn aluminosilicates (ZAS)

3.1. Tectosilicate join ($R=1$)

²⁷Al NMR spectroscopy

Table 58. Deconvolution parameters obtained for ²⁷Al NMR spectra of Zn tectosilicate glasses. δ_{iso} is isotropic chemical shift (in ppm) and C_Q is quadrupolar coupling constant (in MHz). Population is in %.

	ZA75.12	ZA63.18	ZA50.25	ZA42.29
	δ_{iso}			
AlO₄	63.9	63.9	65.8	68.1
AlO₅	36.7	36.5	38.1	38.5
AlO₆	11.4	7.4	7.2	7.5
	C_Q			
AlO₄	10.3	9.8	8.5	9.6
AlO₅	8.0	8.0	7.9	8.7
AlO₆	5.6	3.3	3.6	4.0
	Population			
AlO₄	86.4	87.6	84.6	84.0
AlO₅	11.9	11.2	13.9	14.7
AlO₆	1.8	1.2	1.6	1.3

Table 59. Barycentre position (in ppm) of ²⁹Si NMR spectra of Zn tectosilicate glasses.

	ZA75.12	ZA63.18	ZA50.25	ZA42.29
Barycentre	-102.6	-98.6	-91.3	-89.2

Neutron diffraction

Table 60. The position of the first sharp diffraction peak (in \AA^{-1}) in $S(q)$ and positions of first two peaks in $g(r)$ (in \AA) of Zn tectosilicate glasses.

	ZA75.12	ZA63.18	ZA50.25
$S(q)$			
FSDP	1.59	1.69	1.78
$g(r)$			
1 st peak	1.62	1.64	1.68
2 nd peak	2.65	2.67	2.72

Raman spectroscopy

Table 61. Bands position (in cm^{-1}) observed in Raman spectra of Zn tectosilicate glasses.

	ZA75.12	ZA63.18	ZA50.25	ZA42.29
Boson	70.7	72.2	79.8	81.3
D ₁	486.0*	-	-	-
D ₂	602.3	596.2*	-	-
T _{2b}	798.6	795.6	785.0*	763.9*
HF band ^a	1049.6	1034.4	1012.6	1002.5

* observed as a shoulder

^a barycentre of a high-frequency envelope

Table 62. Gaussian bands positions (in cm^{-1}) and relative areas (in %) after the deconvolution of the high-frequency envelope of Raman spectra of Zn tectosilicate glasses.

	ZA75.12	ZA63.18	ZA50.25	ZA42.29
Wavenumber				
T _{2s}	917	914	922	923
Q ^{4,II}	1073	1041	1042	1041
Q ^{4,I}	1189	1149	1144	1140
Relative area				
T _{2s}	23.3	21.7	39.5	44.0
Q ^{4,II}	68.6	59.9	47.3	44.6
Q ^{4,I}	8.1	18.4	13.2	11.4

Macroscopic properties

Table 63. Chemical composition (theoretical and analysed), density (in g/cm³) and molar volume V_m (in cm³/mol) of Zn tectosilicate glasses. The values in parentheses are standard deviation.

Glass		SiO ₂	Al ₂ O ₃	ZnO	density	V_m	T_g
	mol% ¹	75.00	12.50	12.50			
ZA75.12	wt% ²	66.29	18.75	14.96	2.494(13)	27.26(13)	1029*
	an wt% ³	67.28(66)	18.55(31)	10.09(60)			
	mol%	63.00	18.50	18.50			
ZA63.18	wt%	52.74	26.28	20.98	2.786(1)	25.76(1)	1014*
	an wt%	53.04(38)	26.65(11)	21.16(13)			
	mol%	50.00	25.00	25.00			
ZA50.25	wt%	39.59	33.59	26.81	3.091(1)	24.55(1)	998.2
	an wt%	38.26(15)	34.24(1.74)	28.84(31)			
	mol%	42.00	29.00	29.00			
ZA42.29	wt%	32.19	37.71	30.10	3.159(2)	24.82(2)	1000*
	an wt%	32.89(21)	38.45(12)	30.39(13)			

¹ theoretical content in mol%

² theoretical content in wt%

³ analysed content in wt%

* T_g value was obtained from DSC measurements

3.2. Peralkaline domain (R = 3)

²⁷Al NMR spectroscopy

Table 64. Deconvolution parameters obtained for ²⁷Al NMR spectra of Zn glasses on the join R = 3. δ_{iso} is isotropic chemical shift (in ppm) and C_Q is quadrupolar coupling constant (in MHz). Population is in %.

	ZA75.06	ZA60.10	ZA50.12	ZA42.14
	δ_{iso}			
AlO ₄	64.5	63.9	65.0	67.3
AlO ₅	36.8	35.4	35.7	37.5
AlO ₆	6.9	6.6	6.7	7.2

	C_Q			
AlO ₄	9.19	8.69	8.67	8.43
AlO ₅	8.84	7.22	7.95	8.50
AlO ₆	4.43	2.94	3.34	4.15
	Population			
AlO ₄	93.8	93.1	93.8	91.5
AlO ₅	5.9	6.1	5.7	7.6
AlO ₆	0.3	0.8	0.5	0.8

Table 65. Barycentre position (in ppm) of ²⁹Si NMR spectra of Zn glasses on the join R = 3.

	ZA75.06	ZA60.10	ZA50.12	ZA42.14
Barycentre	-97.2	-93.7	-89.7	-85.1

Neutron diffraction

Table 66. The position of the first sharp diffraction peak (in Å⁻¹) in $S(q)$ and positions of first two peaks in $g(r)$ (in Å) of Zn glasses on the join R = 3.

	ZA75.06	ZA60.10	ZA50.12	ZA42.14
$S(q)$				
FSDP	1.60	1.70	1.80	1.88
$g(r)$				
1 st peak	1.62	1.64	1.66	1.69
2 nd peak	2.65	2.67	2.69	2.73

Raman spectroscopy

Table 67. Bands position (in cm^{-1}) observed in Raman spectra of Zn glasses on the join $R = 3$.

	ZA75.06	ZA60.10	ZA50.12	ZA42.14	ZA33.17
Boson	68	72	75	77	79
D ₁	487	-	-	-	-
D ₂	602	597*	-	-	-
T _{2b}	791	789	778*	-	-
HF band ^a	1021	1003	999	977	954

* observed as a shoulder

^a barycentre of a high-frequency envelope

Macroscopic properties

Table 68. Chemical composition (theoretical and analysed), density (in g/cm^3) and molar volume V_m (in cm^3/mol) of Zn glasses on the join $R = 3$. The values in parentheses are standard deviation.

Glass		SiO₂	Al₂O₃	ZnO	density	V_m	T_g
	mol%	75.00	6.25	18.75			
ZA75.06	wt%	67.57	9.55	22.88	2.659(2)	25.08(2)	972*
	an wt%	66.28(50)	9.26(9)	19.95(24)			
	mol%	60.00	10.00	30.00			
ZA60.10	wt%	51.02	14.43	34.55	3.051(1)	23.16(1)	964*
	an wt%	49.93(46)	14.20(21)	32.58(35)			
	mol%	50.00	12.50	37.50			
ZA50.12	wt%	40.98	17.39	41.63	3.271(1)	22.41(1)	964*
	an wt%	41.98(36)	18.27(10)	41.11(25)			
	mol%	42.86	14.28	42.86			
ZA42.14	wt%	34.25	19.36	46.39	3.480(1)	21.61(1)	949*
	an wt%	34.81(21)	18.94(25)	43.39(51)			

¹ theoretical content in mol%

² theoretical content in wt%

³ analysed content in wt%

* T_g value was obtained from DSC measurements

Alexey NOVIKOV

Structure et dynamique des aluminosilicates vitreux et fondus

Trois systèmes ternaires (SAS, BAS et ZAS) ont été étudiés dans le cadre de la thèse. Les principaux objectifs étaient l'élaboration et la caractérisation de verres aluminosilicatés de Sr, Ba et Zn peu étudiés auparavant. Une étude systématique a été réalisée sur des aluminosilicates vitreux et dans certains cas sur des aluminosilicates fondus avec différents rapports MO/Al_2O_3 ($M = Sr, Ba, Zn$) et SiO_2/Al_2O_3 . Les compositions étudiées couvrent une partie significative des diagrammes ternaires (des silicates aux verres peralumineux, des compositions pauvres en silice à celles riches en silice). Cela a permis d'accroître nos connaissances sur les domaines de vitrification de ces systèmes.

Afin d'obtenir des informations sur la structure et les propriétés macroscopiques des verres SAS, BAS et ZAS, une approche multi-technique a été mise en place. Une telle approche permet d'avoir une vue d'ensemble sur les systèmes étudiés et de trouver des origines nano- à microscopiques aux propriétés macroscopiques. La spectroscopie de résonance magnétique nucléaire, la diffractométrie de neutrons et la spectroscopie Raman ont été utilisées au cours de la thèse afin de sonder l'échelle à courte et à moyenne distance. Les propriétés macroscopiques mesurées ont été : la densité, la viscosité et la température de transition vitreuse.

Les données issues de cette thèse permettent une meilleure compréhension des changements de structures et des propriétés macroscopiques des verres aluminosilicatés produits par les variations de MO/Al_2O_3 ou SiO_2/Al_2O_3 , ou par la nature des cations non-formateurs de réseau.

Mots clés : aluminosilicates vitreux et fondus, Sr, Ba, Zn, structure, propriétés macroscopiques, dynamique, RMN, diffraction de neutrons, Raman, viscosité, densité

Structure and Dynamics of Aluminosilicate Glasses and Melts

Three ternary systems (SAS, BAS and ZAS) have been investigated within the framework of the PhD thesis. The main goals were the elaboration and characterization of previously poorly studied Sr, Ba and Zn aluminosilicate glasses. A systematic study has been carried out on glasses and in some cases on melts with various MO/Al_2O_3 ($M = Sr, Ba, Zn$) and SiO_2/Al_2O_3 ratios. The compositions studied cover a significant part of the ternary diagrams (from silicates to peraluminous glasses, from silica-poor to silica-rich compositions). This allowed expanding our knowledge of the vitrification domains in these systems.

In order to obtain information on the structure and macroscopic properties of SAS, BAS and ZAS glasses, a multi-technique approach has been implemented. Such approach allows having a broad view on the systems and finding nano- to microscopic origins of macroscopic properties. The techniques used during the thesis probe short- (NMR, ND) to medium-range (Raman) scale and among the properties studied were density, viscosity and glass transition temperature.

The data resulting from this thesis provides a better understanding of the changes in the structure and macroscopic properties of the aluminosilicate glasses produced by variations in MO/Al_2O_3 or SiO_2/Al_2O_3 , or by the nature of non-network forming cation.

Keywords : aluminosilicates, glasses, melts, Sr, Ba, Zn, structure, macroscopic properties, dynamics, NMR, neutron diffraction, Raman, viscosity, density



CEMHTI-CNRS UPR3079
Conditions Extrêmes et Matériaux :
Hautes Températures et Irradiation
1D, avenue de la Recherche Scientifique
45071 Orléans Cedex 2

